Analytical Techniques for Evaluating Seal Capacity for Carbon Dioxide Storage in Selected Australian Basins

Michael Edward Gray

BSc (Honours) Petroleum Geology and Geophysics
Australian School of Petroleum, The University of Adelaide

This thesis is submitted to the University of Adelaide in fulfillment of the requirement for the degree of Doctor of Philosophy

Thesis Supervisors: Prof. John Kaldi and Dr. Richard Daniel.

Australian School of Petroleum,

The University of Adelaide

March 2017

ACKNOWLEDGEMENTS

The author would like to begin by acknowledging his fortunate position of studying at the University of Adelaide and in particular the Australian School of Petroleum. Undoubtedly the Australian School of Petroleum is what it is because of the people. In particular, the author would like to thank Maureen Sutton, Andrew Mitchell, Kathryn Amos and Ian West for their help and support.

The author would like to express his gratitude to the CO2CRC, for both their financial support and access to data – specific acknowledgments to Dr. Mathias Raab, Tess Dance and David Hilditch. Further, the author would like to thank the generous donors of scholarships; Adelaide University, Santos, Formation Evaluation Society of Australia, American Association of Petroleum Geologists (AAPG), Petroleum Exploration Society of Australia (PESA) and the International Energy Agency for Greenhouse Gas (IEAGHG).

In addition to friends and colleagues for their help and support; Dr. Mark Bunch, Dr. Ulrike Schmidt, Angie Qu, Nachiketa Mishra (Sunny), Alex Robson, Kunakorn Pokalai, Dr. Tony Hall, Dr. Stefan Loer, Robyn Williamson, Dr. Benjamin Wade, Aoife McFadden, Mark Raven and Lionel Esteban. The author would like to formally acknowledge the encouragement and support received from colleague and friend David Kulikowski.

The author would most importantly like to acknowledge the unwavering support from his primary supervisor (Prof. John Kaldi) and secondary supervisor (Dr. Richard Daniel) throughout the PhD journey. John and his ability to seek out and secure opportunities for collaborations and constant support in helping the author highlight the importance of the research and Richard for his patience, constant technical guidance and for keeping the author on track.

Finally the help and support from his friends and family, in particular, his father (David Gray).

Michael Gray

March 2017

THESIS DECLARATION

I certify that this work contains no material which has been accepted for the award of any other degree or diploma in any university or other tertiary institution to Michael Edward Gray and, to the best of my knowledge and belief, contains no material previously published or written by another person, except where due reference has been made in the text. In addition, I certify that no part of this work will, in the future, be used in a submission in my name for any other degree or diploma in any university or other tertiary institution without the prior approval of the University of Adelaide and where applicable, any partner institution responsible for the joint award of this degree.

I give consent to this copy of my thesis, when deposited in the University Library, being made available for loan and photocopying, subject to the provisions of the Copyright Act 1968.

I also give permission for the digital version of my thesis to be made available on the web, via the University's digital research repository, the Library Search and also through web search engines, unless permission has been granted by the University to restrict access for a period of time.

I acknowledge the support I have received for my research through the provision of an Australian Government Research Training Program Scholarship.

Michael Edward Gray 1/03/2017

ABSTRACT

The geological storage of carbon dioxide (CO_2) is a mitigation strategy for the continued use of fossil fuels without the release of CO_2 to the atmosphere. The successful geological storage of CO_2 requires, among other properties, adequate caprocks; to provide a seal for the safe storage of CO_2 on a geological time scale.

This study identifies and evaluates various technologies to determine the suitability of caprocks from selected Australian Basins to contain stored CO_2.

The primary technique for assessing the amount of CO_2 that can be contained in a geological formation by the overlying caprock is mercury injection capillary pressure (MICP) analysis. MICP is used to test sealing lithologies to determine the maximum column height of carbon dioxide that can be retained. The study has been broken down into four aspects critical to evaluating and improving MICP analyses. These are (i) Evaluation of the accuracy, repeatability and comparability of MICP analytical techniques; (ii) Reviewing the influence of different sample types on MICP analysis; (iii) Investigating the effects of warehousing (long-term core storage) on MICP data and (iv) Developing a technique to produce synthetic MICP curves from nuclear magnetic resonance (NMR) data over caprock (sealing) intervals.

The results of the study demonstrate that MICP analysis is accurate and by using a method derived from this study, a viable correction for conformance is possible. The MICP derived porosity and permeabilities (poroperms) were compared to poroperms from both helium pycnometry and NMR analyses. The porosity results indicate that there is a trend between measurements from different techniques within the same well, but this trend does not extend to other wells tested.

The sample type and subsequent effects on MICP analysis were evaluated by analysing conventional core (CC) samples using (i) "Routine" preparation techniques, (ii) Samples where mercury was allowed to enter by vertical intrusion only, and (iii) Synthetic cuttings prepared from crushed CC. Also, drill cuttings from equivalent depths as the conventional core were analysed. The MICP analyses of all CC samples show no significant differences from one another other than a consistent and predictable change in porosity across sample types. The analyses of the drill cutting samples, however, indicate significant variation in the MICP analyses to the conventional core samples.

The investigations into warehousing of CC samples demonstrate that the MICP analyses performed on the warehoused samples differ from results of the original samples by varying

degrees, suggesting that the storage of samples does lead to alteration of the pore networks. The degree of variation appears to be formation specific; significant changes are observed in MICP analyses of the Muderong Shale while only minor differences are observed in MICP analyses of Belfast Mudstone.

Synthetic MICP curves were generated from NMR analyses using both laboratory and well data. The synthetic MICP curves from the laboratory NMR data are similar to the CC MICP curves. The extension of this technique to wellbore NMR data produces synthetic MICP curves too variable to that of CC MICP curves to be considered reliable.

CONTENTS

LIST OF FIGURES

LIST OF TABLES

Caprock/ Seal – These words are used interchangeably and refer to low permeable rock that is capable of retaining CO_2 or other non-wetting fluid in the subsurface.

Warehoused – Rock material that has been removed from in-situ conditions and stored in a warehouse, core library or similar for greater than 12 months without preservation (i.e. immersed in oil).

Conventional Core (CC) – Core taken with a core barrel also known as full core. The conventional core barrel is run on a drill string. The drill bit has a hole through which the core is collected. The core barrel is brought to the surface to retrieve the conventional core held within.

Drill Cuttings (DC) - Rock chips as a result of drilling. The drill cuttings are circulated in the drilling fluid to the surface where they are separated from the mud, often washed and dried and stored in airtight bags.

Synthetic Drill Cuttings (SC)–Synthetic cuttings have been generated by taking a conventional core sample and crushing the rock to represent drill cuttings.

Reservoir Rock – A rock sample with a threshold pressure <100 psia as interpreted from the MICP curve.

Airtight bags – Zip lock sandwich bags.

Low Sealing Capacity Rock – A rock sample with a threshold pressure between 100-999 psia as interpreted from the MICP curve.

High Sealing Capacity Rock – A rock sample with a threshold pressure >1000 psia as interpreted from the MICP curve.

Mercury Injection Capillary Pressure (MICP) Analysis Key Definitions:

Pressure Equilibrium Points – The mercury porosimeter is programmed to user defined pressure increments to establish equilibrium, for a defined period, after which it records pressure and mercury intrusion which results in pressure equilibrium points on the mercury injection curve (Figure 1-1).

Maximum Inflection Point – The maximum turning point of the MICP curve where the curve changes from low mercury saturation toward high mercury saturation (Figure 1-1).

Linear Upward Trend – This is defined at the portion of the mercury intrusion curve beginning directly after the maximum inflection point and continuing to the plateau (Figure 1-1).

Plateau – The point at which the MICP curve stops its linear upward trend and the rate at which the mercury saturation is increasing diminishes indicating that there is no more pore space accessible by the mercury (Figure 1-1).

Conformance – The intrusion of mercury into fractures and rugosities but not into the pore network of the sample.

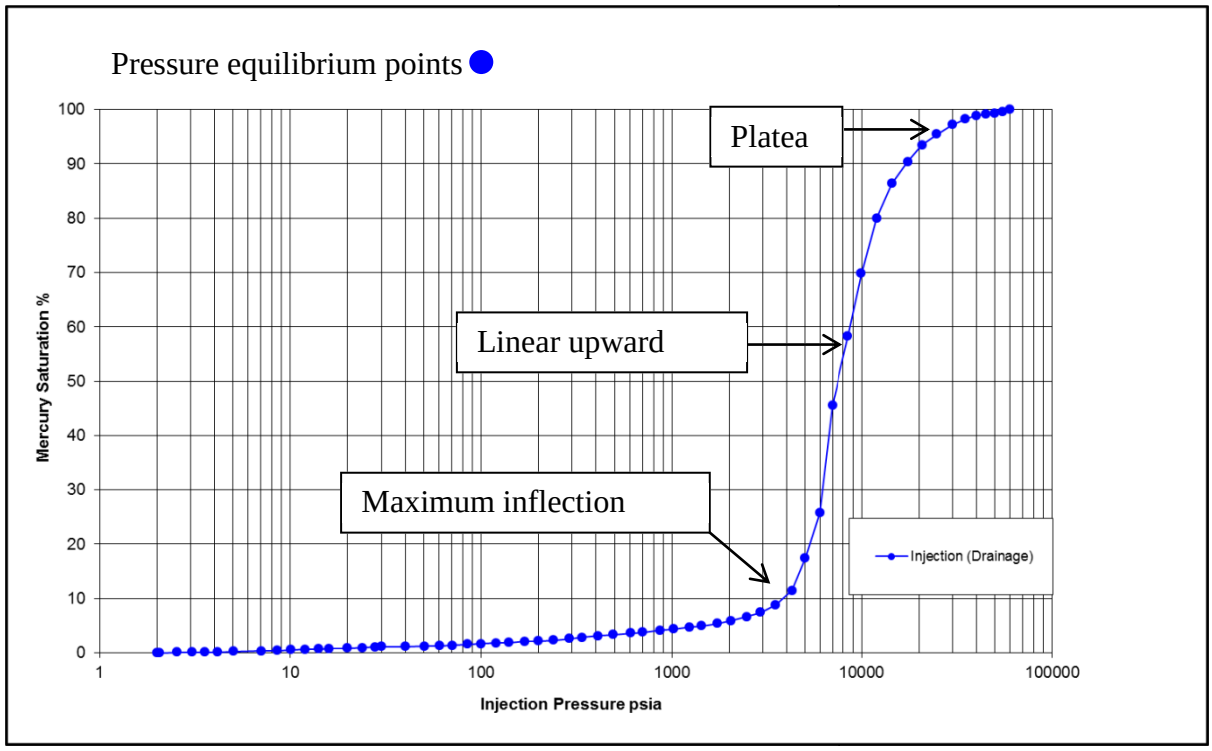

Figure 1-1: MICP curve with key descriptors shown; pressure equilibrium points, maximum inflection point, linear upward trend, and plateau.

Synthetic Mercury Injection Capillary Pressure Analysis Key Definitions:

Wellbore Synthetic (WS) MICP curve – A synthetic MICP curve produced from the wellbore nuclear magnetic resonance log.

Laboratory Synthetic (LS) MICP curve - A synthetic MICP curve produced from laboratory nuclear magnetic resonance analysis on a conventional core plug.

Nuclear Magnetic Resonance T_2 Distribution–The T_2 distribution data reflects the NMR relaxation data that has undergone a Laplace inversion or equivalent. The T_2 distribution reflects the total porosity and the size of the pores present in the sample being analysed.

CHAPTER 1: INTRODUCTION

1.1 AIMS AND OBJECTIVES

- To determine the accuracy and repeatability of Mercury Injection Capillary Pressure (MICP) analyses.
- To determine the comparability of MICP analyses to other techniques and identify any relationships that may allow inferences to be made where other analyses exist i.e. helium porosity and permeability results.
- To develop a reliable method of conformance correction for MICP analyses.
- To determine the effect of sample type on MICP analyses of caprock.
- To determine if repeatable MICP analysis and seal capacity determination are achievable from warehoused caprock. If there are changes and if those changes are predictable, can an adjustment or safety margin be estimated?
- To determine how representative/ appropriate the use of synthetic MICP curves from NMR analyses are for the determination of seal capacity measurements for caprock intervals. More specifically can the calibrated NMR data be used to produce indicative synthetic MICP curves over caprock intervals?
- To propose new methodologies from the research including extending the production of synthetic MICP curves to the hydrocarbon industry.
- To highlight areas of concern and future research.

1.2 SUMMARY OF THESIS CHAPTERS

This thesis has been set out into chapters beginning with an introduction (Chapter 1) which covers the rationale of the research, followed by a brief summary of anthropogenic climate change, geological storage of CO_2 and concludes with a description of seal potential including seal capacity. The second chapter provides the methodology and background to the various analyses conducted in the research; mercury injection capillary pressure (MICP) and the calculation of maximum CO_2 column heights therefrom, nuclear magnetic resonance (NMR), helium pycnometry, X-ray diffraction (XRD) analysis and scanning electron microscope (SEM) imaging. Chapter 2 is supported by Appendix A which provides detailed methodologies for the analyses undertaken; the equipment used, methods and preparation of samples for analyses in Chapters 4, 5, 6 and 7. The third chapter covers the regional geology of the basins from which well data is used in this study. The existence of specific well data was the only consideration in picking suitable wells. Each basin is summarised with a brief geological background including location, evolution, lithostratigraphy and caprocks (seals)

present. The background to the wells is provided within each basin description. The fourth chapter focuses on establishing the accuracy, repeatability and comparability of MICP analyses and provides the foundations for chapter 5, 6 and 7. Chapter 5 focuses on different sample types and preparation techniques and the resulting MICP analyses. A proposed methodology is also detailed in Appendix C as a result of the research. Chapter 6 concentrates on the effects of warehousing on MICP analyses and includes both XRD analyses and SEM imaging to describe the mineralogy and fabric of the samples being analysed. Chapter 7 concentrates on generating synthetic MICP curves from NMR data. To evaluate the technique, the synthetic MICP curves are compared to the MICP curves from the corresponding rock material. Two proposed methodologies are provided in Appendix E including a methodology to extend the technique to the hydrocarbon industry. While this is not the primary focus of the research, the applicability of the techniques will overlap, and the use of the techniques in either industry will aid seal capacity evaluation in general. Chapter 8 provides the conclusions, recommendations and future works respectively.

Complimentary to the thesis is an Appendix providing a detailed methodology for the analyses undertaken; (Appendix A). Appendices B, C, D and E provide graphical evidence of the results described within the text.

Chapters 4, 5, 6 and 7 begin with a summary of any results followed by an introduction/ rationale detailing the reasons for the research. This is followed by a literature review specific to the chapter, a brief description of the data or well, methodology modifications, results and discussion. Each chapter concludes with a discussion of the data sets/ wells in the context of the literature and the significance of these.

1.3 RATIONALE

The purpose/ rationale of each component of this research is summarised as follows:

1.3.1 Accuracy, Repeatability and Comparability of MICP Analyses

This study is carried out to establish the foundations of MICP analyses for the subsequent work and to establish the extent to which the MICP analyses can be applied. The accuracy of the MICP analyses is investigated including; the requirement for a blank correction (analyses with no sample) of the mercury porosimeter, analysing Micromeritics ®Silica Alumina standards and assessing a method derived in this study to correct for conformance. Further, to determine if there are any compressional effects, fragile samples are analysed in the porosimeter with pressures up to 60,000 psia.

The repeatability of MICP analyses on samples taken next to each other at the same depth (adjacent samples) and over a 1.6m interval of conventional core are compared to gauge the heterogeneity that could be expected from fairly uniform core. These analyses provided a range of the heterogeneity that can be expected between adjacent samples from fairly uniform core.

The comparability of MICP porosity and permeability results are compared to other techniques; helium pycnometry and NMR analyses. This provides the opportunity to determine if there is a calibration or relationship between the results from the different techniques.

1.3.2 **The Effect of Sample Type on MICP Analyses of Caprock Rationale**

Drill cuttings (DC) and conventional core (CC) can all be obtained from wells during drilling. The DC samples are rock fragments that have been broken from the parent rock during the drilling process, travelled through the mud column, over the shale shakers, collected at depth intervals, washed and dried. This process introduces numerous variables which may affect the MICP analyses but the sample type is relatively inexpensive to obtain. On the other hand, CC samples can be taken during the drilling of the well with a special bit which allows rock material to remain in a cylindrical core inside the drill bit and drill pipe. This CC is subsequently retrieved, but the process is expensive. It has been observed that the MICP analysis from DC samples varies significantly from the CC samples. Subsequently, in an attempt to bridge the gap between the two sample types synthetic cuttings (SC) samples were produced by breaking a sample of CC to represent a DC sample without the effects of heterogeneity as would be observed over a depth interval from which the DC samples were taken. The sample types and their subsequent MICP analyses are reviewed.

The CC samples can be prepared for MICP analysis in a number of fashions; as a cube with mercury intrusion from all sides, with araldite on five sides for vertical intrusion only and as a synthetic cutting. The effects of these preparation techniques are unknown and are also investigated.

1.3.3 **The Effects of Warehousing Rationale**

Suitable locations for the geological storage and containment of CO_2 often exist in basins that are producing hydrocarbons. In many instances, these basins have a wealth of information including existing wells, detailed knowledge of reservoir and seal couplets, seismic data and infrastructure making them attractive sites for geological storage of CO_2.

Samples of sealing intervals can often be obtained from existing petroleum wells within the basin that have DC or CC samples available. However, the representativeness of the seal capacity results from samples that have been removed from in-situ pressures, stored and dried out for long periods of time is greatly unknown. Additionally, the DC samples have also been exposed to drilling muds, shakers and often washed making their warehoused seal capacity results even less certain. These uncertainties are investigated.

1.3.4 **Synthetic MICP Curves Rationale**

Seal capacity in the petroleum industry can be derived from MICP analysis. This type of analysis requires some form of rock material, preferably CC which is expensive to obtain especially over numerous intervals. The process of determining seal capacity for numerous sealing intervals is thus difficult and expensive. To overcome this difficulty, it is hoped that MICP analysis on a few CC or side wall core (SWC) samples can be used to calibrate synthetic MICP curves from NMR which can easily be produced over numerous sealing intervals to predict the ~~–~~effective seal capacity" accurately. It is envisaged that this technique will be better able to represent the heterogeneous intervals once a suitable calibration interval has been found. The technique relies on converting the NMR T_2 distribution into a synthetic MICP curve which entails a number of data manipulations. Firstly, from the T_2 distribution, a number of properties can be obtained; (1) everything under the T_2 distribution curve is considered the total porosity of the sample which reflects a pore volume and (2) The T_2 relaxation time reflects pore size. Short relaxation times reflect small pores and long relaxation times reflect large pores. The pore size along with a conversion from pore size to pore throat size can be used to predict a pressure through the modified Washburn Equation (See Chapter 2, section 2.4). The amplitude provides the relative number of pores of a specific size and thus a volume at each T_2 relaxation time. This volume loosely corresponds to the volume of mercury at specific pore sizes which is converted to a percentage of the cumulative amplitude to produce equivalent percentage mercury saturation for each pressure.

1.3.5 **Background**

Anthropogenic climate change is accepted in the scientific community with much of the debate occurring in the political and media communities. The greenhouse gasses released during the burning of fossil fuels for energy are warming the earth leading to an array of climate changes which may have significant impacts for the future (IPCC, 2014). Coupled with this are the worlds increasing need for energy predicted to grow by ~34 % by 2035 and a heavy reliance on fossil fuels for this energy (BP Energy Outlook to 2035, (2016)). While

renewables may be the solution to this problem in the long-term (> 100 years) the expected increases in the use of renewables in the short term (< 20 years) is unlikely to abate the future energy requirements (Bree, 2011). It is thus suggested that storage of carbon dioxide be used in the interim to curb the greenhouse gas emissions and limit anthropogenic climate change. One such storage mechanism showing great promise which has been demonstrated to be feasible is the geological storage of carbon dioxide (Cook, 2014).

1.3.6 **Basic Principles of CO_2 Geological Storage**

The storing of CO_2 in the subsurface requires many of the same components as the petroleum system including a caprock or seal, a reservoir rock and a structural or stratigraphic trap. In the case of CO_2 subsurface storage, CO_2 can be stored in a depleted hydrocarbon field or saline aquifer. This study concentrates on the later. It is suggested that CO_2 should be stored in a supercritical phase as it will be denser than in a gaseous phase but still more buoyant than formation brine. To maintain the supercritical state, the temperature must be > 31.1 ° C and the pressure must be > 7.38 MPa which will require a minimum depth of injection and storage (Nordbotten et al., 2005). The reservoir will also require a sufficient permeability to allow the 1-5 Mt/yr. of CO_2 to be injected while being below the fracture gradient of the reservoir rock. Further complications will include mineral reactivity of the seal and reservoir with CO_2 as it potentially mixes with brine formation fluid. However, this is outside the scope of this research (Gibson-Poole et al., 2006).

One of the major concerns in the geological storage of carbon dioxide is the competence of the sealing lithologies to retain CO_2 for long periods of time. Thus the understanding of leakage risks and leakage rates is vital to the successful geological storage of CO_2 (Wollenweber et al., 2009). This study focuses on analysing the sealing lithologies for CO_2 containment using numerous techniques and data sources including mercury injection capillary pressure analyses (MICP), nuclear magnetic resonance (NMR), scanning electron microscopy (SEM) and X-ray diffraction (XRD) analyses.

1.3.7 **Sealing Lithologies**

In water-wet rocks, non-wetting fluids including oil, gas and CO_2 will migrate upwards due to buoyancy (Schowalter, 1979). Within a rock medium, this means migrating through the pore network. Capillary forces, determined by the diameter of the pore throats, the interfacial tension between the non-wetting fluid (oil, gas or CO_2) and wetting fluid (formation brine) and wettability (contact angle) all oppose the buoyancy force. A seal or caprock is considered to be a confining impermeable barrier overlying a porous reservoir rock (Kaldi et al., 2011). The seal in this system is required to retain the buoyant non-

wetting phase. Kaldi et al., (2011) suggest that sealing lithologies are commonly shales and evaporites, but theoretically, any lithology can act as a seal providing the threshold pressure is greater than the buoyancy force of the non-wetting fluid. The threshold pressure is dependent on the size and connectedness of the pore throats and the density of the non-wetting and wetting fluids. The threshold pressure (Pth) is considered to be the pressure at which the non-wetting fluid flows through the rock (Kaldi and Atkinson, 1997).

1.3.8 **Seal Potential**

The ability of a seal or caprock to retain non-wetting fluid is investigated using the seal potential definition described by Kaldi and Atkinson, (1997). Seal potential is a combination of three elements; seal geometry, seal integrity and seal capacity (Kaldi and Atkinson, 1997).

1.3.8.1 Seal Geometry

Seal geometry; the thickness, structural position and the areal extent of the seal. Thickness refers to the thickness of the sealing formation and thus the likelihood for faults to breach the seal (Kaldi and Atkinson, 1997).

1.3.8.2 Seal Integrity

Seal integrity refers to the sealing lithologies mechanical properties; ductility or brittleness, i.e. the likelihood of fractures allowing a breach of the seal (Kaldi and Atkinson, 1997).

1.3.8.3 Seal Capacity

Seal capacity is defined as the maximum column of non-wetting fluid a water wet seal can retain assuming that it is homogeneous (Kaldi and Atkinson, 1997). Seal capacity should be analysed in conjunction with reservoir/ aquifer capillary properties. The difference between the threshold pressure of the seal and reservoir is the critical value allowing a column height of non-wetting fluid to be retained. Thus a seal may have a high threshold pressure with a low threshold pressure reservoir in one location allowing an economic height of non-wetting fluid to be retained, however, that same seal in another location with the same threshold pressure may not be able to retain economic heights of non-wetting fluid due to a high threshold pressure reservoir (Root, 2005). The following research has concentrated on MICP analyses rather than the CO_2 column heights predicted therefrom and has thus only analysed the caprock sample and not the couplet reservoir sample. The calculated CO_2 column heights in the research have assumed a reservoir threshold pressure of 10 psia. This was due to the logistics, economics and scope of the study. This needs to be taken into account when interpreting the predicted CO_2 column heights.

CHAPTER 2: METHODOLOGY

2.1 INTRODUCTION

This chapter outlines the methodologies and equipment used in this study. The chapter focuses on mercury injection capillary pressure (MICP) and nuclear magnetic resonance (NMR) analyses. In addition, X-Ray diffraction (XRD) analyses, scanning electron microscope (SEM) imaging and helium pycnometry techniques are used in this study to support the results and interpretation. The main methodologies discussed are porosity and permeability measurements from various analytical techniques, the production of synthetic mercury injection capillary pressure curves from NMR data and interpreting threshold pressures from the MICP curves (real and synthetic). Further, the determination of contact angle and interfacial tensions for the brine/ CO_2/ rock system and how to use these values to determine the maximum column of CO_2 that can be retained by the sealing rock are discussed.

Further details of the methodologies are presented in Appendix A.

2.2 MERCURY INJECTION CAPILLARY PRESSURE (MICP) ANALYSIS

Capillary pressure curves can be produced by several techniques including centrifuge and porous plate. These techniques are limited in the pressures that can be applied, so while they are often adequate for reservoir samples, they are not so for fine-grained caprock samples. Thus the use of a mercury porosimeter is employed which can reach pressures of 60,000 psia (~413 MPa). Analyses can be performed on conventional core (CC), side wall core (SWC) and drill cuttings (DC) (Purcell, 1949, Al-Ghamdi, 2006, Schowalter, 1979 and Daniel pers comm., 2013).

The samples are firstly dried using one of the following techniques depending on the author; air drying, vacuum drying, pump drying and oven drying (Dewhurst et al., (2002). The sample is placed in a penetrometer, sealed with a cap and sealant and, placed in the porosimeter. A two-stage process is applied. The first stage involves applying a vacuum to the sample. Once a constant vacuum has been reached mercury is then allowed to flow into the penetrometer. The vacuum draws the mercury into the sample. The second stage involves removing the penetrometer and contained sample from the vacuum and applying pressure, which is applied in pressure increments. At each pressure increment, the pressure is allowed to stabilise for twenty seconds and a measurement of pressure and volume of mercury injected is recorded. This procedure is continued until 60,000 psia is reached

producing the *injection* or *drainage* curve. This is referred to as the MICP curve in the results of this study. Once the maximum pressure is reached the pressure is reduced in the same stepwise manner and the *withdrawal* or *imbibition* curve is recorded. The imbibition curves records the amount of mercury that is released as the pressure is decreased. These data are recorded along with porosity, bulk density and grain density of the sample and are displayed in an Excel worksheet and pdf (Al-Ghamdi, 2006 and Purcell, 1949). Often a conformance correction needs to be applied to the MICP analyses to remove any effects of sample surface rugosities and fractures allowing an accurate MICP curve and porosity to be obtained. Please see Appendix A, A.1 - A.4 for details of the mercury porosimeters, the preparation of the samples and details of the conformance correction used in this study.

2.3 MICP ANALYSIS TO PREDICT PERMEABILITY

MICP analyses have been used to predict permeability by numerous authors including Purcell, (1949), Katz and Thompson, (1986), Marschall et al., (1995), Comisky et al., (2007) and Lu et al., (2011). The early works tended to concentrate on conventional reservoirs, but the later works have begun to apply these methods to unconventional reservoirs (Rezaee et al., 2012 and Clarkson et al., 2012). The Winland's equation using r_{35} mercury saturation has been demonstrated to work sufficiently for sandstones and carbonates (Pittman, 1992) and will be applied to caprocks in this research. Please see Appendix A, A.5 for detailed information on how permeability was calculated.

2.4 CO_2 SEAL CAPACITY DETERMINATION BY MERCURY INJECTION CAPILLARY PRESSURE ANALYSIS

The seal capacity of a caprock is determined by the largest connected pore throat network, the interfacial tension (γ) between the brine and CO_2, and the contact angle (θ) between the CO_2 and mineral substrate (Chiquet and Broseta, 2005).

Seal capacity was determined using MICP analysis conducted on a Mercury Porosimeter. The relationship between pressure (Pc) and the radius (r) of a capillary pore is given by the modified Washburn Equation (Equation 1), (Washburn, 1921, Purcell, 1949, Schowalter, 1979 and Kaldi et al., 2011). This requires the interfacial tension (σ) and contact angle (θ) for the air/ mercury/ rock system which has been defined.

$$Pc = \frac{2\sigma cos\theta}{r} \quad \text{Eq.1}$$

The capillary pressures from the air/ mercury/ rock (*a/m*) system can be converted to the brine/ CO_2 / rock (*b/ CO_2*) system provided the interfacial tensions (σ) and contact angles (θ) are known for both systems (Equation 2, Kaldi et al., 2011). The interfacial tensions in a brine/ CO_2/ rock system increase with increasing temperature and salinity and decrease with increasing pressure as shown by experimental data (Bennion and Bachu, 2008), (Chalbaud et al, 2009), (Chiquet et al., 2007), (Aggelopoulos et al., 2010) among others.

$$Pc\ b/CO2 = Pc\ a/m * \frac{\sigma b/CO2 \cos\theta b/CO2}{\sigma a/m \cos\theta a/m} \quad \text{Eq.2}$$

These equations were originally used in the hydrocarbon industry to convert the air/ mercury system to the brine/ hydrocarbon system. The interfacial tension and contact angle can also be predicted for the properties of hydrocarbon.

2.4.1 **Brine/ CO_2/ Rock Contact Angle**

Studies on contact angle (wettability) measurements between the brine/ CO_2/ rock system under varying pressure, temperature and salinity conditions are contentious and further exacerbated by the various methods and equipment employed to study these changes. Studies by Farokhpoor et al., (2013) indicate that there is no significant change in contact angle for feldspar, calcite and quartz minerals with increasing pressure in a brine/ CO_2/ rock system. However, their results for muscovite mica did show a significant increase in contact angle from 16 ° to 36 ° with increasing pressure from 1 MPa to 30 MPa. Quartz showed an increase in contact angle with increasing temperature and salinity. Salinity also increased the contact angle for feldspar. In a study by Espinoza and Santamarina, (2010) contact angles for silica and calcite remained quite constant in response to increasing pressure. They also demonstrated that NaCl dissolved in water to represent brine increased the contact angle for both substrates. Studies by Chiquet et al., (2005) however, evidence significant changes in contact angle for mica and quartz as pressures increased to 10 MPa. Their results indicate that contact angles for mica at a low-pressure range between 0-20 ° and upon increasing the pressure to 10 MPa the contact angle ranged between 60-80 °. Under the same conditions, quartz has a contact angle of between 20 - 30° and upon increasing pressure to 10MPa, the contact angle increases to 40-55 °. They also note changes in contact angle with increasing salinity in a non-linear manner. Kim et al., (2012) evidenced significant changes in contact angle with increasing NaCl concentrations where they experimented with engineered micro

models at 8.5 MPa and temperatures of 45° C and demonstrated that the average contact angle at 0.01 M was 53.7 ° which increased to 75.1 ° at 5.0 M.

The disaccord in contact angle studies for the brine/ CO_2/ rock substrate system has led to significant uncertainties when trying to predict the contact angle or wettability in the system. J Kaldi, (pers. comm. 20 September 2013) has suggested that a contact angle range between 0 ° and 60 ° be presented to account for most of the variation observed in the research. Please see Appendix A, A.6 for detailed information on how the contact angle and interfacial tension were predicted for the research.

2.4.2 Conversion of the Air Mercury Rock System to the Brine/ CO_2/ Rock System

Seal capacity has been determined using various methods and terminologies; entry pressure (Pe), displacement pressure (Pd) and threshold pressure (Pth). In a further complication, the terminology has been defined differently by various authors (Schowalter, 1979, Daniel and Kaldi, 2009 and Kivior, 2000) as shown in Hildenbrand et al., (2002). This has also led to an overlap of meanings (Dewhurst et al., 2002). For this study, Pe is defined as the point at which mercury is identified to intrude the sample on the MICP curve (surface rugosities). It represents conformance of the sample and delineates where the mercury is intruding into the fractures and rugosities of the sample. Pd is defined as the pressure at which mercury begins to intrude the larger pore throats on the outer margin of the rock sample. The difference between Pe and Pd is considered to be conformance. Please see A. Appendix A.4 for details on conformance and a method outlined by this study for conformance correction. Pth is considered to be the point at which the mercury begins to flow through the rock sample (Dewhurst et al., 2002). The point just before Pth is used to determine the seal capacity of rock samples although it is commonly just referred to as Pth. The Pth is considered to be the most representative point of seal failure and is thus used to determine seal capacity.

Seal capacity was determined by picking the threshold pressure (Pth) from the MICP curve. The threshold pressure was then used to determine the maximum column of CO_2 that could be retained.

Once the threshold pressure has been converted from the air/ mercury/rock system to the brine/ CO_2/ rock system it can be used to predict the maximum column height of CO_2 that the seal can retain (Equation 3, Kaldi et al., 2011). This equation requires the seal and reservoir threshold pressures (PthS and PthR respectively). MICP analysis can acquire the PthR on the reservoir rock or be predicted. The density of the brine (ρb) and CO_2 (ρCO_2) are also required.

$$Hmax = \frac{PthS - PthR}{(\rho b - \rho CO2) * 0.132} \qquad \text{Eq.3}$$

This equation was originally used in the hydrocarbon industry to predict the maximum oil and/ or gas column heights within a prospect. The densities of the hydrocarbon can be measured by laboratory analysis of a hydrocarbon sample from the prospect.

2.4.3 **Methods for Determining Threshold Pressures**

Daniel and Kaldi in Cook, (2014) review the different methods of determining threshold pressures from MICP analysis on sealing lithologies. The methods reviewed include that suggested by Schowalter (1979), Sneider (1997) and Sneider et al., (1997), Boult (1996) and Boult et al., (1997), Kivior (2000) and Boult, (1996) and Dewhurst et al., (2002). Daniel and Kaldi in Cook, (2014) demonstrate that the methods suggested by Sneider, (1997) and Boult, (1996) are both affected by conformance. The method proposed by Sneider et al., (1997) is to draw a horizontal line at 7.5 % mercury saturation from the y-axis and at the intersection with the MICP curve the pressure is read from the x-axis giving the threshold pressure. The method suggested by Boult, (1996) is to draw a tangential straight line along the upper slope of the upper inflection (linear upward trend) and the intersection of this line with the x-axis gives the threshold pressure. Their results indicate that the conformance effect was most pronounced in the cutting samples.

Daniel and Kaldi in Cook, (2014) conclude that the methods suggested by Kivior, (2000) and Boult, (1996)/ Dewhurst et al., (2002) provide consistent results without the need for a conformance correction. The method suggested by Kivior, (2000) consistently picks a higher threshold pressure than the method proposed by Boult, (1996)/ Dewhurst et al., (2002) and it was therefore suggested that the safer repeatable method by Boult, (1996)/ Dewhurst be utilised. A key point noted by Daniel and Kaldi in Cook, (2014) is the significant variation in the interpreted threshold pressures by the methods mentioned above.

Interpreting the maximum point of inflection of the MICP curve is another common method of determining the threshold pressure (Pittman, 1992 and Chehrazi et al., 2011). Daniel and Kaldi in Cook, (2014) didn't review this. Thompson et al., (1987) proposed this method after their experimental work on three sandstones and a sintered glass bead pack. Thompson et al., (1987) setup a stepper motor, screw driven mercury injection apparatus with stainless steel electrodes attached to the top and bottom of the samples. The electrodes measured the

resistance across the samples as they injected mercury. On the primary injection into a fresh sample, their results indicated that electrical continuity is achieved after the discontinuous step or maximum inflection point. It must be noted that their results show a maximum attained pressure of 200 kPa or 29 psia. When this method is applied to the MICP curves (both conventional core and drill cuttings) of Daniel and Kaldi in Cook, (2014) consistent threshold pressures can be obtained for both the corrected and uncorrected MICP curves.

Watson, (2012) applied a variant of the maximum inflection point method mentioned above. To determine the point of maximum inflection of the MICP curve Watson, (2012) draws a straight line at 45 ° from the horizontal and moves the line from the y-axis towards the maximum point of inflection of the MICP curve. The point at which the 45 ° line first comes in contact with the maximum inflection of the MICP curve is taken as the threshold pressure read from the x-axis.

Please see A, Appendix A.7 for details of how the threshold pressures are picked in this study.

2.5 MICP SHORTFALLS

The shortfalls of MICP analyses have been broken down into those that are confirmed and those that are suspected; MICP analyses are destructive and repeat analyses after the sample is filled with mercury does not lead to the same results (Thompson et al., 1987). The use of the Washburn equation to predict pore throat radius is based on the pore being cylindrical, which is often not the case (Kaldi e al., 2011). The displacement pressure or threshold pressure is only to be viewed as an approximation to the capillary sealing ability of a caprock (Schlömer and Kross, 1997). It is suspected that MICP analyses above 70 MPa are not meaningful due to pore sample alteration such as particle breakdown, the opening of closed pores and pore throat alterations (Cao et al., 2016). Further, the preparation methods may affect the results; drying may alter clay fabric and the omnidirectional intrusion of mercury does not take into account the rock anisotropy (Hildenbrand et al., 2002). This may be overcome by drying at ~55 °C and applying araldite for vertical intrusion only, representing field conditions (Kaldi et al., 2011).

2.6 NUCLEAR MAGNETIC RESONANCE

The nuclear magnetic resonance tools are tuned to the hydrogen Lamour frequency. The tool firstly aligns all hydrogen atoms in the B_0 vertical direction with a primary static magnetic field (Figure 2-1). A pulsed secondary oscillating magnetic field B_1 (Radio Frequency field (RF)) perpendicular (90 °) to B_0 is pulsed which tips the hydrogen atoms making them

precess. Hydrogen atoms precessing produce a measurable signal that is recorded by the antenna on the NMR tool. As the hydrogen atoms begin to relax and realign with the B_0 magnetic field they stop producing a measurable signal. The B_1 magnetic field is then pulsed (180 °) to tip the protons in the opposite direction, realigning the protons and once again allowing them to dephase producing a measurable signal. This is repeated and is called a CPMG sequence. Each repeated sequence produces a spin echo (Kenyon et al., 1995, Coates et al., 1999 and Freedman, 2006).

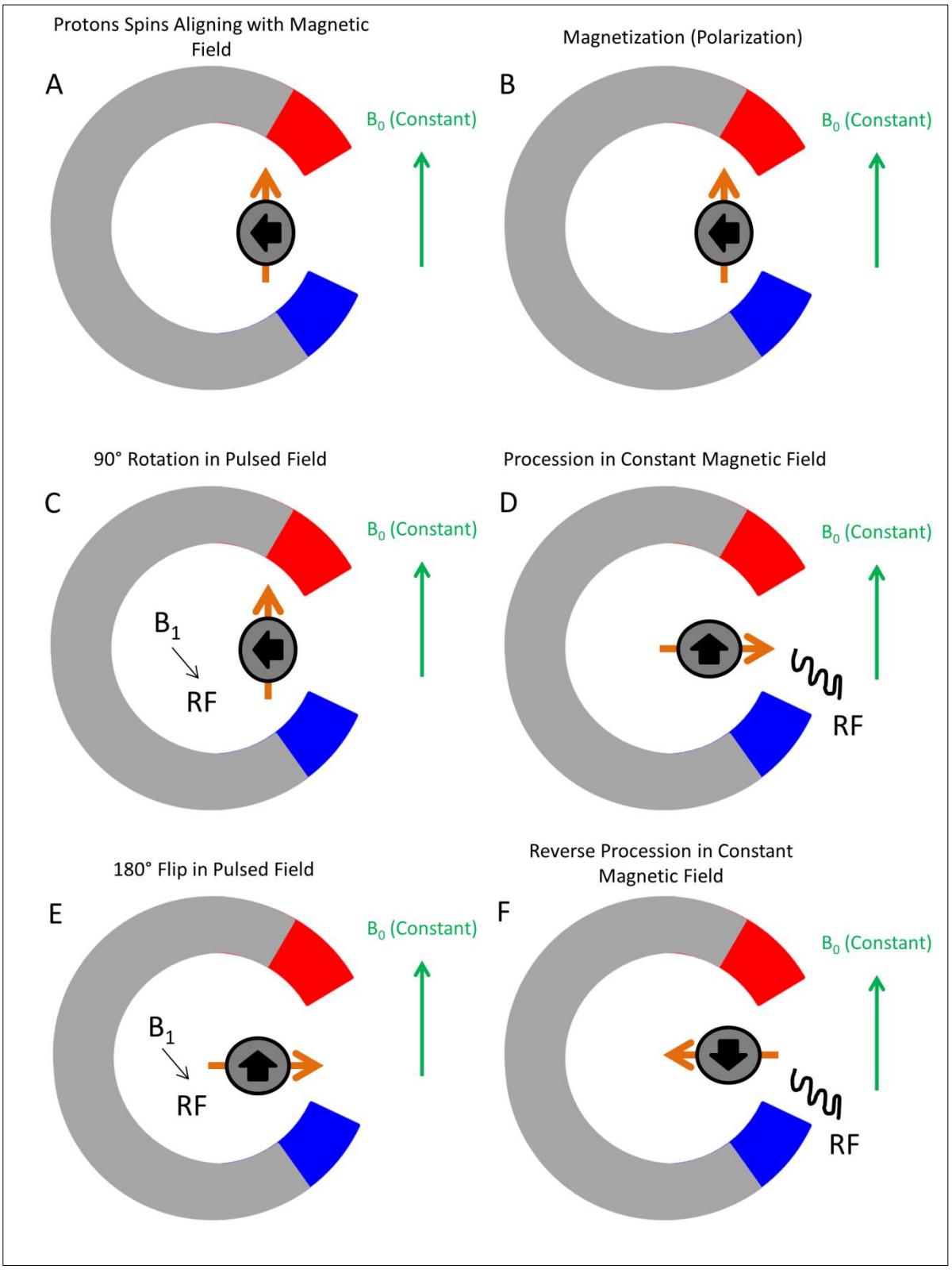

Figure 2-1: Diagram showing the manipulation of hydrogens in the pore fluid to obtain a transverse relaxation measurement. A-B shows the polarization and alignment of hydrogens with the primary magnetic field. C-F shows the CPMG sequence. Diagram after Al-Ghamdi, (2006).

There are three relaxation mechanisms that cause alignment of hydrogens with the B_0 magnetic field; grain surface relaxation, relaxation by molecular diffusion in magnetic field gradients and bulk fluid relaxation. Bulk fluid relaxation is considered negligible for most

siliciclastics but may be important in vuggy carbonates. Relaxation by molecular diffusion in magnetic field gradients is another possible source of relaxation but is kept to a negligible level by keeping the CPMG echo spacing short and keeping the B_0 magnetic field small. Grain surface relaxivity is the parameter that is measured – specifically the relaxation times which reflect the pore size distribution in the sample. The first amplitude of the uncorrected data represents the total porosity for the rock sample and with time represents only larger and larger pores. A mathematical inversion is then applied to this relaxation data to produce a T_2 distribution. The T_2 distribution represents the pore body size range from the smallest being the shortest T_2 times to largest being the longer T_2 times. Everything under the T_2 distribution curve represents the porosity of the sample (Kenyon et al., 1995, Coates et al., 1999 and Keating and Knight, 2007).

Please see Appendix A, A.8 -A.10 for detailed information on the laboratory NMR equipment, wellbore NMR equipment and extraction of wellbore NMR data from DLIS files.

2.7 NMR ANALYSIS TO PREDICT PERMEABILITY

The two most commonly used predictions of permeability from NMR data are the Timur-Coates Model and the Schlumberger-Doll-Research (SDR) model (Coates et al., 1999). Both models were used to predict permeability from laboratory and well log NMR data. Please see Appendix A, A.11 for the equations.

2.8 SYNTHETIC MICP CURVES FROM NMR DATA

NMR data provides information on the pore size distribution as observed from the T_2 time distribution. The amplitude of the T_2 distribution provides information on the proportion and size of the pores. This information can be related to the MICP pressure and mercury saturation. The cumulative amplitude is equivalent to total porosity. Each amplitude measurement can be calculated as a percentage of the cumulative amplitude to determine the equivalent percentage mercury saturation (Rezaee pers com., 2012; Al-Ghamdi, 2006). If the inverse of the T_2 relaxation time is used, it can be related to the pressure required to force a non-wetting fluid through a water wet porous medium at various pore sizes; i.e. long relaxation times are from large pores and short relaxation times are from small pores. However, a degree of uncertainty arises because MICP analysis measures pore throat diameter while NMR measures pore size (Kenyon et al., 1995). In siliciclastics, it is possible to predict a relationship between pore bodies and pore throats. In carbonates, this is more difficult (Ausbrooks et al., 1999), but this relationship or proportionality constant can be determined by correcting to MICP analyses.

Please see Appendix A, A.12 for the methodology used to produce synthetic MICP curves from both the laboratory and wellbore NMR data and how this was calibrated to the MICP curves from conventional core samples for this study.

2.9 NMR SHORTFALLS

The NMR log and corresponding T_2 distribution are affected by the hydrogen index of the fluid (should approximate ~1), the ability to completely polarize the hydrogen protons and the inter-echo spacing (needs to be short enough to record the small pores). The measurement is also affected by the surface relaxivity of the lithology for which the fluid resides, the signal to noise ratio, paramagnetic ions within the lithology, the drilling fluid used (oil or water based), magnetic field gradients, temperature, magnetic susceptibility contrast between the rock and the pore fluid, bulk fluid relaxation (large pores and the presence of hydrocarbon). The tool also has a shallow depth of investigation (Kenyon et al., 1995, Coates et al., 1999, Kleinberg, 2001)

2.10 HELIUM PYCNOMETRY

Helium pycnometry is considered to be the most accurate method of determining porosity (Lucia et al., 2003). The technique utilises a chamber of known volume and helium gas to determine the rock sample volume under dry and saturated conditions. The helium gas is injected into a chamber and then allowed to expand into a second compartment where the rock sample is enclosed and the subsequent pressure reduction recorded. Using Boyle laws, the pressure change is used to calculate the volume of the sample and the porosity (Brooks, 1957). The helium pycnometer can also be used to calculate permeability. Please see Appendix A, A.13 for details of the helium pycnometers used in this study.

2.11 X-RAY DIFFRACTION ANALYSIS

X-ray diffraction is a routine analysis used for mineral identification. It is helpful to use this analysis in conjunction with other mineral-identifying techniques (SEM, BSE with EDX). The analysis is relatively fast and reliable; it can be applied to mixtures and can be used to provide the proportion of minerals present (Flohr, 1997).

Most minerals are crystalline which means that they have planes of regular and repeating arrays of atoms stacked to form a crystal lattice (Nesse, 2000). The focused X-ray beam interacts with the atoms in the crystal lattice where it is partly absorbed, partly refracted and partly diffracted. When the X-ray wavelength is the same distance as the distance between mineral atom planes a diffraction pattern occurs (Petruk, 2000).

The XRD machine generates X-rays in a vacuum sealed chamber by applying a current that heats a filament within the tube (cathode). The filament emits electrons that are then accelerated by applying a voltage; when the electrons collide with the target, they produce X-rays. The wavelength of the X-rays depends on the target (i.e. copper, cobalt or copper/potassium). The X-rays are focussed and directed towards the powdered mineral sample. The X-rays collide with the electrons in the regular repeating units of atoms and scatter producing spherical waves away from the collision. In most directions, these waves cancel out through destructive interference, but in specific directions, they add through constructive interference. This phenomenon is described by Bragg‘s law Equation 4 (Flohr, 1997 and Nesse, 2000):

$$2dsin\theta = n\lambda \quad \text{Eq.4}$$

Where d is the spacing between atomic planes, θ is the angle of incidence, n is any integer, and λ is the wavelength of the X-rays.

As the wavelength and angle of incidence are both known, the d spacing can be calculated. For a powdered rock sample, the resulting XRD scan can be compared to known d spacing‘s (patterns) for mineral standards allowing the identification of the minerals present in the powdered rock sample. This is made possible as the atomic plane spacing‘s between minerals are unique (Flohr, 1997 and Nesse, 2000). The mineralogy can also be semi-quantified using the relative intensity of X-ray diffraction peaks to one another or to an added standard such as corundum. Please see Appendix A, A.14-A.16 for detailed information on the XRD analysis undertaken in this study.

2.12 SCANNING ELECTRON MICROSCOPE IMAGING

The scanning electron microscope (SEM) and energy dispersive X-ray (EDX) allows photomicrographs of the minerals, matrix and general fabric of shales (fine-grained rocks) in conjunction with the ability to identify minerals present (Petruk, 2000). The SEM can provide clear magnification down to the micron scale and poorly imaged results at the 500-nanometre scale. Unfortunately, this is still not able to resolve pores in < 500-nanometre scale commonly found in shales, but it does provide information about the clay and mineral fabric of the rock sample that can be used in conjunction with other mineral analysis (i.e. XRD) (Welton, 2003).

The SEM produces an electron beam in a chamber under high vacuum. A tungsten filament in an electron gun is heated until the material emits electrons. The electrons are accelerated through a column by an accelerating voltage set by the user; they are focussed and de-magnified into a precise beam. This electron beam is aimed at the platinum coated sample. This results in several types of electrons being emitted by the sample which can provide distinct information regarding the sample; type 1 and type 2 secondary electrons (SEM), type 1 and type 2 backscatter electrons (BSE), characteristic X-rays including bremsstrahlung X-rays which can be used to produce an image and elemental composition (Huang et al., 2013). The analysis of rock samples is typically achieved using SEM, BSE and characteristic X-rays (EDX).

The SEM image is a combination of the sample topography and atomic number of the minerals present. The primary beam interacts with the surface of the rock to a depth of 50-500 Angstrom releasing the low energy electrons. The primary beam scans the sample and the captured secondary electrons are processed to produce a SEM image (Petruk, 2000 and Welton, 2003).

The BSE image is the most informative and sensitive application as it provides the distributions of minerals, matrix free, and topography-free effects that are often dominant in SEM images. The BSE can display minor changes in atomic number between minerals as different shades of grey which is advantageous for trace minerals (Petruk, 2000).

The elemental analysis of the rock substrate is produced by capturing the energy dispersive X-rays produced as the primary electron beam scans the sample. The primary electron beam ionizes the atoms being examined resulting in the ejection of electrons from the inner shells of the atoms. The electrons in outer shells drop back into the inner shell vacancies releasing a specific quantity of energy in the form of X-rays. The energies of the inner shell electrons are precisely defined with characteristic values and thus the characteristic X-rays are elemental specific. An X-ray detector is mounted adjacent to the secondary electron detector (Huang et al., 2013). Each element that makes up a mineral within the sample produces characteristic X-rays with specific energies and wavelengths that can be identified. The EDX system works well with an accelerating voltage of 20 KV and only the strongest of those transitions are detected. All X-rays collected are separated according to energy level and displayed on a graph (EDX spectrum). Any major element will result in a peak on the graph (silicon, oxygen, and aluminum will all have a semi-unique location on the graph). The unique position of the peak or peaks allows the identification of the elements making up the mineral or rock substrate (Welton, 2003).

The identified elements from their peaks on the EDX spectrum and the crystal morphology can then be used to identify the minerals present by comparing the EDX spectrums, elements and crystal morphology to known properties of suspected minerals. The relative heights of the identified elements on the EDX spectrum indicate relative concentrations (Welton, 2003).

Please see Appendix A, A.17 for detailed information on the scanning electron microscope used and the interpretation of minerals in the samples for this research.

2.13 WELL AND SAMPLE LOCATIONS FOR ANALYSES

The wells used for this research were all chosen because of available pre-existing data. For more details on the well and sample locations please see Appendix A, A.18.

CHAPTER 3: REGIONAL GEOLOGY OF SELECTED BASINS

3.1 INTRODUCTION

The basin evolution and lithostratigraphy of basins from which wells have been used in this study are described. These basins may not presently be targets for CO_2 storage. However, their logs and core will provide the necessary data for any future such evaluations. Each basin has a description which covers the location, geological evolution, stratigraphic and lithological units of only the intervals for which analyses were conducted as well as references to comprehensive works by others should the reader require more information. Included in each of the basin studies is a summary of caprocks present in the basin and any previous work undertaken on seal capacity. Accompanying well descriptions, which give basic well information from well completion reports (WCR's) used in the research are also provided.

3.2 OTWAY BASIN

The Otway Basin is a rift basin trending northwest-southeast along the coast of southeastern Australia covering an area of 155,000 km^2 (Figure 3-1). The basin extends offshore (80 %) and onshore (20 %), from South Australia to Victoria and into the waters controlled by Tasmania (O'Brien and Thomas, 2007).

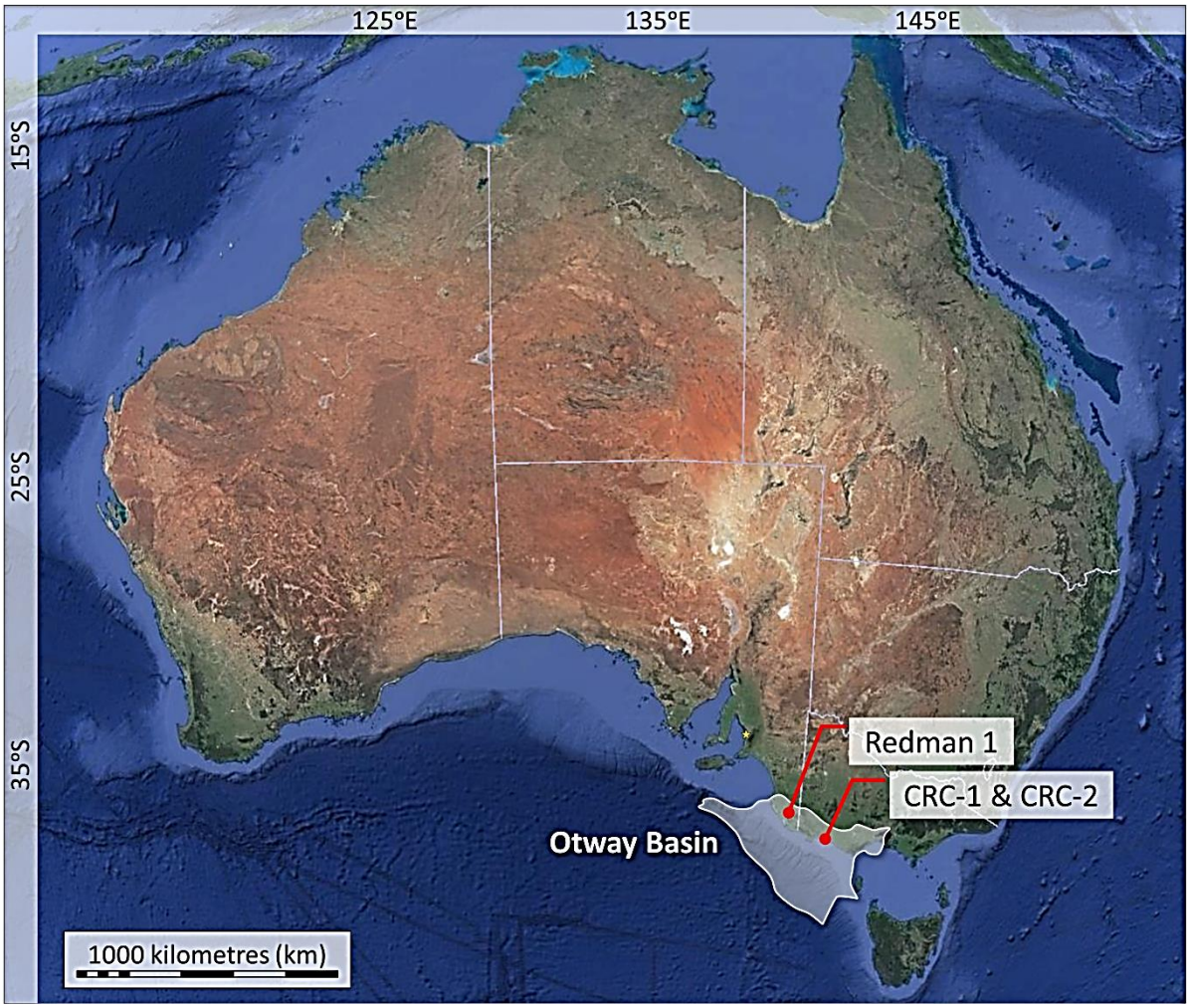

Figure 3-1: Location map of the Otway Basin showing Redman-1, CRC-1 and CRC-2 (Modified from Kulikowski et al., 2016).

3.2.1 Otway Basin Evolution

The Otway Basin evolved as part of the episodic breakup of Gondwana. Teasdale et al., (2003) have modeled seven significant basin events leading to the present day structure of the southern margin basins. The reader is directed to key works by Willcox and Stagg, (1990) Hill et al., (1994), Cockshell in Morton and Drexel, (1995) and Teasdale et al., (2003) for more information on the evolution of the basin.

3.2.2 Otway Basin Lithostratigraphy

The generalised Otway Basin stratigraphy is broken down into five groups commencing from the late Jurassic and extending through to the Tertiary; the Otway Group including the Crayfish Sub-group, Sherbrook, Wangerrip, Nirranda and Heytesbury Groups respectively (Figure 3-2). These sediments overlie Pre-Mesozoic basement rocks of the Lachlan and Kanmantoo Fold belts, consisting of metasediments, metavolcanics and intrusives (Mehin and Constantine, 1999 and Krassay et al., 2004). The reader is directed to Partridge, (2001),

Little and Phillips, (1995), Woollands and Wong, (2001) and Morton et al., in Morton and Drexel, (1995) for more information on the stratigraphy of the Otway Basin.

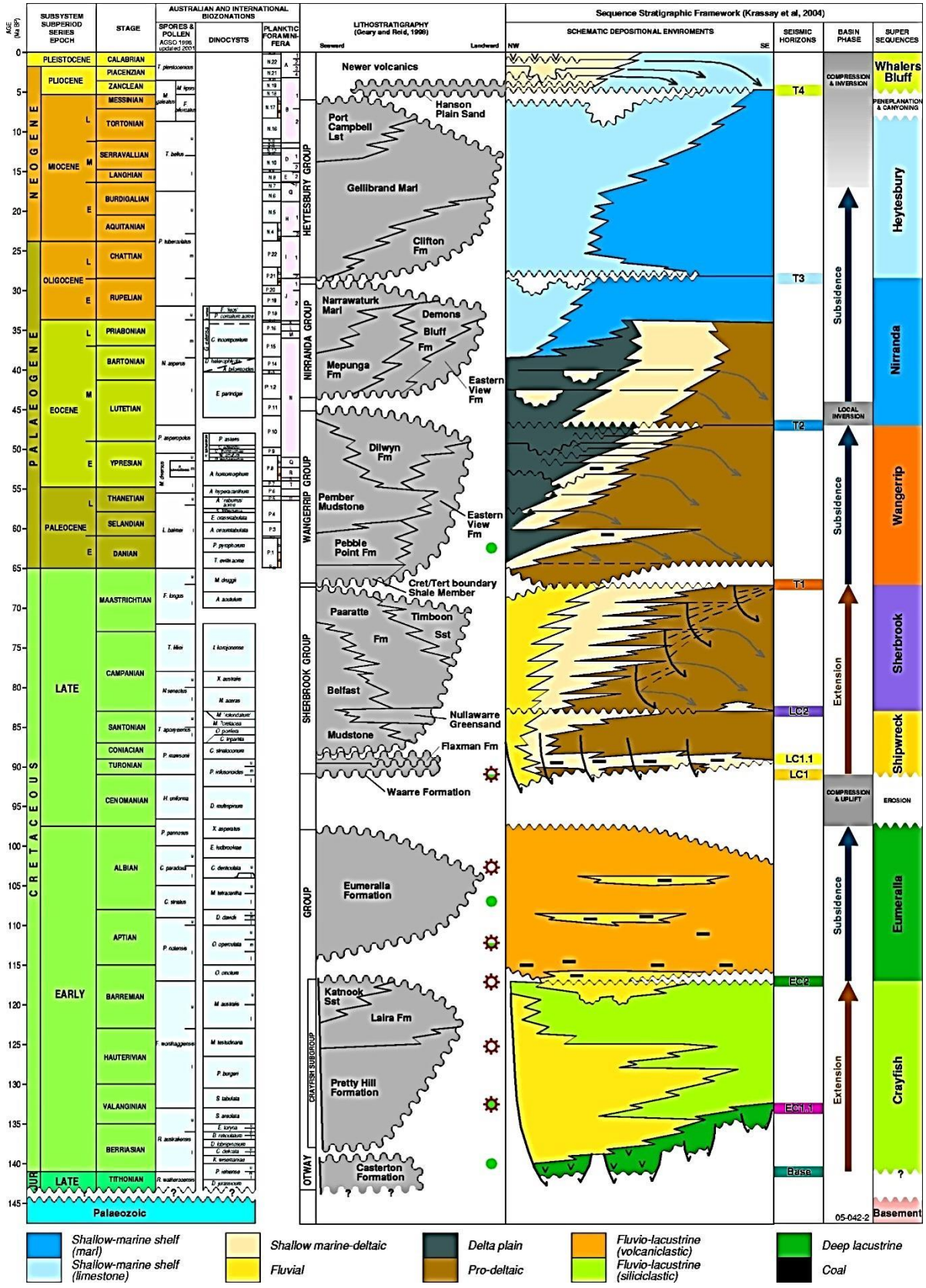

Figure 3-2: Otway Basin Stratigraphic Column (Image from Geoscience Australia, 2016).

The Otway Group (Tithonian-Albian) is divided into three units; Casterton Formation, Crayfish Subgroup- which contains the Pretty Hill and Laira Formation, and the Eumeralla Formation.

The Crayfish Subgroup‘s (Valanginian- Barremian) Pretty Hill Formation consists of a coarsening upwards sandstone unit that conformably succeeds the Casterton Formation or unconformably rests on the Palaeozoic basement. These sandstone units are interbedded with siltstones, shales and infrequent thin beds of pebbles and conglomerates. The sandstone varies from a grey to green litharenite to feldspathic litharenite (Boult and Hibburt, 2002). Visual estimations of grain size suggest that > 90 % of the grain sizes are less than or equal to 0.4 mm. In some wells, a layer of this unit is overlain by an interbedded organic shale-fine to medium grained quartz sandstone. The formation is observed to have dramatic facies changes between wells only a short distance apart. Little and Phillips, (1995) indicate a broad trend of decreasing porosity and permeability with increasing depth. The depositional environment is interpreted to be a braided river system with evidence of lacustrine influence (Little and Phillips, 1995).

The Sherbrook Group contains the Belfast Mudstone (Coniacian–Late Maastrichtian) which conformably overlies the Flaxman Formation and unconformably overlies the Waarre Formation. The Belfast Mudstone is described as an organic mudstone with fine-grained interbeds of siltstone and sandstone, interpreted to have been deposited in a deep submarine fan environment. The Belfast Mudstone is found to interdigitate with the Nullawarre Greensand and Paaratte Formation (Morton et al., in Morton and Drexel, 1995).

The Skull Creek Mudstone (Early Campanian) conformably overlies the Nullawarre Greensand. It is described as a prodelatic thin carbonaceous mudstone with infrequent interbedded siltstones and sandstones. It is lithologically similar to the Belfast Mudstone and where the Nullawarre Greensand is thin or absent, it is difficult to differentiate (Partridge, 2001, Woollands and Wong, 2001, and Dance, 2013).

The Paaratte Formation (Coniacian-Maastrichtian) conformably succeeds the Belfast Mudstone and unconformably overlies the Eumeralla Formation. The Formation is considered to be a gradational change that laterally interdigitates with the Belfast Mudstone, Skull Creek Mudstone and the Nullawarre Greensand (Woollands and Wong, 2001).The formation is described as a fine to coarse grained sandstone interbedded with organic mudstone thought to have been deposited in an offshore to marginal marine environment. More specifically the sandstones are interpreted as channel fill of low sinuosity river

systems deposited in the lower delta plain environment with distributary channels, lagoons, barrier reefs, shoreface and estuarine environments all present (Morton et al., in Morton and Drexel, 1995).

The Pember Mudstone (Early Eocene) conformably overlies the Pebble Point Formation. The formation is described as a silty claystone that was deposited in a pro-deltaic environment (Woollands and Wong, 2001).

3.2.3 **Otway Basin Caprocks**

There is limited literature focussing on seals in the Otway Basin. The formations that are considered or have the potential to act as seals include the Laira Formation, Eumeralla intraformational mudstones, Belfast Mudstone, Skull Creek Mudstone, Paaratte Formation intraformational mudstones and the Pember Mudstone. The following are the principle studies conducted on seal capacity in the Otway Basin; Jones et al., (2000) ‗Integrated hydrocarbon seal evaluation in the Penola Trough, Otway Basin'. Damte, (2002) ‗Analysis of the sealing capacity of the Flaxmans Formation and the Belfast Mudstone in the vicinity of the Shipwreck Trough, Otway Basin, Victoria'. Svendsen, (2004) ‗Seal evaluation of a fluvial-lacustrine rift to post-rift succession, the Early Cretaceous Eumeralla Formation, Otway Basin, Australia'. Daniel, (2007) ‗Carbon dioxide seal capacity study, CRC-1, CO2CRC Otway Project, Otway Basin, Victoria'. That study included MICP analysis, XRD analysis and SEM imaging. Watson, (2012) ‗Natural CO_2 accumulations as analogues for CO_2 geological storage and CO_2-induced diagenesis in the Otway Basin, Australia' which included several MICP analyses from the Belfast Mudstone.

3.3 WELL DESCRIPTIONS

3.3.1 **Redman-1**

Redman-1 was drilled in Pel 32 tenement by Boral Energy Resources Ltd. in the Otway Basin South Australia in January 1998. The well was drilled as an exploration well to appraise an elongate fault dependent closure targeting the anticipated Pretty Hill Formation. The conventional core was cut from the top of the Pretty Hill Formation from a depth of 2828.81 mKB to 2846.81 mKB and was observed to have indications of hydrocarbon. The wireline logs and reservoir formation tests confirmed that the well had encountered a 74 m gas column in the Pretty Hill Formation. Included in the suite of wireline logs was the CMR log from Schlumberger. The well was suspended and completed as a gas discovery (Baker and Skinner, 1999). The well had 18 m of conventional core (CC) cut over the Pretty Hill Formation which included both reservoir rock and tight/ sealing intervals.

3.3.2 **CRC-1**

CRC-1 was drilled as part of the CO2CRC Otway Project in 2007, in the PPL13 tenement at Nirranda, near Port Campbell, Victoria. CRC-1 was drilled to a depth of 2249 mRT into the lower limb of anticline feature of a depleted gas reservoir. The well was drilled as part of a pilot project to safely inject and store carbon dioxide in the subsurface. The well had a full suite of wireline logs including the CMR log by Schlumberger run over the reservoir intervals. Also Elemental Capture Spectroscopy and Formation Micro-Imager logs were run and several Modular Formation Dynamic Tests were conducted. Six conventional cores were cut during the drilling totaling ~43 metres of recovered core sampling both reservoir and sealing rock.

3.3.3 **CRC-2**

The CRC-2 well was also drilled in the Otway Basin in the PPL13 tenement at Nirranda, near Port Campbell, Victoria, Australia in 2010 as part of a pilot project by the CO2CRC to inject CO_2 into a virgin (no hydrocarbons; no pressure depletion) saline aquifer. The well was drilled to a depth of 1565 mKB and had a complete suite of logs run including the CMR log by Schlumberger. Also, 29 conventional cores cut totaling 183 m of recovered core. The core included both reservoir and sealing intervals.

3.4 NORTH WEST SHELF WESTERN AUSTRALIA

The North West Shelf of Western Australia consists of four basins; The Northern Carnarvon, offshore Canning, Browse and Bonaparte Basins and one orogenic belt; the Timor Banda Orogeny. These basins are collectively known as the Westralian Superbasin (Hocking et al., 1994).

The Carnarvon Basin (Figure 3-3) covers an area of approximately 650,000 km^2 and lies predominantly offshore. The basin formed as Australia separated from India during the episodic breakup of Gondwana (Purcell and Purcell, 1988) and consists of numerous sub-basins which are grouped into the Southern Carnarvon and Northern Carnarvon Basin also referred to as the Palaeozoic and Mesozoic Sub-basins respectively. The Southern Carnarvon Basin comprises the Gascoyne, Merlinleigh, Byro and Bidgemia Sub-basins while the Northern Carnarvon Basin consists of the Barrow, Exmouth, Dampier, Beagle, Dixon and, Investigator Sub-basins and the Kangaroo Trough. The Northern Carnarvon Basin contains sediments up to 15 km thick ranging in age from Mesozoic to Palaeozoic (Hocking, 1988). The Barrow and Dampier Sub-basins are considered to be complex inner grabens (Hocking et al., 1994) that are similar, but with distinct depocentres for only part of their past (Woodside Offshore Petroleum, 1988).

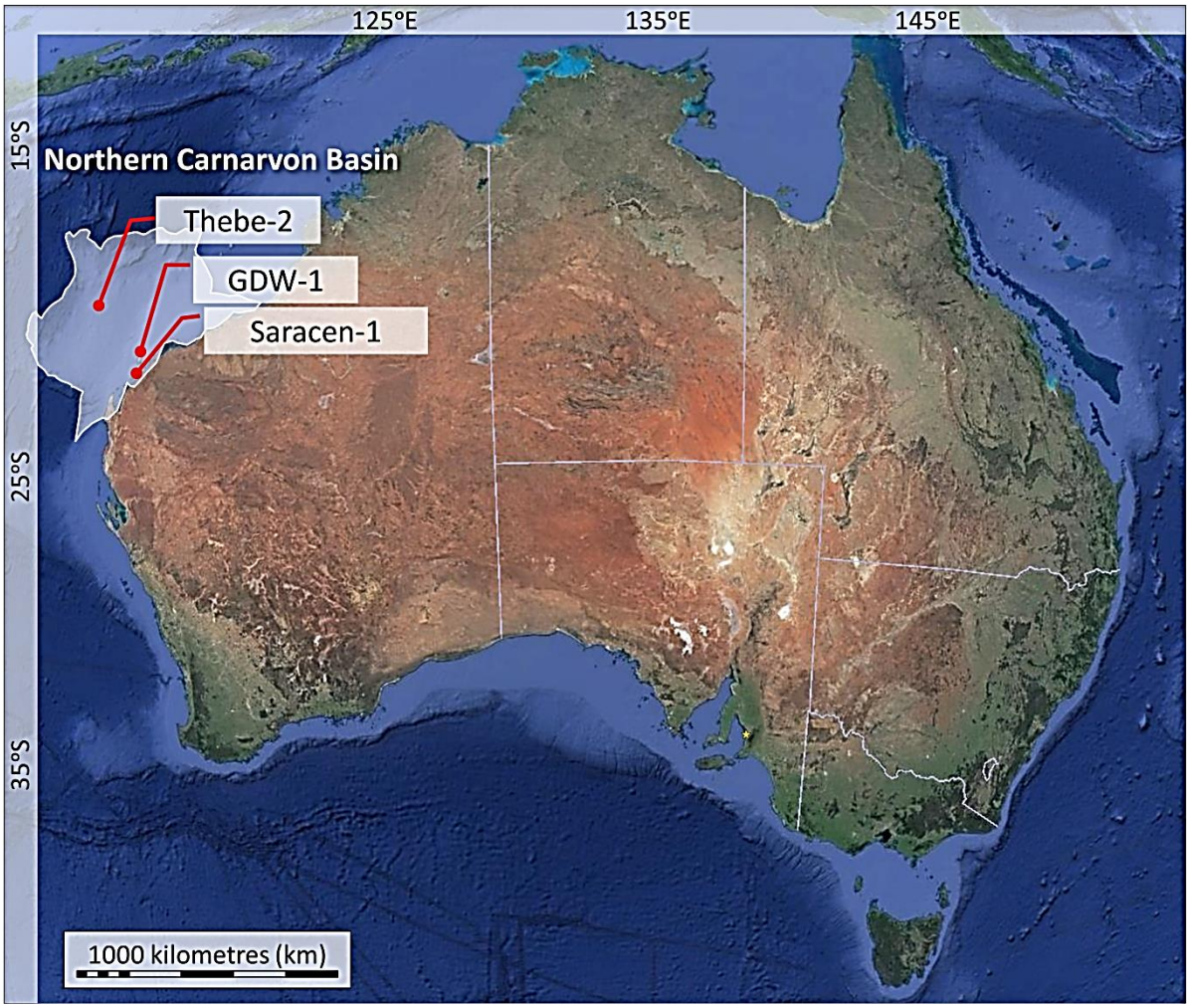

Figure 3-3: Location map of the Northern Carnarvon Basin showing Thebe-2, Gorgon CO2 Data Well-1 & Data Well-1ST1 (GDW-1) and Saracen-1 (Modified from Kulikowski et al., 2016).

3.4.1 Northern Carnarvon Basin Evolution

Most research on the formation of the Westralian Superbasin links its development to the breakup of Gondwana as India separated from Australia and Antarctica (Purcell and Purcell, 1988, Veevers, 1988, Heine and Muller, 2005 and, Longley et al., 2003) as either a failed rift system or a wrench complex. In contrast, Daim and Lennox, (1998) proposed a tectonic model where they suggest that many of the basins in Australia formed and are controlled by west northwest lineaments that have been identified with aeromagnetic, gravity, geological maps and Landsat data. The reader is directed to key works by Purcell, 1988, Purcell, 1994, Purcell, 1998, Keep and Moss, 2002 and Longley et al., 2003 for more information.

3.4.2 Generalised Northern Carnarvon Basin Lithostratigraphy

The Northern Carnarvon Basin stratigraphy (Figure 3-4) and the details of the formations rely on exploration focussed wells in the region. Thus only a few wells have penetrated the deepest formations and those that have occurred on the margins of the basin in the Peedamulla Shelf and Rankin Platform. The oldest rocks encountered in the Carnarvon

Basin are of Carboniferous to Devonian age (Parry and Smith, 1988). The reader is directed to Condon, (1954), Tait, (1985), Hocking et al., (1987) and Parry and Smith, (1988) for more information on the stratigraphy of the Northern Carnarvon Basin.

The following provides a description of the lithostratigraphy in order of age and depositional history:

The Mungaroo Formation (Mid-Late Triassic) conformably overlies the Locker Shale. The formation is a sequence of interbedded sandstone, siltstone and shales dominated by marine processes. The formation on the Exmouth Plateau reaches a thickness > 3000 m. The formation contains many giant gas accumulations (Hocking et al., 1987).

The Brigadier Formation conformably overlies the Mungaroo Formation. The Brigadier Formation is a sequence of narrow alternating beds of sandstone and carbonaceous shale formed in a shallow marine environment; commonly in a coastal lagoon environment. The Brigadier Formation extends from north of the Barrow Sub-basin southwards possibly into the Exmouth Sub-basin (Hocking et al., 1987, Parry and Smith, 1988).

The Dupuy Formation describes the upper sandy sequence of the Dingo Claystone. The formation is regionally extensive and comprises an argillaceous, commonly bioturbated sandstone with thin interbedded sandy claystone and conglomerate facies. The formation has been characterised in detail by Tait, (1985) and divided into three lithofacies. The depositional environment is interpreted to be a prograding shelf edge, below wave base, with turbidite and mass flows (Tait, 1985).

The Barrow Group is divided into two formations that can be identified seismically as the Malouet and Flacourt Formations (Westphal and Aigner, 1997). The formations are both part of a large delta system that prograded from the south, northward into the basin. The Malouet Formation comprises the bottomsets (mainly sandstone) of the distal part of the delta which are interpreted as submarine fans. The Flacourt Formation comprises both topset (mainly sandstone) deposited in the offshore slope, and foresets (mainly claystone) of the delta that were deposited in a shallow marine-fluvial environment (Hocking et al., 1987, Parry and Smith, 1988)

The Winning Group (Early Cretaceous) is divided into the following four units; Birdrong Sandstone, Muderong Shale, Windalia Radiolarite and Gearle Siltstone. These units are regionally extensive over the onshore and offshore Carnarvon Basin (Parry and Smith, 1988). The Winning Group represents a major sea level transgression with the base of the

group being dominated by sand which transitions into marine claystone and siltstones (Hocking et al., 1987).

The Muderong Shale is a marine glauconitic claystone and siltstone formation. The shale is conformably bounded by the higher Windalia Radiolarite and where present the lower Birdrong Sandstone or subsequently the Barrow Group (Parry and Smith, 1988). The shale unit consists of the Mardie Greensand Member at the base and the Windalia Sand Member at the top (Condon, 1954). The shale is the regional seal for the Barrow Dampier Sub-basins sealing majority of the hydrocarbon accumulations found in the Sub-basins (Woodside Offshore Petroleum 1988). In fact, the shale seals the majority of the hydrocarbons in the Carnarvon Basin (Dewhurst et al., 2004). Westphal and Aigner, (1997) interpreted the Muderong Shale as a late transgressive deposit and Woodside Offshore Petroleum, (1988) propose that it was deposited during a sizable sea level transgression during the Valanginian.

The Mardie Greensand Member extends thinly over the Peedamulla Trough through the eastern region of the Barrow Sub-basin and through to Barrow Island (Hocking et al., 1987). The member is a glauconitic sandy siltstone interbedded with siltstone and shale (Parry and Smith, 1988).

The Windalia Sand Member is a fine grained, argillaceous, glauconitic and bioturbated sandstone (Parry and Smith, 1988) which is conformably overlain by the Windalia Radiolarite. The Windalia Sand Member has been identified on Barrow Island and the Robe River area (Hocking et al., 1987).

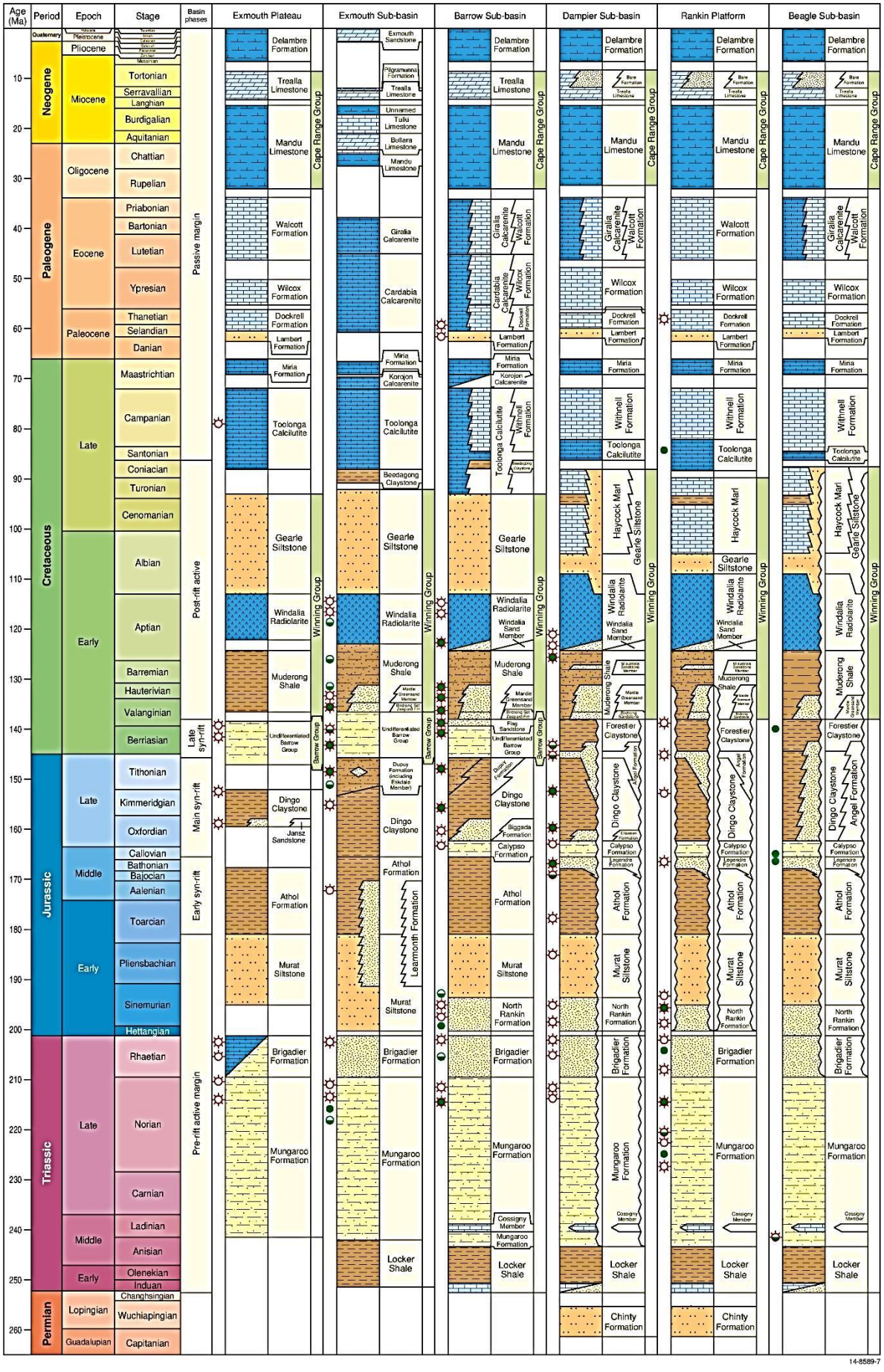

Figure 3-4: Northern Carnarvon Basin Stratigraphic Column (Image from Geoscience Australia, 2016).

3.4.3 **Carnarvon Basin and Barrow Sub-basin Caprocks**

Several journal articles and reports focus on the seals in the Northern Carnarvon and Barrow Sub-basin. The Muderong Shale is the formation recognised as the regional seal to both the Barrow Sub-basin and the Carnarvon Basin. It traps more than 90 % of the hydrocarbon discoveries (Kovack et al., 2004). Other formations acting as seals include the Windalia Radiolarite, Gearle Siltstone, the Dockrell Formation of the Cardabia Calcarenite Group and the Murat Siltstone. Also, a number of intraformational shales have acted as seals to hydrocarbon accumulations of the Barrow Group, Dupuy, Dingo Claystone, Brigadier and the Mungaroo Formations (Australia Government, 2009, and Bailey et al., 2006).

For studies conducted on seal capacity in the Carnarvon Basin the reader is directed to; Dewhurst et al., (2002), Kovack et al., (2004), Daniel, (2006) and Bailey et al., (2006). Dewhurst et al., (2002) concentrated on characterising the mineralogy and the effects of different drying methods on MICP analysis from 13 samples of conventionally cored Muderong Shale in Saracen-1, Barrow sub-basin. Kovack et al., (2004) focused on threshold pressures and subsequent seal capacities from Muderong Shale samples from various wells and depths across the Carnarvon Basin where they varied in composition, diagenesis and compaction. Bailey et al., (2006) undertook an investigation into the Pyrenees and Macedon fields in the Exmouth sub-basin. Both fields are not filled to structural closure and the study aimed to determine whether the weak link was fault seal capacity or the top seal capacity of the Muderong Shale (caprock) over the field. Daniel, (2006) compiled a comprehensive report in which seal samples from Gorgon CO2 Data Well-1 & Data Well-1ST1 on Barrow Island were analysed extensively. MICP, XRD and SEM analyses were carried out on 22 conventional core samples.

3.5 WELL DESCRIPTIONS

3.5.1 **Saracen-1**

The Saracen-1 offshore well, under production license TL/4, was drilled by WAPET with the primary goal of testing the hydrocarbon potential of the Mardie Greensand member of the Muderong Shale; the secondary goal was to evaluate the uppermost Muderong Shale and the lower Gearle Siltstone. The prospect was described as a prominent anticline with an associated seismic amplitude anomaly (Banfield, 2000). The well was spudded in January 2000, drilled to a depth of 1350 m but encountered no hydrocarbons. The well had basic geophysical logs run and thirty sidewall cores recovered. The well also had conventional coring carried out between 1118.00 m and 1123.2 m totaling 4.38 m of core. The core was in the Muderong Shale. The well was plugged and abandoned as a dry hole (Banfield, 2000).

3.5.2 **Thebe-2**

Thebe-2 was drilled in 2008 by BHP as an exploration well in the WA-346-P tenement on the Exmouth Plateau, Northern Carnarvon Basin. The well had a complete set of wireline logs run including a CMR log from Schlumberger. Also, the well had ten conventional cores cut through the Brigadier and Mungaroo Formations totaling 81.23 m of recovered core. The wireline logs and reservoir formation tests confirmed a ~65 m gross gas column. The well was plugged and abandoned as a gas discovery (Ellis, 2009).

3.5.3 **Gorgon CO_2 Data Well-1 & Data Well-1ST1**

The Gorgon CO2 Data Well-1 & Data Well-1ST1 well was drilled on Barrow Island by Chevron in a joint venture with ExxonMobil, Shell, Osaka Gas, Tokyo Gas and Chubu Electric power in 2006. The objective of the well was to collect data and reduce uncertainty about the proposed storage of carbon dioxide from their offshore oil and gas fields. The well evaluated the Dupuy Formation and secondarily evaluated the overlying Barrow Group as possible targets for carbon dioxide injection. The well was drilled to a total depth of 2619 m mdRT. A full suite of wireline logs were run including the CMR tool by Schlumberger. Also 11 conventional cores were cut totaling 502 m of recovered core through the formation of interest. Numerous petrological analyses were conducted on the core. The well was plugged and abandoned (Beacher, 2007).

3.6 DARLING BASIN

The Darling Basin is located onshore western New South Wales and covers an area of more than 100,000 km^2 (Figure 3-5). The basin stretches from Broken Hill in the west to Cobar Basin in the east and as far north as White Cliffs and Louth and possibly under the Eromanga Basin. To the south, the basin extends to Ivanhoe and Roto and under the Murray Basin (Cooney and Mantaring, 2004 and NSW Department of Industry, 2016).

The basin is divided into thirteen sub-basins or troughs. The basin was sparsely explored for petroleum during the 1960‘s and 1970‘s during which time approximately 20 petroleum wells were drilled, many of which were shallow. More recently, 1550 km of multi-fold, seismic coverage has been acquired as well as a magnetic survey which provides the data for the interpretation of the geological evolution and stratigraphy of the basin (NSW Department of Industry, 2016).

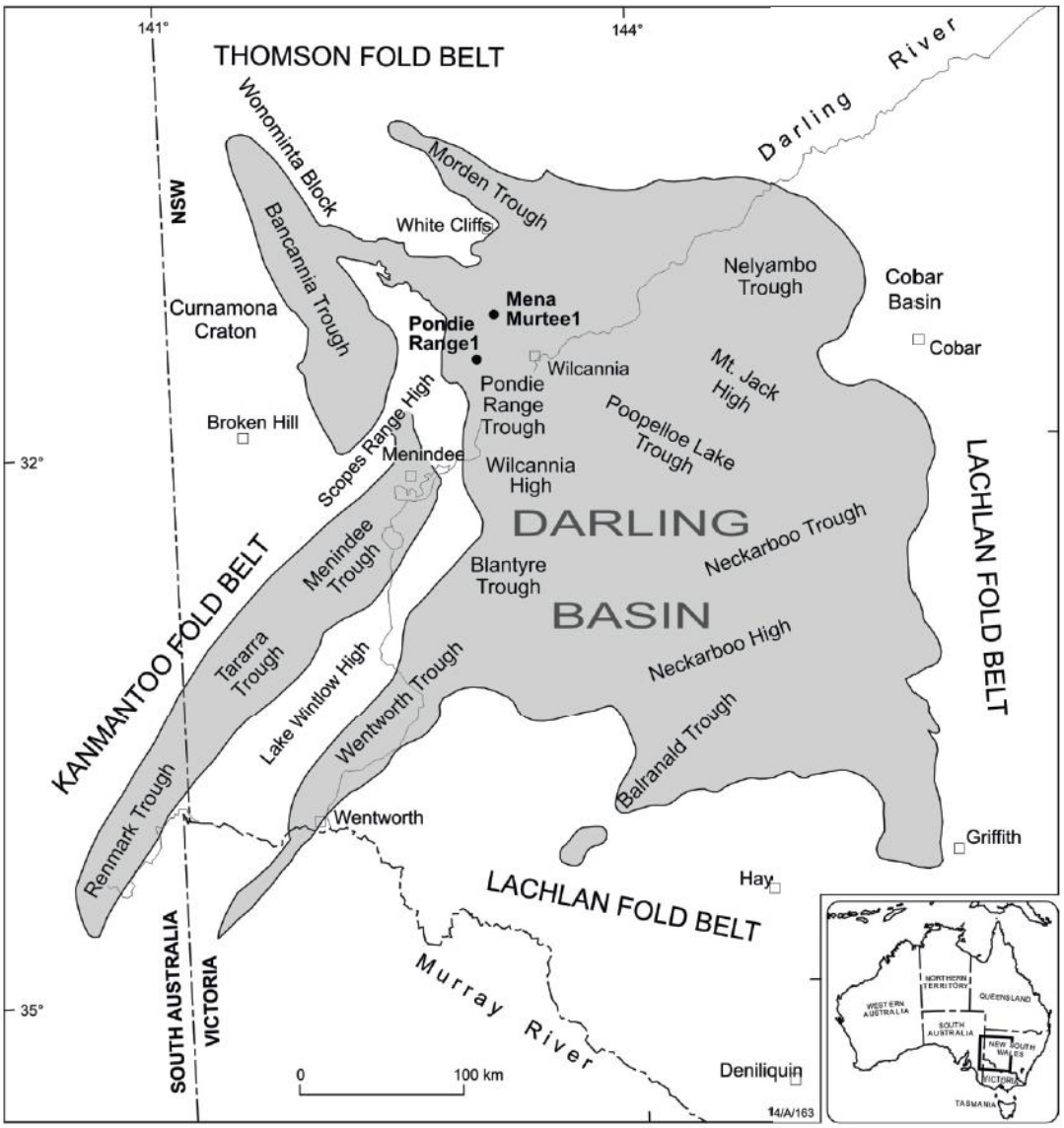

Figure 3-5: Darling Basin location map highlighting the troughs and the Mena Murtee-1 (Image from Bunch, 2014).

3.6.1 **Darling Basin Evolution**

The basin initiated from extension during the Silurian-Devonian. Kobussen and Dick, (2011) suggest that weak Kanmantoo crust surrounded by stronger crust underwent extension. This extension was strongly localised and associated with the pre-existing fault network developed during the Neoproterozoic and Palaeozoic which has led to localised Silurian to early Carboniferous sediments being deposited, reaching up to 10 km in depth. The age of the basement sediments is largely unconfirmed but based on current geological models are likely to be of Neoproterozoic to Middle Cambrian Kanmantoo aged rocks in the west and Cambro-Ordovician age metasediments in the east. There are also indications of Silurian aged granite bodies below many parts of the basin (Kobussen and Dick, 2011).

Sediment deposition was halted during the Kanimblan Orogeny. This compressional event led to the compartmentalization of the basin into thirteen sub-basins and troughs. These sub-basins and troughs are typically steep-sided and fault-bounded and the strata have been moderately folded and faulted with some igneous activity. Post Kanimblan extension has resulted in unconformable, discontinuous sedimentation of Late Carboniferous to Early Permian age. Above these are Cretaceous sediments of the Eromanga Basin in the north and Palaeocene to present sediments of the Murray Basin in the south (Watson et al., 2014).

3.6.2 **Darling Basin Lithostratigraphy**

The Darling Basin stratigraphy has been classified by a number of authors including Evans, (1977), Alder et al., (1998) and Khalifa, (2009) (Figure 3-6). Unfortunately, due to the paucity of petroleum exploration, the basin is only coarsely broken down into a number of identifiable groups. Fortunately, several authors have built on one another‘s work allowing the new groups and formations to be placed in the context of earlier work although there is still confusion as groups and formations have been reassigned, classified and reclassified as lateral equivalents in the different sub-basins. The stratigraphy described here is based on the most recent stratigraphic information published in Rajabi et al., (2015) which appears to be the most comprehensive. For further information on the stratigraphy of the Darling Basin the reader is directed to works by Evans, (1977), Neef and Botrill, (1991), Bembrick, (1997), Neef, (2004), Khalifa, (2010), Khalifa and Ward, (2009), Khalifa and Ward, (2010).

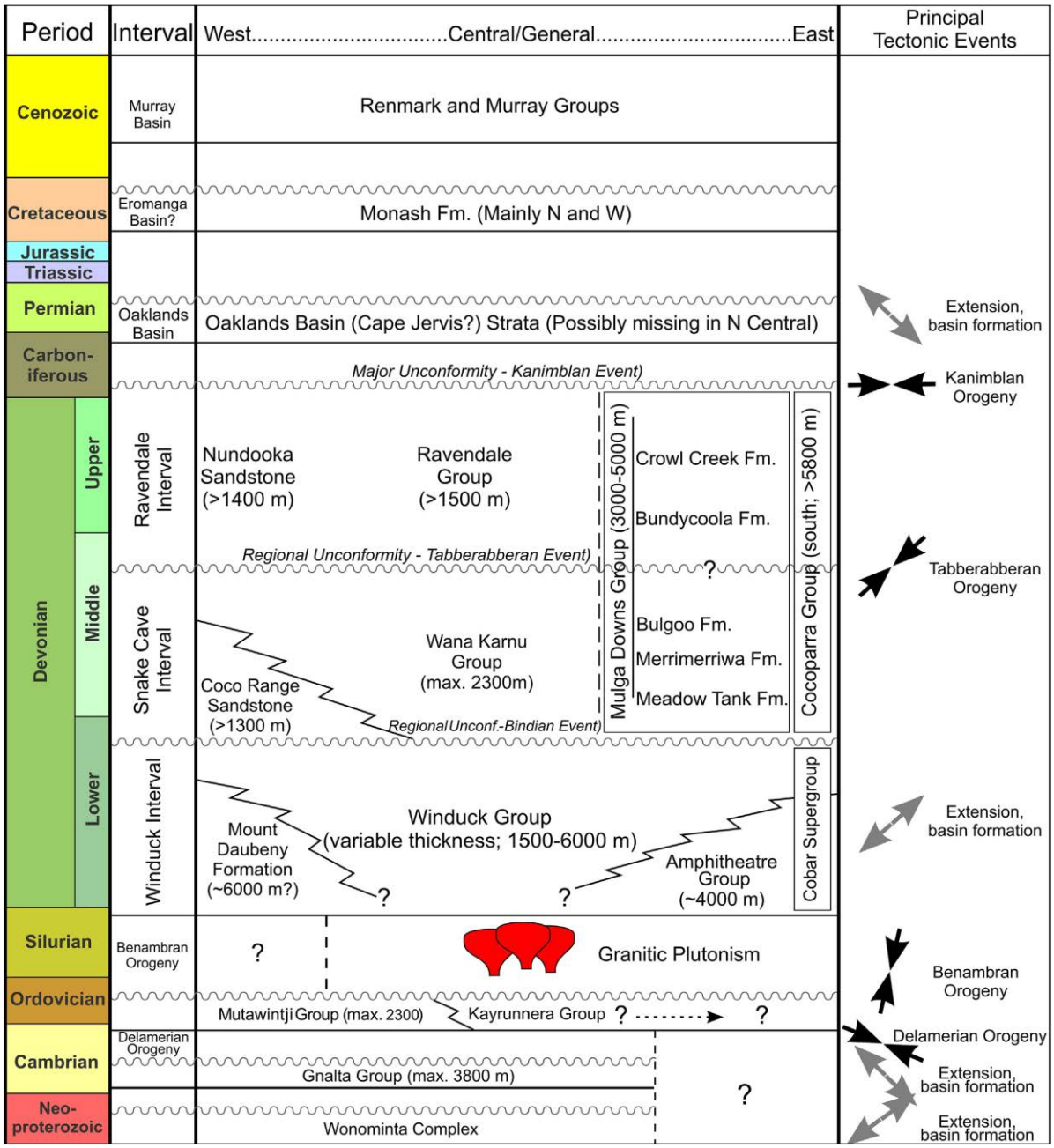

Figure 3-6: Darling Basin stratigraphic column (Image from Rajabi et al., 2015).

The Ravendale Formation (Upper Devonian-Lower Carboniferous) was deposited in a braided stream environment (Neef et al., 1996). The unit is identified at the top of the red bed sequence which is conformably overlain by Permo-Carboniferous, Cretaceous or Tertiary sediments (Neef et al., 1996). The unit commonly contains interbedded sand reservoir intervals and overlays the Snake Cave Sandstone (Bembrick, 1997). Nine core samples of the Ravendale interval were described in detail by Khalifa and Ward, (2010).

3.6.3 **Darling Basin Caprocks**

The identification of sealing formations/ groups within the Darling Basin is poor due to the lack of geological knowledge compounded by the coarsely described stratigraphy. Willcox

et al., (2003) suggest that finding suitable sealing formations in the middle to late Devonian stratigraphy is likely to be difficult. They suggest that effective sealing formations will most likely be argillaceous/ carbonate layers that formed as a result of marine transgressions or restricted lacustrine settings.

Bembrick, (1997) provides limited information on the sealing potential of the three intervals (Figure 3-6). He suggests that the Winduck interval is likely to provide local or intraformational seals throughout the basin. The Snake Cave interval is generally absent of possible sealing lithologies. However, Bembrick (1997) suggests the possibility of a siltstone/ shale unit at the top of the Snake Cave interval with possible regional extent and another possible local seal identified in Pondie Range -1. The Ravendale interval (red bed facies) is considered to host the most promising reservoir units within the basin (Wilcox et al., 2003). Sealing units within this interval are not well developed. However, in the Blantyre -1 well a 1000 m thick unit of siltstone and shale overlie the reservoir unit. It is expected that this sealing interval will have significant lateral extent although it has only been intersected in Blantyre-1 (Bembrick, 1997). Local sealing units were also intersected in Pondie Range-1, Jupiter-1 and Pamameroo-1) (Cooney and Mantaring, 2007) and (Bembrick, 1997).

Seal capacity analysis has been conducted on two wells drilled in the Darling Basin; Tiltagoonah-1 and Mena Murtee-1 by Daniel, (2014); in Watson et al., (2014) report produced by the CO2CRC for the NSW Division of Resources and Energy. These wells were drilled to determine the potential for CO_2 storage in the basin.

The findings of Daniel, (2014) in Watson et al., (2014) indicate that the sealing rocks and intraformational barriers analysed in Tilitagoonah-1 had higher seal capacities than those analysed in Mena Murtee-1; 124-985 m and 62 to 493 m column height of carbon dioxide. Also, Watson et al., (2014), state that the sealing intervals in Mena Murtee-1, in the majority of instances, have sealing capacity column heights greater than the underlying reservoir unit thickness.

3.7 WELL DESCRIPTION

3.7.1 **Mena Murtee-1**

Mena Murtee-1 was drilled in 2014 by the NSW Department of Trade and Investment in the EL8066 tenement, Pondie Range Trough, Darling Basin, NSW. The well was drilled to a total depth of 2279 m. The well was drilled to test possible Devonian reservoirs for the storage of carbon dioxide. The well had conventional core cut with a total of 86.5 m recovered between 1598 m and 2039 m depth over the Ravendale Formation. Petrological analyses were conducted and a full suite of wireline logs were run including an NMR log by Weatherford. The well was plugged and abandoned (NSW Government, Trade and Investment WCR, 2014).

3.8 COOPER BASIN

The late Carboniferous-Triassic aged Cooper Basin is located onshore in eastern central Australia and extends into South Australia and Queensland, covering an area of 130,000 km^2 (Figure 3-7). The Cooper Basin overlies the Warburton Basin and is succeeded by the Eromanga Basin. It described as a northeast-trending structural depression directly overlying the Warburton Basin and Thomson Fold Belt (Apak et al., 1997). The sediments were deposited in environments varying from glacial, fluvial and lacustrine in the Permian-Triassic. The Permian sediments are thickest (1600 m) in the south while the Triassic sediments are thicker in the north of the basin. The southern part of the basin is made up of three major troughs; Patchawarra, Nappamerri, and Tanappera which are separated by structural ridges; Gidgealpa, Merrimelia, Innamicka and Murteree (Kulikowski et al., 2016).

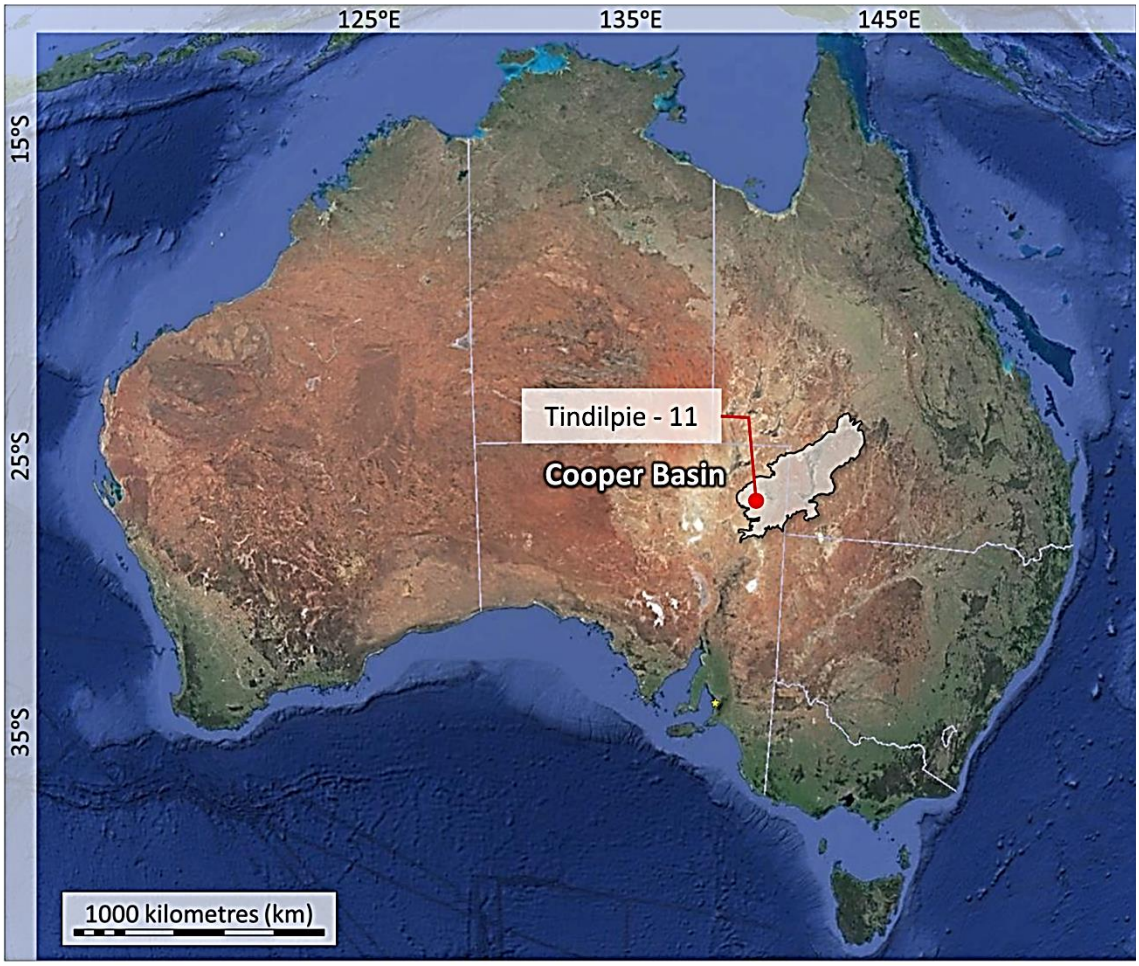

Figure 3-7: Location map of the Cooper Basin showing Tindilpie-11 (Modified from Kulikowski et al., 2016).

3.8.1 Cooper Basin Evolution

The Cooper Basin is a structurally complex intra-cratonic depression that is mildly compressive (Apak et al., 1997 and Kulikowski et al., 2016). The reader is directed to key works by Apak et al., (1997), Haines et al., (2001), Muller et al., (2012) and Kulikowski et al., (2016) for further information.

3.8.2 Cooper Basin Lithostratigraphy

The Cooper Basin stratigraphy is broken down into four depositional cycles; glacial cycle (Merrimelia Formation), fluviatile cycle (Tirrawarra Sandstone to the Patchawarra Formation), lacustrine deltaic cycle (Murteree Shale to the Daralingie Formation) and fluviatile cycle (Toolachee Formation to the Nappamerri Group) (Apak et al., (1997) (Figure 3-8). For further information not covered below, please see Apak, (1994), Apak et al., (1997), Gravestock et al., (1998) and McGowen et al., (2007)

The Patchawarra Formation is the primary reservoir target in the Cooper Basin and has thus been extensively studied and stratigraphically divided into five units (Apak et al., 1997).

Unit 5 was deposited in a lacustrine environment with the sediments restricted to topographic lows. The primary depocenter for this unit was the Pina area. The sandstone-rich Unit 4 was deposited during a stage of sag across the basin that was pronounced in the south and north margins. This Unit was also deposited around the perimeter of intra-basin highs and along the basin margins due to differing rates of subsidence. Unit 3 comprises interbedded shales and coals dominated by sandstone. Unit 3 is eroded throughout much of the basin as a result of compressional tectonic activity. The Unit is present over the Moomba field and likely present in the Patchawarra syncline. Unit 2 was deposited extensively over the basin, covering topographic highs including Moomba, Toolachee, Della, Daralingie, Gidgelapa, the southern margin and extending into the northern Cooper Basin. The depositional environment of Unit 1 and 2 are shoreline and offshore deltas. There is evidence of syndeposition around topographic highs. Unit 1 was deposited extensively over the basin during the transition from a fluvial environment to a lacustrine environment, transgressing from the east or northeast. Channel development in the west and south of the basin is likely to have been controlled by faulting. Mouth bars, shorelines and offshore sandstones are present throughout this area. Unit 1 and 2 have been eroded as a result of compression and subsequent uplift in the late Permian over the Gidgealpa Merrimelia and Innamincka trend (Apak et al., 1997).

The Patchawarra Formation consists of interbedded sandstones, siltstones, shales and coals. The sandstones vary locally from pebbly, coarse grained to fine grained with minor chert and rock fragments, quartz overgrowths and cements (Gravestock et al., 1998).

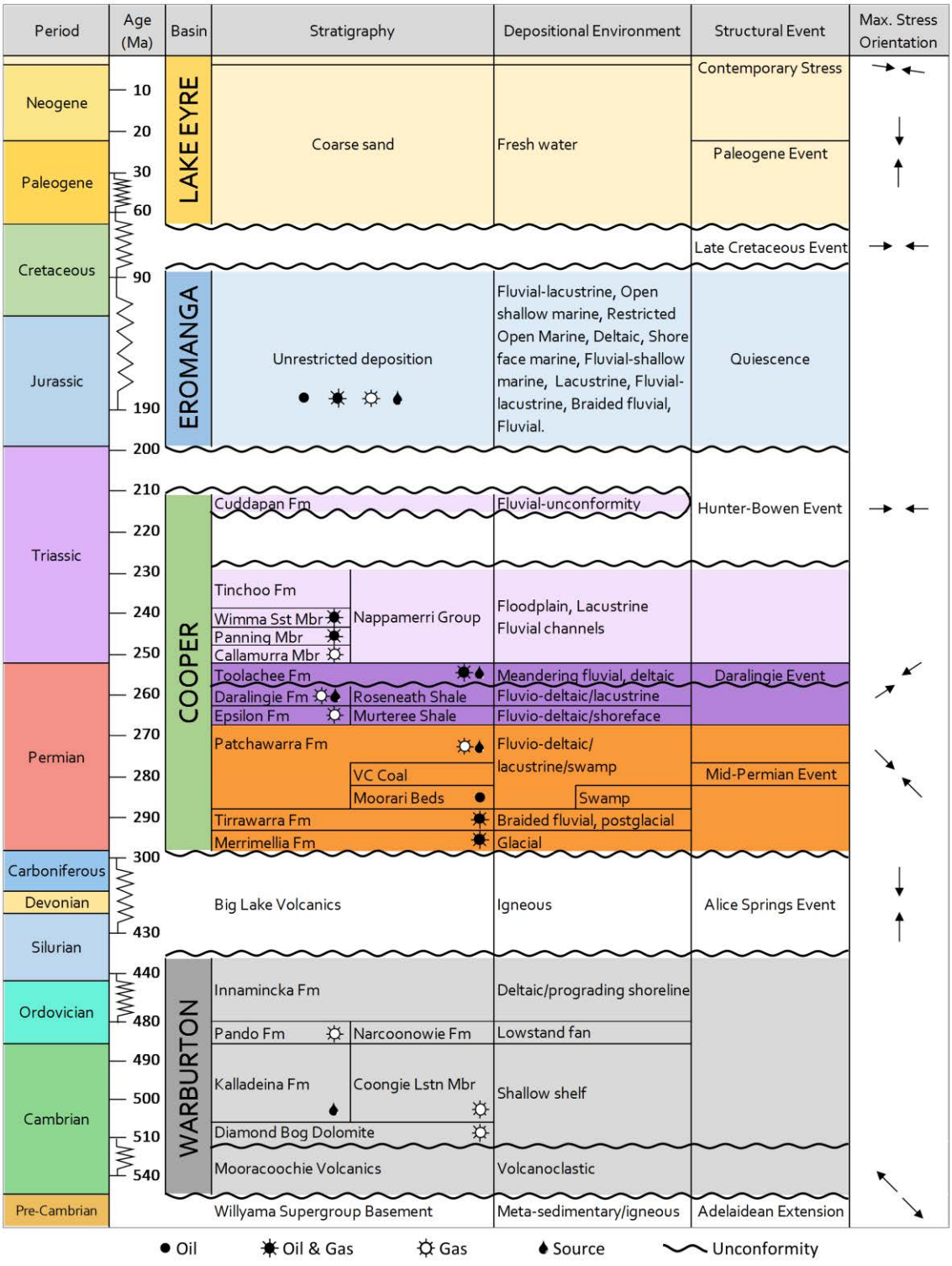

Figure 3-8: Cooper Basin Stratigraphic Column (after Kulikowski et al., 2016).

3.8.3 Cooper Basin Caprocks

There is limited literature on seal capacity analyses in the Cooper Basin. The following references provide research on MICP analyses conducted in the basin or nearby; Boult, (1996) investigated reservoir and seal couplets in the Eromanga Basin, Rezaee and Lemon, (1997) investigated permeability estimates using the Winland and Pittman methods from MICP analysis. Dragomirescu et al., (2001), evaluated the seal potential of four sealing

lithofacies from the Nappamerri Group and Cuddapan Formation of the Cooper Basin with MICP and mineralogical analysis. Wust et al., (2014) compared and contrasted the Eagle Ford (USA), Montney (Canada) and the Roseneath, Epsilon and Murteree Shale in the Cooper Basin. That study focussed on gas and liquid transport and used MICP to determine porosity and the diameter of the majority of the pore throats in the samples. Ahmad, (2014) investigated the unconventional potential of shale gas reservoirs in the Cooper Basin. Ahmad, (2014) concentrated on the Roseneath and Murteree shales and performed QEMSCAN, Micro and Nano-CT Scanning, SEM/EDX, XRD, MICP, helium and liquid pycnometry analyses.

3.9 WELL DESCRIPTION

3.9.1 **Tindilpie-11**

Tindilpie-11 was drilled in 2011 in PPL140 tenement by Santos in the Cooper Basin, South Australia in July 2011. The well was drilled on an anticlinal structure to a depth of 3165 m as a gas development well to the Greater Tindilpie field. The well objective was to determine the extent of channel sandstones within the Patchawarra Formation and to provide information on development well spacing. The Tirrawarra Sandstone was a secondary objective. The well had a total of six conventional coring runs totaling ~42 m over two separate objective intervals. A complete suite of geophysical logs were run in the well including an NMR log by Baker Hughes (MREX). The well encountered gas pay in both the Patchawarra and the Tirrawarra Formation. The well was classified as a single completion gas well (Kicas, 2012)

CHAPTER 4: EVALUATION OF MICP ANALYSIS – ACCURACY, REPEATABILITY AND COMPARABILITY

4.1 SUMMARY

Mercury Injection Capillary Pressure (MICP) analysis at the Australian School of Petroleum (ASP) is an accurate technique, within certain tolerance parameters, as demonstrated by running experimental standards of silica-alumina samples. The conformance correction method derived from this study is applied to the silica-alumina samples allowing minor corrections to be made to the raw MICP curves and porosities. This conformance correction methodology is used for MICP analyses in subsequent chapters. Compression of samples during MICP analysis was not observed; MICP analysis of fragile samples resulted in no disintegration, fracturing or dislodgement of grains following analyses.

The repeatability of MICP analyses on fairly uniform samples of a conventional cored interval of shale was investigated and provides a baseline of observable variation. Lastly, results of MICP analyses were compared to Nuclear Magnetic Resonance (NMR) analyses and helium pycnometry. This was undertaken to determine if there were any relationships between the techniques and to gauge the reliability of techniques. The results suggest that these techniques can be used reliably within individual wells but that any relationships between the techniques do not extend beyond the individual well.

4.2 INTRODUCTION

The investigation into MICP analysis is separated into three subsections: accuracy, repeatability and comparability.

Accuracy; this section reviews the following: 1) the use of blank corrections for calibrating the mercury porosimeter and removing artefacts from the results: 2) the analysis of Micromeritics silica alumina ® samples (standards) in the ASP‘s Micromeritics Autopore III Mercury Injection Porosimeter: 3) the method derived by this study for correcting MICP curves for conformance and 4) discussion on the compression of samples during MICP analyses. This section also provides the level of accuracy achievable from the ASP‘s

mercury porosimeter and the level of accuracy achievable from comparable mercury porosimeters at other laboratories.

Repeatability; this section reviews MICP analysis of samples taken as close as possible to one another at approximately the same depth (<5 cm apart); these are referred to as adjacent samples. Further, the section establishes the degree of variability that can be expected from MICP analyses of samples taken along 1.6 m of conventionally cored shale described by Dewhurst et al., (2002) as being fairly uniform. The degree of variability observed establishes the baseline to determine changes occurring as a result of warehousing (Chapter 7). This section also includes research into the effects of sample size and drying methods. The evidence is provided from the re-interpretation of results from Dewhurst et al., (2002).

Comparability; the section establishes the comparability of porosity and permeability measurements from three different techniques: 1) MICP analysis, 2) Nuclear Magnetic Resonance (NMR) and 3) helium pycnometry. The reliability of each technique is presented. All samples were taken from the conventional core and included both reservoir and sealing lithologies.

4.3 LITERATURE REVIEW

Accuracy

The accuracy of mercury porosimetry has been investigated by numerous authors (Winslow, 1978, Smitwick, 1982, Smith and Schentrup, 1986, y Leon, 1998, Sigal, 2009 and the ASTM International, 2011). In the discussion of the accuracy of mercury porosimetry three aspects are commonly focussed upon; the blank correction, compression of the sample and the conformance correction (Sigal, 2009).

The blank correction can be carried out in two ways; (i) As suggested by the American Society for Testing and Materials (ASTM International, 2011) a blank correction is carried out with a nonporous specimen with a similar compressibility to the rock sample being tested. This means that the MICP analysis is conducted with the blank sample and this allows the correction due to any compressibility in the system as a result of the penetrometer, porosimeter and temperature increases with pressure increases. The intruded volumes from the blank correction are then subtracted from the rock MICP analysis (y Leon, 1998, Sigal, 2009 and the International ASTM, 2011).(ii) The same blank correction can be carried out without a sample; the mercury porosimeter is run in the same method as if a sample was being analysed. The intruded volumes are stored as a blank correction and removed from all rock analysis, which is conducted for each penetrometer.

Smitwick, (1981), Smith and Schentrup, (1987) y Leon, (1998), Sigal, (2009) and International ASTM, (2011) suggest that there is the added effect of compression of the sample being tested. Further, Smith and Schentrup, (1987) suggest that depending on the composition of the sample and pore structure; the measured mercury intrusion volume may be entirely the result of sample compression. In a complication of the above y Leon, (1998) suggests that the mercury porosimeter pressures are applied equally in all directions and thus the collapse of the sample pore walls are unlikely, but in principle, samples could compress leading to additional mercury intrusion.

The conformance correction of MICP analysis is dealt with in different ways by different authors. The International ASTM does not mention a conformance correction for MICP analysis of rock samples. Schmitt et al., (2013) worked with uncorrected data that did have a blank correction, but not a conformance correction applied. On the other hand, Bailey, (2009) in Comisky et al., (2011) describes a conformance correction for samples of unconventional reservoirs. The rock sample is crushed for MICP analysis to allow pore access. The crushing of the rock increases conformance and hence the need for a conformance correction. Bailey, (2009) in Comisky, (2011) attributes mercury intrusion below 1000 psia for tight shales to the compressibility of the crushed particles. Bailey, (2009) conformance correction involves calculating pore volume per gram compressibility directly from the MICP analysis at each pressure equilibrium point. This allows the modelled compressibility to be graphed against the MICP analysis on a log-log plot and conformance and intrusion pressure to be interpreted. Sigal, (2009) suggests that the bulk volume calculation from the mercury porosimeter analysis should be compared to the bulk volume calculation from independent analysis to determine if conformance is affecting the MICP analysis. As acknowledged by Sigal, (2009) this is complicated by the fact that the rock volumes being analysed with MICP are often small and to obtain an accurate independent bulk volume requires larger samples. This is often not possible and may introduce error if the MICP sample is not representative of the larger sample. Sigal, (2013) suggests that a blank correction must be applied before applying a conformance correction. The conformance can be identified as a low-level incremental intrusion that resembles a saw blade edge. He then states that after a blank correction low-level incremental intrusion values can be zeroed and that any apparent intrusion below a few thousand psia for shales is a combination of blank correction and conformance correction.

Repeatability

Investigation of rock properties from well samples is somewhat problematic, especially when comparing results between adjacent samples or samples taken in close proximity with one another from within a formation. The problem with this analysis is that the adjacent samples and alike may not be homogeneous and heterogeneity may be influencing the results in combination with treatment effects. It then becomes difficult to separate what effects are due to heterogeneity and what effects are due to the treatments. To remove the added variable of heterogeneity, many authors perform analysis on homogeneous or model rock types (Olafuyi et al., 2006).

Perrin and Benson, (2009) investigated sub-core heterogeneities on CO_2 distribution in reservoir rocks. While this is not directly relevant to this study, it does provide an indication of possible heterogeneity within conventional core. The conventionally cored reservoirs were obtained from CRC-1 in the Otway Basin Australian and a Berea Sandstone. The core samples were between 6.35 cm - 20.32 cm in length and 5.08 cm in diameter. Both cores were injected with CO_2 and imaged with an X-ray CAT scanner to map porosity and CO_2 saturation during the experiment. The results of the CRC-1 core demonstrated CO_2 saturation is heterogeneous and low CO_2 saturations corresponded to low porosity regions and vice versa. The Berea Sandstone was also investigated and is described as having moderate heterogeneities by Perrin and Benson (2009) when investigating CO_2 saturation, although it was later described in Krause et al., (2009) as being relatively homogeneous when investigating permeability.

Comparability

Darlak et al., (2011) investigated the accuracy of MICP analysis of shale rock and the accuracy of the calculated porosity. The bulk density and grain density for the non-crushed samples were calculated from mercury pycnometry, while helium pycnometry was used for dry and powdered samples. These parameters and the mass of the sample can be used to calculate the porosity. This result was then compared to the porosity measurements with mercury porosimetry. The mercury porosimeter reached pressures that allowed the mercury to penetrate pore throats with diameters less than 40 micron. Their results indicate that the mercury is only penetrating 36-47 % of the pore space of non-crushed samples. They attribute the lack of mercury intrusion to inefficient extraction and drying, standard procedure parameters that are not suitable for shale porosity and/or due to the percentage of nanopores. To improve the porosity measurement from MICP analysis samples were granulated and powdered.

In a similar experiment Comisky et al., (2011) experimented with sample size and subsequent MICP porosity from a section of core (8050-8250 feet) taken from the Eagle Ford Formation in Central Texas. The core was crushed and analysed with helium pycnometry. The results show that the porosity was up to 4 % of the bulk volume. The samples then underwent hydrocarbon extraction and humidity oven drying. This resulted in an increase in porosity; a maximum of 10 % porosity of the bulk volume was recorded. Comisky et al., (2011) attribute this to water and oil affecting the initial porosity of fresh core samples.

Comisky et al., (2011) further experimented with sample size and the resulting porosity, bulk density and grain density measurements from MICP and low pressure helium pycnometry (LPP). Samples between -20+35 sieve sizes had the best agreement between results and bulk density from MICP agrees well with the measured bulk density from LPP via simple mercury immersion. Grain density agreement was unsuccessful due to a number of difficulties.

Comisky et al., (2011) presents the MICP curves before and after correction for conformance using the method of Bailey (2009) described in Comisky et al., (2011). The uncorrected MICP curves show a decreasing sharpness of the maximum point of inflection of the MICP curve with decreasing sample size. The initial mercury injection at low pressures increases with a decreasing sample size shown by the MICP curve. The conformance correction described by Bailey (2009) is applied firstly as a conformance correction and secondly as an intrusion correction. After each of these corrections, the MICP curves of the different sample sizes appear more similar. After the last correction process, the MICP curves closely overlay one another and this would likely lead to a similar threshold pressure interpretation had Comisky et al., (2011) decided to do so.

The advent of unconventional oil and gas plays has led to considerable research being published on porosity measurements and techniques as well as the subsequent determination of permeability for tight sands and shales (Glover et al, 2006 and Rezaee et al., 2012, Labani et al., 2012, Josh et al., 2012 and Anovitz and Cole, 2015). The following results are from authors who studied shales or tight sandstones with helium, MICP or NMR techniques on the same samples allowing a comparison of techniques and results. Mbia et al., (2014) investigated the Fjerritslev Formation in the Norwegian –Danish Basin which acts as a sealing lithology to Triassic sandstone reservoirs. They found that MICP porosities were 6-10 % lower than helium and NMR porosities from the same core. In a study by Lonnes et al., (2003) in which they compared NMR and helium porosity they found that NMR

porosity, in general, appears to predict porosity reasonably well. Coates et al., (1999) concurs suggesting that thousands of laboratory experiments verify an agreement of better than 1 % porosity between NMR porosity and helium porosity. However, Coates et al., (1999)‘s research is likely to have been primarily performed on conventional reservoir samples. Conversely, Dellinger and Esteban, (2014) found that NMR tended to overestimate porosity by 3-5 % in comparison to helium porosity for coarse and fine grained (tight) sandstone samples.

4.4 SECTION 1: ACCURACY

4.4.1 Blank Correction

The Mercury Porosimeter at the ASP (Figure 4-1) has a blank correction applied to all four penetrometers used in the analysis of seal and reservoir rock. A blank correction is carried out by performing MICP analyses without a sample and removing any apparent mercury intrusion (Sigal, 2009). The blank correction is applied to nullify the compressibility caused by the equipment. Newsham et al., (2004) suggest that pressures of up to 60,000 psia may cause changes in the volumes of the mercury porosimeter components, mercury, penetrometer and stem, the oil reservoir and system frame. All analyses conducted on the ASP mercury porosimeter have had such a blank correction applied.

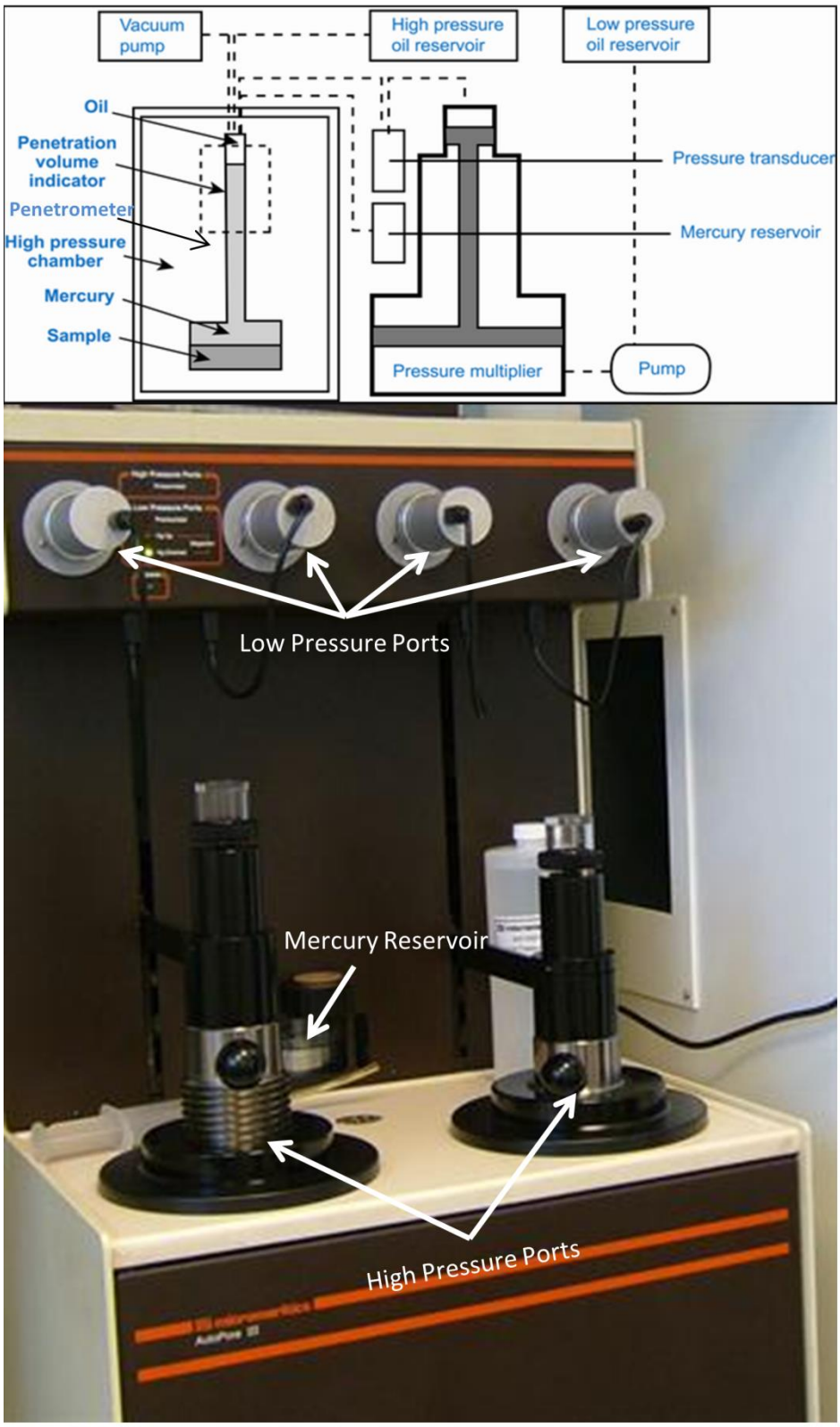

Figure 4-1: Micromeritics Autopore III Mercury Injection Porosimeter including technical diagram (Modified from Plymouth University, 2016 and Medicines Complete © 2016 Royal Pharmaceutical Society).

Methodology: The selected penetrometer is run without a rock sample to calibrate the equipment. This blank analysis provides the pressures and identifies any mercury intrusion i.e. any intrusion that occurs as a result of the equipment. Any such artefactual intrusion is subtracted from the results whenever that specific penetrometer is used to analyse a rock sample.

Results: The results of the blank correction for the four penetrometers at the ASP are shown in Table 4-1. The results indicate that the blank corrections can vary between 0 ml/g and 0.0332 ml/g. This correction can remove up to the equivalent of 5 % porosity from the final results.

Table 4-1: The blank corrections for penetrometers used for MICP analysis at the Australian School of Petroleum (ASP).

Bulb (cc)	Stem	Total Intrusion Volume (ml/g)	Equivalent Porosity (%)
5	1.31	0.0002	1
3	0.39	0	0
5	1.31	0.0332	3
3	0.39	0.0197	5

Discussion: The total intrusion and porosity measurements (Table 4-1) indicate that mercury intrusion is recorded in some penetrometers where no sample is being analysed. Further, the mercury intrusion volume varies between penetrometers and thus a blank correction is required for each penetrometer for accurate data interpretation. Thus the variation is penetrometer specific and not occurring as a result of the mercury porosimeter system.

4.4.2 **Silica-Alumina Standards**

The Micromeritics Autopore III Mercury Injection Porosimeter at the ASP is serviced yearly and calibrated with Micromeritics Silica Alumina ® standards regularly to ensure that the machine is within the standard tolerances. This yearly calibration is required as part of the quality assurance for analytical analysis. The standards are normally run on the high-pressure cycle only and have thus not been included in the following analysis. Upon this

study‘s request, the last three accuracy checks (i.e. where the Micromeritics Silica Alumina ® standard is analysed by the mercury porosimeter to check the MICP analyses is within the standard parameters) were run in full and establish the maximum amount of variation that can be expected between MICP analyses. This allows a determination of the level of achievable accuracy from the mercury porosimeter.

Methodology: Approximately 1 g of Silica Alumina ® standard sample is analysed with the mercury porosimeter. The total intrusion from the data file is checked against the standard parameters of the silica-alumina to determine if the porosimeter is working within the given tolerances.

Results: The MICP results for the analysis of the standard samples indicate that the bulk density and grain density vary by 0.03 g/ml and 0.05 g/ml with a standard deviation of 0.01 and 0.02 respectively (Table 4-2.). The porosity averaged 57.88 % with a maximum variation between samples of 1.03 %. The total intrusion volume for the standard sample at 60,000 psia should be between 0.50 ml/g ±0.02 ml/g. The results for the mercury porosimeter and penetrometer are all within the given tolerances.

The threshold pressures using the Incremental Pore Volume (IPV) technique and Maximum Inflection (MI) technique are in nearly perfect agreement with one another (Table 4-2), where the threshold pressures average 20728 psia. Both techniques pick the threshold pressure at the same pressure equilibrium point for all three standards (refer to keywords and their meanings for a description of pressure equilibrium point).

Table 4-2: MICP results from analysis of Micromeritics Silica Alumina standards.

Standards	Sample Weight (g)	Total Intrusion (ml/g)	Bulk Density (g/ml)	Grain Density (g/ml)	Porosity (%)	IPV Threshold Pressure (psia)	MI Threshold Pressure (psia)
		Raw	Raw	Raw	Raw	Raw	Raw
002-270 Silica Alumina	1.04	0.506	1.15	2.76	58.29	20733	20733
002-278 Silica Alumina	1.07	0.494	1.18	2.81	58.10	20697	20697
002-086 Silica Alumina	1.03	0.485	1.18	2.76	57.26	20756	20756
Average	1.04	0.495	1.17	2.78	57.88	20728.67	20728.67
SD	0.02	0.010	0.01	0.02	0.55	29.74	29.74

The MICP curves and incremental pore volumes for the three standard samples are in nearly perfect agreement with one another with an almost perfect match of MICP curves (Figure 4-2). The only minor discrepancy observed is in sample 002-086 which has an MICP curve with slightly lower mercury saturation at ~20,000 psia.

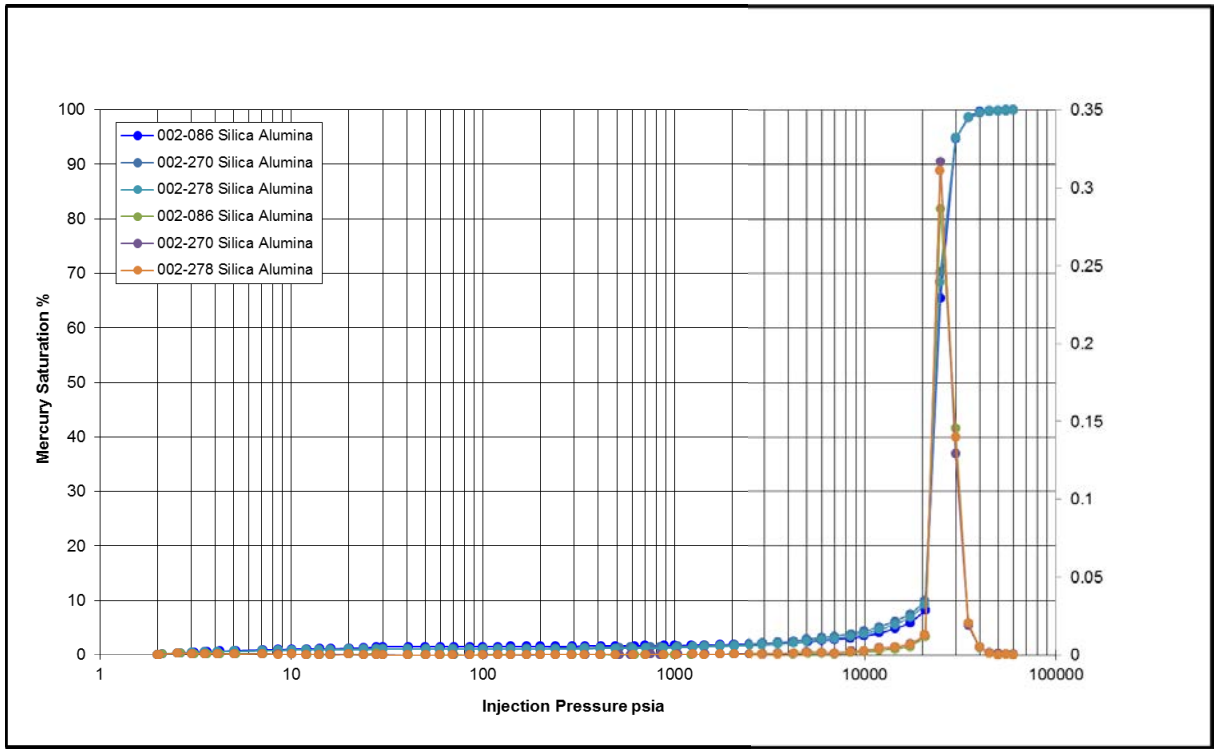

Figure 4-2: MICP curves and incremental pore volumes from analysis of Micromeritics Silica Alumina standards.

Discussion: The threshold pressure results interpreted with the IPV and MI techniques give the same results which indicate that both techniques are comparable for the analysis of Micromeritics Silica Alumina standard and can be used for subsequent rock sample analysis.

The minimum level of accuracy obtainable with the ASP mercury porosimeter is ± 0.015 g/ml and ± 0.025 g/ml and ± 0.515 % for bulk density, grain density and porosity measurements respectively. The given tolerance for the Micromeritics Silica Alumina standard is 0.50 ml/g ± 0.02 ml/g total intrusion volume. The three standards run are all within these tolerances and the average of the three samples is 0.4949 ml/g suggesting that on average the machine is reading slightly lower than the optimum 0.50 ml/g but is still well within the tolerances.

The MICP curves and incremental volumes are in nearly perfect agreement with one another indicating a high level of accuracy. These results are considered the minimum level of

accuracy achievable from the mercury porosimeter as the results reflect the variation of both the Micromeritics Silica Alumina standard and the mercury porosimeter.

4.4.3 **Conformance Correction**

Conformance or closure as defined by Vavra et al. (1992) as ―The process whereby mercury fills surface irregularities, such as nicks, gouges, small fractures, or vugs on the sample". Conformance can be further defined as the difference between entry pressure (Pe) and the displacement pressure (Pd) which can be estimated from the MICP curve and incremental pore volume. Conformance and compressibility are considered the two most likely causes of error in MICP measurements (Newsham et al., 2004). Newsham et al. (2004) and McPhee et al., (2015) suggest that there are no published standards for correcting conformance, that the methods are often subjective, commonly not released by the laboratory and thus the following method is suggested by this study.

Methodology: Please see Appendix A, A.4 for the conformance correction methodology.

Results: MICP analysis of standard samples and subsequent conformance correction resulted in the bulk density increasing from an average of 1.17 g/ml to 1.18 g/ml and the standard deviation increasing from 0.01 to 0.02 (Table 4-3). The grain density remained the same at 2.78 g/ml after conformance correction. However, the standard deviation increased from 0.02 to 0.03. The porosity decreased from an average of 57.88 % to 57.42 % and the standard deviation increased from 0.55 to 0.61. The average total intrusion volume for the three samples was 0.495 ml/g and after conformance correction, the average decreased to 0.486 ml/g. The changes after conformance correction were all very minor.

Table 4-3: MICP results from analysis of Micromeritics Silica Alumina standards with and without conformance correction.

Standards	Sample Weight (g)	Total Intrusion (ml/g)		Bulk Density (g/ml)		Grain Density Raw (g/ml)		Porosity (%)		IPV Threshold Pressure (psia)		MI Threshold Pressure (psia)	
		Raw	Cor.	Raw	Cor.	Raw	Cor.	Raw	Cor.	Raw	Cor.	Raw	Cor.
002-270 Silica Alumina	1.04	0.506	0.496	1.15	1.17	2.76	2.76	58.29	57.84	20733	20733	20733	20733
002-278 Silica Alumina	1.07	0.494	0.486	1.18	1.19	2.81	2.81	58.10	57.69	20697	20697	20697	20697
002-086 Silica Alumina	1.03	0.485	0.476	1.18	1.19	2.76	2.76	57.26	56.72	20756	20756	20756	20756
Average	1.04	0.495	0.486	1.17	1.18	2.78	2.78	57.88	57.42	20728.67	20728.67	20728.67	20728.67
SD	0.02	0.0104	0.0102	0.01	0.02	0.02	0.03	0.55	0.61	29.74	29.74	29.74	29.74

The conformance corrected MICP curves for the Micromeritics Silica Alumina standard samples are similar to one another (Figure 4-3). In comparison to the uncorrected sample analysis (Figure 4-2), the conformance corrected MICP curves have no mercury saturation until ~4000 psia whereas the uncorrected samples have minor saturation from ~1000 psia upwards. The conformance correction has not altered the location of the maximum inflection point in this case but has resulted in a change of shape to a more gradual maximum inflection.

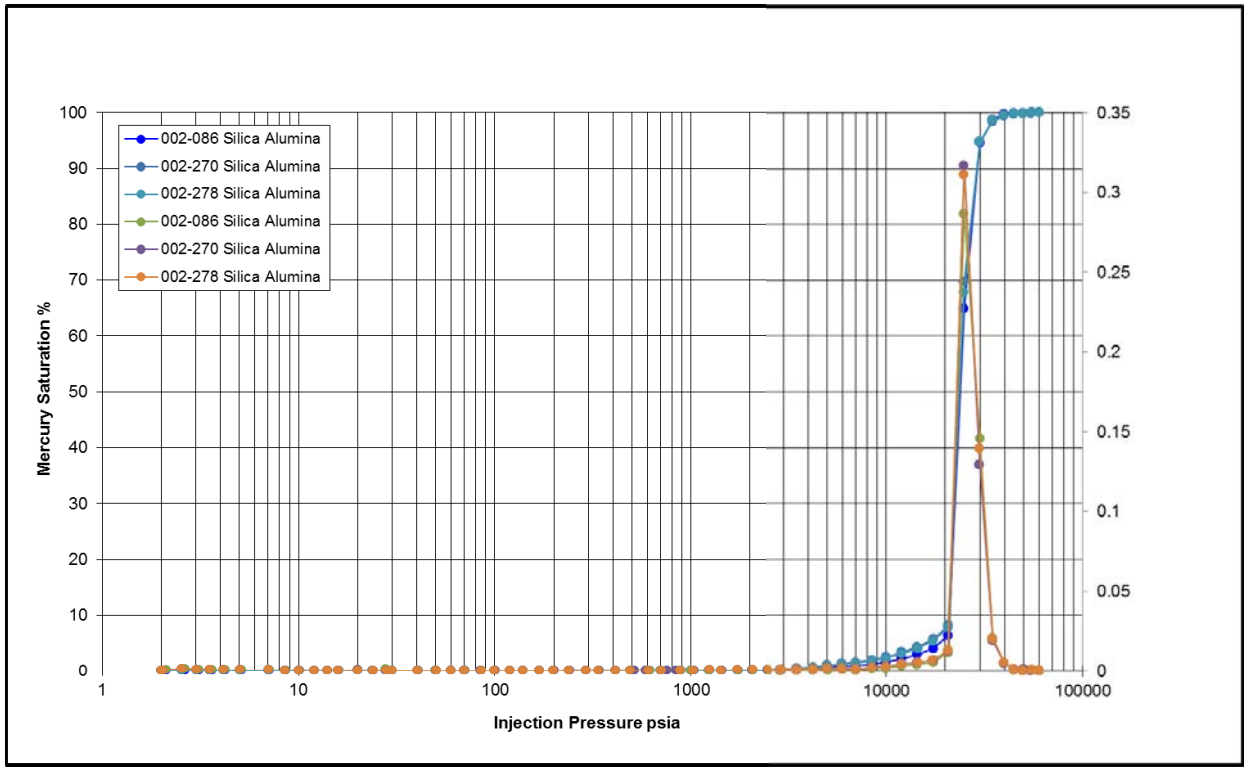

Figure 4-3: MICP curves and incremental pore volumes from analysis of Micromeritics Silica Alumina standards with conformance correction.

Discussion: The conformance correction of the standard samples has decreased the total intrusion volume average from 0.495 ml/g to 0.486 ml/g (Table 4-3). This is still within the tolerance parameters for the standard being 0.50 ml/g ± 0.02 ml/g. The conformance correction has reduced the total intrusion standard deviation between samples from 0.0104 to 0.0102. However, it has resulted in one standard sample (002-086) being outside of the tolerance parameters with a total intrusion after conformance correction of 0.476 ml/g. This, however, is to be expected as the tolerance parameters are for standard samples results without conformance correction.

The conformance correction has reduced the average porosity from 57.88 % to 57.42 % which is only minor and is to be expected with standard samples. The uncorrected bulk

density and grain density average result is 1.17 g/ml and 2.78 g/ml respectively. After conformance correction, the bulk density increases slightly to 1.18 g/ml and the grain density remains the same at 2.78 g/ml. The standard deviation of the bulk density, grain density and porosity has increased slightly suggesting that the conformance correction has introduced more variation than was observed in the uncorrected results. Firstly, the increase in standard deviation is minor. Secondly, there is little conformance that requires correction on the standard samples. Thus the conformance correction may not be quite perfect, providing the increased variation observed is not a property of the standard samples, which has been assumed in this case. The conformance corrected MICP curves and incremental pore volumes are in nearly perfect agreement with one another indicating that no visible variation has been introduced and the conformance correction is in agreement with the uncorrected samples. Given that the porosities have only shifted marginally (0.46 %), the MICP curves remain in agreement and the standard deviation between results (porosity, bulk density and grain density) have only increased slightly over the uncorrected samples, it is suggested that the proposed method for conformance correction is effective.

4.4.4 **Compression of Samples During MICP Analysis**

This section addresses the concern that mercury porosimetry is compressing the sample; causing particle breakdown and opening otherwise closed pores as the mercury is injected into the penetrometer, thus not reflecting the actual pore throat network of the sample (Shafer and Neasham 2000, Bustin et al., 2008 and McPhee et al., 2015). These authors have suggested that a blank cell correction should be applied with the addition of a non-porous sample with a bulk volume and composition similar to the samples being analysed. This study suggests that compression of the sample does not occur, even with mercury intrusion pressures up to 60,000 psia. This evidence for this comes from detailed analyses of samples from the Brigadier and Mungaroo Formations from Thebe-2, Exmouth Plateau.

Thebe-2

Please see section 3.5.2 for Thebe-2 well description.

The Thebe-2 core was stabilised at the well site with Aptane resin by ACS Laboratory technicians and subsequently shipped to the ACS Laboratories in Perth. The core in barrels was cut into 1 m sections (both the barrel and the core) and stored in 2/ 3 barrels in the WA core library in Carlisle. The cored sand intervals were mostly unconsolidated and required freezing for analysis.

Samples were taken by Paul Stephenson (Core Librarian) at the Department of Mines and Petroleum, Western Australia. There were difficulties in sampling the core due to its friability and it was described in one section as being similar to beach sand (Stephenson pers.com, 2015). The Thebe-2 samples were analysed with MICP as part of the NMR synthetic MICP analysis detailed later in Chapter 7.

Methodology: The Thebe-2 samples included sandstone, shale and siltstones, which during preparation often disintegrated into grains. Some of the grains were dislodged during the cutting operation and, while being transported to the drying oven and mercury porosimeter. These samples had a similar strength to soil clods.

The shales were more lithified than the sandstones although they were still fragile and also partially disintegrated during the cutting process. They crumbled into smaller shale pieces rather than into individual grains like the sandstones.

Results: Table 4-4 provides the sample depth, interpreted lithology and whether the sample disintegrated after being analysed with the mercury porosimeter. Significantly, none of the samples broke after being analysed at pressures of up to ~60,000 psia and no grains were dislodged and found in the penetrometer as might be expected from such fragile samples. The sample from a depth of 2298.13 m broke apart two days after being analysed while drying in the fume hood.

Table 4-4: Thebe -2 sample depths, lithology and subsequent state after MICP analysis.

Sample Depth (m)	Lithology	Disintegration after MICP Analysis Yes/No	Dislodged grains in penetrometer after analysis
2182.35	Fine Sandstone	No	No
2188.37	Siltstone	No	No
2246.5	Shale	No	No
2247.2	Sandstone	No	No
2259.05	Siltstone	No	No
2269.35	Shale	No	No
2275.8	Sandstone	No	No
2298.13	Fine Sandstone	No – sample broke into two pieces two days after analysis	No
2381.66	Fine Sandstone	No	No

The samples are imaged in (B. Appendix Figure B-1) after MICP analysis. Unfortunately, sample (2246.5 m was lost). Sample 2298.13 m broke two days after analysis. Sample 2259.05 m was cut to fit the penetrometer and during cutting, it broke into two pieces. It was subsequently analysed as two pieces due to the fragile nature of the rock and the concern of not being able to produce another cube without disintegration.

Discussion: The anecdotal evidence above suggests that there is no compression of the sample during MICP analysis. If compression occurs during MICP analysis, then these fragile samples would have disintegrated. Thus the production of the vacuum during the first stage of the MICP analysis is sufficient to allow intrusion without producing an opposing force leading to the breakage/ damage of the sample. Further, the anecdotal evidence would suggest that the force of the mercury intruding into the sample does not compress the sample but only enters the sample pore space. The sample that broke apart two days after analysis may have been a result of the capillary forces produced as the mercury from the sample evaporated, further evidencing the fragility of the samples.

4.5 SECTION 2: REPEATABILITY

The repeatability of MICP analysis on adjacent samples and samples over a conventionally cored (CC) interval are investigated in the Saracen-1 well.

4.5.1 Saracen-1, Barrow Sub-basin

Please see section 3.5.1 for Saracen-1 conventional core and well description.

The 4.38m of core retrieved from Saracen-1 was determined to be the Muderong Shale and was transported in an aluminum barrel to Core Laboratories, Perth on the 1st of February 2000. The CC lithology was described as claystone in the WCR (Banfield, 2000). The core was wiped clean of drilling fluids before being slabbed using mineral oil as blade lubricant. Subsequently, 13 core plugs were drilled with mineral oil as the lubricant, in the top 1.6 m of core. These plugs were placed in jars filled with mineral oil.

Dewhurst et al., (2002) investigated the microstructural and petrophysical properties of plugs from the conventional core. As part of their investigations, they analysed 29 samples and, based on numerous analyses including MICP, XRD and the BSE microscope described the core as being fairly uniform. The aim of their research was to determine if the capillary breakthrough of the top seal was a factor limiting hydrocarbon column heights in the basin. The analyses were performed using different drying methods to evaluate the effect on MICP threshold pressures. The three drying techniques were air drying, freeze drying and vacuum pump drying.

The replication of MICP analyses on relatively uniform core allowed the results to be re-interpreted and the MICP curves, bulk densities, grain densities, porosities and interpreted threshold pressures, with and without the conformance correction derived from this study, to be compared. This provides an indication of the accuracy and repeatability of MICP analysis on adjacent samples and samples over the 1.6 m interval of the densely sampled conventional core. These results will demonstrate the similarity of adjacent samples and whether adjacent samples can be used as a guide to the effects of warehousing (Chapter 7).

The samples were analysed with XRD and semi-quantified by Mark Raven at the CSIRO (Appendix B Table B-1). The mineralogical analyses demonstrate that the samples have a similar mineralogy and are dominated by quartz and smectite, with moderate mica and kaolinite and, trace amounts ($\leq$ 5 %) of chlorite, pyrite, siderite, albite and orthoclase. The BSE images (Appendix B Figure B-2) show quartz and glauconitic grains and, pyrite framboids dispersed in a matrix of illite/ smectite clays and other unidentified minerals. The

quartz and glauconite grains are generally not in contact with one another but are distributed throughout the clay matrix (Dewhurst et al., 2002).

Methodology modifications specific to Saracen-1: The rock samples were not oven dried at ~55° C but were air dried for a two week period, freeze dried or vacuum pump dried. The BSE images taken of the rock samples were acquired by impregnating resin into the samples before polishing and imaging.

Results: The uncorrected MICP curves from the 11 air dried Muderong Shale samples from the 1.6 m cored interval from Saracen-1 are shown in the Appendix B Figure B-3. The MICP curves are similar to one another; both in shape and position on the graph but with two exceptions; samples 1118.34 m and 1119.24 m which have MICP curves that differ from the remaining nine samples. These nine samples have MICP curves that show a variation of cumulative mercury saturation up to15 %, after which they show similar mercury saturation with minor separation.

The 11 air dried conformance corrected MICP curves (Appendix B Figure B-4) are similar to one another. The 11 MICP curves from the maximum inflection point upwards to 70 % mercury saturation all are similar. The MICP curves show slight variation from 70 % mercury saturation upward to the mercury porosimeter pressure limit of 60,000 psia.

The MICP curve of sample 1118.34 m is no longer an outlier after the conformance correction has been applied. The greater conformance of this sample is also indicated by the jumps in cumulative mercury saturation between 50 psia and 100 psia relative to the maximum inflection point at ~6000 psia in the uncorrected MICP curve (Appendix B Figure B-3). The analysis of sample 1119.24 m shows an unusual MICP curve with a number of equilibrium points having little or no further injection of mercury with increased pressure in contrast to the other samples. These points of little mercury injection are followed by significant jumps in the injection of mercury with further increases in pressure which results in the realignment of the MICP curve. This is observed between 10,000 psia and 30,000 psia (Appendix B Figure B-4).

The results shown in Table 4-5 indicate that the air dried samples have relatively homogeneous properties. The corrected bulk density and grain density for all samples are similar, with an average of 2.28 g/ml for the bulk density and an average of 2.74 g/ml for the grain density. The threshold pressures interpreted using the incremental pore volume method (IPV) are also similar with most of the samples having a threshold pressure of ~4990 psia. There are three exceptions where the threshold pressure was interpreted at the pressure

equilibrium point before or after ~4990 psia.The threshold pressures interpreted using the maximum inflection (MI) point method are all at the same pressure equilibrium point ~5980 psia. There is no observed relationship between the interpreted threshold pressure and sample weight, bulk density or corrected grain density for the 11 samples.

The average corrected porosity, sample volume per gram, grain volume per gram and pore volume per gram for the samples is 16.88 %, 0.439 ml/g, 0.365 ml/g and 0.074 ml/g respectively (Table 4-5). The sample at 1119.42 m weighing 0.52 g has the highest corrected porosity with 1.75 % greater porosity than the average of the samples. However, the sample at 1118.34 m weighing 1.95 g has porosity 0.09 % less than sample 1119.42 m weighing 0.52 g. Thus, there was no observed relationship between the weight of the samples (The 11 samples weighed between 0.52 g and 2.23 g and their corrected porosities.

Table 4-5: MICP data for the 11 air dried original samples from the 1.6m interval of conventional cored Muderong Shale from Saracen-1 (Re-interpretation of Dewhurst et al., 2002 analyses).

Sample Depth (m)	Sample Weight (g)	Porosity (%)		Bulk Density (g/ml)		Grain Density (g/ml)		Sample Volume (ml/g)		Pore Volume (ml/g)		Grain Volume (ml/g)		IPV Threshold Pressure (psia)		MI Threshold Pressure (psia)	
		Raw	Cor.	Raw	Cor.	Raw	Cor.	Raw	Cor.	Raw	Cor.	Raw	Cor.	Raw	Cor.	Raw	Cor.
1118.15	1.58	16.80	15.6	2.26	2.29	2.71	2.71	0.443	0.436	0.074	0.068	0.369	0.369	4976	4976	5971	5971
1118.22	1.68	16.56	15.39	2.28	2.3	2.73	2.72	0.439	0.434	0.073	0.067	0.366	0.366	5095	5095	5991	5991
1118.34	1.95	21.27	18.54	2.22	2.3	2.82	2.82	0.450	0.435	0.096	0.081	0.354	0.354	4995	4995	5976	5976
1118.79	1.39	17.46	17.46	2.22	2.23	2.69	2.69	0.450	0.448	0.079	0.077	0.371	0.371	5993	5993	5993	5993
1118.87	1.44	16.13	15.55	2.25	2.26	2.68	2.68	0.445	0.442	0.072	0.069	0.373	0.373	4985	4985	5980	5980
1118.96	1.52	17.07	16.23	2.32	2.32	2.8	2.8	0.431	0.427	0.074	0.069	0.358	0.358	4986	4986	5983	5983
1119.08	0.94	17.31	17	2.22	2.23	2.69	2.68	0.450	0.449	0.078	0.076	0.373	0.373	4326	4326	5976	5976
1119.24	0.92	17.38	16.99	2.24	2.25	2.71	2.71	0.446	0.444	0.078	0.076	0.369	0.369	4987	4987	5984	5984
1119.42	0.52	19.23	18.63	2.27	2.29	2.81	2.81	0.440	0.437	0.084	0.081	0.356	0.356	5007	5007	5981	5981
1119.58	2.23	17.22	16.35	2.23	2.26	2.7	2.7	0.448	0.443	0.077	0.073	0.371	0.371	5980	5980	5980	5980
1119.75	1.82	18.88	17.95	2.29	2.31	2.82	2.82	0.437	0.432	0.082	0.078	0.355	0.355	4982	4982	5980	5980
Average	1.45	17.76	16.88	2.25	2.28	2.74	2.74	0.443	0.439	0.079	0.074	0.365	0.365	5119	5119	5981	5981
SD	0.50	1.48	1.17	0.03	0.03	0.06	0.06	0.006	0.007	0.007	0.005	0.008	0.008	475	475	6	6

The uncorrected MICP curves from the 13 samples of Muderong Shale from Saracen-1 were freeze dried (Appendix B Figure B-5). The MICP curves show similar general agreement with one another and are similar to the MICP curves of the 11 air dried adjacent samples from the same interval. The MICP curve for sample 1119.58 m is a notable outlier. The MICP curves are least well grouped between 0 % and 20 % mercury saturation; notably, sample 1119.58 m. However, the 13 samples do show a similar trend. The MICP curves for all samples between 20 % and 70 % mercury saturation are all in close agreement as is the maximum point of inflection. Similar to the MICP curves of the air dried samples, the MICP curves from 70 % mercury saturation upwards show increased separation (become less constrained) before once again coming into agreement at 100 % mercury saturation. This coming into agreement of the MICP curves at 60,000 psia was not observed in the air-dried samples.

The MICP curves for the freeze-dried samples with conformance correction are shown in Appendix B Figure B-6. These MICP curves show much better grouping and agreement between 0 % and 20 % mercury saturation, including the maximum inflection point than without conformance correction. This includes sample 1119.58 m. The MICP curves above 20 % mercury saturation remain consistent or more similar to one another than the uncorrected MICP curves.

The results shown in Table 4-6 indicate that the samples are fairly homogeneous with properties similar to the air dried samples (Table 4-5). The corrected porosities for the 13 samples averaged 17.15 %, the corrected bulk densities averaged 2.24 g/ml and the grain densities averaged 2.71 g/ml. The threshold pressures interpreted with the IPV method vary between 4978 psia and 5988 psia while the threshold pressures interpreted with the MI method are all at the same pressure equilibrium point 5980 psia. The corrected sample volume per gram was similar with an average of 0.45 ml/g and a maximum difference between samples of 0.023 ml/g. The grain volume per gram was an average of 0.370 ml/g. The pore volume per gram showed greater variation with an average of 0.076 ml/g and a maximum difference of 0.013 ml/g between samples. There is no observed relationship between threshold pressures and sample weights, corrected porosities, bulk densities or grain densities. There is also no relationship between sample weight and the corresponding porosity as was found with the air dried samples in Table 4-5

Table 4-6: MICP data for the 13 freeze dried original samples from a 1.6m interval of conventionally cored Muderong Shale from Saracen-1 (Re-interpretation of Dewhurst et al., 2002 analyses).

Sample Depth (m)	Sample Weight (g)	Porosity (%)		Bulk Density (g/ml)		Grain Density (g/ml)		Sample Volume (ml/g)		Pore Volume (ml/g)		Grain Volume (ml/g)		IPV Threshold Pressure (psia)		MI Threshold Pressure (psia)	
		Raw	Cor.	Raw	Cor.	Raw	Cor.	Raw	Cor.	Raw	Cor.	Raw	Cor.	Raw	Cor.	Raw	Cor.
1118.15	1.83	17.29	16.96	2.22	2.23	2.68	2.68	0.451	0.449	0.078	0.076	0.373	0.373	4995	4995	5975	5975
1118.22	0.81	19.46	18.15	2.2	2.24	2.73	2.73	0.455	0.445	0.089	0.081	0.366	0.364	4993	4993	5983	5983
1118.34	1.6	19.08	18.4	2.22	2.24	2.75	2.75	0.450	0.443	0.086	0.082	0.366	0.366	5003	5003	5980	5980
1118.79	2.1	16.74	15.58	2.24	2.28	2.69	2.69	0.446	0.440	0.075	0.069	0.371	0.371	4992	4992	5980	5980
1118.87	1.3	19.49	18.57	2.27	2.3	2.82	2.82	0.441	0.436	0.086	0.081	0.355	0.355	5986	5986	5986	5986
1118.96	1.77	17.16	16.27	2.21	2.23	2.66	2.66	0.453	0.449	0.078	0.073	0.376	0.376	4984	4984	5981	5981
1119.08	1.14	16.53	15.72	2.2	2.22	2.64	2.64	0.454	0.450	0.075	0.071	0.379	0.379	4992	4992	5977	5977
1119.19	0.78	18.23	16.69	2.19	2.24	2.68	2.68	0.456	0.447	0.083	0.075	0.373	0.373	5988	5988	5988	5988
1119.24	0.82	18.64	17.81	2.23	2.26	2.74	2.75	0.449	0.444	0.084	0.079	0.366	0.366	4989	4989	5983	5983
1119.42	1.06	17.75	17.62	2.23	2.24	2.72	2.72	0.448	0.447	0.080	0.079	0.368	0.368	4978	4978	5979	5979
1119.5	1.97	17.25	16.42	2.16	2.18	2.61	2.60	0.464	0.459	0.080	0.075	0.384	0.384	4986	4986	5980	5980
1119.58	0.98	18.5	16.24	2.19	2.25	2.69	2.69	0.456	0.443	0.085	0.072	0.371	0.371	5973	5973	5973	5973
1119.75	1.61	19.77	18.49	2.23	2.26	2.77	2.78	0.449	0.442	0.089	0.082	0.360	0.360	4994	4994	5993	5993
Average	1.37	18.15	17.15	2.21	2.24	2.71	2.71	0.452	0.446	0.082	0.076	0.370	0.370	5219	5219	5981.38	5981
SD	0.47	1.11	1.08	0.03	0.03	0.06	0.06	0.006	0.006	0.005	0.005	0.008	0.008	435	435	5.38	5

The results shown in Table 4-7 indicate that the MICP results are relatively consistent between the air dried and freeze dried adjacent samples. The results from the vacuum pump method of drying tend to have more variation than is observed between the other drying methods. Although the results from the vacuum pump drying method can be within the range of the adja*c*ent sample results of the other drying methods, they commonly have one or more measured properties that are inconsistent. For example, sample 1118.15 m which has a high threshold pressure, sample 1119.58 m which has a higher corrected porosity by ~1.2 % over the average. Sample 1119.75 m which has a lower porosity by 1.06 % and a higher threshold pressure over the average of the samples. The vacuum pump dried sample analysis of 1118.34 m has inconsistent results for all measured properties. Thus the results from the samples dried using the vacuum pump method will not be taken into account in the comparison of adjacent samples and have not been taken into account in the average and standard deviation (SD) Table 4-7.

Table 4-7: MICP data for the 11 adjacent original samples of conventional cored Muderong Shale from Saracen-1 dried using one of three techniques; air drying, freeze drying and vacuum pump drying (Re-interpretation of Dewhurst et al., 2002 analyses).

Sample Depth (m)	Drying Method	Sample Weight (g)	Porosity (%)		Bulk Density (g/ml)		Grain Density (g/ml)		Sample Volume (ml/g)		Pore Volume (ml/g)		Grain Volume (ml/g)		IPV Threshold Pressure (psia)		MI Threshold Pressure (psia)	
			Raw	Cor.	Raw	Cor.	Raw	Cor.	Raw	Cor.	Raw	Cor.	Raw	Cor.	Raw	Cor.	Raw	Cor.
1118.15	Air	1.58	16.8	15.6	2.26	2.29	2.71	2.71	0.443	0.436	0.074	0.068	0.369	0.369	4976	4976	5971	5971
	Freeze	1.83	17.29	16.96	2.22	2.23	2.68	2.68	0.451	0.449	0.078	0.076	0.373	0.373	4995	4995	5975	5975
	Vac and Pump	0.97	18.79	16.71	2.24	2.3	2.76	2.76	0.447	0.436	0.084	0.073	0.363	0.363	6977	6977	5975	5975
Average		1.71	17.05	16.28	2.24	2.26	2.70	2.70	0.45	0.44	0.08	0.07	0.37	0.37	4985.50	4985.50	5973.00	5973.00
SD		0.18	0.35	0.96	0.03	0.04	0.02	0.02	0.01	0.01	0.00	0.01	0.00	0.00	13.44	13.44	2.83	2.83
1118.22	Air	1.68	16.56	15.39	2.28	2.3	2.73	2.72	0.439	0.434	0.073	0.067	0.366	0.367	5095	5095	5991	5991
	Freeze	0.81	19.46	18.15	2.2	2.24	2.73	2.73	0.455	0.447	0.089	0.081	0.366	0.366	4993	4993	5983	5983
Para Inject	Vac and Pump	0.72	15.93	15.68	2.09	2.09	2.48	2.48	0.479	0.478	0.076	0.075	0.403	0.403	4983	4983	5973	5973
	Vac and Pump	1.79	18.7	17.61	2.19	2.21	2.69	2.69	0.457	0.451	0.085	0.079	0.371	0.371	5977	5977	5977	5977
Average		1.25	18.01	16.77	2.24	2.27	2.73	2.73	0.45	0.44	0.08	0.07	0.37	0.37	5044.00	5044.00	5987.00	5987.00
SD		0.62	2.05	1.95	0.06	0.04	0.00	0.01	0.01	0.01	0.01	0.01	0.00	0.00	72.12	72.12	5.66	5.66
1118.34	Air	1.95	21.27	18.54	2.22	2.3	2.82	2.82	0.45	0.435	0.096	0.081	0.354	0.354	4995	4995	5976	5976
	Freeze	1.6	19.08	18.4	2.22	2.24	2.75	2.75	0.45	0.446	0.086	0.082	0.366	0.366	5003	5003	5980	5980
Outlier	Vac and Pump	0.44	27.38	27.29	2.17	2.181	3	3	0.458	0.458	0.125	0.125	0.333	0.333	6978	6978	6978	6978
Average		1.78	20.18	18.47	2.22	2.27	2.79	2.79	0.45	0.44	0.09	0.08	0.36	0.36	4999.00	4999.00	5978.00	5978.00
SD		0.25	1.55	0.10	0.00	0.04	0.05	0.05	0.00	0.01	0.01	0.00	0.01	0.01	5.66	5.66	2.83	2.83
1118.79	Air	1.39	17.46	17.46	2.22	2.23	2.69	2.69	0.45	0.448	0.079	0.077	0.371	0.371	5993	5993	5993	5993

	Freeze	2.1	16.74	15.58	2.24	2.28	2.69	2.69	0.446	0.440	0.075	0.069	0.371	0.371	4992	4992	5980	5980
Average		1.75	17.10	16.52	2.23	2.26	2.69	2.69	0.45	0.44	0.08	0.07	0.37	0.37	5492.50	5492.50	5986.50	5986.50
SD		0.50	0.51	1.33	0.01	0.04	0.00	0.00	0.00	0.01	0.00	0.01	0.00	0.00	707.81	707.81	9.19	9.19
1118.87	Air	1.44	16.13	15.55	2.25	2.26	2.68	2.68	0.445	0.442	0.072	0.069	0.373	0.373	4985	4985	5980	5980
	Freeze	1.3	19.49	18.57	2.27	2.3	2.82	2.82	0.441	0.436	0.086	0.081	0.355	0.355	5986	5986	5986	5986
Average		1.37	17.81	17.06	2.26	2.28	2.75	2.75	0.44	0.44	0.08	0.07	0.36	0.36	5485.50	5485.50	5983.00	5983.00
SD		0.10	2.38	2.14	0.01	0.03	0.10	0.10	0.00	0.00	0.01	0.01	0.01	0.01	707.81	707.81	4.24	4.24
1118.96	Air	1.52	17.07	16.23	2.32	2.32	2.8	2.8	0.431	0.427	0.074	0.069	0.358	0.358	4986	4986	5983	5983
	Freeze	1.77	17.16	16.27	2.21	2.23	2.66	2.66	0.453	0.449	0.078	0.073	0.376	0.376	4984	4984	5981	5981
Average		1.13	17.12	16.25	2.27	2.28	2.73	2.73	0.44	0.44	0.08	0.07	0.37	0.37	4985.00	4985.00	5982.00	5982.00
SD		0.90	0.06	0.03	0.08	0.06	0.10	0.10	0.02	0.02	0.00	0.00	0.01	0.01	1.41	1.41	1.41	1.41
1119.08	Air	0.94	17.31	17	2.22	2.23	2.69	2.68	0.45	0.449	0.078	0.076	0.373	0.373	4326	4326	5976	5976
	Freeze	1.14	16.53	15.72	2.2	2.22	2.64	2.64	0.454	0.450	0.075	0.071	0.379	0.379	4992	4992	5977	5977
Average		1.04	16.92	16.36	2.21	2.23	2.67	2.66	0.45	0.45	0.08	0.07	0.38	0.38	4659.00	4659.00	5976.50	5976.50
SD		0.14	0.55	0.91	0.01	0.01	0.04	0.03	0.00	0.00	0.00	0.00	0.00	0.00	470.93	470.93	0.71	0.71
1119.24	Air	0.92	17.38	16.99	2.24	2.25	2.71	2.71	0.446	0.444	0.078	0.076	0.369	0.369	4987	4987	5984	5984
	Freeze	0.82	18.64	17.81	2.23	2.26	2.74	2.75	0.449	0.442	0.084	0.079	0.366	0.366	4989	4989	5983	5983
Average		0.87	18.01	17.40	2.24	2.26	2.73	2.73	0.45	0.44	0.08	0.08	0.37	0.37	4988.00	4988.00	5983.50	5983.50
SD		0.07	0.89	0.58	0.01	0.01	0.02	0.03	0.00	0.00	0.00	0.00	0.00	0.00	1.41	1.41	0.71	0.71
1119.42	Air	0.52	19.23	18.63	2.27	2.29	2.81	2.81	0.44	0.437	0.084	0.081	0.356	0.356	5007	5007	5981	5981
	Freeze	1.06	17.75	17.62	2.23	2.24	2.72	2.72	0.448	0.447	0.080	0.079	0.368	0.368	4978	4978	5979	5979
Average		0.79	18.49	18.13	2.25	2.27	2.77	2.77	0.44	0.44	0.08	0.08	0.36	0.36	4992.50	4992.50	5980.00	5980.00
SD		0.38	1.05	0.71	0.03	0.04	0.06	0.06	0.01	0.01	0.00	0.00	0.01	0.01	20.51	20.51	1.41	1.41
1119.58	Air	2.23	17.22	16.35	2.23	2.26	2.7	2.7	0.448	0.443	0.077	0.073	0.371	0.371	5980	5980	5980	5980

	Freeze	0.98	18.5	16.24	2.19	2.25	2.69	2.69	0.456	0.443	0.085	0.072	0.371	0.371	5973	5973	5973	5973
	Vac and Pump	0.89	17.87	17.57	2.25	2.26	2.74	2.74	0.444	0.442	0.079	0.078	0.364	0.364	4983	4983	5982	5982
Average		1.61	17.86	16.30	2.21	2.26	2.70	2.70	0.45	0.44	0.08	0.07	0.37	0.37	5976.50	5976.50	5976.50	5976.50
SD		0.88	0.91	0.08	0.03	0.01	0.01	0.01	0.01	0.00	0.01	0.00	0.00	0.00	4.95	4.95	4.95	4.95
1119.75	Air	1.82	18.88	17.95	2.29	2.31	2.82	2.82	0.437	0.432	0.082	0.078	0.355	0.355	4982	4982	5980	5980
	Freeze	1.61	19.77	18.49	2.23	2.26	2.77	2.78	0.449	0.442	0.089	0.082	0.360	0.360	4994	4994	5993	5993
	Vac and Pump	1.16	17.47	16.89	2.23	2.24	2.7	2.7	0.449	0.446	0.079	0.075	0.371	0.371	5975	5975	5975	5975
Average		1.72	19.33	18.22	2.26	2.29	2.80	2.80	0.44	0.44	0.09	0.08	0.36	0.36	4988.00	4988.00	5986.50	5986.50
SD		0.15	0.63	0.38	0.04	0.04	0.04	0.03	0.01	0.01	0.00	0.00	0.00	0.00	8.49	8.49	9.19	9.19

The results shown in Table 4-7 indicate that the corrected porosity standard deviation for all samples is 0.38. Between adjacent samples, the standard deviation varies between a low of 0.08 (Sample 1119.58m) and a high of 2.14 (sample 1118.87m). The corrected bulk density difference between adjacent samples was a minimum of 0.01 g/ml and a maximum of 0.06 g/ml. The corrected grain density varied between 0 g/ml and 0.1 g/ml. The interpreted threshold pressure using the IPV method remained constant at the ~ 4990 psia pressure equilibrium point for most samples. Notable exceptions include sample 1119.08 m that was air dried with a threshold pressure at the pressure equilibrium point below (4236 psia). Four samples were interpreted to have a threshold pressure at the pressure equilibrium point above at ~ 5980 psia; one air dried sample and one freeze dried sample at 1118.79 m and 1118.87 m respectively and both the freeze and air dried adjacent samples at 1119.58 m. This equates to 23 % of the samples having an IPV threshold pressure that varied from the majority by one pressure equilibrium point. The threshold pressures interpreted with the MI method are in much better agreement with all threshold pressures at the same pressure equilibrium point ~ 5980 psia.

Discussion: The MICP curves for the Saracen-1 samples indicate the repeatability, reliability and accuracy of the MICP analysis over 1.6 m of Muderong Shale, which is described as being fairly uniform (Dewhurst et al., 2002). This is further evidenced when comparing adjacent samples. The MICP curves tend to show variation up to 20 % mercury saturation after which they are similar to 70 % mercury saturation, followed by slight separation before regrouping at 100 % mercury saturation for both the air dried and freeze dried samples. The variation observed in the MICP curves up to 20 % mercury saturation is interpreted to represent conformance and is further supported by re-graphing the MICP curves with conformance correction. This highlights the importance of accurate conformance correction for threshold pressures that are interpreted using saturation percentages as was suggested and utilised by Schowalter, (1979) and Sneider et al., (1997). The separation in MICP curves upward of 70 % mercury saturation hints at the possible variation in the pore throat distribution at approximately (10,000 psia =~0.01µm and 60,000 psia= ~ 0.00178 µm radius). The MICP curves for all samples show a continued upward trend to 100 % mercury saturation indicating that there is still pore space being accessed by the mercury and that the porosities are likely lower than those from other apparatus (i.e. helium pycnometry) that is capable of accessing pore space with a radius below ~0.00178 µm. The threshold pressures using the IPV method are in agreement with one another with a maximum of one pressure equilibrium point discrepancy between samples no matter whether the samples were air dried or freeze dried. Five of the twenty-two samples showed a

one pressure equilibrium point change from the average with four of these samples being higher. The threshold pressures using the MI method are all similar and interpreted at the same pressure equilibrium point 5980 psia. Considering the uniformity of the MICP curves, porosities, bulk densities and grain densities it is likely that the differences in threshold pressures interpreted with the IPV method in the five samples are a result of the IPV method. However, this is a structured and consistent method of determining threshold pressure that is not open to interpretation or the effects of conformance as is the MI method.

The average porosity for the 11 air dried samples was 17.76 % (SD 1.48) without conformance correction. When conformance corrected, the average porosity was reduced to 16.88 % (SD 1.17) indicating a reduction in variation. The average porosity for the freeze-dried samples was 18.15 % (SD 1.11) without the conformance correction and 17.15 % (SD 1.08) with the conformance correction. An improvement in the standard deviation was observed with conformance correction for both drying methods. This assumes that the core is fairly uniform as shown by XRD analysis and suggested by Dewhurst et al., (2002); the conformance correction is reducing the variation and producing a more accurate result, validating its use. This is further supported by the improved uniformity observed in the conformance corrected MICP curves.

The minimum porosity for any sample was 15.39 % and the maximum was 18.63 % giving a maximum possible range of 3.44 % for conformance corrected samples. The maximum difference in porosity between adjacent samples was 3.02 % indicating that the maximum variation over the 1.6 m interval of the conventional core was slightly more than the maximum variation observed between adjacent samples that were treated with different drying methods.

The conformance corrected bulk density and grain density results were similar among all samples with an average of 2.28 g/ml and 2.74 g/ml for the air-dried samples and 2.24 g/ml and 2.71 g/ml respectively for the freeze-dried samples. The grain volume per gram results and pore volume per gram results suggest that there is more relative variation observed in the pore volume per gram than the grain volume per gram which is then translating into the observed minor differences in porosity.

Overall these results confirm the uniformity of the 1.6 m of conventionally cored Muderong Shale from Saracen-1 and the repeatability, reliability and accuracy of the MICP analysis over the 1.6 m interval of core and of samples adjacent to one another. The maximum variation in the bulk and grain density between any of the samples was 0.14 g/ml and 0.22

g/ml respectively. When comparing adjacent samples, this difference drops to a maximum of 0.09 g/ml for the bulk density and 0.14 g/ml for the grain density. This is a significant improvement and indicates that the variation between adjacent samples is considerably less than the variation seen vertically over the 1.6 m of cored Muderong Shale interval.

There was no relationship identified between the weight of the sample and the interpreted threshold pressure, corrected bulk density and grain density results. There was also no relationship observed between the weight of the samples and their corrected porosities. This indicates that the weight and inferred size of the sample does not need to be taken into account when comparing sample analysis.

The results from this analysis will provide the original (fresh) sample baseline for the evaluation of warehoused samples taken from the same core over the same 1.6 m interval from Saracen-1. Also, the variation seen in measurements will be used as a guide in subsequent chapters for determining the uniformity of core and differences between original core samples and warehoused adjacent samples for CRC-1 and Gorgon CO2 Data Well-1& Data Well-1ST1.

4.6 SECTION 3: COMPARABILITY

4.6.1 Tindilpie-11, Cooper Basin

Please see section 3.9.1 for Tindilpie-11 conventional core and well description. The well had a total of six conventional cores cut totaling ~ 42 m over the Patchawarra Formation and VC50 coal between 2740 m and 2907 m.

The core barrels were cut at 3 feet intervals and transported to the regional distribution centre, Port Adelaide. There is no other information on the treatment of the core subsequently. However, the special core analysis reports suggest that core plugs were received in the Perth Core Laboratories Australia for analysis. The well completion report also details the depth correction of the core using the core gamma ray and wireline gamma ray which was used to correct the sample depths. The well has a comprehensive log suite run including NMR (MREX) by Baker Hughes.

Methodology modifications specific to Tindilpie-11: Please see Appendix A, A.13 for details of the helium pycnometry analysis.

Laboratory NMR data was provided in porosity units and while the Coates and SDR permeabilities were provided they were re-calculated to remain consistent with the wellbore NMR log.

Results: The porosities from the helium pycnometry vary between 14.9 % and 5.8 % (Table 4-8) for the six samples. The Laboratory NMR results show a similar trend to the helium pycnometry results with a variation between 14.8 % and 5.3 % porosity. The MICP results for the samples show more variation with porosity varying between 14.5 % and 5.2 %. The log NMR results show more variation again to the other analyses on core plugs; however, a similar range of variation in porosities between 13.94 % and 4.32 % is still found.

The permeability results (Table 4-8) from the different techniques show significant variation appearing to compound the differences observed in porosity measurements from the different techniques. The air permeability measurements vary between 12.4 md and 0.015 md for the six samples. The helium permeability with Klinkenberg correction was a reduction on the air permeability results for all samples so that the permeability range fell between 10.6 md and 0.004 md. The laboratory NMR Coates permeability results produce a much larger range of permeability values for the samples (265.24 md – 0.01 md). The SDR model also increased the range in permeabilities values in comparison to helium permeability (503.32 md - 0 md). The well log Coates permeability results indicate that there is no permeability with the highest permeability recorded being 0.0000095 md. The well log SDR permeability estimates were higher than those predicted the by the Coates method but still less than 0.21 md. The MICP permeability, however, was the most optimistic with a range between 5478 md – 4.5 md over the six samples. It is also noted that the high and low permeabilities are consistent across the samples (i.e. the samples from high to low permeability are always in the same order no matter the technique or type of analysis) however the magnitudes and differences between samples do vary.

Sample 2755.72 m (Table 4-8) porosities are fairly consistent for helium, laboratory and well log NMR (5.8 %, 5.3 % and 4.3 % respectively). The MICP porosity is slightly higher at 8.6 %. The permeabilities are consistently low for this sample with all techniques and models ranging between 4.5 md from MICP and 0 md from the NMR well log using the Coates model.

The porosities for sample 2849.3m (Table 4-8) are consistent between helium (6.5 %) and laboratory NMR (6.5 %) and show slight variation to the well log NMR (7.4 %) and MICP (5.2 %) results. The permeabilities from all techniques are consistently low; the permeability ranged between an MICP permeability of 5.9 md and the well log NMR Coates permeability of 0 md.

Sample 2851.87 m (Table 4-8) results show consistent helium, laboratory NMR and MICP porosities of 14.9 %, 14.8 % and 14.5 % respectively. The log NMR averaged porosity over 2851.87 m is significantly less (6.87 %). The permeabilities show considerable variation. The MICP permeability estimate is extremely high in comparison to the other techniques. The laboratory SDR Model and Coates model are the second and third highest estimates of permeability; 503 md and 265 md respectively but still considerably less than the MICP predicted permeability. The permeability estimated from the air and the helium techniques with Klinkenberg correction is 12.4 md and 10.6 md respectively. The well log SDR and Coates permeabilities are all below 0.008 md.

The porosities for sample 2851.92m (Table 4-8) are consistent for helium (12.4 %), laboratory NMR (11.6 %) and MICP (11.5 %) analytical techniques. The well log NMR porosity is considerably lower (6.9 %). The permeability results show considerable variation between techniques. The MICP permeability estimate is the highest at 2015.04 md followed by the laboratory NMR SDR (123.5 md) and Coates (79.94 md) permeability estimates. The air permeability is 2.18 md and the helium permeability with the Klinkenberg correction is 1.66 md. The well log NMR estimates were the lowest; the Coates model estimated 0 md and the SDR model estimated 0.007 md.

The porosities for sample 2872.07 m (Table 4-8) are consistent for helium, laboratory NMR and MICP (9.3 %, 9.1 % and 8.4 % respectively). The well log NMR porosity is higher at 13.29 %. The permeability results show that MICP is considerably higher than the other techniques (113.5 md) which range between 5.0 md from the laboratory NMR and Coates model and 0 md for the well log NMR Coates model.

Sample 2872.7 m (Table 4-8) porosities show more variation between helium, laboratory and well log NMR, and MICP (10.1 %, 9 %. 13.9 % and 12.2 % respectively) than observed in the other samples. The subsequent permeability results from the different techniques are variable. MICP permeability was the highest estimate of 293.5 md followed by the NMR laboratory SDR model (8 md) and the NMR laboratory Coates Model (4.5 md). The air permeability (0.29 md) and helium permeability with Klinkenberg correction (0.087 md) along with the NMR well log Coates model (0 md) and SDR model (0.21 md) were all low estimates.

Table 4-8: Tindilpie-11 porosity and permeability results from helium pycnometry, laboratory NMR, log NMR and MICP analyses.

Sample	Depth (m)	Helium porosity (air) (%)	Lab NMR porosity (%)	Log NMR porosity (%)	MICP porosity (%)	Kair (md)	Klinkenberg Helium Kinf (md)	Lab NMR Coates (md)	Lab NMR SDR (md)	Log NMR Coates (md)	Log NMR SDR (md)	MICP permeability (md)	Radius 35 % (µm)
14	2755.72	5.8	5.3	4.32	8.6	0.015	0.004	0.00	0.00	0.0000000	0.0001	4.50	0.038
30	2849.3	6.5	6.5	7.36	5.2	0.043	0.016	0.01	0.13	0.0000095	0.0020	5.92	0.069
4A	2851.87	14.9	14.8	6.87	14.5	12.4	10.6	265.24	503.32	0.0000000	0.0077	5478.42	1.580
2A	2851.92	12.4	11.6	6.87	11.5	2.18	1.66	79.94	123.54	0.0000000	0.0077	2015.04	1.072
48	2872.07	9.3	9.1	13.30	8.4	0.175	0.045	2.17	4.97	0.0000000	0.1670	113.51	0.259
49	2872.7	10.1	9.0	13.94	12.2	0.294	0.087	4.53	8.09	0.0000000	0.2100	293.54	0.328

Discussion: The porosities from the different techniques indicate that the core plug porosity can differ up to 3.3 % for the same sample. The well log NMR porosity differed up to 8.03 % from the techniques which measured the core plug but is to be expected as the well log NMR porosity result was a measurement over a 20 cm interval. It is likely to have considerably more heterogeneity from this sample volume than observed over the core plug. The helium porosities were either higher or the same as the results from the laboratory NMR with a maximum of 1.1 % variation observed.

The helium pycnometry and MICP porosities showed more variation to one another. The four samples (2849.3 m, 2851.97 m, 2851.92 m and 2872.07m) show a decrease of between 1.3 % and 0.4 % porosity from helium pycnometry to mercury injection. However, two of the MICP porosities (Sample 14 and 49) are higher than the helium pycnometry porosities which is contrary to the theoretical limitations of mercury versus helium as suggested by the following authors (Mbia et al., 2014, Webb, 2001, Anovitz and Cole, 2015 and Mastalerz, 2013). This suggests there was considerable heterogeneity over the core plug sample as the mercury molecules are larger in comparison to the helium molecules, allowing the helium molecules to access more pore volume per gram than the mercury and thus the helium porosity values should be the same or greater.

NMR has been verified to have a similar porosity measurement to that of helium pycnometry; better than 1 porosity unit or 1 % (Coates et al., 1999). The laboratory NMR results above agree with this finding with a slightly higher variation of 1.1 %. This suggests that the helium pycnometry analyses are accurate. Thus the higher MICP porosities are most likely a result of the NMR and helium analysis being conducted on the same sample while the MICP is a destructive test and would have been conducted on the adjacent sample. Thus this would suggest that there is a porosity variation on the centimetre scale (within the length of a core plug) of > 2.8 % for sample 2755.72 m and > 2.1 % for sample 2872.07 m. This centimetre heterogeneity in porosity is also likely to be affecting the larger scale measurements of the NMR log which has a much greater contrast to the core plug porosity indicating significant porosity heterogeneity over the metre scale.

The permeability results from the different techniques show some significant trends. Firstly for samples 2755.72m and 2849.3 m, no matter the technique, the permeability results are all low (< 5.9 md). These samples also have the lowest porosity independent of technique. The remaining four samples all have higher porosities and some varying permeabilities depending on technique. In a study conducted by Comisky et al., (2007) the Klinkenberg steady state permeability was used as the reference standard while this was not available the

Klinkenberg corrected permeability by unsteady state principles was available and is used as the reference for this analysis. The air permeability estimate was an increase on the helium with the Klinkenberg correction permeability in all cases; a maximum increase of 1.8 md was recorded for sample 2851.87 m. Sample 2851.87 m was the most permeable with all other samples having Klinkenberg helium permeabilities ≤ 1.66 md. The laboratory NMR Coates permeability prediction showed a similar trend over the samples although it overestimated permeability by varying amounts. The laboratory SDR model shows the same permeability trends as the Klinkenberg helium permeability and the laboratory NMR Coates model. The SDR model similar to the Coates model overestimates the permeability of the samples when compared to the Klinkenberg corrected helium permeability. SDR model estimates of permeability are higher than those predicted by the Coates model.

The well log calculated permeabilities are the lowest of all techniques. The Coates model estimates the highest permeabilities to be 0.0000095 md while the SDR model estimates are slightly higher with permeabilities reaching a maximum of 0.21 md. Thus the NMR log in conjunction with the Coates and SDR model suggests that these intervals of rock are of low permeability and may be considered as non-permeable. This is in line with the helium Klinkenberg corrected permeabilities for all core plug samples except sample 2851.87m. Sample 2851.92 m taken 5 cm deeper has a Klinkenberg corrected helium permeability of 1.66 md and sample 2849.3 m (shallower) has a Klinkenberg corrected helium permeability of 0.016 md. This indicates that sample 2851.87 m was taken through a streak of higher permeability and is thus not representative of the 1.6 m sampled by the NMR log. It is concluded that the NMR log and the calculated permeabilities are representative of the formations on a broad scale but are unable to pick up streaks (~10 cm) of permeability. The SDR model was an improvement over the Coates Model for predicting permeability for the well log data when using the Klinkenberg helium permeabilities as the standard reference.

The MICP permeability results using the Winland‘s equation are the highest of all techniques although showing a similar trend to the Klinkenberg corrected helium permeability estimates. The permeability estimates show the correct trend in comparison to the other techniques but are not scaled correctly suggesting the constants used in the Winland‘s equation are not appropriate for these samples. The Winland‘s equation was formulated using sandstone samples relating porosity and pore throat diameter. This relationship is likely to differ for tight sandstones, siltstones and shales. The change in pore throat to porosity ratio of these sealing intervals can partially explain the extremely high

permeability predictions. The prediction of Darcy scale permeability from this equation is puzzling.

4.6.2 **Mena Murtee-1, Darling Basin**

Please see section 3.7.1 for Mena Murtee-1 conventional core and well description. The core plugs for analysis were taken within 12 months of the well being drilled. The core is stored at the NSW Core Library in Londonderry, NSW.

The well logs were run by Weatherford including NMR. The conventional core had MICP analysis carried out soon after drilling by Intertek Geotech in Perth. A total of 12 samples were analysed and reported in Watson et al., (2014). Subsequently, a number of samples (both reservoir and sealing) were analysed with laboratory NMR to calibrate the NMR log and were reported in Esteban, (2015). Three of these samples were at or near the location of samples analysed with MICP. Additionally, two reservoirs intervals and a further two sealing intervals were collected at the same depths as previous NMR analyses. This MICP analysis was carried out at the ASP.

Methodology modifications specific to Mena Murtee-1: Three samples analysed with MICP, laboratory NMR and helium pycnometry were taken at slightly different depths; MM1-041-LE2 was taken at a depth of 1859.025 m for NMR and helium analysis while the sample for MICP analysis was taken at 1859.75 m. MM1-043-LE2 was taken at a depth of 1866.035m for NMR and helium analysis. The sample for MICP analysis was taken at 1865.06m. MM1-044 was taken at a depth of 1873.03 m for NMR and helium analysis while the sample for MICP analysis was taken at 1872.32 m.

Please see Appendix A, A.14 for details of the helium pycnometry analysis.

Results: The porosities show a clear trend between analytical techniques (Table 4-9). The laboratory NMR porosity is consistently higher or equal to the other techniques for all samples. The helium pycnometry produces results equal or less to the porosity from the laboratory NMR. The MICP porosity, excluding sample MM1-15, are the lowest of all techniques (up to 2.85 % below laboratory NMR and up to 1.25 % below helium pycnometry). The results also indicate that there is no consistent variation/ change in porosity between techniques.

The permeability results from the different techniques also show considerable variation (Table 4-9). The helium permeability and the laboratory NMR Coates model permeability results are most similar to one another showing a similar trend across samples. The

laboratory NMR SDR model permeability shows a similar trend to both the helium permeability results and the laboratory NMR Coates model permeability results excluding the permeability estimates for samples 1629.05 m and 1629.98 m which are at least 350 % higher than the laboratory NMR Coates permeability model and higher again over the helium permeability results. However, the remaining three samples with lower porosity and, low helium and laboratory NMR Coates permeability results show the opposite trend and are predicted to have a lower permeability than the laboratory NMR SDR model. The MICP permeability predictions using the Winland‘s equation show a similar trend to the helium permeability results across the samples. However, the estimates of permeability are significantly higher than those predicted by both helium and NMR techniques to the point where the results may be considered erroneous. The well log NMR Coates permeability predictions excluding sample MM1-50V are generally conservative in comparison to the helium permeability predictions. The well log NMR SDR model predicts no permeability over any of the sampled intervals.

The porosities for the core plug sample MM1-11 (1604.97m) indicate that there is considerable variation between the analytical techniques; 9.8 % laboratory NMR porosity, 2.5 % well log NMR porosity and 4.8 % MICP porosity (Table 4-9). The permeability estimates from the laboratory NMR Coates model is slightly less than the SDR model; 0.0013 md and 0.002 md respectively. The well log NMR Coates model permeability estimate is higher than both laboratory models (0.012 md) while the well log NMR SDR model permeability estimates 0 md.

The porosities for the core plug sample MM1-15 (1606.91 m) indicate that there is considerable variation between the analytical techniques similar to sample MM1-11; 0.67 % helium porosity, 9.4 % laboratory NMR porosity, 2.4 % well log NMR porosity and 4.2 % MICP porosity (Table 4-9). The helium permeability estimate and the laboratory NMR permeability estimate are quite consistent at 0.0004 md. The laboratory NMR SDR model estimates the permeability to be slightly higher at 0.00136 md. The well log NMR Coates model estimates the permeability to be slightly higher again at 0.00337 md while the well log NMR SDR model estimates the lowest permeability of all techniques.

The porosities for the core plug sample MM1-036-LE (1629.05m) vary between 10.8 % for the laboratory NMR and 7.95 % for the MICP analysis (Table 4-9). The well log NMR porosity is considerably lower but is measuring a much larger interval. The permeability results are quite similar for the helium pycnometry and the laboratory NMR using the Coates model; 3.92 md and 4.63 md respectively. The laboratory NMR SDR model predicts

a considerably higher permeability of 29.27 md while the well log NMR predicts low permeabilities; 1.31 md for the Coates model and 0 md for the SDR model. The MICP permeability prediction using the Winland‘s equation is erroneous at 97313.45 md.

The porosities for the core plug sample MM1-037V (1629.98m) indicate that the helium pycnometry and NMR laboratory analysis porosity are consistent at 9.5 % (Table 4-9). The MICP porosity result is also close at 9.03 %. The well log NMR, however, indicates that the porosity result is indeed much lower over the 1.6 m interval at 1.22 %. The similar porosity for the helium pycnometry and the NMR laboratory analysis did result in similar permeability predictions using the Coates Model only; 8.57 md and 10.2 md respectively. The NMR laboratory data in conjunction with the SDR model estimated a permeability of 35.1 md more than 26 md higher than the helium permeability prediction. The log NMR data estimated low permeabilities with both the Coates and SDR model in line with the low porosity predictions; 0.008 md and 0 md respectively. The MICP permeability prediction using the Winland‘s equation is erroneous at 149850.34 md.

The porosities for the core plug sample MM1-041-LE2 (1859.05 m) indicate that the laboratory NMR and well log NMR differ significantly; 4.2 % porosity as opposed to 0.82 % porosity respectively (Table 4-9). The MICP and helium porosity were not available (N/A) or not done (ND).

The porosities from sample MM1-043-LE2 (1866.035 m) show a different trend to those observed in the other samples (Table 4-9). The helium pycnometry results indicate a porosity of 0.9 % while the laboratory NMR results indicate a much higher porosity of 6.5 %. However, the log NMR porosity (0.66 %) is showing similar agreement with the helium porosity. The MICP porosity was not available (N/A).

The porosities for sample MM1-044 (1873.03 m) are only available from the laboratory NMR and well log (Table 4-9). The laboratory NMR has a much higher porosity (5.9 %) as opposed to the well log NMR (1.16 %).

The porosities for the core plug sample MM1-50V (2035.39 m) indicate that the helium porosity result and the MICP porosity result are consistent (1.2 % and 1.1 % respectively). However, the laboratory NMR result is higher at 3.8 % (Table 4-9). The NMR well log porosity is the lowest at 0.61 %. The helium permeability prediction is 0.007 md which is higher than both the laboratory NMR Coates model and SDR model. The well log SDR model predicts a lower permeability again; however, in contrast, the log NMR Coates model predicts a permeability of 175.5 md. The MICP permeability is predicted to be 3.15 md.

Table 4-9: Mena Murtee-1 porosity and permeability results from helium pycnometry, laboratory NMR, log NMR and MICP analyses.

Sample	Depth (m)	Helium porosity (%)	Lab NMR porosity (%)	Log NMR porosity (%)	MICP porosity (%)	Helium Permeability (md)	Lab NMR Coates (md)	Lab NMR SDR (md)	Log NMR Coates (md)	Log NMR SDR (md)	MICP permeability (md)	Radius 35 % (µm)
MM1-11	1604.965	ND	9.8	2.51	4.75	ND	0.00	0.00	0.01	0.00	10.46	0.10
MM1-15	1606.91	0.67	9.4	2.41	4.24	0.00	0.00	0.00	0.00	0.00	8.85	0.01
MM1-036-LE	1629.05	9.2	10.8	5.40	7.95	3.92	4.63	29.27	1.31	0.00	765.60	0.83
MM1-037V	1629.98	9.5	9.5	1.22	9.03	8.57	10.20	35.10	0.00	0.00	36096.60	7.22
MM1-041-LE2	1859.025	ND	4.2	0.82	N/A	ND	0.00	0.00	0.61	0.00	N/A	N/A
MM1-043-LE2	1866.035	0.9	6.5	0.66	N/A	2.28	0.00	0.00	0.00	0.00	N/A	N/A
MM1-044	1873.03	ND	5.9	1.16	N/A	ND	0.00	0.00	0.00	0.00	N/A	N/A
MM1-50V	2035.39	1.2	3.8	0.61	1.08	0.01	0.00	0.00	175.5	0.00	3.15	0.19

Discussion: The core porosities indicate that there is a maximum variation of 8.7 % porosity for sample MM1-15 (1606.91 m) between helium pycnometry (0.67 %) and laboratory NMR (9.4 %). The well log NMR porosities differed by a maximum of 8.29 % between both the laboratory NMR and helium pycnometry for sample MM1-037V (1629.98 m). The results show a number of trends between techniques; laboratory NMR porosity is higher than helium porosity which is generally higher than MICP porosity which is generally higher than well log NMR porosity. MM1-15 shows a slightly different trend with the helium porosity being the lowest result. The porosity difference between techniques is not consistent. The well log NMR consistently has very low porosity in comparison to the other techniques over all core plug locations which is unlikely to be a result of the tool measuring a 20 cm interval but more likely to be a result of the tool having a poor resolution of small pores.

The helium porosities were higher than the MICP porosities for all samples except MM1-15 in alignment with the theoretical limitations of mercury in comparison to helium porosity (Webb, 2001, Mastalerz, 2013, Ernest et al., 2014 and Cole, 2015). This suggests that there was considerable heterogeneity over the core plug MM1-15 which is supported by the significant differences in porosity measurement from the different analytical techniques.

NMR has been verified as having a similar porosity result to helium pycnometry of better than 1 porosity unit or 1 % (Coates et al., 1999). The laboratory NMR and helium pycnometry results from Mena Murtee-1 do not agree with this finding. There are two possible explanations; (i) the sensitivities are greater than 1 % between the two techniques or, (ii) there is significant heterogeneity over the core plug. Given that sample MM1-037V is within the 1 % variation for all three techniques (helium, laboratory NMR and MICP) it is thought that the other plugs have significant heterogeneity affecting the results and that this heterogeneity is occurring on the centimetre scale.

The permeability estimates show a number of different trends; Samples MM1-036-LE and MM1-037V show an increasing permeability estimate from well log NMR SDR method to the well log NMR Coates method to the helium pycnometry to laboratory NMR to the Coates prediction to the SDR prediction to the Winland‘s prediction from MICP. However, Samples MM1-15, MM1-043-LE2 and MM1-50V show no consistent trend between techniques. The Winland‘s permeability predicted from MICP analysis was consistently the highest permeability estimate of all techniques on core plug samples. The laboratory NMR permeability predicted from the Coates technique has the best agreement with the helium permeability.

The well log permeabilities are all low in comparison to the results from the other techniques on core samples except for the measurement over MM1-50V sample location using the Coates prediction which is anomalously high. The SDR well log permeabilities are all predicted to be 0 md. This suggests that the NMR well log and the SDR model are not appropriate for these formations.

The MICP permeability results using the Winland‘s equation are the highest of all techniques. The permeability estimates show a semi-similar trend in comparison to the other techniques but are not scaled correctly suggesting the constants used in the Winland‘s equation are not appropriate for these samples. The Winland‘s equation was formulated using sandstone samples relating porosity and pore throat diameter. This relationship is likely to differ for tight sandstones, siltstones and shales. The change in pore throat to porosity ratio of these sealing intervals can partially explain the extremely high permeability predictions.

4.6.3 **Saracen-1, Barrow Sub-basin**

Please see section 3.5.1 and 4.5.1.for Saracen-1 conventional core and well description. The conventional core was stored at the Western Australian Core Library (WACL). The WACL is a warehouse facility located in Carlisle, Perth. The facility is not temperature controlled; temperatures vary between 8 ° and 27 ° C throughout the year (pers. comm. Paul Stephenson WA Core Librarian). No information is available on the humidity for the facility, but past humidity data is available from Bureau of Meteorology for Perth which is likely to be semi-indicative of that experienced by the core.

The Saracen-1 core analysis was conducted in two stages. The first stage, on the original (fresh) core in 2001, was conducted under the supervision of Dr. Dave Dewhurst at the CSIRO in Perth. Among many other tests helium pycnometry and MICP analysis were performed on the samples. In the second stage of testing, warehoused core stored in the WACL was analysed with MICP, helium pycnometry and NMR by this study. The four samples analysed with NMR were subsampled; two of the sub-samples were saturated with water and two of the sub-samples were saturated with oil.

The analysis will firstly compare helium porosity, MICP porosity and permeability estimates of the fresh core tested in 2001 with the same tests repeated on the warehoused core in 2013. Secondly, the analysis will compare the helium porosity, MICP porosity and NMR laboratory porosity and subsequent permeability predictions from 2013 warehoused core only.

Methodology modifications specific to Saracen-1: The original samples (2001) analysed with MICP were air dried not oven dried. The warehoused samples (1118.65 m and 1119.30 m) analysed with laboratory NMR were saturated with oil, not brine.

Please see Appendix A, A.14 for details of the helium pycnometry analysis.

Results: The Saracen-1 original (fresh) core (2001) analysed with helium pycnometry and MICP shows a number of trends (Table 4-10). Firstly, the helium porosities are much higher (approximately twice) that of the MICP porosities of the same samples. The helium porosity from the 11 samples has up to 18 % variation in porosity while the MICP analyses suggest that the samples have more similar porosities with a variation of 3.23 %. Secondly, the samples with high and low helium porosity do not correspond to the same samples with high and low MICP porosity.

The Saracen-1 warehoused core had two water-saturated samples analysed with helium to determine porosity only (Table 4-11). Thus a lack of repetition makes it difficult to determine any trends with certainty. With this in mind, similar trends to those observed in the original core can be observed. The helium porosities are approximately 50 % higher than those observed in the MICP analysis. However, there is a similar variation in porosity between the two techniques (1.3 % and 1.13 % for helium and MICP respectively) bearing in mind the lack of samples analysed with helium. Once again the samples with high and low helium porosity do not correspond to the samples with high and low MICP porosity.

The helium pycnometry analyses of the two sample types (fresh and warehoused) indicate that there is nearly an ~18 % reduction in the porosity of the warehoused samples; bearing in mind the lack of warehoused samples analysed. However, the MICP porosities indicate an average porosity reduction of only 4.61 % in the warehoused samples.

The permeability prediction from the MICP analyses using the Winland‘s equation suggests that the fresh core had a permeability of between 3.41 md and 4.68 md while the warehoused core has a predicted permeability of between 0.569 md and 0.825 md.

The porosity analysis of the warehoused Saracen-1 samples indicates a clear grouping of results for each of the analytical techniques (Table 4-11). One outlier is noted (sample 1119.3 m) which has an anomalously low laboratory NMR porosity result. The MICP porosities are the lowest averaging 12.21 %, followed by the helium porosities averaging 17.65 % and the laboratory NMR porosities averaging 28.54 %.

The calculated permeability results from the laboratory NMR using the Coates and SDR models indicate a similar trend but are more pronounced in the oil saturated samples with the Coates model (Table 4-11). The water saturated samples have permeabilities of 0.003 md with the Coates model and between 0.143 md and 0.150 md with the SDR model. The oil saturated samples have Coates permeabilities of between 2.749 md and 4.289 md while the SDR model predicts permeabilities of between 0.163 md and 0.167 md. The MICP permeability predictions using the Winland‘s equation vary between 0.569 md and 0.825 md for the four samples.

Table 4-10: Saracen-1 original samples porosity and permeability results from helium pycnometry and MICP analyses.

Sample	Depth (m)	Helium porosity (%)	MICP porosity (%)	MICP permeability (md)	Radius 35 % (µm)
1H	1118.15	36	15.56	4.647	0.0118
1V	1118.22	36	15.39	4.647	0.0118
2A	1119.24	50	16.99	3.419	0.0099
2H	1118.34	33	18.54	4.647	0.0118
3A	1119.24	39	18.62	3.419	0.0099
3H	1118.79	32	17.12	3.419	0.0099
4H	1118.96	43	16.23	3.419	0.0099
5A	1119.58	36	16.35	4.681	0.0119
5H	1119.08	46	17.00	4.647	0.0118
6A	1119.75	34	17.95	4.647	0.0118
45	1118.87	37	15.55	4.647	0.0118

Table 4-11: Saracen-1 warehoused samples porosity and permeability results from helium pycnometry, laboratory NMR and MICP analyses.

Depth (m)	Helium porosity (%)	Lab NMR porosity (%)	MICP porosity (%)	Lab NMR Coates (md)	Lab NMR SDR (md)	MICP permeability (md)	Radius 35 % (µm)
1118.45	18.3	31.85	11.95	0.003	0.150	0.741	0.0099
1118.65	ND	29.12	11.72	2.749	0.163	0.720	0.0099
1119.05	17.0	30.92	12.32	0.003	0.143	0.569	0.0083
1119.3	ND	22.25	12.85	4.289	0.167	0.825	0.0099

Discussion: The MICP and helium porosity analyses indicate consistently that the helium porosity values are much higher, although not by the same percentage; values of 100 % greater porosity are observed in the original samples while values of 50 % greater porosity are observed in the warehoused samples. As the helium molecules are much smaller than the mercury molecules (60,000 psia= ~ 0.00178 µm radius) it is possible that the helium has accessed a greater volume of small pores not accessible by the larger mercury molecules. However, this would indicate that approximately 50 % of the pore volume per gram of the original Saracen-1 samples had a pore throat diameter below the size of the mercury molecules but larger than the size of the helium molecules. This is considered unlikely to be entirely responsible for the observed changes.

The warehoused samples show a consistent decrease in porosity in comparison to the original samples using both the helium and MICP analyses. The helium analysis indicates a much greater reduction in porosity (~18 %) compared to the MICP analyses (4.61 %) suggesting that the porosity accessible by both the mercury and the helium in warehoused samples has reduced by 4.61 %. It further suggests that the pores with pore throat diameters below the diameter of the mercury molecules have reduced by 13.39 % indicating that the warehousing has the greatest effect on pores with pore throat diameters between the diameter of mercury molecules and helium molecules providing both analytical techniques measure porosity accurately.

The resultant permeability predictions using the MICP data and the Winland‘s equation show a decrease in permeability of the warehoused samples which is to be expected as a

result of the decrease in pore throat diameter at 35 % mercury saturation and reduction in porosity. The decrease in pore throat diameter at which 35 % mercury saturation is achieved suggests that pore throats are constricted not that pores are no longer accessible reducing the porosity. The constriction of pore throats is thought to be an effect of one or a combination of both of the following factors: (i) shrinkage of the entire sample as a result of drying or (ii) lining of the pores and pore throats with a precipitant due to a reaction taking place during warehousing.

The porosity analysis and permeability predictions for the warehoused samples show a clear grouping of the porosity and permeability techniques while also showing that the samples have similar porosity using the same technique. This indicates that the samples are still quite uniform after being warehoused as was suggested about the original samples by Dewhurst et al., (2002) and as also found in Section 4.5.1. This indicates that the differences in porosity are a result of the instrument or technique used to measure the porosity. Thus some key inferences can be made from this analysis. Firstly the MICP analysis gives the lowest porosity result. The helium porosities are approximately 50 % larger than the MICP result – note the lack of samples but at the same time the uniformity of the samples tested. Lastly, the laboratory NMR porosity is ~133 % larger than the MICP results and 62 % larger than the helium porosity. The oil saturated sample (1118.65m) porosity result appears similar to the two water-saturated samples suggesting there is little difference in porosity no matter the wetting fluid – this requires more samples to confirm this. The fourth sample saturated with oil appears to be anomalous as this type of variation has not been observed in the MICP porosity or other samples and is possibly a result of incomplete oil saturation.

The permeability results using the laboratory NMR with the Coates and SDR models show a number of clear differences between the samples and the saturating fluids. Firstly, it can be observed that the water-saturated samples have the lowest Coates permeability results (0.003 md) followed by the SDR model (~0.158 md) and the MICP permeability results (~0.655 md). However, the oil saturated samples show a different trend with the Coates permeability predicted to be considerably higher (~3.519 md) including the sample with the anomalous porosity result) suggesting that the T_2 distribution has moved into the Free Fluid Zone (>33 msec relaxation times). This indicates that the hydrogen‘s in the oil were much slower to relax than the hydrogens in the water which is likely indicating a difference in viscosity between the two fluids. However, the SDR permeability model predicted oil saturated sample permeabilities much more in line with the water saturated samples with a slight difference in the average permeability (0.019 md). Thus it would be suggested that the SDR

permeability model is the most appropriate model to compare oil saturated and water saturated permeabilities.

4.7 CHAPTER 4 DISCUSSION

Accuracy

The results from Section 4.4.1 suggest there is indeed an intruded volume when the mercury porosimeter is run without a sample for some penetrometers. This is thought to be a result of the compressibility of the system (y Leon, 1998, Sigal, 2009, International ASTM, 2011) however, given variation in results between penetrometers it is suspected to be a result of the penetrometer only. This blank correction without the sample has been applied to all subsequent analysis conducted by this study. The result from Section 4.4.2 where the Silica-Alumina samples were run and the total intrusion is compared to the given parameters indicates that this analysis minus the blank correction is providing accurate results.

This study acknowledges the need for a conformance correction of MICP analysis data as observed in the Saracen-1 results (Section 4.5.1) and concurs with the observations of Sigal, (2013) where there is low-level incremental intrusion resembling saw teeth for tight shales. The conformance correction method suggested by this study (Appendix A, A.4) is different to that proposed by Bailey, (2009) in Comisky, (2011) and Sigal, (2009) above but attempts to align with the statement by Sigal, (2013). Thus a blank correction is applied to all MICP analysis specific to the penetrometer used. The effect of the conformance correction on the MICP curves, porosity, bulk density and grain density results (Chapter 4.4.3) can be compared to the uncorrected data (Chapter 4.4.2.). The silica alumina standards have little conformance as indicated by the lack of low-level incremental intrusion; lack of saw blade appearance. Thus as would be expected the conformance correction is rather minimal; slight changes in MICP curves, porosity, bulk density and grain density results. The conformance correction was applied to 10 % of the threshold pressure or to the highest pressure equilibrium point where the incremental intrusion was zero below the threshold pressure. In this case, it was to ~2100 psia for the standard samples. As the threshold pressure was beyond that observed for any shale tested (20,000 psia) the ~2100 psia conformance correction is considered to be appropriate and concur with the statement by Sigal, (2013) who suggests that any intrusion for a shale sample below a few thousand psia is a combination of blank and conformance effect. The method suggested by this study is considered to be more appropriate than that by Bailey (2009) in Comisky et al., (2011) as Bailey‘s method removes nearly all of the maximum inflection point from Comisky et al.,

(2011) example MICP curves and removes all incremental pore volume up to ~6000 psia which is considerably higher than the expected conformance as suggested by Sigal, (2013).

The anecdotal results from Section 4.4.4 suggest that there is no compression of the samples contrary to common opinion. It is thought that with the fragility of the samples any compressive force would have led to fracturing and subsequent disintegration of samples. As this was not observed it is suggested that sample compression is not occurring during MICP analysis. The stepped intrusion with equilibration at each pressure equilibrium point nullifies compression because the system is in contact with the outside of the sample.

Repeatability

The investigations by Darłak et al., (2011) and Comisky et al., (2011) into the effects of sample size on MICP provide general agreement that sample size does affect the porosity and MICP curves even after being conformance corrected. However, when compression correction is applied to the MICP curves of Comisky et al., (2011) from different sample sizes the MICP curves do become in agreement. Both authors sampled core and subsequently broke the sample into adjacent sub-samples. The sub-samples were broken down into a number of treatments from whole rock samples to granules to powders. In Section 4.5.1 all samples were whole rock and not broken down in granules or powders. In contradiction to Darłak et al., (2011) and Comisky et al., (2011) there was no relationship observed between sample size and MICP curve position or shape on the graph, interpreted threshold pressure or porosity from Saracen-1. However, it must be noted that sample size analysed was between 2.23 g and 0.52 g and these samples are likely to have been considerably larger than the granules or powder utilised by Darłak et al., (2011) and Comisky et al., (2011).

The investigations of Perrin and Benson, (2009) suggest that there are sub-core heterogeneities in the CO_2 distribution in reservoir rocks. While the rock type and the fluid type are not relevant to this study, the variations in porosity and to some degree the permeability over the ~6.5 cm -20 cm scale can be used to infer the variation in porosity and pore throat diameter that may be plausible between adjacent samples of sealing rock and samples taken in close proximity to one another. The results from Section 4.5.1 demonstrate that the 1.6 m of the Saracen-1 core is relatively homogeneous as was suggested by the original authors (Dewhurst et al., (2002). The variation in porosity between samples along the 1.6 m of core was 3.44 % and this was reduced to 3.01 % between adjacent samples that were dried using two different techniques. The similarity in MICP curves is improved upon

after conformance correction which further supports these statements. While these results suggest that the 1.6 m of core from Saracen-1 is fairly uniform, this study does recognise that this may not be the case with sealing and tight reservoir rock from other wells as significant heterogeneities may be observed similar to that of Perrin and Benson (2009).

Comparability

This study confirms the variation in results from different analytical techniques as observed by the following authors Coates et al., (1999), Lonnes et al., (2003), Mbia et al., (2014) and Dellinger and Esteban, (2014). The Tindilpie-11 samples have at most a 1.1 % variation in porosity between helium pycnometry and laboratory NMR with helium pycnometry tending to predict slightly higher porosities. These results agree with Lonnes et al., (2003) and Coates et al., (1999) and disagree with Dellinger and Esteban, (2014). The log NMR porosity shows considerable variation from the different analytical techniques, but due to the much larger sampling volume, it cannot be deciphered as to whether this is a result of the NMR tool or the core sample not being representative of the larger sampling volume. The MICP porosity showed more variation in comparison to the helium and laboratory NMR porosity and no constant trend. Two samples had MICP porosities higher than both the helium and laboratory NMR. The other three samples were all lower than helium porosity by ~1.5 %. The MICP results from Tindilpie-11 do not align with the findings of Mbia et al., (2014).

Conversely, the results in Mena Murtee-1 show a different trend between the different techniques measuring porosity. The laboratory NMR porosities tends to be the same as the helium porosities or higher which are tending to be in better alignment with the results of Dellinger and Esteban, (2014) while still being in alignment with the findings of Lonnes et al., (2003) and Coates et al., (1999). The well log NMR results will not be taken into account due to the larger sampling volume. The MICP porosity is consistently lower than the helium and NMR porosity by ~1-2 % which is in general agreement with findings in Tindilpie-11 but in disagreement with the large variations observed by Mbia et al., (2014).

The Saracen-1 original sample porosities for the Muderong Shale are in contradiction to the results of other authors, the results from Tindilpie-11 and the results from Mena Murtee-1. The helium porosities are greater than 50 % higher than porosities from MICP analysis. While this trend is in alignment with the results of Cui et al., (2013) and Mbia et al., (2014) it is significantly greater than the 0.7 -2.1 % and 6-10 % (respectively) decrease in porosity estimation of MICP analysis found in their results. The warehoused Saracen-1 results,

however, show a decrease of between ~5 - 6 % between the helium and MICP porosity in trend alignment and a similar range of results to Mbia et al., 2014. The laboratory NMR results, however, are in complete contradiction to all results with the laboratory NMR porosity being on average nearly ~16 % higher than the MICP porosity and nearly 11 % higher than the helium porosity. This trend is in line with the results of Dellinger and Esteban, (2014) but on a much greater scale. Dellinger and Esteban, (2014) explained the higher estimations of porosity by laboratory NMR as a result of interactions between water and clay minerals during water saturation of the core plugs. Additionally, Dellinger and Esteban, (2014) suggest that water may have percolated through some of the large, well-connected sample pores and may have accumulated around the sample due to the water saturation process and NMR measurements leading to higher porosity estimates. The Saracen-1 samples mineralogy (Dewhurst et al., 2002 and Appendix B, Table B-1) indicates that the samples are co-dominated by quartz and smectite. Smectite is swelling clay that absorbs polar solvents (Laird, 2006); in this case water. As shown in Appendix B Figure B-2 BSE image the quartz grains are dispersed between the clays and it is envisaged that with no grain framework the clays (including smectite) would be unconstrained when introduced to the solvent and could potentially swell significantly leading to the high NMR porosity result. The clay fraction is likely to be less in the Dellinger and Esteban, (2014)‘s samples and even if the clay type is swelling it will likely be constrained by the grain framework of the tight sandstones. Also, the Saracen-1 samples were observed to have discontinuous fractures parallel to the shale fissility that is likely to have affected the porosity similar to the large pore network in the Dellinger and Esteban, (2014) samples.

The permeability analysis from Tindilpie-11, Mena Murtee-1 and Saracen-1 show a number of interesting trends. As mentioned earlier the helium permeability will be used as the reference (Comisky et al., 2007). The Tindilipie-11 and Mena Murtee-1 helium, NMR and MICP Winland‘s permeabilities in nearly all cases show a consistent trend; a sample with relatively low helium permeability is predicted to be low relative to the other samples by NMR and MICP techniques. However, the variation observed between the predicted permeability from the different techniques is highly variable. Thus no scaling factor can predict from one technique to the other. In general, the following was observed from the three wells; MICP permeability using the Winland‘s equation was the highest predicted permeability followed by laboratory NMR using the SDR model, NMR using the Coates model, helium permeability and the lowest permeability was Klinkenberg corrected helium permeability.

The permeability variations/contradictions observed have also been observed by others (Cui et al., 2013, Yang and Aplin, 2007). Cui et al., (2013) suggest that the permeability estimates can vary by several orders of magnitude depending on sample orientation, sample size, fluid type, and analytical technique. It is further suggested that the results from different analytical techniques are not a contradiction but complement one another to provide the full picture of a complex, heterogeneous reservoir.

In a study conducted by Musu and Widarsono, (2007) using the Coates model and the SDR model to determine permeability they found that both methods gave different permeability results for low permeability, ductile, shaly sandstones. Their results suggest that the T_2 cut-offs of 22.6 msec and 33 msec significantly underestimated the Bulk Volume Irreducible (BVI) porosity leading to overestimation of rock permeability in rocks with high ductility; ductile rock fragments, kaolinite matrix and clay cement. These results may help to explain the variation in this study‘s results.

In a study by Rezaee et al., (2012) in which they investigated the permeability estimates from MICP and NMR data of tight gas sands they suggest that the Coates model T_2 cut off should be obtained from core analysis. They further suggest a value of R_{10} (the pore throat radius at 10 % mercury saturation) for the estimation of permeability using the Winland‘s equation instead of R_{35} for tight gas sands gives the best correlation with permeability. This saturation would occur at lower pressures and hence larger pore throat diameters leading to a higher prediction of permeability. This result would appear to be in contrast with the MICP Winland‘s permeability results of this study which were already high estimates compared to the other techniques utilised.

4.8 CHAPTER 4 CONCLUSIONS

The mercury porosimeter is accurate and repeatable as demonstrated on silica- alumina samples (standards). A blank correction without a sample is necessary to calibrate the mercury porosimeter. A blank sample is suggested to be used as part of the blank correction, but as demonstrated by the analysis of the fragile Thebe-2 samples there is no compression of the sample during the MICP analysis and is thus not required. The results from the standards indicate that a maximum variation of ± 0.015 g/ml and ±0.025 g/ml and ± 0.515 % for bulk density, grain density and porosity respectively is achievable and that results outside this variation will likely be due to sample variation and not the accuracy of the mercury porosimeter. The MICP curves from standard samples are in near perfect agreement and set the achievable level of accuracy of the mercury porosimeter. Both the IPV and MI techniques for threshold pressure determination are comparable.

The conformance correction as suggested by this study has not adversely affected the results of standard samples with minor conformance. As a result of the conformance correction, there has been a slight increase in the standard deviation between standard samples for bulk density, grain density and porosity. However, the conformance corrected MICP curves remain in agreement after conformance correction. The conformance correction method derived from this study is considered adequate.

The analysis of Saracen-1 comparing adjacent samples and samples from the 1.6m interval demonstrate that the conformance correction improves the agreement of MICP curves and porosity agreement between the samples. The MI method threshold pressures were ~5980 psia ± 10 psia for all samples while only 77 % of the samples were interpreted at this threshold pressure using the IPV method. Porosity variation between conformance corrected adjacent samples was 3.02 %, bulk density variation was 0.09 g/ml and grain density variation was 0.14 g/ml. This is considered to be a good gauge of the variation that can be observed between adjacent samples without any differing treatments. The sample weight was not found to have a relationship with porosity, bulk density or grain density results.

The adjacent samples dried with two different techniques are in better agreement for porosity, bulk density and grain density than samples from the 1.6 m interval of core dried with the same method. The air drying and freeze drying did not adversely affect MICP results. The freeze drying did tend to produce results with slightly less standard deviation than the air drying. The use of a vacuum pump to dry samples led to erroneous MICP results.

The porosity of the adjacent samples from Tindilpie-11, Mena Murtee-1 and Saracen-1 measured with helium, NMR and MICP show no consistent trends among the three wells. Any trends present are possibly masked by suspected heterogeneity between adjacent samples. The permeability results from the different techniques show a poor relationship between one another with the permeability estimates from the MICP analysis and Winland's permeability equation often leading to erroneous results. The porosity and permeability results from the different techniques highlight the need to analyse samples with a number of techniques to remove anomalous results.

CHAPTER 5: SAMPLE TYPE AND THE EFFECT ON MICP ANALYSIS

5.1 SUMMARY

The MICP analyses on four different sample types were investigated; conventional core, core coated with araldite on five sides allowing only vertical intrusion of mercury, synthetic cuttings made from crushed conventional core and drill cuttings taken from the well in close proximity to the conventional core samples.

The conformance correction (Appendix A, A.4) brought the MICP curves of the conventional core, vertical intrusion only and synthetic cutting samples into good agreement with one another. However, the MICP porosity values were not in agreement, suggesting that the samples were affected. The differences are thought to be a result of the surface area to volume ratio of the samples suggesting that the pores in the samples are not uniformly connected.

The drill cutting sample MICP analyses suggest that these samples are significantly different to the conventional core, vertical intrusion only and synthetic cutting samples. It is thought that this variation is a result of the heterogeneity of the drill cuttings being collected over a large sampling interval, the destructive effect of samples being agitated and disaggregated on the shale shakers and/ or the effect of sample washing and drying.

5.2 INTRODUCTION

Four types of samples and their effects on MICP analysis are analysed and discussed. Sample types are drill cuttings (DC), synthetic cuttings (SC), conventional core prepared for vertical intrusion (VI) only and conventional core (CC). The objective of this was to determine whether DC samples produce MICP analysis commensurate with CC samples. The research also evaluates the use of SC samples to approximate DC samples and compares results of CC samples to VI samples.

A number of authors including Sneider et al., (1997), Kivior (2005), Watson, (2012), Purcell, (1949), Schowalter, (1979) and Daniel and Kaldi, (2014) in Cook, (2014) have attempted to evaluate the usefulness of DC samples. Two different methodologies have been employed. The first methodology involves producing an SC sample by taking a CC plug and dividing it into two adjacent samples, leaving one intact and crushing the other. From the crushed sample, rock chips are taken and are considered to be representative of a DC

sample. The advantage of this methodology is the location of the SC sample is precisely known which allows a direct comparison with the adjacent CC sample. This is in contrast to the DC sample which undoubtedly has heterogeneity due to a large (5-10 m) sampling interval, which may contain different lithologies/ formations affecting the result.

The second methodology to evaluate the usefulness of DC samples relies on finding wells with DC samples taken near or over the conventional core interval and attempting to relate the MICP analysis between the DC and CC samples. The uncertainties with this method result from attempting to relate a DC sample interval (metres) to a CC plug or plugs (centimetres). Thus it is difficult to suggest if the differences in MICP analyses are a result of the drilling process or a result of heterogeneity that was not accounted for in the sampling and analyses of the CC interval.

The main challenge with understanding the effect of sample type on MICP analyses is distinguishing whether these differences (such as between DC and CC) are due to the sample type or to sample heterogeneity. The rock material used in the following analyses are sourced from petroleum wells and commonly do not have accompanying mineralogical analysis, which makes it difficult to distinguish between these two variables. Where both MICP analysis and mineralogical analysis are available for both DC and CC samples and the mineralogies are similar then the MICP analyses are also expected to be similar. Where there are similar mineralogies and differences in MICP analysis, there is a strong indication that these differences are due to sample type or sample preparation.

The chapter includes a re-interpretation of the results of Watson, (2012), Sneider et al., (1997) and Kivior, (2005) using the conformance correction suggested by this study in Appendix A, A.4. These results will be compared to the analyses of Saracen-1 CC and DC samples from the same 1.6 m interval using the same conformance correction. As observed in the analysis by Daniel and Kaldi, (2014) in Cook (2014) the conformance observed in DC samples is considerably higher than in CC samples. Thus the conformance correction applied needs to be accurate to compare DC samples with CC samples and make inferences regarding the observed changes. This analysis incorporates mineralogy from X-ray diffraction (XRD) analyses and images of shale fabric from the backscatter electron (BSE) microscope in addition to MICP analyses.

5.3 LITERATURE REVIEW

The effects of sample type on MICP analysis have been investigated by numerous authors including Purcell, (1949), Schowalter (1979), Sneider et al., (1997), Kivior (2005), Watson,

(2012), and Daniel (2014) in Cook (2014). Their research aims to investigate the differences between the MICP analysis from DC and CC samples. Conventional core allows sampling of specific sealing intervals and baffles on a centimetre scale allowing a considerable degree of certainty in the results. However, in many instances, the only rock samples of sealing intervals are from drill cuttings and these have been subjected to the impact of drilling, drilling muds, cave-ins from higher in the wellbore, shale shaker disaggregation and the effects of washing and drying. Further, the time taken for the DC samples to circulate to the surface needs to be estimated and assigned a depth adding another degree of uncertainty. Also, DC samples are commonly from a large interval (5-10 m) depending on the sampling regime and the proximity to the formation of interest. This could lead to other formations than the target sealing formation being sampled not to mention the natural heterogeneity within the sealing formation. Thus the MICP analysis from DC samples has a great degree of uncertainty in comparison to samples from CC.

Purcell, (1949) indicated that one of the advantages of MICP is that the method can obtain accurate capillary pressure measurements results from not only large regular shaped core plugs but also from small irregular shaped DC samples.

Schowalter, (1979) investigated the reliability of MICP analysis from SC samples. He evaluated four cutting samples; two from sandstone formations, one from interbedded sand and shale formation and one from a chalk sample. The samples were crushed and divided into four groups from large to small; the group with the largest samples were approximately ~2.5 cm in width and the average sample size in the groups decreased to approximately < 0.5 cm in the group with the smallest samples. The resulting MICP curves displayed three general trends; a slight increase in irreducible saturation with decreasing sample size, a slight reduction in estimated displacement pressure (10 % saturation) and capillary pressure plateaus with decreasing sample size. Schowalter, (1979) concluded that satisfactory capillary pressure analysis could be obtained from full diameter cores, sidewall cores and drill cuttings.

Sneider et al., (1997), Kivior, (2005) and Watson, (2012) attempted to characterise the differences in MICP analysis between CC and DC samples by creating synthetic cutting samples. Sneider et al., (1997) created the synthetic cuttings by sampling the rock adjacent to the core plug and crushing the sample. Watson, (2012) compared conventional core unglued, conventional core glued (stops horizontal intrusion) and synthetic cuttings. The synthetic cuttings were produced by crushing the conventional core plug sample.

Kivior, (2005) undertook a comprehensive study investigating the differences in MICP analysis of core, glued core (vertical intrusion only), cuttings (taken above and below the conventional core) and synthetic cuttings (crushed core samples). As detailed above Kivior, (2005) used the 1st derivative method to remove conformance (Pd) and then added 10 % to estimate threshold pressure (Pth). The analysis and subsequent interpretation suggest that the displacement pressures (Pd) for each sample type, for each well vary by ± 3 %. The subsequently interpreted threshold pressures vary between 6 and 20 %.

Watson, (2012) also attempted to determine if there were any differences between conventional core, glued conventional core and synthetic cuttings. Conventional cored Belfast Mudstone was sampled from FI1-1943 well in the Port Campbell Embayment. Watson, (2012) interpreted a clear decrease in threshold pressure in the synthetic cuttings which he attributed to compromised (deformed or altered) pore throats as a result of the crushing.

The reader is directed to section 4.3 for a review of the work by Comisky et al., 2011 and Darlak et al., (2011). Both experimented with crushed samples which are considered in the effects of sample size. The act of crushing the conventional core leads to samples that are similar to the synthetic cuttings produced by Snieder et al., (1997), Kivior, (2005) and Watson, (2012) and should thus be taken into account.

5.3.1 **Flaxman-1, Otway Basin**

Flaxman-1 was drilled in 1961 by Frome-Broken Hill Company in the Otway Basin, Southwest Victoria. The well was drilled to a depth of 3513 m with forty-four conventional cores collected totaling 116 m of recovered core. MICP analysis was conducted on the Belfast Mudstone samples in 2002 and presented in Watson, (2012) and subsequently re-interpreted herein.

Methodology: Watson, (2012) followed the following procedure to compare the MICP analysis of different sample types. The first two samples of Belfast Mudstone were cut into cubes; one sample was analysed using standard methodology. The second sample was orientated and coated with araldite resin on five sides allowing only vertical intrusion (VI) of mercury. A third SC sample was created by crushing a piece of the CC. This provided the raw data for re-interpretation.

This study interpreted the threshold pressures for the uncorrected data using both the IPV and MI method. Subsequently, the uncorrected data were conformance corrected and the threshold pressures were re-interpreted. The uncorrected porosities, bulk densities and grain

densities were then compared to the conformance corrected porosities, bulk densities and grain densities.

Results: The uncorrected MICP curves for the three sample types are shown in Appendix C Figure C-1. The three MICP curves show a similar shape and position on the graph. The three curves, however, do show differences in mercury saturation at low pressures which become more significant. When pressure increases to 20,000 psia the MICP curves come into agreement. At pressures approximating the threshold pressures (5500 psia) of the samples, the mercury saturation is highest for the SC sample, followed by the VI sample, followed by the CC sample. The conformance corrected MICP curves for the three sample types are shown in Appendix C Figure C-2. The three MICP curves show excellent agreement with one another with minor variation observed at pressures above 20,000 psia.

The uncorrected (raw) and conformance corrected MICP analysis is shown in Table 5-1. The conformance corrected porosities indicate that the SC sample has the highest porosity (10.53 %) followed by the CC (7.78 %) and lastly the VI sample (5.5 %). The pore volume per gram shows the same trend while the grain volume per gram shows the reverse trend. The sample volume per gram is largest for the VI followed by the SC sample and lastly by the CC sample. The bulk density was highest for the CC sample (2.38 g/ml) followed by the SC sample (2.34 g/ml) and lowest for the VI sample (2.33 g/ml). The threshold pressures using the IPV method were interpreted at the same pressure equilibrium point for both the CC and VI samples (~6970 psia). The SC sample was interpreted at the pressure equilibrium point below (5982 psia). The threshold pressure was interpreted at 5974 psia using the MI method for the CC sample, the pressure equilibrium point below for the VI sample (4976 psia) and SC sample (4977 psia).

Table 5-1: MICP results from Belfast Mudstone samples, Flaxmans-1 (Re-interpretation of results from Watson, 2012).

Sample Type	Sample Weight (g)	Porosity (%)		Bulk Density (g/ml)		Grain Density (g/ml)		Sample Volume (ml/g)		Pore Volume (ml/g)		Grain Volume (ml/g)		IPV Threshold Pressure (psia)		MI Threshold Pressure (psia)	
		Raw	Cor.	Raw	Cor.	Raw	Cor.	Raw	Cor.	Raw	Cor.	Raw	Cor.	Raw	Cor.	Raw	Cor.
Core	9.7	8.36	7.78	2.36	2.38	2.58	2.58	0.423	0.420	0.036	0.033	0.387	0.387	6969	6969	5974	5974
Vertical Intrusion	2.33	6.44	5.5	2.31	2.33	2.47	2.47	0.433	0.429	0.028	0.024	0.405	0.405	6970	6970	4976	4976
Cutting	2.15	13.36	10.53	2.26	2.34	2.61	2.62	0.442	0.427	0.059	0.045	0.382	0.382	5982	5982	5982	4977
Average	4.73	9.39	7.94	2.31	2.35	2.55	2.56	0.432	0.425	0.041	0.034	0.391	0.391	6640	6640	5644	5309
SD	4.308	3.572	2.519	0.050	0.026	0.074	0.078	0.009	0.004	0.016	0.011	0.012	0.012	570	570	579	576

Discussion: Conformance correction of the MICP curves brought the curves into excellent agreement for all three sample types. The breaking of the CC into an SC did not affect the pore throats or the ability for mercury to intrude the sample. Further, the coating of the sample allowing vertical intrusion did not affect the pore throats or the ability of mercury to intrude the sample. This is demonstrated by the MICP curves showing excellent agreement and hence having the same mercury saturations for the same pressure (pore throat diameter).The threshold pressures interpreted with the IPV and MI method shows a maximum of one pressure equilibrium point variation. This is within the variation observed between adjacent Saracen-1 samples (Section 4.5.1) and is not considered significant.

Sample preparation did affect the porosity, bulk density and grain density results of the different sample types even after conformance correction. The porosity showed the following trend; the SC samples had the highest porosity (13.36 % to 10.53 % after conformance correction), followed by the CC sample (8.36 % to 7.78 % after conformance correction) and lastly the VI sample (6.44 % to 5.5 % after conformance correction). The variation in porosity is greater than that observed in Saracen-1 (Section 4.5) over the 1.6 m interval (3.24 %) and between adjacent samples (3.02 %). On review of the pore volume per gram and grain volume per gram, it can be determined which parameter is leading to the variation in porosity. The grain volume per gram shows a slight variation in a reverse trend to the pore volume per gram. It can be observed that the samples with high pore volume per gram results have lower grain volume per gram results and vice versa. Thus it can be suggested that sample type and preparation affects the accessible pore volume per gram but not the pore throats of the rock sample. The greatest accessibility to the pore network was found from the SC sample, followed by the CC sample and lastly the VI sample. It can thus be suggested that the ratio of exposed surface to volume of rock sample affects the porosities significantly. In this example, the porosity result varied up to ~50 % after conformance correction depending on sample type and preparation.

5.3.2 **Five Sealing Formations from Unknown Well/S**

Sneider et al., (1997) describe five sealing formations from unknown well/s., Four of these have descriptions and SEM photographs provided. Sneider et al., (1997) conducted the MICP analyses, but the uncorrected analyses were unavailable. The results have been re-interpreted by this study.

Methodology: Sneider et al., (1997) conducted the MICP analysis on a vertical epoxy sealed plug (VI) and the adjacent surrounding material was crushed to form an SC. The mercury pressure was increased stepwise to 60, 000 psia. The sample was closure corrected. Sneider

et al., (1997) state that closure pressure (conformance) is the pressure at which mercury first enters the rock pore space. Conformance corrections are particularly important for drill cuttings which have higher closure due to the irregularity of the sample and its surface. Sneider et al., (1997) use the terminology entry pressure (Pe) to describe the point at which mercury first enters the pore network and Pe 7.5 % to describe the point at which continuous filaments of mercury are formed. This is defined as the threshold pressure by other authors (Daniel and Kaldi, 2014 in Cook, 2014).

In an attempt to remain consistent with the other analysis, this study has re-interpreted the threshold pressures from the Sneider et al., (1997) conformance corrected MICP curves using the MI method. The IPV method for picking threshold pressures could not be used due to the absence of the raw information.

Results: The MICP curves for the VI sample and the SC sample are shown in Appendix C Figure C-3. The SC sample has clearly higher mercury saturation than the VI sample during the initial pressure equilibrium points up until 179 psia, where the MICP curves come into agreement. Based on the pressure limited MICP curves presented, the MI threshold pressures are interpreted at 179 psia for both samples. No porosity, bulk density or grain density data are available.

The MICP curves of the two sample types (VI and SC) for the four (A-D) sealing formations are shown in Appendix C Figure C-4. The MICP curves for ~~–A~~" seal VI and SC samples show variation up to 20 % mercury saturation and subsequently show excellent agreement with one another; both shape and position on the graph. The variation between MICP curves has led to different threshold pressures interpreted using the MI method. Table 5-2 shows the threshold pressures interpreted for the SC and VI sample. The VI sample has been interpreted at a pressure equilibrium point higher than the SC sample (4000 psia and 3500 psia respectively).

The MICP curves for ~~–B~~" seal SC sample and VI sample are shown in Appendix C Figure C-4.The MICP curves for ~~–B~~" seal VI and SC samples show variation up to 30 % mercury saturation and subsequently show excellent agreement with one another; both shape and position on the graph. The variation between MICP curves has led to different threshold pressures interpreted using the MI method. Table 5-2 shows the threshold pressures interpreted for the SC and VI sample. The VI sample has been interpreted at a pressure equilibrium point higher than the SC sample (800 psia and 720 psia respectively).

The MICP curves for ―C" seal VI and SC samples are shown in Appendix C Figure C-4. Both VI and SC samples are similar in position on the graph with some minor differences in the shape of the MICP curve. The SC sample MICP curve shows higher mercury saturation from ~40 psia to ~300 psia before coming into agreement with the VI sample at ~1000 psia and subsequently showing lower mercury saturation than the VI sample up to 60,000 psia. The variation between ~40 psia to ~300 psia occurs where the MI threshold pressure is interpreted and has led to the threshold pressure interpreted at a higher pressure for the VI sample (Table 5-2).

The VI and SC sample MICP curves for ―D" seal are shown in Appendix C Figure C-4. Both samples are similar in position on the graph but have some minor differences in the shape of the MICP curves. The SC sample MICP curve shows slightly higher mercury saturation from ~30 psia to ~150 psia before overlaying the VI sample at ~200 psia. Post ~200 psia the SC sample shows lower mercury saturation than the VI sample up to 60,000 psia. The variation between ~30 psia to ~150 psia occurs at the pressure where the MI threshold pressure is interpreted and has led to the threshold pressure being interpreted higher for the VI sample (Table 5-2).

Table 5-2: Re-interpreted of threshold pressures using the maximum inflection point (MI) methodology (Re-interpretation of results from Sneider et al., 1997)

Sample	Description	Threshold Pressure (MI method) Convent. Core	Threshold Pressure (MI method) Syn. Cuttings
A	Predominant clay structure no grain contact	4000 psia	3500 psia
B	Grain support and limited diagenetic clay	800 psia	720 psia
C	Grain support with intergranular clay particles	250 psia	200 psia
D	Grain support with quartz overgrowths	800 psia	720 psia

Discussion: The threshold pressure results using the MI method indicate that other than the first sample, there is a difference in the threshold pressures between the VI and SC samples. The results from seal samples A-D indicate that there is approximately a one pressure equilibrium point difference in the threshold pressures interpreted from the MICP curves. The SC samples consistently have the lower threshold pressures. However, the MICP curves for sample A and B only show variation over the maximum inflection point where the threshold is interpreted using the MI method. Additionally, samples C and D show variation over the maximum inflection point of the MICP curve and only slight variation towards higher mercury saturations.

The heterogeneity that can be expected in adjacent samples can be observed in the results from Section 4.5 analysing the repeatability of adjacent samples from Saracen-1. These results suggest that the variation in MICP curves over the 70 % to 100 % mercury saturation in samples C and D is not more than that observed in adjacent samples from Saracen-1. However, the variation in MICP curves between samples A, B, C and D over the 0 % to 20 % mercury saturation including the maximum inflection point are greater than the heterogeneity observed in Saracen-1 samples that were conformance corrected. The variation observed is more reminiscent of the variation in uncorrected Saracen-1 MICP curves.

The variation of the MICP curves over the 0 % to 20 % mercury saturation of the VI and SC sample MICP curves is most likely due to an inadequate conformance correction. This has led to partial conformance altering the initial MICP curve of the SC sample (where more conformance is expected) from the VI sample. This has resulted in the incorrect picking of the maximum inflection point and subsequent interpretation of a lower threshold pressure. The rationale for attributing the differences in the MICP curves between 0 % and 20 % mercury saturation to the conformance correction stems from the relationship between pressure and pore throat radius as established by Washburn, (1921) section 2.4 Equation 1. When converting pressure to pore throat radius for the four seal types more ~~"l~~arge" pore throats occur between 0 % and 20 % mercury saturation for each SC sample type. However, the pore throat radii are not affected beyond this initial 0 % to 20 % mercury saturation (both MICP curves match). It is reasoned that if the creation of an SC sample was going to alter the pore throats of the sample and the resulting MICP curve, then it would alter all pore throats not just the ~~"l~~arge" ones. Note these ~~"l~~arge" pore throats occur at different pore throat radii for the different samples thus it is not occurring at a certain pore throat radius.

Thus it is suggested that the higher initial mercury saturation in the SC samples is not representing ~~l~~arge" pores but conformance as a result of crushing the sample.

5.3.3 **Swan-1, Vulcan Sub-basin**

Swan-1 was drilled in 1972 by Arco Australia Limited and partners in the Vulcan Sub-basin, Bonaparte Basin Western Australia. The well was drilled into the limb of a structural high and encountered a number of thin gas bearing sand intervals in the Upper Cretaceous and Upper Jurassic sections. The well was drilled to a depth of 3284 m. A conventional core was cut from 2830 m to 2836.5 m and is described as shale in the well completion report (WCR).

Methodology: Kivior, (2005) undertook a comprehensive study examining the differences in MICP analysis from; conventional core (CC), vertical intrusion (VI) prepared conventional core and synthetic cuttings (SC) from Swan-1. The preparation of samples was similar to Sneider et al., (1997) and Watson, (2012). To compare and contrast results from Swan-1 with other analyses, the results have been re-interpreted using the conformance correction suggested in this study (Appendix A, A.4) and the IPV and MI method to pick threshold pressures. As the uncorrected MICP data are available, the porosity, bulk density and grain density results can be compared, both with and without conformance correction.

There is limited background information provided on the samples from the analysis. The SEM images of samples from Swan-1 in Kivior, (2005) show a dominant clay fabric with a possible quartz grain. Kivior, (2005) further describes the samples as having carbonate support in the clay fabric.

Results: The MICP curves for the three sample types are shown in Appendix C Figure C-5. The MICP curves for the three sample types show a similar shape but poor agreement up until ~70 % mercury saturation where they begin to overlay and show a continued upward trend to 100 % mercury saturation. The conformance corrected MICP curves (Appendix C Figure C-6) show excellent agreement. The CC and VI samples have excellent agreement while the SC MICP curve shows very slight offset. The CC sample and the VI sample have zero mercury intrusion for at least one pressure equilibrium point higher, respectively than the SC sample.

The conformance corrected porosity is 5.17 % for the CC sample, 3.55 % for the VI sample and 6.1 % for the SC sample (Table 5-3). The highest bulk density is for the CC sample (2.5 g/ml) followed by the SC sample (2.45 g/ml) and lastly the VI sample (2.26 g/ml). The corrected grain density results show the same pattern (2.63 g/ml, 2.61g/ml and 2.34 g/ml respectively). The corrected sample volume per gram results for the CC sample is 0.399

ml/g and increases to the SC sample (0.409 ml/g) and again to the VI sample (0.442 ml/g). The grain volume per gram shows the reverse trend with the VI sample having the highest grain volume (0.426 ml/g) followed by the SC sample (0.384 ml/g) and the CC sample (0.380 ml/g). The pore volume per gram follows a different pattern with the highest pore volume per gram recorded for the SC sample, followed by the CC sample and lastly the VI sample. The threshold pressures interpreted with the IPV method are consistent across the three sample types (~9970 psia) while the threshold pressures interpreted with the MI method are also consistent at the pressure equilibrium point below the IPV method (~8507 psia).

Table 5-3: Swan-1 MICP analyses of different sample types from conventional core at a depth of 2835.9m.

Sample Depth (m)	Sample Weight (g)	Porosity (%)		Bulk Density (g/ml)		Grain Density (g/ml)		Sample Volume (ml/g)		Pore Volume (ml/g)		Grain Volume (ml/g)		IPV Threshold Pressure (psia)		MI Threshold Pressure (psia)	
		Raw	Cor.	Raw	Cor.	Raw	Cor.	Raw	Cor.	Raw	Cor.	Raw	Cor.	Raw	Cor.	Raw	Cor.
Conventional Core	4.58	5.17	4.93	2.5	2.5	2.64	2.63	0.400	0.399	0.020	0.020	0.380	0.380	9970	9970	8517	8517
Vertical Intrusion	5.03	5.65	3.55	2.21	2.26	2.35	2.34	0.452	0.442	0.025	0.016	0.426	0.426	9994	9994	9994	8470
Synthetic Cutting	3.2	7.81	6.1	2.4	2.45	2.6	2.61	0.417	0.409	0.033	0.025	0.384	0.384	9956	9956	9955	8507
Average	4.27	6.21	4.86	2.37	2.40	2.53	2.53	0.42	0.42	0.03	0.02	0.40	0.40	9973.33	9973.33	9488.67	8498.00
Stdev.	0.954	1.406	1.276	0.147	0.127	0.157	0.162	0.027	0.023	0.006	0.005	0.026	0.026	19.218	19.218	841.714	24.759

Discussion: The differences observed in the uncorrected MICP curves of the different sample types in comparison to the similarity observed in the conformance corrected MICP curves highlights the importance of accurately removing conformance. The MICP curves suggest that the samples have a very similar pore throat networks and that there are no significant differences between the MICP curves of the different sample types.

The conformance corrected threshold pressure interpretations using the two methods indicate that the samples are relatively homogeneous with both methods being consistent over the three sample types. However, the two techniques differ in threshold pressures interpretations by one pressure equilibrium point, i.e. the IPV method has a threshold pressure of ~9970 psia and the MI method has a threshold pressure of~8507 psia.

The uncorrected and corrected conformance porosity indicates that the sample type does affect the result. However, the variation in porosity is not greater than the variation observed in Saracen-1 (Section 4.5) samples over the 1.6m interval (3.24 %) and between adjacent samples (3.02 %).The SC sample has the highest porosity followed by the CC sample and the VI sample; 6.1 %, 4.93 % and 3.55 % respectively. The sample volume per gram and grain volume per gram indicate that the sample type is affecting the analyses. The SC sample has the highest pore volume followed by the CC sample and the VI sample indicating that the sample type is affecting the pore volume that is accessible. Thus a relationship between surface area and pore accessibility is again suggested. The grain volume per gram should theoretically show the opposite trend because of the added porosity not being filled by the mercury and thus being included in the grain volume per gram measurement which should result in a higher grain volume while the weight remains consistent. This is observed in the VI sample, however, this appears to be extreme. It is thus suggested that the application of araldite resin to the five sides of the sample cube has affected the grain volume per gram measurement. The Araldite resin has no porosity and has a low relative density (between 0.95 and 1.20 Selleys, (2014)) which in combination is thought to have led to an increased grain volume with only minor changes in weight resulting in a higher grain volume per gram result.

This trend is not observed between the CC and SC samples with the CC sample having a slightly lower grain volume per gram than the SC sample. If the rock is uniform, then the result in not in line with the theory.

The bulk density and grain density results of the CC, SC and VI sample reflect the variations in pore volume per gram and grain volume per gram which has led to the bulk density being

highest for the CC sample followed by the SC sample and VI sample. The grain density is slightly higher for the CC sample over the SC sample and much higher than the VI sample.

5.3.4 **Puffin-2, Vulcan Sub-basin**

Puffin-2 was drilled in 1974 by Arco Australia Limited and partners in the Vulcan Sub-basin, Bonaparte Basin Western Australia. The well was drilled on a large faulted anticline structure and encountered numerous oil and gas shows in the Palaeocene - Upper Cretaceous section. The well was drilled to a depth of 2560 m. A conventional core was cut 2035 m to 2045.5 m and is described in the WCR as an interbedded sand shale package.

Methodology: The analysis conducted by Kivior, (2005) on Puffin-2 provides a rare opportunity to compare the results from a conventional core (CC) sample, a vertical intrusion (VI) sample, a synthetic cutting (SC) sample taken (between 2042.47 m and 2043.39 m depth), and a drill cutting (DC) sample taken from between 2045 m and 2048 m depth.

The preparation of samples was similar to Sneider et al., (1997) and Watson, (2012), though DC samples were included. To compare and contrast the results from Puffin-2 with other analyses, the results were re-interpreted using the conformance correction herein (Appendix A, A.4) and the IPV and MI method to pick threshold pressures (Appendix A, A.7). Using the uncorrected MICP data, the porosity, bulk density and grain density results can be compared, both with and without conformance correction.

Results: The uncorrected MICP curves for the four different sample types show poor agreement with one another (Appendix C Figure C-7). Both the DC and the SC samples show similar high mercury saturation, although they have a distinctively different MICP curve shape. The CC and VI samples show low initial mercury saturation and similar MICP curves; both shape and position on the graph.

The conformance corrected MICP curves for the different sample types are shown in Appendix C Figure C-8. The MICP curve of the DC sample has a distinctively different curve shape to the other three sample types, which is indicative of different pore throat networks. The CC sample has an MICP curve showing a similar pattern to the VI and SC samples but is in poor agreement due to a smaller diameter pore throat network. The VI and SC curves vary slightly up to 50 % mercury saturation above which saturation they overlay.

The conformance corrected porosity (Table 5-4) show that the DC sample has a much higher porosity (11.87 %) than the CC sample (5.93 %), the SC sample (4.32 %)and the VI sample

(2.89 %). Using the CC sample as a baseline for comparison, the DC samples have low bulk and grain density while the SC and VI samples have only a slightly lower bulk and grain density to the CC samples. The IPV threshold pressure for the samples is at the same pressure equilibrium point for the CC and SC sample (~2068 psia), higher for the VI sample (2936 psia) and much higher for the DC sample (4985 psia). The MI threshold pressures indicate that the CC sample and VI sample are at the same pressure equilibrium point (2936 psia) while the SC sample is at a lower pressure equilibrium point (2483 psia). The DC sample has a significantly higher MI threshold pressure compared to the other three sample types (4985 psia).

Table 5-4: Puffin-2 MICP results of different sample types from conventional core.

Sample Depth (m)	Sample Weight (g)	Porosity (%)		Bulk Density (g/ml)		Grain Density (g/ml)		Sample Volume (ml/g)		Pore Volume (ml/g)		Grain Volume (ml/g)		IPV Threshold Pressure (psia)		MI Threshold Pressure (psia)	
		Raw	Cor.	Raw	Cor.	Raw	Cor.	Raw	Cor.	Raw	Cor.	Raw	Cor.	Raw	Cor.	Raw	Cor.
Conventional Core	1.79	6.29	5.93	2.61	2.63	2.79	2.79	0.382	0.381	0.024	0.023	0.358	0.358	2064	2064	2937	2937
Vertical Intrusion	2.55	3.1	2.89	2.55	2.56	2.63	2.63	0.392	0.391	0.012	0.011	0.380	0.380	2936	2936	2936	2936
Synthetic Cutting	1.51	5.78	4.32	2.5	2.54	2.65	2.65	0.400	0.394	0.023	0.017	0.377	0.377	2071	2071	2483	2483
Drill Cuttings	3.04	16	11.87	2.05	2.16	2.44	2.45	0.488	0.465	0.078	0.055	0.410	0.410	4985	4985	4985	4985
Average	2.22	7.79	6.25	2.43	2.47	2.63	2.63	0.416	0.408	0.034	0.026	0.381	0.381	3014.00	3014.00	3335.25	3335.25
Stdev.	0.70	5.65	3.95	0.256	0.212	0.144	0.140	0.049	0.038	0.030	0.020	0.021	0.021	1376.3	1376.3	1120.4	1120.4

Discussion: The uncorrected MICP curves indicate that the SC and DC samples have high initial mercury saturation at pressures below ~1000 psia that are not observed in the CC and VI samples. The conformance corrected MICP curves confirm that this initial saturation is due to conformance of the samples. The conformance corrected MICP curves of the four sample types are still not in agreement, indicating that there are differences in pore throat size distributions between the sample types. The general shape of the MICP curves is similar for all samples except the DC sample indicating a significantly different pore throat distribution.

The conformance corrected porosity, bulk density, grain density, sample volume per gram, pore volume per gram and threshold pressures for the DC sample relative to the other sample types show significant differences. This along with the dissimilar MICP curve suggests a very different sample type. Given the core was described as interbedded sand and shale it is likely that the drill cutting sample contains both lithologies as it was from a 3 m interval below the core. This is supported by the bimodal (two inflections of the MICP curve indicating two dominant pore throat sizes) MICP curve. The variation in porosities is greater than the variation observed in the Saracen-1 (Section 4.5) samples along the 1.6 m interval (3.24 %) and more than the variation observed between adjacent samples (3.02 %).

The conformance corrected porosity, bulk density, grain density, sample volume per gram, grain volume per gram, pore volume per gram and threshold pressure results indicate that the CC, VI and SC samples do vary from one another. The VI sample has a significantly lower porosity in comparison to the CC and VI sample that is a result of the low pore volume per gram measurement for that sample. This suggests that the preparation of the VI sample is restricting the access of mercury to the sample pore system leading to a low porosity. The other results do show variation, but it is not possible to determine whether the variation is a result of the sample preparation or heterogeneity between adjacent samples.

5.3.5 **Tenacious West-1, Bonaparte Basin**

Tenacious West-1 was drilled in 1999 by Woodside Offshore Petroleum Pty. Ltd in the Vulcan Sub-basin, Bonaparte Basin Western Australia. The well was drilled as an offset well to test the Tenacious structure. The target was the late Jurassic sandstone member which was found to be water bearing. The well was drilled to a depth of 3060 mRT. Drill cutting (DC) samples were collected at 10 m intervals. One set of samples were washed and air dried and subsequently split into five sets. The second set of unwashed samples were not split but retained in their cloth bags. The third set of samples were collected in ~~–s~~amplex" trays. The first and second sets of samples were sent to the Bureau of Research Sciences

(BRS) and to the Northern Territory Geological Survey (NTGS) respectively. Woodside retained the remaining sets. Also, a conventional core was cut from a depth of 2801 mRT to 2855 mRT. The core was described as predominantly sandstone with minor silty sandstone and siltstone intervals in the WCR (Willis, 1999).

Methodology: Two conventional core samples from Tenacious West-1 were used to test sample type/ preparation and the subsequent effects on MICP analyses (Kivior, 2005). The first sample was taken at a depth of 2810.04 m and was divided into three adjacent samples. Two of the adjacent samples were prepared with araldite resin for vertical intrusion (VI) only, the third sample was analysed as a CC sample.

A second core sample was taken at a depth of 2846.04 m and divided into five adjacent samples. Two of the adjacent samples were prepared as VI samples, two adjacent samples were crushed to produce synthetic cuttings (SC) and the last sample was analysed as a CC sample.

In addition, Kivior, (2005) took two DC samples and divided the DC samples by lithology and subsequently analysed the samples with MICP to gauge the variability within a DC sample. The DC samples were taken from a 5 m and 10 m interval. The only description of the samples was that attached to the original MICP analyses and that of Kivior, (2005) who described the CC at a depth of 2846.04 m as a ~~"s~~ealing interval consisting of interbedded siltstone and claystone". The following provides a re-interpretation of the MICP analyses.

5.3.5.1 Results – 2810.04 m

The MICP curves for the three sample types (CC, VI and VI repeat) from the conventional core at 2810.04 m depth show poor agreement with one another (Appendix C Figure C-9). The VI sample has a pore throat network that is significantly different to the other two samples; the shape of the MICP curve suggests that the sample is influenced by two common pore throat sizes while the other two samples show a linear trend with no such influence.

The conformance corrected MICP curves (Appendix C Figure C-10) still show significant variation to one another. The conformance corrected porosity, bulk density and grain density results for the different sample types (Table 5-5) indicate that the CC and the VI repeat samples are similar. However, the threshold pressures interpreted with the IPV and MI method are different. The VI sample shows a higher porosity, a lower bulk density, similar grain density and a higher pore volume per gram in comparison to the other two sample

types. Also, the interpreted threshold pressure for this sample is significantly higher than the other two sample types.

Table 5-5: Tenacious West-1 MICP results of different sample types from conventional core at a depth of 2810.04m.

Sample Depth (m)	Sample Weight (g)	Porosity (%)		Bulk Density (g/ml)		Grain Density (g/ml)		Sample Volume (ml/g)		Pore Volume (ml/g)		Grain Volume (ml/g)		IPV Threshold Pressure (psia)		MI Threshold Pressure (psia)	
		Raw	Cor.	Raw	Cor.	Raw	Cor.	Raw	Cor.	Raw	Cor.	Raw	Cor.	Raw	Cor.	Raw	Cor.
Conventional Core	7.73	6.3	6.1	2.51	2.51	2.67	2.68	0.399	0.398	0.025	0.024	0.374	0.374	341	341	602	602
Vertical Intrusion	1.04	10.87	9.52	2.38	2.41	2.67	2.67	0.420	0.414	0.046	0.039	0.374	0.374	4980	4980	4283	4283
Vertical Intrusion Repeat	2.25	6.85	6.85	2.48	2.48	2.66	2.66	0.403	0.403	0.028	0.028	0.375	0.375	1453	1453	2054	2054
Average	3.67	8.01	7.49	2.46	2.47	2.67	2.67	0.407	0.405	0.033	0.030	0.374	0.374	2258.0	2258.0	2313.0	2313.0
Stdev.	3.565	2.495	1.798	0.068	0.051	0.006	0.010	0.011	0.008	0.011	0.008	0.001	0.001	2422.0	2422.0	1854.1	1854.1

Discussion: The MICP curves and threshold pressures for the different samples types, including the VI samples, including post conformance correction have a significant variation to one another. The dissimilarity observed in these MICP curves and interpreted threshold pressures suggest that along with sample preparation there is considerable heterogeneity between the adjacent samples that is affecting the MICP analyses. This is supported by the two VI samples prepared in the same manner but with poor agreement in their MICP curves. It is further supported by the porosity variation being more than that observed between Saracen-1 (Section 4.5.1) samples over the 1.6 m interval (3.24 %) and the variation in threshold pressures being much more than the one pressure equilibrium point apart. The variation in MICP curves and interpreted threshold pressures strongly suggests that samples have significantly different pore throat networks that are not caused by sample preparation but by rock heterogeneity.

5.3.5.2 Results – 2846.04 m

The uncorrected MICP curves (Appendix C Figure C-11) for the different samples show poor agreement with one another. However, both SC samples have similar MICP curve patterns, slightly offset at low pressure and displaying higher initial mercury saturation than the samples prepared as CC and VI. The two samples prepared for VI both show a similar MICP curve pattern although separated by ~800 psia at approximately 10 % mercury saturation and progressively coming together with increased pressure.

The conformance corrected MICP curves for the different sample types show reasonable agreement to one another (Appendix C Figure C-12). The SC MICP curves nearly perfectly overlay one another. The two VI samples have similar shaped MICP curves to the SC samples; the VI sample shows better agreement than the VI repeat sample. The CC sample MICP curve is least similar to the other sample types, although the curve shapes are similar.

The corrected porosities (Table 5-6) indicate a maximum variation between samples of 2.5 %. The bulk density and grain density for all samples except the VI sample are all in reasonable agreement. The VI sample has an anomalously high sample volume per gram in comparison to the other sample types. The interpreted threshold pressures vary by one pressure equilibrium point using the MI method and up to two pressure equilibrium points using the IPV method. The IPV method has a lower average threshold pressure (9072 psia) than the MI method (10759 psia).

Table 5-6: Tenacious West-1 MICP results of different sample types from conventional core at a depth of 2846.04m.

Sample Depth (m)	Sample Weight (g)	Porosity (%)		Bulk Density (g/ml)		Grain Density (g/ml)		Sample Volume (ml/g)		Pore Volume (ml/g)		Grain Volume (ml/g)		IPV Threshold Pressure (psia)		MI Threshold Pressure (psia)	
		Raw	Cor.	Raw	Cor.	Raw	Cor.	Raw	Cor.	Raw	Cor.	Raw	Cor.	Raw	Cor.	Raw	Cor.
Conventional Core	4.43	5.67	5.26	2.55	2.56	2.71	2.71	0.391	0.390	0.022	0.021	0.369	0.369	6970	6970	9972	9972
Vertical Intrusion	4.2	5.13	5.11	2.4	2.4	2.53	2.53	0.417	0.417	0.022	0.021	0.395	0.395	9950	9950	9950	9950
Vertical Intrusion Repeat	3.13	6.32	6.15	2.53	2.53	2.7	2.7	0.396	0.395	0.025	0.024	0.371	0.371	9950	9950	9950	9950
Synthetic Cutting	2.41	8.96	5.92	2.43	2.51	2.67	2.67	0.412	0.398	0.037	0.024	0.375	0.375	9985	9985	11947	11947
Synthetic Cutting Repeat	1.45	10.6	7.61	2.48	2.57	2.77	2.78	0.403	0.390	0.043	0.030	0.360	0.360	8503	8503	11978	11978
Average	3.12	7.34	6.01	2.48	2.51	2.68	2.68	0.404	0.398	0.030	0.024	0.374	0.374	9071.60	9071.60	10759.40	10759.40
Stdev.	1.243	2.343	0.995	0.064	0.068	0.089	0.092	0.011	0.011	0.010	0.004	0.013	0.013	1333.93	1333.93	1098.37	1098.37

Discussion: The uncorrected MICP curves and accompanying analyses indicate a degree of variability between samples types. However, this variation is not consistent between repeat sample types indicating that either conformance and/ or rock heterogeneity is masking any effects of sample type. The conformance corrected MICP curves and MICP results are in better agreement than the uncorrected data but still show a degree of variability that is inconsistent across sample types indicating that sample heterogeneity is affecting the result. However, this variation is still less than the porosity variation observed between Saracen-1 samples (Section 4.5.1) over the 1.6m interval (3.24 %) and between adjacent samples (3.02 %). Additionally, the threshold pressure variation between the same sample types is also not more than that observed between Saracen-1 samples. Thus it is concluded that all though heterogeneity is minor, it is still sufficient to affect the MICP curves.

5.3.5.3 Results 2160-2165 m

Drill cuttings from this interval are described as ~~"d~~dark marl" and ~~"w~~white lithology" (Table 5-7). The uncorrected MICP curves from the separated DC sample taken from this depth interval show considerable variation (Appendix C Figure C-13). The separated white lithology has a lower initial mercury saturation than the dark marl lithology. The MICP curve suggests that the white lithology has a larger pore throat network than the dark marl lithology.

The conformance corrected MICP curves from the separated DC sample taken between 2160-2165 m depth still show considerable variation (Appendix C Figure C-14). The MICP curves indicate that the white lithology has a larger pore throat network than the dark marl lithology. The threshold pressure interpreted with the MI method is1759 psia while the dark marl threshold pressure has dropped to 4283 psia. The threshold pressures interpreted with the IPV method vary between 1439 psia and 4981 psia. There is considerable variation in the conformance corrected porosity, bulk density and grain density between the samples; 8.52 %, 0.69 g/ml and 0.57 g/ml respectively (Table 5-7).

Table 5-7: Tenacious West-1 drill cuttings from a depth interval between 2160-2165m which were divided up on visible lithology.

Sample Depth (m)	Sample Weight (g)	Porosity (%)		Bulk Density (g/ml)		Grain Density (g/ml)		Sample Volume (ml/g)		Pore Volume (ml/g)		Grain Volume (ml/g)		IPV Threshold Pressure (psia)		MI Threshold Pressure (psia)	
		Raw	Cor.	Raw	Cor.	Raw	Cor.	Raw	Cor.	Raw	Cor.	Raw	Cor.	Raw	Cor.	Raw	Cor.
Dark Marl	1.04	10.87	9.52	2.38	2.42	2.67	2.67	0.420	0.414	0.046	0.039	0.374	0.374	4981	4981	4981	4981
White Lithology	0.68	19.39	18.27	1.69	1.72	2.10	2.1	0.590	0.582	0.114	0.106	0.476	0.476	1439	1439	1759	1759
Average	0.86	15.13	13.90	2.04	2.07	2.39	2.39	0.505	0.498	0.080	0.073	0.425	0.425	3210	3210	3370	3370
Stdev.	0.255	6.025	6.187	0.488	0.495	0.403	0.403	0.120	0.119	0.049	0.047	0.072	0.072	2504.6	2504.6	2278.3	2278.3

5.3.5.4 Results – 2200-2210 m

Drill cuttings from this interval are described as ~~–b~~lack shale", ~~–d~~ark lithology" and ~~–w~~hite carbonate" (Table 5-8). The uncorrected MICP curves for the DC sample from this depth have been grouped into three separate lithologies (Appendix C Figure C-15). The three MICP curves show poor agreement with one another. The black shale has higher initial mercury saturation and a maximum inflection point at a higher pressure, while the dark lithology and the white carbonate samples show less initial mercury saturation and general agreement up to 30 % mercury saturation where there is a maximum inflection point for both MICP curves. Above 30 % mercury saturation the MICP curves separate and the white carbonate sample's MICP curve indicates a larger pore throat network than the dark lithology sample.

The conformance corrected MICP curves still show poor agreement between the samples (Appendix C Figure C-16). The black shale MICP curve shows poor agreement with the dark lithology and the white carbonate sample. The white carbonate and dark lithology samples are similar up to 15 % mercury saturation above which they separate. The conformance corrected porosity, bulk density and grain density (Table 5-8) show significant variation (12.5 % porosity variation between the black shale and the white carbonate samples). The interpreted threshold pressures show significant variation using both the IPV method and the MI method. The IPV method indicates that the black shale samples have a threshold pressure of 9981 psia while both the dark lithology and the white carbonate samples have much lower threshold pressures (1441 psia and 1427 psia respectively). The MI method indicates that the threshold pressures are lower for the black shale (5993 psia), slightly higher for the dark lithology (1755 psia) and lower for the white carbonate sample (1020 psia).

Table 5-8: Tenacious West-1 drill cuttings from a depth interval between 2200-2210m which were divided up on visible lithology.

Sample Depth (m)	Sample Weight (g)	Porosity (%)		Bulk Density (g/ml)		Grain Density (g/ml)		Sample Volume (ml/g)		Pore Volume (ml/g)		Grain Volume (ml/g)		IPV Threshold Pressure (psia)		MI Threshold Pressure (psia)	
		Raw	Cor.	Raw	Cor.	Raw	Cor.	Raw	Cor.	Raw	Cor.	Raw	Cor.	Raw	Cor.	Raw	Cor.
Black Shale	0.22	31.17	24.41	1.68	1.85	2.44	2.44	0.595	0.541	0.185	0.132	0.409	0.409	9981	9981	6970	5993
Dark Lithology	1.98	13.87	11.87	2.25	2.31	2.62	2.62	0.444	0.434	0.062	0.052	0.382	0.382	1441	1441	2057	1755
White Carbonate	1.42	20.8	18.5	2.12	2.19	2.68	2.68	0.471	0.458	0.098	0.085	0.373	0.373	1427	1427	1259	1020
Average	1.21	21.95	18.26	2.02	2.12	2.58	2.58	0.503	0.478	0.115	0.089	0.388	0.388	4283.00	4283.00	3428.67	2922.67
Stdev.	0.899	8.707	6.273	0.299	0.239	0.125	0.125	0.080	0.056	0.064	0.041	0.019	0.019	4934.62	4934.62	3092.73	2684.26

Discussion: The Tenacious West-1 DC sample from (2160-2165 m), separated into two lithologies, highlights the significant variation that is possible within a DC sample from a 5 m interval. Even with the separation of the sample into different lithologies, it is not possible to match any of the lithologies to specific horizons or depths with any certainty. It is envisaged that if this DC sample was not separated and analysed with MICP, it would reflect the average of the cuttings used in the analyses. Thus if the sample was composed of 50 % white lithology and 50 % dark lithology drill cuttings, the MICP analyses would reflect an average of the MICP analyses.

The Tenacious West-1 DC sample from 2200-2210 m also shows significant variation when divided into the three different lithologies. The experiment highlights the significant problems with the use of DC samples to determine subsurface rock properties. Without the division of these DC samples into the respective lithologies, the resultant MICP analyses would have produced an MICP analyses reflecting the percentage of each formation present in the sample analysed. Unfortunately, there is little advantage in dividing the DC samples into their different lithologies without having the specific depth location of each lithology, other than knowing, that most likely within the DC sampling interval there is a certain lithology with these properties. Also, the effects of drilling, passage through the mud column, the disaggregating effects of the shale shakers and being washed and dried can also affect the results. With all of these effects the analyses of DC samples may have limited value due to the large uncertainties.

This type of sample may, however, be a viable way of averaging rock properties over formations (metre scale) or at least provide indicative MICP properties over the metre scale. For instance, the MICP analyses of DC samples can provide average reservoir or sealing properties for the reservoir or seal rock or allow the matching of MICP analyses to log properties taken on a much coarser scale than individual core plugs. Improved accuracy of the DC samples could be achieved by quantifying the effects of the mud column, shale shakers and, washing and drying of the DC samples which could be achieved experimentally.

5.3.6 **Saracen-1, Barrow Sub-basin**

Please see Section 3.5.1 and 4.6.3 for Saracen-1 conventional core and well description.

Drill cutting (DC) samples were taken by this study throughout the well including over the cored interval. The DC sample from above the cored interval at 1115-1118 m depth was described in the WCR as 100 % siltstone with a trace of glauconitic sandstone while the DC

sample below (1118-1121 m) was described as 70 % siltstone and 30 % glauconitic sandstone. The DC sample from 1121-1124 m below the cored interval was described as 60 % siltstone and 40 % glauconitic sandstone and the DC sample from 1120-1125 m was described as 70 % siltstone and 30 % glauconitic sandstone (Banfield, 2000). The DC samples were not analysed originally in Dewhurst et al., (2002) but were analysed as part of the investigations in this study.

Methodology: Four core plugs from the CC Muderong Shale from Saracen-1 were analysed in 2013 after being warehoused in the Western Australia Core Library since early 2001. Additionally, four subsamples of DC samples were also collected and analysed in 2014. The analyses included; MICP, XRD (to determine sample mineralogy) and BSE imaging to detail the mineral fabric of the samples. The additional mineralogy and SEM/BSE analysis will indicate similarities/ differences between the CC and DC mineralogies and the likelihood of these having originated from the same depth interval.

Results: The four CC samples have MICP curves in close agreement with one another (Appendix C Figure C-17). Sample 1118.45 m has slightly higher initial mercury saturation than the other samples. Between 8 % mercury saturation and 35 % mercury saturation the MICP curves almost overlap one another. Above 35 % mercury saturation the MICP curves separate suggesting some variation in pore throat sizes between the samples. The MICP curves re-converge at 100 % mercury saturation. Sample 1119.30 m and 1118.45 m show slight curvature at the top of the MICP curve (>80 % mercury saturation) while 1118.65 m and 1119.05 m both show a steep increasing MICP curve up to 100 % mercury saturation.

The conformance corrected MICP curves (Appendix C Figure C-18) show better agreement between 0 % and 8 % mercury saturation. The threshold pressures interpreted using the IPV and the MI methods (Table 5-9) are selected at the same pressure equilibrium point (~6970 psia). The average corrected porosity is 12.21 % and all samples are within a maximum of 1.13 % of one another confirming the similarity of the samples. The average corrected bulk density and corrected grain density are 2.19 g/ml and 2.50 g/ml, respectively, with a maximum variation of 0.04 g/ml and 0.06 g/ml. The sample volume per gram and pore volume per gram reflect these minor variations.

Table 5-9: MICP results for four warehoused samples from a 1.6m interval of conventional cored Muderong Shale from Saracen-1.

Sample Depth (m)	Sample Weight (g)	Porosity (%)		Bulk Density (g/ml)		Grain Density (g/ml)		Sample Volume (ml/g)		Pore Volume (ml/g)		Grain Volume (ml/g)		IPV Threshold Pressure (psia)		MI Threshold Pressure (psia)	
		Raw	Cor.	Raw	Cor.	Raw	Cor.	Raw	Cor.	Raw	Cor.	Raw	Cor.	Raw	Cor.	Raw	Cor.
1118.45	2.83	12.510	11.954	2.190	2.206	2.510	2.505	0.456	0.453	0.057	0.054	0.399	0.399	6970	6975	6975	6975
1118.65	3.13	12.190	11.717	2.160	2.174	2.460	2.462	0.463	0.460	0.056	0.054	0.406	0.406	4.796	6972	6972	6972
1119.05	3.12	12.590	12.320	2.190	2.196	2.500	2.505	0.457	0.455	0.058	0.056	0.399	0.399	6970	6965	6965	6965
1119.3	3.22	13.260	12.846	2.180	2.192	2.510	2.515	0.458	0.456	0.061	0.059	0.398	0.398	4.796	6966	6966	6966
Average	3.08	12.64	12.21	2.18	2.19	2.50	2.50	0.456	0.456	0.058	0.056	0.401	0.401	6970	6969.50	6970	6969.50
SD	0.169	0.446	0.493	0.014	0.017	0.025	0.026	0.003	0.003	0.002	0.002	0.004	0.004	4.796	4.796	4.796	4.796

The four DC samples have MICP curves with initial mercury saturations and pore throat distributions that differ significantly (Appendix C Figure C-19). The samples all have MICP curves that taper at high pressures (>30,000 psia). The samples from 1121-1124 m and 1118-1121 m depth intervals have MICP curves with similar shapes and sharper points of maximum inflection. The sample from 1121-1124 m has a maximum inflection point nearly 1000 psia lower than the sample from 1118-1121 m but otherwise, has a similar shape. The samples from 1115-1118 m and 1120-1125 m also have similar MICP curves with gently sloping maximum inflection points and higher initial mercury saturation. However, with increasing pressure (> 9,000 psia) both the 1115-1118 m and the 1118-1121 m samples have MICP curves that are in close agreement or overlay. The same pattern occurs with the MICP curves for samples 1121-1124 m and 1120-1125 m, above 30,000 psia these curves align with one another.

The conformance corrected MICP curves (Appendix C Figure C-20) show better agreement with one another but still have different pore throat size distributions. The threshold pressures interpreted with the IPV method (Table 5-10) for the DC samples vary by three pressure equilibrium points (2450 -3520 psia). The threshold pressures interpreted with the MI method show greater variation between 4249 psia and 2928 psia. The corrected porosity, bulk density and grain density (Table 5-10) indicate that DC samples from 1115-1118 m and 1118-1121 m have similar properties with porosities between 15 and 17 %, bulk densities of ~2.1 g/ml and grain densities between 2.49 g/ml and 2.53 g/ml. The deeper DC samples between 1121-1124 m and 1120-1125 m have higher porosities (20 % and 22 %), lower bulk densities (1.95-1.96 g/ml) but similar grain densities (2.46 g/ml and 2.52 g/ml).

Table 5-10: MICP results for the four warehoused drill cutting samples taken in close proximity to the 1.6m interval of conventional cored Muderong Shale from Saracen-1.

Sample Depth (m)	Sample Weight (g)	Porosity (%)		Bulk Density (g/ml)		Grain Density (g/ml)		Sample Volume (ml/g)		Pore Volume (ml/g)		Grain Volume (ml/g)		IPV Threshold Pressure (psia)		MI Threshold Pressure (psia)	
		Raw	Cor.	Raw	Cor.	Raw	Cor.	Raw	Cor.	Raw	Cor.	Raw	Cor.	Raw	Cor.	Raw	Cor.
1115-1118	1.31	17.35	15.09	2.059	2.11	2.49	2.49	0.486	0.473	0.084	0.071	0.402	0.402	2911	2911	4266	3516
1118-1121	1.31	18.84	17.22	2.06	2.1	2.53	2.53	0.487	0.477	0.092	0.082	0.395	0.395	3520	3520	4249	4249
1120-1125	0.86	27.78	22.74	1.82	1.95	2.52	2.52	0.549	0.514	0.152	0.117	0.397	0.397	2457	2457	2928	2928
1121-1124	0.77	21.89	20.31	1.92	1.96	2.45	2.46	0.522	0.522	0.115	0.115	0.407	0.407	2938	2938	2938	2938
Average	1.06	21.47	18.84	1.96	2.03	2.50	2.50	0.511	0.494	0.111	0.094	0.400	0.400	2957	2956.50	3595	3407.75
SD	0.288	4.615	3.369	0.117	0.087	0.036	0.032	0.031	0.022	0.031	0.021	0.006	0.006	436	435.68	765	624.57

Mineralogy: The mineralogy was semi-quantified using bulk XRD for both the CC and DC samples by Mark Raven at CSIRO using the methodology described in Appendix A, A.14-A.16.The CC samples had clay analysis performed; unfortunately, no DC samples were available for clay analysis. The mineralogy results (Figure 6.1) indicate that CC samples are similar to one another with a maximum of 2 % difference between the concentrations of any minerals present. The DC samples are all similar except for sample 1115-1118 m which has ~40 % less smectite than the other samples; does not contain calcite or barite but does have jarosite present. The other three samples have mineralogies within 1 % concentration of one another.

The mineralogy varies between the DC and CC samples. The CC samples have a lower concentration of quartz, smectite and pyrite, and do not contain calcite siderite or barite. The CC samples have a higher concentration of kaolinite and illite-smectite. They also all contain jarosite. The 1115-1118 m DC sample has mineralogy reflective of the CC samples with jarosite present, lower smectite, higher kaolinite concentration and no calcite or barite.

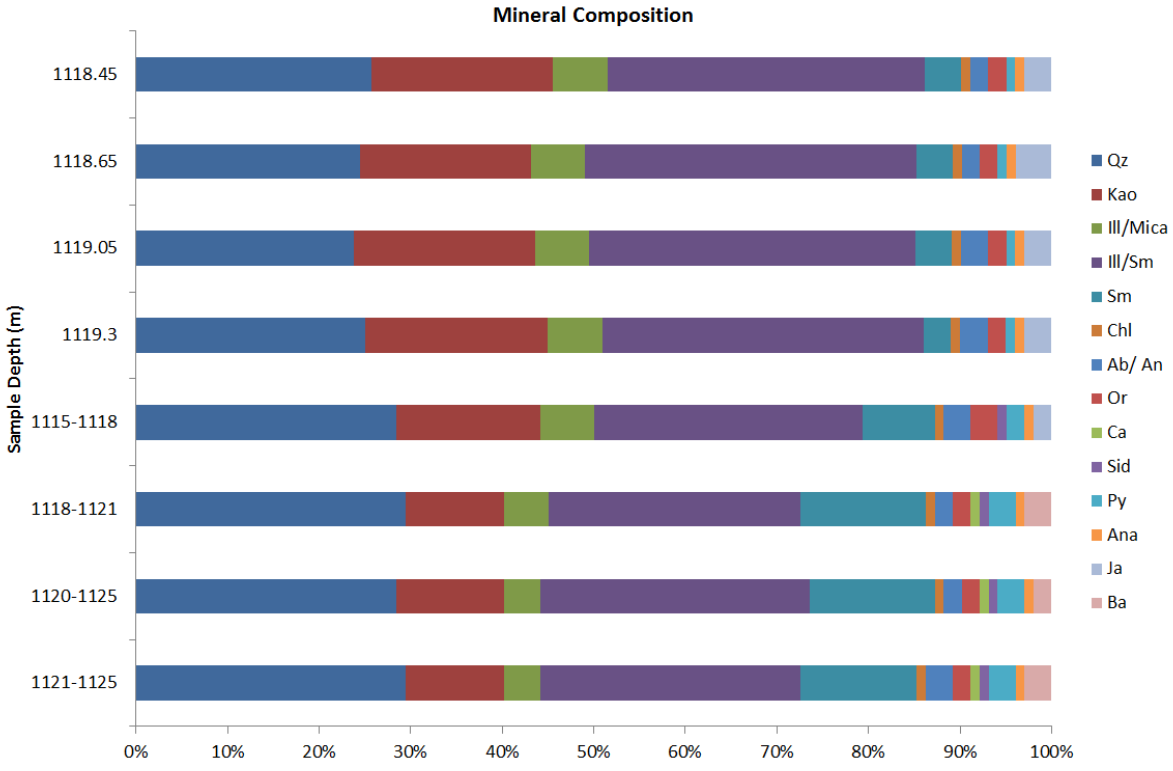

Figure 5-1: XRD Mineralogy of warehoused Saracen-1 conventional core and drill cutting samples (Analysed in 2013/2014).

The CC and DC samples were analysed with the BSE microscope. The CC samples (Figure 5-2) under low magnification show a distinctive fissility. The fissility appears as discontinuous micro fractures approximately 1 mm apart throughout the samples. The shale fabric is clay dominated with quartz grains speckled throughout an illite/ smectite matrix with minor pyrite framboids, glauconite and plagioclase. The DC samples have significant fracturing/ fissility throughout the sample and in some cases, these fractures have significant apertures (Figure 5-3). These fractures appear to link up and in some cases span the entire width of the DC sample. On higher magnification, black features are visible throughout the rock matrix (Figure 5-3). These black features are not in contact with one another but are linked by the fractures. Also, the edges of the DC sample have poorly consolidated rock material and possibly a rind of dried mud cake attached (Figure 5-3 top of the image on the LHS and circled in red). The mineral fabric of the DC samples is loosely similar to the core samples although, the fracture connectivity is greater in the DC samples.

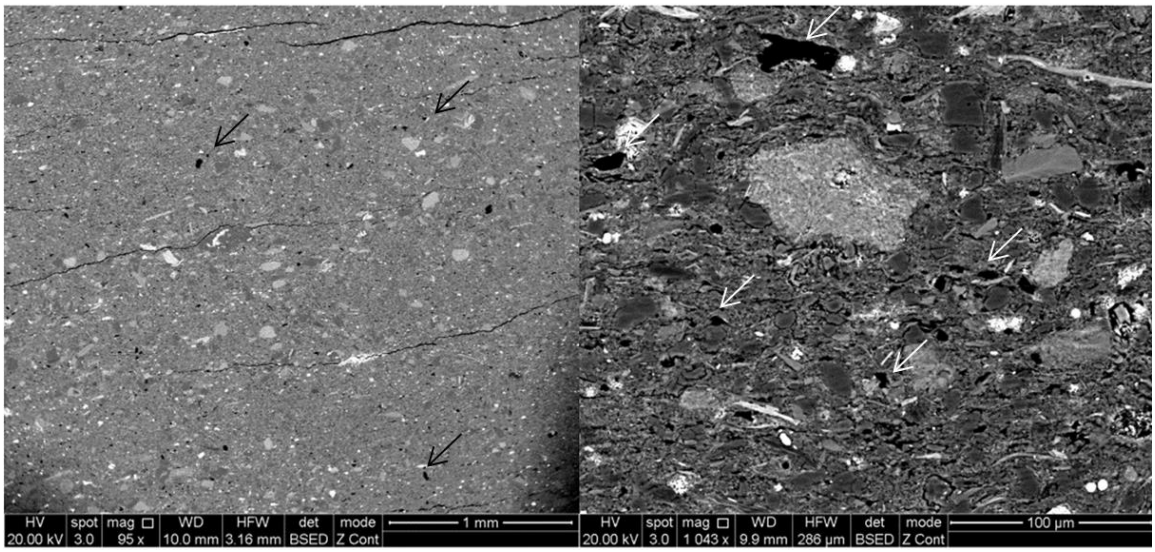

Figure 5-2: Saracen-1 BSE images of a warehoused conventional core sample taken in 2013. The arrows indicate the black features identified throughout the samples.

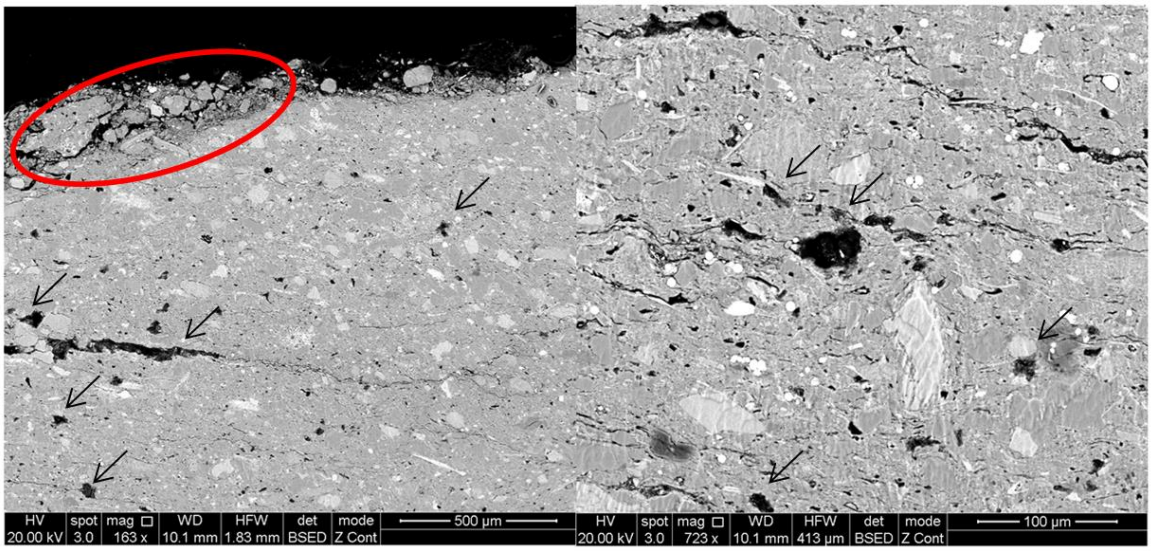

Figure 5-3: Saracen-1 BSE images of a drill cutting sample taken in 2014. Drill cuttings were orientated with their long sides up and stabilised in araldite. The red oval in the LHS image shows the rind of dried mud. The arrows indicate the black features identified throughout the samples.

Comparison of conventional core and drill cutting sample MICP pore throat distributions

The pore throat distributions for the CC sample 1118.65m and the DC sample at 1118-1121m are shown in Appendix C, Figure C-21. The pore throat distributions from the sample show a different distribution of pores between the samples. The CC sample has a smaller diameter pore throat radii distribution between 0.01675 µm and 0.0019µm that are less constrained than the DC sample. The DC sample has a larger pore throat radii distribution between 0.03365 µm and 0.00335 µm that is tightly constrained.

Discussion: The CC samples from the 1.6m interval are similar in porosity, bulk density and grain density. The MICP curves interpreted threshold pressures using both the IPV and MI method (~6970 psia), mineralogy and BSE images are all similar to one another. Of the four DC samples, only sample 1118-1121m was from the same interval as the CC samples. Sample 1118-1121m has the highest interpreted threshold pressure (3520 psia for the IPV and 4249 psia for the MI method) of any of the DC samples. However, this is approximately half of the threshold pressure of the CC samples taken between 1118.45m and 1119.30 m. The DC samples taken from above and below the cored interval all have similar mineralogies but have threshold pressures one to two pressure equilibrium points below the DC sample at 1118-1121 m. Also, the DC samples have consistently higher porosities than the CC sample, with a minimum difference of 2 % to 11 % between DC samples, with an average difference of 6.3 %. The average corrected grain density for both sample types is 2.50 g/ml while the bulk densities vary due to the variations in sample volume per gram which is predominantly a result of the variation in pore volume per gram.

The MICP, XRD and BSE images from the samples taken in 2013 confirm that this interval of CC is relatively homogeneous. The DC samples from the 10 m interval covering the CC depth have mineralogy and MICP curves that differ from the CC although they are similar to one another (excluding the sample from 1115-1118 m). This is not unexpected as the mud logging report suggests that the DC sample lithology grades from 100 % siltstone with a trace of glauconitic sandstone at 1115 m depth into approximately 30 % and 40 % glauconitic sandstone and 70 % and 60 % siltstone respectively indicating significant heterogeneity over the 10 m interval (Banfield, 2000). Further, it suggests that the formation intergrades between siltstone and glauconitic sandstone. The 1.6 m interval of CC is interpreted as claystone in the WCR and thus the lithologies from the surrounding ten-metre interval are probably a mix of claystone, the more porous siltstone and glauconitic sandstone. This results in MICP analyses suggest a formation with higher porosity and larger pore throats (lower threshold pressure). This is before the effects of drilling, drilling mud, shale shakers, washing and drying are taken into account. Thus the lower threshold pressures and higher porosities of the DC samples in comparison to the CC samples can be explained.

The mineralogy analysis of the DC samples suggests that the sample at 1115-1118 m has several key differences to the other three depth intervals. The other three depth intervals have similar mineralogies and yet have threshold pressures that differ by more than two pressure equilibrium points and have porosities differing up to 5.5 %. These results show a maximum variation that is considerably higher than the samples from the 1.6 m interval of Saracen-1 (Section 4.5) CC (3.24 %) and between the adjacent samples (3.02 %). However, both the bulk density and grain density variation are within the limits observed for the 1.6 m interval of Saracen-1 core and adjacent samples. If storage, washing and drying of the samples was the same, then it is possible that the lag time for the samples to return to the surface was longer than the actual return time of the DC samples. Thus the DC samples were returning quicker than was reported and may be from a shallower depth. Alternatively, the samples were only collected at the end of the depth interval. Thus the DC sample from 1115-1118 m could have been from deeper. This could explain why the DC samples are considerably different from the CC samples over the (supposed) same interval.

The BSE images of the DC samples show several different properties to the images of the CC; poorly consolidated rock material and possibly a rind of dried mud cake can be observed attached to the edge of the DC sample, an extensive fracture network with

considerable aperture, often continuous and linking the black features to one another and providing a conduit for fluid flow can also be observed.

The poorly consolidated rock material and rind of dried mud cake attached to the DC sample edge are a likely result of one of the following three processes; (i) the sanding and polishing of the DC sample has resulted in rock debris being removed and subsequently lodging in the araldite at the edge of the sample. This is considered unlikely as sanded rock material would be expected to spread further than the edge of the DC sample and this material would not appear to be attached to the edge of the sample, (ii) the poorly consolidated rock material and rind of dried mud cake has attached itself to, or become semi-detached from the edge of the DC sample during the drilling process; the passage through the mud column and across the shale shakers and, during the washing and drying of the samples. This is supported by the XRD mineral identification of barite (a common drilling mud constituent) in three of the DC samples, (iii) this material may be a result of the capillary forces during the washing and drying of the samples leading to fracturing and dislodgement of weakly held rock material. The last two hypotheses are considered the likely cause of the extensive fracturing and black features throughout the DC sample.

It was expected that the differences in CC and DC samples, and between DC samples themselves is in part a result of the extensive fracturing and poorly consolidated rock material and possibly the rind of dried mud attached to the DC samples. These factors would also affect the MICP curve primarily at the lower pressures (larger pore throats). However, given the pore throat radii distributions of the two samples and the lack of overlaying pore throats, it is suggested that the two samples contain a different pore throat network which is either a result of the processes experienced by the drill cuttings or that the drill cuttings are not from the same interval. Thus, it is thought the fractures and poorly consolidated rock material are not affecting the MICP curves and have likely been removed in the conformance correction.

5.4 CHAPTER 5 DISCUSSION

The following discussion concentrates on the differences in results between the interpretations of the authors noted in Section 5.3 and the re-interpretation of their results in this study.

Watson, (2012) analysed CC, VI and SC adjacent samples with MICP in Flaxman-1 and determined threshold pressures. Watson, (2012) interpreted a decrease in threshold pressure from the CC and VI samples to the SC sample and attributed this to the pore throats being

compromised. The re-interpretation and conformance correction of these three MICP analyses suggest that, contrary to the interpretation of Watson, (2012), there is no discernible/conclusive difference in the interpreted threshold pressures and MICP curves between the sample types. The IPV method suggests that there is only one pressure equilibrium point difference between the CC and SC samples. However, the VI sample has the same threshold pressure as the SC sample. Thus the variation is similar to the variation observed between adjacent samples of Saracen-1 in Section 4.5.1 and is thus not significant. Furthermore, the threshold pressures interpreted with the MI method from the uncorrected MICP curves indicate that the CC and SC samples have the same threshold pressure (~5980 psia) while the VI sample is interpreted at a lower threshold pressure (4976 psia). The MI threshold pressures from the conformance corrected MICP curves led to a change for the SC sample only. The threshold pressure is interpreted as 4977 psia which is the same pressure equilibrium point as the VI sample.

Sneider et al., (1997) analysed five seal samples with MICP, taking adjacent samples of CC and SC sample types and subsequently interpreting threshold pressures that decrease from the CC to the SC sample. Sneider et al., (1997) subsequently suggested empirical adjustment factors that could be added to DC samples to approximate the higher threshold pressures of CC samples. The re-interpretation of these results was hindered by the absence of the uncorrected data and was subsequently carried out on the conformance corrected data provided by Sneider et al., (1997). The threshold pressures were interpreted with the MI method and show a clear trend; the CC samples have a one pressure equilibrium point higher threshold pressure than the SC samples for four seal samples. The fifth sample, however, has the threshold pressures interpreted at the same pressure equilibrium point for both sample types. It is noted that this variation in threshold pressures is within the variation range observed in adjacent samples from Saracen-1 Section 4.5.1. Furthermore, it is suggested that as the variation in MICP curves consistently occurs at low mercury saturation, the conformance correction methodology is not adequate. This is evidenced by the excellent agreement of MICP curves (both shape and position on the graph) above ~20 % mercury saturation indicating no discernible difference in pore throat radii. Thus, it is postulated that below ~20 % mercury saturation the pore throats are similarly unaltered and that the observable differences are a result of conformance. This conformance has led Sneider et al., (1997) to picking the incorrect threshold pressures for the SC sample. It is thus concluded that there is no discernible difference between these CC and SC samples. These results are in agreement with the re-interpretation of Flaxman-1 in this study.

Kivior, (2005) analysed adjacent samples of CC, VI and SC sample types from Swan-1 with MICP analysis and showed that the interpreted threshold pressures increased from the CC (14441 psia) to the SC (15927 psia) sample by approximately one pressure equilibrium point. The VI sample had a threshold pressure at the same pressure equilibrium point as the CC sample. These findings are in contradiction to the findings of Watson, (2012), Sneider et al., (1997) and this study‘s re-interpretation of results. The re-interpretation suggests that there is no discernible difference between the threshold pressures interpreted with the IPV and MI method. This concurs with the re-interpretation of the Flaxman-1 and the five sealing formations from Sneider et al., (1997). The threshold pressures interpreted with the IPV and MI method on the uncorrected MICP curves are all at the same pressure equilibrium point (~9970 psia) as interpreted with the MI method for the CC sample (8517 psia). The threshold pressures interpreted with the IPV method on the conformance corrected MICP curves remain the same, but the threshold pressures interpreted with the MI method were all interpreted on the same pressure equilibrium point (~8470 psia). The conformance corrected MICP curves show similar general agreement, but with slightly more variation in the CC sample MICP curve. It is thus concluded for Swan-1 that there is no discernible difference between the MICP curves or threshold pressures of the CC, VI and SC samples.

Kivior, (2005) performed MICP analysis on CC and SC samples between 2042.47 m and 2043.39 m and on a DC sample from 2045 m and 2048 m depth from Puffin-2. The threshold pressures show a decreasing trend from the CC (9300 psia) to the DC (7800 psia) to the SC (7250 psia) sample. The re-interpretation of these results includes a VI sample and is contrary to the findings of Kivior, (2005). The new results show a higher threshold pressure for the DC (4985 psia for IPV and MI) sample in comparison to the SC (2071 psia and 2483 psia for the IPV and MI), VI (2936 psia and 2936 psia for the IPV and MI) and CC (2064 psia and 2937 psia for the IPV and MI) samples respectively. Furthermore, the conformance corrected MICP curves are not in agreement with one another over the entire pressure range; especially the DC sample. These results are contrary to the re-interpreted results from Flaxman-1, Swan-1 and the five sealing lithologies analysed by Sneider et al., (1997). They are also in contrast to the original interpretations for Flaxman-1, Swan-1 and the five sealing lithologies from Sneider et al., (1997). This variation is interpreted to be a result of heterogeneity rather than of sample type.

The samples from Tenacious West-1 2810.04 m, 2846.04 m and, Puffin-2 2042.47 m and 2043.39 m demonstrate the degree of heterogeneity that occurs between adjacent

conventional core samples. In the Tenacious West-1 samples, the repeat sample types confirm that the variation is not a result of sample type but a result of heterogeneity (on a cm scale). Kivior, (2005) also suggests that the variation in interpreted threshold pressures for the CC and VI samples is a result of heterogeneity on a core scale as a result of a larger interconnected pore network in the horizontal direction as opposed to the vertical. However, there is variation between repeat sample types before and after conformance correction and it is suggested that this variation is a result of heterogeneity between adjacent samples. The conformance corrected MICP curves show loose agreement indicating minor to moderate heterogeneity between adjacent samples.

The results from Tenacious West-1 DC samples separated into "dark marl" and "white lithology" over the 5 m interval from 2160-2165 m and over the10 m interval from 2200-2210 m both indicate the degree of heterogeneity that can be observed in DC samples. This is not unexpected given the degree of heterogeneity observed in adjacent core samples (cm scale) in the re-interpreted results from Tenacious West-1 samples 2810.04 m and 2846.04 m. This analysis highlights the limitations of using DC samples for detailed information but hints at the possibility of using the DC samples to provide averaging information over a formation for coarse scale correlation. The heterogeneity in the Tenacious West-1 DC samples further supports the hypothesis that heterogeneity is a factor affecting the MICP analysis of DC samples from Puffin-2 which showed considerable variation to the MICP analysis of CC, VI and SC samples.

The Saracen-1 MICP analysis of CC and DC samples indicate that the DC samples have significantly different MICP curves both from one another and from the CC samples. Further, the interpreted threshold pressures are all lower for the DC samples than for the CC samples no matter the method used. Sneider et al., (1997) also observed the lower threshold pressures for the DC samples in comparison to the CC samples. The variation in the DC samples to one another was similar to the variation observed in the Tenacious West-1 samples which were divided into lithologies and suggests that heterogeneity between the different sampling intervals is affecting the MICP curves and subsequent threshold pressures. However, the XRD mineralogical analysis of Saracen-1 samples suggests only minor mineralogical variations between three of the DC samples and the CC samples. While undoubtedly, these mineralogical variations lead to differing rock fabric and subsequently pore network variations resulting in modification of the MICP curves, it is thought that the drilling, transport through the mud column, time on the shale shakers, washing and drying of the samples has led to further alteration of the pore throat radii distributions.

The results of SC sample analyses suggest that the breaking of the rock sample does not affect the MICP curve and interpreted threshold pressure as shown in the re-interpretation of Flaxman-1, Swan-1 and the five sealing formations of Sneider et al., (1997). Thus the differences observed in the DC samples can then be attributed to artefacts of the drilling, transport through the mud column, time on the shale shakers and the washing and drying of the DC sample altering the pore throat network leading to modified MICP curves and threshold pressures. However, equally the differences can be attributed to the larger sampling interval of DC samples in conjunction with the heterogeneity that can be observed over these larger sampling intervals. This makes it near impossible to quantify these effects or to suggest a correction factor that would consistently correlate DC analyses with CC analyses.

The sample types and their effects on the MICP curves and threshold pressures have been investigated by Watson, (2012), Kivior, (2005), Sneider et al., (1997) and Daniel and Kaldi, (2014) in Cook, (2014), however, these investigations have not extended to the porosity, bulk density and grain density which are also measured as part of the MICP analysis. From the wells that were re-interpreted (in this study) and found to have relatively homogeneous samples (Flaxman-1 and Swan-1), there is a common trend with the porosity; the DC sample has the highest porosity followed by the SC sample, the CC sample and lastly the VI sample. Darlak et al., (2011) demonstrated that the MICP porosities were constantly higher for shale rocks that were crushed to between 0.5-1 mm, as opposed to samples that were not crushed. Darlak et al., (2011) suggested that the crushing of samples allowed better extraction and drying. While this is possible it is thought that this is a result of the connectivity of the pore network and thus is a relationship between surface area and rock volume of the sample. Thus the smaller the sample the higher the surface area to rock volume allowing more of the pore network to be accessed by mercury. This is supported by the conformance corrected pore volume per gram results for the different sample types from Flaxman-1 and Swan-1. The high DC porosities compared to the CC, VI and SC samples, indicates that the SC samples are only partially representative of the DC samples.

5.4.1 **Methodology for the Use of Drill Cuttings for MICP Analysis**

A proposed methodology for the use of drill cuttings for MICP analysis is provided in Appendix C, C.1.

5.5 CHAPTER 5 CONCLUSIONS

The accurate conformance correction for CC, VI and especially SC and DC samples is crucial for threshold pressure interpretations using the MI method and for the comparison of MICP curves as shown in Flaxman-1 and Swan-1. This is further highlighted in the results from the five sealing formations analysed by Sneider et al., (1997) in which the differences observed in the MICP curves between 0 % and 20 % mercury saturation have been attributed to inadequate conformance correction.

The re-interpretation of Flaxman-1 and Swan-1 data to include conformance correction indicates that there is no significant difference in the MICP curves of an SC, VI or CC sample. Further, there are no significant differences in the interpreted threshold pressures using the IPV or MI method. Thus these sample types do not affect the pore throat size distribution in the sample, nor in the MICP curve or interpreted threshold pressures.

The MICP results do indicate that the sample type affects the accessible pore volume per gram of the sample and subsequently the porosity. The pore volumes per gram results suggest that the surface area to rock volume (inferred from weight) ratio will affect the porosity indicating that the pore network is not all connected in the samples. Samples with high surface area to rock volume have the highest porosity. The porosity variation between samples is greater than the variation observed between Saracen-1 adjacent samples (3.02 %) and Flaxman-1 but less than 3.02 % for Swan-1. The porosity trend for both Flaxman-1 and Swan-1are SC > CC> VI.

The re-interpretation of results from Puffin-2 and Tenacious West-1 sample 2846.04 m indicate that heterogeneity can occur between adjacent samples influencing the MICP curves and porosity. Tenacious West-1 sample 2810.04 m indicates that heterogeneity can be significant. This was confirmed in the Tenacious West-1 samples where repeat sample types were analysed and showed significantly different MICP curves and threshold pressure interpretations with more than two pressure equilibrium point variations between repeat samples. This heterogeneity is magnified when collecting DC samples over 5 m and 10 m sampling intervals as shown in Tenacious West-1 samples 2160-2165 m and 2200-2210 m.

The analysis of Puffin-2 and Saracen-1 which compared DC samples to CC samples illustrates that there can be significant differences between conformance corrected MICP analyses; DC sample porosity is the highest of all sample types including the SC samples which are meant to replicate DC samples. This high porosity is suspected to be a result of the transport through the mud column, the destructive effect of samples being agitated and

disaggregated on the shale shakers and the effect of sample washing and drying but may equally likely be an effect of heterogeneity. The analyses from these two wells led to the conclusion that a correction factor or empirical correction factor cannot be applied that will consistently correlate the DC results to those of CC samples.

The DC samples are nonetheless useful in that they provide average properties which may be advantageous for correlating rock properties with coarse scale well logs and formation modelling.

CHAPTER 6: THE EFFECTS OF WAREHOUSING ROCK SAMPLES ON MICP ANALYSIS

6.1 SUMMARY

The long term storage (warehousing) of conventional core samples results in various effects on MICP analyses. The warehoused samples of Muderong Shale from Saracen-1 show a shift in the MICP curves to higher pressures for the same mercury saturation in comparison to the original analyses. The warehoused samples have a threshold pressure two pressure equilibrium points higher than the original analyses. The warehoused samples also have jarosite precipitated although this is unlikely to be the main reason for the shift in the MICP curves or reduced porosity. The Saracen-1 Muderong Shale samples stored in zip lock bags show fewer differences in MICP analyses and reduced jarosite precipitation in comparison to the samples stored in core boxes in the Perth Core Library.

The warehoused Belfast Mudstone samples from CRC-1 showed no change in the MICP curves in comparison to the original samples. The only difference in later MICP analyses of these samples was a slight drop in the MICP porosities.

The Gorgon CO_2 Data Well-1 & Data Well-1ST1 and, the Pember and Paaratte Formations from CRC-1 showed inconsistent changes between the analyses on warehoused and original samples. This is thought to be a result of heterogeneity between adjacent samples. However, the warehousing effect cannot be conclusively ruled out.

The storage of samples in airtight bags reduced the effects of warehousing but didn‘t remove them entirely. Thus there is the opportunity to improve the storage of warehoused samples possibly through the use of plastic wrap in conjunction with aluminum foil as suggested by Auman, (1989).

6.2 INTRODUCTION

The effect of warehousing (core storage) on samples used for MICP analysis and veracity of the resultant seal capacity determinations has been a subject of considerable debate. This study attempts to address the concern by comparing the original analyses undertaken on the original rock to the analysis undertaken on the same rock, after being warehoused for

upwards of 10 years. Where possible, both the original and warehoused analyses were interpreted using the same techniques and software.

MICP analyses were conducted to identify changes in threshold pressures, porosity, MICP curves, bulk density and grain density. Also, XRD analyses were conducted to identify the minerals present, specifically any minerals that have precipitated during storage. SEM/ BSE imaging of the rock fabric and mineral identification were also conducted.

The research on the effects of warehousing was conducted on three wells and focussed on sealing intervals of Saracen-1, CRC-1 and Gorgon CO2 Data Well -1& Data Well-1ST1. The threshold pressures were converted to maximum CO_2 column height retentions to show any differences between the original analyses on fresh core and the analyses on warehoused core.

To attribute the differences observed between sample types to either heterogeneity (a factor noted in Chapter 5) or the effect of the sample warehousing, the following protocol was followed. Firstly the samples were grouped into their formations and the original samples were assessed for consistency or grouping of conformance corrected MICP curves. Consistent grouping of the MICP curves suggests the samples are alike and uniform. Secondly, the warehoused samples need also to show a consistent grouping of conformance corrected MICP curves between samples of the same formation. The grouping of the conformance corrected MICP curves from the warehoused samples need to be offset from the MICP curves of the original samples to suggest that there is a warehousing effect. Lastly, the interpreted threshold pressures, porosity, bulk density, grain density and mineralogy results need to provide supporting evidence for the interpretation that warehousing has affected the MICP analyses.

6.3 LITERATURE REVIEW

Most of the available literature is focussed on attempting to restore the original core to in situ conditions to measure permeability and its associated parameters or in situ fluids (Wendell et al., 1987, Torsaeter and Beldring, 1987 and Auman, 1989).

Auman, (1989) investigated different core preservation materials for native state fluid saturated conventional core. Auman, (1989) measured the weight loss of 100 % brine saturated Berea Sandstone plugs stored in a variety of different preservation materials; no plastic or aluminium foil, plastic only, punctured plastic, different amounts of plastic, aluminium foil only and plastic, aluminium foil covered with heat sealed plastic and different types of strippable plastic. The results suggest that undamaged plastic has the least

amount of water loss from the sample. Further the more plastic used to wrap the core samples the less water loss. The addition of plastic wrap and aluminum foil again reduced the loss of water from the core samples. Type C strippable plastic is comparable to the plastic wrap and foil preservation methods.

Comisky et al., (2011) analysed original core which was subsequently stored in sealed plastic bags for two years before being re-analysed with a low-pressure helium pycnometer. The porosities from the original stored core were close to that of the clean and dried porosities measured two years prior but were higher than the original core analysis. This was interpreted to be a consequence of desiccation as a result of storage at room temperatures, atmospheric pressure and the remaining hydrocarbon.

6.3.1 **Saracen-1, Barrow Sub-basin**

The effects of warehousing on seal capacity analyses is evaluated on Muderong Shale conventional core (CC) samples that were analysed in 2001 (Dewhurst et al., 2002) with samples analysed a decade later (2013/14) from the same core that had been warehoused in the Western Australia Core Library (WACL). Drill cutting (DC) samples stored in airtight bags from the WACL were also sampled at and in close proximity to the depth of the conventional cored interval. Also, the remaining original samples analysed by Dewhurst et al., (2002) were located and analysed. These samples had been stored in airtight bags (zip-lock sandwich bags).

6.3.1.1 Original (fresh) samples, Saracen-1, Barrow Sub-basin

Please see section 3.5.1, 4.5.1 and 5.3.6 for Saracen-1 conventional core, drill cuttings and well description.

Methodology modifications: The MICP analyses were performed on samples that had been air dried at laboratory temperature over a two-week period. The sub-sample cubes were coated on five sides with epoxy glue allowing mercury injection normal to the laminae as to best represent field conditions. The BSE images available have no specific details as to which subsample they were attributed too.

Results: The uncorrected MICP curves from 11 samples covering 1.6 m of CC from Saracen-1 were air dried and are displayed in Appendix D Figure D-1. In general, the MICP curves are similar to one another in shape and position on the graph. Samples 1118.34 m and 1119.24 m show MICP curves differing significantly from the other nine samples. Sample 1118.34 m is showing increased mercury saturation at low pressures. The MICP curve re-aligns with the other samples after 30 % mercury saturation. Sample 1119.24 m has an

MICP curve consistent with the other nine samples up until 16 % mercury saturation where it then shows a horizontal stepping out followed by a linear increase until it steps out horizontally at 62 % mercury saturation (Appendix D Figure D-1).

The conformance corrected MICP curves are displayed in Appendix D Figure D-2. These MICP curves show an improved agreement with one another, excluding sample 1119.24 m. Sample 1118.34 m is now consistent with the other samples suggesting the sample had increased conformance. Sample 1119.24 m shows similar initial agreement but still shows an unusual MICP curve above 15 % mercury saturation.

The threshold pressures interpreted with the incremental pore volume (IPV) method are in close agreement with one another differing by a maximum of one pressure equilibrium point (Table 6-1). The majority of the samples are approximately ~4990 psia while two samples are interpreted to have threshold pressures at the next pressure equilibrium point ~5980 psia and one sample at the pressure equilibrium point below 4326 psia. The conformance corrected porosities have a maximum variation of 3.24 % between sample 1119.42 m (18.63 %) and sample 1118.22 m (15.39 %). The corrected sample volume per gram has a maximum variation of 0.007 ml/g, the grain volume per gram has a maximum variation of 0.019ml/g while the pore volume per gram varies by a maximum of 0.014 ml/g between the 11 samples. Conformance corrected bulk density varies between 2.23 g/ml and 2.31 g/ml for sample 1119.08 m and 1119.75 m respectively leading to a maximum variation of the 0.08 g/ml. The grain density varies between 2.68 g/ml and 2.82 g/ml for the same samples respectively.

Table 6-1: MICP results for the original conventional core samples from a 1.6m interval of Muderong Shale from Saracen-1 (Re-interpretation of Dewhurst et al., (2002)).

Sample Depth (m)	Sample Weight (g)	Porosity (%)		Bulk Density (g/ml)		Grain Density (g/ml)		Sample Volume (ml/g)		Pore Volume (ml/g)		Grain Volume (ml/g)		IPV Threshold Pressure (psia)		MI Threshold Pressure (psia)	
		Raw	Cor.	Raw	Cor.	Raw	Cor.	Raw	Cor.	Raw	Cor.	Raw	Cor.	Raw	Cor.	Raw	Cor.
1118.15	1.58	16.80	15.6	2.26	2.29	2.71	2.71	0.443	0.436	0.074	0.068	0.369	0.369	4976	4976	5971	5971
1118.22	1.68	16.56	15.39	2.28	2.3	2.73	2.72	0.439	0.434	0.073	0.067	0.366	0.366	5095	5095	5991	5991
1118.34	1.95	21.27	18.54	2.22	2.3	2.82	2.82	0.450	0.435	0.096	0.081	0.354	0.354	4995	4995	5976	5976
1118.79	1.39	17.46	17.46	2.22	2.23	2.69	2.69	0.450	0.448	0.079	0.077	0.371	0.371	5993	5993	5993	5993
1118.87	1.44	16.13	15.55	2.25	2.26	2.68	2.68	0.445	0.442	0.072	0.069	0.373	0.373	4985	4985	5980	5980
1118.96	1.52	17.07	16.23	2.32	2.32	2.8	2.8	0.431	0.427	0.074	0.069	0.358	0.358	4986	4986	5983	5983
1119.08	0.94	17.31	17	2.22	2.23	2.69	2.68	0.450	0.449	0.078	0.076	0.373	0.373	4326	4326	5976	5976
1119.24	0.92	17.38	16.99	2.24	2.25	2.71	2.71	0.446	0.444	0.078	0.076	0.369	0.369	4987	4987	5984	5984
1119.42	0.52	19.23	18.63	2.27	2.29	2.81	2.81	0.440	0.437	0.084	0.081	0.356	0.356	5007	5007	5981	5981
1119.58	2.23	17.22	16.35	2.23	2.26	2.7	2.7	0.448	0.443	0.077	0.073	0.371	0.371	5980	5980	5980	5980
1119.75	1.82	18.88	17.95	2.29	2.31	2.82	2.82	0.437	0.432	0.082	0.078	0.355	0.355	4982	4982	5980	5980
Average	1.45	17.76	16.88	2.25	2.28	2.74	2.74	0.443	0.439	0.079	0.074	0.365	0.365	5119	5119	5981	5981
SD	0.50	1.48	1.17	0.03	0.03	0.06	0.06	0.006	0.007	0.007	0.005	0.008	0.008	475	475	6	6

Mineralogy: The mineral composition of the 11 original samples was semi-quantified with XRD analysis. The results shown in Figure 6-1 indicate that the mineralogies of the samples are similar with slight variations in smectite and kaolinite. The samples are dominated by quartz, smectite, mica and kaolinite. There are minor concentrations (< 5 %) of chlorite, pyrite, siderite, albite and orthoclase (Dewhurst et al., 2002). The BSE images (Appendix D Figure D-3) show quartz and glauconite grains, and pyrite framboids dispersed in a matrix of illite/smectite clays and other unidentified minerals. The grains are generally not in contact with one another (Dewhurst et al., 2002).

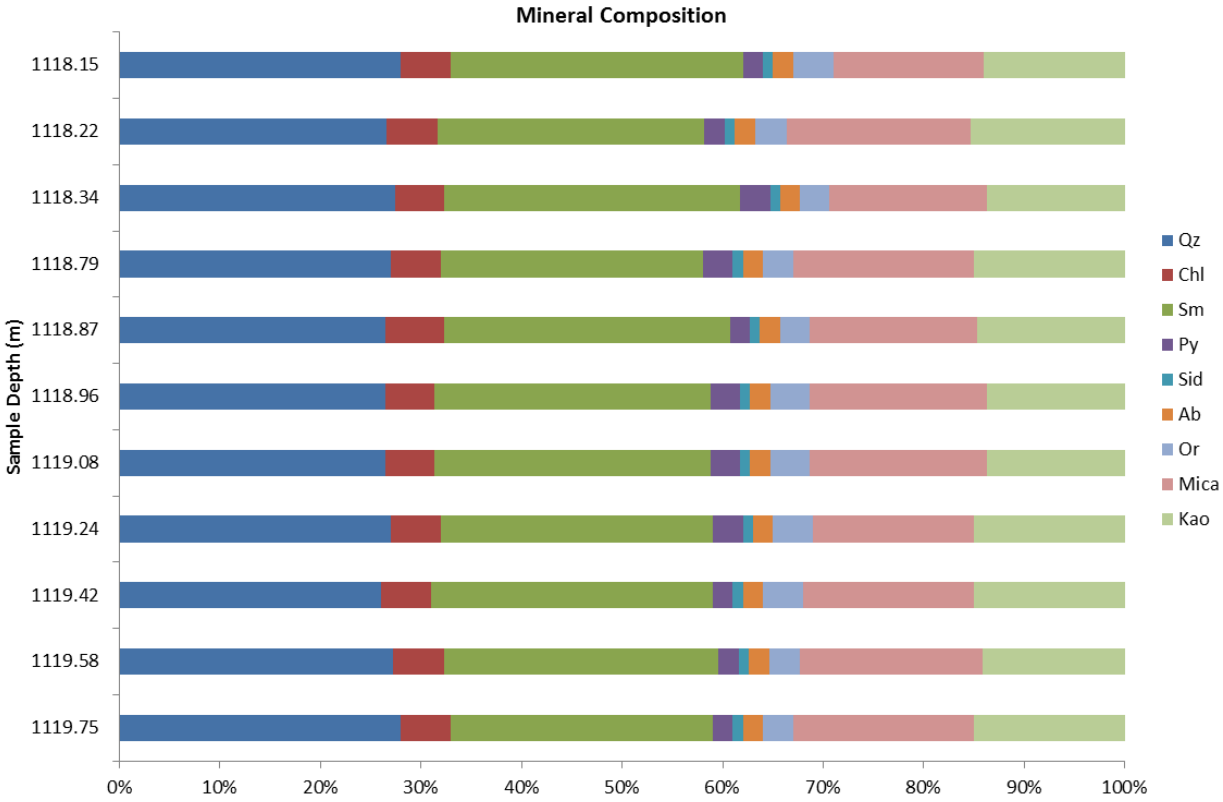

Figure 6-1: XRD Mineralogy of original Saracen-1 conventional core samples (Analysed in 2001 and reported in Dewhurst et al., 2002).

Discussion: The MICP curves, porosities, interpreted threshold pressures and mineralogies indicate that the 11 original samples are all similar over the 1.6 m interval of Muderong Shale. The variations in MICP curves are interpreted to be a result of minor heterogeneity over the 1.6 m interval as the results from the standards (Section 4.4.2) indicate that the MICP curves are perfectly matched. The variation is most pronounced over the 70 % to 100 % mercury saturation interval of the conformance corrected MICP curves indicating minor variation in pore throat diameters in the range of 0.0138 µm and 0.0032 µm.

The variation in porosity from a minimum of 15.39 % to a maximum of 18.63 % is a result of the combination of variation observed in both the grain volume per gram and the pore

volume per gram. The bulk density and grain density results reflect this variation. There is no relationship between sample volume per gram and pore volume per gram nor is there a relationship between grain volume per gram and pore volume per gram. The bulk density and grain density results reflect this variation. These results indicate that there is no relationship between the variables measured and there are also no trends in either the mineralogical or MICP analyses over the 1.6 m that would be expected if the depositional environment and associated variables had changed.

These results confirm that the MICP and mineralogical properties are similar over the 1.6 m interval of CC Saracen-1. This replication with only minor variation set the parameters for the testing of warehoused sample from the same core.

6.3.1.2 Airtight bag sample storage, Saracen-1, Barrow Sub-basin

The following analysis was conducted after some of the remaining original samples from Dewhurst et al., (2002) were located in 2015. The major difference between these samples and those stored in the WACL is that they have been stored in airtight bags at the CSIRO in Adelaide since their sampling in early 2000. The results from this analysis in comparison to the original and those stored in the WACL will allow recommendations to be made about how samples are stored and if there is an advantage in storing samples in airtight bags.

Methodology modifications: The MICP analysis was replicated where possible and the samples were orientated and glued for vertical intrusion only. However, for two samples their orientation could not be deciphered and they were run as whole unglued samples. Sample 1119.08 m and sample 1119.58 m were not glued and orientated. This needs to be taken into account when interpreting the MICP analyses.

The XRD methodology for the remaining original samples of Dewhurst et al., (2002) was modified due to the lack of sample available. Four of the five samples had bulk XRD analysis performed by mixing the original powdered sample from 2001 that had been stored in an air tight container with the whole sample stored in an airtight bag. Sample 1119.58 m was the only sample where the XRD was performed on the original whole rock stored in the sample bag. This is less than ideal but due to the lack of sample was required. This needs to be considered when interpreting any mineralogical changes.

Results: The uncorrected MICP curves for the remaining original samples stored in airtight bags are in excellent agreement with one another (Appendix D Figure D-4). Slight variation in MICP curves can be observed between 30 % and 90 % mercury saturation after which the MICP curves overlay one another. The MICP curves show a linear vertical trend from 15 %

mercury saturation up to 80 % mercury saturation after which the MICP curves show a 45 ° inclined trend.

The conformance corrected MICP curves show little to no improvement in agreement over the uncorrected MICP curves (Appendix D Figure D-5). The interpreted threshold pressures (Table 6-2) are within one pressure equilibrium point of one another and remain consistent with the uncorrected results interpretation. Three samples have interpreted IPV threshold pressures of ~5970 psia while two samples have interpreted threshold pressures at the next pressure equilibrium point (~6970 psia). This equates to 40 % of the samples having an interpreted threshold pressure at a higher pressure equilibrium point. The corrected porosities vary between 12.92 % for sample 1118.15 m and 14.87 % for sample 1118.34 m giving a maximum variation of 1.95 % between samples. The sample volume per gram shows considerable variation between 0.464 ml/g and 0.482 ml/g, the grain volume per gram shows less variation and varies between 0.395 ml/g and 0.411ml/g and the pore volume per gram shows less variation again between 0.061 ml/g and 0.072 ml/g. The bulk density varies between 2.08 g/ml and 2.24 g/ml while the grain density varies between 2.43 g/ml and 2.59 g/ml.

Table 6-2: MICP analysis of the remaining original samples taken by Dewhurst et al., (2002) that had been stored in airtight bags until analysis in 2015.

Sample Depth (m)	Sample Weight (g)	Porosity (%)		Bulk Density (g/ml)		Grain Density (g/ml)		Sample Volume (ml/g)		Pore Volume (ml/g)		Grain Volume (ml/g)		IPV Threshold Pressure (psia)		MI Threshold Pressure (psia)	
		Raw	Cor.	Raw	Cor.	Raw	Cor.	Raw	Cor.	Raw	Cor.	Raw	Cor.	Raw	Cor.	Raw	Cor.
1118.15	2.08	13.35	12.92	2.12	2.12	2.44	2.44	0.473	0.471	0.063	0.061	0.410	0.410	5979	5979	6971	6971
1118.34	1.85	15.26	14.87	2.07	2.08	2.44	2.44	0.484	0.482	0.074	0.072	0.410	0.410	6969	6969	6969	6969
1119.08	2.31	15.28	14.82	2.14	2.15	2.53	2.53	0.467	0.464	0.072	0.069	0.395	0.395	5974	5974	5974	5974
1119.58	1.67	14.01	13.68	2.23	2.24	2.59	2.59	0.449	0.447	0.063	0.061	0.386	0.386	6974	6974	6974	6974
1119.75	2.24	14.66	14.18	2.08	2.09	2.44	2.43	0.481	0.479	0.070	0.068	0.411	0.411	5974	5974	5974	5974
Average	2.03	14.51	14.09	2.13	2.14	2.49	2.49	0.471	0.469	0.068	0.066	0.403	0.403	6374	6374	6572	6572
SD	0.27	0.833	0.819	0.06	0.06	0.069	0.071	0.014	0.014	0.005	0.005	0.011	0.011	545	545	546	546

Mineralogy: The mineralogical analysis of the remaining Saracen-1 samples stored in airtight bags indicates that the samples are rather consistent except for the sample at 1118.15 m which shows a higher concentration of pyrite, the formation of jarosite and a decreased concentration of illite-smectite in comparison to the other samples. Sample 1118.34 m also has jarosite present at 1 % concentration (Figure 6-2) but otherwise, has mineralogy similar to the other samples.

The mineralogy is dominantly illite/ smectite, illite/ mica, quartz and kaolinite. There are trace amounts (≤ 2 %) of chlorite, albite/ anorthite, orthoclase/ microcline, pyrite and anatase.

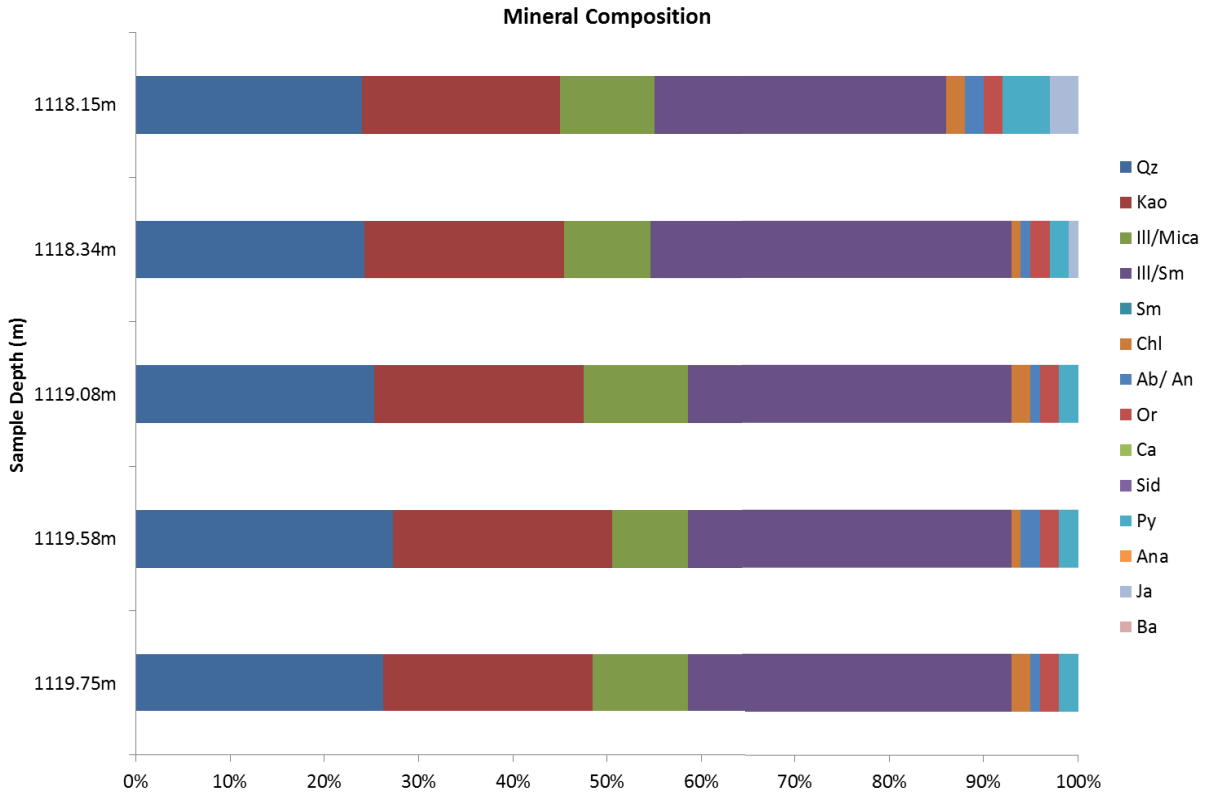

Figure 6-2: XRD Mineralogy of warehoused Saracen-1 samples stored in air lock bags (Analysed in 2016).

The BSE images of the CC samples stored in airtight bags show silt-sized grains dotted throughout a clay matrix (Appendix D Figure D-6 to D-9). The silty grains have their long axes oblique to the fracture in the middle of the image (Appendix D Figure D-6). In the higher magnification images, EDAX has identified; quartz, potassium feldspar, illite, anatase, albite, carbon and iron framboids. The silt grain edges are distinct and there is no evidence of dissolution. The clay matrix appears to fold around these grains.

Discussion: The MICP analysis of the CC samples stored in airtight bags indicates that all of the MICP curves are similar over the 1.6 m interval of Saracen-1 core. The IPV and MI

threshold pressures have a one pressure equilibrium point variation between samples (5970 psia- 6970 psia). This suggests that the effects of warehousing were not uniform for each of the five samples. This is supported by the mineralogical results which identified jarosite in two of the samples (1118.15 m and 1118.34 m). There was no relationship found between the presence of jarosite in the samples and porosity, bulk density, grain density, sample volume per gram, pore volume per gram, IPV threshold pressure or MI threshold pressure.

6.3.1.3 Warehoused samples, Saracen-1, Barrow Sub-basin

Please see section 4.6.3 for a description of the warehouse conditions for the CC and DC cuttings and a description of the CC. For a description of the DC samples please see section 5.3.6

*Methodology modifications***:** Four core plugs were dry drilled in 2013 from the same section of the core as the original samples taken by Dewhurst et al., (2002). The plugs were orientated and subsequently, 2-3 g cube sub-samples were taken for MICP analysis. The sub-sample cubes were coated on five sides with epoxy araldite allowing mercury injection normal to the laminae as to best represent field conditions. The remaining material was sent to the CSRIO where Mark Raven semi-quantified the mineralogy or the material was used for BSE imaging.

Saracen-1 DC samples stored in airtight bags in the WACL from four depth intervals proximal to the depth of the CC samples were also analysed with MICP. The DC samples were vetted for DC‘s not representative or which appeared to be refused and dried together. The largest DC samples were selected and analysed with MICP. Orientations could not be determined and mercury intrusion was from all sides.

The warehoused CC samples were all imaged with the BSE microscope perpendicular to the bedding of the sample. The DC samples were placed in araldite resin containers and orientated so that the sample view was perpendicular to the long side of the sample. Numerous issues were encountered with the araldite resin and the polishing of the samples. Subsequently, two samples were viewed by breaking the samples and imaging with the SEM microscope (1120-1125 m and 1121-1124 m).

Results: The uncorrected MICP curves from the warehoused Saracen-1 samples are displayed in Appendix D Figure D-10. The MICP curves are similar to one another up until 30 % mercury saturation, upon which, they show slight separation before regrouping at 100 % mercury saturation.

There is a slight improvement in the agreement between conformance corrected MICP curves for the four CC samples (Appendix D Figure D-11). The IPV threshold pressures (Table 6-3) are all at the same pressure equilibrium point (~6970 psia) while the MI threshold pressures are picked at the pressure equilibrium point higher (~8475 psia) for two of the samples with the other three remaining at (~6970psia). The corrected porosities have a maximum variation of 1.13 % between sample 1119.30 m (12.85 %) and sample 1118.65m (11.72 %). The corrected bulk density varies between 2.17g/ml and 2.2 g/ml and the grain density varies between 2.51 g/ml and 2.46 g/ml. The average sample volume per gram, grain volume per gram and pore volume per gram are 0.456 ml/g, 0.401 ml/g and 0.056 ml/g respectively with minor variation between samples.

Table 6-3: MICP analysis of warehoused (2013) Saracen-1 samples from a 1.6m of CC Muderong Shale.

Sample Depth (m)	Sample Weight (g)	Porosity (%)		Bulk Density (g/ml)		Grain Density (g/ml)		Sample Volume (ml/g)		Pore Volume (ml/g)		Grain Volume (ml/g)		IPV Threshold Pressure (psia)		MI Threshold Pressure (psia)	
		Raw	Cor.	Raw	Cor.	Raw	Cor.	Raw	Cor.	Raw	Cor.	Raw	Cor.	Raw	Cor.	Raw	Cor.
1118.45	2.83	12.510	11.954	2.190	2.206	2.510	2.505	0.456	0.453	0.057	0.054	0.399	0.399	6970	6975	8488	8488
1118.65	3.13	12.190	11.717	2.160	2.174	2.460	2.462	0.463	0.460	0.056	0.054	0.406	0.406	6972	6972	6972	6972
1119.05	3.12	12.590	12.320	2.190	2.196	2.500	2.505	0.457	0.455	0.058	0.056	0.399	0.399	6965	6965	8470	8470
1119.3	3.22	13.260	12.846	2.180	2.192	2.510	2.515	0.458	0.456	0.061	0.059	0.398	0.398	6966	6966	6966	6966
Average	3.08	12.64	12.21	2.18	2.19	2.50	2.50	0.456	0.456	0.058	0.056	0.401	0.401	6970	6969.50	7724	7724
SD	0.169	0.446	0.493	0.014	0.017	0.025	0.026	0.003	0.003	0.002	0.002	0.004	0.004	4.796	4.796	872	872

The uncorrected MICP curves for the warehoused DC samples analysed in 2014 are shown in Appendix D Figure D-12. The MICP curves show poor agreement with one another; the point of maximum inflection and shape are not consistent up until 90 % mercury saturation.

The conformance corrected MICP curves (Appendix D Figure D-13) show improved agreement with one another. However, the shapes of the MICP curves do show variation especially the DC sample from 1121-1124 m which crosses the MICP curve from 1115-1118 m. The other samples also show variation in the ~~"ti~~ghtness" of the maximum point of inflection of the MICP curve. The IPV interpreted threshold pressures (Table 6-4) vary between 2457 psia and 3520 psia. The threshold pressures interpreted with the MI method are picked slightly higher leading to an average threshold pressure of 3407psia as opposed to the IPV method 2956 psia. The conformance corrected porosities vary significantly between samples; 17.22 % for sample 1115-1118 m and 22.74 % for sample 1120-1125 m. The corrected bulk densities vary between 1.95 g/ml and 2.11 g/ml while the grain density varies between 2.46 g/ml and 2.53 g/ml. The conformance corrected sample volume per gram and pore volume per gram show a consistent trend of increasing sample volume per gram with increasing pore volume per gram.

Table 6-4: MICP analysis of warehoused (2013) Saracen-1 samples DC samples taken above, over and below the 1.6m of CC Muderong Shale.

Sample Depth (m)	Sample Weight (g)	Porosity (%)		Bulk Density (g/ml)		Grain Density (g/ml)		Sample Volume (ml/g)		Pore Volume (ml/g)		Grain Volume (ml/g)		IPV Threshold Pressure (psia)		MI Threshold Pressure (psia)	
		Raw	Cor.	Raw	Cor.	Raw	Cor.	Raw	Cor.	Raw	Cor.	Raw	Cor.	Raw	Cor.	Raw	Cor.
1115-1118	1.31	17.35	15.09	2.059	2.11	2.49	2.49	0.486	0.473	0.084	0.071	0.402	0.402	2911	2911	4266	3516
1118-1121	1.31	18.84	17.22	2.06	2.1	2.53	2.53	0.487	0.477	0.092	0.082	0.395	0.395	3520	3520	4249	4249
1120-1125	0.86	27.78	22.74	1.82	1.95	2.52	2.52	0.549	0.514	0.152	0.117	0.397	0.397	2457	2457	2928	2928
1121-1124	0.77	21.89	20.31	1.92	1.96	2.45	2.46	0.522	0.522	0.115	0.115	0.407	0.407	2938	2938	2938	2938
Average	1.06	21.47	18.84	1.96	2.03	2.50	2.50	0.511	0.494	0.111	0.094	0.400	0.400	2957	2956.50	3595	3407.75
SD	0.288	4.615	3.369	0.117	0.087	0.036	0.032	0.031	0.022	0.031	0.021	0.006	0.006	436	435.68	765	624.57

Mineralogy: The mineralogy has been semi-quantified with XRD analysis (Figure 6-3). The four CC samples show a similar mineralogy to one another. The samples are dominantly illite/ smectite, quartz and kaolinite. There are minor amounts (< 6 %) of illite/ mica, smectite, jarosite and, trace amounts (≤ 2 %) of albite/ anorthite, orthoclase, pyrite and anatase.

Three of the DC samples have a mineralogy with notable differences and changes in mineral concentration to the CC samples while the fourth sample from 1115-1118 m has a mineralogy that more closely resembles the CC samples. The three DC samples (1118-1121 m, 1120-1125 m and 1121-1124 m) are dominantly illite/ smectite, quartz, kaolinite, smectite. There are minor amounts (< 6 %) illite/ mica, pyrite, barite and, trace amounts (≤ 2 %) of albite/ anorthite, orthoclase, calcite, siderite and anatase. The fourth DC sample (1115-1118 m) is dominantly quartz, illite/ smectite, kaolinite, and smectite. There are minor amounts (< 6 %) of illite/ mica, albite/ anorthite, orthoclase and, trace amounts (≤ 2 %) of chlorite, siderite, pyrite, anatase and jarosite.

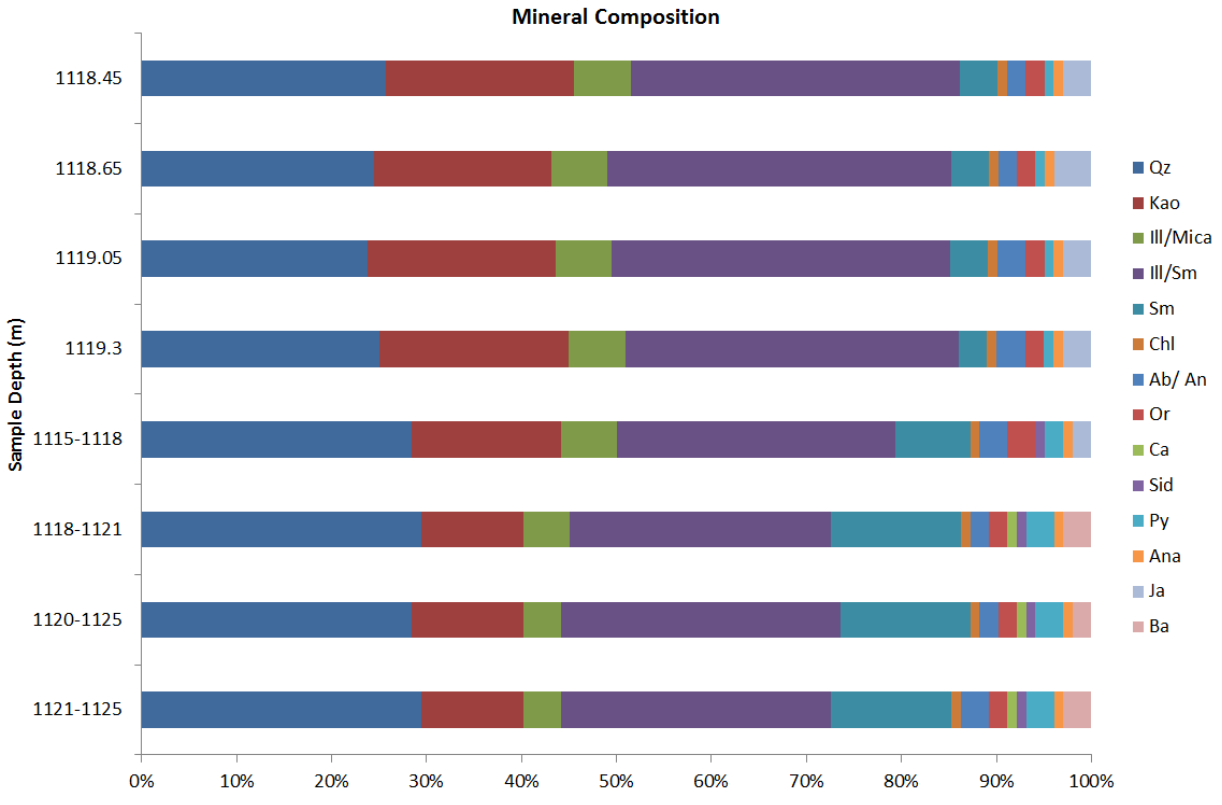

Figure 6-3: XRD Mineralogy of warehoused Saracen-1 conventional core and drill cutting samples (Analysed in 2013/2014).

The BSE images of the CC sample show silty grains floating throughout a clay matrix (Appendix D Figure D-14 to D-17). The silty grains tend to show a degree of orientation parallel to the bedding. The fractures or fissility is slightly oblique to the bedding (Appendix

D Figure D-17). In the higher magnification images, there are a number of grains that have been identified using the EDAX; quartz, potassium feldspar, plagioclase and iron framboids all floating within the clay matrix. The silty grain edges are distinct and there is no evidence of dissolution. The clay matrix often appears to fold around silt-sized grains.

The BSE and SEM images of the DC samples show a similar fabric to the CC samples with silty grains floating throughout the clay matrix (Appendix D Figure D-18 to D-21). The silty grains do not show a preferred orientation. There are numerous fractures throughout the sample. The fractures are linking up to dark black bodies which are either carbon or porosity and are continuous throughout the image. Portions of the fractures have material deposited in them. In the higher magnification image, there are a number of grains that have been identified using the EDAX; quartz, glauconite and illite/ smectite clays. The fractures can clearly be observed around the edges of some of the silty grains. The silty grain edges appear less distinct/ sharp in some cases. The clay matrix appears to fold around the silt-sized grains.

Discussion: The MICP analyses of the warehoused CC samples indicate that the MICP curves, porosities, interpreted threshold pressures and mineralogies are all similar to one another over the re-sampled Saracen-1 core. The DC samples, however, show much more variation in MICP curves to the CC samples and to a lesser extent one another. The interpreted threshold pressures of the DC samples are at best four pressure equilibrium points less than the warehoused CC samples indicating that the samples are significantly different. However, the DC samples, while showing variation in interpreted threshold pressures between one another are not significantly different; there is no more than one pressure equilibrium point difference from the common threshold pressure which is the same variation observed in Saracen-1 Section 4.5.1. However, the corrected porosities and MICP curves of the DC samples are significantly different from the CC as well as each other.

The mineralogy of three of the DC samples (1118-1121 m, 1121-1124 m and 1120-1125 m) are all quite similar to one another. They vary from the warehoused CC slightly in the concentration of the primary minerals (quartz, kaolinite, illite/smectite and smectite) but also in that they contain calcite, siderite and barite. However, the DC sample from 1115-1118 m has mineralogy distinct from the other three DC samples and reflecting the CC samples. The BSE images of the DC samples show key differences to the CC sample images with numerous fractures and black, dark black bodies being observed.

6.3.1.4 Maximum CO_2 column Height Retentions

The maximum CO_2 column heights have been calculated to determine the effects of the revised interpretations of threshold pressure as calculated using IPV method.

Results: The calculated maximum CO_2 column height retentions (Figure 6-4) indicate that at a minimum the DC sample from 1121-1124 m with the lowest threshold pressure and a contact angle of 60 ° is capable of retaining 100 m of CO_2. The CC samples with a threshold pressure of ~6970 psia and a contact angle of 0 ° are capable of retaining a maximum of a 568m column of CO_2. This puts the range of maximum CO_2 column heights for the Muderong Shale interval at 468 m depending on sample type, threshold pressure and contact angle.

The DC samples are consistently lower than the original and warehoused CC samples (Figure 6-4). The highest maximum CO_2 column height for a DC sample is for the DC sample from the interval from which the CC samples were taken. The original samples generally have a maximum calculated CO_2 column height of ~400 m with a contact angle of 0 ° down to ~200 m with a contact angle of 60 °. The warehoused CC samples have a maximum calculated CO_2 column height of ~567 m with a contact angle of 0 ° down to 283 m with a contact angle of 60 °. The CC samples stored in airtight bags have a maximum CO_2 column that falls between 567 m at 0° and 243 m with a contact angle of 60 °.

The warehoused CC samples show an increase in maximum CO_2 column heights in comparison to the original samples. The CC samples stored in airtight bags on average show a similar trend of increased maximum CO_2 column heights compared to the original samples although to a lesser extent than the warehoused samples.

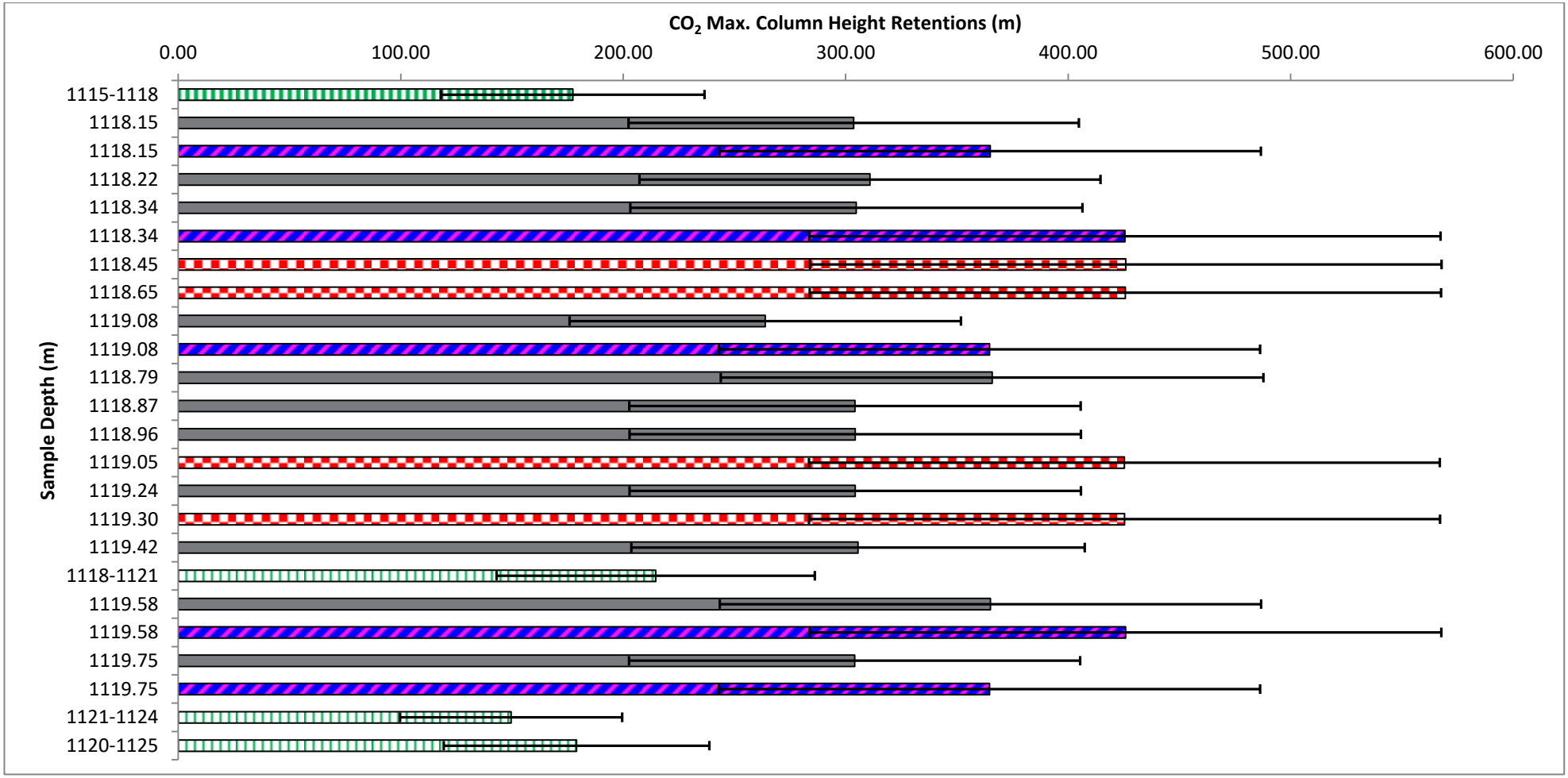

Figure 6-4: Maximum CO_2 column height retentions calculated for the original samples (grey), the warehoused conventional core samples (red checks), the warehoused drill cutting samples (green and white stripes) and the samples stored in airtight bags (pink and blue diagonal stripes). The error bars represent the range of contact angle (brine/ CO_2/ rock) from 0° (right) to 60° (left).

6.3.1.5 Comparison of original conventional core MICP results with MICP results of conventional core samples stored in airtight bags

The MICP curves of the original CC samples analysed in 2001 are shown in blue, the samples stored in airtight bags and analysed in 2015 are shown in orange and are displayed in Appendix D Figure D-22. The grouping and subsequent differentiation between the two sample types are slight. The CC samples stored in airtight bags appear to have the maximum inflection points of the MICP curves at slightly higher pressure than the original CC samples after which the MICP curves of the CC samples stored in airtight bags move back into agreement with the original CC sample MICP curves up to 80 % mercury saturation. After that the MICP curves follow a steeper pattern and close grouping up to 100 % mercury saturation. The MICP curves follow the same pattern after conformance correction (Appendix D Figure D-23).

The IPV method interpreted threshold pressures for the different sample types are similar to one another; the average threshold pressure for the original CC samples is 5119 psia threshold while the average threshold pressure for the CC samples stored in airtight bags is 6374 psia. Forty percent of the CC samples stored in airtight bags have an interpreted threshold pressure of ~6969 psia while the remaining 60 % have threshold pressures of ~5975 psia. The original CC samples, as mentioned above have 18 % of samples with an interpreted threshold pressure of ~5980 psia, 9 % interpreted as having a threshold pressure of 4326 psia and 73 % of samples with an interpreted threshold pressure of ~4990 psia.

The MI interpreted threshold pressures for the different sample types show improved agreement over the IPV method for the original CC samples but similar variation for the CC samples stored in airtight bags. The original CC samples all have their interpreted threshold pressures at the same pressure equilibrium point ~5970 psia while the CC samples stored in airtight bags have 60 % of samples interpreted at the pressure equilibrium point higher ~6970 psia. The remaining 40 % of samples are interpreted at the same pressure equilibrium point ~5970 psia.

The porosities of the CC samples stored in airtight bags vary between 14.87 % and 12.92 % while the original CC samples have porosities between 18.63 % and 15.39 %. The bulk density and grain density are highest for the original CC samples with an average of 2.28 g/ml and 2.74 g/ml respectively. The average bulk density and grain density for the CC samples stored in airtight bags are 2.14 g/ml and 2.49 g/ml respectively.

The comparison of the mineralogical analyses between the original samples and the samples stored in airtight bags is complicated by the slightly different mineral breakdown and groupings. However, clear differences can be observed in the mineralogy of the samples stored in airtight bags from 1118.15 m and 1118.34 m which have had jarosite formed. Anatase at < 1 % was also found in all warehoused samples that was not identified in the original samples. Also, a number of the concentrations of minerals have changed with a general reduction in the concentration of chlorite, orthoclase/microcline and pyrite (except sample 1118.15 m). There is a general increase in the concentration of kaolinite. The BSE images show no obvious differences from the images of the original CC samples and the CC samples stored in airtight bags.

6.3.1.6 Comparison of original conventional core MICP results with warehoused conventional core and drill cuttings MICP results

The MICP curves of the original CC samples analysed in 2001 are shown in blue, the warehoused CC samples analysed in 2013 are shown in red and the warehoused DC samples analysed in 2014 are shown in green and are displayed in Appendix D Figure D-24. The graph clearly shows the grouping of the MICP curves of the different sample types. The groupings are clearer in the conformance corrected MICP curves in Appendix D Figure D-25. The MICP curves for the warehoused DC samples are indicative of a larger pore throat network than the other sample types; higher mercury saturation at lower pressure. They also show the poorest agreement between one another. The original CC samples from 2001 have smaller pore throat networks than the DC samples with good agreement between one another. The warehoused CC samples have MICP curves indicative of the smallest pore throat network; highest pressure and lowest mercury saturation of all samples. The warehoused CC MICP curves are similar.

The interpreted IPV threshold pressures for the different sample types show similar groupings; the average threshold pressure for the warehoused DC samples is 2957 psia, 6970 psia for the warehoused CC samples and 6069 psia for the original CC samples. The DC samples have 50 % of samples with an interpreted threshold pressure of ~2920 psia and 25 % have threshold pressures of 2457 psia and 3520 psia each. All of the CC warehoused samples have a threshold pressure of ~6969 psia while the original CC samples had 18 % of samples with an interpreted threshold pressure of ~5980 psia, 9 % interpreted as having a threshold pressure of 4326 psia and 73 % of samples with an interpreted threshold pressure of ~4990 psia.

The interpreted MI threshold pressures for the different sample types show similar agreement with one another; the average threshold pressure for the original CC sample samples is 5980 psia with all samples having an interpreted threshold pressure at the same pressure equilibrium point. The warehoused CC samples have an average threshold pressure of 7724 psia with the four samples split between adjacent pressure equilibrium points. The DC samples show more variation with threshold pressures between 2939 psia and 4249pisa.

The conformance corrected porosity for the different sample types follow a similar trend; the warehoused DC samples have the highest porosity between 22.74 % and 15.1 %, the original CC samples have porosities between 18.63 % and 15.39 % and the warehoused CC samples have porosities between 12.85 % and 11.72 %.

The conformance corrected bulk density and grain density, however, show a different pattern. Both the bulk density and grain density are highest for the original CC samples with an average of 2.28 g/ml and 2.74 g/ml respectively. The average bulk density and grain density for the warehoused CC samples are 2.19 g/ml and 2.50 g/ml respectively while the warehouse DC samples have the lowest average bulk density of 2.03 g/ml and an average grain density of 2.50 g/ml.

The mineralogical analysis highlights mineral differences between the sample types and changes in mineral concentration between the samples. The warehoused CC samples have jarosite and anatase interpreted as present that were not identified in the original CC samples. The warehoused CC samples do not have siderite identified that was found in the original CC samples. Also, a number of the concentrations of minerals have changed. The comparison between these concentrations of minerals is made complicated by the slightly different mineral breakdown and, identification and the presence/ absence of minerals. However, in general, there is a reduction in the concentration of chlorite and pyrite. There is an increase in the concentration of kaolinite and possibly albite/ anorthite.

Three of the four warehoused DC samples have similarly interpreted mineralogy while the fourth (1115-1118 m) has key differences. The three warehoused DC samples have calcite, barite and anatase present that was not present in the original CC samples. The mineral concentrations of quartz and chlorite all appear to have decreased while kaolinite appears to have increased. The fourth warehoused DC sample (1115-1118 m) has jarosite and anatase present that were not identified in the original CC samples. The concentrations of chlorite also appear to have decreased while kaolinite is possibly present in slightly higher concentrations.

The BSE images of the original CC samples and the warehoused CC samples show no obvious differences. However, the warehoused DC samples show prevalent continuous fracturing throughout the samples. These fractures often have linked together with black fragments throughout the rock fabric that is either carbon or porosity as identified with EDAX. The DC samples also have a rind of mud cake and unconsolidated material around the edge that appears semi-attached.

6.3.1.7 Comparison of MICP results from warehoused conventional core and drill cutting samples with MICP results from conventional core samples stored in airtight bags.

The MICP curves of the CC samples stored in airtight bags analysed in 2015 are shown in orange, the warehoused CC samples taken in 2013 are shown in red and the warehoused DC samples taken in 2014 are shown in green and are displayed in Appendix D Figure D-26. The mercury injection graph shows the clear grouping of the MICP curves for the different sample types. The CC samples stored in airtight bags and the CC samples stored in the warehouse have similar MICP curves; the key difference being the linear part of the MICP curve after the maximum inflection point for the warehoused samples is at a higher pressure for the same mercury saturation indicating the samples have smaller diameter pore throat networks. The warehoused DC samples have distinctly higher initial mercury saturation and maximum inflection points at much lower pressures than both the warehoused CC samples and the CC samples stored in airtight bags. The conformance corrected MICP curves still show the same trend but with a better agreement between samples and between sample types (Appendix D Figure D-27).

The interpreted IPV threshold pressures for the different sample types show similar trends; the average threshold pressure for the CC samples stored in airtight bags is 6374 psia while the average for the warehoused CC and DC samples is 6969 psia and 2965 psia respectively. Forty percent of the CC samples stored in airtight bags have an interpreted threshold pressure of ~6969 psia while the remaining 60 % have threshold pressures of ~5975 psia. One hundred percent of the CC warehoused samples have a threshold pressure of ~6969 psia while the warehoused DC samples have 50 % of samples with an interpreted threshold pressure of ~2920 psia and 25 % had threshold pressures of 2457 psia and 3520 psia each.

The interpreted MI threshold pressures for the warehoused CC samples are similar to one another; the warehoused CC samples all have an interpreted threshold pressure at the same pressure equilibrium point (~6970 psia). The warehoused DC samples, however, show considerable variation (2928pisa to 4249 psia). The CC samples stored in airtight bags show

more variation (5970 psia and ~6970 psia) than the warehoused CC samples, but less variation than the warehoused DC samples.

The conformance corrected porosity for the CC samples stored in airtight bags varies between 12.92 % and 14.82 % while the warehoused CC samples vary between 11.72 % and 12.85 %. The warehoused DC sample porosities vary between 15.1 % and 22.74 %. Thus the sample types show a clear grouping as with the MICP curves. The variation between the minimum and maximum porosity is less for the warehoused CC samples (~1 %) than the variation observed in the airtight bag CC samples (~2 %) and much less than the variation observed between warehoused DC samples (~7.7 %).

The conformance corrected average bulk density and grain density for the CC samples stored in airtight bags is 2.14 g/ml and 2.49 g/ml respectively while the warehoused CC samples have a bulk density of 2.19 g/ml and a grain density of 2.50 g/ml. The warehouse DC samples have the lowest average bulk density of 2.03 g/ml and an average grain density of 2.50 g/ml. Notably, the grain density for all the sample types is nearly the same while the bulk density varies.

The mineralogy of the warehoused CC samples and those stored in airtight bags show both similarities and key differences. The samples show similar concentrations of anatase, orthoclase/ microcline, illite/ smectite, kaolinite and quartz. The sample stored in the airtight bag from 1118.15 m has jarosite formed in a similar concentration to the warehoused CC samples. This sample also has a high concentration of pyrite relative to both sets of samples. The sample below (1118.34 m) stored in an airtight bag also has jarosite formed but at a concentration of 1 % as opposed to 3 % and 4 %. The other three samples stored in airtight bags do not have jarosite present. There are minor changes in concentrations of pyrite, albite/ anorthite, chlorite and illite/ mica between the warehoused CC samples and the samples stored in airtight bags. The mineral concentrations do not vary by more than 6 % between any of the samples.

The mineralogies of the warehoused DC samples and those stored in airtight bags have a number of key differences. Siderite was identified in low concentrations in the DC samples but not identified in the CC samples stored in airtight bags. Three of the DC samples have barite and calcite present which was not identified in the CC samples stored in airtight bags. Notably, jarosite was found in the DC sample from 1115-1118 m and in two of the samples stored in airtight bags (1118.15 m and 1118.34 m). In general, the DC samples have a lower

concentration of illite/ smectite, illite/ mica, chlorite and kaolinite while the concentration of pyrite, albite, anorthite and quartz are higher.

The BSE images of CC samples stored in airtight bags and the warehoused CC samples show no obvious differences. However, the warehoused DC samples show prevalent continuous micro-fracturing throughout the samples. These micro-fractures often link up to one another and black fragments throughout the rock fabric that is either carbon or porosity as identified with the EDAX. The DC samples also have a rind of mud cake and unconsolidated material around the edge that appears semi-attached.

Discussion: The MICP results of the original CC samples analysed in 2001 and the CC samples stored in airtight bags analysed in 2015 show a number of distinct differences. The IPV threshold pressure of the samples stored in airtight bags is interpreted to be at ~5990 psia for 60 % of the samples while only 18 % of the original samples had threshold pressures at ~5990 psia. The remaining 40 % of samples stored in airtight bags were interpreted at the pressure equilibrium point higher (~6970 psia). The average porosity decreased from 16.88 % to 14.09 %, the bulk density decreased from 2.28 g/ml to 2.14 g/ml and the grain density decreased from 2.74 g/ml to 2.49 g/ml. The mineralogy of the samples stored in airtight bags show a key difference with the samples from 1118.15 m and 1118.34m having jarosite ($KFe^{3+}_3(OH)_6(SO_4)_2$) and anatase (TiO2) (<1 %) present that were not found in the original samples or the other samples stored in airtight bags. This suggests that the airtight bag environments varied for the samples and it is thought that this may have resulted from the efficacy with which the zip lock bags sealed and thus stopped the influence of the atmosphere.

The uniform changes in MICP analyses of the samples stored in airtight bags and the formation of jarosite in only two of the samples allows the conclusion that there is no relationship between the formation of jarosite and the changes in MICP analyses between the original samples and the samples stored in airtight bags. This suggests that jarosite is not forming in significant concentrations within the pore network of the rock samples as might be hypothesised. The anatase is suspected to be in too low a concentration to have caused the variations observed in MICP analyses of the samples stored in airtight bags.

The warehoused CC samples show significant differences to the original samples and to the samples stored in airtight bags. The warehoused CC samples have MICP curves with the maximum inflection point and subsequent linear upward trend at a higher pressure than the original CC samples. The interpreted threshold pressures for the warehoused CC samples

are all at ~6969 psia while the highest threshold pressure for any of the original samples is ~5980 psia. The warehoused CC samples all have a distinctly lower porosity (11.75 %-12.85 %) as opposed to the original CC samples (15.39-18.54 %). The bulk density and grain density are highest for the original CC samples with an average of 2.28 g/ml and 2.74 g/ml respectively while the warehoused CC samples are 2.19 g/ml and 2.50 g/ml respectively. The mineralogy also shows a number of distinct differences with jarosite and anatase present and the absence of siderite in the warehoused samples.

These differences can be attributed to two likely causes; heterogeneity between samples or the effects of warehousing. Heterogeneity between samples is unlikely as the results are consistent within the original sample analysis and within the warehousing sample analysis. Also, the sampling regime for both the original analysis and the warehousing analysis overlap one another and thus any heterogeneity should be identified in both analyses with distinct differences observed. Thus, as the differences were identified between the original and warehousing samples and not within these sample types, the differences are attributed to the warehousing of the CC.

It is thought that the precipitated minerals jarosite and anatase are formed during the storage of the core as a result of the contact with the atmosphere (oxygen and humidity). However, as demonstrated by the samples stored in airtight bags, with a reduction in porosity and constriction of pore throats in all the samples, including the samples without jarosite forming, it cannot be suggested that this is a result of the precipitation of jarosite. It is thought that this is also the situation with the warehoused samples which also have jarosite present. It is thought given the consistent grain volume per gram and inconsistent reduction in pore volume per gram between warehoused samples and samples stored in airtight bags that the entire sample has not constricted only the pore space. It is thought that clays have lost their bound water constricting the pore space. This is possible because the samples have a clay matrix with no grain to grain contact which would act as a brace and stop the constriction. If the sample fabric had grain to grain contact, then it would be envisaged that the porosity and pore throats would increase and enlarge in contrast to these results.

The precipitation of jarosite in the warehouse CC and samples stored in airtight bags is suggested to have formed as a result of the pyrite being oxidised in the presence of oxygen and water and subsequently reacting with potassium ions from the illite clay. The oxidation of pyrite may have been accelerated if acidophilic bacteria were present. The suggested reaction is below (Espana, 2008 and Nazari et al., 2014):

$$FeS_2 + 3.5O_2 + H_2O \rightarrow Fe^{2+} + 2\,SO_4^{2-} + 2H^+$$

$$14Fe^{2+} + 3.5O_2 + 14H^+ \rightarrow 14Fe^{3+} + 7H_2O$$

$$Fe^{3+} + H_2O \rightarrow Fe\,(OH)_3 + H^+$$

$$Fe(OH)_3 + SO_4^{2-} + H^+ \rightarrow Fe(OH)SO_4 + H_2O$$

$$Fe\,(OH)SO_4 + K^+ + Fe_{3+} + +H_2O \rightarrow K[Fe(OH)_2]_3(SO_4)_2 + H^+$$

(Espana, 2008 and Nazari et al., 2014)

Anatase is thought to form as a result of the dissolution of Titanium bearing minerals. Anatase crystals and agglomerates (TiO_2) form in the pore water, at low to high temperatures, under low pH conditions and increased ionic strength. The necessary acidic conditions often occur as a result of the diagenetic products from organic matter found in black shales (Schulz et al., 2016). However, in the case of Saracen-1, the necessary acidic conditions would likely have been brought about by the precipitation of jarosite and associated acidic conditions.

A comparison of MICP analysis between DC and CC samples is provided in Section 5.3.6. The MICP curves of the warehoused DC samples have much lower interpreted threshold pressures than the original (fresh) samples. This is indicative of the warehoused DC samples having larger pore throats and higher average porosity. It is suggested that the DC sample from 1115m-1118m, given its distinct mineralogy and its similarity to the CC taken just below the sampling interval is most representative of the CC samples. It is thus suggested that this sample was stored in an airtight bag that wasn‘t properly sealed.

The three DC samples (1118-1121 m, 1120-1125 m, 1121-1124 m) show differences in mineralogy when compared to the original CC samples. The anatase identified is interpreted to have formed during the storage of the samples suggesting that this mineral does not require exposure to the atmosphere to form. Thus the storage in airtight bags has not prevented the precipitation of anatase. The differences in mineral concentrations of quartz,

chlorite and kaolinite are likely representative of the heterogeneity in mineralogy over the seven-metre interval from which the DC samples were taken.

In conclusion, the warehoused Saracen-1 DC samples have lower threshold pressure than the original (fresh) CC samples and even lower threshold pressure than the CC samples stored in airtight bags and lower again to the CC samples stored in the warehouse. It is suggested that the storage of samples in airtight bags reduces changes in mineralogy and improves the similarity of MICP analyses to the original core analyses.

6.3.2 **CRC-1, Otway Basin**

The CRC-1 well was drilled in the Otway Basin in 2007 by the CO2CRC. The well had conventional core from a number of sealing intervals, reservoirs and intraformational baffles; Pember Mudstone, Paaratte Formation and the Belfast Mudstone. Daniel, (2007) investigated the sealing capacity and mineralogy of the original samples providing the basis for comparison to the warehoused samples analysed by this study in 2014.

6.3.2.1 Original samples, Paaratte Formation and Pember Mudstone, CRC-1, Otway Basin

Please see section 3.3.2 for CRC-1 well description. The core was originally sampled at the CRC-1 well site immediately after drilling. A total of nine samples were taken and analysed with MICP, XRD and SEM (Daniel, 2007). The Pember Mudstone was sampled at 917 m, the Paaratte Formation at 1262.95 m, 1264.95 m and 1268.80 m, the Belfast Mudstone was more densely sampled at 1900.70 m, 1900.99 m, 1901.50 m, 1901.85 m and 1902.25 m depths. The results have subsequently been re-interpreted in the same manner as the warehoused samples to identify the effects of warehousing.

Methodology modifications: The CO_2 maximum column height retentions were calculated with the brine salinities recorded in Daniel, (2007) for the formations.

The methodology for the characterisation of the mineralogy of the CRC-1 samples has undergone a number of changes. Firstly, the imaging of the original samples from 2007 was acquired using a broken rock sample under the SEM (Daniel, 2007). No BSE imaging of polished rock sections were acquired. Secondly, the XRD interpretation is achieved by comparing the diffractograms and their peak positions and intensities, which reflect the mineralogies present. No mineralogy was interpreted due to the nature and variability of interpretation and due to the differences in methodologies and equipment used to undertake the XRD analysis (cobalt source vs. copper).

Results: The uncorrected MICP curves for the original (fresh) Pember Mudstone and Paaratte intraformational baffles are shown in Appendix D Figure D-28. The Pember Mudstone shows a clearly distinct MICP curve to the three intraformational baffles of the Paaratte Formation. The three MICP curves from the Paaratte Formation were taken nearly six meters apart and show poor agreement with one another. The conformance corrected MICP curves (Appendix D Figure D-29) do not significantly improve the agreement between the MICP curves. The MICP data (Table 6-5) show that the IPV threshold pressures vary considerably between the four samples (71 psia-2923 psia). The threshold pressures interpreted with the MI method show similar variation and are generally consistent with the IPV method.

The conformance corrected porosity show considerable variation (Table 6-5). The Pember Mudstone has a corrected porosity of 16.78 % while the intraformational baffles have a corrected porosity varying between 19.72 % for the sample taken at a depth of 1268.8m and 26.64 % for the sample taken at 1264.95 m. The corrected sample volumes per gram show some variation between samples, however, there is significant variation in corrected grain volume per gram and the pore volume per gram between samples. The corrected bulk densities and grain densities show some variation; 2.17 g/ml and 2.61 g/ml respectively for the Pember Mudstone while the Paaratte Formation intraformational baffles vary between 2.07 g/ml and 2.26 g/ml for the corrected bulk density and 2.77 g/ml and 2.82 g/ml for the corrected grain density.

Table 6-5: CRC-1 (2007) MICP results for the original Paaratte Formation and Pember Mudstone samples (Re-interpreted from Daniel, 2007).

Sample Depth (m)	Sample Weight (g)	Porosity (%)		Bulk Density (g/ml)		Grain Density (g/ml)		Sample Volume (ml/g)		Pore Volume (ml/g)		Grain Volume (ml/g)		IPV Threshold Pressure (psia)		MI Threshold Pressure (psia)	
		Raw	Cor.	Raw	Cor.	Raw	Cor.	Raw	Cor.	Raw	Cor.	Raw	Cor.	Raw	Cor.	Raw	Cor.
917	2.83	17	16.78	2.17	2.17	2.61	2.61	0.461	0.461	0.078	0.077	0.383	0.383	71	71	71	71
1262.95	1.95	26.34	25.42	2.04	2.07	2.78	2.77	0.489	0.483	0.129	0.123	0.361	0.361	2923	2923	2923	2923
1264.95	2.11	28.09	26.64	2.02	2.07	2.81	2.81	0.494	0.484	0.139	0.129	0.355	0.355	2048	2048	2048	2048
1268.8	1.64	20.00	19.72	2.25	2.26	2.82	2.82	0.444	0.442	0.089	0.087	0.355	0.355	140	140	199	199
Average	2.13	22.83	22.14	2.12	2.14	2.75	2.75	0.472	0.468	0.109	0.104	0.364	0.364	1295.50	1295.50	1310.25	1310.25
SD	0.51	5.28	4.67	0.11	0.09	0.10	0.10	0.024	0.020	0.030	0.026	0.013	0.013	1420.05	1420.05	1404.26	1404.26

Mineralogy: The bulk XRD diffractograms for the 2007 samples of Pember Mudstone and Paaratte Formation are shown in Appendix D Figure D-30. This analysis was conducted by Daniel, (2007). There are a number of clear differences in peak position, peak shape and peak intensities between the samples. Peak 1 is minor and occurs in all the samples with slightly higher intensity in the sample from 1268.80 m. Peak 2 shows some variation in shape and intensity between the samples. The Pember Mudstone sample has a small rounded peak while the sample from 1262.95 m is much larger but still rounded. The samples taken at 1264.95 m and 1268.80 m show a slightly smaller peak but much steeper. Peak 3 shows considerable variation in intensity and shape between the samples. The sample of Pember Mudstone has a tall dominant peak 3 with an adjacent peak at a lower 2-theta angle. The sample from 1262.95 m has a peak 3 which is less intense; however, the adjacent peak at a lower 2-theta angle has much less intensity than the Pember Mudstone sample. The sample from 1264.95 m has a peak with a similar intensity to the Pember Mudstone sample without the adjacent peak at a lower 2-theta angle. The sample from 1268.80 m has a peak 3 with intensity between the sample at 917 m and the sample at 1262.95 m. Peak 4 is strong for all samples with adjacent peaks at higher 2-theta angle observed for all samples but the Pember Mudstone sample at 917 m. Between peak 4 and peak 5, there are a number of small peaks that vary in shape and position between samples. Peak 5 shows considerable variation between samples, being most intense in the sample at 1268.80 m and least intense in the sample at 1264.95 m. Peak 6 is quite consistent in position and intensity for all samples. Peak 7 is showing a higher intensity peak for the Pember mudstone sample and the sample at 1264.95 m in comparison to the samples from 1262.95 m and the sample from 1268.80 m. This pattern is also observed for peak 8 and peak 9.

The clay XRD diffractograms are shown in Appendix D Figure D-31. The samples show similar peak locations but clear differences in the shape and intensities of the peaks. Peak 1 is most intense for the sample at 1264.95 m while being broader in the samples from 1262.95 m and 917 m and being less intense in the sample at 1268.80 m. Peak 2 is quite consistent in shape and intensity for the three Paaratte Formation samples. Peak 2 is more intense for the sample at 917 m. Peak 3 is similar in shape for all samples but varies in intensity. The samples at 917 m and 1268.80 m appear most intense while the samples at 1262.95 m and 1264.95 m show much less intensity. Peak 4 is prominent in the sample at 917 m while having much less intensity in the samples at 1262.95 m, 1264.95 m and 1268.80 m. The peak is similar in shape and intensity for all samples except the sample at 1262.95 m. Peak 6 and 7 show similar patterns to peak 3 where the samples at 917 m and 1268.80 m have much higher intensity than the other samples. Peak 8 has a similar shape

and intensity for all samples except the sample at 1268.80 m. Peak 9 is most intense for the sample at 917 m while the other three samples are similarly less intense.

The original SEM images of the Pember Mudstone (Appendix D Figure D-32) samples from the CC sample at 917 m show a dominant clay matrix with interspersed silty grains identified as quartz and mica (Daniel, 2007). The original SEM images of the Paaratte Formation samples at 1262.95 m, 1264.95 m and1268.90 m (Appendix D Figure D-33, 34 and 35) show a clay matrix with broken silt-sized fragments dotted throughout the samples. Iron framboids were also identified in two of the samples (Daniel, 2007).

6.3.2.2 Warehoused Samples, Paaratte Formation and Pember Mudstone, CRC-1, Otway Basin - Introduction

The CRC-1 core was initially transported from the well site to the Victorian Department of Primary Industries core laboratory for storage. It was subsequently removed for sampling and stored at the core labs at Geoscience Australia, Canberra. A total of nine samples were taken from the same depth, where possible, as the original samples and analysed in 2014 in this study with MICP, XRD and SEM. The Pember Mudstone was sampled at 917 m depth, the Paaratte Formation intraformational baffles were sampled at 1262.95 m, 1264.95 m and 1268.80 m. The results have been re-interpreted in the same manner as the re-interpreted original samples to compare and infer the effects of warehousing on the analytical results.

Methodology modifications: Please see section 6.3.2.1 for XRD methodology. Both SEM images of broken samples and BSE images of polished samples were acquired.

Results: The MICP curves for the warehoused CC samples of Pember Mudstone and Paaratte Formation (Appendix D Figure D-36) show poor agreement with one another. The Pember Mudstone CC sample has an MICP curve indicative of a much larger pore throat network than the Paaratte Formation. The Paaratte Formation samples have MICP curves in poor agreement with one another but all indicative of potential sealing formations. Their MICP curves all show a tapering off towards the pressure limits of the mercury porosimeter and 100 % mercury saturation indicating that all accessible porosity is filled with mercury**.** The conformance corrected MICP curves for the warehoused CC samples of Pember Mudstone and Paaratte Formation (Appendix D Figure D-37) still show poor agreement with one another with little improvement over the uncorrected MICP curves.

The conformance corrected MICP results (Table 6-6) show that the interpreted threshold pressures vary considerably. The Pember Mudstone has the lowest interpreted threshold pressure of 41 psia (Both IPV and MI methods). The lowest interpreted threshold pressure

for the Paaratte Formation is from the sample at a depth of 1264.95 m; 1431 psia for the IPV method and 1736 psia for the MI method. The highest interpreted threshold pressure for the Paaratte Formation is 3496 psia for the IPV method and 4265 psia for the MI method for the sample taken at 1262.95 m. The conformance corrected porosity result for the Pember Mudstone is 16.24 % while the Paaratte Formation samples have similar porosities for the samples taken at a depth of 1262.95 m and 1264.95 m; 23.23 % and 22.71 % respectively. The sample at 1268.8m has a much lower porosity; 10.31 %. The conformance corrected sample volumes per gram results appear similar for the Pember Mudstone sample at 917 m and the two Paaratte Formations samples at 1262.95 m and 1264.95 m. The major difference between the three samples is the pore volume per gram which is much less for the Pember Mudstone sample and similar for the two Paaratte Formation samples. The third Paaratte Formation sample (1268.8 m) has a significantly different sample volume per gram (0.443 ml/g) and a significantly different pore volume per gram (0.046 ml/g) to the Pember Mudstone sample (917 m) and the two Paaratte Formation samples (1262.95 m and 1264.95 m)

The corrected bulk densities are quite similar (2.01-2.06 g/ml) for the Pember Mudstone sample and the two Paaratte Formation samples (1262.95 m and 1264.95 m) while the sample from 1268.8 m has a higher bulk density of 2.28 g/ml. The corrected grain densities show variation between 2.46 g/ml and 2.67 g/ml.

Table 6-6: CRC-1 (2014) MICP results from warehoused Paaratte Formation and Pember Mudstone samples.

Sample Depth (m)	Sample Weight (g)	Porosity (%)		Bulk Density (g/ml)		Grain Density (g/ml)		Sample Volume (ml/g)		Pore Volume (ml/g)		Grain Volume (ml/g)		IPV Threshold Pressure (psia)		MI Threshold Pressure (psia)	
		Raw	Cor.	Raw	Cor.	Raw	Cor.	Raw	Cor.	Raw	Cor.	Raw	Cor.	Raw	Cor.	Raw	Cor.
917	1.62	16.24	16.18	2.06	2.06	2.46	2.46	0.486	0.485	0.079	0.079	0.407	0.407	41	41	41	41
1262.95	1.45	23.79	23.23	2.03	2.05	2.67	2.67	0.492	0.488	0.117	0.113	0.375	0.375	3496	3496	4265	4265
1264.95	1.86	23.19	22.71	2.00	2.01	2.60	2.61	0.500	0.497	0.116	0.113	0.384	0.384	1431	1431	1736	1736
1268.8	1.85	10.31	9.54	2.26	2.28	2.51	2.52	0.443	0.439	0.046	0.042	0.397	0.397	2929	2929	856	856
Average	1.70	18.38	17.91	2.09	2.10	2.56	2.56	0.480	0.477	0.090	0.087	0.391	0.391	1974.25	1974.25	1724.50	1724.50
SD	0.20	6.38	6.44	0.11	0.12	0.09	0.09	0.025	0.026	0.034	0.034	0.014	0.014	1555.62	1555.62	1829.64	1829.64

Mineralogy: The bulk XRD diffractograms for the 2014 warehoused samples of Pember Mudstone and Paaratte Formation are shown in Appendix D Figure D-38. There are a number of clear differences in peak position, peak shape and peak intensities between the samples. Firstly, peak 1 is identifiable for sample 1268.80 m and possibly for sample 1264.95 m while there is no peak for sample 1262.95 m and a slight broad hump for sample 917 m. Peak 1 varies in both shape and intensity between the samples. Peak 2 varies considerably in intensity and shape. Peak 3 is in the same position and has a similar shape amongst the samples. It does appear to vary in intensity with the Pember Mudstone sample having a higher intensity than the sample from Paaratte Formation sample 1268.80 m. There also appears to be an adjacent peak to peak 3 at a lower 2-theta angle that is distinct in the samples at 917 m and 1268.80 m while being minor in the other two samples. Peak 4 is quite similar in shape and position between samples. Notably, the samples from 1268.80 m and 1264.95 m have an adjacent peak at a higher 2-theta angle that is much more intense than in the samples at 1262.95 m and 917 m. The minor peaks observed between peak 4 and 5 vary in shape, intensity and presence. Peak 5 is most intense in the sample 1268.80 m followed by the samples at 917 m, 1264.95 m and 1262.95 m. A similar pattern is observed for peak 6, 7, 8 and 9. However, the shape of these peaks is consistent with only the intensity varying.

The clay XRD diffractograms of the 2014 warehoused samples of Pember Mudstone and Paaratte Formation are shown in Appendix D Figure D-39. Peak 1 and 2 have the highest intensity in the sample from 1268.80 m followed by the sample at 1262.95 m, 917 m and 1264.95 m. Peak 3 is most intense in the sample at 917 m followed by the sample at 1268.80 m, 1262.95 m and 1264.95 m. Peak 3 appears to be broader in the sample at 1262.95 m than in the other samples. Peak 4 is clearly identifiable in the sample at 917 m while being much less distinct in the Paaratte Formation samples. Peak 5 has the highest intensity in sample 917 m followed by the sample at 1268.80 m, 1264.95 m and 1262.95 m. Peak 6 has a similar shape in the samples from 917 m and 1268.80 m but is slightly more intense in the sample from 917 m. Peak 6 is broader and less intense in the samples from 1262.95 m and 1264.95 m. Peak 7 has a similar shape in all samples but is less intense in the samples from 1262.95 m and 1264.95 m. Peak 8 is just detectable in the samples from 917 m and 1268.80 m and undetectable against background levels for the samples at 1262.95 m and 1264.95 m. Peak 9 shows a similar pattern but is slightly more intense than peak 8.

The warehoused BSE images of the Pember Mudstone (Appendix D Figure D-40) show poorly consolidated clay dominated porous samples with interspersed grains. The BSE

images of the Paaratte Formation sample from 1262.95 m (Appendix D Figure D-41) show much more consolidation and less porosity. The images show silt-sized grains identified as quartz and potassium feldspar surrounded by clays including illite. Iron framboids were also identified. The BSE images of the Paaratte sample taken at 1264.95 m (Appendix D Figure D-42) appear more porous than the previous sample. The images show silt-sized grains identified as quartz and potassium feldspar, on occasion in contact with one another scattered throughout a clay matrix. The BSE images of the Paaratte sample at 1268.80 m show dominant quartz in grain to grain contact throughout the sample (Appendix D Figure D-43). Sites of high and low porosity are also observed.

6.3.2.3 Maximum CO_2 Column Height Retentions

The calculated maximum CO_2 column heights for the original and the warehoused samples from CRC-1 are shown in Figure 6-5. The Pember Mudstone samples at 917 m show minor discernible differences in the maximum calculated CO_2 column heights; both samples indicate that the Pember Mudstone has little to no sealing capacity (< 5 m). The Paaratte Formation samples are considerably more promising for the retention of carbon dioxide. The original sample at 1262.95 m has a calculated maximum CO_2 column height of 285 m at 0 ° contact angle that reduces to 142 m when the contact angle is shifted to 60 °. The warehoused sample MICP threshold pressure results show an increased calculated maximum CO_2 column height between 341 m and 170 m as the contact angle changes from 0 ° to 60 °. The sample from 1264.95 m shows a decreased seal capacity and associated maximum column height for both the original and warehoused samples in comparison to the sample from 1262.95 m depth. The original sample (1264.95m) varies between ~200 m and ~100 m column height while the warehoused sample varies between 139 m and 69 m for 0 ° and 60 ° respectively. The last Paaratte sample at a depth of 1268.80 m varies significantly between the original sample and the warehoused sample. The original sample has a calculated maximum CO_2 column height between 13 m and 6.5 m while the warehoused sample has a calculated column height between 286 m and 143 m for a contact angle of 0 ° and 60 ° respectively.

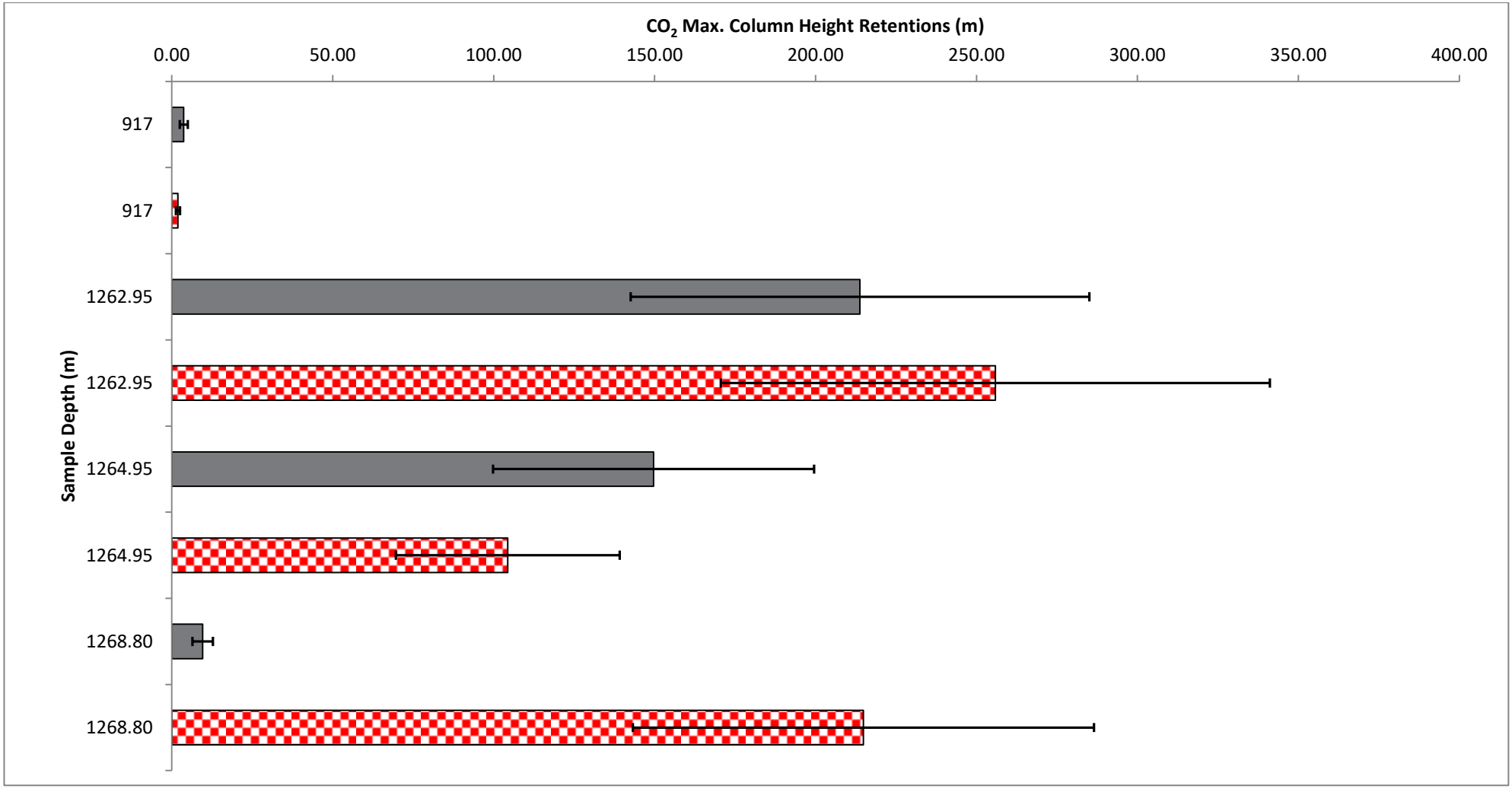

Figure 6-5: Maximum CO_2 column height retentions calculated for the original conventional core samples (grey) and the warehoused conventional core samples (red checks). The error bars represent the range of contact angle (brine/ CO_2/ rock) from 0 ° (right) and 60 ° (left).

6.3.2.4 Comparison of MICP analysis from original 2007 and warehoused 2014 samples from the Pember Mudstone and Paaratte Formation, CRC-1

The uncorrected MICP curves for the original and warehoused samples of the Pember Mudstone show a similar pattern but are offset from one another (Appendix D Figure D-44). The original sample has an MICP curve indicative of a smaller diameter pore throat network in comparison to the warehoused sample. The MICP curves show a similar shape to one another and come into agreement from approximately 80 % mercury saturation and overlap with one another from 90 % mercury saturation. The conformance corrected MICP curves (Appendix D Figure D-45) show no significant improvement in agreement with one another.

The conformance corrected porosity show a slight decrease from 16.78 % for the original samples to 16.18% for the warehoused samples. The same trend was observed for the bulk density and grain density results decreasing from 2.17 g/ml to 2.06 g/ml and 2.61 g/ml to 2.46 g/ml respectively. The interpreted threshold pressures (IPV and MI method), however, show the opposite trend with the original Pember Mudstone sample showing a higher threshold pressure of 71 psia as opposed to the warehoused Pember Mudstone sample which had a threshold pressure of 41 psia.

The uncorrected MICP curves for the original and warehoused samples (Appendix D Figure D-44) for the Paaratte Formation show varied agreement. The samples at 1262.95 m depth show a similar pattern to one another with the warehoused sample having an MICP curve offset at 10 % mercury saturation towards a higher pressure indicative of a smaller pore throat network than the original sample. However at a mercury saturation of 60 % upwards the samples are similar. The conformance corrected MICP curves show a slight improvement in agreement (Appendix D Figure D-45).

The conformance corrected porosity for 1262.95m sample shows a slight decrease from 25.42 % to 23.23 % from the original to the warehoused sample. The bulk density decreased marginally from 2.07 g/ml to 2.05 g/ml while the grain density decreased more significantly from 2.77 g/ml to 2.67 g/ml. The interpreted threshold pressure increased from the original sample (2923 psia) to the warehoused sample (3496 psia) which equates to one pressure equilibrium point.

The uncorrected MICP curves for the original and warehoused samples at 1264.95 m are similar to one another (Appendix D Figure D-44). The conformance corrected MICP curves show slightly poorer agreement due to a slight offset of the original sample to a higher pressure for the same mercury saturation (Appendix D Figure D-45).

The conformance corrected porosities for the 1264.95 m sample show a decrease from the original sample (26.64 %) to the warehoused sample (22.71 %). The bulk density decreased from 2.07g/ml in the original samples to 2.01 g/ml in the warehoused samples while the grain density decreased from 2.81 g/ml to 2.60 g/ml. The interpreted threshold pressures decrease from 2048 psia in the original sample to 1431 psia in the warehoused sample.

The uncorrected MICP curves for the original and warehoused samples taken at 1268.80 m depth show a distinctly different pattern to one another (Appendix D Figure D-44). The conformance correction does not improve the agreement between the MICP curves (Appendix D Figure D-45). The warehoused MICP curve shows significant offset to higher pressure for the same mercury saturation in comparison to the original sample which is indicative of a smaller pore throat network.

The porosities for the samples taken at 1268.80 m show a significant decrease from the original sample (19.72 %) to the warehoused sample (9.54 %). The bulk density shows a slight change from 2.26 g/ml for the original sample to 2.28 g/ml for the warehoused sample. The grain density decreases significantly from 2.82 g/ml for the original sample to 2.52 g/ml for the warehoused sample. The interpreted threshold pressures increase significantly from the original sample (140 psia) to the warehoused sample (2929 psia).

The task of comparing the sample XRD diffractograms from the original samples to the warehoused samples is made difficult due to the use of different XRD machines, with different sensitivities and different sources for the X-rays. Thus the X-rays have different wavelengths and the subsequent diffraction peaks occur at different 2-theta angles. However, with this in mind, the following provides an interpretation of the key mineralogy and mineralogical differences. The peaks that are being compared have been numbered to save confusion.

The Pember Mudstone sample bulk XRD diffractogram from the warehoused sample shows a number of distinct differences to the original sample. The first significant peak (Peak 1) is much taller and thinner in the warehoused sample than in the original sample, where it is less intense and broader. Peak 2 in the warehoused sample is similar in both the warehoused and original samples. Peak 3 and 4 appear comparable for both the original and warehoused samples. Peak 5 appears broader and more intense in the original sample while in the warehouse sample the peak is broad and has a low intensity. Peak 6 is comparable in both sample types in intensity but shows evidence of a side peak in the warehoused samples. Peak 7, 8 and 9 show a number of low-intensity peaks between the numbered peaks in the

original samples that were not observed in the warehoused samples. The identified peaks have similar intensities between samples, but the warehoused samples all have side peaks. The clay XRD diffractograms show similar peaks with variation in intensity for peak 1, peak 3, peak 6, peak 8 and peak 9.

The warehoused Paaratte Formation sample at a depth of 1262.95 m analysed with XRD has a number of distinct differences to the original bulk XRD sample. The first two peaks show similar intensities to one another and shape. The third peak appears to be more intense, has fewer side peaks and is much thinner in the warehouse sample. Peak 4 is much less pronounced in the warehoused sample. Peak 5 is minor in the original sample and not observed in the warehoused sample. Peak 6, 7, 8 and 9 are also more intense in the original sample. The warehoused sample also appears to have evidence of side peaks on peak 6, 7, 8, 9. The clay XRD diffractograms show variation in peak 1, peak 8 and peak 9.

The warehoused Paaratte Formation from a depth of 1264.95 m shows a number of differences to the original bulk XRD sample. Peak 1 in the warehoused sample is more prominent and sharper than the minor peak in the original sample. Peak 2 and 3 are consistent between the samples although there is a minor peak observed between peak 2 and 3 in the original sample that is not observed in the warehoused sample. Also, the side peak to peak 4 in the warehoused sample is much more prominent than in the original sample. Peak 5 is barely detectable in the warehoused sample but more prominent in the original sample. Peak 6, 7, 8 and 9 are of lower intensity and show evidence of a side peak in the warehoused samples whereas the original samples show much sharper peaks of higher intensity. The clay XRD diffractograms show variation between peak 1, peak 6, peak 7, peak 8 and peak 9.

The warehoused Paaratte Formation sample from a depth of 1268.80 m exhibits a number of key differences to the original sample. Peak 1 and 2 are more prominent and sharper in the warehoused sample than in the original sample. Peak 3 and 4 appear very similar in both samples. The side peak of peak 4 appears sharper in the warehoused samples than the original samples. Peak 5 is more prominent in the original samples than the warehoused samples while peak 6, 7, 8 and 9 are of similar intensity. The warehoused samples all show side peaks toward the high 2-theta angle (peak 6, 7, 8, 9). The clay XRD diffractograms show variation between peak 1, peak 8 and peak 9.

The images from the scanning electron microscope were obtained using two different techniques (BSE and SEM) which led to a number of difficulties when making fair

comparisons or inferences. With this in mind, it can be observed that the original samples, in general, show a clay matrix with visible porosity, angular silt-sized grains with iron framboids and mica present. This is consistent with the mineralogy observed in the warehoused samples although no mica was observed.

Discussion: The comparison of the original sample MICP curves to the MICP curves of the warehoused samples (Appendix D Figure D-44, D-45) show no clear trend; both the warehoused Pember Mudstone sample (917 m) and the sample from the warehoused Paaratte Formation (1264.95 m) show an MICP curve indicative of a sample that has a larger pore throat diameter network. However, the two samples from the warehoused Paaratte Formation (1262.95 m and 1268.80 m) clearly show MICP curves offset to higher pressure for the same mercury saturation indicative of samples with a smaller diameter pore throat network. The warehoused Pember Mudstone sample (917 m) and the warehoused Paaratte Formation sample (1264.95 m) both show a decreased threshold pressure while the two samples from the warehoused Paaratte Formation (1262.95 m and 1268.80 m) show an increased threshold pressure.

The conformance corrected porosity, bulk density and grain density results all show similar trends from the original samples to the warehoused samples. The porosity, bulk density and grain density all show a general decreasing trend with warehousing. The only exception is the bulk density result for the warehoused Paaratte Formation sample (1268.8 m) which increased from 2.26 g/ml to 2.28 g/ml. The decrease in porosity of the warehoused samples in comparison to the original samples increases with depth.

The mineralogical interpretation from the XRD analysis indicates that the samples from the warehoused Pember Mudstone and Paaratte Formation have minor changes to some peaks and their intensities while overall remaining similar. It can thus be suggested that minor changes in the mineralogy are present.

It is difficult to determine the effects of warehousing as opposed to the effects of sample heterogeneity from the MICP, XRD and SEM analysis due to the lack of consistent results from the MICP curves and the interpreted threshold pressures of the Pember Mudstone and Paaratte Formation. However, while still considering possible sample heterogeneity effects, there is a general trend of decreasing porosity, bulk density and grain density in the warehoused samples.

6.3.2.5 Original samples, Belfast Mudstone, CRC-1, Otway Basin

Methodology: The methodology modifications are consistent with the Pember and Paaratte Formation samples (Section 6.3.2.1).

Results: The uncorrected MICP curves for the Belfast Mudstone samples from 1.6m of conventional core from CRC-1 are similar to one another (Appendix D Figure D-46). The sample from 1900.70 m exhibits higher initial mercury saturation in comparison to the other samples. The other four MICP curves are similar to one another up until the maximum point of inflection at approximately 15 % mercury saturation, after which, the samples show some separation up until 100 % mercury saturation where they match. The MICP curves of all samples show a continuing upward trend to 100 % mercury saturation indicating that there is still porosity being filled up to the 60,000 psia mercury porosimeter pressure limit.

The conformance corrected MICP curves (Appendix D Figure D-47) show improved agreement with one another below 20 % mercury saturation after which they show similar separation to the uncorrected MICP curves. The IPV threshold pressures(Table 6-7) are all consistent at the same pressure equilibrium point (~6970 psia).The MI threshold pressures are ~6970 psia for three of the five samples with the remaining two samples interpreted at the pressure equilibrium point higher (~8500 psia).

The corrected porosities (Table 6-7) vary between 7.84 % and 10.57 % giving a maximum variation of 2.73 %. The samples at 1901.50 m and 1901.85 m have the lowest porosities (~8 %) while the samples above (1900.99 m and 1900.70 m) and the sample below (1902.25 m) have porosities of ~10 %. The sample volume per gram, grain volume per gram and pore volume per gram show some variation. The bulk density results show an increasing trend with depth until sample 1902.25 m where the bulk density once again decreases. The average grain density for the five samples is 2.65 g/ml and there is no obvious trend with depth.

Table 6-7: CRC-1 (2007) MICP results from original Belfast Mudstone samples (Re-interpreted from Daniel, 2007).

Sample Depth (m)	Sample Weight (g)	Porosity (%)		Bulk Density (g/ml)		Grain Density (g/ml)		Sample Volume (ml/g)		Pore Volume (ml/g)		Grain Volume (ml/g)		IPV Threshold Pressure (psia)		MI Threshold Pressure (psia)	
		Raw	Cor.	Raw	Cor.	Raw	Cor.	Raw	Cor.	Raw	Cor.	Raw	Cor.	Raw	Cor.	Raw	Cor.
1900.7	2.45	10.75	10.11	2.37	2.39	2.66	2.66	0.422	0.419	0.045	0.042	0.376	0.376	6966	6966	6966	6966
1900.99	2.29	10.74	10.57	2.40	2.40	2.69	2.69	0.417	0.416	0.045	0.044	0.372	0.372	6981	6981	6981	6981
1901.5	3.13	8.18	8.09	2.41	2.41	2.62	2.62	0.416	0.415	0.034	0.034	0.382	0.382	6972	6972	8500	8500
1901.85	3.10	7.97	7.84	2.46	2.47	2.68	2.68	0.406	0.406	0.032	0.032	0.374	0.374	6982	6982	8487	8487
1902.25	2.89	10.22	9.95	2.35	2.36	2.62	2.62	0.425	0.424	0.043	0.042	0.382	0.382	6969	6969	6969	6969
Average	2.77	9.57	9.31	2.40	2.40	2.65	2.65	0.417	0.416	0.040	0.039	0.377	0.377	6974.00	6974.00	7580.60	7580.60
SD	0.38	1.39	1.25	0.04	0.04	0.03	0.03	0.007	0.007	0.006	0.006	0.004	0.004	7.18	7.18	833.39	833.39

Mineralogy: The bulk XRD analysis of the five original Belfast Mudstone samples indicates that the samples are all similar except the sample at 1900.70 m which has a few minor peaks missing and a general decrease in intensity of the peaks (Appendix D Figure D-48). Peak 1 is similar in intensity and shape in sample 1901.50 m, 1901.85 m and 1902.25 m. The samples at shallower depth; 1900.70 m and 1900.99 m show diminished peak intensity. Peak 3 shows two peaks which merge at the base and show an increasing prominence with increasing sample depth. The side peak of peak 4 towards the lower 2-theta angle shows a similar pattern increasing in intensity with sample depth while peak 4 appears relatively constant except for sample 1900.70 m which appears to have the peak slightly offset, thinner and less intense. Peak 5 appears relatively constant but does seem to diminish in the 1900.70 m sample. Peak 6, 7, 8 and 9 appear to increase in intensity with sample depth. This is especially noticeable in sample 1900.70 m.

The clay XRD analysis of the five original Belfast Mudstone samples indicates that the samples are fairly uniform with minor differences in the intensity and shape of peaks (Appendix D Figure D-49). The intensity of the peaks for the sample at 1901.50 m appears on general to be less intense than the other four samples which is clearly observed in peak 1, 2, 5, 8 and 9. Peak 2 shows variation in shape between the samples with the sample at 1900.70 m having a thin peak as opposed to the broader peaks observed in the other samples. Peak 3 is consistent in shape and intensity for all samples. Peak 4 and 5 appear less intense in the samples from 1900.99 m and 1901.50 m. Peak 6 shows a similar intensity for all samples but is much broader in the samples from 1900.99 m, 1901.85 m and 1902.25 m. Peak 7 is generally consistent for all samples. Between peak 7 and 8 there is a clear intense peak for the sample at 1901.85 m. This can be observed in the sample at 1900.99 m and to a lesser extent 1901.50 m, 1900.99 m and 1902.25 m. Peak 8 is the least intense in the samples from 1900.99 m and 1901.50 m. Peak 9 is relatively consistent in shape and intensity between samples.

The original SEM images of the Belfast Mudstone (Appendix D Figure D-50 and D-54) show clay dominated samples with quartz, pyrite, glauconite and mica throughout. The SEM images of the Belfast Mudstone sample at 1900.70 m (Appendix D Figure D-50) shows a dominant clay fabric. The high magnification image shows microporosity and possible mica platelets. The SEM images of the Belfast Mudstone sample at 1900.99 m (Appendix D Figure D-51) are consistent with the sample at 1900.70 m with identified quartz and pyrite present. The Belfast Mudstone sample at 1901.50 m (Appendix D Figure D-52) has glauconitic pellets identified in the images and shows the dominant clay matrix. Quartz and

pyrite were also identified. The SEM images of the Belfast Mudstone sample at 1901.85 m (Appendix D Figure D-53) appears to show a greater dominance of clay matrix with identified microporosity under high magnification. The clay was identified as kaolinite/ illite/ smectite. The SEM image from 1902.25 m (Appendix D Figure D-54) is consistent with the samples at 1900.70 m, 1900.99 m and 1901.50 m showing a dominant clay matrix with quartz and pyrite grains scattered throughout the sample. Under high magnification, the microporosity can be observed within the clay matrix.

Discussion: The MICP curves, porosities, interpreted threshold pressures and mineralogies indicate that the five original samples are all similar over the 1.6 m interval of Belfast Mudstone from CRC-1. The variations in MICP curves are interpreted to be a result of minor heterogeneity over the 1.6 m interval. The variation is most pronounced over the 20 % to 90 % mercury saturation interval of the conformance corrected MICP curves indicating minor variation in pore throat diameters in the range of 0.0282μm and 0.0067 μm.

The variation in porosity from a minimum of 7.97 % to 10.75 % is a result of the combination of variation observed in both the sample volume per gram and the pore volume per gram. There is no relationship between sample volume per gram and pore volume per gram. The bulk density and grain density results reflect this variation.

There does appear to be a relationship between the threshold pressures interpreted with the MI method and the porosity; low porosities are found in combination with higher threshold pressures. This trend is not observed for the threshold pressures interpreted with the IPV method. Also, it is observed in the SEM images that the sample from 1901.85 m appear to have a higher dominance of clay than was observed in the other samples which may have contributed to the lower porosity and higher threshold pressures for this sample. However, the observed variation is not beyond the observed variation in the replication of samples along the 1.6 m interval of Saracen-1 Muderong Shale core or the variation observed between adjacent samples (Section 4.5.1). Thus, while there is likely minor heterogeneity between the samples, they are still considered fairly uniform.

6.3.2.6 Warehoused Samples, Belfast Mudstone, CRC-1, Otway Basin

Methodology modifications: The sample location for the warehoused sample of the Belfast Mudstone at a depth of 1902.25 m was taken 2 cm deeper due to a lack of sample. Please see section 6.3.2.1 for the XRD methodology. Both SEM images of broken samples and BSE images of polished samples were acquired for the warehoused samples.

Results: The MICP curves from the warehoused samples (Appendix D Figure D-55) are similar to one another. The MICP curves show slight separation below 20 % mercury saturation after which the MICP curves come into agreement for the linear upward trend with a slight tapering off towards 100 % mercury saturation.

The conformance corrected MICP curves (Appendix D Figure D-56) show improved agreement below 20 % mercury saturation and similar agreement to the uncorrected results thereafter. The interpreted IPV threshold pressures (Table 6-8) for all samples except sample 1900.70 m are at the same pressure equilibrium point (~6970 psia). The sample at 1900.70 m has an MICP curve similar to the other four samples but has an interpreted threshold pressure two equilibrium points higher (9959 psia). The MI threshold pressures are interpreted as ~6970 psia threshold pressure for the samples at 1900.99 m, 1901.50 m and 1902.27 m while the samples at 1900.70 m and 1901.85 m have their threshold pressures interpreted at the pressure equilibrium point above (~8490 psia).

The corrected porosities (Table 6-8) vary between 10.04 % and 7.19 % giving a maximum variation of 2.85 %. The samples at 1901.50 m and 1901.85 m have the lowest porosity (< 7.5 %) while the samples above and below have higher porosities (> 8 %). The sample volume per gram varies between 0.43 ml/g and 0.40 ml/g, while the pore volume per gram varies between 0.043 ml/g and 0.030 ml/g. The grain volume per gram for all samples is consistent (0.389 g/ml average). The bulk density is highest for samples at 1901.50 m and 1901.85 m (2.38 g/ml) while the other three samples from above and below have lower bulk densities. The grain density results are consistent between samples with an average of 2.57 g/ml.

Table 6-8: CRC-1 (2014) MICP results from warehoused Belfast Mudstone samples.

Sample Depth (m)	Sample Weight (g)	Porosity (%)		Bulk Density (g/ml)		Grain Density (g/ml)		Sample Volume (ml/g)		Pore Volume (ml/g)		Grain Volume (ml/g)		IPV Threshold Pressure (psia)		MI Threshold Pressure (psia)	
		Raw	Cor.	Raw	Cor.	Raw	Cor.	Raw	Cor.	Raw	Cor.	Raw	Cor.	Raw	Cor.	Raw	Cor.
1900.7	2.94	9.47	8.89	2.32	2.34	2.57	2.57	0.430	0.427	0.041	0.038	0.389	0.389	9959	9959	8499	8499
1900.99	2.46	10.22	10.04	2.31	2.31	2.57	2.57	0.433	0.432	0.044	0.043	0.389	0.389	6968	6968	6968	6968
1901.5	3.02	7.58	7.30	2.37	2.38	2.57	2.57	0.422	0.421	0.032	0.031	0.390	0.390	6969	6969	6969	6969
1901.85	2.66	7.49	7.19	2.37	2.38	2.56	2.56	0.422	0.420	0.032	0.030	0.390	0.390	6981	6981	8477	8477
1902.27	3.05	8.69	8.11	2.35	2.37	2.57	2.57	0.426	0.423	0.037	0.034	0.389	0.389	6979	6979	6979	6979
Average	2.83	8.69	8.31	2.35	2.36	2.57	2.57	0.426	0.425	0.037	0.035	0.389	0.389	7571.20	7571.20	7578.40	7578.40
SD	0.25	1.18	1.19	0.03	0.03	0.00	0.00	0.005	0.005	0.005	0.006	0.001	0.001	1334.83	1334.83	830.39	830.39

Mineralogy: The warehoused samples of Belfast Mudstone have similar bulk XRD diffraction patterns with slight variations in peak intensity (Appendix D Figure D-57). Peak 1 varies in intensity across the samples; both 1900.70 m and 1900.99 m show a low-intensity peak while the samples from 1901.50 m, 1901.85 m and 1902.27 m show a sharper peak with greater intensity. Peak 2 is similar across all samples with slightly diminished intensity for samples 1900.70 m and 1900.99 m. Peak 3 is consistent between samples. Peak 4 is also consistent in sharpness and intensity between samples. Notably, there is a peak at 2.808 angstrom in the samples from 1900.70 m and 1900.99 m that is not present or possibly only broadly present as a low-intensity hump in the samples from lower in the formation. Peak 5 is consistent in shape and intensity between all samples except sample 1900.70 m where it has a higher intensity. The broad peak 6 is consistent in shape and intensity across all samples. Peak 7 and its adjacent peak at higher 2-theta angle are consistent between all samples except 1900.70 m where the adjacent peak is higher intensity than the other samples. Peak 8 and 9 appear to slightly increase in intensity with depth from 1900.70 m through to 1902.27 m.

The clay XRD analysis of the five warehoused Belfast Mudstone samples indicates that the samples are fairly uniform with minor differences in peak intensity (Appendix D Figure D-58). The intensity of the peaks for the samples from 1901.50 m and 1902.27 m appear in general to be less intense than the other three samples which is clearly observed in peak 1, 4, 6, 7 and 9. Peak 1 appears more intense in sample 1900.70 m and 1900.99 m. Peak 2 is similar in shape among the samples with higher intensities observed in 1901.50 m and 1901.85 m. Peak 3 is consistent in shape and intensity between all samples. Peak 4 varies considerably between the five samples. The sample from 1900.99 m has the highest intensity and broadest peak followed by the sample at 1900.70 m, 1901.85 m, 1901.50 m and 1902.27 m. Peak 5 is minor in all samples but appears more prominently in the sample from 1900.70 m. Peak 6 follows a similar pattern to peak 4. Peak 7 shows a decreasing intensity with depth. Peak 8 is not detectable in the warehoused samples. Peak 9 is most prominent in 1900.99 m, 1900.70 m and 1901.85 m.

The SEM and BSE images of sample 1900.70 m show a clay matrix with interspersed silt-sized grains; generally potassium feldspar (Appendix D Figure D-59 and D-60). The clay matrix was identified as illite. A glauconite pellet can be observed in the SEM image Appendix D Figure D-59. Iron framboids were also identified in the BSE images (Appendix D Figure D-60) and microporosity within the clay matrix can be seen in the SEM and BSE images.

The SEM and BSE images of sample 1900.99 m show clay dominated samples with silt-sized grains of potassium feldspar present in high concentrations locally (Appendix D Figure D-61 and D-62). The clay matrix was identified as illite. A glauconite pellet and imprint can be observed in the SEM image. The BSE images (Appendix D Figure D-62) show iron framboids scattered throughout the samples. The higher magnification images have identifiable authigenic iron framboids.

The SEM images of sample 1901.50 m show a dominant clay fabric (Appendix D Figure D-63). On higher magnification, the microporosity within the illite clay matrix can be observed. The BSE image shows the dominant clay matrix with minor potassium feldspars, iron framboids and porosity or carbon. On higher magnification, quartz grains and anatase can be observed (Appendix D Figure D-64).

The SEM images of sample 1901.85 m show a dominant clay matrix with angular muscovite grains extruding the sample (Appendix D Figure D-65). The BSE image shows a similar dominant clay matrix with carbon or porosity dotted throughout the sample (Appendices Figure 7-66). A discontinuous microfracture can also be observed.

The SEM images of sample 1902.27 m show a similar dominant clay matrix although the clay is identified as smectite (Appendix D Figure D-67). Muscovite is also identified folded over in the top of the high magnification image. The BSE images show potassium feldspar, quartz and iron framboids dotted throughout the sample (Appendix D Figure D-68).

Discussion: The MICP curves, porosities, interpreted threshold pressures and mineralogies indicate that the five warehoused samples are all generally similar over the 1.6 m interval of Belfast Mudstone from CRC-1. The minor variations in MICP curves are interpreted to be a result of minor heterogeneity over the 1.6 m interval similar to the results from Saracen-1 (Section 4.5.1). The variation is most pronounced over the 20 % to 90 % mercury saturation interval of the conformance corrected MICP curves indicating minor variation in pore throat diameters in the range of 0.0282 μm and 0.0067 μm.

The IPV threshold pressures are similar to one another other than sample 1900.70 m which has the threshold pressure interpreted two pressure equilibrium points higher. The MI threshold pressures are all interpreted within one pressure equilibrium point of one another. This variation may be attributed to the minor differences in the mineralogy as identified in the bulk XRD diffractograms, SEM and BSE images. The four deeper samples all had bulk XRD diffractograms in excellent agreement with one another suggesting the mineralogy and concentrations of minerals were all very similar between the samples.

The variation in conformance corrected porosity from a minimum of 7.19 % to 10.04 % is primarily a result of the variation observed in the pore volume per gram which equates to ~30 % as opposed to the sample volume per gram variation which equates ~3 %. The bulk density shows slight variation while the grain density remains similar among samples which are consistent with the poor agreement in pore volume per gram results. The variation (excluding the IPV threshold pressure for sample 1900.70 m) in threshold pressures and porosity is not greater than the variation observed in samples along the 1.6m interval of Saracen-1 or between adjacent samples of Saracen-1 (Section 4.5.1) indicating that the samples can be considered fairly uniform. There are no strong relationships observed with any of the measured parameters and depth. Sample 1900.70 m appears to show more heterogeneity than the other samples.

6.3.2.7 Maximum CO_2 Column Height Retentions

The Belfast Mudstone original and warehoused samples have almost uniform calculated maximum CO_2 column heights other than for the warehoused sample at 1900.70 m depth (Figure 6-6). The samples excluding 1900.70 m have calculated CO_2 column heights between ~788 m and ~395 m for 0 ° and 60 ° contact angles respectively. The warehoused sample from a depth of 1900.70 m has a calculated maximum CO_2 column height of between 1127 m and 563 m for 0 ° and 60 ° contact angles respectively.

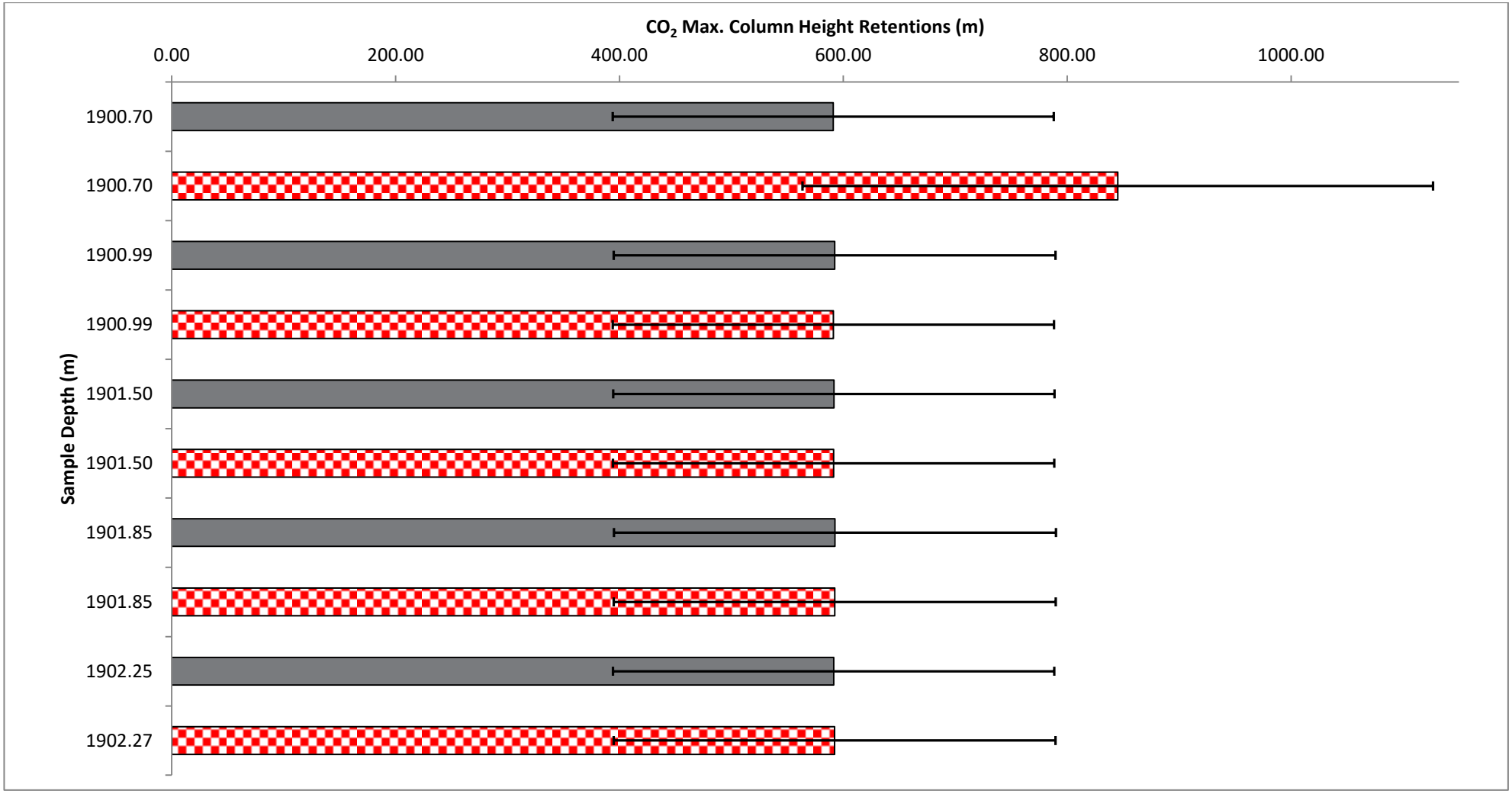

Figure 6-6: Maximum CO_2 column height retentions calculated for the 2007 original samples (grey) and the 2014 warehoused conventional core samples (red checks). The error bars represent the range of contact angle (brine /CO_2/ rock) from 0 ° (right) and 60 ° (left).

6.3.2.8 Comparison of MICP analysis of the original and warehoused samples from the Belfast Mudstone, CRC-1

The uncorrected MICP curves of the original and warehoused samples are displayed in Appendix D Figure D-69. There is slight variation in MICP curves for both the original samples and warehoused samples, however, the MICP curves of the warehoused samples match and fit between the variations of the MICP curves of the original samples. The conformance correction improves agreement between all the MICP curves (Appendix D Figure D-70). There is no discernible difference between the MICP curves of the original samples and the warehoused samples other than the warehoused samples show less variation between one another. With the exception of the warehoused sample from 1900.7 m depth, there is no difference in the interpreted threshold pressures.

The conformance corrected porosity from Table 6-7 and 6-8 show a decreasing trend and average from the original samples to the warehoused samples; 9.31 % average porosity for the original samples which reduced to 8.31 % average porosity for warehoused samples. This represents a decrease of 1 % in the average porosity of the samples. The average bulk density and grain density both decrease with warehousing from 2.40 g/ml and 2.65 g/ml respectively for the original samples to 2.36 g/ml and 2.57 g/ml respectively for the warehoused samples. These results indicate that the grain density was affected to a greater extent than the bulk density. However, this variation is not greater than that observed between samples along the 1.6 m interval of Saracen-1 or between the adjacent samples (Section 4.5.1).

The XRD analysis of both the original and the warehoused samples are remarkably similar to one another. The key differences observed include a decrease in the intensity of the adjacent peak to peak 3 at higher 2-theta angle, a decrease in intensity of the minor peak between peak 3 and 4 (3.577 angstrom in the original samples) and a clear change in the side peak at low 2-theta angle side of peak 4 and a broadening with decreased intensity of peak 5 of the warehoused samples.

Discussion: The comparison of MICP curves of the original samples to the adjacent warehoused sample suggests that warehousing has had no effect on the MICP curves of the Belfast Mudstone. This indicates that the pore throat network diameter remains the same for both the original and warehoused samples. The MICP curves of the warehoused samples show less variation between one another than the original samples. The interpreted IPV threshold pressures other than the warehoused sample from 1900.70 m show no variation

between one another. The threshold pressures interpreted with the MI method show a maximum of one pressure equilibrium point variation between one another within a sample group and show a maximum of one pressure equilibrium point variation increase and decrease between the original and warehoused samples.

The average porosity of the Belfast Mudstone warehoused samples suggest that the warehousing does affect the porosity; in this case decreasing the porosity by an average of 1 %. Further, the warehousing results show an increased maximum variation in porosity from 2.73 % in the original samples to 2.85 % in the warehoused samples indicating that not all samples are affected equally by the warehousing.

The sample volume per gram of the warehoused samples has increased on average by 2.1 % suggesting that one or both of two variables has changed; weight or sample volume. Theoretically, the weight loss could be explained by the loss of interstitial water and the loss of water from the clays above and beyond what would have been lost from the 48 hours of oven drying at ~55 ° C. Equally likely, the Belfast Mudstone samples could have expanded as a result of being removed from their insitu pressure conditions. The clay matrix with interspersed grains would have allowed this to occur. It is unlikely to have led to fractures due to the relatively small change (1.1 %).

The pore volume per gram of the warehoused samples has decreased on average by 10 %. However, the MICP curves of the warehoused samples remain consistent with the original samples suggesting that there is no change in the pore throat diameter network. In conjunction, there has been a decrease in weight and/ or an increase in sample volume per gram of the warehoused samples. The change in weight is not expected to have affected the pore volume per gram measurements however if there was an increase in volume due to expansion then theoretically this should have increased the pore volume per gram marginally. Thus, the decrease in the pore volume per gram of the warehoused samples theoretically can have occurred for two reasons; a decrease in pore body size but no effect on the pore throat or a blocking of pore throats and the associated pore body. These results (sample volume per gram and pore volume per gram) are also reflected in the bulk density and related grain density measurements where there is a slight decrease in bulk density and a greater decrease in grain density.

6.3.3 **Gorgon CO2 Data Well-1 & Data Well-1ST1, Barrow Island**

The effect of warehousing on seal capacity results from Gorgon CO2 Data Well-1& Data Well-1ST1 core is investigated. The report by Daniel and Kaldi, (2006) on the original samples on which numerous MICP analyses were performed to evaluate the sealing potential for CO_2 storage is compared to analyses of adjacent warehoused samples analysed by this study (2015).

6.3.3.1 Original samples, Gorgon CO2 Data Well-1& Data Well-1ST1, Barrow Sub-basin

Please see section 3.5.3 for Gorgon CO2 Data Well-1 & Data Well-1ST1 well description. The original conventional core samples were selected and supplied to Dr. Ric Daniel at the Australian School of Petroleum for MICP analysis and seal capacity determination. The samples were also analysed with XRD and SEM. The core samples were taken as ~~"~~discs" removing an entire section of core approximately 10 cm in height. This sample was then wrapped in aluminum foil, coated with wax and sent to Adelaide from the well site at Barrow Island. A total of twenty-one samples were taken and analysed with MICP, XRD and SEM and reported in Daniel and Kaldi, (2006). The Basal Barrow Group was sampled at 2011 m and 2023.82 m and the Upper Dupuy Formation was sampled at 2101.57 m, 2164.23 m and 2179.68 m. The results have subsequently been re-interpreted in the same manner as the warehoused samples to compare and infer the effects of warehousing from the analytical results.

Methodology modifications: The original samples were taken as 10 cm disc intervals of the conventional core which meant that the exact location from which the sample was taken for MICP analysis is not precisely known but is approximately correct. The methodology for the characterisation of the mineralogy has undergone a number of changes. Firstly, the imaging of the original samples from 2006 was acquired using a broken rock sample under the SEM. No BSE imaging of polished rock sections was acquired. Secondly, the XRD interpretation is achieved by comparing the diffractograms and their peak positions and intensities, which reflect the mineralogies present. No mineralogy was interpreted due to the nature and variability of interpretation and due to the differences in methodologies and equipment used to undertake the XRD analysis (cobalt source vs. copper). The CO_2 maximum column height retentions were calculated with the brine salinities recorded in Daniel and Kaldi, (2006) for the formations.

Results: The uncorrected MICP curves from Gorgon CO2 Data -1 well & Data Well-1ST1 (Appendix D Figure D-71) original samples show significant variation between one another. The samples from 2164.23 m and 2179.68 m depth have much higher initial mercury

saturation than the other three samples taken at shallower depths and have MICP curves with similar shape and position on the graph but offset from one another.

The conformance corrected MICP curves show better agreement with one another (Appendix D Figure D-72). The sample from a depth of 2023.82 m shows a similar initial MICP curve up to 20 % mercury saturation after which it progresses in a much steeper vertical direction than the samples from 2011 m and 2164.23 m. The 2179.68 m sample has an MICP curve pattern similar to the 2011 m and 2164.23 m sample except offset to a higher pressure. Towards ~50,000 psia the MICP curve of 2179.68 m sample matches with these two samples. The MICP curve for sample 2101.57 m is offset to a lower pressure for equivalent mercury saturation to the other samples. It also shows a distinct tapering towards the pressure limits (60,000 psia) of the mercury porosimeter indicating, unlike the other samples that the available pore space is becoming limited. The interpreted threshold pressures for the samples show a similar pattern to the position of the MICP curves for the different samples. The samples with similar MICP curves (2011 m and 2164.23 m) have the same interpreted threshold pressure (~9970 psia) while the sample from (2023.82 m) with a steeper inclined MICP curve has a lower interpreted threshold pressure (6985 psia) (Table 6-9). The sample from a depth of 2179.68 m has the highest interpreted threshold pressure of 10014 psia and the highest pressure to mercury saturation ratio. The sample from 2101.57 m has the lowest threshold pressure of 2940 psia.

The conformance corrected porosities (Table 6-9) show considerable variation to one another. The porosities vary between 9.87 % for the sample at a depth of 2101.57 m to 2.28 % for the sample at 2164.23 m. The conformance corrected sample volume per gram, grain volume per gram and pore volume per gram vary significantly. The corrected bulk densities vary significantly between samples with no relationship to sampling depth (2.02 g/ml to 2.57 g/ml). The grain density follows a similar pattern varying between 2.24 g/ml and 2.67 g/ml.

Table 6-9: Gorgon CO2 Data Well-1 & Data Well-1ST1 MICP (2006) results from original samples of Barrow Group and Dupuy Formation (Re-interpreted from Daniel and Kaldi, 2006).

Sample Depth (m)	Sample Weight (g)	Porosity (%)		Bulk Density (g/ml)		Grain Density (g/ml)		Sample Volume (ml/g)		Pore Volume (ml/g)		Grain Volume (ml/g)		IPV Threshold Pressure (psia)		MI Threshold Pressure (psia)	
		Raw	Cor.	Raw	Cor.	Raw	Cor.	Raw	Cor.	Raw	Cor.	Raw	Cor.	Raw	Cor.	Raw	Cor.
2011	4.07	8.25	4.89	2.19	2.27	2.39	2.39	0.456	0.440	0.038	0.022	0.418	0.418	9967	9967	12053	8503
2023.83	4.41	9.00	8.27	2.38	2.40	2.62	2.61	0.419	0.417	0.037	0.035	0.383	0.383	6985	6985	6985	6985
2101.57	4.71	10.05	9.87	2.02	2.02	2.25	2.24	0.451	0.495	0.049	0.049	0.446	0.446	2940	2940	2491	3534
2164.23	3.25	2.94	2.28	2.52	2.54	2.60	2.62	0.396	0.394	0.012	0.009	0.385	0.385	9970	9970	9970	6979
2179.68	5.35	4.22	3.39	2.56	2.57	2.67	2.67	0.391	0.389	0.015	0.015	0.376	0.376	10014	10014	11955	11955
Average	4.36	6.89	5.74	2.34	2.36	2.51	2.51	0.423	0.427	0.030	0.026	0.401	0.401	7975.20	7975.20	8690.80	7591.20
SD	0.78	3.12	3.23	0.23	0.22	0.18	0.18	0.030	0.043	0.016	0.016	0.030	0.030	3099.88	3099.88	4029.36	3044.56

Mineralogy: The bulk XRD analysis of the original samples suggests that there are significant differences in both the mineralogy and concentration of the minerals identified in the samples (Appendix D Figure D-73). This analysis was carried out by Daniel and Kaldi, (2006). Peak 1 is minor in all samples but most pronounced in sample 2164.23 m. Peak 2 shows considerable variation in shape and intensity between the samples. The sample from 2011 m has a sharp peak with the highest intensity while the samples from 2023.82 m and 2101.57 m have a diminished broader peak. The sample from 2164.23 m has a similar intensity to the sample from 2011 m but a much broader shape while the sample from 2179.68 m is of moderate intensity and quite sharp. Peak 3 has a similar shape for all samples but varies in intensity. The samples from 2011 m and 2023.82 m have moderate to low intensity peaks in conjunction with a broad shape adjacent peak on the lower 2-theta angle side. The sample from 2101.57 m has the highest peak 3 of all samples with a minor adjacent peak at the higher 2-theta angle. The peak 3 intensity and shape is very similar for the samples at 2164.23 m and 2179.63 m. Peak 4 has a similar shape and intensity for all samples. Peak 5 is observed in the sample from 2011 m with low intensity. This peak is not identified in the sample from 2023.82 m. The sample from 2101.57 m has a broad peak while the sample from 2164.23 m has a high-intensity peak relative to the other samples. The sample from 2179.68 m has a moderate to low intensity peak. Peak 6 has the highest intensity in sample 2101.57 m and 2179.68 m while the other three samples are similarly less intense. Peak 7 shows a similar pattern to peak 6. Peak 8 has a similar shape for all samples although varies in intensity between the sample at 2101.57 m which has the highest intensity and the sample at 2179.68 m which has the lowest intensity. Peak 9 is a minor peak which is most prominent in the sample 2101.57 m.

The clay XRD diffractograms of the five samples show significant differences between one another (Appendix D Figure D-74). This analysis was carried out by Daniel and Kaldi, (2006). Peak 1 is similar in shape and intensity for samples 2011 m, 2023.82 m and 2179.68 m. The sample at 2101.57 m shows a higher intensity for peak 1 while the sample at 2164.23 m does not have a peak present at that 2-theta angle. Peak 2 has a broad and intense shape for samples 2023.82 m and 2101.57 m while the samples from 2011 m, 2164.23 m and 2179.68 m have a peak which is much sharper and less intense. Peak 3 is similar in shape and intensity for samples at 2011 m and 2023.82 m. The sample 2101.57m has a high intensity peak 3 while the sample below at 2164.23 m has the least intensive peak. Peak 3 for the sample at 2179.63 m is more intense that the samples at 2011 m and 2023.82 m but less intense than the sample at 2101.57 m. Peak 4 is similar in shape and intensity for the samples at 2023.82 m and 2101.57 m. The sample at 2011m has the least intense peak 4.

The sample at 2164.23 m has the most intense peak but shows a distinctly different shape to the other samples. Peak 4 for sample 2179.68 m is slightly more intense than the sample at 2011 m. Peak 5 shows the same pattern as peak 3 with more variation in the shape/ broadness of the peak between samples. Peak 6 shows considerable variation between samples. The samples at 2023.82 m and 2101.57 m are the most intense followed by the sample at 2179.68 m, 2011 m and 2164.23 m.

The SEM images of the 2011 m sample indicate a dominant clay matrix with microporosity (Appendix D Figure D-75). The sample at 2023.82 m shows a clay matrix of different morphology that is identified as smectite/ kaolinite in the high-resolution image (Appendix D Figure D-76). The sample below at 2101.57 m shows a clay matrix with quartz grains interspersed (Appendix D Figure D-77). On higher magnification, illite clays can be identified. The sample at 2164.23 m again shows a different clay morphology that is identified as smectite-illite with interspersed quartz grains (Appendix D Figure D-78). The sample at 2179.68 m appears more consolidated than the previous samples and again shows a differing clay morphology that is identified at smectite-illite (Appendix D Figure D-79). Quartz grains were also identified dotted throughout the sample (Daniel and Kaldi, 2006).

Discussion: The MICP analysis, XRD analysis and SEM imaging suggest that the samples are significantly different from one another. This is to be expected as the samples were from 168m interval covering two distinct formations representing different depositional environments.

6.3.3.2 Warehoused Samples, Gorgon CO2 Data Well-1& Data Well-1ST1, Barrow Sub-basin– Introduction

The Gorgon CO2 Data Well-1 & Data Well-1ST1 conventional core was slabbed on return from the well site to Perth. 2/ 3rd of the core was stored at the Core Laboratories in Perth while the remaining 1/3rd was kept by the Western Australian Department of Mines and Petroleum in Perth. The samples were stored in an open air warehouse with no climate control (pers.comm. Justin Tomlinson, 2015).

Methodology: The sampling of original 10 cm interval discs of the conventional core has meant that the exact location from which the sample was taken for MICP analysis is not precisely known. Subsequently, the warehoused samples were taken from the disc if it was remaining or above or below that interval. Thus there may be a variation of a maximum of ~ 10 cm in the vertical direction of the adjacent sample. Five warehoused samples were taken

from the slabbed 2/ 3rd conventional core adjacent to the original samples in the seals report by Daniel and Kaldi, (2006).

Results: The MICP curves of the warehoused samples analysed in 2015 show considerable disparity between one another and reflect different pore throat networks of the samples (Appendix D Figure D-80). The conformance corrected MICP curves (Appendix D Figure D-81) indicate that the samples from a depth of 2164.23 m and 2010.90 m are similar in position on the graph and have a similar shape. These samples have the highest pressure to mercury saturation ratio. The samples from 2101.57 m and 2179.68 m also have MICP curves in a similar position on the graph and a somewhat similar MICP curve shape. These two MICP curves have the lowest pressure to mercury saturation ratio. The sample from 2023.82 m depth has an MICP curve between these two groups of similar samples. The MICP curve shape is most similar to the samples at 2164.23 m and 2010.90 m.

The conformance corrected porosities (Table 6-10) vary significantly between 14.45 % and 2.37 % for samples 2101.57m and 2010.9m respectively. The sample volume per gram and pore volume per gram also vary significantly in a reverse trend to the porosity. The grain volume per gram shows minor variation between 0.375 ml/g and 0.388 ml/g for samples 2101.57m and 2179.68m respectively. The bulk density shows significant variation (0.32 g/ml) while the grain density has minor variation only (0.08 g/ml).

Table 6-10: Gorgon CO2 Data Well-1 & Data Well-1ST1 (2015) MICP results from warehoused samples of the Barrow Group and Dupuy Formation.

Sample Depth (m)	Sample Weight (g)	Porosity (%)		Bulk Density (g/ml)		Grain Density (g/ml)		Sample Volume (ml/g)		Pore Volume (ml/g)		Grain Volume (ml/g)		IPV Threshold Pressure (psia)		MI Threshold Pressure (psia)	
		Raw	Cor.	Raw	Cor.	Raw	Cor.	Raw	Cor.	Raw	Cor.	Raw	Cor.	Raw	Cor.	Raw	Cor.
2010.9	2.74	2.77	2.37	2.54	2.54	2.61	2.61	0.394	0.393	0.010	0.009	0.384	0.384	9952	9952	9952	11954
2023.83	2.88	8.69	8.12	2.41	2.42	2.63	2.63	0.416	0.414	0.036	0.034	0.380	0.380	6972	6972	6972	6972
2101.57	2.58	16.71	14.45	2.22	2.28	2.66	2.66	0.451	0.439	0.076	0.063	0.375	0.375	2913	2913	2913	2459
2164.23	3.10	3.75	3.15	2.50	2.52	2.60	2.60	0.399	0.397	0.015	0.013	0.384	0.384	11953	11953	11953	11953
2179.68	2.50	11.77	11.02	2.28	2.30	2.58	2.58	0.439	0.436	0.052	0.048	0.388	0.388	2935	2935	2935	2935
Average	2.76	8.74	7.82	2.39	2.41	2.62	2.62	0.420	0.416	0.038	0.033	0.382	0.382	6945.00	6945.00	6945.00	7254.60
SD	0.24	5.77	5.14	0.14	0.12	0.03	0.03	0.025	0.021	0.027	0.023	0.005	0.005	4076.15	4076.15	4076.15	4634.00

Mineralogy: The bulk XRD diffractograms for the five samples show numerous differences in peak shape and intensity along with a number of minor peaks presences and absences (Appendix D Figure D-82). Peak 1 shows a distinct shape and intensity for each of the five samples; the sample at 2010.9 m has a low-intensity sharp peak 1 while the sample from 2023.82 m has a higher intensity broad peak 1. Peak 1 has the highest intensity for the sample at 2101.57 m followed by the sample at 2164.23 m and 2179.68 m. Peak 2 is similar in shape and intensity for the samples from 2101.57 m, 2164.23 m and 2179.68 m where it has a slightly higher intensity. The peak 2 in samples from 2010.9 m and 2023.82 m show diminished intensity in comparison to the other samples. The side peak of peak 3 at a low 2-theta angle is similar in shape and intensity for the samples at 2010.9 m, 2023.82 m and 2164.23 m. The sample at 2101.57 m has a low-intensity side peak to peak 3 at a low 2-theta angle while this side peak is barely detectable for the sample at 2179.63 m. Peak 3 appears similar in shape and intensity between the samples. Peak 5 is similar in shape but varies in intensity; highest for the sample at 2101.57 m followed by 2179.63 m, 2164.23 m, 2010.9 m and 2023.82 m. Minor side peaks to peak 5 at a high 2-theta angle are observed in the samples from 2010.9 m and 2101.57 m. Between peak 5 and peak 6 both samples at 2010.9 m and 2164.23 m show a peak at 2.708 angstrom that is not observed in the other samples. A broad peak is also observed between 2.2708 angstrom and 2.457 angstrom for the samples at 2010.9 m, 2023.82 m and 2164.23 m. Peak 6 has a similar shape between samples but varies in intensity; highest for the sample at 2179.63 m followed by 2101.57 m, 2164.23 m, 2023.82 m and 2010.9 m. A side peak to peak 6 at a high 2-theta angle can be observed for the samples at 2010.9 m, and 2164.23 m. Peak 7, 8 and 9 have a similar pattern to peak 6.

The clay XRD diffractograms show considerable differences between peak shapes and their intensities for the five samples (Appendix D Figure D-83). Peak 1 is generally uniform for all five samples with minor variation in intensity. Peak 2 shows much more variation between the five samples. The samples from 2010.90 m and 2179.68 m both show a skewed peak towards low 2-theta angle. The peak 2 for sample 2164.23 m shows a broader shape with a flat top in comparison to the other samples. The intensity is highest for the sample at 2023.82 m and lowest for the sample at 2101.57 m. Peak 3 is similar in shape and position but varies in intensity from the highest for sample 2179.68 m followed by 2164.23 m, 2101.57 m, 2010.90 m and 2023.82 m. Between peak 3 and peak 4 there are 2 minor peaks that vary in shape and intensity between the samples. Peak 5 shows similar variation to peak 3. Peak 6 varies in intensity; the highest intensity is for sample 2179.63 m followed by 2023.82 m, 2010.90 m, 2164.23 m and 2101.57 m. The sample from 2101.57 m also has a distinctive peak after peak 6 at a higher 2-theta angle that is not present in the other samples.

The SEM images of the sample from 2010.90 m indicate a dominant clay matrix with interspersed angular silt-sized quartz grains and imprints of glauconite pellets visible (Appendix D Figure D-84). The BSE image illustrates a mixture of potassium feldspar grains and quartz grains often in direct contact with one another. The clay matrix is littered with iron framboids and microporosity/ carbon. It can also be observed that there are discontinuous fractures trending along grain edges within the sample (Appendix D Figure D-85).

The SEM images of the sample at 2023.82 m show a clay matrix with interspersed angular silt-sized quartz grains (Appendix D Figure D-86). The silt-sized grains appear randomly orientated within the sample. The BSE images show quartz and glauconite grains providing the rock structure with cemented primary porosity. The cement contains iron framboids. Secondary porosity appears to have formed within the cemented primary porosity (Appendix D Figure D-87).

The SEM images of the sample at 2101.57 m show a dominant clay matrix with sparsely interspersed silt-sized grains (Appendix D Figure D-88). The BSE images show silt-sized grains including quartz and potassium feldspar forming the framework of the rock. Zones of high porosity/ carbon can be observed throughout the sample. The clay matrix is observed to fold or mould to the grain framework which is a likely result of compaction (Appendix D Figure D-89).

The SEM images of the sample at 2164.23 m indicate distinctly different clay morphology to the other samples. Silt-sized grains can be observed throughout the clay matrix (Appendix D Figure D-90). The BSE image illustrates silts sized grains in contact with one another with zones of high porosity surrounding primarily the quartz grains suggesting dissolution of the matrix. Fractures can also be observed traversing the samples (Appendix D Figure D-91).

The SEM images of the sample at 2179.68 m (Appendix D Figure D-92) show an undulating clay matrix with interspersed silt-sized grains. Under high magnification, illite clay quartz overgrowths can be observed. The BSE images show dominant quartz grains interspersed by clay matrix. The matrix appears to have undergone localised areas of diagenesis eroding the matrix and leaving angular fine grains behind. Localised precipitation of matrix also appears to have occurred (Appendix D Figure D-93).

Discussion: The MICP analysis, XRD analysis and SEM/ BSE imaging suggest that the samples are distinctly different from one another. This is to be expected as the samples were from a 168 m interval covering two distinct formations representing different depositional environments.

6.3.3.3 Maximum CO_2 column Height Retentions

The maximum CO_2 column heights for the warehoused samples are rather similar to the original samples except for the sample at 2179.68 m which shows considerable disparity (Figure 7-7). The maximum CO_2 column heights for the samples vary between a maximum of 1347 m and an average of 168 m for the sampling intervals tested. The variation in contact angle between 0 ° and 60 ° results in a maximum change in column height of 674 m which is approximately half of the maximum calculated CO_2 column height.

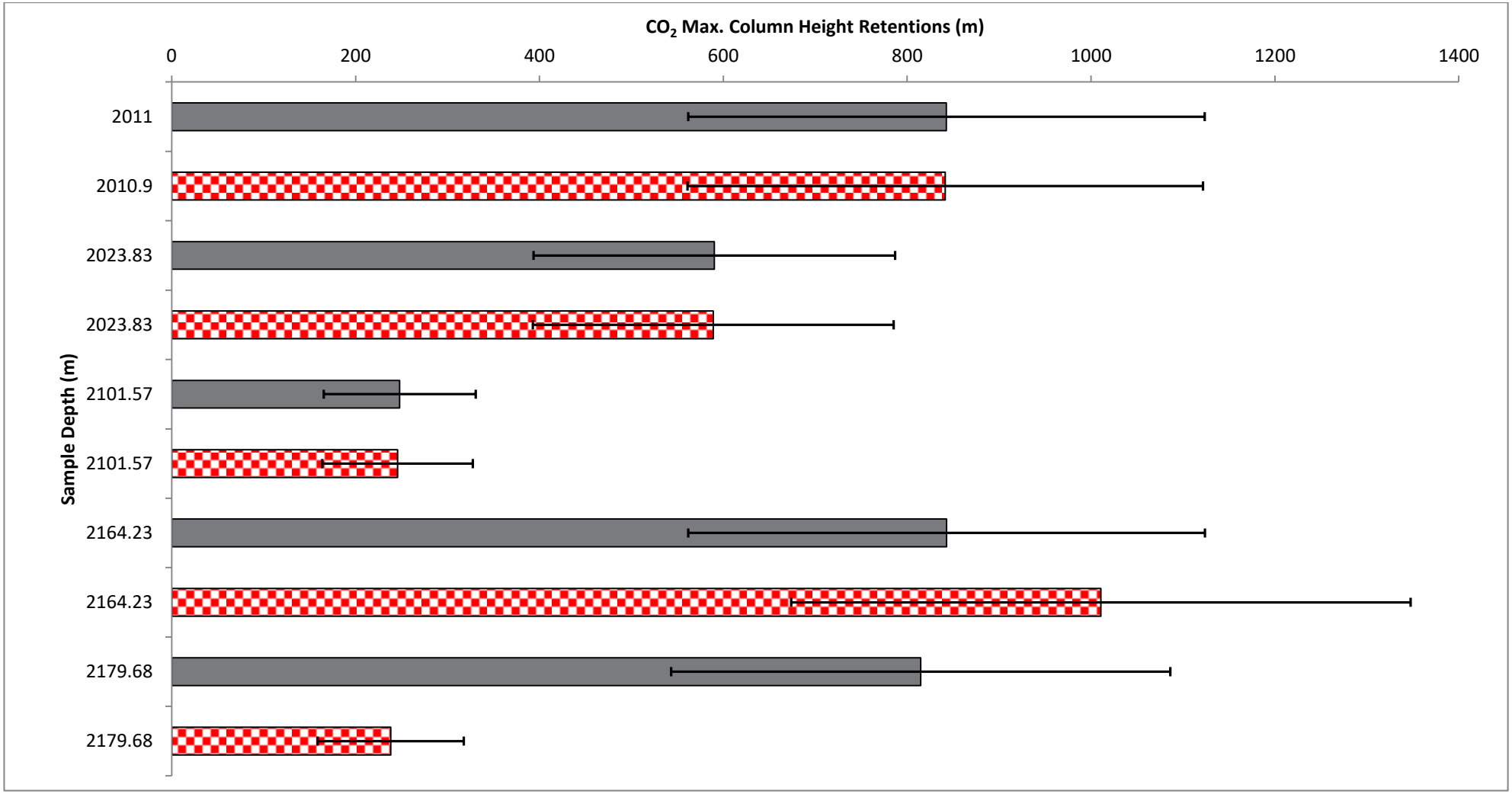

Figure 6-7: Maximum CO_2 column height retentions calculated for the original samples (grey) and the warehoused conventional core samples (red checks) of the Barrow Group and the Dupuy Formation. The error bars represent the range of contact angle (brine/ CO_2 / rock) from 0 ° (right) and 60 ° (left).

6.3.3.4 *Comparison of MICP analysis from the original 2006 and warehoused 2015 samples of the Barrow Group and Dupuy Formation, Gorgon CO2 Data Well-1 & Data Well-1ST1*

The comparison of MICP curves (Appendix D Figure D-94) indicates that the original samples and the warehoused samples have no consistent relationships or trends to one another. The MICP curves of the warehoused samples show a shift to higher pressure and lower pressure for the same mercury saturation in comparison to the original samples (i.e. samples 2164.23 m and 2101.57 m). The conformance correction of the MICP curves still shows considerable disparity for all samples except that from 2023.82 m (Appendix D Figure D-95). The following is a description of the two extremes in relationships between the original and warehoused MICP curves. The 2023.82 m samples show an excellent agreement with one another; both MICP curves show a similar shape and position on the graph often matching with one another. The 2179.68 m samples show disparity in the position of the MICP curve on the graph and the shape suggesting that original sample has a much higher ratio of pressure to mercury saturation in comparison to the warehoused sample and a different pore throat diameter network. The conformance corrected MICP curves show improved agreement between the original and warehoused samples except in the case of the sample from 2179.68 m which shows similar disagreement. The original and warehoused samples from 2010.90 m, 2101.57 m and 2164.23 m show variation between that observed for the samples 2023.82 m and 2179.68 m.

The interpreted IPV threshold pressures from both the original and warehoused samples for the following depths were all interpreted to be at the same pressure equilibrium point; ~2011 m, 2023.82 m and 2101.57 m. The warehoused sample from 2164.23 m has an interpreted IPV threshold pressure (11953 psia) one pressure equilibrium point higher than the original sample (9970 psia). The warehoused sample from 2179.68 m has a large discrepancy between the interpreted IPV threshold pressure for the original sample (10014 psia) and the warehoused sample (2935pisa) equating to seven pressure equilibrium points difference between samples.

The MI threshold pressures show more disparity than the IPV threshold pressures. The sample from 2023.82 m is the only sample where the MI threshold pressure is interpreted at the same pressure equilibrium point for the original and warehoused samples. The samples at ~2011 m and 2101.57 m show a disparity of two pressure equilibrium points in the MI threshold pressures for the original and warehoused samples. The samples at 2164.23 m show a disparity of three pressure equilibrium points between the original and warehoused

samples. A variation of seven pressure equilibrium points is observed between the MI threshold pressures of the original and warehoused samples from 2179.68 m.

The threshold pressures using both techniques (IPV and MI methods) show no common trend with agreement to considerable disparity observed between original and warehoused samples. Further, the disparity between the threshold pressures and the sample type shows no common change; warehoused samples can have a higher or lower interpreted threshold pressure than the corresponding original sample.

The conformance corrected porosity (Table 6-9 and 6-10) for the original and the warehoused samples show no clear pattern. The ~2011 m and 2023.82 m samples both show a decrease in porosity with warehousing. However, the samples from 2101.57 m, 2164.23 m and 2179.68 m show the opposite trend with porosity increasing after warehousing. The bulk density increased for the following warehouse samples; 2011 m, 2023.82 m and 2101.57 m and decreased for 2164.23 m and 2179.68 m. The grain density of the warehoused samples followed the same trend with the grain density increasing for 2011 m, 2023.82 m and 2101.57 m samples and decreasing for 2164.23 m and 2179.68 m samples.

The XRD bulk mineralogical analyses of the original sample (Appendix D Figure D-73) from 2011 m and the warehoused sample (Appendix D Figure D-82) from 2010.90 m show a number of key differences; Peak 2 shows diminished intensity in the warehoused sample. Peak 3 shows increased intensity. The peak between peak 3 and 4 for the original sample is not observed in the warehouse sample. Peak 5 in the original sample has a number of adjacent peaks at a higher 2-theta angle that is not observed in the warehoused sample. Peak 6, 7, 8 and 9 are more pronounced in the warehoused samples. The clay XRD mineralogical analyses indicate a much more prominent peak 2 in the warehoused sample (Appendix D Figure D-83) in comparison to the original sample (Appendix D Figure D-74). Peak 5 and 6 also appear slightly diminished in the warehoused samples.

The XRD bulk mineralogical analyses of the original sample (Appendix D Figure D-73) and the warehoused sample (Appendix D Figure D-82) from 2023.82 m show a number of crucial differences; Peak 1 is more intense in the warehoused samples. Peak 5 is prominent in the warehoused sample. Peak 6 and 7 are more intense in the warehoused sample. However, peak 8 appears similar in both samples and peak 9 appears diminished in the warehoused sample. The clay XRD mineralogical analyses indicate a more intense peak 1 in the original sample and a less prominent peak 2 (Appendix D Figure D-83) in comparison to

the warehoused sample (Appendix D Figure D-74). Peak 3, 4, 5 and 6 also appear significantly diminished in the warehoused sample.

The XRD bulk mineralogical analyses of the original sample (Appendix D Figure D-73) and the warehoused sample (Appendix D Figure D-82) from 2101.57 m show key differences; Peak 1 appears more intense in the warehoused sample. Peak 6, 7, 8 and 9 appear higher in intensity in the warehoused sample than in the original sample. The clay XRD mineralogical analyses indicate significantly more intensive peaks in the original sample (Appendix D Figure D-74) in comparison to the warehoused sample (Appendix D Figure D-83).

The XRD bulk mineralogical analyses of the original sample (Appendix D Figure D-73) and the warehoused sample (Appendix D Figure D-82) from 2164.23 m show a number of differences; Peak 2 appears more intense in the original sample than in the warehoused sample. The adjacent peak to peak 3 at a lower 2-theta angle is present in the warehoused sample but not in the original sample. Peak 5 is much more prominent in the original sample than in the warehoused sample. Peak 6, 7, 8 and 9 appear higher in intensity in the warehoused sample than in the original sample. The clay XRD mineralogical analyses indicate a less intense peak 1 in the original sample and a less prominent peak 2 (Appendix D Figure D-74) in comparison to the warehoused samples (Appendix D Figure D-83). Peak 4 which is observed in the original sample is not observed in the warehoused sample. Peak 5 and 6 show a different shape and slightly different intensities in the warehoused sample in comparison to the original sample.

The XRD bulk mineralogical analyses of the original sample (Appendix D Figure D-73) and the warehoused sample (Appendix D Figure D-82) from 2179.68 m show numerous differences; peak 2 and peak 3 appear more intense in the warehoused sample. Peak 6, 7, 8 and 9 are much more intense in the warehoused sample than in the original sample. The clay XRD mineralogical analyses indicate a broader peak 2 in the warehoused sample and a less prominent peak 3 (Appendix D Figure D-83) in comparison to the original sample (Appendix D Figure D-74). Peak 4 which is observed in the original samples is not observed in the warehoused sample. Peak 5 and 6 show a different shape and slightly different intensities in the warehoused samples in comparison to the original samples. Peak 4, 5 and 6 appear similar.

The SEM images of the original sample at 2011 m (Appendix D Figure D-75) and the warehoused sample at 2010.90 m (Appendix D Figure D-84) appear to have a different clay

morphology. The warehoused sample also appears to have angular silt-sized grains present that are not observed in the original sample.

The SEM images of the original sample at 2023.82 m (Appendix D Figure D-76) and the warehoused sample (Appendix D Figure D-86) show some similarities in clay morphology although they appear different under high magnification. The warehoused sample appears to have more angular silt-sized grains present that is not obvious in the original sample.

The SEM images of the original sample at 2101.57 m (Appendix D Figure D-77) and the warehoused sample (Appendix D Figure D-88) show a similar clay morphology.

The SEM images of the original sample at 2164.23 m (Appendix D Figure D-78) and the warehoused sample (Appendix D Figure D-90) show a similar shale fabric.

The SEM images of the original sample at 2179.68 m (Appendix D Figure D-79) and the warehoused sample (Appendix D Figure D-92) show a similar shale fabric. However, under high magnification, the clay morphology appears vastly different.

Discussion: With the inconsistent changes in MICP analysis between the original samples and the warehoused samples, it is difficult to determine if the changes are due to sample heterogeneity or the effects of the warehousing. No conclusions can be drawn.

6.4 CHAPTER 6 DISCUSSION

The investigations into the effects of warehousing with samples from Saracen-1, CRC-1 and Gorgon CO2 Data Well-1 & Data Well-1ST1 have brought to light a number of findings; both intentional and unintentional. The investigations of the Saracen-1 Muderong Shale CC samples stored in the WACL show a shift of the MICP curves towards higher pressure for the same mercury saturation, an increase in the average IPV threshold pressure by nearly two pressure equilibrium points, a decrease in porosity which is mostly attributed to the reduction in pore volume per gram, decrease in the bulk density and grain density. This resulted in an increase in the average maximum CO_2 column height retentions of between 163 m and 80 m as the brine/ CO_2/ rock contact angle is varied from 0 ° to 60 °. Also, the mineralogical interpretation has identified jarosite and anatase in the warehoused samples that were not identified in the original samples. The investigations into the original samples stored in airtight bags have demonstrated that these minerals have not primarily formed in the pore space and have not caused the reduction in porosity of the samples. It is thus thought that the loss of clay bound water has led to the constriction of the pore bodies and

pore throats which in turn has led to a reduction in porosity but no significant changes in the grain volume per gram.

The CC samples stored in airtight bags showed similar changes but to a lesser extent suggesting that the storage of CC samples in airtight bags reduced the changes in rock properties observed in the CC samples stored in the WACL. It is thus concluded that the warehoused DC samples stored in airtight bags have MICP results that have changed similarly to the CC samples stored in airtight bags; a MICP curve with higher pressure for the same mercury saturation on average, higher average threshold pressure, reduced average porosity and the precipitation of jarosite and anatase in comparison to the original DC samples.

The warehoused Belfast Mudstone CC samples from CRC-1, in contrast to Sarcen-1 CC samples, show no changes in MICP curves; both position and shape, no significant changes in the threshold pressures interpreted with either the IPV method or MI method, and no significant mineralogical changes. However, the samples do show a slight decrease in the average bulk density and grain density but to a lesser extent than observed in the Muderong Shale from Saracen-1. The decrease in porosity of the warehoused samples concurs with the results from the Muderong Shale from Saracen-1 but has occurred to a much lesser extent (1.2 % vs. 5.2 % average decrease respectively). It is thus suggested that the differences between the warehousing effects for the Muderong Shale and Belfast Mudstone are a result of different storage conditions, clay types present, the degree of lithification and compaction of the original samples.

In contrast to the warehousing results from the Muderong Shale samples and the Belfast Mudstone, the Paaratte and Pember Mudstone samples from CRC-1 and, the Barrow Group and the Dupuy Formation from Gorgon CO2 Data Well-1 & Data Well-1ST1 show few consistent trends between the original and warehoused MICP analyses. The only consistent trend observed from these warehoused samples is a decrease in porosity for the CRC-1 Pember Mudstone and Paaratte Formation in comparison to the original samples. Unfortunately, without consistent trends in the warehousing MICP analysis, it is not possible to separate the effects of the warehousing from possible effects of heterogeneity between adjacent samples. The mineralogical results show that there are differences between the original and warehoused samples but whether these variations are a result of the warehousing or heterogeneity is unknown.

The results of this research are in contrast to the investigations by Comisky et al., (2011) who investigated samples stored for a period of two years with helium pycnometry and found an increase in helium porosity after storage. However, the results are consistent with the finding of Auman, (1989) who found that the storage of rock samples in airtight bags reduced the water loss from rock samples while in this case reduced the effects of warehousing.

The results of Auman, (1989) suggest that storage of CC samples in plastic wrap and aluminum foil sealed with a heat sealer are not stopping the effects of the external storage environment but are limiting them. This was also observed in the Saracen-1 CC samples stored in airtight bags where the observed changes were significantly less than those observed in the CC samples stored in the WACL. The American Petroleum Institute, (1998) in the Recommended Practices for Core Analysis suggests that plastic bags be only used for short term storage which concurs with the results observed in Saracen-1.

6.5 CHAPTER 6 CONCLUSIONS

The warehousing (storage) of CC samples affects the resulting MICP analysis. The effects vary depending on the rock being stored. In the case of the Saracen-1 Muderong Shale samples, both jarosite and anatase precipitated, the MICP curves had higher threshold pressures with both the IPV and MI methods. Also, both the grain density and bulk density were lower than in the original analyses. In CRC-1Belfast Mudstone samples, the MICP curves and threshold pressures remained consistent with the original samples and the only changes were an average of 1 % decrease in porosity and a slight decrease in the average bulk density and grain density.

The storage of samples in airtight bags reduced the effects of warehousing but didn‘t remove the effects entirely. It is thus likely that the warehoused Saracen-1 DC samples have had similar modifications to their MICP analysis. Thus there is the opportunity to improve the storage of warehoused samples possibly through the use of plastic wrap in conjunction with aluminum foil as suggested by Auman, (1989).

The effects of warehousing may not be consistent between samples taken from the same well over different formations (CRC-1 Pember Mudstone and Paaratte Formations and Gorgon CO2 Data Well-1 & Data Well-1ST1 Barrow Group and Dupuy Formation). Unfortunately, due to the inconsistent nature of the changes, it is not possible to distinguish these changes from heterogeneity between adjacent samples. Further, adjacent samples are

not necessarily uniform or homogeneous and care needs to be taken when comparing any results from adjacent samples.

CHAPTER 7: NMR SYNTHETIC MICP CURVES

7.1 SUMMARY

The synthetic MICP curves, produced from higher resolution laboratory nuclear magnetic resonance (NMR) apparatus are compared to those produced from the lower resolution wellbore NMR tools. Synthetic MICP curves generated from laboratory NMR data are generally similar to the MICP curves analysed on the same conventional core (CC) sample. However, even in the laboratory NMR analyses with small sample volumes, there are infrequent sample mismatches between the synthetic and CC MICP curves. These infrequent differences may be due to sample heterogeneities.

The heterogeneity effects are thought to be greatly magnified when the synthetic MICP curves are produced from the wellbore NMR tool. Thus the match between the CC and synthetic MICP curves are even more variable; good agreement is observed in Redman-1 between CC and well synthetic MICP curves while in contrast poor agreement is observed between CC and well synthetic MICP curves from Mena Murtee-1. These two wells demonstrate the extremes of the scale of variation in MICP curve agreement that was observed with the technique. Conventional core samples in close proximity (<1.6 m apart) to one another are analysed to gauge the degree of heterogeneity being measured by the NMR tool over the 1.6 m, interval. This allows a distinction to be made between synthetic MICP curves that are inaccurate and those that have a non-representative CC sample.

It is concluded that the laboratory data highlight the future possibilities of using wellbore NMR tools for producing synthetic MICP curves. The wellbore NMR data from well logs show present capability as well as a comparison of different logs from a number of service providers.

7.2 INTRODUCTION

The aim of this component of the research is to produce synthetic mercury injection capillary pressure (MICP) curves from nuclear magnetic resonance (NMR) data and to calibrate these to MICP curves from conventional core (CC) samples. It is envisaged that these calibrated synthetic MICP curves will allow the prediction of capillary pressure properties (e.g. threshold pressure) of caprocks to predict ~~–~~effective" seal capacity of entire sealing intervals, even where conventional core is not available.

The techniques using both laboratory and wellbore data to produce laboratory synthetic (LS) MICP curves and well synthetic (WS) MICP curves are evaluated. Laboratory data was made available for two wells; Tindilipie-11 in the Cooper Basin and Mena Murtee-1 in the Darling Basin. Wellbore data were available from the above wells as well as CRC-2 and Redman-1 in the Otway Basin, Gorgon CO2 Data Well-1& Data Well-1ST1 Barrow Island and Thebe-2 in the Exmouth Plateau. Tindilipie-11 has a Baker Hughes MREX well log, Mena Murtee-1 has a Weatherford's NMR log and CRC-2, Redman-1, Gorgon CO2 Data Well-1& Data Well-1ST1 and Thebe-2 all have a Schlumberger CMR log.

The wells used for this analysis have numerous CC samples with MICP analyses to allow comparison with the synthetic MICP curves produced from the NMR well log. A large number of samples are only required to evaluate the technique of producing synthetic MICP curves and their ability to predict threshold pressures for seal capacity evaluation. It is envisaged that the success of this technique will require fewer MICP samples to calibrate the synthetic MICP curves.

The MICP curves produced from CC rock material and the NMR data were compared to one another to evaluate the representativeness of the synthetic MICP curve. The evaluation of the synthetic MICP curves includes the comparison of the shape and position of the curve as well as the determined threshold pressures and subsequent calculated maximum CO_2 column height retentions. It should be noted that CC MICP curves which have been obtained from samples that are ~ 1cm^3 in volume, are inherently very different to well log NMR measurements, which are taken every ~20 cm and then averaged over anywhere between 4 and 8 measurements (0.8 m-1.6 m). This variability can lead to significant differences in MICP curves which complicate the assessment of the technique.

7.3 LITERATURE REVIEW

The production of synthetic or pseudo MICP curves from NMR has been successfully achieved for reservoir and tight reservoir rocks (Marschall et al., 1995, Lowden et al., 1998, Agut et al, 2000, Volokitin et al., 2001 and, Mardi et al., 2014, Xiao et al., 2016). This has been attained with both laboratory NMR and wellbore NMR using various methods to produce the synthetic MICP curves. Al-Ghamdi, (2006) was the only author who attempted to produce synthetic MICP curves over sealing intervals. This was unsuccessful.

Volokitin et al., (2001) investigated the production of capillary pressure curves from NMR core log that were scaled to MICP data. Their investigations were conducted on the NMR sandstone catalogue compiled by Applied Reservoir Technology Ltd. Their results, using a

fixed pore body to pore throat correction factor, show similar variation in MICP curve shape to Mardi et al., (2014). Mardi et al., (2014) investigated the production of pseudo (synthetic) capillary pressure curves from well log NMR calibrated to MICP data in the heterolithic Granite Wash Formation. Two of the six pseudo MICP curves show similar to excellent agreement, while the remaining four samples show reasonable to poor agreement. Similar variation was also observed in Grattoni et al., (2003) NMR-derived capillary pressure curves.

Al-Ghamdi, (2006) undertook the original analyses of Redman-1 in which he attempted to produce synthetic capillary pressure curves from the wellbore NMR log unsuccessfully. Al-Ghamdi, (2006) attributes the lack of agreement between the WS and CC MICP curves to internal field gradients due to the concentration of paramagnetic ions in the samples leading to internal magnetic field gradients primarily affecting the samples with larger pores.

This study has attempted to extend the production of synthetic MICP curves to sealing rock. While it is possible to shift the synthetic MICP curves using the pore body to pore throat correction factor to align the MICP curves of sealing rock it is also important to identify zones that are not sealing rock. Thus the production of synthetic MICP curves over both sealing and reservoir rock types has been conducted.

7.3.1 **Tindilpie-11, Cooper Basin**

Please see section 3.9.1 for Tindilpie-11 well description.

*Methodology modifications specific to the Tindilpie-11 analysis***:** The pore body to pore throat correction for the well log NMR was 100 which gave the best agreement between the CC MICP curves and the WS MICP curves. The pore body to pore throat correction for the LS MICP curves was 5 which gave the best agreement with the CC MICP curves.

The depth correction applied to the core was that described in the WCR. This was achieved by correlating the well gamma log to the conventional core gamma log (Kicas, 2012).

Results: The threshold pressures for the synthetic MICP curves and the MICP curves from the CC samples are presented in Table 7-1 as well as the difference between the interpreted values. The threshold pressures interpreted from the LS MICP curves show less disparity than those interpreted from the wellbore NMR. The WS MICP curves have overestimated the threshold pressures of reservoir rock (0-100 psia threshold pressures) samples (2852.28 m, 2852.33m) and have had mixed results with the low sealing capacity intervals (threshold pressures between 101 psia and 999 psia). The sample from 2849.71 m has been

significantly underestimated while the sample from 2756.05 m is underestimated to a lesser degree. The low sealing capacity samples from 2872.50 m and 2873.13 m are in the vicinity of the of threshold pressures from the CC MICP curves.

Table 7-1: Tindilpie-11 MICP and Synthetic MICP threshold pressure results from the laboratory and the well log NMR.

Sample	Sample Depth MICP (m)	MICP Threshold Pressure (psia)	Lab Synthetic MICP Threshold Pressure (psia)	Well Synthetic MICP Threshold Pressure (psia)	Difference MICP Lab (psia)	Difference MICP Well (psia)
14	2759.69	605	677	468	72	-137
30	2854.17	862	538	178	-324	-684
4A	2856.74	19	21	245	2	226
2A	2856.80	46	43	245	-3	199
48	2877.59	264	170	178	-94	-86
49	2877.88	163	107	178	-56	15

The maximum CO_2 column height retentions calculated from the interpreted threshold pressures of the CC samples and the synthetic MICP curves are shown in Figure 7-1. In general, the maximum CO_2 column heights derived from the LS MICP curves are in much better agreement with the CC column heights than the column heights derived from the WS MICP curves. The variation observed in the samples is often greater than the variation due to the contact angle changing between 0 ° and 60 °.

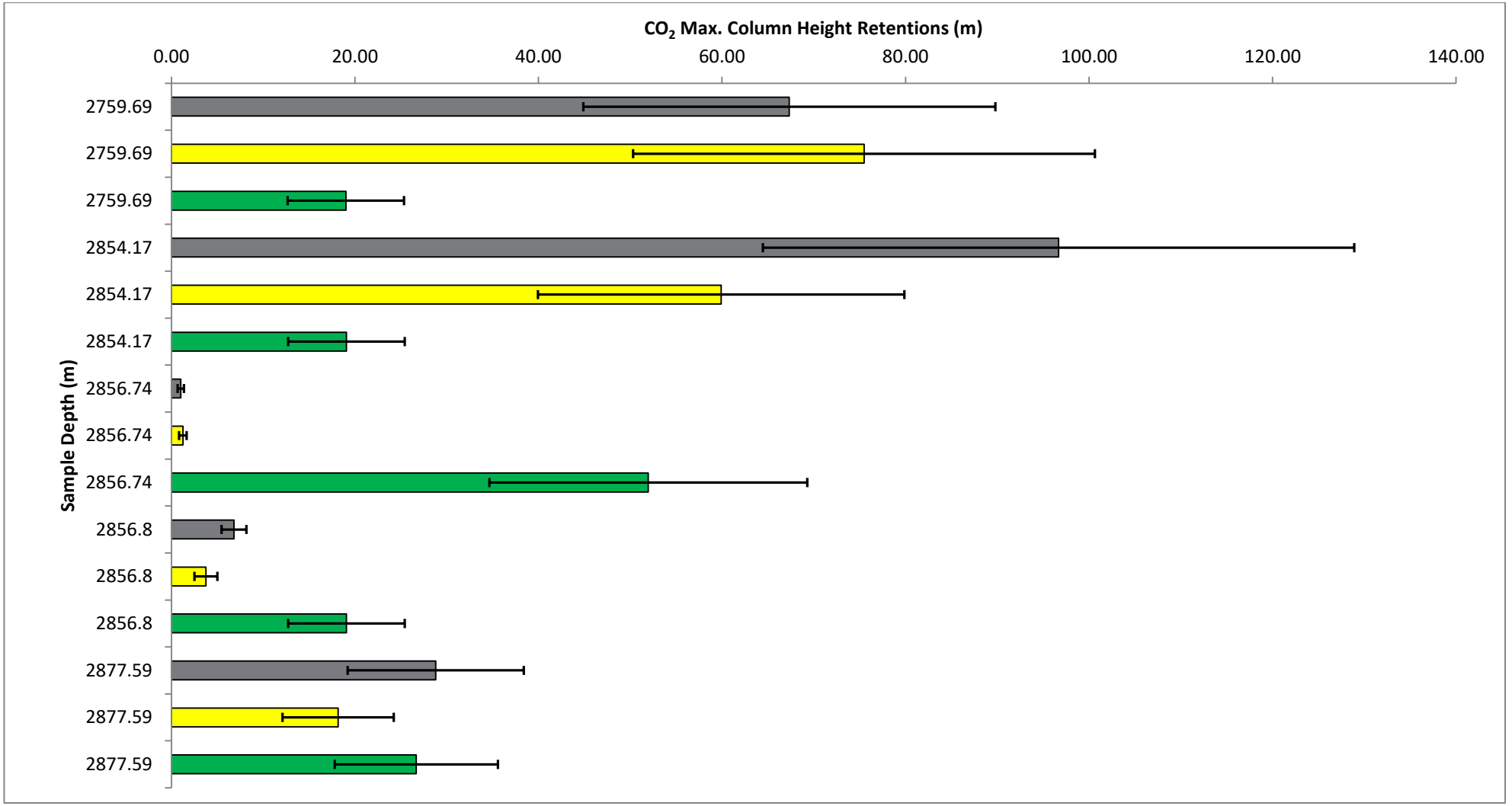

Figure 7-1: The maximum CO_2 column height retentions estimated from CC sample MICP curves are shown in grey, the LS MICP curves are shown in yellow and the WS MICP curves are shown in Green. The error bars represent the range of contact angle (brine/ CO_2 / rock) from 0 ° (right) and 60 ° (left).

The LS MICP curve at 2759.69 m is similar in shape to the CC MICP curve with a slight offset in graph position towards higher pressure for the equivalent mercury saturation (Appendix E Figure E-1). The WS MICP curve also has a semi-similar shape to the CC MICP curve up until ~90 % mercury saturation after which the synthetic MICP curve continues in an upward linear fashion while the CC mercury curve tapers off. The position on the graph is also semi-similar with slight offset towards lower pressure for the same mercury saturation. The T_2 distributions used to produce the WS MICP curve are in agreement (Appendix E Figure E-2). The T_2 distribution from the laboratory sample has a poor agreement with the well log T_2 distributions. The primary peak of the laboratory T_2 distribution occurs at ~80 msec while the well log primary peak occurs at approximately 2 msec (Appendix E Figure E-3).

The LS MICP curve at 2854.17 m and the CC MICP curve are in excellent agreement (Appendix E Figure E-4). The WS MICP curve has a poor agreement with both the LS MICP curve and the CC MICP curve in position on the graph although it has a similar shape. The WS MICP curve has the maximum inflection point at much lower pressure and the subsequent linear upward trend is much earlier than the CC MICP curve and the LS MICP curve. The T_2 distributions used to produce the WS MICP curve are not in agreement with one another (Appendix E Figure E-5). The position of the primary peak average (time axis) of the wellbore T_2 distribution is offset to the laboratory T_2 distribution. The shape of the laboratory T_2 distribution peak (Appendix E Figure E-6).is similar to the average peak for the well T_2 distributions

The LS MICP curve at 2856.74 m and the CC MICP curve are in agreement with one another with only minor variations in shape (Appendix E Figure E-7). The shape and position on the graph of WS MICP curve is dissimilar to the CC MICP curve. The WS MICP curve has the maximum inflection point at much higher pressure and the subsequent linear upward trend occurs much later. The WS MICP curve has a much sharper maximum inflection point, a steeper linear trend and a much more acute plateau than the CC sample. The T_2 distributions used to produce the WS MICP curve are in excellent agreement with one another (Appendix E Figure E-8). Further, the position of the T_2 distribution peak (time axis) is not in agreement with the laboratory T_2 distribution peak. The shape is also considerably different in the laboratory T_2 distribution (Appendix E Figure E-9).

The LS MICP curve at 2856.80 m and the CC MICP curve are in the same position on the graph with similar shape; slight variation in the maximum inflection point, linear upward trend and the mercury saturation at which the plateau occurs (Appendix E Figure E-10). The

WS MICP curve has a poor agreement with both the LS MICP curve and the CC MICP curve in both shape and position on the graph. The WS MICP curve has the maximum inflection point at higher pressure and the subsequent linear upward trend is much steeper. Further, the WS MICP curve has a more acute plateau at 100 % mercury saturation than was not observed in the other MICP curves. The T_2 distributions used to produce the WS MICP curve are in excellent agreement with one another (Appendix E Figure E-11). The position of the primary peak (time axis) is in no agreement with the laboratory T_2 distribution and the shape of the peak is considerably broader in the laboratory T_2 distribution (Appendix E Figure E-12).

The LS MICP curve at 2877.59 m and the CC MICP curve are in excellent agreement; both shape and position on the graph (Appendix E Figure E-13). The WS MICP curve is in agreement with the CC MICP curve up to 50 % mercury saturation above which the synthetic MICP curve continues on a steeper linear upward trend and has a plateau occurring at ~100 % mercury saturation. The T_2 distributions used to produce the WS MICP curve are similar with minor variations in the intensity of the primary peak at ~6 msec (Appendix E Figure E-14). The T_2 distribution of the laboratory sample (Appendix E Figure E-15) occurs at much shorter relaxation times than in the well log T_2 distribution. However, the shape of the peaks is in general agreement.

The LS MICP curve at 2877.88 m and the CC MICP curve are in agreement; both shape and position on the graph with minor variation in the maximum inflection point and the subsequent upward linear trend (Appendix E Figure E-16). The WS MICP curve is similar to the CC MICP curve up to 70 % mercury saturation after which the synthetic MICP curve continues on a much steeper linear upward trend and has an acute plateau occurring at 100 % mercury saturation. The T_2 distributions used to produce the WS MICP curve have a similar position on the graph but show variation in the intensity of the primary peak at ~6 msec (Appendix E Figure E-17). The T_2 distribution of the laboratory sample (Appendix E Figure E-18) has reasonable primary peak shape agreement although broader and skewed in comparison to the primary peak from the well log T_2 distribution , however, the T_2 time at which the peaks occur is ~6 msec for the well log T_2 distribution and ~90 msec for the laboratory sample.

Discussion: The interpreted threshold pressures from the LS MICP curves are similar to the interpreted threshold pressures of the CC samples with only slight discrepancies in the exact pressures excluding sample 2854.17 m. The threshold pressures interpreted from the WS MICP curves are mixed. Two samples show reasonable agreement (2877.59 m and 2877.88

m) in threshold pressures while the other four samples show discrepancies (2759.69 m, 2854.17 m, 2856.74 m and 2855.80 m). The CC samples taken in close proximity to one another (2854.17 m, 2856.74 m and 2856.80 m) suggest that there is considerable variation in threshold pressures over the 2.5 m interval. The WS threshold pressures predict a different trend to that observed in the CC samples. The samples in close proximity to one another at 2877.59 m and 2977.88 m show that the WS MICP curve is predicting accurately at 2877.88 m while underestimating the threshold pressure at 2877.59 m. The observed variation is difficult to explain. The CC MICP curves indicate that there is heterogeneity over the 1.6 m interval used to produce the WS MICP curve. However no significant heterogeneity is observed in the T_2 distributions of these samples. This suggests that either the heterogeneity is on too fine a scale and the NMR tool is averaging the results or that the NMR tool is failing to accurately measure the pore body distribution leading to inaccurate synthetic MICP data.

The calculated CO_2 column heights for the LS MICP curves and the CC MICP curves are similar with the variation between column heights less than the variation due to contact angle change between 0 ° and 60 °.

The synthetic MICP curves generated from the laboratory samples are similar to the CC sample MICP curves confirming the technique and that the T_2 distribution is representative of the sample. In contrast, the WS MICP curves have had mixed results. The T_2 distributions for all samples except that from 2854.17 m are similar suggesting that the 1.6 m measurement interval is fairly homogeneous. However, as discussed above the CC samples in close proximity to one another (2877.59 m and 2977.88 m) differ in threshold pressures threshold pressures (19 psia and 46 psia respectively). As 33 % of the WS MICP curves are similar, it is unlikely that the NMR tool is inaccurate. It is more likely that the tool is measuring a much greater volume than the 20 cm measurement interval. Furthermore, all of the laboratory T_2 distributions show different primary peak locations to the well T_2 distributions. In all cases, the primary peak of the laboratory T_2 distribution is at higher T_2 relaxation times than observed in the well T_2 distributions. This may be a result of the calibration or the inversion process used to convert the relaxation times to a T_2 distribution.

7.3.2 **CRC-2, Otway Basin**

Please see section 3.3.3 for CRC-2 well description. The CRC-2 well provides a unique opportunity to test this methodology. The well not only has an NMR log over the entire seal interval, intraformational baffles, reservoir and following seal but also has twenty MICP

analyses from numerous cored intervals throughout the well that allow the evaluation of the accuracy of synthetic MICP curves and methodology.

*Methodology modifications specific to the CRC-2 analysis***:** The pore body to pore throat correction for the well log NMR was 4 which gave the best agreement between the CC MICP curves and the WS MICP curves.

The depth correction applied to the core was that provided by CO2CRC. The correction was achieved by correlating the well gamma log to the conventional core gamma log.

Results: The threshold pressures for the WS and CC MICP curves are presented in Table 7-2 including the differences between the interpreted values. The results of the threshold pressure interpretations from the well WS MICP curves indicate that the threshold pressures of the reservoir intervals (0-100 psia) are being overestimated (+~65 psia). The low sealing capacity intervals (threshold pressures between 101 psia and 999 psia) have minor differences for two (930.66 m and 1320.42 m) of the three samples while the third (1491.43 m) sample has a threshold pressure difference of 188 psia. The eight high sealing capacity (>1000 psia) intervals have much less success in accurately predicting threshold pressures for the WS MICP curves. Seven of the eight samples were predicted to have a lower threshold pressure from the WS MICP curve while sample 1521.65 m had a threshold pressure considerably higher (+1602 psia) than the MICP curve from the CC sample. Table 7-2 shows a clear pattern in the column titled difference; the WS MICP curves are overestimating the threshold pressure of the reservoir intervals and significantly underestimating the threshold pressures of the high sealing capacity intervals.

Table 7-2: CRC-2 threshold pressures from MICP CC samples and WS MICP curves. The samples have been grouped in reservoir (R), low seal capacity (LS) and high seal capacity (HS) intervals.

Sample	Sample Depth MICP (m)	MICP Threshold Pressure (psia)	Well Synthetic MICP Threshold Pressure (psia)	Difference MICP Well (psia)
Pember Mudstone (LS1)	930.66	119	120	1
Pember Mudstone (HS1)	933.21	2938	1105	-1833
Paaratte Formation (LS2)	1320.42	849	804	-45
Paaratte Formation (HS2)	1321.93	1731	614	-1117
Paaratte Formation (HS2)	1323.09	3526	608	-2918
Paaratte Formation (HS2)	1328.96	4993	614	-4379
Paaratte Formation (HS2)	1330.63	4990	804	-4186
Paaratte Formation (HS2)	1433.33	4392	1518	-2874
Paaratte Formation (LS3)	1433.97	171	225	54
Paaratte Formation (R1)	1438.63	71	119	48
Paaratte Formation (R1)	1440.7	9	63	54
Paaratte Formation (R1)	1443.52	5	63	58
Paaratte Formation (R1)	1447.89	87	412	325
Paaratte Formation (R1)	1448.32	40	87	47
Paaratte Formation (R1)	1472.02	20	226	206

Paaratte Formation (HS3)	1480.28	4985	2865	-2120
Paaratte Formation (LS4)	1491.43	414	226	-188
Paaratte Formation (R2)	1498.32	4	87	83
Paaratte Formation (R2)	1504.45	5	63	58
Paaratte Formation (R2)	1507.65	3	87	84
Paaratte Formation (R2)	1509.88	4	46	42
Skull Creek Formation (HS4)	1521.65	1263	2865	1602

The maximum CO_2 column height retentions calculated from the interpreted threshold pressures of the CC samples and the WS MICP curves are shown in Figure 7-2. The calculated maximum CO_2 column heights from the WS MICP curves for the high sealing (HS) capacity intervals show clear discrepancies to the column heights calculated from the MICP curves of the CC samples. The WS MICP curves have threshold pressures and subsequent maximum CO_2 column heights consistently less than the column heights calculated from CC samples that are beyond the range from the change in contact angle (0 ° to 60 °). The low seal (LS) capacity intervals generally have similar maximum CO_2 column heights to the CC samples. The maximum calculated CO_2 column heights for the reservoir samples are being slightly overestimated using the WS threshold pressures.

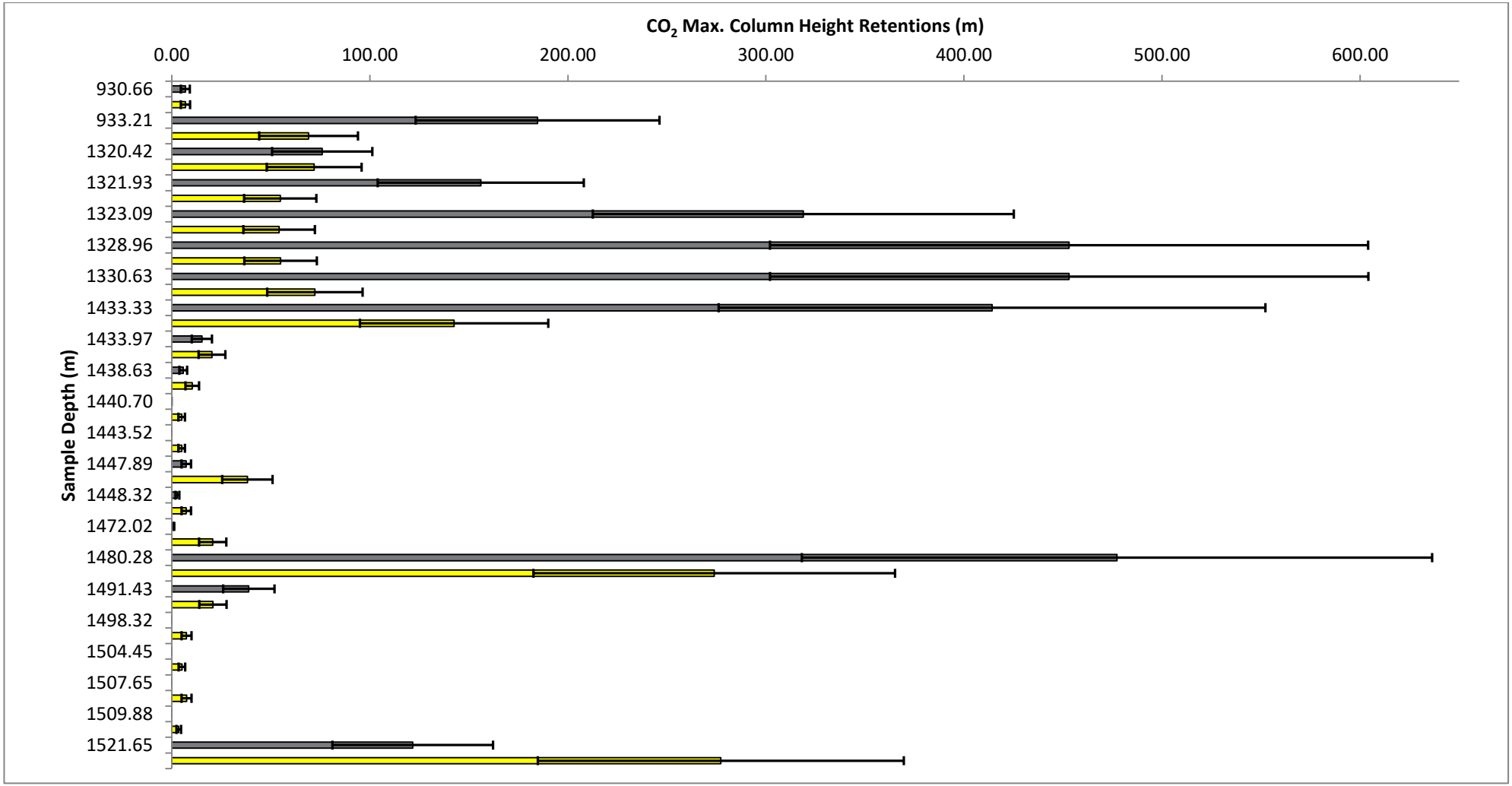

Figure 7-2: The maximum CO_2 column height retentions estimated from CC sample MICP curves (Grey) and WS MICP curves (Yellow). The error bars represent the range of contact angle (brine/ CO_2 / rock) from 0 ° (right) and 60 ° (left).

The Pember Mudstone sample at 930.66 m (LS1) has a WS MICP curve in agreement with the MICP curve taken from the core sample (Appendix E Figure E-19). Both curves have the same shape and position on the graph. There is a slight deviation between the two curves between 600 psia and 8000 psia where the WS MICP curve shows higher mercury saturation at the same pressure. The T_2 distributions (Appendix E Figure E-20) for the eight measurements over the depth of 930.66 m are similar to one another except for two outliers; 929.9 m and 930.1 m.

The Pember Mudstone sample from 933.21 m (HS1) has a WS MICP curve which shows fair agreement with the MICP curve from the CC sample (Appendix E Figure E-21). Both MICP curves show a flat linear increase before the maximum inflection point, however, there is significant separation between the two. The MICP curve from the CC sample shows much greater mercury saturation for pressures between 80 psia and 2000 psia. Above 2000 psia both the WS and CC sample MICP curves are similar. The T_2 distributions used to produce the WS MICP curve are similar from 0.3 msec to ~90 msec (Appendix E Figure E-22). Post ~90 msec the T_2 distributions show disparity to ~800 msec. This disparity is approximately where the separation between the MICP curve and the WS MICP curve occurs.

The Paaratte Formation sample 1320.42 m (LS2) has a similar threshold pressures and MICP curve (position on graph and shape) to the CC MICP curve (Appendix E Figure E-23). There is a slight disparity between curves from 6000 psia and 60,000 psia where the WS MICP curve shows a lower saturation than the CC MICP curve at the same pressure. The T_2 distributions used to produce the WS MICP curve (1.6 m interval) show poor agreement with one another (Appendix E Figure E-24,). It is observed that these T_2 distributions show a loose relationship between shape and the depth of the sample.

The Paaratte Formation (HS2) samples between 1321.93 m and 1328.96 m have core sample MICP curves and WS MICP curves in poor agreement with one another which is also reflected in the threshold pressures (Table 7-2). These samples all show significant disparity in the position (lower pressure) of the linear upward trend of the WS MICP curve graph (after the maximum inflection point) in comparison to the MICP curve from the CC samples (Appendix E Figure E-25, E-27 and E-29). The T_2 distributions for these samples all show a similar shape with a major peak between 8 msec and 100 msec and a secondary subtle minor peak between 3 msec and 8 msec (Appendix E Figure E-26, E-28 and E-30).However, the T_2 distribution peaks for the samples over the 1.6 m intervals show significant variation in the signal distribution/ amplitude of the major peak.

The Paaratte Formation (HS2) samples from 1330.63 m and 1433.33 m both have WS MICP curves displaying a similar trend and difference to the CC MICP curves (Appendix E Figure E-31, E-33). The WS MICP curves for both samples show loose agreement up to ~600 psia and subsequently, show significant separation up to ~20,000 psia where they cross. This is more pronounced in sample 1330.63 m. This has led to the maximum inflection point of the WS MICP curves occurring much earlier than the CC MICP curves and a reduced threshold pressure interpretation. The T_2 distribution from sample 1330.63 m (Appendix E Figure E-32) shows poor agreement within the major peak similar to the samples above (1321.93 m, 1323.09 m and 1328.96 m) while the T_2 distributions from sample 1433.33 m (Appendix E Figure E-34) have a loosely similar shape but differ in their position on the graph.

The Paaratte Formation (LS3) sample 1433.97 m has a threshold pressure and MICP curve in agreement with the CC MICP curve (position on graph and shape) (Appendix E Figure E-35). There is a slight disparity in MICP curves between 200 psia and 2000 psia before matching with the CC MICP curve and then again showing disparity between 10,000 psia and 60,000 psia. The T_2 distributions used to produce the WS MICP curve (1.6 m interval) show poor agreement with one another (Appendix E Figure E-36).

The Paaratte Formation (R1) samples between 1438.63 m and 1472.02 m depth show a number of different relationships between the WS MICP curves and the CC MICP curves (Appendix E Figure E-37, E-39, E-41, E-43, E-45 and E-47) as do corresponding T_2 distributions (Appendix E Figure E-38, E-40, E-42, E-44, E-46 and E-48).

The Paaratte Formation (R1) samples 1438.63 m and 1448.32 m have WS MICP curves with a reasonable agreement to the MICP curves from the CC samples; the general shape, maximum inflection point and position on the graph are all loosely agreeable (Appendix E Figure E-37, E-45). The T_2 distributions over the 1438.63 m sample interval show poor agreement between one another, both in position and shape (Appendices Figure E-38). These changes are observed to vary with depth over the 1.6 m interval. The T_2 distributions over the 1448.32 m sample interval (Appendix E Figure E-46) show reasonable agreement in shape but do show variation in the primary peak intensity at ~500 msec.

The Paaratte Formation (R1) samples 1440.7 m and 1443.52 m have WS MICP curves with similar shapes but offset from the MICP curves of the CC samples (Appendix E Figure E-39, E-41). In both samples, the WS MICP curve is showing a higher pressure for the same saturation as the MICP curves from the CC samples. This offset is more pronounced in these samples because of the logarithmic scale. The T_2 distributions from the 1440.7m (Appendix

E Figure E-40) show poor agreement with one another with a clear trend in the T_2 distribution shape with depth. The T_2 distributions from the sample at 1443.52 m (Appendix E Figure E-42) are similar to one another.

The Paaratte Formation (R1) sample at 1447.89 m has a WS MICP curve showing the opposite trend to the two samples above (1440.7 m and 1443.52 m) with the WS MICP curve having a similar shape to the MICP curve from the CC sample but offset to a lower pressure for the same mercury saturation (Appendix E Figure E-43). The T_2 distributions over the sample location show poor agreement with one another and a clear trend in the T_2 distribution shape with depth (Appendix E Figure E-44).

The Paaratte Formation (R1) samples from 1448.32 m and 1472.02 m both have higher estimated threshold pressures from the WS MICP curves in comparison to the MICP curves from the CC samples. The WS MICP curve for sample 1448.32 m shows loose agreement with the MICP curve from the CC sample (Appendix E Figure E-45). The maximum inflection point of the WS MICP curve occurs at higher pressure and the upward linear trend post maximum inflection point is much steeper than the MICP curve from the CC sample. The WS MICP curve for sample 1472.02 m shows poor agreement between 20 psia and 600 psia after which the MICP curves follow a similar trend (Appendix E Figure E-47). The poor agreement between MICP curves from 20 psia and 600 psia has led to the significant difference in threshold pressures; the WS threshold pressure suggests the sample is not reservoir quality. The T_2 distributions for sample 1448.32 m generally have similar shape, but the intensity of the primary peaks is observed to vary significantly (Appendix E Figure E-46). The variation in heights of the peaks is observed to vary with depth. The T_2 distributions for sample 1472.02 m show poor agreement (Appendix E Figure E-48).

The Paaratte Formation (HS2) sample from 1480.28 m depth has a WS MICP curve with a similar shape to the CC MICP curve (Appendix E Figure E-49). The CC sample MICP curve has considerable interpreted conformance which explains the increase in mercury saturation at pressures below 10 psia. The T_2 distributions over that sample interval show loose general agreement with a change in shape of the T_2 distribution with depth (Appendix E Figure E-50).

The Paaratte Formation low seal capacity interval 3 (LS3) sample from 1491.43 m has a WS MICP curve that has a similar position on the graph to the CC MICP curve but has a distinctly different shape (Appendix E Figure E-51). The T_2 distributions over the sample

interval used to produce the WS MICP curve are in poor agreement with one another (Appendix E Figure E-52).

The Paaratte Formation (R2) samples 1498.32 m, 1504.45 m, 1507.65 m and 1509.88 m all have MICP curves from CC samples indicating low threshold pressures and similar quality reservoir rock. The WS MICP curves produced over these sample locations have somewhat similar shaped MICP curves although offset to a higher pressure for the same mercury saturation indicative of a lower quality reservoir rock (Appendix E Figure E-53, E-55, E-57 and E-59). The agreement in shape of the WS MICP curves with the CC samples appears to correspond with the agreement in T_2 distribution over the sample interval used to produce the WS curve; sample 1498.32 m and 1509.88 m have similarly shaped MICP curves to CC samples and similar T_2 distributions (Appendix E Figure E-54 and E-60) over the sample interval while the sample from 1507.65 m has a more varied WS MICP curve and more variation in the T_2 distributions (Appendix E Figure E-58) used to produce the WS.

The Skull Creek Formation sample from a depth of 1521.65 m has a WS MICP curve with a similar shape and slight offset in position on the graph to the MICP curve from the CC sample (Appendix E Figure E-61). The T_2 distributions over the sample interval are similar with one another excluding the two measurements from 1522.2 m and 1522.4 m where there is a secondary peak in the T_2 distribution (Appendix E Figure E-62).

Discussion: The comparison of threshold pressure interpretations from the WS MICP curves and the CC sample MICP curves indicates that threshold pressure interpretations are almost consistently (excluding the Skull Creek Formation) being underestimated for the sealing intervals and being overestimated for the reservoir intervals. It is expected that the correction factor for pore body size to pore throat size would be unable to accurately correct for both types of samples (reservoir and sealing) and thus the overestimation of reservoir threshold pressures is expected. However, the underestimation of threshold pressures from the WS MICP curves over sealing intervals is unexpected. Excluding samples from the HS2 the MICP curves are quite well aligned. However, the maximum inflection point of the WS MICP curves continually occurs earlier than in the MICP curves from the CC samples. If the maximum points of inflection were aligned using the pore body to pore throat correction factor, then the position of the linear upward trending part of the WS MICP curves would be misaligned. This was considered undesirable as the capillary pressure curve (excluding the maximum point of inflection) would not be representative.

The calculated CO_2 column heights are reflective of the interpreted threshold pressures. The calculated CO_2 column heights clearly show that the differences in interpreted threshold pressures from the WS MICP curves will lead to considerable differences in the maximum CO_2 column heights. In general, this will lead to an underestimation of sealing capacity and maximum column heights retainable.

The HS2 from 1321.93 m to 1433.33 m has WS MICP curves and interpreted threshold pressures with significant disparity in comparison to the CC samples. The T_2 distributions used to produce the WS MICP curves do show considerable disparity over the 1.6 m interval. However, the T_2 distribution peaks are consistently low between 3000 msec and approximately 100 msec before beginning the peak indicating the pores are below 100 msec in size. This 100 msec point at which the T_2 distribution peaks begin corresponds to the point at which the MICP curve begins to inflect and begin its upward linear trend. Thus, as this point is consistent across the T_2 distributions, it suggests that the pore to pore throat ratio used over this baffle zone is not appropriate and not providing enough shift. The T_2 distributions are unlikely to be in error or measuring filter cake as the WS MICP curves show a similar pattern to those obtained from the CC samples indicating the NMR tool was indeed measuring the rock. Thus there are two possibilities for the results observed; the pore body to pore throat ratio used throughout the well is not appropriate for this formation, or a property unique to the formation is leading to a shift in the T_2 distribution and the corresponding WS MICP curve.

There are a number of factors which can lead to a shift in T_2 distributions and thus affect the point at which the WS mercury inflection and upward linear trend occur. These include minerals with magnetic properties and pore fluids with different hydrogen indexes from the brine including gas and oil. The minerals with magnetic properties will lead to a shortening of T_2 relaxation times indicating that the pores are smaller than in reality and resulting in an MICP curve pushed towards lower mercury saturation for the same pressure and thus indicating better sealing properties. This is the opposite of what is occurring over the HS2. If hydrocarbons were present over HS2, then the effects would be dependent on the fluid type. If gas was present, then hydrogen index would be considerably lower than brine and this would lead to low porosity measurements. However, as the gas would be present in water wet rock and the two fluids are immiscible this would reduce the surface relaxivity effect and suggest the fluids were in larger pores than the reality. This effect would also occur with oil although the porosity would be high as the hydrogen index of oil is similar to that of brine. Thus if oil or gas was present this would result in T_2 distribution with longer

relaxation times and thus be indicative of larger pores resulting in a WS MICP curve with the same mercury saturation occurring at lower pressures than the CC sample MICP curves. This is consistent with the MICP curves observed in the HS2 however, the presence of hydrocarbons was not observed in the mud log; no hydrocarbon fluorescence in the cutting samples and no significant mud gas. Further, the resistivity log has no indication of a non-conductive fluid being present over this interval. Thus the shift in the T_2 distribution is unlikely to have been caused by the presence of hydrocarbon.

The shift in the T_2 distribution is likely to be a result of either a change in the ratio of pore throat to pore body over this interval, surface relaxivity efficacy changes or equally likely due to the bioturbation noted in the sedimentary log of the conventional core over this interval. It is thought that the bioturbation observed in the conventional core has led to numerous large pores/cavities that resulted in long relaxation times within the rock volume and shifted the T_2 distribution towards larger pores and thus resulted in a WS mercury curve which represents the pore throat distribution of both the bioturbations and the rock porosity. Unfortunately, the bioturbation is not uniform and has therefore likely been missed or not sampled for MICP analysis.

The agreement between MICP curves (shape and position) loosely correlates to the agreement between T_2 distributions over the 1.6 m interval used to construct the WS MICP curves i.e. reservoir samples 1433.52 m, 1498.32 m, 1509.88 m where the MICP curves are in agreement in shape, but the position is incorrect due to correction factor being scaled for sealing rock. The Skull Creek formation (1521.65 m) where the MICP curves have consistent shape, but there is a slight shift in the position of the MICP curve which is a likely result of the two measurements and resulting T_2 distributions from 1521 m and 1521.2 m which are not consistent with the six deeper measurements which are summed to give the average over eight measurements. Even with a loose agreement between T_2 distributions the WS MICP curves produced are of the general shape of those from the CC i.e. 1320.42 m, 1433.97 m, 1440.70 m, 1480.28 m, 1504.45 m and 1507.65 m. However, when there is little to no agreement between the T_2 distributions the resulting WS MICP curves show no agreement in shape and often show a significant change in the position on the graph i.e. sample 1472.02 m and 1491.43 m.

7.3.3 **Redman-1, Otway Basin**

Please see section 3.3.1 for Redman-1 well description. Boult et al., (1999), Ramamoorthy et al., (2000) and Al-Ghamdi, (2006) published on this well. Boult et al., (1999) and Ramamoorthy et al., (2000) focus on using the wellbore NMR tool to determine gas

saturation while Al-Ghamdi focusses on calibrating NMR response to capillary pressure curves. Al-Ghamdi, (2006) provides the MICP analyses for the calibration and comparison of the WS MICP curves.

Methodology modifications specific to the Redman-1 analysis: The WS MICP curves were constructed from four samples over 0.8 m for each MICP sample instead of eight samples over 1.6 m. This methodology was undertaken because the samples of CC for which the MICP analysis was taken were often taken close together. The WS MICP curves had a pore to pore throat correction of 9 applied which best aligned the WS MICP curves to the CC MICP curves. To make sure that the technique was working adequately, a reservoir sample at 2834.31 m was taken to distinguish between reservoir rock and sealing rock.

The depth correction applied was + 3.81 m to the core depth to match the wireline log depth (Al-Ghamdi, 2006).

Results: The threshold pressures interpreted from the MICP curves of CC samples and the WS MICP curves are shown in Table 7-3. The results clearly show a mismatch between the interpreted threshold pressures of the CC samples and the WS MICP curves. The greatest observed difference is for sample 2841.21 m with the WS MICP curve having a threshold pressure of 8561 psia; twice that of the CC sample. None of the sample locations have the same interpreted threshold pressures for both methods. However, a number of patterns can be observed from the data; firstly the threshold pressures from the WS MICP curves and the CC samples show similar trends i.e. Sample locations with low CC sample MICP threshold pressures also have low interpreted threshold pressures from the WS MICP curves. Secondly due to the close proximity of CC MICP analysis the WS MICP curves over the same interval often overlap (4 samples over 80cm) and it can be observed that the CC threshold pressures are varying while the WS MICP threshold pressures are remaining constant; samples 2841.21 m and 2841.3 m and, samples 2841.66 m and 2841.99 m.

Table 7-3: Redman-1 threshold pressures from MICP CC samples and WS MICP curves.

Sample	Sample Depth MICP (m)	MICP Threshold Pressure (psia)	Well Synthetic MICP Threshold Pressure (psia)	Difference MICP Well (psia)
Pretty Hill Formation	2834.31	20	100	80
Pretty Hill Formation	2837.57	6970	4981	-1989
Pretty Hill Formation	2840.66	997	260	-737
Pretty Hill Formation	2840.86	864	260	-604
Pretty Hill Formation	2841.21	4288	8560	4272
Pretty Hill Formation	2841.3	5984	8561	2577
Pretty Hill Formation	2841.66	4993	6231	1238
Pretty Hill Formation	2841.99	4305	6231	1926
Pretty Hill Formation	2843.08	492	927	435
Pretty Hill Formation	2843.42	6983	4254	-2729
Pretty Hill Formation	2843.61	4994	4536	-458
Pretty Hill Formation	2844.08	6974	4536	-2438

The maximum calculated CO_2 column heights for Redman-1 are shown in Figure 7-3. The calculated column heights for both CC samples and the WS MICP curves show a similar trend often not varying by more than the potential variation as a result of contact angle change between 0 ° and 60 ° as shown by the error bars. The maximum CO_2 column heights for both the CC samples and the WS MICP curves show no specific patterns; the threshold pressures from the WS samples are above and below that from the CC samples. The maximum CO_2 column heights indicate that there are three zones over the sampled interval with high seal capacity and three zones with low seal capacity/ reservoir potential.

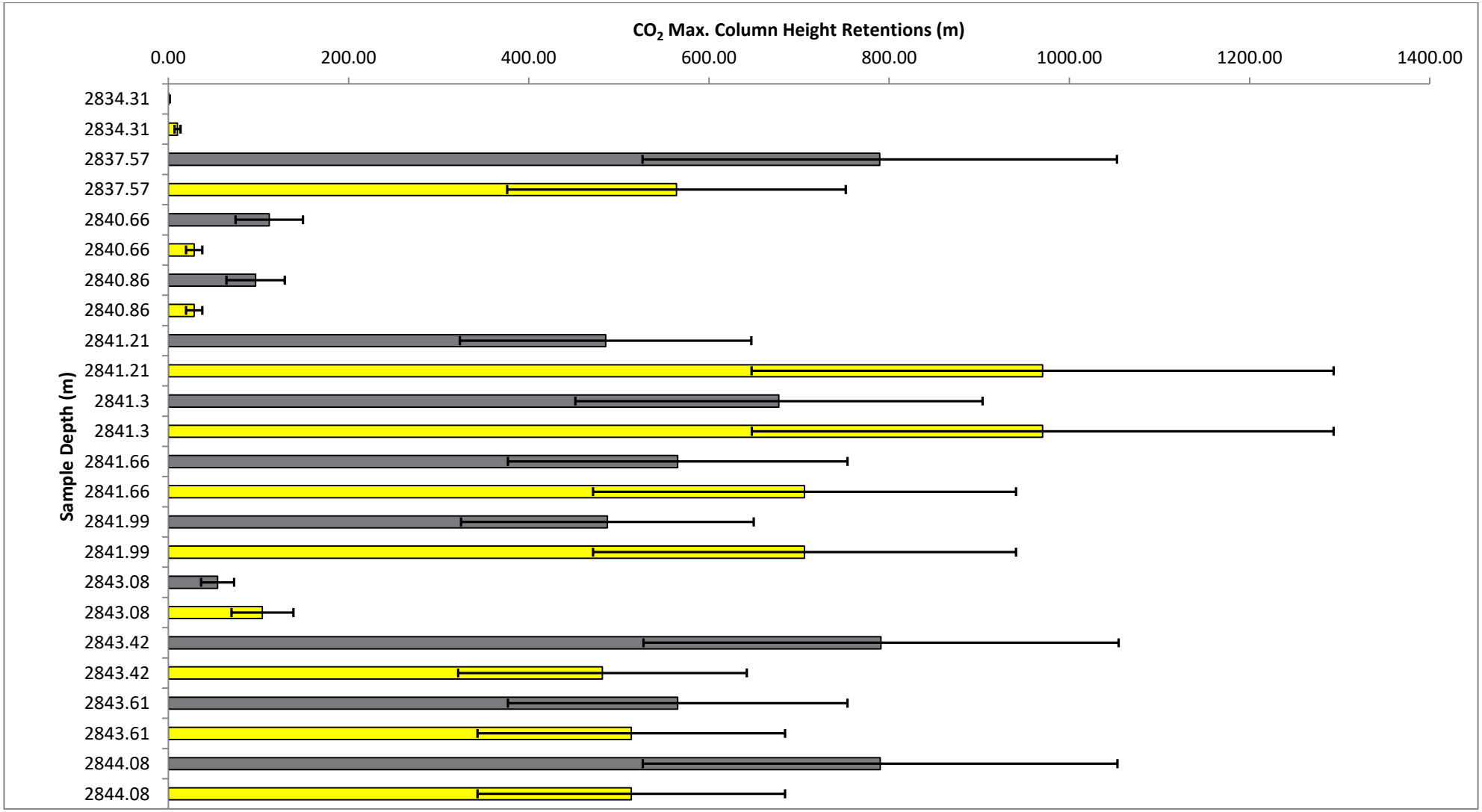

Figure 7-3: The maximum CO_2 column height retentions from CC samples (grey) and WS MICP curves (yellow) over the Pretty Hill Formation, Redman-1. The error bars represent the range of contact angle (brine/ CO_2 / rock) from 0 ° (right) and 60 ° (left).

The WS MICP curve at a 2834.31 m shows poor agreement up to 50 % mercury saturation, after which, the WS MICP curve comes into alignment with the CC MICP curve (Appendix E Figure E-63). The WS MICP curve has only one point of maximum inflection while the CC MICP curve has two points of inflection. The T_2 distribution used to construct the WS MICP curve is similar in all samples except that from the lowest depth at 2834.49 m which has a varied shape to the other samples (Appendix E Figure E-64).

The WS MICP curve at a depth of 2837.57 m (Appendix E Figure E-65) shows poor agreement up to 30 % mercury saturation with the CC MICP curve. However, at mercury saturations > 30 % the MICP curves show a similar position on the graph and alignment of the maximum inflection point and the subsequent linear upward trend towards 100 % mercury saturation. The WS MICP curve has two points of inflection; 70 psia and 4980 psia while the CC sample MICP curve shows one maximum inflection point and a considerably different shaped curve. The second inflection point of the WS MICP curve aligns well with the maximum inflection point of the CC MICP curve. The T_2 distributions used to produce the WS MICP curves show general shape agreement between the three samples with differences in peak intensity while the sample from 2837.84 m has an extra peak between 80 msec and 500 msec (Appendix E Figure E-66).

The WS MICP curve at 2840.66 m depth has a poor agreement with the CC MICP curve (Appendix E Figure E-67). The MICP curves are disimilar from approximately 40 psia through to 10,000 psia. The MICP curve from the WS sample has higher mercury saturation for the same pressure as opposed to the CC MICP curve. The T_2 distributions over this interval show a similar trend and shape with some offset and peak intensity variation from 0.3 msec to 100 msec after which the samples show more variation (Appendix E Figure E-68). The measurement from 2840.43 m has a significant T_2 peak between 100 msec and 1000 msec while the two measurements below have a much lower intensity peak. The measurement from 2840.89 m has no peak present over this interval.

The WS MICP curve at 2840.86 m has a similar general agreement with the CC MICP curve (Appendix E Figure E-69). Both MICP curves have a similar position on the graph and similar shape although the WS MICP curve has a more prominent jump in mercury saturation at approximately 1000 psia. The T_2 distributions used to produce the WS MICP curve show little agreement with one another improving towards the short relaxation times (Appendix E Figure E-70). The peak offsets and variation intensities follow somewhat of a similar pattern. However, between 100 msec and 1000 msec, the T_2 peak from the

measurement at 2841.04 m depth is completely absent while at the shallowest depth (2840.58 m) there is a sizeable peak.

The WS MICP curve over the interval at 2841.21 m is in near perfect shape agreement with the CC MICP curve (Appendix E Figure E-71). There is a slight offset in the position of the MICP curves with the WS at slightly higher pressure for the same mercury saturation. The T_2 distributions have a shape, peak intensity and position in similar alignment to one another excluding the shallowest measurement at 2841.04 m which has a slight offset and a slight change in peak intensity (Appendix E Figure E-72).

The WS MICP curve over the interval at 2841.3 m has a similar shape and graph position to the CC MICP curve (Appendix E Figure E-73). The WS MICP curve over this interval is created from the same four measurements used to create the WS MICP curve for the sample at 2841.21 m and thus has the same T_2 distributions (Appendix E Figure E-74). The WS MICP curve appears to plot in between the CC MICP curves for the samples at 2841.21 m and 2841.3 m.

The WS MICP curve for the sample at 2841.66 m has similar agreement in shape and position on the graph to the CC MICP curve (Appendix E Figure E-75). The CC MICP curve has a slight plateau at ~15000 psia that is not observed in the WS MICP curve which has led to a slight offset between the two linear portions of the MICP curves. The T_2 distributions over the sampling interval have similar peak position and peak intensity with the measurement at 2841.95 m having a slightly higher peak intensity at 1 msec and 30 msec (Appendix E Figure E-76).

The WS MICP curve at 2841.99 m has good agreement with the CC MICP curve. The WS MICP curve has slight variation below 20 % mercury saturation and slight offset of the maximum point of inflection, however, the linear upward trend of the MICP curve above 20 % mercury saturation matches the CC MICP curve in near perfect agreement (Appendix E Figure E-77). The T_2 distributions used to produce the WS MICP curves are in similar/ reasonable agreement with slight variation in the intensity of the peak at 1 msec and variation in position and intensity of minor peaks at 30 msec (Appendix E Figure E-78).

The MICP curve for the CC sample at 2843.08 m is unlikely to be representative of the true rock properties (Appendix E Figure E-79). This CC sample should have been re-analysed upon inspection of the MICP curve. However, with this in mind and drawing a linear line between the two linear upward sections it can be suggested that the MICP curves from the CC sample and the WS MICP curve are similar in shape but are offset to the WS MICP

curve predicting higher pressure for the same mercury saturation (Appendix E Figure E-79).The T_2 distributions used to create the WS MICP curve over this interval have some agreement with one another showing a similar shape (Appendix E Figure E-80). Notably, the sample from 2842.87 m at the shallowest depth shows more contrast than the other three samples.

The WS MICP curve at 2843.42 m is similar to the CC sample MICP curve (Appendix E Figure E-81). The MICP curves do have some disparity in the maximum inflection points. As a result of the disparity, the WS MICP curve underestimates the threshold pressure and subsequently the seal capacity. The T_2 distributions over the interval show some agreement with differences in shape and peak intensity (Appendix E Figure E-82).

The WS MICP curve created for the depth interval 2843.61 m has a similar shape to the CC MICP curve (Appendix E Figure E-83). The WS MICP curve has a slightly earlier maximum point of inflection and shows less pore space being invaded at initial pressures unlike the CC sample. The CC sample is likely being affected by conformance. The T_2 distributions over the sampling interval show some agreement in shape, peak location and peak intensity (Appendix E Figure E-84). Notably, the measurement from 2843.33 m has a peak at approximately 1 msec, of lower intensity and slightly different shape.

The WS MICP curve at 2844.08 m is similar to the CC sample MICP curve (Appendix E Figure E-85). Both the maximum inflection point and the subsequent upward linear curve match. There is a slight discrepancy in MICP curves between 0 % and 10 % mercury saturation. The T_2 distributions over this interval are similar in shape, peak locations and peak intensity (Appendix E Figure E-86). The T_2 distribution from 2844.24 m has a slight offset in the peak at 1 msec and a higher intensity peak at 100 msec.

Discussion: The threshold pressures interpreted from the WS MICP curves follow a similar trend to that observed in the CC sample threshold pressures; i.e. high threshold pressures are interpreted by both techniques and low threshold pressures are interpreted by both techniques. However, the exact value does vary considerably and more so where the threshold pressures are higher i.e. sample 2841.21 m where there is a 4272 psia difference. This is a result of the logarithmic scale on the graph where small changes in the position of the maximum inflection point lead to large changes in the interpreted threshold pressures. In conjunction with this, for the example above, the CC sample 2841.3 m (7 cm deeper) has an interpreted threshold pressure of 5984 psia (~1600 psia greater) and this zone would have been used in the production of the WS MICP curve. Thus the WS MICP curve may be

representative of the 80 cm rock interval and the CC MICP curve may be representative of the core sample but the core sample is unlikely to be representative of the 80 cm interval used to create the WS MICP curve. This is supported by the CC sample MICP curves having threshold pressures differing by 1600 psia 7 cm apart.

The maximum CO_2 column heights do vary considerably between the WS MICP curves and the CC MICP curves (up to 280 m for sample 2841.3 m). However, often this variation is not more than the variation due to the change in contact angle from 0 ° to 60 °. Moreover, the column heights for the WS MICP curves do follow the same trend as the column heights for the CC MICP curves; high and low relative column heights are interpreted at the same location by both techniques. This suggests that the technique is working adequately over this formation.

The WS MICP curves are generally similar to the MICP curves from the CC samples. However, there are three exceptions; samples 2837.57 m, 2840.66 m and to a lesser extent 2843.08 m. The lack of agreement in MICP curves has a strong relationship with the lack of agreement between the T_2 distributions and vice versa. The sample location at 2840.66 m (Appendix E Figure E-68) has T_2 distributions that have peaks of different intensities and at different relaxation times. The sample location at 2837.57 m (Appendix E Figure E-66) has T_2 peaks in similar alignment, however, the peaks vary significantly in intensity and there is a peak at approximately 200 msec for measurement at 2837.84 m that isn‘t observed in the other samples. The T_2 distribution for the sample at 2843.08 m has considerable variation in T_2 distributions between 5 msec and 90 msec which is likely to have contributed to the discrepancy in the position of the linear upward trend of the MICP curve. This is further complicated by the MICP curve that required re-analysis as it is unlikely to be representative. However, the similar samples at 2841.21 m, 2841.3 m, 2841.66 m, 2841.99 m, 2843.42 m, 2843.61 m and 2844.08 m show much better agreement between T_2 distributions from the 0.8 m interval to produce the WS MICP curve. This indicates that the rock volume over the 0.8 m interval is much more uniform than in the three exceptions. Thus, the three exceptions where there is a poor agreement between the WS MICP curves and the CC MICP curves is a result of the 0.8 m interval over which the WS MICP curve was constructed being heterogeneous and the CC sample not being representative of the larger volume. This can be observed where CC samples are taken in close proximity to one another and yet show considerable variation; samples at 2841.21 m and 2841.30 m. Thus the technique is working accurately and both the CC and WS MICP curves are accurate but are representative of different sample volumes.

7.3.4 **Mena Murtee-1, Darling Basin**

Please see section 3.7.1 for Mena Murtee-1 well description.

Methodology modifications specific to Mena Murtee-1 analysis: There was a depth discrepancy for three CC samples (MM1-041LE2, MM1-043-LE2 and MM1-044). The location of the MICP analysis relative to the laboratory NMR analysis is slightly offset. This has meant that sample locations are up to 1.29 m apart which needs to be taken into account when comparing the CC and LS MICP curves. The correction for the pore body to pore throat ratio for the laboratory NMR data was 100. The WS MICP curves were generated for the MICP sample location not the location of the laboratory NMR. The WS MICP curves had a pore body to pore throat correction of 4 applied which best aligned the WS MICP curves to the CC MICP curves.

The following samples were analysed in 2016 at the Particle and Surface Sciences; MM1-11, MM1-15 and MM1-50Von request of this study.

Results: The synthetic MICP curves generated from laboratory NMR data have interpreted threshold pressures in general agreement with the interpreted threshold pressures from CC samples (Table 7-4) excluding the samples MM1-11, MM1-15 and MM1-50V. The synthetic MICP curves generated from the well log have threshold pressures that show no agreement with the CC sample threshold pressures or the threshold pressures predicted from LS MICP curves. The well threshold pressures show no pattern or consistency with the CC samples and their interpreted threshold pressures. All threshold pressures interpreted from the synthetic well log NMR are indicative of reservoir intervals.

Table 7-4: Mena Murtee-1 threshold pressures from MICP CC samples, LS MICP curves and WS MICP curves.

Sample	Sample Depth MICP (m)	Sample Depth Lab NMR (m)	MICP Threshold Pressure (psia)	Lab Synthetic MICP Threshold Pressure (psia)	Well Synthetic MICP Threshold Pressure (psia)	Difference MICP Lab (psia)	Difference MICP Well (psia)
MM1-11	1604.965	1604.965	66	370	34	304	-32
MM1-15	1606.91	1606.91	2937	457	34	-2480	-2903
MM1-036-LE	1629.05	1629.05	9	3	50	-6	41
MM1-037V	1629.98	1629.98	10	6	54	-4	44
MM1-041-LE2	1859.75	1859.025	1368	1318	31	-50	-1337
MM1-043-LE2	1865.06	1866.035	967	1466	31	499	-936
MM1-044	1872.32	1873.03	968	960	50	-8	-918
MM1-50V	2035.39	2035.39	292	1067	60	775	-232

The maximum CO_2 column height retentions generated from LS mercury injection data are similar with maximum CO_2 column heights for the CC samples (Figure 7-4). The sample from MM1-15 shows the most variation in maximum CO_2 column heights between the LS and CC MICP curves beyond the range in maximum column height as a result of contact angle variation between 0 ° and 60 °. The maximum CO_2 column height retentions from the synthetic NMR well log data show no agreement with the CC or laboratory NMR maximum CO_2 column heights. The wellbore NMR maximum CO_2 column heights are all indicative of non-sealing intervals.

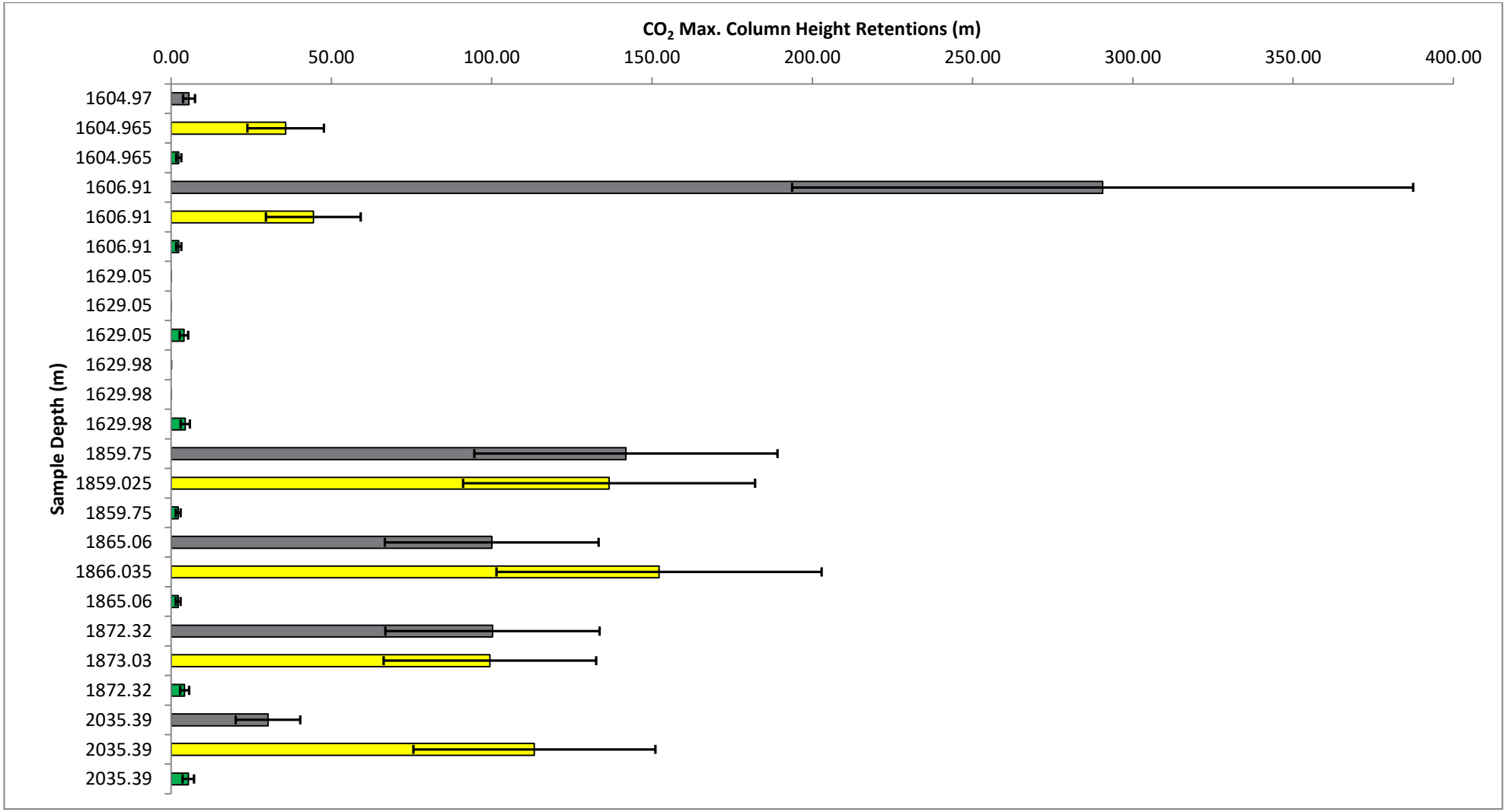

Figure: 7-4: The maximum CO_2 column height retentions from CC samples (grey), laboratory synthetic MICP curves (yellow) and well synthetic MICP curves (green) over the Ravendale Formation, Mena Murtee-1. The error bars represent the range of contact angle (brine/ CO_2 / rock) from 0 ° (right) and 60 ° (left).

The LS MICP curve at 1604.965 m (MM1-11) and CC MICP curve are in a similar position on the graph but show poor agreement in shape (Appendix E Figure E-87). The CC MICP curve has higher initial mercury saturation than the LS MICP curve. The synthetic MICP curve generated from the NMR well log has no agreement in shape or position with either the CC sample or LS MICP curves. The T_2 distributions from the well log used to produce the synthetic MICP curve are in reasonable agreement with one another with slight variances in the peak intensities and location at ~40 msec and slight variances in peak intensity at 900 msec (Appendix E Figure E-88). The T_2 distribution used to create the LS MICP curve is in poor agreement with the well log T_2 distribution for the same depth (Appendix E Figure E-89). The primary peak for the Laboratory T_2 distribution is occurring at 1000 msec while the well log T_2 distribution has two dominant peaks at ~30 msec and 900 msec.

The LS MICP curve at 1606.91 m (MM1-15) is in poor agreement in both shape and position with the CC MICP curve (Appendix E Figure E-90). The LS MICP curve has lower initial mercury saturation up to ~450 psia after which there is a maximum inflection point and a steep linear upward section while the CC MICP curve is more progressive. The maximum inflection point is occurring at ~3000 psia and the upward linear section of the MICP curve is occurring at much higher pressure than observed in the LS MICP curve. The WS MICP curve shows no relationship to the CC MICP curve. The T_2 distributions used to generate the WS MICP curve show poor agreement in both peak location and intensity (Appendix E Figure E-91). The laboratory T_2 distribution has a primary peak occurring at 1000 msec that is similar to the coherent peak observed in the well T_2 distributions occurring at ~900 msec (Appendix E Figure E-92).

The LS MICP curve for the sample at 1629.05 m (MM1-036-LE) is in nearly perfect agreement with the CC MICP curve; both shape and position on the graph (Appendix E Figure E-93). The WS MICP curve is similar in shape to the CC MICP curve but is significantly offset to higher pressure. The well T_2 distributions show poor agreement between one another in peak location, shape and intensity over the 1.6 m interval (Appendix E Figure E-94). The laboratory T_2 distribution is similar in shape to the well T_2 distribution measurements from 1629.2 m - 1629.8 m but is offset to higher relaxation times; 500000 msec as opposed to 500 msec respectively (Appendix E Figure E-95).

The LS MICP curve at a depth of 1629.98 m (MM1-037V) has a similar shape to the CC MICP curve but is significantly offset to lower pressure for the same mercury saturation (Appendix E Figure E-96). The LS MICP curve also has the inflection point occurring at lower pressures and higher mercury saturations than the CC MICP curve. The WS MICP

curve has no agreement with the CC MICP curve in both shape and position on the graph. The well T_2 distributions are similar with one another with only slight variations in peak intensities (Appendix E Figure E-97). The laboratory T_2 distribution is similar in shape to the well T_2 distributions. However, the laboratory T_2 distribution is offset to higher relaxation times (Appendix E Figure E-98).

The LS MICP curve at 1859.025 m (MM1-041-LE2) next to the CC MICP curve at 1859.75 m is in a similar position on the graph and has a similar shape (Appendix E Figure E-99). The MICP curve from the CC sample has higher mercury saturation at lower pressure to the LS MICP curve. The WS MICP curve generated from the NMR well log has no agreement in shape or position on the graph with either the CC sample or laboratory NMR MICP curves. The T_2 distributions from the well log used to produce the synthetic MICP curve are in agreement with one another with slight variances in the peak intensity at ~900 msec and a slight peak at 5 msec for the measurement at 1859.6 msec (Appendix E Figure E-100). The laboratory T_2 distribution is similar to the well T_2 distributions with a slight offset (Appendix E Figure E-101).

The LS MICP curve at 1866.035 m (MM1-043-LE2) next to the CC sample MICP curve at 1865.06 m depth have a similar shape and position to one another on the graph (Appendix E Figure E-102). However, the CC MICP curve has higher mercury saturation at low-pressure that is not observed in the LS MICP curve. The WS MICP curve has no agreement in shape or position on the graph with either the CC or LS MICP curves. The T_2 distributions between 1864.4 m and 1865.2 m are similar to one another with only slight differences in peak intensity at ~900 msec (Appendix E Figure E-103). The samples below this, however, show completely different T_2 shape distributions with an initial peak at ~10 msec and a secondary peak of similar intensity at 500-700 msec. The laboratory T_2 distribution is similar to the well T_2 distributions between 1864.4 m and 1865.2 m (Appendix E Figure E-104).

The LS MICP curve at 1873.03 m (MM1-044) next to the CC sample MICP curve at 1872.32 m depth have a similar shape and position to one another on the graph (Appendix E Figure E-105). There is slightly higher mercury saturation for the same pressure observed in the MICP curve from the CC sample and a slight discrepancy in the trajectory of the linear upward section post the maximum inflection point. The synthetic MICP curve generated from the NMR well log has a similar position on the graph to the CC and synthetic MICP curves, however, it has a poor agreement in shape and maximum inflection point location. The T_2 distributions used to generate the WS MICP curve show poor agreement between

one another (Appendix E Figure E-106). The laboratory T_2 distributions show no alignment with any of the peak locations of the T_2 distributions from the well log (Appendix E Figure E-107).

The LS MICP curve at 2035.39 m (MM1-50V) and CC MICP curve have a similar shape on the graph but are offset from one another (Appendix E Figure E-108). The LS MICP curve shows lower initial mercury saturation and, a maximum inflection point and linear upward trend at higher pressure. The synthetic MICP curve generated from the NMR well log has no agreement in shape or position on the graph with either the CC sample or laboratory NMR MICP curves. The T_2 distributions from the well log used to produce the synthetic MICP curve are in no agreement with one another with variation in peak position and intensity (Appendix E Figure E-109). The T_2 distribution used to create the LS MICP curve has a primary peak at a similar relaxation time to some of the well measurements; 2035 m, 2035.2 m, 2035.4 m and 2035.8 m (Appendix E Figure E-110).

Discussion: The interpreted threshold pressures from the LS MICP curves have mixed results when compared to the interpreted threshold pressures from the CC MICP curves. The original samples analysed with MICP have a better agreement between the interpreted threshold pressures, however, the samples taken later and analysed on the mercury porosimeter at the Particle and Surface Sciences show less agreement. It is suggested that the changes may be a result of heterogeneity, warehousing, incorrect interpretation of pore body to pore throat ratio for the intervals either side of 1629.05 m and 1873.03 m or that a property unique to this interval is leading to a shift in the T_2 distribution and the corresponding LS MICP curves. Without further information, it is difficult to determine the cause of the poor relationship in threshold pressures observed in these samples.

The interpreted threshold pressures from the WS MICP curves have a poor correlation with the interpreted threshold pressures from the CC MICP curves. The threshold pressures from the WS MICP curves are all interpreted as reservoir intervals suggesting that either the wellbore NMR has been unable to record the short T_2 relaxation times corresponding to small pores found in sealing intervals or that there are reservoir intervals within the 1.6 m interval used to produce the WS MICP curve. There are clear differences in the shape of the T_2 distribution peaks and the position of the peaks between the wellbore NMR and laboratory NMR T_2 distributions suggesting that the pore body network is differing between the two samples volumes and hence indicating that heterogeneity is affecting the results of the WS MICP curve and subsequently the interpreted threshold pressure.

The calculated CO_2 column heights are reflective of the interpreted threshold pressures. The calculated CO_2 column heights from the LS MICP curve and the CC MICP curves are similar for the samples between 1629.05 m and 1873.03 m with all variation between calculated column heights below that of the variation due to contact angle change between 0 ° and 60 °. The samples outside of this interval have significant variation between the maximum calculated CO_2 column heights from the threshold pressures interpreted from the LS and WS MICP curves. This variation is beyond the variation due to contact angle change between 0 ° and 60 °. The maximum calculated CO_2 column heights from the threshold pressures interpreted from the WS MICP curve are all indicative of reservoir rock and show no relationship with the maximum calculated CO_2 column heights from the LS and CC MICP curves.

The LS MICP curves have three trends occurring; similarity of the LS MICP curve in shape and position on the graph to the CC MICP curve (1629.05 m), similarity in shape of the LS MICP curve but offset from the CC MICP curve (1606.91 m, 1629.98 m, 1859.75 m, 1865.06 m, 1872.32 m and 2035.39 m) and poor/ little agreement of the LS MICP curve with the CC MICP curve (1606.91 m). The samples with similar LS and CC MICP curves suggest both techniques are measuring the same pore network and that the correction between pore body and pore throat is correct. The samples with similarity in shape but offset from one another suggest that both techniques are measuring the pore network but the correction between pore body and pore throat is incorrect or the surface relaxivity efficacy has changed. This has occurred in the majority of the samples. However, there is no trend in the offset suggesting that the correction factor is not appropriate over the well and may only be appropriate over formations. The samples with no agreement in shape and position suggest that the two techniques are measuring different pore networks and that heterogeneity is affecting the results.

The WS MICP curves show a similar shape to the CC and LS MICP curves in the two reservoir samples 1629.05 m and 1629.98 m but are offset from one another. This is to be expected as the pore body to pore throat correction was only applicable for sealing intervals. The other sealing samples have WS MICP curves with no agreement in shape or position on the graph to the CC MICP curves suggesting the NMR tool is unable to measure short T_2 relaxation times or that there is significant heterogeneity within the 1.6 m interval used to produce the WS MICP curve. It is suspected that given the agreement between the T_2 distributions used to produce the WS MICP curves that both factors are in effect. Poor agreement in the WS MICP curve with the CC MICP curve can be observed in sample

1859.75 m (Appendix E Figure E-99) where the T_2 distributions are in agreement (Appendix E Figure E-100) and to a lesser extent sample 1604.965 m (Appendices Figure E-87, E-88) suggesting heterogeneity is not in effect. Poor agreement in the WS MICP curve with the CC MICP curve can also be observed in sample 1606.91 m, 1865.06 m, 1872.32 m and 2035.39 m (Appendix E Figure E-90, E-102, E-105 and E-108 respectively) where the T_2 distributions are in general poor agreement over the 1.6 m interval (Appendix E Figure E-91, E-103, E-106, E-109 respectively) suggesting that heterogeneity is in effect.

7.3.5 **Gorgon CO2 Data Well-1 & Data Well-1ST1, Barrow Island**

Please see section 3.5.3 for the Gorgon CO2 Data Well-1 & Data Well-1ST1 well description.

The production of synthetic MICP curves from the Thebe-2 NMR well log was unsuccessful. The following explains the likely causes; either technique, log or MICP analysis issues.

Methodology modifications specific to Gorgon CO2 Data Well-1& Data Well-1ST1 analysis: A selection of CC MICP curves covering high sealing capacity, low sealing capacity and reservoir rock were selected to compare to the WS MICP curves. Once it was established that the technique was not successful only a few of the samples were presented in the following although many more were tested. The WS MICP curves have a pore to pore throat correction of 4 applied which best aligned the high sealing capacity WS MICP curves to the CC MICP curves.

The CO_2 maximum column height retentions were calculated with the brine salinities recorded in Daniel, (2006) for the formations.

Results: The synthetic MICP curves generated from well log NMR data have interpreted threshold pressures similar to the CC sample MICP curves over high capacity sealing intervals; both the shape and position of the curve on the graph (Table 7-5). However, the low capacity sealing intervals and especially the reservoir zones show a poor correlation in MICP curves (both shape and position on the graph). This has resulted in threshold pressures in reasonable agreement for the Barrow Group sample at 2023.82m. However, the reservoir samples at 2046.25 m and 2295.6 m have synthetic threshold pressures indicative of sealing intervals while the CC MICP curve threshold pressures indicate reservoir rock.

Table 7-5: Gorgon CO2 Data Well-1 & Data Well-1ST1 threshold pressures from MICP CC samples and WS MICP curves.

Sample	Sample Depth MICP (m)	MICP Threshold Pressure (psia)	Well Synthetic MICP Threshold Pressure (psia)	Difference MICP Well (psia)
Barrow Group	2023.82	6985	5407	-1578
Dupuy Formation	2046.25	10	2865	2855
Dupuy Formation	2243.69	25	585	560
Dupuy Formation	2267.73	295	1518	1223
Dupuy Formation	2307.6	18	804	786
Dupuy Formation	2335.77	347	426	79
Dupuy Formation	2367.53	13	426	413

The maximum CO_2 column heights generated from the threshold pressures interpreted from WS and CC MICP curves are similar over the Barrow Group sealing interval at 2023.82 m with a difference less than the difference as a result of the contact angle being varied between 0 ° and 60 ° (Figure 7-5). The maximum CO_2 column heights generated for other samples show that the synthetic MICP curves are consistently having a threshold pressure indicative of sealing intervals while the CC samples are indicative of reservoir or low sealing capacity intervals. The variation observed is greater than the variation as a result of changing the contact angle between 0 ° and 60 °.

Figure 7-5: The maximum CO_2 column height retentions from CC samples (grey) and synthetic MICP curves (yellow) for the Barrow Group and Dupuy Formation, Gorgon CO2 Data Well-1 & Data Well-1ST1. The error bars represent the range of contact angle (brine/ CO_2 / rock) from 0 ° (right) and 60 ° (left).

The WS MICP curve at the sampling depth of 2023.82 m is in a similar position on the graph to the CC sample MICP curve with a slight offset towards higher pressure for the same mercury saturation (Appendix E Figure E-111). The synthetic MICP curve has a similar general shape, however, the synthetic MICP curve has lower saturation at pressures between 200 psia and 8000 psia and a more gradual incline of the MICP curve thereafter. The T_2 distributions used to produce the synthetic MICP curve are similar in shape with slight variation in the peak intensity at ~3 msec (Appendix E Figure E-112).

The WS MICP curve at the sampling depth of 2046.25 m has no agreement with the CC sample MICP curve; both position on the graph and shape (Appendix E Figure E-113). The T_2 distributions used to produce the synthetic MICP curve show some agreement in shape with discrepancies in the intensity of the peak at ~5 msec (Appendix E Figure E-114). The T_2 distributions indicate that there are some pores in the range between ~20 msec and 3000 msec, however, most of the pores are between 0.3 msec and ~20 msec indicative of small pores.

The WS MICP curve at the sampling depth of 2243.69 m has a reasonable agreement in shape but poor agreement in graph position with the CC sample MICP curve (Appendix E Figure E-115). The T_2 distributions used to produce the synthetic MICP curve are similar to one another (Appendix E Figure E-116). Note the T_2 distributions from the two deepest measurements (2243.1375 m and 2243.328 m) have slight offset and reduced peak intensity.

The WS MICP curve at the sampling depth of 2267.73 m has a reasonable agreement in graph position and to a lesser extent shape with the MICP curve from the CC sample; most notably the disparity in the location of the maximum inflection point and subsequent linear upward trend to approximately 40 % mercury saturation (Appendix E Figure E-117). These larger pore throats are not observed in the synthetic MICP curve. This has led to a significant disparity in interpreted threshold pressures. The T_2 distributions are in agreement in shape and peak intensity with slight offsets observed in the major peak at approximately 9 msec (Appendix E Figure E-118). There are varied, minor peaks observed between 300 msec and 3000 msec.

The WS MICP curve at the sampling depth of 2307.60 m has no agreement with the CC sample MICP curve; both position on the graph and shape (Appendix E Figure E-119). The T_2 distributions used to produce the synthetic MICP curve are similar except for the two shallowest T_2 distributions (2306.955 m and 2307.1455 m) which have a secondary peak at ~150 msec (Appendix E Figure E-1120).

The WS MICP curve at the sampling depth of 2335.77 m is in agreement with the CC MICP curve; both position on the graph and to a lesser extent shape (Appendix E Figure E-121). The MICP curve has a slightly earlier maximum inflection point and a slight deflection thereafter as the curve approaches 50 % mercury saturation. The T_2 distributions have a similar position on the graph but show some variation in the two peaks and their intensities (Appendix E Figure E-122).

The WS MICP curve at the sampling depth of 2367.53 m has no agreement with the CC sample MICP curve; both position on the graph and shape (Appendix E Figure E-123). The T_2 distributions are similar in position on the graph and to a lesser extent shape about which there is a slight variation between 1 msec and 10 msec (Appendix E Figure E-124).

Representative sections of the well composite log including the T_2 distributions over the cored interval have been added to Appendix E, Figure E-125 and E-126. It can be observed from Appendix E Figure E-125 that the high gamma is associated with T_2 distributions skewed to the low T_2 relaxation times and vice versa over the well log until a depth of 1960 m. A low gamma zone (65API) can be observed between 1745 m and 1765 m with associated long relaxation T_2 distributions. The permeability log over this interval approximates 1000 md with one major drop in permeability associated with a peak in gamma (100API) at ~1762.5 m. This log was taken first and subsequently, the second part of the well was cored and then logged. The composite log interval from 2300 m to 2450 m has few high gamma zones (2008 m- 2030 m and 2267 m-2279 m). The log has a low gamma interval between 2340 m and 2370 m (Appendix E Figure E-126) that is slightly higher than the low gamma zone observed in the log above between 1745 m and 1765 m. However, in this instance, the T_2 distribution has a strong cut off at 200 msec. This cut off is observed over the entire interval shown other than in the minor high gamma zones (Appendix E Figure E-126). The permeability log over this interval approximates a maximum of ~100 md with major drops in permeability associated with peaks in gamma (2354 m, 2360 m and 2364 m).

The NMR log also had a number problems over the well. The tool failed and was abandoned for the first suite 2 run 2. The failure was a result of the tool becoming stuck and not being able to retune the tool. During suite 3 run 4 the software compensation failed due to a software bug. During the fourth run, the logging software froze and had to be rebooted. During suite 6 run 3 the run had to have more weight added to the tool but was successful. Also, there are three instances during the 1960 m to 2620 m interval for which there are

noise flags, BADF CMR, wait for flags, tuning mode, and no update counts recorded on the log (Beacher, 2007).

The conventional core also had a gamma and permeability log run (Appendix E Figure E-127). The gamma log over the interval between 2340 m and 2370 m approximates 70API with the odd spike up to 100 API. The permeability log over the CC interval approximates 1000 md that has a number of low spikes in permeability that often correspond to gamma spikes (100 API).

Discussion: The threshold pressures interpreted from the WS MICP curves have worked quite well for the samples with high sealing capacity; 2023.82 m, 2335.77 m and to a lesser extent 2267.73 m. However the conventional samples with low sealing capacities/ reservoir properties have poor to no agreement with the synthetic MICP curves and the threshold pressures reflect this; 2046.25 m, 2307.60 m, 2367.53 m and to a lesser extent 2243.69 m.

The maximum column heights follow the trend of the threshold pressures with major discrepancies for samples 2046.25 m, 2307.60 m, 2267.73 m, 2307.6 m and 2367.53 m for which the differences in calculated column heights are greater than the variation observed as a result of contact angle change between 0 ° and 60 °.

The T_2 distributions over the sampling intervals for all samples show a generally similar correlation suggesting that the 1.6 m interval for which the measurement are taken are fairly homogenous with only slight variations. Unusually there is little or no signal in the long relaxation times for the reservoir/ low sealing capacity intervals that would be expected as suggested by the CC sample MICP curves.

The NMR log and possibly the gamma log to a lesser degree over the cored interval from 1960-2620 m are dubious. Upon inspection of the permeability core and well log, there are strong indications of significant differences; there is approximately a 900 md discrepancy between the well log and the core log over the interval 2340 m to 2370 m. However, as the permeability was logged with different tools, it is not possible to make a definitive decision on the accuracy of the well log. The most definitive evidence for the existence of a problem with the log is that the initial CMR log to 1960 m has T_2 distributions with short relaxation times and long relaxation times changing with the gamma log. However, over the interval from 1960 m to 2620 m, there are no/ minimal T_2 distributions with relaxation times greater than ~200 msec. Furthermore, these T_2 distributions appear to align perfectly for 100 m intervals in two sections of the well which is unusual.

7.3.6 **Thebe-2, Exmouth Plateau**

Please see section 3.5.2 for Thebe-2 well description.

Methodology modifications specific to the Thebe-2 analysis: Thebe-2 encountered gas in the Mungaroo Formation. The gas affects the relaxation rate and hydrogen index comparatively to the brine encountered throughout the rest of the well. The CMR log subsequently underwent a density correction to remove the gas effect as described by Freedman et al., (1998) and Freedman (2006).

The WS MICP curves had a pore to pore throat correction of 18 applied which best aligned the high sealing capacity WS MICP curves to the CC MICP curves.

The depth correction applied was +1.15 m to the core depth to match the wireline logging depth. This was achieved using the borehole image log and core photographs.

Results: The threshold pressures interpreted from the WS MICP curves are almost consistently underestimating the high sealing capacity rock and overestimating the low sealing capacity/ reservoir rocks (Table 7-6). The exception to this is the three deepest reservoir rock samples where the synthetic threshold pressures are similar to that derived from the CC sample MICP curves. The synthetic MICP curves, in general, have a poor agreement with the MICP curves from CC samples; exceptions include sample 2270.5 m, 2382.81 m and to a lesser extent sample 2247.65 m and 2277.05 m.

Table 7-6: Thebe-2 threshold pressures from MICP CC samples and WS MICP curves.

Sample	Sample Depth MICP (m)	MICP Threshold Pressure (psia)	Well Synthetic MICP Threshold Pressure (psia)	Difference MICP Well (psia)
Brigadier Formation	2183.5	41	637	596
Brigadier Formation	2189.52	100	463	363
Mungaroo Formation	2247.65	2930	1202	-1728
Mungaroo Formation	2248.35	5	1202	1197
Mungaroo Formation	2260.2	14	463	449
Mungaroo Formation	2270.5	3513	1202	-2311
Mungaroo Formation	2276.95	7	637	630
Mungaroo Formation	2277.05	2476	637	-1839
Mungaroo Formation	2298.28	16	69	53
Mungaroo Formation	2382.81	16	14	-115

The maximum CO_2 column heights from the interpreted threshold pressures from the generated WS mercury injection data, in general, show poor agreement (Figure 7-6). The column heights interpreted from the WS MICP curves for the deepest two reservoir samples are an exception. The samples from shallower depths show that the reservoir intervals as interpreted from the CC sample MICP curves are being consistently estimated as having sealing properties while the samples that have high sealing capacity are being consistently estimated as having low sealing capacity.

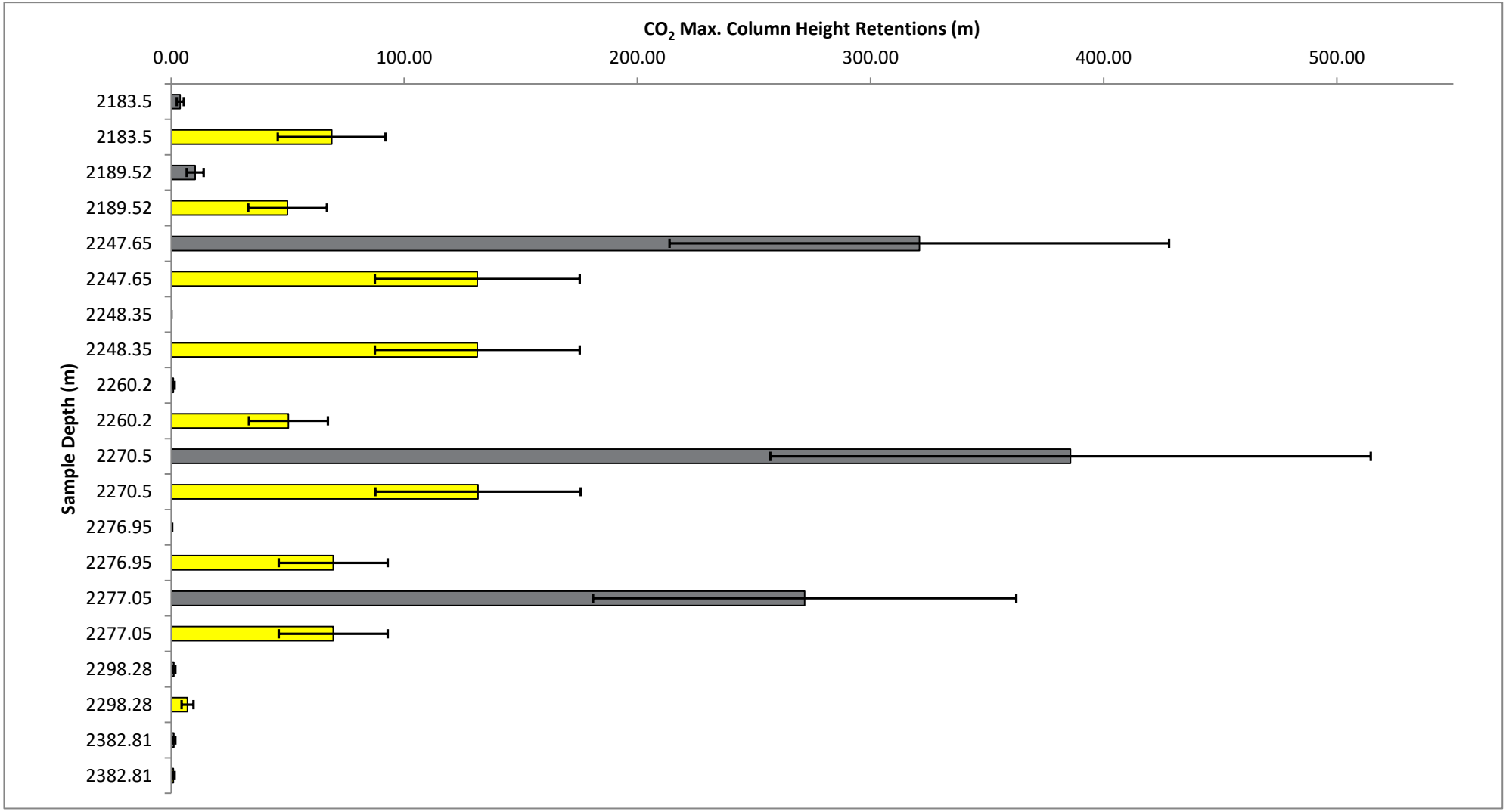

Figure 7-6: The maximum CO_2 column height retentions from CC samples (grey) and synthetic MICP curves (yellow) from the Brigadier and Mungaroo Formations, Thebe-2. The error bars represent the range of contact angle (brine/ CO_2 / rock) from 0 ° (right) and 60 ° (left).

The WS MICP curve at the sampling depth of 2183.5 m has a reasonable agreement in shape but poor agreement in position on the graph with the CC sample MICP curve (Appendix E Figure E-128). The T_2 distributions used to produce the synthetic MICP curve are in agreement with one another with only slight variations in peak intensity and near perfect agreement in peak position (Appendix E Figure E-129).

The WS MICP curve at the sampling depth of 2189.52 m has a reasonable agreement in shape but poor agreement in position on the graph in comparison to the CC sample MICP curve. The WS MICP curve is offset towards higher pressure for the same mercury saturation (Appendix E Figure E-130). The T_2 distributions used to produce the synthetic MICP curve are similar to one another; the position and intensity of the primary peak at approximately 5 msec (Appendix E Figure E-131). There is only slight variation in the secondary peak location and intensity at ~500 msec.

The WS MICP curve at the sampling depth of 2247.65 m has a similar general shape to the CC sample MICP curve. However, the CC MICP curve has a much higher mercury saturation at low pressures up to 40 % mercury saturation where both MICP curves match; both shape and position on the graph (Appendix E Figure E-132). The T_2 distributions used to produce the synthetic MICP curve show similar general agreement with one another (Appendix E Figure E-133). There is similarity in the graph location of the primary peak at ~4 msec with slight variations in intensity with depth, however, the secondary peak at approximately 100 msec shows some variation; both shape and intensity with depth.

The WS MICP curve at the sampling depth of 2248.35 m has no agreement in shape or position on the graph (Appendix E Figure E-134). The T_2 distributions primary peak show variation in intensity but have a similar position at ~3 msec (Appendix E Figure E-135). The secondary peak has variation in location and shape at ~100 msec.

The WS MICP curve at the sampling depth of 2260.2 m has no agreement in shape or position on the graph (Appendix E Figure E-136). The T_2 distributions primary peak at ~3 msec show some variation in location and intensity which vary with depth (Appendix E Figure E-137). There is also variation observed on the limb of the primary peak at ~90 msec followed by two minor peaks observed at ~250 msec and ~2000 msec.

The WS MICP curve at the sampling depth of 2270.5 m has agreement in general shape and position on the graph with the CC MICP curve although the CC MICP curve has much higher mercury saturation at low pressures up to 25 % mercury saturation where both MICP curves come into close agreement in both shape and position on the graph (Appendix E

Figure E-138). The T_2 distributions used to produce the synthetic MICP curve have a common primary peak at ~2 msec over the measurement interval; both graph position and intensity (Appendix E Figure E-139). The secondary peaks vary in intensity and graph position with the measurement depth from minimal to significant i.e. measurement 2271.2 m.

The WS MICP curve at the sampling depth of 2276.95 m has some similarities in shape and agreement in position on the graph with the CC sample MICP curve; the peak at 30 psia on the CC sample MICP curve is observed at 100 psia on the WS MICP curve, however, the mercury saturation at which it occurs is much higher for the CC MICP curve (Appendix E Figure E-140). The position of the WS MICP curve is offset in comparison to the CC MICP curve and has much lower mercury saturation for the same pressure. The T_2 distributions show some agreement with one another; there are two primary peaks at ~4 msec and ~250 msec with variations in intensity that vary with depth (Appendix E Figure E-141).

The WS MICP curve at the sampling depth of 2277.05 m has a general agreement in shape and position with the CC sample MICP curve (Appendix E Figure E-142). However, the WS MICP curve is offset at low pressure and high pressure from the CC MICP curve. The T_2 distributions show reasonable agreement with one another; there are two primary peaks at ~4 msec and ~250 msec with variations in intensity that vary with depth (Appendix E Figure E-143).

The WS MICP curve at the sampling depth of 2298.28 m has some similarities in shape with the CC sample MICP curve; there is a minor inflection in both MICP curves at approximately 25 % mercury saturation and the maximum inflection points occur at approximately 5 % mercury saturation (Appendix E Figure E-144). The position of the WS MICP curve is offset towards higher pressures for the same mercury saturation. Further, at approximately 50 % mercury saturation, the WS MICP curve appears more concave whereas the CC MICP curve appears more convex. The T_2 distributions used to produce the synthetic MICP curve are similar except the shallowest measurement at 2296.6 m (Appendix E Figure E-145). The T_2 distributions show slight variations in peak intensity, but peak location remains consistent.

The WS MICP curve at the sampling depth of 2382.81 m is in agreement with the CC MICP curve; both shape and position on the graph (Appendix E Figure E-146). The WS MICP curve has a slightly earlier maximum inflection point and a slightly later deflection thereafter as the curve approaches 65 % mercury saturation. The WS MICP curve also has

higher mercury saturation for the same pressure as opposed to the CC MICP curve. The T_2 distributions are similar with minor variations in the intensity of the primary peak at ~500 msec (Appendix E Figure E-147).

Discussion: The threshold pressures interpreted from the synthetic MICP curves have a rather poor agreement with those interpreted from CC samples other than; 2276.95 m, 2298.28 m and 2382.81 m samples. The associated maximum CO_2 column heights derived from the threshold pressures show that the variation observed is greater than as a result of contact angle change between 0 ° and 60 °.

The WS MICP curves show significant discrepancies with the CC MICP curves which in turn has led to the inconsistencies in threshold pressures which suggest the technique of producing synthetic MICP curves from the NMR log is unsuccessful. However, upon review of samples in close proximity to one another, it can be observed that significant variation in rock properties occur within the 1.6 m interval used to produce the synthetic MICP curve. The CC sample at 2247.65 m depth and the sample at 2248.35 m depth are 0.7 m apart and show contrasting sealing capacities. The CC sample at 2247.65 m has an MICP curve with a threshold pressure of 2930 psia while the CC sample (2248.35 m) below has an MICP curve with a threshold pressure of 5 psia. The WS mercury curve created over both sample intervals has a threshold pressure of 1202 psia. Thus, it is suggested that the NMR tool is averaging the rock properties over the interval to produce a synthetic mercury curve representing both rock types. This is further evidenced by the CC samples at 2276.95 m and 2277.05 m which have contrasting MICP curves while the WS MICP curve made from the same eight measurements for both samples appears to average the pore throat properties over the 1.6 m interval. The threshold pressures reflect this change in MICP curves; the sample from 2276.95 m has a threshold pressure of 7 psia while the sample from 2277.05 m has a threshold pressure of 2476 psia. The WS MICP curve has a threshold pressure of 637 psia. If indeed the device is averaging the properties then this would suggest that the 1.6 m interval consists of more of the rock type at 2276.95 m than the rock type at 2277.05 m.

The T_2 distributions over the 2247.65 m and 2248.35 m intervals show minimal variation between one another over the 1.6 m interval and certainly not the variation that would be expected as suggested from the MICP curves from the CC samples. This suggests that the NMR tool cannot resolve small-scale heterogeneity (> 0.2 m) and that the tool while measuring in 0.2 m intervals measures a much larger volume than is suggested by the measurement interval. To a lesser extent, this is also observable with the samples from

2276.95 m and 2277.05 m although the T_2 distributions over this interval show more variation.

The results and their interpretation pose both a problem and an advantage in the production of synthetic MICP curves over heterogeneous lithologies. It is envisaged that this technique would be utilised with minimal CC material or SWC where it will be difficult to assess the scale of heterogeneity over which the sample was taken and the subsequent synthetic MICP curve will be produced. Hence, the sample which will be used as the calibrator and subsequently derive the correction factor will need to be carefully selected. Thus, if the core sample used to calibrate the synthetic MICP curve was selected at either 2247.65 m or 2248.35 m then both corrections would result in synthetic MICP curves that are inaccurate. However, if the sample for the calibration is from a relatively homogeneous interval and the correct shift has been made to the samples then the technique will be able to produce synthetic MICP curves over the entire formation evaluating 1.6 m at a time and accounting for the heterogeneity observed in the formation that won‘t be captured by the small samples taken for MICP analysis. This will be advantageous over heterogeneous intervals where CC samples will provide analysis that is representative of the sample but not of the formation as observed with the samples at 2247.65 m and 2248.35 m and, 2276.95 m and 2277.05 m.

7.4 CHAPTER 7 DISCUSSION

The LS MICP curves have the best agreement with the CC MICP curves. This translates to having the best agreement in threshold pressures and derived maximum CO_2 column heights. This is a result of the greater sensitivity of laboratory based NMR equipment, the proximity of samples being analysed by MICP and NMR and the smaller rock volume being analysed by laboratory NMR. A larger rock volume increases the likelihood of the sample taken for MICP analyses not being representative and thus the two instruments measuring two different pore networks.

A maximum variation in threshold pressure of 324 psia and 3 psia over low seal capacity rock and reservoir rock respectively was observed in Tindilpie-11. In Mena Murtee-1 this jumped to 499 psia for sealing rock and 4 psia for reservoir rock excluding the three samples taken later which are in poor agreement (MM1-11, MM1-15 and MM1-50V). The maximum CO_2 column heights are all in agreement with no variation beyond the variation as a result of varying the contact angle between 0 ° and 60 ° excluding the three samples above. The LS MICP curves show similar to excellent agreement with the CC MICP curves that is not always evident in the interpreted threshold pressures due to a mismatch in the maximum inflection point of the MICP curves.

The WS MICP curves have mixed results; Redman-1 has been successful while CRC-2, Thebe-2 and Tindilpie-11 have had mixed results. Gorgon CO2 Data Well-1 & Data Well-1ST1 and Mena Murtee-1 well logs were unsuccessful in producing accurate WS MICP curves.

Redman-1 demonstrates that the technique of producing synthetic MICP curves over a formation can be achieved successfully. The threshold pressures predicted from the synthetic MICP curves are observed to have significant differences to the CC MICP curves. However, the WS threshold pressures and the CC threshold pressures follow a similar trend over the 4 m of conventional core. Furthermore, where there is more than one CC sample taken within the 0.8 m interval used to construct the WS MICP curve, significant variation in the CC threshold pressures can be observed hinting at the heterogeneity (Table 7-3). It is thus suggested, while there are differences in the threshold pressures between the CC and WS threshold pressures, they are a result of the CC sample not being representative of the 0.8 m used to construct the WS MICP curve. Further, given the similarity of the WS synthetic and CC MICP curves, the differences in threshold pressures, while appearing large, are often only one or two pressure equilibrium points as a result of slight offset or slight changes in the shape of the MICP curves.

The laboratory results from Tindilpie-11 and Mena Murtee-1 in conjunction with the successful results from Redman-1 wellbore NMR have demonstrated that the technique of producing synthetic MICP curves from NMR analysis works. The mixed results observed in CRC-2, Thebe-2 and Tindilpie-11 are a likely result of three factors; the incorrect pore body to pore throat correction factor or change in surface relaxivity over different formations, the CC sample not being representative of the volume measured by the NMR tool and the accuracy of the NMR tool.

The CRC-2 WS MICP curves show a strong relationship with agreement in T_2 distributions and the agreement with the CC MICP curve suggesting that there can be significant heterogeneity over the 1.6 m interval used to construct the WS MICP curve. Further, the samples over the Paaratte Formation have had mixed results with a common offset of the similar shaped WS MICP curve to lower pressure for the same mercury saturation as the CC curve. This suggests that the pore body to pore throat ratio or the surface relaxivity is not valid for this formation while it worked rather well for the Pember Mudstone and Skull Creek Formation. The pore body to pore throat ratio may have been affected by bioturbation. It is unlikely to be a result of pore network heterogeneity as the T_2 distributions all show similar peak positions and alignment with the variation often only being in the

intensity of the peak. The T_2 peak position which relates to a T_2 time determines at what pressure the WS MICP curve begins its linear upward trend and thus its alignment with the CC MICP curve.

The Thebe-2 WS MICP curves show similar trends to CRC-2. The WS MICP curves for some samples have a similar shape to the CC MICP curves but are offset suggesting that the pore body to pore throat ratio is not correct for those samples. Further, while the T_2 distributions show similarity, the CC samples taken in close proximity to one another suggest significant heterogeneity and the subsequent WS MICP curve appears to have averaged these properties. This is a likely result of the CC sample not being representative of the 1.6 m interval used to construct the WS MICP curve. This occurred because of the fragility of the conventional core which led to samples being taken where rock fragments had dislodged from the conventional core. This was primarily in the sandstone lithology while the siltstone and mudstone intervals remained consolidated. Thus the CC samples were often sandstone which produced reservoir MICP curves while the siltstone and mudstone were rarely sampled. This sampling bias has affected the agreement of the WS MICP curves with the CC MICP curves. This highlights the importance of selecting a CC sample that is representative of the 1.6 m interval used to construct the WS MICP curve.

The Tindilpie-11 WS MICP curves appear rather primitive often failing to show a similar shape to the CC MICP curves. On inspection of the T_2 distribution, it can be observed that often there is little difference between the T_2 distributions with near perfect alignment of measurements from the 1.6 m interval. The subsequent WS MICP curves often show a very linear upward trend unlike that of the CC MICP curves. This linear trend suggests that all of the pore throats are of a uniform diameter which is not supported by the CC or LS MICP curves. It is thus suspected that the accuracy of the wellbore NMR tool is debatable.

The WS MICP curves for the Gorgon CO2 Data Well-1 & Data Well-1ST1 well was unsuccessful in identifying reservoir and low sealing capacity intervals. The T_2 distributions show a most unusual alignment of relaxation times terminating at approximately 200 msec with little to no distribution beyond this T_2 relaxation time. The lack of success in adequately producing synthetic MICP curves over low sealing capacity/ reservoir intervals is a direct result of the lack of long relaxation times observed in the well log (T_2 relaxation times all less than ~200 msec). Thus all reservoir intervals have sealing synthetic MICP curves and threshold pressures. It is considered highly unlikely that this alignment is a true of measurement of the Dupuy Formation reservoir intervals. Thus the NMR well log is dubious. It is thought that this peculiar T_2 distribution alignment may be a result of the NMR

tool becoming unstuck from the wellbore and measuring the mud and filter cake and not the formations (pers comm. Lionel Esteban, 2016). Alternatively, as the NMR tool was recorded as having problems in the WCR, it may have had a malfunction stopping the tool from recording T_2 relaxation times beyond 200msec.

The Mena Murtee-1 WS MICP curves are all indicative of reservoir to low sealing capacity formations. In the instances where the CC samples were of reservoir lithology, the WS MICP curves show a similar shape indicating that the NMR tool is measuring the pore bodies within the rock. Often the WS curves are offset but this is to be expected as the pore body to pore throat correction was selected for sealing formations. The WS curves for the sealing intervals show no shape agreement with the CC MICP curves for any of the sealing samples even where the agreement in the T_2 distributions is similar suggesting that it is unlikely that the NMR tool is measuring the small pores in these rock types and is the limiting factor, not the technique.

The variation in WS and MICP curves from CC samples in CRC-2, Thebe-2 and Tindilpie-11 show similar variation in shape agreement to those produced by Volokitin et al., (2001), Grattoni et al., (2003) and Mardi et al., (2014) whom all investigated the production of capillary pressure curves from NMR data.

The synthetic MICP curves of Al-Ghamdi, (2006) are distinctly different to the synthetic MICP curves produced in Section 7.3.3 for Redman-1. The similarity of WS and CC MICP curves in Section 7.3.3 suggests that the methodology used by Al-Ghamdi, (2006) to produce the synthetic MICP curves was not working adequately.

7.4.1 Methodology to use NMR Synthetic MICP Curves to Determine Seal Capacity and Perforation Zones for Hydrocarbon Reservoirs

Please see Appendix E.1 for a methodology to produce synthetic MICP curves to predict seal capacity and Appendix E.2 for a methodology to produce MICP curves to determine perforation zones in hydrocarbon reservoirs as a result of this study.

7.5 CHAPTER 7 CONCLUSIONS

The LS MICP curves have a consistently better agreement than the WS MICP curves because of the greater sensitivity of the laboratory NMR equipment and due to the reduced rock volume being measured. These results hint at the future possibilities, with the technological progression of NMR well tools, and what the sensitivities of the WS MICP curves might be.

The WS MICP curves have a complete mix of results due to suspected heterogeneity of the 1.6 m interval used to construct the WS MICP curve, the CC sample not being representative of the 1.6 m interval used to construct the WS MICP curve and NMR tool malfunction and sensitivities. The research suggests that the Schlumberger CMR tool is best able to measure the small pores associated with sealing intervals. Further, that the sample location for pore body to pore throat correction needs to be very carefully chosen with the most uniform sealing interval being selected from which to sample and carry out the technique. Additionally that the pore body to pore throat correction may only be suitable for one formation and that the confidence in the produced WS mercury curve decreases with distance from the depth from which the pore to pore throat correction was made.

The Redman-1 WS MICP curves have the best agreement with the CC MICP curves of any of the wells where the technique was tested. However, even minor differences in the MICP curves have led to significant differences in the interpreted threshold pressures which in turn have led to considerable differences in the maximum CO_2 column height retentions calculated. In most cases, this variation is less than the differences as a result of brine/ CO_2/ rock contact angle change from 0 ° to 60 °. Where there are discrepancies with the WS MICP curve shape and position, there is often a poor agreement between the T_2 distributions over the 0.8 m interval for which the WS MICP curve is produced.

The variation observed in MICP analyses of CC samples in close proximity to one another has been interpreted to lead to synthetic MICP curves that are an average of both rock types i.e. Thebe-2. This has subsequently led to MICP curves and threshold pressures with significant differences to the CC sample rock properties suggesting the technique isn‘t working whereas in reality, the synthetic MICP curves may be a better representation of the 1.6 m interval.

The NMR measurements being averaged over the 1.6 m interval poses both a problem and an advantage; the selection of a CC sample to calibrate the well log needs to be taken from a homogeneous interval. If it is taken from a heterogeneous interval, the synthetic MICP curve shift will be incorrect leading to non-representative synthetic MICP curves throughout the well. The synthetic MICP curve being representative of a much larger interval will be advantageous when evaluating heterogeneous formations allowing a much better indication of the capillary pressure properties providing the pore body to pore throat calibration is correct.

The study identified a number checks that need to be made to determine the quality of the NMR log and the subsequent WS MICP curves; The NMR log needs to be checked against what was expected over formations and what the T_2 distributions show. This can be achieved by checking the gamma against the T_2 distributions where there should be a relationship between short T_2 relaxation distributions and high gamma and vice versa. Further, the log should be checked for any abnormalities; the T_2 distributions should show the movement of the distribution peaks over the entire relaxation scale 0.3-3000 msec or equivalent. The log should also be checked for commonalities that would not be expected in nature.

CHAPTER 8: CONCLUSIONS AND RECOMMENDATIONS

8.1 CONCLUSIONS

The geological storage of carbon dioxide is a mitigation strategy for the continued use of fossil fuels with minimal release of carbon dioxide to the atmosphere. This study has advanced the understanding of the study of caprocks for the geological storage of carbon dioxide through the following:

a) The mercury porosimeter analysis is demonstrated as an accurate tool for providing reliable and repeatable data for determining seal capacity. The study demonstrates that the study‘s conformance correction methodology is viable, with the variation in MICP analyses between adjacent samples attributable to sample preparation and/ or warehousing.

b) Samples prepared from conventional core have no significant differences in MICP curves from conventional core samples prepared for vertical intrusion and synthetic cuttings after the study‘s conformance correction. However, measured porosities have a systematic variation, with the synthetic cutting samples having the highest porosity, followed by the traditional conventional core samples and lastly by the conventional core samples prepared for vertical intrusion only. The drill cutting samples from the same interval as the conventional core have differences in both porosity and MICP curves indicating that some other processes than the mechanical breaking of the sample is altering the pore networks and subsequently affecting the MICP curves.

c) The comparison of adjacent samples demonstrates that there can be significant heterogeneities that are unlikely to be a result of preparation or storage. Thus caution needs to be exercised when using adjacent samples in data analysis.

d) The warehousing of conventional core samples affects MICP analysis. The effects can be reduced by storing the samples in airtight bags. Further improvements may be possible with other storage options; alfoil, different plastics, vacuum sealing and pre-packed desiccants.

e) The results from MICP analyses of shale samples stored in warehouses should be adjusted by interpreting threshold pressures two pressure equilibrium points lower than would be interpreted on fresh samples. The porosity results should also be increased ~1%.

f) The methodology of producing synthetic MICP curves from NMR data over sealing intervals can be used to predict threshold pressure and estimate maximum column height retention in wells where core is not available. The laboratory NMR data derived from core is the most reliable and the resulting synthetic MICP curves show the best correlation with the MICP curves from conventional core samples. The wellbore NMR data and derived synthetic MICP curves are correlatable in some wells but show poor agreement in others. This is attributed to the rock sample not being representative of the larger rock volume measured by the well log NMR tool and a lack of tool sensitivity.

g) Three wells (Tindilpie-11, Mena Murtee-1 and Saracen-1) were studied to compare variations in poroperms from helium, NMR and MICP techniques. The lack of any consistent trend or relationship in the three wells indicates that no correction or calibration factor can be applied to the data.

8.2 RECOMMENDATIONS

- **Evaluation of MICP Analysis**

The blank correction process should be investigated further. It is suggested the mercury porosimeter blank correction method be conducted first without a sample, then with a quartz sample and possibly a shale sample wrapped in a balloon to support the results and interpretation of this study that there is no compression of the sample during MICP analysis.

- **Sample Type and the Effects on MICP Analysis**

To determine the exact process resulting in the differences observed in the MICP analysis of conventional core and drill cutting samples the following experimental analysis is suggested:

Sample a conventional core that is described as being fairly uniform (i.e. Saracen-1). Visually observe the sample for obvious heterogeneity and do not continue if observed. If the sample appears uniform then send the centre portion away for XRD mineralogical analysis. Divide the remaining sample into 5 groups of 3 replicates (15 total samples). The first group would provide the constant and simply be a conventional core cube. The second group would be immersed in drilling mud under pressure for a period of time similar to that experienced while drilling. The third group would be washed and dried. The fourth group would be shaken similar to the shale shakers on the drilling rig. The fifth group would be crushed to produce a cutting. The differences in the analysis could then be attributed to

individual processes. Those processes under control of the operator may be managed to prevent the changes observed in MICP analysis of drill cutting samples.

- **The Effects of Warehousing Rock Samples on MICP Analysis**

Further studies on the effects of warehousing on MICP analysis should be conducted on additional wells having different sealing formations to gauge the amount of variability that can be expected. It is also suggested that this work is regularly conducted over time i.e. after 1 month, 6 months, 1 year and 5 years.

- **NMR Synthetic MICP Curves**

Where well synthetic MICP curves (produced from the NMR logs) have significant variation from the conventional core MICP curve, it is likely to be a result of the conventional core sample not being representative of the 1.6 m interval used to produce the well synthetic MICP curve. It is thus suggested intervals of interest be densely sampled for MICP analyses and then compared with the well synthetic MICP curve.

Aggelopoulos, C. A., Robin, M., Perfetti, E., & Vizika, O. (2010). $CO_2/CaCl_2$ solution interfacial tensions under CO_2 geological storage conditions: influence of cation valence on interfacial tension. Advances in Water Resources, 33(6), 691-697.

Agut, R., Levallois, B., & Klopf, W. (2000, January). Integrating core measurements and NMR logs in complex lithology. In SPE Annual Technical Conference and Exhibition. Society of Petroleum Engineers.

Ahmad, M. (2014). Petrophysical and mineralogical evaluation of shale gas reservoirs (A Cooper Basin Case Study) (Doctoral dissertation, The University of Adelaide Australia).

Alder, J. D., Bembrick, C., Hartung-Kagi, B., Mullard, B., Pratt, D. A., Scott, J., & Shaw, R. D. (1998). A re-assessment of the petroleum potential of the Darling Basin: a Discovery 2000 initiative. The APEA Journal, 38, 278-310.

Al-Ghamdi, A. (2006). Calibrating NMR response to capillary pressure curves in fine grained lithologies: Pretty Hill Formation, Otway Basin. Master‘s Thesis, Australian School of Petroleum, University of Adelaide, Adelaide.

Altunbay, M., Martain, R., & Robinson, M. (2001, January). Capillary pressure data from NMR logs and its implications on field economics. In SPE annual technical conference and exhibition. Society of Petroleum Engineers.

American Petroleum Institute. (1998). Recommended practices for core analysis. Recommended Practice 40, Second Edition. Url: http://w3.energistics.org/RP40/rp40.pdf. Accessed on the 20/12/2015

Anovitz, L. M., & Cole, D. R. (2015). Characterization and analysis of porosity and pore structures. Reviews in Mineralogy and geochemistry, 80(1), 61-164.

Apak, S. N. (1994). Structural development and control on stratigraphy and sedimentation in the Cooper Basin, northeastern South Australia and southwestern Queensland/by Sukru N. Apak (Doctoral dissertation).

Apak, S. N., Stuart, W. J., Lemon, N. M., & Wood, G. (1997). Structural evolution of the Permian-Triassic Cooper Basin, Australia: relation to hydrocarbon trap styles. AAPG bulletin, 81(4), 533-555.

ASTM International. (2011). Standard test method for determination of pore volume and pore volume distribution of soil and rock by mercury intrusion porosimetry. Designation:D4404-10

Auman, J. B. (1989). A laboratory evaluation of core-preservation materials. SPE Formation Evaluation, 4(01), 53-55.

Ausbrooks, R., Hurley, N. F., May, A., & Neese, D. G. (1999, January). Pore-size distributions in vuggy carbonates from core images, NMR, and capillary pressure. In SPE annual technical conference and exhibition. Society of Petroleum Engineers.

Australian Government. (2009). Regional geology of the Northern Carnarvon Basin, Department of Resources, Energy and Tourism. Url: http://www.petroleum-acreage.gov.au/sites/prod.petroleum-acreage.gov.au/files/files/2009/geology/rankin/RankinPlatform-RegionalGeology.pdf

Bailey, W. R., Underschultz, J., Dewhurst, D. N., Kovack, G., Mildren, S., & Raven, M. (2006). Multi-disciplinary approach to fault and top seal appraisal; Pyrenees–Macedon oil and gas fields, Exmouth Sub-basin, Australian Northwest Shelf. Marine and Petroleum Geology, 23(2), 241-259.

Baker Hughes. (2010). MR eXplorer; magnetic resonance logging service‘ Drilling and Evaluation, URL: https://assets.www.bakerhughes.com/system/2f021fff98402c23a68b071b38858c85_29111-mrex_brochure-0810.pdf.

Baker, D. and Skinner, J. (1999). Well completion report, Otway Basin, South Australia, Boral Energy Resources Ltd. Open File Envelope No. 7539/6.

Banfield, J.A. (2000). Well completion report; Saracen-1 production licence TL/4 Carnarvon Basin, Chevron Australia. Document No. BTAR-120.

Beacher, G. (2007). Gorgon Project: Gorgon CO2 data well-1 & Data well-1ST1 Well completion report – basic data. Document ID: G1-TE-Z-0000-REPX105

Bembrick, C. (1997). A re-appraisal of the Darling Basin Devonian sequence. Geological Survey of New South Wales Quarterly Notes, 105, 1-16.

Bennion, D. B., & Bachu, S. (2008, January). correlations for the interfacial tension between supercritical phase CO2 and equilibrium brines at in situ conditions. In SPE annual technical conference and exhibition. Society of Petroleum Engineers.

Boult, P. J. (1996). An investigation of reservoir/seal couplets in the Eromanga Basin; implications for petroleum entrapment and production: development of secondary migration and seal potential theory and investigation techniques (Doctoral dissertation).

Boult, P. J., & Hibburt, J. E. (2002). The petroleum geology of South Australia. In Otway Basin (Vol. 1). Department of Primary Industries and Resources South Australia.

Boult, P. J., Ramamoorthy, R., Theologou, P. N., East, R. D., Drake, A. M., & Neville, T. (1999). Borehole technology-Use of nuclear magnetic resonance and new core analysis technology for determination of gas saturation in Pretty Hill Sandstone reservoirs, onshore Otway Basin. APPEA Journal-Australian Petroleum Production and Exploration Association, 39(1), 437-450.

Boult, P. J., Theologou, P. N., & Foden, J. (1997). Capillary seals within the Eromanga basin, Australia: Implications for exploration and production. Memoirs-American Association of Petroleum Geologists, 143-168..

BP Energy Outlook (2016) Edition Url: https://www.bp.com/content/dam/bp/pdf/energy-economics/energy-outlook-2016/bp-energy-outlook-2016.pdf

BP Statistical Review of World Energy June. (2016). Url:

https://www.bp.com/content/dam/bp/pdf/energy-economics/statistical-review-2016/bp-statistical-review-of-world-energy-2016-full-report.pdf

BREE. (2011). Australian energy projections to 2034–35, BREE report prepared for the Department of Resources, Energy and Tourism, Canberra, December. Url: www.industry.gov.au/Office-of.../australianenergyprojections2034-35report.docx

Brooks, C. S. (1957). An Evaluation of the Procedures Used in the Determination of the Grain Densities of Petroleum Reservoir Minerals.

Bunch, M. (2014). A live test of automated facies prediction at wells for CO_2 storage projects. Energy Procedia, 63, 3432-3446.

Bustin, R. M., Bustin, A. M., Cui, A., Ross, D., & Pathi, V. M. (2008, January). Impact of shale properties on pore structure and storage characteristics. In SPE shale gas production conference. Society of Petroleum Engineers.

Cao, Z., Liu, G., Zhan, H., Li, C., You, Y., Yang, C., & Jiang, H. (2016). Pore structure characterization of Chang-7 tight sandstone using MICP combined with N2GA techniques and its geological control factors. Scientific Reports, 6.

Chehrazi, A., Rezaee, R., & Rahimpour, H. (2011). Pore-facies as a tool for incorporation of small-scale dynamic information in integrated reservoir studies. Journal of Geophysics and Engineering, 8(2), 202.

Chalbaud, C., Robin, M., Lombard, J. M., Martin, F., Egermann, P., & Bertin, H. (2009). Interfacial tension measurements and wettability evaluation for geological CO_2 storage. Advances in Water Resources, 32(1), 98-109.

Chiquet, P., Broseta, D. F., & Thibeau, S. (2005, January). Capillary alteration of shaly caprocks by carbon dioxide. In SPE Europec/EAGE Annual Conference. Society of Petroleum Engineers.

Chiquet, P., Daridon, J. L., Broseta, D., & Thibeau, S. (2007). CO_2/water interfacial tensions under pressure and temperature conditions of CO_2 geological storage. Energy Conversion and Management, 48(3), 736-744.

Clarkson, C. R., Wood, J., Burgis, S., Aquino, S., & Freeman, M. (2012). Nanopore-structure analysis and permeability predictions for a tight gas siltstone reservoir by use of low-pressure adsorption and mercury-intrusion techniques. SPE Reservoir Evaluation & Engineering, 15(06), 648-661.

Coates, G. R., Xiao, L., & Prammer, M. G. (1999). NMR logging: principles and applications. Gulf Professional Publishing.

Cockshell, CD. (1995). Structural and tectonic history in Morton, J.G.G., and Drexel, J.F., (1995). Petroleum geology of South Australia, Volume 1: Otway Basin. SA Department of Mines and Energy. ISBN 0 7308 0643 X

Comisky, J. T., Newsham, K., Rushing, J. A., & Blasingame, T. A. (2007, January). A comparative study of capillary-pressure-based empirical models for estimating absolute permeability in tight gas sands. In SPE Annual Technical Conference and Exhibition. Society of Petroleum Engineers.

Comisky, J. T., Santiago, M., McCollom, B., Buddhala, A., & Newsham, K. E. (2011, January). Sample size effects on the application of mercury injection capillary pressure for determining the storage capacity of tight gas and oil shales. In Canadian unconventional resources conference. Society of Petroleum Engineers.

Geoscience Australia. (2016). Petroleum Geology. Url: http://www.ga.gov.au/scientific-topics/energy/province-sedimentary-basin-geology/petroleum. Viewed on the 20/2/2015.

Condon, M. A. (1954). Progress report on the stratigraphy and structure of the Carnarvon Basin, Western Australia (No. 15). Bureau of Mineral Resources, Geology and Geophysics.

Cook, P. (2014). Geologically storing carbon: Learning from the Otway Project experience. CSIRO Publishing.

Cooney, P. M., & Mantaring, R. M. (2004). Interpretation of the Petroleum Potential of the Darling Basin, a Process of Integration and Iteration. ASEG Extended Abstracts, 2004(1), 1-4.

Cui, A. Wust, R., Nassichuk, B., Glover, K., Brezovski, R. and Twemlow, C., (2013). A nearly complete characterization of permeability to hydrocarbon gas and liquid for unconventional reservoirs: a challenge to conventional thinking. Unconventional Resources Technology Conference (URTEC).

Damte, S. W. (2002). Analysis of the Sealing Capacity of the Flaxmans Formation and the Belfast Mudstone in the Vicinity of the Shipwreck Trough, Otway Basin, Victoria. University of Adelaide, National Centre for Petroleum Geology and Geophysics.

Dance, T. (2013). Assessment and geological characterisation of the CO2CRC Otway Project CO 2 storage demonstration site: From prefeasibility to injection. Marine and Petroleum Geology, 46, 251-269.

Daniel, R. F. (2007). Carbon Dioxide Seal Capacity Study, CRC-1, CO2CRC Otway Project, Otway Basin, Victoria. CO2CRC Report No: RPT07-0629.

Daniel, R.F. and Kaldi, J.G. (2006). Carbon dioxide seal capacity study, Gorgon Data Well No.1, Barrow Island, Western Australia. CO2CRC Report No:RPT06-0169.

Daniel, R., & Kaldi, J. (2008). Evaluating seal capacity of caprocks and intraformational barriers for the geosequestration of CO2.

Daniel, R.F. and Kaldi, J.G. in Cook P.J. (2014). Geologically storing carbon: Learning from the Otway Project Experience. CSIRO Publishing, Melbourne.

Darłak, B., Kowalska-Włodarczyk, M., & Such, P. (2011). Methodological aspects of porosity and pore space measurements in shale rocks. Nafta-Gaz, 67(5), 326-330.

Dillinger, A., & Esteban, L. (2014). Experimental evaluation of reservoir quality in Mesozoic formations of the Perth Basin (Western Australia) by using a laboratory low field Nuclear Magnetic Resonance. Marine and Petroleum Geology, 57, 455-469.

Dewhurst, D. N., Jones, R. M., & Raven, M. D. (2002). Microstructural and petrophysical characterization of Muderong Shale: application to top seal risking. Petroleum Geoscience, 8(4), 371-383.

Dragomirescu, R., Kaldi, J., Lemon, N., & Alexander, E. (2001). Triassic seals in the Cooper Basin. In Eastern Australasian Basins Symposium, a refocused energy persepctive for the future. Petroleum Exploration Society of Australia Limited.

Ellis, C. (2009). Well completion report: Thebe-2/2CH WA-346-P, BHP Billiton Petroleum Pty. LTD.

Ennis-King, J., 2001, _Calculator for CO2 properties, URL: http://www-old.dpr.csiro.au/people/jonathan/codecomp/

Espinoza, D. N., & Santamarina, J. C. (2010). Water-CO_2-mineral systems: Interfacial tension, contact angle, and diffusion—Implications to CO2 geological storage. Water resources research, 46(7).

Evans, P. R. (1977). Petroleum geology of western New South Wales. The APEA Journal, 17, 42-49.

Farokhpoor, R., Bjørkvik, B. J., Lindeberg, E., & Torsæter, O. (2013). Wettability behaviour of CO_2 at storage conditions. International Journal of Greenhouse Gas Control, 12, 18-25.

Flohr, J.K.M. (1997). X-ray powder diffraction. U.S. Department of the Interior, U.S. Geological Survey. Url: http://pubs.usgs.gov/info/diffraction/html/.

Freedman, R. (2006). Advances in NMR logging. Journal of Petroleum Technology, 58(01), 60-66.

Freedman, R., Minh, C. C., Gubelin, G., Freeman, J. J., McGinness, T., Terry, B., & Rawlence, D. (1998, January). Combining NMR and density logs for petrophysical analysis in gas-bearing formations. In SPWLA 39th Annual Logging Symposium. Society of Petrophysicists and Well-Log Analysts.

Geoscience Australia. (2016). Australian Government: Geoscience Australia. Url: http://www.ga.gov.au/scientific-topics/energy/province-sedimentary-basin-geology/petroleum/offshore-southern-australia/otway#heading-4. Accessed on the 6th of December 2016.

Gibson-Poole, C., Svendsen, L., Underschultz, J., Watson, M., Ennis-King, J., Van Ruth, P., & Cinar, Y. (2006). Gippsland Basin geosequestration: a potential solution for the Latrobe Valley brown coal CO2 emissions.

Glover, P. W., Zadjali, I. I., & Frew, K. A. (2006). Permeability prediction from MICP and NMR data using an electrokinetic approach. Geophysics, 71(4), F49-F60.

Grattoni, C. A., Al-Mahrooqi, S. H., Moss, A. K., Muggeridge, A. H., & Jing, X. D. (2003, September). An improved technique for deriving drainage capillary pressure from NMR T 2 distributions. In Proceedings of the International Symposium of the Society of Core Analysts (Vol. 25).

Gravestock, D. I., Hibburt, J. E., & Drexel, J. F. (1998). The petroleum geology of South Australia, vol 4: Cooper Basin. South Australia. Department of Primary Industries and Resources. Report Book, 98, 9.

Haines, P. W., Hand, M. A. R. T. I. N., & Sandiford, M. I. K. E. (2001). Palaeozoic synorogenic sedimentation in central and northern Australia: a review of distribution and timing with implications for the evolution of intracontinental orogens. Australian Journal of Earth Sciences, 48(6), 911-928.

Hamada, G. M., El Oraby, M., & Abushanab, M. A. (2007, January). Integration of NMR with other open hole logs for improved porosity, permeability and capillary pressure of gas sand reservoirs. In SPE Saudi Arabia Section Technical Symposium. Society of Petroleum Engineers.

Heine, C., & Müller, R. D. (2005). Late Jurassic rifting along the Australian North West Shelf: margin geometry and spreading ridge configuration. Australian Journal of Earth Sciences, 52(1), 27-39.

Hildenbrand, A., Schlömer, S., & Krooss, B. M. (2002). Gas breakthrough experiments on fine-grained sedimentary rocks. Geofluids, 2(1), 3-23.

Hill, K. A., Cooper, G. T., Richardson, M. J., & Lavin, C. J. (1994). Structural framework of the eastern Otway Basin: inversion and interaction between two major structural provinces. Exploration Geophysics, 25(2), 79-87.

Hocking, R. M., Moors, H. T., & Van de Graaff, W. E. (1987). Geology of the Carnarvon Basin, Western Australia (Vol. 133). State Print. Division.

Hocking, R. M. (1988, August). Regional geology of the northern Carnarvon Basin. In The North West Shelf, Australia: Proc. Pet. Expl. Soc. Aust. Symp (pp. 97-114).

Hocking, R. M., Mory, A. J., & Williams, I. R. (1994, July). An atlas of Neoproterozoic and Phanerozoic basins of Western Australia. In The Sedimentary Basins of Western Australia: Proceedings of the Petroleum Exploration Society of Australia Symposium, Perth (pp. 21-43).

Huang, J., Cavanaugh, T., & Nur, B. (2013). 1 An Introduction to SEM Operational Principles and Geologic Applications for Shale Hydrocarbon Reservoirs.

Intergovernmental Panel on Climate Change. (2014). Climate Change 2014–Impacts, Adaptation and Vulnerability: Regional Aspects. Cambridge University Press.

Jones, R., Boult, P., Hillis, R., Mildren, S., & Kaldi, J. (2000). Integrated hydrocarbon seal evaluation in the Penola Trough, Otway Basin.

Josh, M., Esteban, L., Delle Piane, C., Sarout, J., Dewhurst, D. N., & Clennell, M. B. (2012). Laboratory characterisation of shale properties. Journal of Petroleum Science and Engineering, 88, 107-124.

Kaldi, J. G., & Atkinson, C. D. (1997). Evaluating seal potential: example from the Talang Akar Formation, offshore northwest Java, Indonesia. Memoirs-American Association of Petroleum Geologists, 85-102.

Kaldi, J., Daniel, R., Tenthorey, E., Michael, K., Schacht, U., Nicol, A., ... & Backe, G. (2011). Caprock systems for CO 2 geological storage. IAEGHG Rep, 1, 149.

Katz, A. J., & Thompson, A. H. (1986). Quantitative prediction of permeability in porous rock. Physical review B, 34(11), 8179.

Keating, K., & Knight, R. (2006). A laboratory study to determine the effect of iron oxides on proton NMR measurements. Geophysics, 72(1), E27-E32.

Keep, M. & Moss, S.J. (Eds). (2002). The Sedimentary Basins of Western Australia 3: Proceedings of the Petroleum Exploration Society of Australia Symposium, Perth, WA, 2002.

Kenyon, B., Kleinberg, R., Straley, C., Gubelin, G., & Morriss, C. (1995). Nuclear magnetic resonance imaging—technology for the 21st century. Oilfield Review, 7(3), 19-33.

Khalifa, M. K. H. (2010). Correlation of the Devonian formations in the Blantyre sub-basin. New South Wales with the Adavale Basin, Queensland. J Proc R Soc NSW, 143, 19-33.

Khalifa, M. K., & Ward, C. R. (2009). Stratigraphic correlation of the Devonian sequence in the Blantyre Sub-basin, Darling Basin, western New South Wales∗. Australian Journal of Earth Sciences, 56(2), 111-133..

Khalifa, M. K., & Ward, C. R. (2010). Sedimentological analysis of the subsurface Mulga Downs Group in the central part of the Darling Basin, western New South Wales. Australian Journal of Earth Sciences, 57(1), 111-139.

Kickas, K. (2012). Tindilpie 11 well completion report. Compiled for Santos Limited.

Kim, Y., Wan, J., Kneafsey, T. J., & Tokunaga, T. K. (2012). Dewetting of silica surfaces upon reactions with supercritical CO_2 and brine: pore-scale studies in micromodels. Environmental science & technology, 46(7), 4228-4235.

Kivior, T. (2005). Characterising top seal in the Vulcan Sub-Basin, North West Shelf, Australia (Doctoral dissertation).

Kleinberg, R. L. (2001). NMR well logging at Schlumberger. Concepts in Magnetic Resonance, 13(6), 396-403.

Kleinberg, R. L. (1996). Utility of NMR T 2 distributions, connection with capillary pressure, clay effect, and determination of the surface relaxivity parameter ρ 2. Magnetic resonance imaging, 14(7), 761-767.

Kobussen, A.F., Dick, S. (2011). Assessment of Carbon Storage Capacity in NSW: the Scientific Basis, Site Selection Criteria and Preliminary Well Prognoses for Research Drilling in the Darling Basin, Western NSW. NSW Division of Resources & Energy, NSW Department of Trade and Investment, Regional Infrastructure and Services, p. 25.

Kovack, G., Dewhurst, D., Raven, M., & Kaldi, J. (2004). The influence of composition, diagenesis and compaction on seal capacity in the Muderong Shale, Carnarvon Basin.

Krassay, A. A., Cathro, D. L., & Ryan, D. J. (2004, September). A regional tectonostratigraphic framework for the Otway Basin. In Eastern Australasian Basins Symposium II, Petroleum Exploration Society of Australia, Special Publication (pp. 97-116).

Kulikowski, D., Amrouch, K., & Cooke, D. (2016). Geomechanical modelling of fault reactivation in the Cooper Basin, Australia. Australian Journal of Earth Sciences, 63(3), 295-314.

Labani, M. M., Rezaee, R., Saeedi, A., & Al Hinai, A. (2013). Evaluation of pore size spectrum of gas shale reservoirs using low pressure nitrogen adsorption, gas expansion and mercury porosimetry: a case study from the Perth and Canning Basins, Western Australia. Journal of Petroleum Science and Engineering, 112, 7-16.

Laird, D. A. (2006). Influence of layer charge on swelling of smectites. Applied Clay Science, 34(1), 74-87.

Little, B. M., & Phillips, S. E. (1995). Detrital and authigenic mineralogy of the Pretty Hill Formation in the Penola Trough, Otway Basin: implications for future exploration and production. APEA JOURNAL, 35, 538-538.

Lonnes, S., Guzman-Garcia, A., & Holland, R. (2003, January). NMR petrophysical predictions on cores. In SPWLA 44th Annual Logging Symposium. Society of Petrophysicists and Well-Log Analysts.

Longley, I. M., Buessenschuett, C., Clydsdale, L., Cubitt, C. J., Davis, R. C., Johnson, M. K. & Thompson, N. B. (2002). The North West Shelf of Australia–a Woodside perspective. The sedimentary basins of Western Australia, 3, 27-88.

Lowden, B. D., Porter, M. J., & Powrie, L. S. (1998, January). T2 relaxation time versus Mercury injection capillary pressure: Implications for NMR logging and reservoir characterisation. In European Petroleum Conference. Society of Petroleum Engineers.

Lu, J., Milliken, K., Reed, R. M., & Hovorka, S. (2011). Diagenesis and sealing capacity of the middle Tuscaloosa mudstone at the Cranfield carbon dioxide injection site, Mississippi, USA. Environmental Geosciences, 18(1), 35-53.

Lucia, F. J., Kerans, C., & Jennings Jr, J. W. (2003). Carbonate reservoir characterization. Journal of petroleum technology, 55(06), 70-72.

Mardi, C. (2014). A Practical Method to Predict Deliverability and Water-Cut in the Granite Wash Formation, Anadarko Basin, USA, Using Pseudo-Capillary Pressure Curves From NMR Data. Unconventional Resources Technology Conference (URTEC).

Marschall, D., Gardner, J. S., Mardon, D., & Coates, G. R. (1995, September). Method for correlating NMR relaxometry and mercury injection data. In 1995 SCA Conference, paper (No. 9511).

Mastalerz, M., Schimmelmann, A., Drobniak, A., & Chen, Y. (2013). Porosity of Devonian and Mississippian New Albany Shale across a maturation gradient: Insights from organic petrology, gas adsorption, and mercury intrusion. AAPG bulletin, 97(10), 1621-1643.

Mbia, E. N., Fabricius, I. L., Krogsbøll, A., Frykman, P., & Dalhoff, F. (2014). Permeability, compressibility and porosity of Jurassic shale from the Norwegian–Danish Basin. Petroleum Geoscience, 20(3), 257-281.

Medicines Complete. (2016), Diagram of mercury porosimeter, Url: https://www.medicinescomplete.com/mc/rem/2012/c38-fig-38-14.png, Accessed one the 5/6/2016.

Mehin, K. and Constantine, A.E. (1999) Hydrocarbon potential of the Western Onshore Otway Basin in Victoria: 1999 Acreage Release. Victorian Initiative for Minerals and Petroleum Report 62. Department of Natural Resources and Environment.

McGowen, J. M., Gilbert, J. V., & Samari, E. (2007, January 1). Hydraulic Fracturing Down Under. Society of Petroleum Engineers. doi:10.2118/106051-MS

McPhee, C., Reed, J., Zubizarreta, I. "Core Analysis: A Best Practice Guide", chapter 10 about relative permeability, Developments in Petroleum Science, Elsevier, (2015), Volume 64, Pages 519-653.

Morton J.G.G., CD., (1995), "Structural and tectonic history' in Morton, J.G.G., and Drexel, J.F., 1995, "Petroleum geology of South Australia, Volume 1: Otway Basin', SA Department of Mines and Energy. ISBN 0 7308 0643 X

Müller, R. D., Dyksterhuis, S., & Rey, P. (2012). Australian paleo-stress fields and tectonic reactivation over the past 100 Ma. Australian Journal of Earth Sciences, 59(1), 13-28.

Musu, J. T., & Widarsono, B. (2007). Study on the Relationship Between Rock Properties and NMR Measurement of the Low Permeability, Ductile, Shaly Sandstones.

National Inventory Report. (2012). Volume 1, Commonwealth of Australia. The Australian Government submission to the United Nations framework convention on Climate Change. Australian National Greenhouse accounts.

Nazari, B., Jorjani, E., Hani, H., Manafi, Z., & Riahi, A. (2014). Formation of jarosite and its effect on important ions for Acidithiobacillus ferrooxidans bacteria. Transactions of Nonferrous Metals Society of China, 24(4), 1152-1160.

Neef, G., & Bottrill, R. S. (1991). Early Devonian (Gedinnian) nonmarine strata present in a rapidly subsiding basin in far western New South Wales, Australia. Sedimentary Geology, 71(3-4), 195-212.

Neef, G. (2004). Stratigraphy, sedimentology, structure and tectonics of lower Ordovician and Devonian strata of South Mootwingee, Darling Basin, western New South Wales. Australian Journal of Earth Sciences, 51(1), 15-29.

Neef, G., Larsen, D.F. and Ritchie, A. (1996), Australasian sedimentologists group field guide series No. 10: Late Silurian and Devonian fluvial strata in western Darling Basin, far west New South Wales, Geological Society of Australia.

Nesse, W. D. W. D. (2012). Introduction to mineralogy (No. 549 NES).

Newsham, K. E., Rushing, J. A., Lasswell, P. M., Cox, J. C., & Blasingame, T. A. (2004, January). A comparative study of laboratory techniques for measuring capillary pressures in tight gas sands. In SPE Annual Technical Conference and Exhibition. Society of Petroleum Engineers.

Nordbotten, J. M., Celia, M. A., & Bachu, S. (2005). Injection and storage of CO2 in deep saline aquifers: Analytical solution for CO2 plume evolution during injection. Transport in Porous media, 58(3), 339-360.

NSW Department of Industry. (2014). Mena Murtee-1 well completion report, NSW CO2 storage assessment program. EL8066.

NSW Department of Industry. (2016). _Darling Basin. Url: http://www.resourcesandenergy.nsw.gov.au/miners-and-explorers/geoscience-information/nsw-geology-overview/sedimentary-basins/darling-basin. Accessed on the 9/12/2016.

O'Brien, G. W., & Thomas, J. H. (2007). A technical assessment of the Yet-to-Find hydrocarbon resource inventory, offshore and onshore Otway Basin, Victoria, Australia. GeoScience Victoria.

Olafuyi, O. A., Sheppard, A. P., Arns, C. H., Sok, R. M., Cinar, Y., Knackstedt, M. A., & Pinczewski, W. V. (2006, January). Experimental investigation of drainage capillary pressure computed from digitized tomographic images. In SPE/DOE Symposium on Improved Oil Recovery. Society of Petroleum Engineers.

Partridge, A. (2001). Revised stratigraphy of the Sherbrook Group, Otway Basin.

Parry, J. C., & Smith, D. N. (1988). The Barrow and Exmouth sub-basins. In The North West Shelf, Australia. Pet. Expl. Soc. Aust. Symp (pp. 129-145).

Perrin, J. C., Krause, M., Kuo, C. W., Miljkovic, L., Charoba, E., & Benson, S. M. (2009). Core-scale experimental study of relative permeability properties of CO 2 and brine in reservoir rocks. Energy Procedia, 1(1), 3515-3522.

Petroleum, W. O. (1988). A review of the petroleum geology and hydrocarbon potential of the Barrow-Dampier Sub-basin and environs. In The North West Shelf, Australia Proc. Pet. Expl. Soc. Aust. Symp (pp. 115-128).

Petruk, W. (2000). Applied mineralogy in the mining industry. Elsevier.

Pittman, E. D. (1992). Relationship of porosity and permeability to various parameters derived from mercury injection-capillary pressure curves for sandstone (1). AAPG bulletin, 76(2), 191-198.;

Plymouth University. 2016. Pore-scale modelling. Url:https://www1.plymouth.ac.uk/research/cres/Research%20themes/Pages/Pore-scale-modelling.aspx. Accessed on the 20/6/2014.

Purcell, P. G., & Purcell, R. R. (Eds.). (1988). The North West Shelf, Australia: Based on the Proceedings of the North West Shelf Symposium. Petroleum Exploration Society of Australia.

Purcell, P. G., & Purcell, R. R. (Eds.). (1994). The Sedimentary Basins of Western Australia: Based on the Proceedings of the West Australian Basins Symposium Sponsored by the Western Australian Branch of the Petroleum Exploration Society of Australia, Limited and Held in Perth, Western Australia, August 14-17, 1994 (Vol. 1). PESA Limited, WA Branch.

Purcell, P. G. & R. R. (Eds).(1998). The Sedimentary Basins of Western Australia 2: Proceedings of Petroleum Exploration Society of Australia Symposium, Perth, WA, 1998.

Purcell, W. R. (1949). Capillary pressures-their measurement using mercury and the calculation of permeability therefrom. Journal of Petroleum Technology, 1(02), 39-48.

Purcell, P. G., & Purcell, R. R. (Eds.). (1988). The North West Shelf, Australia: Based on the Proceedings of the North West Shelf Symposium. Petroleum Exploration Society of Australia.

Rajabi, M., Tingay, M., & Heidbach, O. (2016). The present-day state of tectonic stress in the Darling Basin, Australia: implications for exploration and production. Marine and Petroleum Geology, 77, 776-790.

Ramamoorthy, R., Boult, P. J., & Neville, T. (2000, January). A Novel Application Of Nuclear Magnetic Resonance And Formation Tester Data For The Determination Of Gas Saturation In Pretty Hill Sandstone Reservoirs, Onshore Otway Basin. In SPWLA 41st Annual Logging Symposium. Society of Petrophysicists and Well-Log Analysts.

Rezaee, M. R., & Lemon, N. (1997). Permeability estimation from mercury injection capillary pressure data, a case study in the Tirrawarra Sandstone, Cooper Basin. Australian Petroleum Production and Exploration Association Journal, 37.

Rezaee, R., Saeedi, A., & Clennell, B. (2012). Tight gas sands permeability estimation from mercury injection capillary pressure and nuclear magnetic resonance data. Journal of Petroleum Science and Engineering, 88, 92-99

Root, R. (2005). Geological evaluation of the Eocene Latrobe Group in the offshore Gippsland Basin for CO_2 geosequestration (Doctoral dissertation).

Sánchez-España, J. (2008). Acid mine drainage in the Iberian Pyrite Belt: an overview with special emphasis on generation mechanisms, aqueous composition and associated mineral phases. Macla, 10, 34-43.

Schlumberger. (2002). Schlumberger CMR-Plus: high speed, high resolution answers, URL: https://www.slb.com/~/media/Files/evaluation/brochures/wireline_open_hole/petrophysics/nmr/cmrplus_br.ashx.

Schmitt, M., Fernandes, C. P., da Cunha Neto, J. A., Wolf, F. G., & dos Santos, V. S. (2013). Characterization of pore systems in seal rocks using nitrogen gas adsorption combined with mercury injection capillary pressure techniques. Marine and Petroleum Geology, 39(1), 138-149.

Schlömer, S., & Krooss, B. M. (1997). Experimental characterisation of the hydrocarbon sealing efficiency of cap rocks. Marine and Petroleum Geology, 14(5), 565-580.

Schowalter, T. T. (1979). Mechanics of secondary hydrocarbon migration and entrapment. AAPG bulletin, 63(5), 723-760.

Schulz, H. M., Wirth, R., & Schreiber, A. (2016). Nano-Crystal Formation of TiO2 Polymorphs Brookite and Anatase Due To Organic—Inorganic Rock–Fluid Interactions. Journal of Sedimentary Research, 86(2), 59-72.

Scott, M. P., Stephens, T., Durant, R., McGowen, J., Thom, W., & Woodroof, R. (2013, November 11). Investigating Hydraulic Fracturing in Tight Gas Sand and Shale Gas Reservoirs in the Cooper Basin. Society of Petroleum Engineers. doi:10.2118/167073-MS

Selleys. (2014). Selleys Material Safety Data Sheet: Hazardous substance, dangerous goods, Url: https://www.colliermiller.com.au/documents/MSDS%5C930069710040501_4.pdf, Accessed on the 10/10/2015.

Shafer, J., & Neasham, J. (2000). Mercury porosimetry protocol for rapid determination of petrophysical and reservoir quality properties. In International Symposium of the Society of Core Analysts, SCA (Vol. 2021, p. 12).

Sigal, R. F. (2009). A methodology for blank and conformance corrections for high pressure mercury porosimetry. Measurement Science and Technology, 20(4), 045108.

Sigal, R. F. (2013). Mercury capillary pressure measurements on Barnett core. SPE Reservoir Evaluation & Engineering, 16(04), 432-442.

Smith, D. M., & Schentrup, S. (1987). Mercury porosimetry of fine particles: Particle interaction and compression effects. Powder technology, 49(3), 241-247.

Smithwick, R. W. (1982). A generalized analysis for mercury porosimetry. Powder Technology, 33(2), 201-209.

Sneider, R. M. (1997). Practical petrophysics for exploration and development. American Association Petroleum Geologist Short Course Lecture Notes.

Sneider, R. M., Sneider, J. S., Bolger, G. W., & Neasham, J. W. (1997). AAPG Memoir 67: Seals, Traps, and the Petroleum System. Chapter 1: Comparison of Seal Capacity Determinations: Conventional Cores vs. Cuttings.

Svendsen, L. (2004). Seal evaluation of a fluvial-lacustrine rift to post-rift succession, the Early Cretaceous Eumeralla Formation, Otway Basin, Australia (Doctoral dissertation, University of Adelaide).

Tait, A. M. (1985). A depositional model for the Dupuy Member and the Barrow Group in the Barrow sub-basin, northwestern Australia. APEA J, 25(1), 282-290

Teasdale, J. P., Pryer, L. L., Stuart-Smith, P. G., Romine, K. K., Etheridge, M. A., Loutit, T. S., & Kyan, D. M. (2003). Structural framework and basin evolution of Australia's southern margin. APPEA Journal, 43(1), 13-37.

Thompson, A. H., Katz, A. J., & Raschke, R. A. (1987). Mercury injection in porous media: A resistance devil's staircase with percolation geometry. Physical review letters, 58(1), 29.

Torsaeter, O., & Beldring, B. (1987). The effect of freezing of slightly consolidated cores. SPE formation evaluation, 2(03), 357-360.

USA Society of Petroleum Engineers. (2007). Petroleum engineering handbook. Vol. 5. Reservoir engineering and petrophysics. E. D. Holstein, & L. W. Lake (Eds.). SPE.

Vavra, C. L., Kaldi, J. G., & Sneider, R. M. (1992). Geological applications of capillary pressure: a review (1). AAPG Bulletin, 76(6), 840-850.

Veevers, J. J. (1988, August). Morphotectonics of Australia‘s northwestern margin—A review. In The North West Shelf, Australia: Proc. Pet. Expl. Soc. Aust. Symp (pp. 19-27).

Volokitin, Y, Looyestijn, W.J., Slijkerman, W. J. L. & Hofman, J. P. (2001). A practical approach to obtain primary drainage capillary pressure curves from NMR core and log data. Petrophysics, 42(04).

Washburn, E. W. (1921). The dynamics of capillary flow. Physical review, 17(3), 273.

Watson, M. N. (2012). Natural CO_2 accumulations as analogues for CO_2 geological storage and CO_2-induced diagenesis in the Otway Basin, Australia (Doctoral dissertation).

Watson, M., Bunch, M., Haese, R.R., Karsten, M., Tenthorey, E., Daniel, R., Black, J. and Knight, J. (2014). Geological interpretation and dynamic modelling of well data from the NSW Darling Basin Drilling Program. CO2CRC Report No: RPT14-5162.

Weatherford. (2010). NMRT^{TM} Nuclear Magnetic Resonance Tool, © 2006–2010 Weatherford.

Webb, P.A. (1993). Micromeritics poresizer 9320 autopore II 9220: Data collection, reduction and presentation, an international sales support document. Url:

http://depts.washington.edu/mseuser/Equipment/RefNotes/Hg%20Porosimetery%20paper.pdf. Accessed on the 10/10/2014.

Webb, P. A. (2001). An introduction to the physical characterization of materials by mercury intrusion porosimetry with emphasis on reduction and presentation of experimental data. Micromeritics Instrument Corp, Norcross, Georgia.

Welton, J. E., & Chevron Oil Field Research Company. (1984). SEM petrology atlas. Tulsa, Okla: American Association of Petroleum Geologists.

Wendell, D. J., Anderson, W. G., & Meyers, J. D. (1987). Restored-state core analysis for the Hutton reservoir. SPE Formation Evaluation, 2(04), 509-517.

Willcox, J. B. (2003). Structural Evolution and Potential Petroleum Plays in the Darling Basin:(Pondie Range Trough--Mount Jack Area) Based on a Seismic Sequence Analysis. Geoscience Australia, Department of Industry, Tourism & Resources.

Willis, S. (1999). Tenacious West-1 Well Completion Report, Basic Data, Part 1. Woodside Energy Limited.

Willcox, J. B., & Stagg, H. M. J. (1990). Australia's southern margin: a product of oblique extension. Tectonophysics, 173(1-4), 269-281.

Winslow, D. N. (1978). The validity of high pressure mercury intrusion porosimetry. Journal of Colloid and Interface Science, 67(1), 42-47.

Wollenweber, J., a Alles, S., Kronimus, A., Busch, A., Stanjek, H., & Krooss, B. M. (2009). Caprock and overburden processes in geological CO 2 storage: An experimental study on sealing efficiency and mineral alterations. Energy Procedia, 1(1), 3469-3476.

Woollands, M. A., & Wong, D. (2001). Petroleum Atlas of Victoria, Australia. The State of Victoria, Department of Natural Resources and Environment, 208.

Wust, J., Raphael, A., Cui, A., Nassichuk, B., Brezovski, R., Letham, E., & Bustin, R. M. (2014, October). Improved Understanding of Gas/Liquid Transport in Unconventional

Shales of the Eagle Ford (USA), Montney (Canada), and REM (Australia) Through Micromorphological and Laboratory Analyses of Rock Fabric and Pore Sizes. In SPE Asia Pacific Oil & Gas Conference and Exhibition. Society of Petroleum Engineers.

Xiao, L., Mao, Z. Q., Zou, C. C., Jin, Y., & Zhu, J. C. (2016). A new methodology of constructing pseudo capillary pressure (P c) curves from nuclear magnetic resonance (NMR) logs. Journal of Petroleum Science and Engineering, 147, 154-167.

Yang, Y., & Aplin, A. C. (2007). Permeability and petrophysical properties of 30 natural mudstones. Journal of Geophysical Research: Solid Earth, 112(B3).

y Leon, C. A. L. (1998). New perspectives in mercury porosimetry. Advances in colloid and interface science, 76, 341-372.

A. APPENDIX

Detailed Methodology

This appendix details the mercury injection capillary pressure (MICP) analyses and sample preparation techniques undertaken at the Australian School of Petroleum (ASP) as well as those undertaken at other laboratories where appropriate. The preparation of different sample types is also discussed.

The appendix further details how the MICP threshold pressures were determined for both fresh and warehoused samples and, the synthetic MICP curves from NMR data. Only one methodology for picking threshold pressure could be employed for synthetic MICP curves as no incremental pore volumes are available and, in order to maintain consistency, both the synthetic and conventional core MICP curves are interpreted in the same manner. A detailed methodology and reasoning are given for the conformance corrections applied in the warehousing investigations of the MICP curves as well as the equations to correct porosity, grain density, bulk density, pore volume, grain volume and bulk volume measurements.

The rationale for the well and sample selection for both the effects of warehousing and the production of synthetic MICP curves including a detailed methodology for each of the analyses performed on rock samples and well logs is provided. This includes well log data extraction, laboratory NMR analyses, helium pycnometry, SEM imaging and XRD analyses. For samples examined for warehouse effects, the best efforts were made to repeat the methodologies that were used on the original samples so as to not introduce non-quantifiable variables. On occasion, this was not possible, but this will be discussed where applicable.

A.1 MICP ANALYSIS AT THE AUSTRALIAN SCHOOL OF PETROLEUM

Samples analysed with mercury porosimeter at the ASP were first inspected for fractures and heterogeneity. A representative sub-sample was cut from the original material. The sample was taken as close as possible to the centre of the core where it is less likely to have been influenced by drilling fluid invasion during the coring process. The sample was cut as large as possible to fit into the penetrometer. Subsequently, the samples were oven dried for a period of 48 hours at ~55 °C and placed in a penetrometer and analysed with the mercury porosimeter.

The excel graph and analysis output were inspected to make sure the parameters and results are –sensible". The analysis output was checked to make sure that the vacuum pressure was attained and that the maximum pressure of 60,000 psia was reached. The MICP curve was also inspected. The curve should move in an upwards direction and in a steady fashion. There should be no large jumps between equilibrium points. Lastly, the percentage intrusion of the penetrometer stem is also checked. The percentage intrusion should be greater than 8 % but less than 90 %. If this is not the case, then a different size penetrometer was used and the sample was re-analysed.

A.2 MICP ANALYSIS AT OTHER LABORATORIES

The Tindilpie -11 core samples were analysed at Core Laboratories Australia. The samples were soxhlet-cleaned with toluene followed by methanol and subsequently oven dried at 95 °C in order to remove any hydrocarbons and salts before analysis. No information was available on the mercury porosimeter or the settings. The samples were injected with mercury from 0 psia to 55,000 psia. The pressure and volume were recorded to produce the MICP curve.

Several samples were analysed by Particle and Surface and Sciences Pty. Limited (PSSPL). The instrument was set up to produce a vacuum less than 25 μm. The samples were injected with mercury from 0.51 psia to 60,000 psia. This included original samples from Gorgon CO2 Data Well-1 & Data Well-1ST1 (samples 2164.23 m and 2179.68 m), CRC-1(917 m) and CRC-2 (samples 1435.31 m, 1440.7 m and 1443.52 m). Several warehoused samples were also analysed by PSSPL; Thebe-2 (2277.05 m), and Mena Murtee-1 (1604.74 m, 1606.91 m and 2035.39 m). These samples were sent away for analysis for three reasons; (1) the numbers of samples were too large to be handled by the one mercury porosimeter, (2) to check the accuracy of results from the mercury porosimeter at the ASP and (3) as a result of the ASP mercury porosimeter not being able to attain the necessary vacuum and subsequently not being used for the analyses. The PSSPL mercury porosimeter is a Micromeritics Autopore IV 9500 V1.06.

Mena Murtee-1 samples (1629.05 m, 1629.98 m, 1859.75 m, 1865.06 m and 1872.32 m) were analysed by Geotech Intertek in Perth. The only details of the mercury porosimeter found, suggest that the machine is capable of injecting mercury in user defined step-like increments up to 60,000 psia.

The uncorrected results from the MICP analyses are provided in the results of the study, however, only the conformance corrected properties are discussed. The mercury

porosimeters used in all laboratories are required to be regularly calibrated although this cannot be confirmed for the Geotech Intertek machine. It is noted that in some instances the MICP analyses being compared in the study are from different mercury porosimeter instruments. However, this is not considered to make quantifiable differences beyond the variation observed in adjacent samples (samples taken at the same depth as close as possible to one another).

A.3 SAMPLE TYPE PREPARATION FOR MICP ANALYSES

The following methodology describes how conventional core (CC), vertical intrusion (VI), synthetic cuttings (SC) and drill cuttings (SC) samples were prepared for MICP analysis. In some cases, the samples were prepared by other authors and the best guess methodology is provided.

CC samples were prepared by taking core plug from the conventional core. The core plug was subsequently cut and a cube was taken from the middle of the sample. The cube was cut as big as possible while still being able to fit into the chosen penetrometer. All attempts to remove roughness and rugosities by clean cutting the sample were carried out. If the sample was fragile or small, often a second sample was added to the penetrometer for MICP analyses. Mercury intrusion is from all sides.

VI samples were prepared by taking the prepared and orientated CC sample and coating the top and sides of the sample with two part resin araldite. Mercury intrusion was from the bottom of the sample only which is considered to best represent field conditions.

SC samples were prepared by taking a conventional core plug and crushing part of the sample. The crushed sample was then analysed in the mercury porosimeter. Mercury intrusion is from all sides.

DC samples were collected at the well site at pre-determined depth intervals. The DC samples may have been exposed to the following; drilling muds (water or oil) and additives, well cave in‘s from younger stratigraphic intervals, shale shakers, washing (potable or sea water) drying (temperature unknown), storage and transport. The DC samples were vetted for composite samples (samples that appeared to have dried and re- amalgamated) and anomalies (samples that are not representative). The largest samples were analysed with MICP. Mercury intrusion was from all sides.

A.4 CONFORMANCE CORRECTIONS FOR ACCURATE MERCURY CURVES, POROSITY, BULK DENSITY AND GRAIN DENSITY MEASUREMENTS

When analysing rock samples with MICP, it is necessary to correct for conformance to accurately determine the point where the mercury is entering the rock‘s pore system rather than entering the fractures and rugosities of the rock sample. There are a number of methods for correcting the conformance of MICP data including the Bailey, (2009) method as well as the automatic conformance correction applied by the newer mercury porosimeters (i.e. Micromeritics Autopore IV). These methods, in the study‘s opinion, are excessive and may remove actual data (i.e. mercury that has intruded the large pores and throats of the rock sample). Commonly, the MICP curve of sealing rock is observed to increase steeply, plateau and after increased pressure begin to increase again producing the maximum inflection point (Figure A-1).Conformance is observed where there is mercury injection at initial injection pressures of a sealing rock followed by little to no mercury injection at higher pressures up to the maximum inflection point of the MICP curve (Figure A-1)

The methodology suggested by this study is to plot the incremental pore volume on a secondary y- axis to the cumulative mercury curve (Figure A-1). The threshold pressure is then interpreted from the MICP curve using the IPV method described in Section A.7 below (The conformance correction should not remove mercury at or past the threshold pressure). The incremental pore volume is used to pick where conformance stops and intrusion into the rock pore network begins. This point is identified by picking the pressure equilibrium point closest to the threshold pressure where there is no incremental pore volume intrusion (Figure A-1). All mercury intrusion below this pressure equilibrium point is zeroed. Secondly, in combination with the methodology above (whichever conformance correction is greater), 10 % of the threshold pressure is calculated and mercury intrusion up to and including this pressure is zeroed. This is often required for drill cutting samples where there are no pressure equilibrium points with zero mercury intrusion. The aim of using this methodology is to remove data not likely to represent an intrusion of mercury into the rock. Thus conformance corrections of up to 1000 psia are common (Figure A-1).

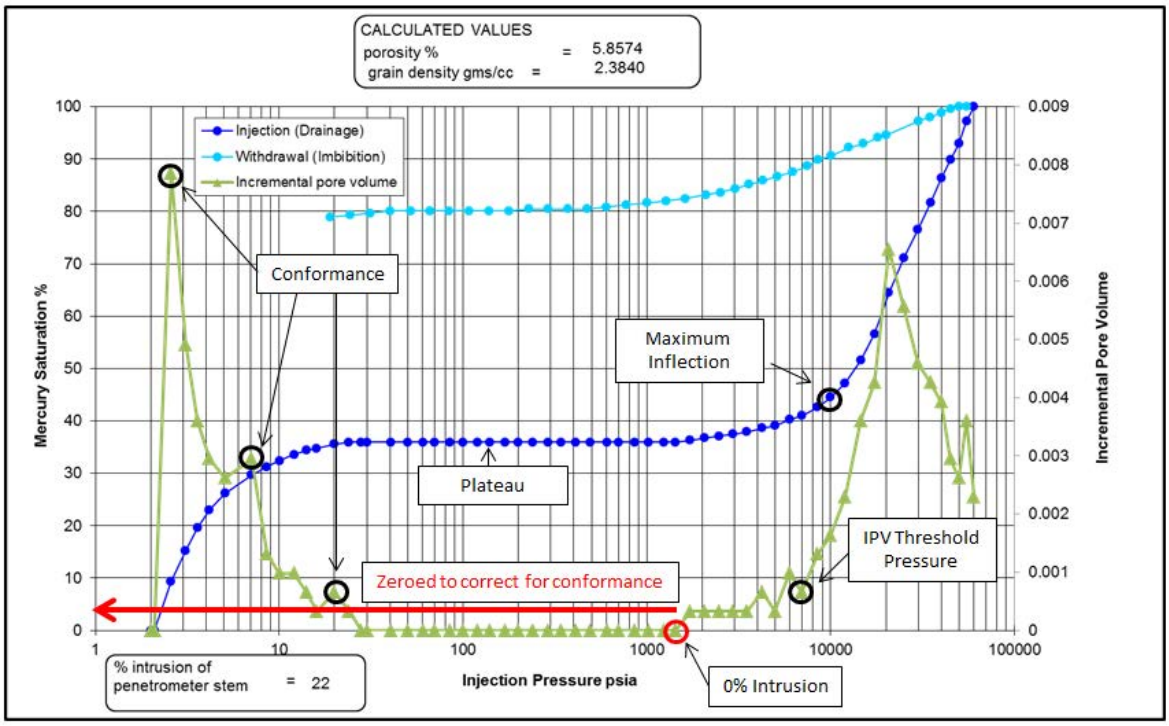

Figure A- 1: Example MICP analysis illustrating the maximum inflection point of the MICP curve, the incremental pore volume, IPV threshold pressure, conformance, the point at which there is 0% mercury intrusion and what is zeroed to correct for conformance (red arrow).

The conformance corrected bulk density, grain density and porosity can be re-calculated using equations 1-6 (modified from Webb, 1993).

Equation 1: To determine the volume of mercury in the penetrometer (measured after applying the vacuum and allowing mercury to fill the space not taken up by the sample in the penetrometer).

$$Vm = \frac{Wpsm - Ws - Wp}{Ym} \quad \text{Eq.1}$$

Equation 2: To determine the bulk volume of sample.

$$Vb = Vp - Vm \quad \text{Eq.2}$$

Equation 3: To determine the bulk density

$$Yb = \frac{Ws}{Vb} \quad \text{Eq.3}$$

Equation 4: To determine grain volume

$$Vs = Vb - Vtot \quad \text{Eq.4}$$

Equation 5: To determine grain density

$$Ys = \frac{Ws}{Vs} \qquad \text{Eq. 5}$$

Equation 6: To determine the porosity of the sample

$$Ppc = \frac{100 \times Vtot}{Vb} \qquad \text{Eq.6}$$

Where Vm = volume of mercury in the penetrometer, Wpsm = user entered weight of penetrometer + sample +mercury, Ws = user entered sample weight, Wp = user entered weight of penetrometer, Ym = user entered density for mercury, Vb = bulk volume, Yb = bulk density, Vs = grain volume, Ys = grain density, Vtot = total mercury intrusion volume and Ppc = porosity %.

A.5 DETERMINATION OF PERMEABILITY FROM MICP CURVES

The permeability prediction for the MICP analyses was achieved using the Winland‘s equation. The Winland‘s equation was chosen as there were no unknown constants unlike the Swanson‘s equation or the requirement for further analysis as with the Katz and Thompson‘s equation (Katz and Thompson, 1986). Further, it was shown by Pittman, (1992) to give reasonable results for sandstones. The Winland‘s equation (Equation 7) is shown below where r_{35} corresponds to the pore throat radius at 35 % mercury saturation, k is the air permeability and ϕ is the porosity (Pittman, 1992).

$$logr35 = 0.732 + 0.588logk - 0.8641log\phi \qquad \text{Eq. 7}$$

A.6 CONTACT ANGLE AND INTERFACIAL TENSION PARAMETERS

To determine the maximum CO_2 column heights that can be retained the mercury/ air/ rock substrate system must be converted to a brine/ CO_2/ rock system. This requires input values of the contact angle and interfacial tension for the two systems. This is well known for mercury/ air/ rock substrate system but for the brine/ CO_2/ rock system it has been shown that there is considerable variation in the contact angle between CO_2 and the rock surface, with most authors concluding that water saturated CO_2 has intermediate wettability (Chiquet et al., 2007 and Kaldi et al., 2011). Thus for this project threshold pressures and CO_2 maximum column heights are given using a calculated interfacial tension and a range of contact angle sensitivities. The interfacial tension for the brine/ CO_2/ rock substrate system was calculated using the Geodisc Calculator for CO_2 Properties ©2001(King, 2001). This required the pressure (Eq.8), temperature (Eq.9) and brine salinity to be estimated. The brine

salinity was estimated at 35000 ppm (approximate marine salinity) where no actual data were available.

$$Pressure\ MPa = Sample\ Depth * 0.0098 \qquad \text{Eq.8}$$

$$Temperature\ °C = 20 + \left(\frac{Sample\ Depth}{1000}\right) * 23.8 \qquad \text{Eq.9}$$

The contact angle for the brine/ CO_2/ rock system was given as sensitivities between 0 ° and 60 °.

A.7 THRESHOLD PRESSURE DETERMINATION FOR WAREHOUSED SAMPLES

The threshold pressure for the warehoused samples is picked using two methodologies; the first method called the incremental pore volume (IPV) method is a slight modification to the method described by Dewhurst et al., (2002) and recommended by Daniel and Kaldi (2014) in Cook (2014). The threshold pressure using the IPV method is picked by plotting the incremental pore volume against pressure on the MICP curve and identifying the zone on the graph where the MICP curve has its maximum inflection and where the incremental pore volume starts to increase steeply. The pressure equilibrium point on the incremental pore volume graph before the significant increase in volume is picked as the threshold pressure. This is identified by observing the distance between equilibrium points on the graph. Often on the incremental pore volume graph, there is a drop before the significant increase and this point is picked as the threshold pressure (Figure A-2).The method described by Dewhurst et al., (2002) picks the point after the drop or the point at which there is a significant intrusion (jump) on the incremental pore volume graph. However, a more conservative point, before the significant increase in intrusion occurs on the incremental pore volume graph is suggested as the threshold pressure.

The second methodology used to pick the threshold pressure is the maximum inflection point (MI) method where the maximum inflection point of the MICP curve is interpreted as the threshold pressure (Figure A-2). The MI method is used in conjunction with the IPV method for the warehoused results (Thesis Chapter 6) to allow comparisons to be made between the warehoused sample threshold pressures and those threshold pressures derived from the synthetic NMR mercury curves where the IPV method could not be used (Chapter 7).

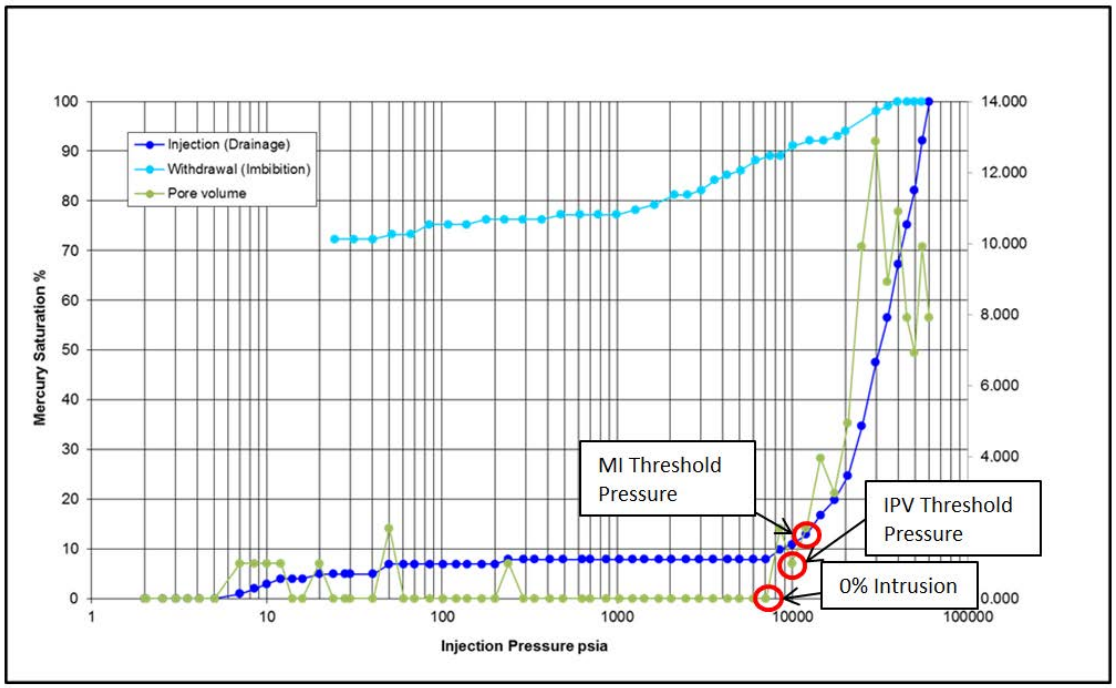

Figure A- 2: Example MICP analysis illustrating the two methods used to pick threshold pressures (Pth). Incremental Pore Volume method (IPV) and Maximum Inflection point (MI) method.

A.8 LABORATORY NMR ANALYSIS

The Tindilpie-11 samples were analysed by Core Laboratory in Perth with a Corespec-1000. The samples were soxhlet-cleaned with toluene followed by methanol and subsequently, oven dried at 95 °C to remove any hydrocarbon and salts. The samples were 100 % saturated with brine (15,000 ppm) before being analysed (Kicas, 2012).

The Corespec-1000 operates under a homogeneous magnetic field, with 1 MHz frequency pulses and an inter-echo spacing of 0.32 msec with no confining stress on the sample. A signal to noise ratio greater than 200 was generally aimed for during the analysis. The relaxation decay record was then processed separately using Numar‘s MAP II software to produce the T_2 distribution curves.

The Laboratory NMR analyses for both the Saracen-1 and Mena Murtee-1 samples were conducted by Lionel Esteban at the CSIRO in Perth. The instrument used to conduct the analysis was a Maran 2 MHz device from Oxford. This device was chosen because it works in a similar way to the NMR logging tools used in the field. The dead time between spin echos is 8µs and the time for magnetization recovery is 120 µs which is considered as low sensitivity. Thus, if the results from this instrument can be used to generate accurate synthetic MICP curves successfully then this would suggest that the same approach will work in the field.

The Maran 2 MHz device can measure both T_1 relaxation and T_2 relaxation times. For this research, the device was set to measure T_2 relaxation times using a CPMG sequence. The data quality was maintained by achieving a signal to noise ratio >> 100. Once the measurement had been taken and the subsequent relaxation decay recorded, the data was transformed using a Laplace transform to produce a T_2 distribution. The software used was WINDXP.

The analysis was conducted using the following settings on the Maran 2MHz device

- Number of scans – 20,000 (equivalent to 2 days of NMR acquisition)
- Relaxation delay – 2 seconds
- Tau- 120 µs
- Dead time before and after pulse – 8 µs
- First spin echo arrival time – (2 * tau) + (2 * dead time) = 256 µs
- Receiver gain – 100 %
- Echo train number – 8000

The Maran 2 MHz device was calibrated against 15 ml of water doped with NaCl or 5 ml of Ondina oil 15 using the above settings. The resulting NMR signal amplitude can be used to determine the volume of water or oil in the rock volumes by comparing the rock NMR signal amplitude to the calibration results.

A.9 WELLBORE NMR LOGS, CMR-PLUS, NMR AND MREX LOGS

The description of the NMR tools for Schlumberger, Weatherford and Baker Hughes is provided below. The description given may not be for the exact NMR tool used to log the well but is expected to be somewhat similar.

The Combinable Magnetic Resonance-Plus (CMR-Plus) is an NMR well logging tool offered by Schlumberger. The tool design involves two 30 inch magnets above and below the antenna allowing high-speed logging. It is advertised as being able to log at speeds of 1097 m/hr in the bound fluid mode and down to 244 m/hr in the long T1 relaxation mode. The vertical resolution can be adjusted between the high resolution (22.86 cm) and the fast mode (76.20 cm) while the horizontal depth of investigation is a maximum of 3.81 cm. The tool offers the Enhanced Precision Mode (EPM) mode allowing the measurement of fine

pores and heavy oils. The tool sends out one long wait pulse followed by stacked short pulses to gain a precise T_2 distribution (Schlumberger, 2002).

The NMRt Nuclear Magnetic Resonance well logging tool is offered by Weatherford. The tool is advertised as having a vertical resolution of 620 mm, a signal to noise ratio ≥ 3, a measurement zone thickness of 0.5-0.8 mm, a minimum echo spacing of 1.2 msec and ≤ 1000 echoes per measurement (Weatherford, 2010).

The MR eXplorer (MREX) is an NMR well logging tool offered by Baker Hughes. The tool is advertised as having the following unique benefits; side antenna with a gradient magnetic field, multiple frequency operations for multiple simultaneous NMR measurements in the one logging run, new acquisition techniques, T_1 and T_2 diffusivity measurements continuously recorded for hydrocarbon typing and 2D NMR imaging. The side looking magnetic antenna measures an arc on one side of the borehole; approximately 120 ° minimising the effects of borehole condition and allowing boreholes of varying sizes to be logged with the same instrument. The logging speed is advertised as 402 m/hr with a horizontal depth of investigation of 5.3-9.7 cm (Baker Hughes, 2010).

A.10 EXTRACTION AND INTERPRETATION OF NMR WELL LOG DATA

The wells investigated were accompanied by DLIS files containing the well log information. The T_2 distribution vector under the constants tab and the T_2 distribution under the logs tab were both extracted (Figure A-3 and A-4). The extracted information was then imported into Microsoft Excel ® for manipulation. The T_2 distribution is plotted on the x-axis and is a set of constants for each amplitude measurement. The T_2 distribution is the amplitude measurement plotted on the y-axis.

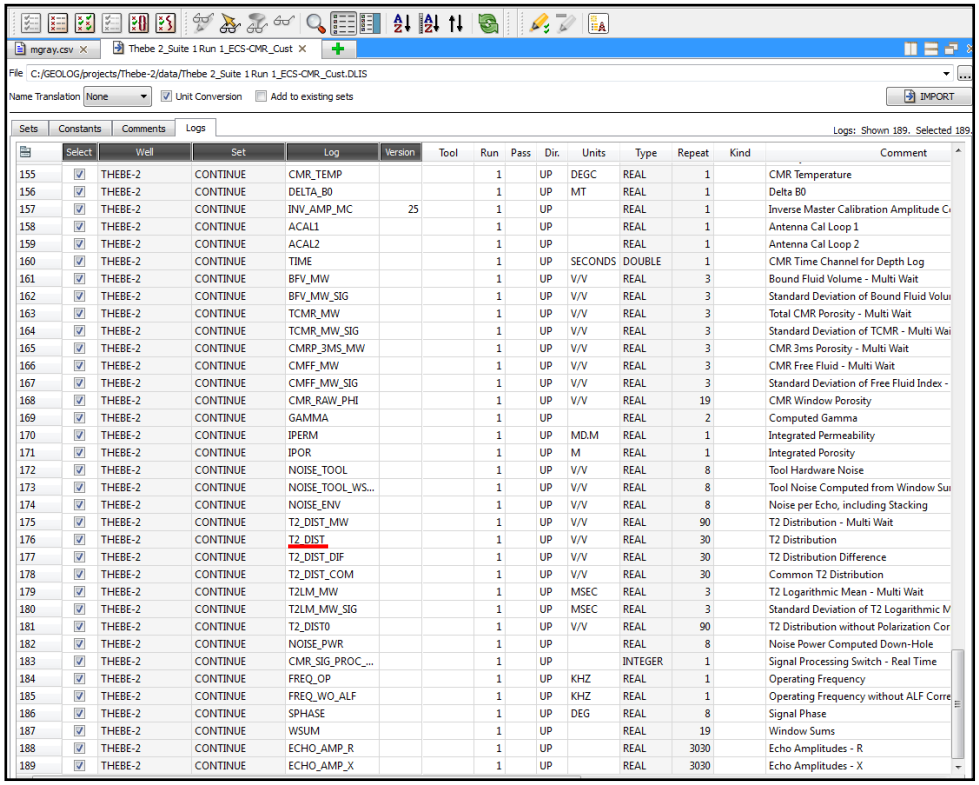

Figure A- 3: Geolog 7.2 ® panel indicating the T_2 distribution file that was extracted from the DLIS file.

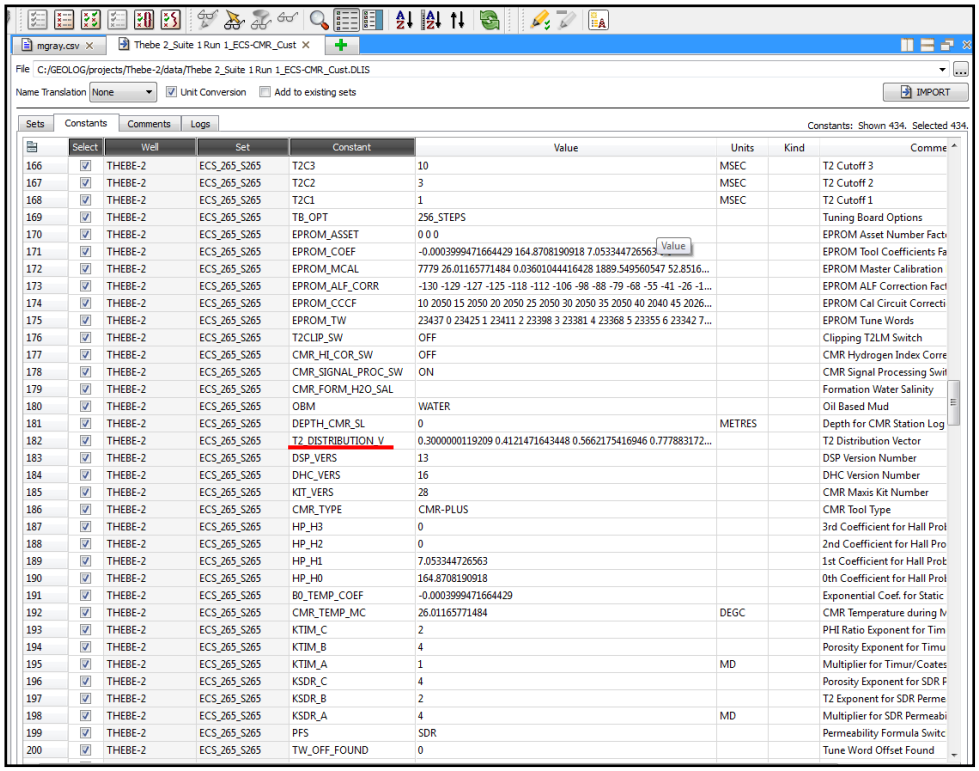

Figure A- 4: Geolog 7.2 ® panel indicating the T_2 distribution vector that was extracted from the dlis file.

A.11 NUCLEAR MAGNETIC RESONANCE PERMEABILITY ESTIMATION

Free fluid or (Timur-Coates model or Coates Model):

$$k_{Coates} = \left[\left\{\frac{\phi}{C}\right\}\frac{FFI}{BVI}\right]^2 \qquad \text{Eq. 10}$$

Where ϕ = porosity, C = is a formation dependent variable (10), Free Fluid Index (FFI) =T_2 distribution > 33 msec and the Bulk Volume Irreducible (BVI) =T_2 distribution < 33 msec

Schlumberger-Doll Research (SDR) model:

$$k_{SDR} = C * T_{2gm}^2 * \phi^4 \qquad \text{Eq.11}$$

Where C = a formation dependent variable (2), T_{2gm} = geometric mean of the T_2 distribution, and ϕ = effective porosity (MPHI) T_2 distribution > 33 msec (Kenyon et al., 1995 and Coates et al., 1999).

A.12 SYNTHETIC MICP CURVES FROM NMR DATA

The synthetic mercury curves are constructed on the premise of a relationship between pore throats measured by MICP and pore bodies measured by NMR. The NMR T_2 distribution is constructed using a number of pre-set T_2 times at which amplitude is recorded for each T_2 time depending on the relaxation signal from the rock volume. These T_2 measurement times and resultant amplitudes are then plotted as the inverse of the T_2 time. Thus they are plotted from long relaxation times to short relaxation times (large pores too small pores) reflecting the MICP curves (large pore throats too small pore throats). The T_2-^{1} time was converted to a pore throat diameter using Equation 12. The T_2-^{1} time was multiplied by a conversion factor from pore body diameter to pore throat diameter. This value is estimated by comparing the MICP curves with the NMR synthetic MICP curves for intervals of interest; sealing or reservoir. The best value found has been noted for each data set in Chapter 7. It is noted that the pore body to pore throat relationship will differ between sealing and reservoir formations. The pore throat diameter is then used to calculate a capillary pressure value using the modified Washburn Equation (Equation 13).

$$P_t = T2^{-1} * C \qquad \textit{Eq. 12}$$

Pore throat (Pt) diameter (μm) = T_2^{-1}(seconds)*(Conversion factor μm/s (C) from pore body to pore throat).

$$P_c = \frac{2\gamma cos\theta}{r} \qquad Eq.\ 13$$

Interfacial tension (γ = 480 dyne cm^{-1}) and contact angle (θ = 140 °) are those used for mercury/ air/ rock substrate.

The amplitudes for the entire T_2^{-1} distribution at each depth were cumulated and each amplitude for each T_2^{-1} time is calculated as a percentage of the cumulated amplitude for the T_2^{-1} distribution. This provides the equivalent of % mercury saturation. These calculations are a modified version to those of Volokitin et al., (2001) and Al-Ghamdi, (2006).

The measurements taken by the wellbore NMR tools were averaged to reduce the effects of noise and take into account any depth correction errors between the rock sample depth and wire line logging depth. The best results were found by averaging 8 NMR measurements (1.6 m) and using the average to produce the synthetic MICP curve.

Assumptions/Uncertainties

- There is a relationship between the pore body measured by NMR and the pore throats measured by MICP in the rock substrate and that this relationship remains constant over the formation of interest; sealing or reservoir.
- The correction from pore body to pore throat is consistent between sealing intervals.
- The surface relaxivity efficacy is constant between sealing lithologies.

A.13 HELIUM PYCNOMETRY ANALYSIS

The Tindilpie-11 samples were analysed by Core laboratory in Perth. The samples were soxhlet-cleaned with toluene followed by methanol and subsequently oven dried at 95°C to remove any hydrocarbons and salts.

To determine the porosity, the results from both the Ultrapore TM porosimeter used to determine grain volume and the CMSTM 300 used to determine pore volume were combined. The sample weight, diameter and length were all measured before the samples were analysed with the Ultrapore TM porosimeter. After every 10 samples, a standard was run. The samples were then analysed with the CMS TM 300 automated core measurement

system at a confining stress of 800 psi. A standard was analysed after every five samples (Kicas, 2012). This machine was also used to measure Klinkenberg permeabilities.

There was no information regarding the methodology and equipment used to determine the helium porosity of the original Saracen-1 samples analysed by Dewhurst et al., (2002).

The helium porosity measurements for both the warehoused Saracen-1 and Mena Murtee-1 well samples were conducted by Lionel Esteban at the CSIRO in Perth. The helium porosity measurements were made on an Accupyc II 1340 pycnometer from Micromeritics.

A.14 BULK XRD

The original Saracen-1 samples for bulk XRD mineralogical analysis were ground using an agate mortar and pestle. The ground samples were pressed into sample holders and analysed. A sub- sample of approximately 5 g was taken, mixed with deionized water and treated with 10 ml of 1 M NaCl. The sub-sample was repeatedly rinsed and centrifuged to recover the <2 μm fraction. The <2 μm fraction was subsequently treated with acetic acid, saturated with 1 M $CaCl_2$, repeatedly rinsed with deionized water followed by alcohol and then dried at 105 °C. The samples were then pressed into sample holders and analysed (Dewhurst et al., 2002).

The warehoused Saracen-1 samples also underwent bulk XRD mineralogical analysis. The samples were ground using an agate mortar and pestle. The ground samples were pressed into sample holders and analysed. The samples stored in zip-lock bags had to be mixed with the original powdered sample that was stored separately in sealed containers to make up the volume. This is also acknowledged as a variable that may have affected the results.

The XRD analysis of the Gorgon CO2 Data Well-1 & Data Well-1ST1 and CRC-1 samples was carried out by Michael Till at Amdel on behalf of Daniel and Kaldi (2006) and (2007). Both the Amdel machine and interpreter are no longer available, but the original XRD scan files were kept. Thus the XRD analysis of the warehoused samples was undertaken by the author under the supervision of Dr. Tony Hall and Dr. Tony Milne at the University of Adelaide. The methodology for preparing samples was kept constant for the Bulk XRD analysis. The X-ray diffraction source used by Amdel was Cobalt with a wavelength of 1.79020 and the X-ray diffraction source for the Bruker D8 machine at the University of Adelaide was a copper source with a wavelength of 1.54060. However, the different sources used to produce the X-ray diffraction patterns will result in a slight shift in peak location and

will still allow a comparison between diffraction patterns and the intensity of the relative peaks.

The warehoused conventional core samples from Gorgon CO2 Data Well-1 & Data Well-1ST1 and CRC-1 wells were sub-sampled (approximately 5 g) and crushed. Before and after each sample was crushed the tungsten carbide container was cleaned by running a sample of quartz and then cleaning the container with ethanol. The crushed rock samples were then loaded into XRD sample containers. All efforts were made to obtain a flat surface of crushed sample in the XRD sample containers.

A.15 XRD CLAYS

The Saracen-1 original samples for clay XRD mineralogical analysis were obtained by redispersing the <2 μm fraction powders with deionized water. The suspensions were applied to cellulose nitrate filter discs to maximise orientation of the clay platelets. One sample was saturated with magnesium and glycerol to aid mineral identification (Dewhurst et al., 2002).

The warehoused conventional core samples only had a sub- sample of approximately 5 g taken, mixed with deionized water and treated with 10 ml of 1 M NaCl. The sub-sample was repeatedly rinsed and centrifuged to recover the < 2 μm fraction and the < 0.2 μm. The <2 μm and <0.2 μm fraction was subsequently treated with acetic acid, saturated with 1M $CaCl_2$, repeatedly rinsed with deionized water followed by alcohol and then dried at 105 °C. The samples were then pressed into sample holders and analysed to give the clay fraction.

The original samples for the both the Gorgon CO2 Data Well-1 & Data Well-1ST1 and CRC-1 wells were both analysed with XRD by Michael Till at Amdel. The XRD clay analysis was performed by taking a sub-sample of pulverised rock. This sub-sample was treated with a mixture of demineralised water and deflocculants and allowed to settle. A pipette was then used to acquire a 2 μm fraction. The acquired 2 μm fraction was then applied to a porous ceramic plate. As the sample is pipetted onto the ceramic plate, a vacuum is applied drawing the water out and leaving the clay platelets orientated on their flat face. The sample was then treated with Mg^{++} ions to remove the exchangeable cations helping to improve the identification of smectite. The sample was then dried and analysed with the XRD machine on the clay setting (Daniel and Kaldi, 2006 and 2007).

The warehoused samples for the both the Gorgon CO2 Data Well-1 & Data Well-1ST1 and CRC-1 wells were analysed with the standard method used by Dr. Tony Hall and Dr. Tony

Milne at the University of Adelaide. A 100 milligram crushed sub-sample was accurately weighed out and used for clay analysis. The samples were placed in centrifuge containers, treated with 5 ml of 1 mol $CaCl_2$ exchange solution, shaken vigorously and left to stand for 30 minutes. The samples were diluted by adding distilled water, filling the centrifuge containers to the 10 ml level. Subsequently, samples were centrifuged for 15 minutes at 2000 rpm. The solvent was poured off and the sample containers were refilled with distilled water (rinsing). The centrifuging and rinsing of the samples was repeated three times. On completion of this, the samples were treated with the ultrasonic machine for 1 minute at 30 %. The samples were assessed for the amount of material in the water column. Samples that were settling to quickly were re-centrifuged, rinsed and treated with the ultrasonic. Once the samples were assessed to be satisfactory they were centrifuged for 4 minutes at 900 rpm. Once again they were assessed for the amount of material in the water column. If the samples had settled and there was minimal material in the water column, then they were re-rinsed, centrifuged and treated with the ultrasonic. On achieving satisfactory samples, a pipette was used to sample the solution in the middle of the water column. This solution was then applied to a silicon slide and dried in the oven at 40 ° C for 2 hours. The prepared slide was then analysed with the XRD machine set to clay.

A.16 XRD INTERPRETATION

To compare and contrast results, the XRD analysis should ideally be analysed in the same manner, on the same machine and by the same interpreter. In the case of the Saracen-1 samples, the XRD machine was upgraded in the intervening warehouse period, but the preparation of the samples and the interpreter (Mark Raven) remained the same.

The samples from Gorgon CO2 Data Well-1 & Data Well-1ST1 and CRC-1 wells were originally analysed by Michael Till at Amdel. The warehoused samples, however, were analysed on a Bruker D8 machine at the University of Adelaide by the author. The preparation of the samples for bulk XRD appears consistent, but the preparation of the clay XRD analysis does differ which may have affected the results. To compare the XRD diffractograms of the original and warehoused samples, the analyses were both plotted using the Xplot software. Due to the different X-ray diffraction sources used, the XRD diffractograms could not be plotted on the same diffractogram. To compare the original and warehoused results, the XRD diffractograms were used to compare peak shape and intensity to gauge any differences between samples. The comparison was further complicated by the greater sensitivity of the Bruker D8 machine used to analyse the warehouse samples. The results and interpretation of differences can be considered as a guide only.

A.17 SCANNING ELECTRON MICROSCOPE

The scanning electron microscope samples are prepared in two ways depending on the desired image; SEM or BSE. The SEM samples are prepared by cutting a 1 cm^3 block that is orientated in a perpendicular direction to the bedding of the sample. The 1 cm^3 block is broken with a small rock chopper producing a fresh clean broken surface for imaging. The bottom of the block is attached to a SEM stub with adhesive (i.e. araldite resin). The sample is thinly vacuum coated with platinum allowing a clear image to be obtained. The samples for BSE imaging are prepared by orientating the sample in a perpendicular direction to the bedding to obtain information on the fabric of the rock. The 1 cm^3 samples are polished instead of being broken. In the first instance, this involves sanding with emery paper followed by ion milling. The sample is attached to a SEM stub and coated with a thin film of platinum as was done with the SEM samples.

The fresh Muderong Shale samples in the original analysis conducted by Dewhurst et al., (2002) were investigated using the SEM machine set to backscatter electron (BSE) microscopy. They were freeze dried, impregnated with resin and polished. The samples were orientated at 90 ° to the bedding and glued to a SEM stub. The SEM machine was setup with the sample at10 mm working distance and an acceleration voltage of 25 kV.

The warehoused Muderong Shale samples were not freeze dried or resin impregnated. The conventional core samples were glued to a SEM stub. The drill cutting samples were orientated with their short sides normal to the viewed surface in an Araldite resin filled the cylinder. The samples were initially hand sanded using emery paper (1200 grit followed by 3000 grit) and then ion milled using a Fischione ion mill to obtain a polished surface, followed by the application of platinum.

In the case of the reports prepared by Daniel and Kaldi, (2006) and Daniel, (2007) for Gorgon CO2 Data Well-1 & Data Well-1ST1 and CRC-1 respectively, the samples were freshly broken and glued to a SEM stub for viewing with the SEM microscope. The warehoused samples were prepared in the same manner. Further, polished stubs for BSE imaging were also prepared for the warehoused samples to obtain more detailed mineralogical information although no original imaging is available for comparison.

All warehoused samples were analysed with the Quanta 450 FEG Environmental SEM+EDAX TEAM EDS with SDD detector. SEM and BSE images were acquired at different levels of magnification to gain information on the mineralogical fabric of the

samples. EDAX scans were taken for all images. With high magnification images, EDAX scans were taken of individual minerals for identification.

A.18 DETAILED WELL AND SAMPLE LOCATIONS

A.18.1 Evaluation of MICP Analysis – Accuracy, Repeatability and Comparability

The evaluation of MICP analysis was undertaken to determine the robustness of the technique. In the first instance, the accuracy of the MICP analysis was checked by analysing Micromeritics Silica-Alumina standard samples. This analysis was regularly undertaken as part of the quality assurance required by the laboratory. Upon request by this study, the standard samples were analysed in full allowing a comparison and determination of the accuracy of MICP analyses.

The Thebe-2 samples were analysed as part of the investigations into the production of synthetic MICP curves from NMR data. The samples were very fragile and it was decided that as a secondary investigation the state of the samples would be recorded before and after MICP analysis providing anecdotal evidence regarding compression. Thus due, to the fragile nature of the samples, it was expected that any compression of the sample during analysis would lead to complete disintegration of the rock sample.

The original Muderong Shale samples from Saracen-1were analysed at the ASP and the finding were reported in Dewhurst et al., (2002). This well and the Muderong Shale analyses was chosen to determine the repeatability of MICP analysis on adjacent samples as the original analyses were available for re-interpretation, the sheer number of samples analysed from the 1.6 m interval of conventional core, and the supporting XRD analysis and BSE imaging indicating the conventional core was fairly uniform.

The Tindilpie-11 and Mena Murtee-1 wells were chosen because they had existing MICP, helium pycnometry, laboratory NMR and well log NMR over both reservoir and low sealing capacity rock allowing the comparison of results from the different techniques.

A.18.2 Sample Type and the Effect on MICP Analysis

The Flaxman-1, Swan-1, Puffin-2, Tenacious West wells were chosen for the investigation of sample type because the analyses had already been undertaken by Watson, (2012) and Kivior, (2005) and was available for re-interpretation. These analyses could be further compared to the similar analyses undertaken on Saracen-1 in this study.

A.18.3 The Effects of Warehousing Rock Samples on MICP Analysis

The ASP has had a Mercury Porosimeter since the 1980‘s. During that time hundreds of samples have been analysed, including original (fresh) samples that have since been stored (warehoused). All of these analyses have been kept and filed allowing a comparison of the original data set to the re-analysed warehouse data. The same Mercury Porosimeter is still in operation and its utilisation provides the opportunity to determine the effects of warehousing while minimising the effects of equipment, techniques and output that may be a variable if another Mercury Porosimeter is employed.

Of particular relevance to this research are one journal paper and two CO2CRC reports that provide the basis for comparison to the present day results to determine the effects of warehousing. These reports were selected because there was a comprehensive analysis conducted on original (fresh) conventional core samples as well as there being stored (warehoused) core available for sampling. The analysis included MICP, XRD and SEM/ BSE imaging that were available.

Dewhurst et al., (2002) conducted seal capacity analysis of the original Muderong Shale samples from Saracen-1. The core was subsequently stored at the Western Australian Geological Survey and was approved for sampling for this study. Four core plug samples were taken within but not next to the original 11 samples (Figure A- 5). The core plugs were taken by Western Australian Geological Survey (WAGS) on the author‘s behalf and were drilled without the use of lubricant. Also 4 drill cutting interval samples were taken; above, over the same interval and below the conventional core. These samples were then placed in airtight bags and sent via the post to Adelaide.

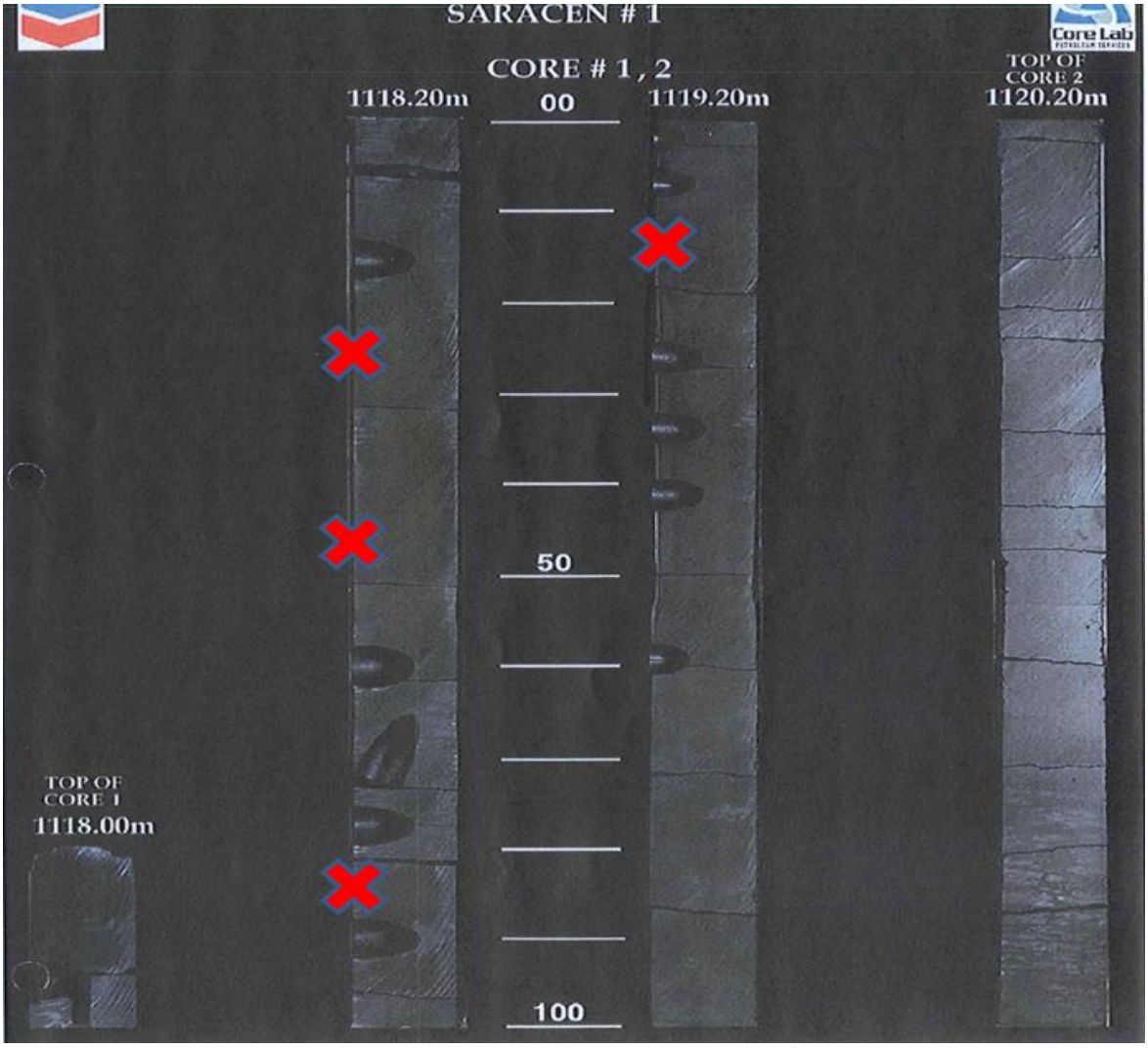

Figure A- 5: Image of conventionally cored Muderong Shale from Saracen-1. The fresh sample locations of Dewhurst et al., (2002) can be observed as well as the sample locations of the warehoused samples marked with red crosses.

In a CO2CRC report on seal capacity of the Gorgon CO2 injection Project on Barrow Island, Carnarvon Basin, Western Australia Daniel and Kaldi, (2006) analysed more than 20 samples of ~~"f~~resh" caprock and intraformational sealing rock with MICP, XRD and SEM. The core was subsequently stored in Western Australia Core Laboratories Australia in an open air warehouse. The reports were released by Chevron and approval was given for sampling of the conventional core. Five samples were taken by the Western Australian Core Laboratories adjacent to five of the original samples and re-analysed. Samples were picked out of the core as broken pieces; no water was used in the retrieval and thus no alteration should have occurred as a result of the sampling.

Daniel, (2007) completed a comprehensive analysis of the sealing formations intersected in CRC-1 in the Otway Basin. The report had 1 sample from the Pember Mudstone, 3 intraformational baffle samples from the Paaratte Formation and 5 samples from the Belfast

Mudstone. The core was subsequently stored in the Victorian Core Library and later moved to Geoscience Australia‘s Core Library in Canberra. Nine samples were taken adjacent to the original samples and re-analysed. The samples were picked out of the core as broken pieces; no water was used in their retrieval.

A.18.4 NMR Synthetic MICP Curves

The wells used for the production of NMR synthetic MICP curves were selected on the basis of available data only. The necessary data included a conventionally cored interval covering both sealing and reservoir rock and an NMR well log over the entire interval. While the reservoir intervals were not of interest for this project they were necessary to prove/ disprove the techniques ability to identify both sealing and reservoir intervals. Thus the conventional core MICP curves and the synthetic mercury curves needed to be similar for both rocks types with the understanding that pore body to pore throat correction factor will likely be wrong for the reservoir rock.

Wells with conventionally cored sealing intervals and NMR logs are rare for conventional petroleum plays and thus the wells identified have come from a number of basins around Australia. As the project has progressed, the exploration and research into unconventional plays with tight sandstone/ siltstone/ shale intervals has occurred. These results are being released concurrently and provide more opportunities to test this methodology.

The Tindilpie-11 well had conventional core cut through the Patchawarra Formation. Numerous samples were taken by the operator (Santos) on the tight reservoir and conventional reservoir samples based on CT scanning.

The CRC-2 well samples were taken at the time of drilling by Dr. Ric Daniel for seal capacity analysis. These samples included reservoir, low seal capacity intraformational baffles within the reservoir formation and sealing intervals above and below the reservoir.

The Redman-1 samples were all taken by Al-Ghamdi, (2006). These samples were all from a fine-grained interval of the Pretty Hill Formation. This study subsequently took a reservoir sample from the conventional core in 2016.

The Mena Murtee-1 samples were taken after coring by identifying possible sealing lithologies by Dr. Ric Daniel. Both an NMR well log and laboratory NMR analysis were carried out. Three additional samples were taken at a later stage adjacent to the laboratory NMR analysis.

The Gorgon CO2 Data Well-1 & Data Well-1ST1 samples were taken at the wellsite by Chevron representatives.

The Thebe-2 sample locations for MICP analysis were governed by the fragility of the core. The fragility of the core prevented the drilling of core plugs for samples analysis. Samples had to be taken where they had broken away from the parent rock material which ultimately was a reflection of the lithology of the sample.

B. APPENDIX

2269.35	2247.20	2275.80	2188.37	2298.13	2182.35	2259.05	2381.66

Figure B- 1: Thebe-2 samples after MICP analysis.

Table B- 1: Original Bulk XRD analysis of Saracen-1 samples by Mark Raven at the CSIRO in 2000/2001 from the well completion report and published in Dewhurst et al., (2002).

Sample	Depth	w	Gs	Porosity	Qz	Chl	Sm	Py	Sid	Ab	Or	Mica	Kao
	m	%	gcm^{-3}	%	%	%	%	%	%	%	%	%	%
MUD 1A	1119.19	21	2.56	35	27	5	30	2	<1	1	2	17	14
MUD 2A	1119.24	39	2.54	50	27	5	27	3	<1	2	4	16	15
MUD 3A	1119.42	25	2.59	39	26	5	28	2	<1	2	4	17	15
MUD 4A	1119.50	22	2.56	36	28	5	29	3	1	2	4	15	14
MUD 5A	1119.58	22	2.55	36	27	5	27	2	1	2	3	18	14
MUD 6A	1119.75	20	2.57	34	28	5	26	2	<1	2	3	18	15
MUD 1H	1118.15	22	2.58	36	28	5	29	2	<1	2	4	15	14
MUD 2H	1118.34	18	2.66	33	28	5	30	3	<1	2	3	16	14
MUD 3H	1118.79	18	2.55	32	27	5	26	3	<1	2	3	18	15
MUD 4H	1118.96	30	2.55	43	27	5	28	3	<1	2	4	18	14
MUD 5H	1119.08	33	2.55	46	27	6	25	2	<1	2	4	19	15
MUD 45	1118.87	23	2.55	37	27	6	29	2	<1	2	3	17	15
MUD 1V	1118.22	22	2.54	36	26	5	26	2	<1	2	3	18	15

Notes: w = water content; Gs = Grain Density; Qz = Quartz; Chl = Chlorite; Sm = Smectite; Py = Pyrite; Sid = Siderite; Ab = Albite; Or = Orthoclase; Mica = combined illite and muscovite; Kao = Kaolinite; N.G. = Not Given. Errors on the last significant figure for the bulk composition are estimated to be ±1 for all minerals except smectite and mica which are ±2.

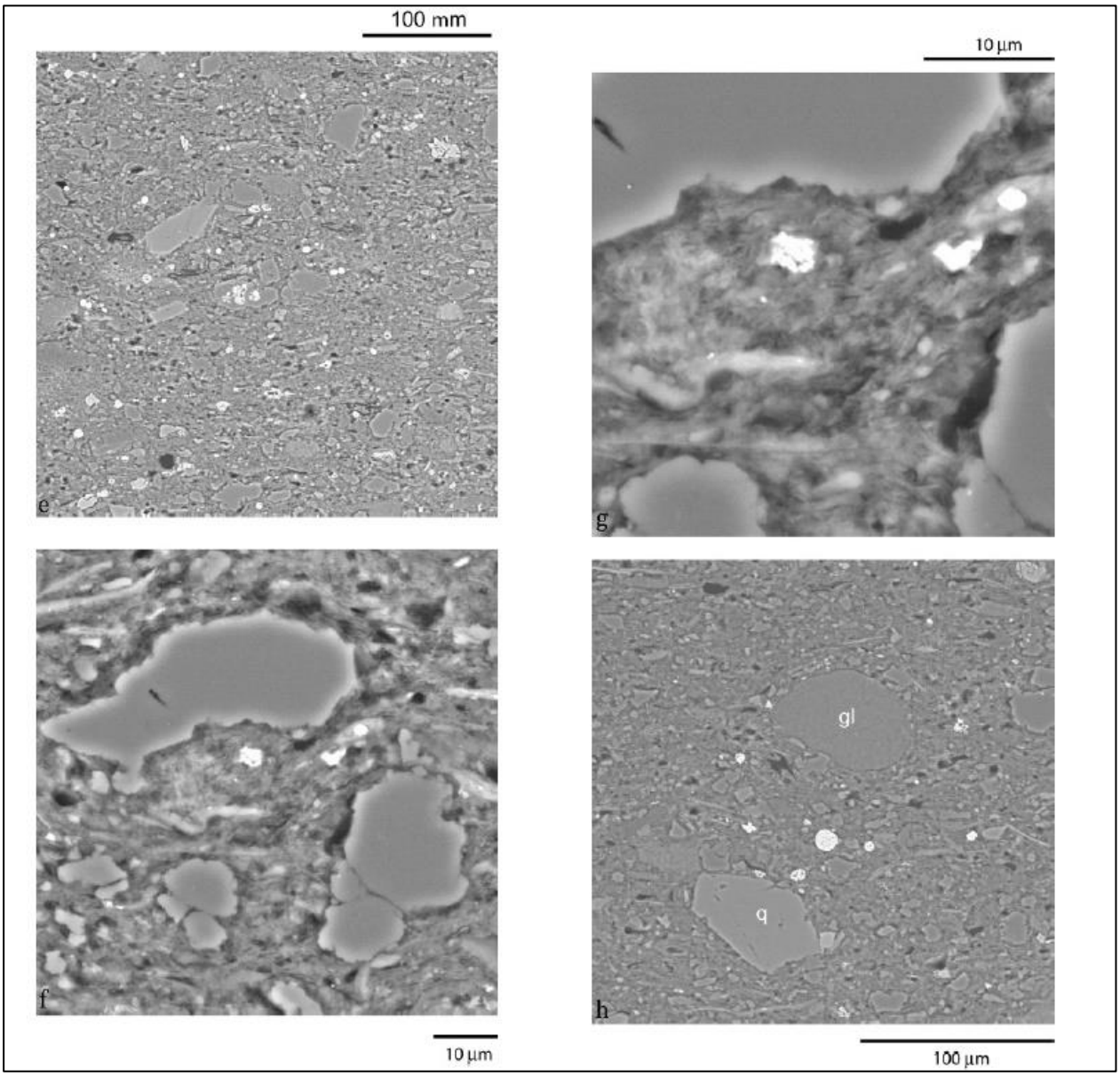

Figure B- 2: BSE images of the Muderong Shale from Saracen-1. (Images taken from Dewhurst et al., (2002)).

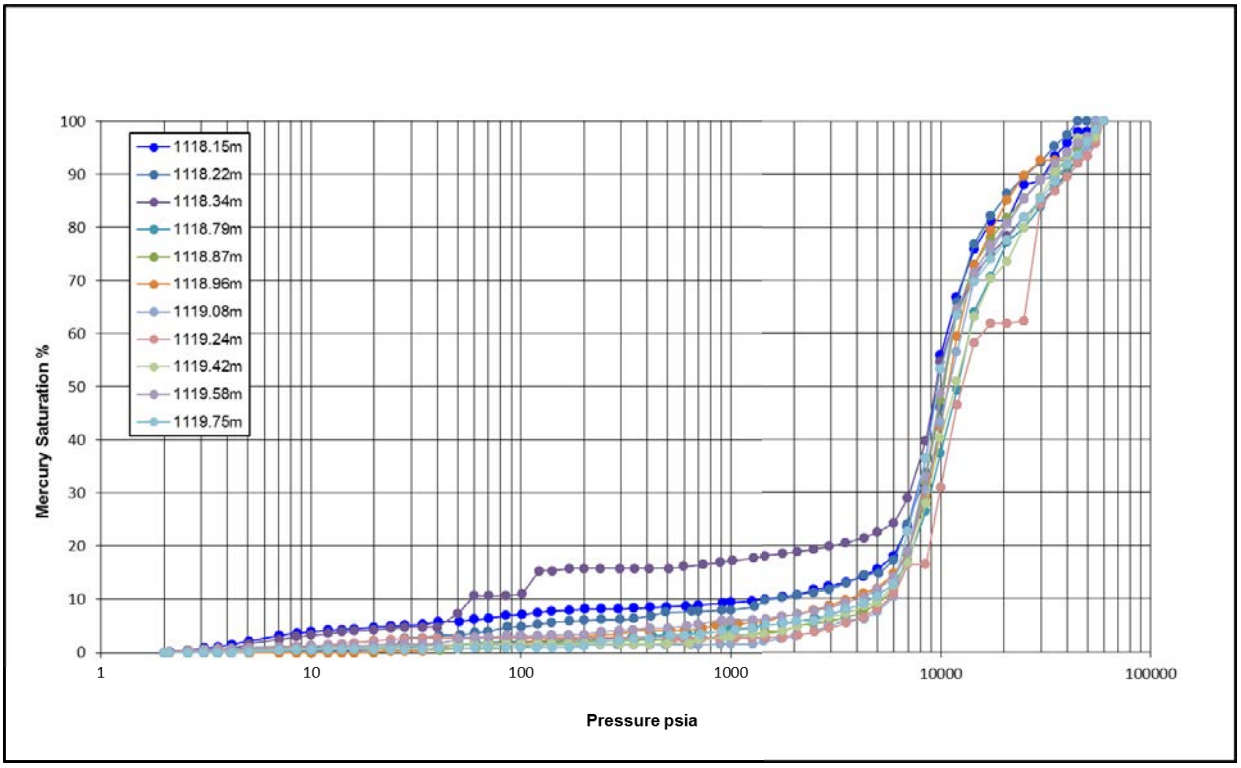

Figure B- 3: Raw MICP curves for the 11 air dried original samples taken over a 1.6 m interval of conventional core of Muderong Shale from Saracen-1. No conformance corrections have been applied (Original analysis was undertaken at the ASP and reported in Dewhurst et al., 2002).

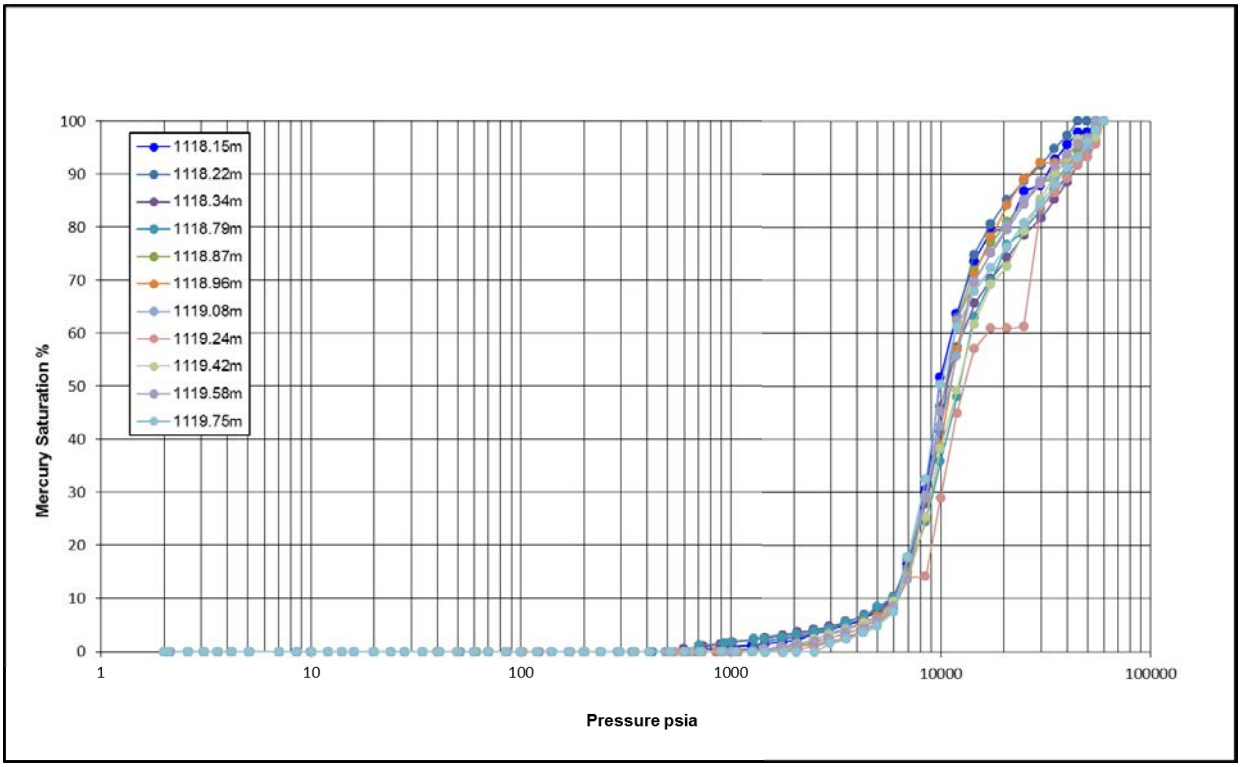

Figure B- 4: MICP curves for the 11 air dried samples taken over a 1.6 m interval of conventional cored Muderong Shale from Saracen-1. Conformance corrections have been applied. (Original analysis was undertaken at the ASP and reported in Dewhurst et al., 2002)

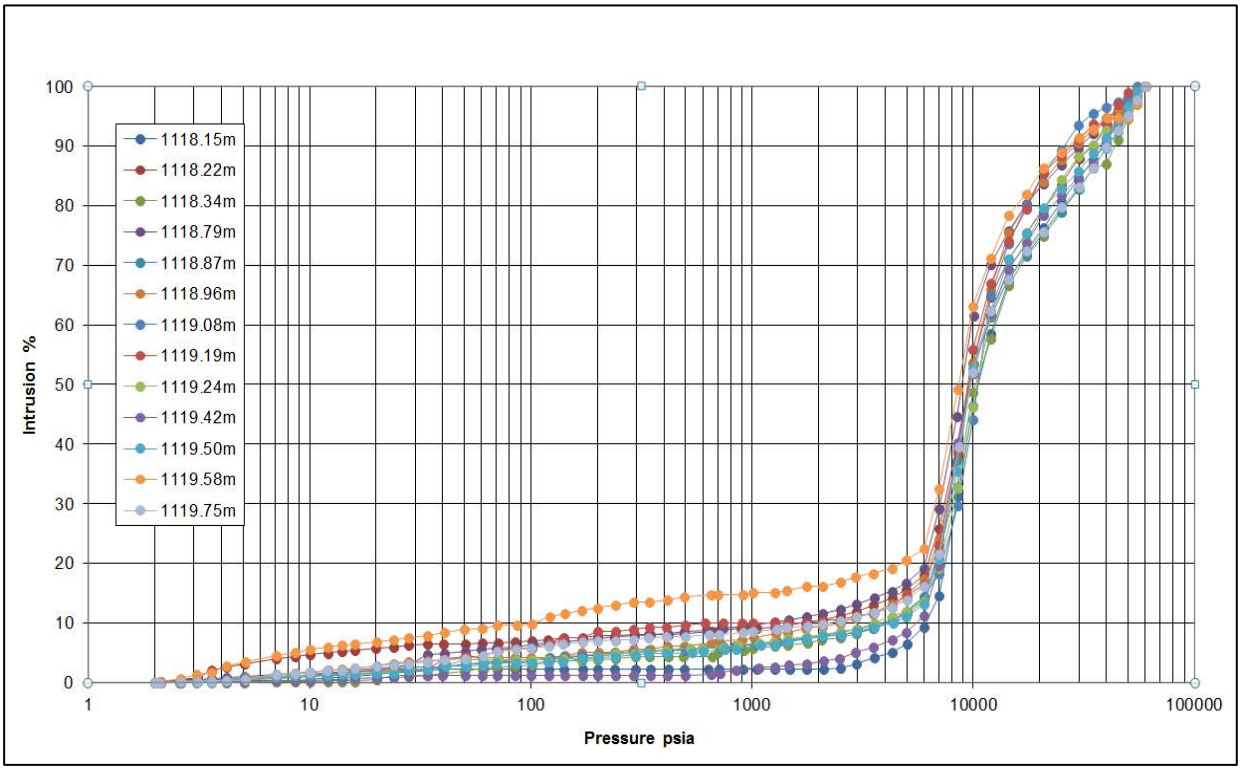

Figure B- 5: Raw MICP curves for the 13 freeze dried samples taken over a 1.6 m interval of conventional cored Muderong Shale from Saracen-1. No conformance corrections have been applied. (Original analysis was undertaken at ASP and reported in Dewhurst et al., 2002)

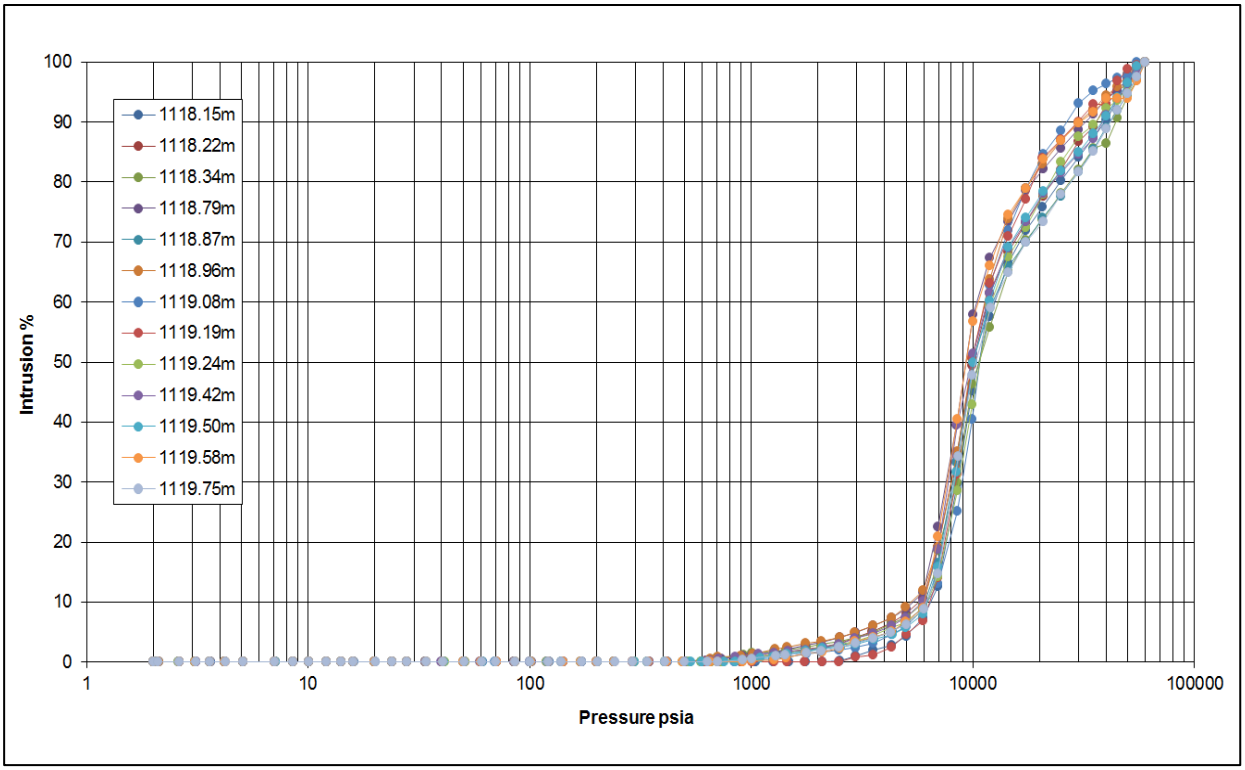

Figure B- 6: MICP curves for the 13 freeze dried samples taken over a 1.6m interval of conventional cored Muderong Shale from Saracen-1. Conformance corrections have been applied. (Original analysis was undertaken at the ASP and reported in Dewhurst et al., 2002).

C. APPENDIX

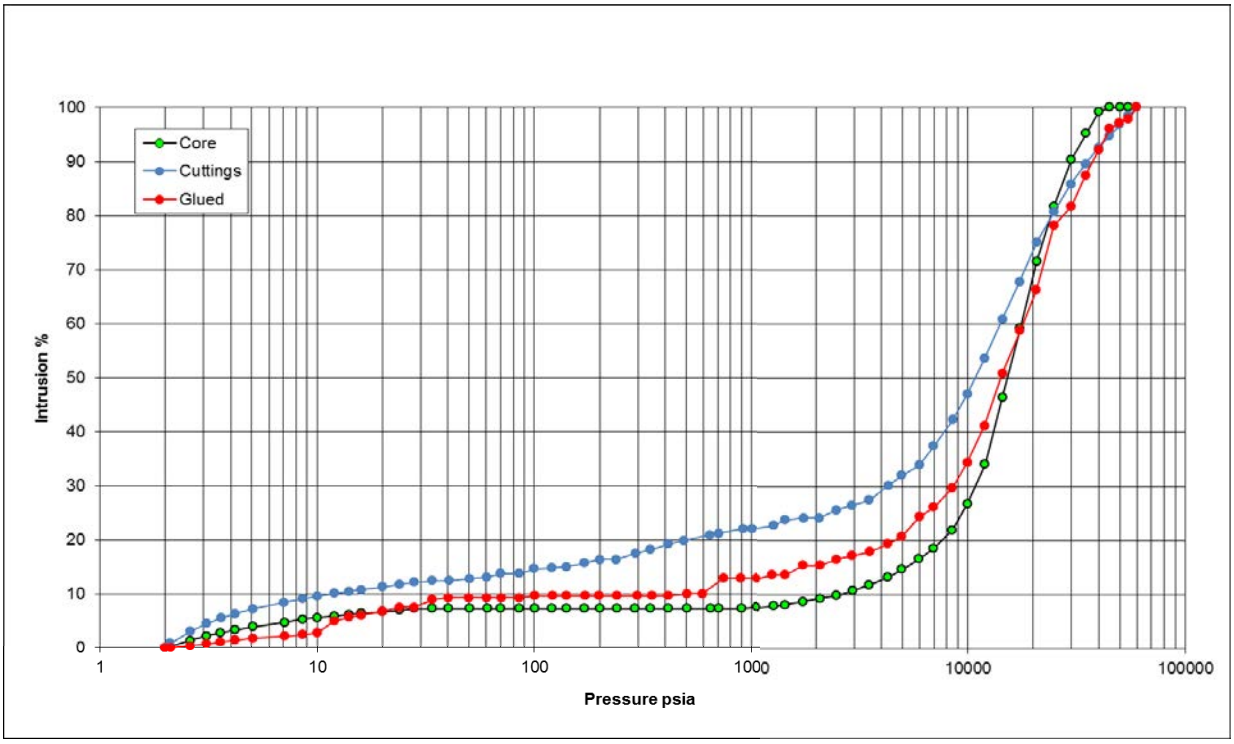

Figure C- 1: Raw MICP injection data for Flaxmans-1 Belfast Mudstone samples; conventional core (Core), conventional core prepared for vertical intrusion only (Glued) and synthetic cuttings (Cuttings). (Original analysis was undertaken by Watson, 2012).

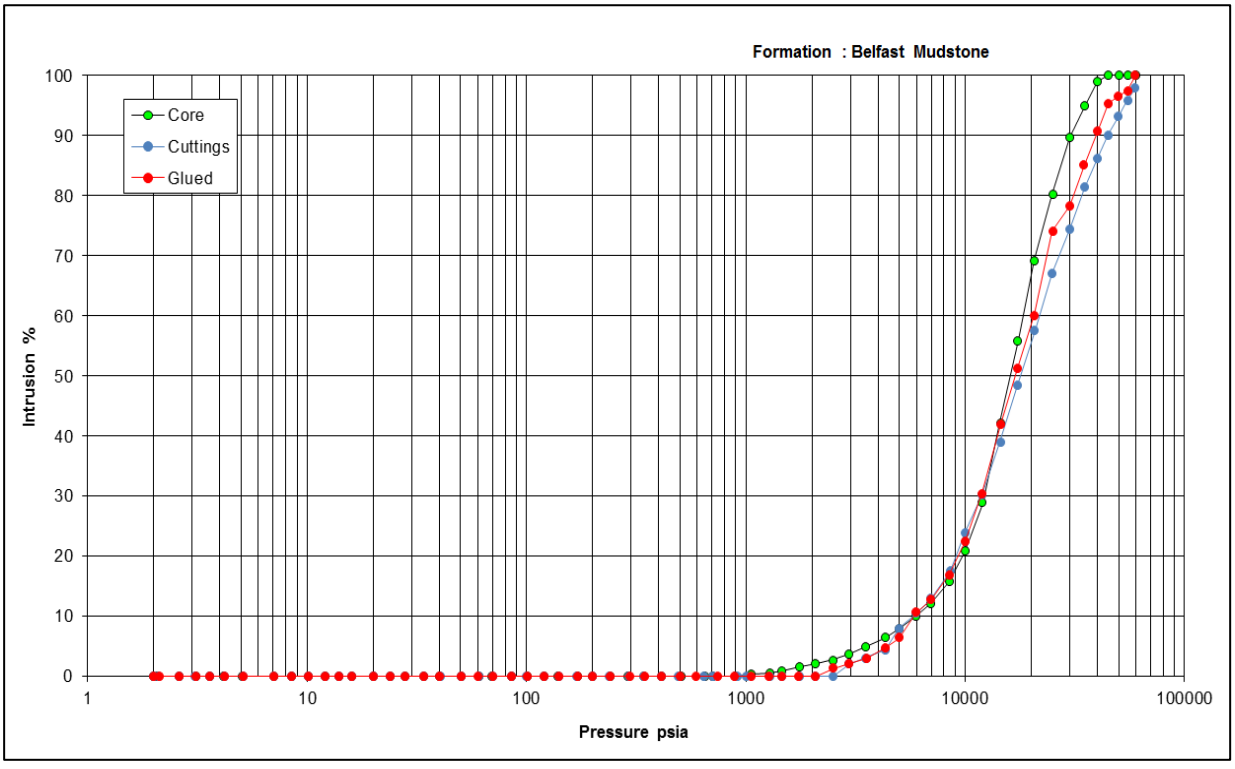

Figure C- 2: Conformance corrected MICP injection data for Flaxmans-1 Belfast Mudstone samples; conventional core (Core), conventional core prepared for vertical intrusion only (Glued) and synthetic cuttings (Cuttings). (Original analysis was undertaken by Watson, 2012)

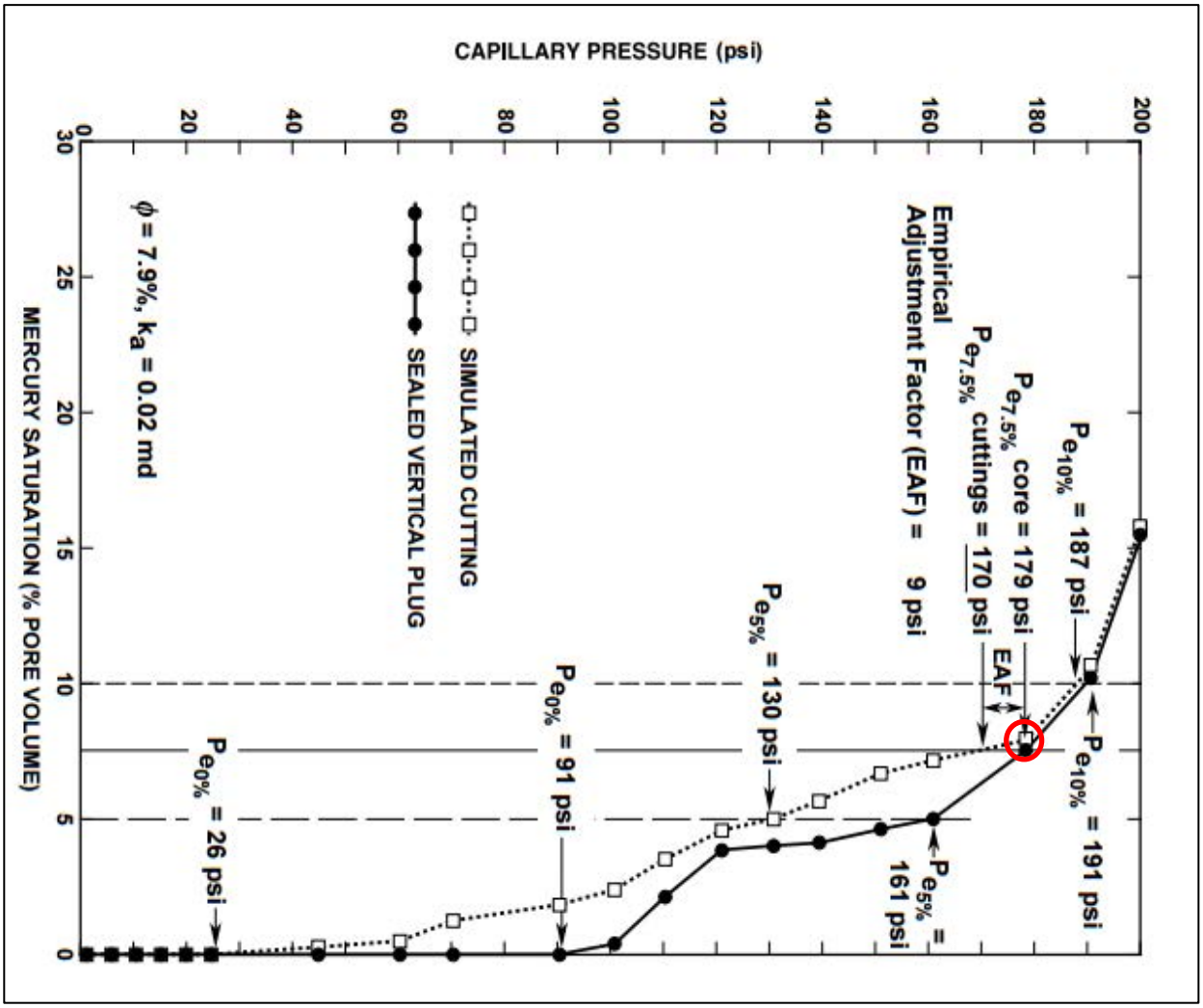

Figure C- 3: A comparison of mercury injection curves from MICP analysis of conventional core prepared for vertical intrusion only and synthetic cuttings. This image is taken from Sneider et al., (1997) and has been re-interpreted.

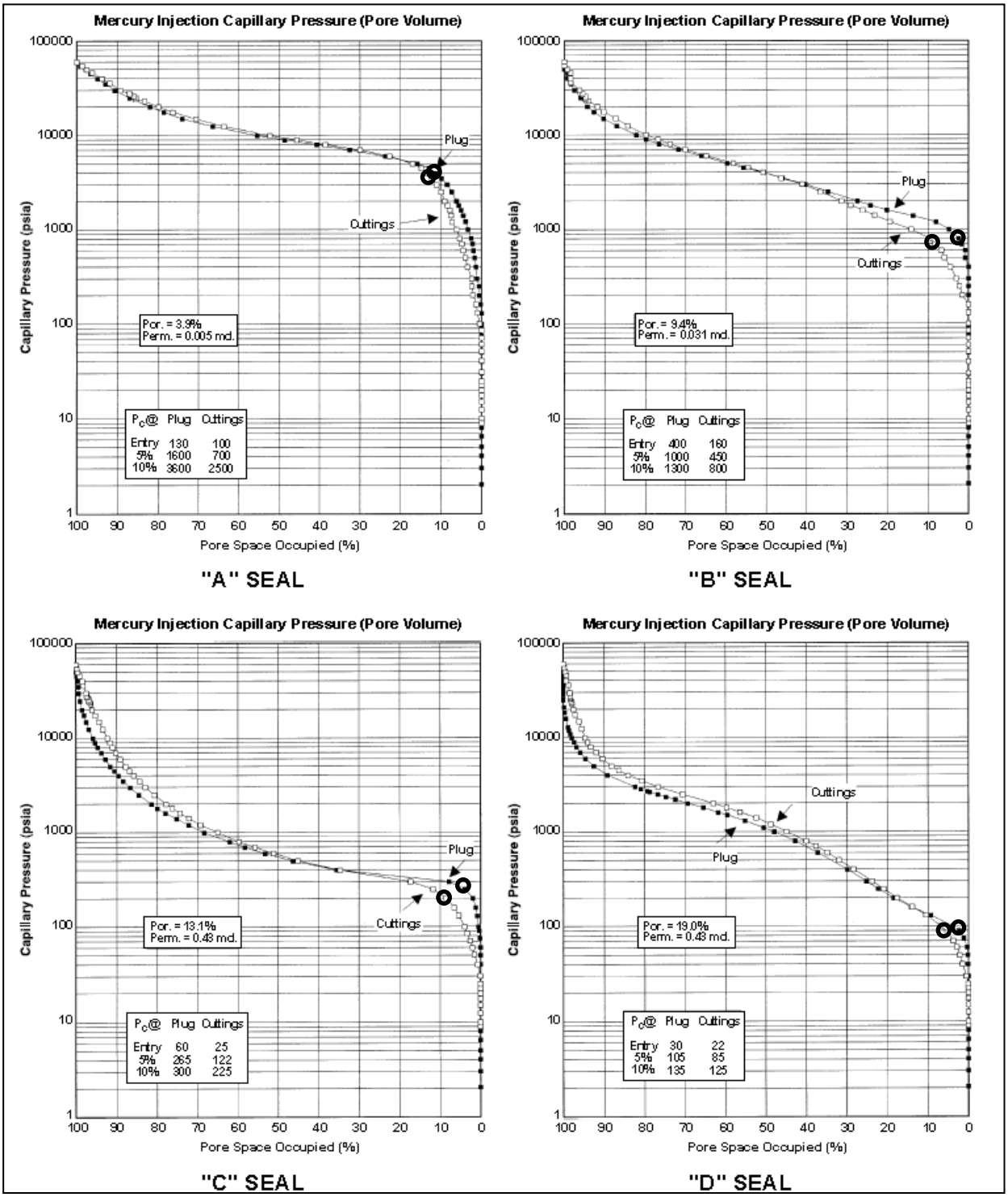

Figure C- 4: MICP results for four seal samples (conventional core prepared for vertical intrusion only and synthetic cuttings). Image and results modified from Sneider et al., (1997).

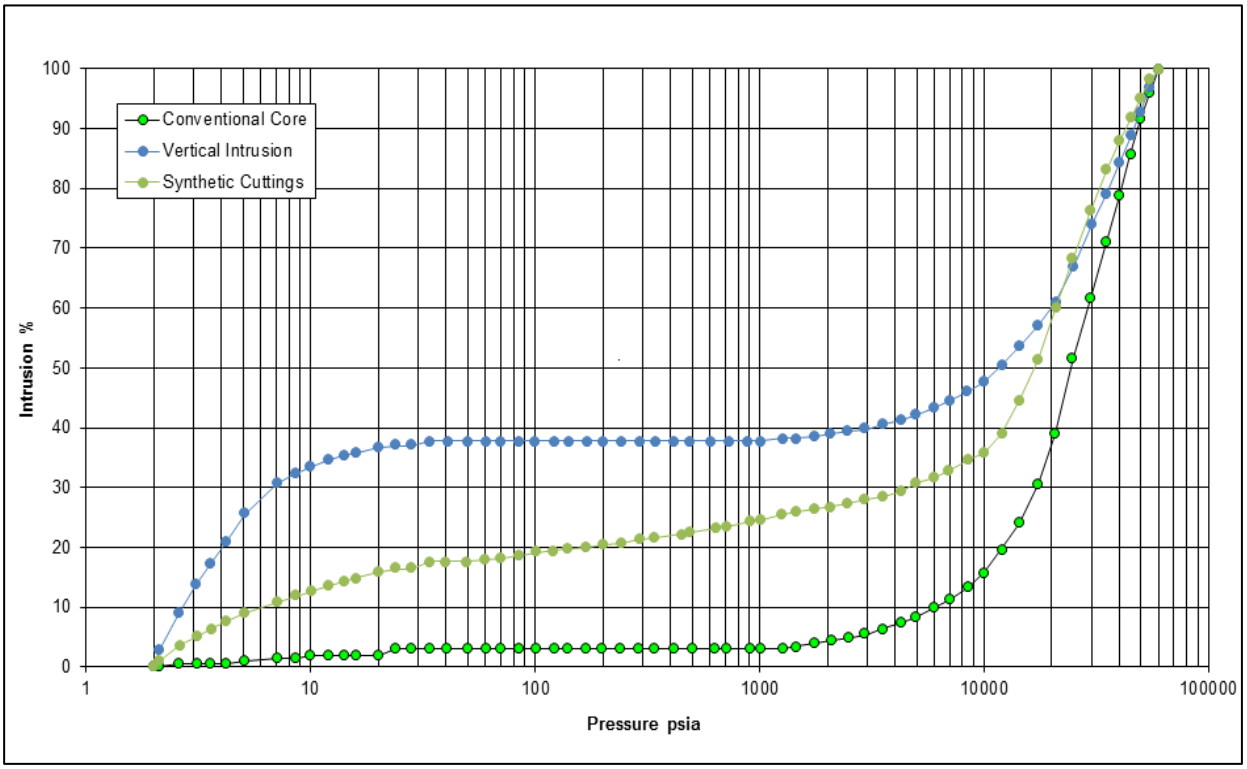

Figure C- 5: Raw MICP curves for Swan-1 sample from a depth of 2835.9 m; conventional core, conventional core prepared for vertical intrusion only and synthetic cuttings. (Original analysis was undertaken by Kivior, 2005)

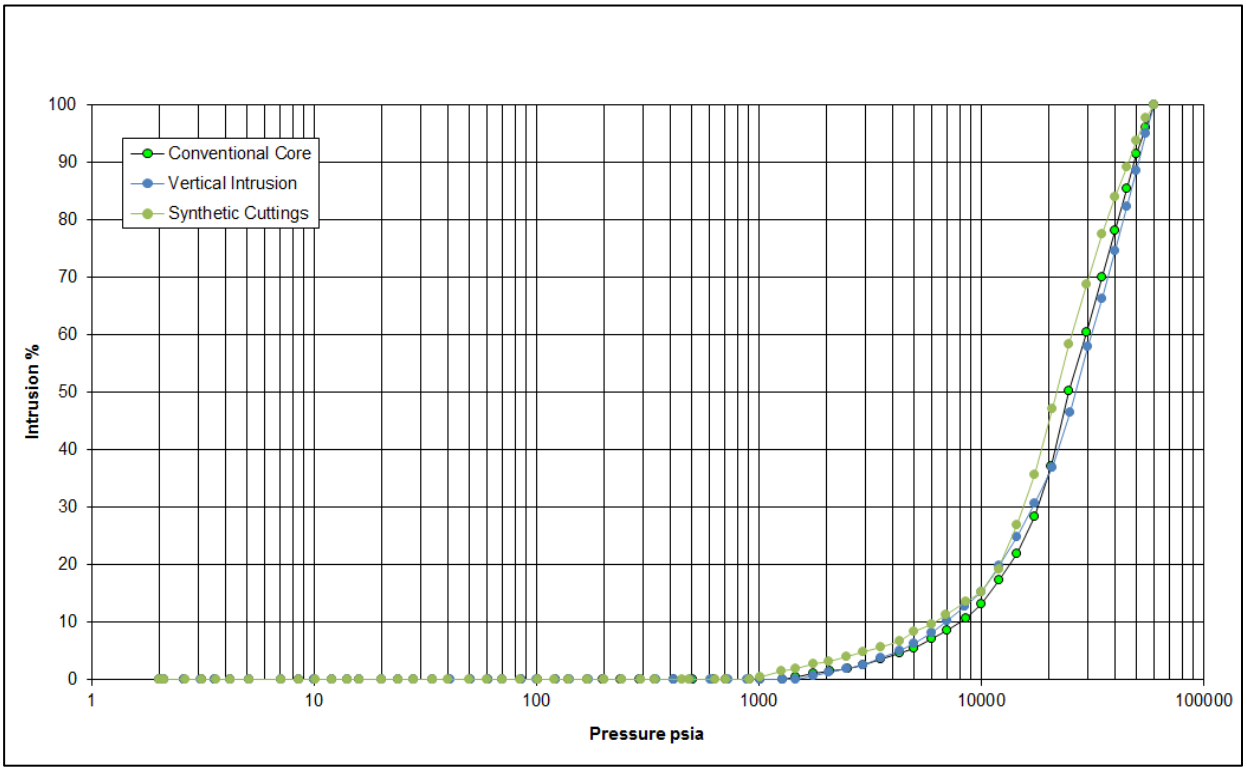

Figure C- 6: Swan1-2835.9 m Conformance corrected MICP curves from the conventional core, conventional core prepared for vertical intrusion only and synthetic cuttings. (Original analysis was undertaken by Kivior, 2005)

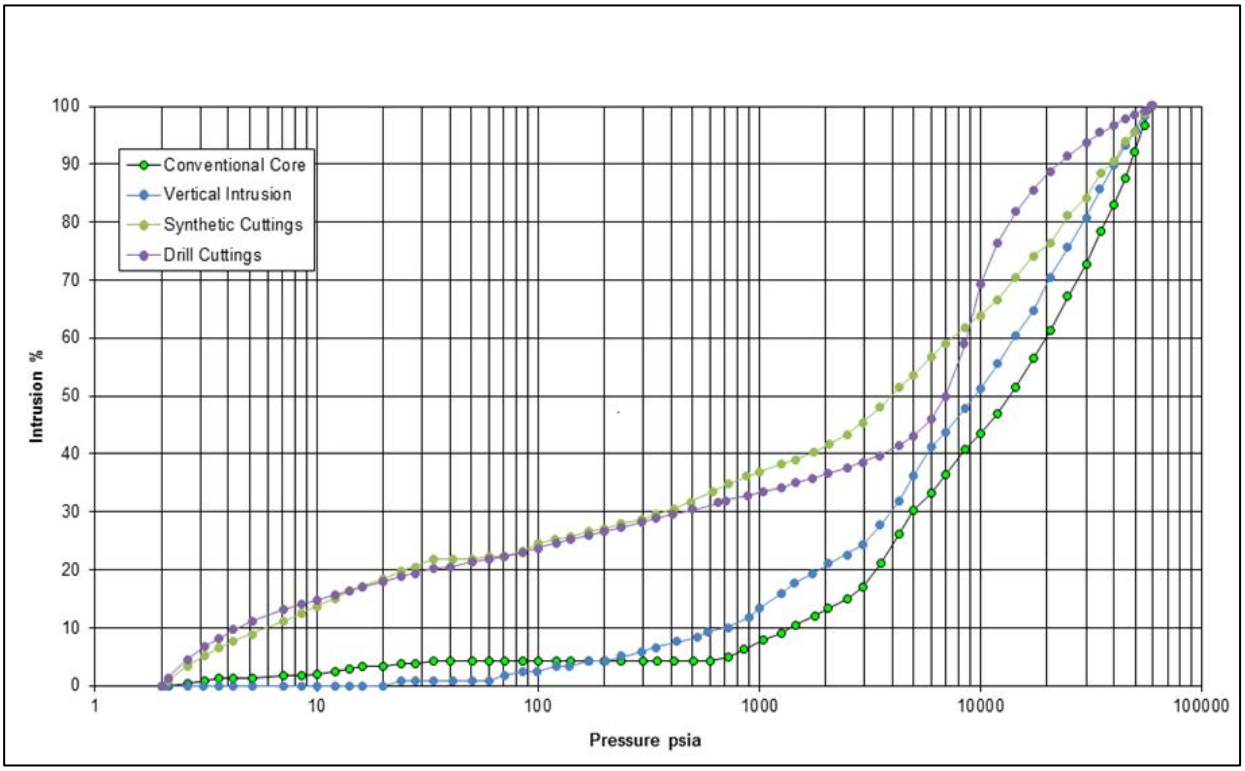

Figure C- 7: Puffin-2 Raw MICP curves. The conventional core, conventional core prepared for vertical intrusion only and the synthetic cutting sample have been taken from a conventional core at a depth between 2042.47 m and 2043.38 m. The drill cutting was taken below at a depth between 2045-2048 m (Original analysis undertaken by Kivior, 2005).

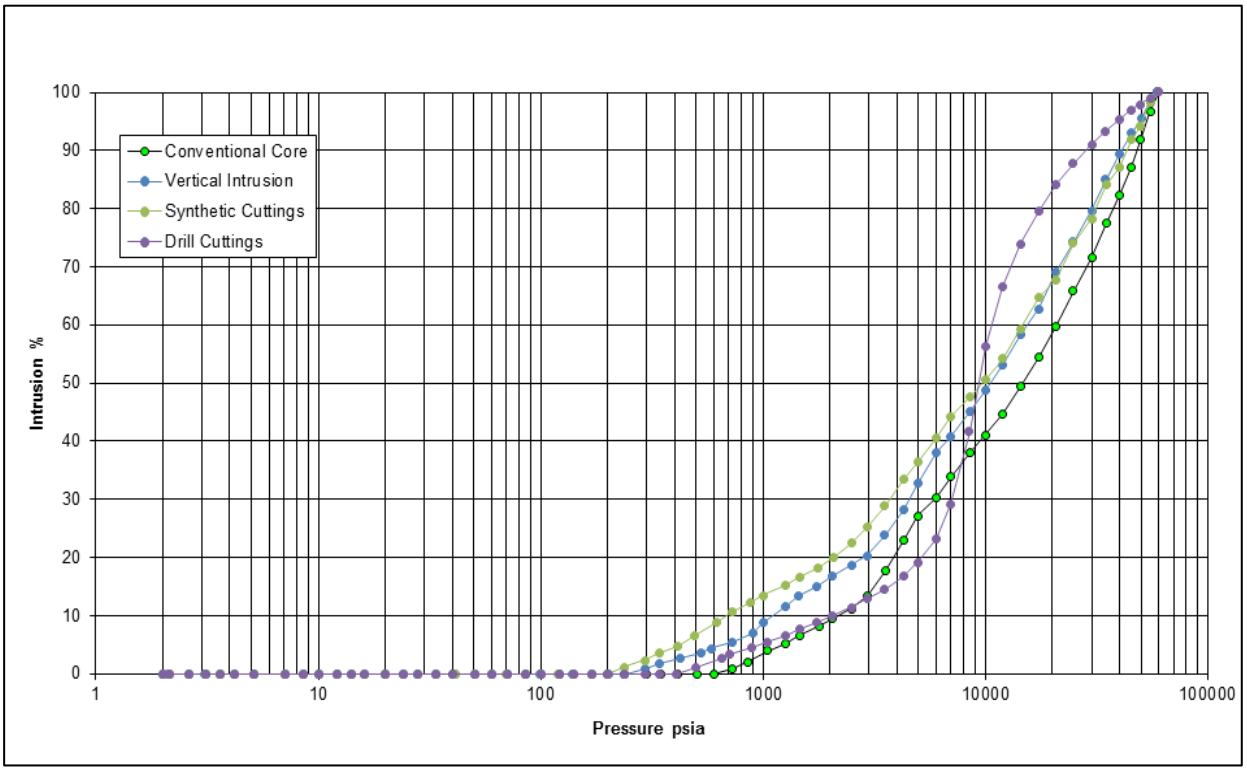

Figure C- 8: Puffin-2 Conformance corrected MICP curves. The conventional core, conventional core prepared for vertical intrusion only and the synthetic cutting sample have been taken from a conventional core at a depth between 2042.47 m and 2043.38 m. The drill cutting was taken below at a depth between 2045-2048 m (Original analysis undertaken by Kivior, 2005).

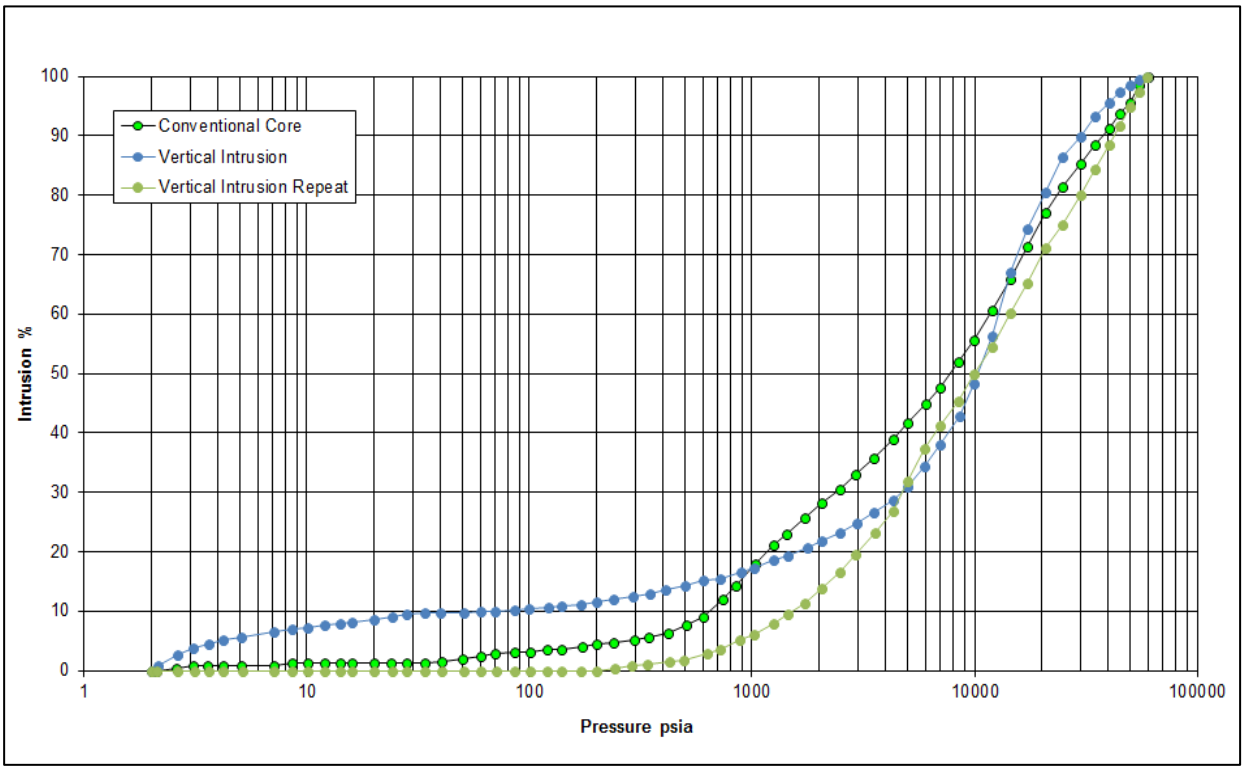

Figure C- 9: Raw MICP curves from Tenacious West-1 sample at a depth of 2810.04 m; prepared as conventional core, conventional core for vertical intrusion only and the repeated conventional core prepared for vertical intrusion only (Original analysis undertaken by Kivior, 2005)

.

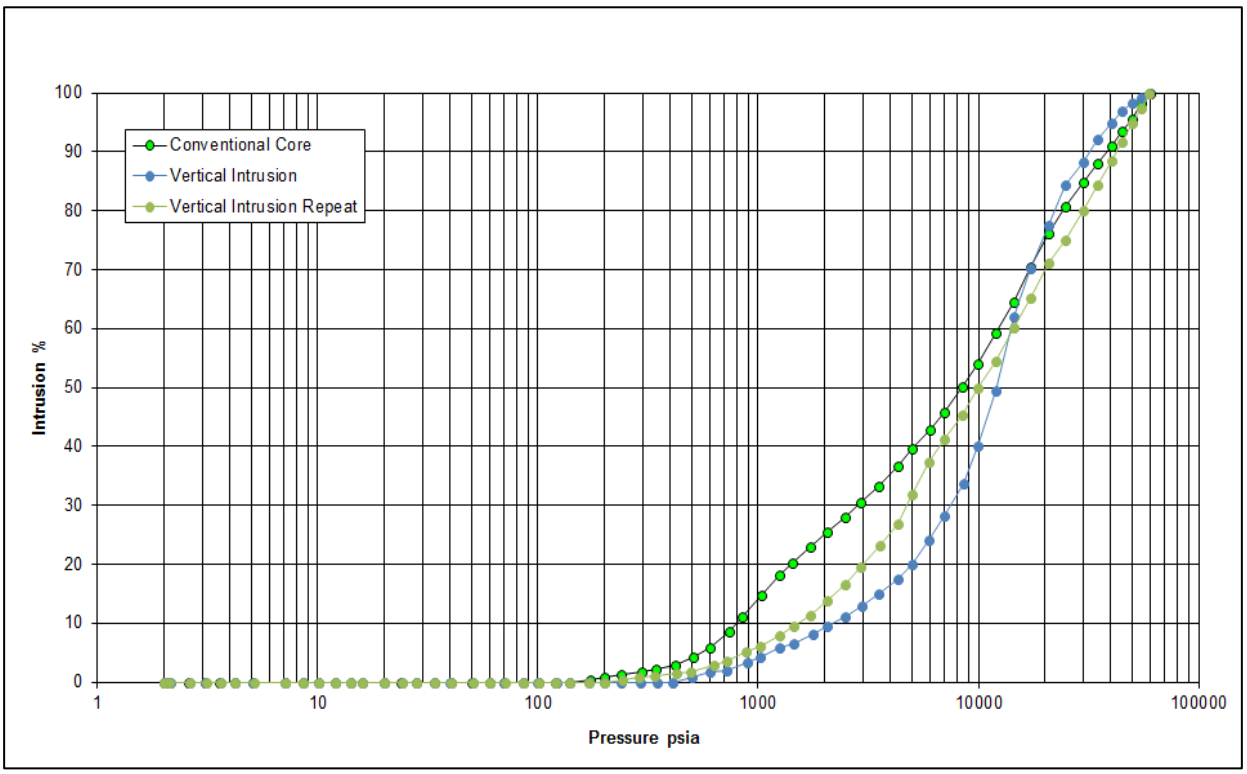

Figure C- 10: Conformance corrected MICP curves from Tenacious West-1 sample at a depth of 2810.04 m; prepared as conventional core, conventional core for vertical intrusion only and the repeated conventional core for vertical intrusion only (Original analysis undertaken by Kivior, 2005).

.

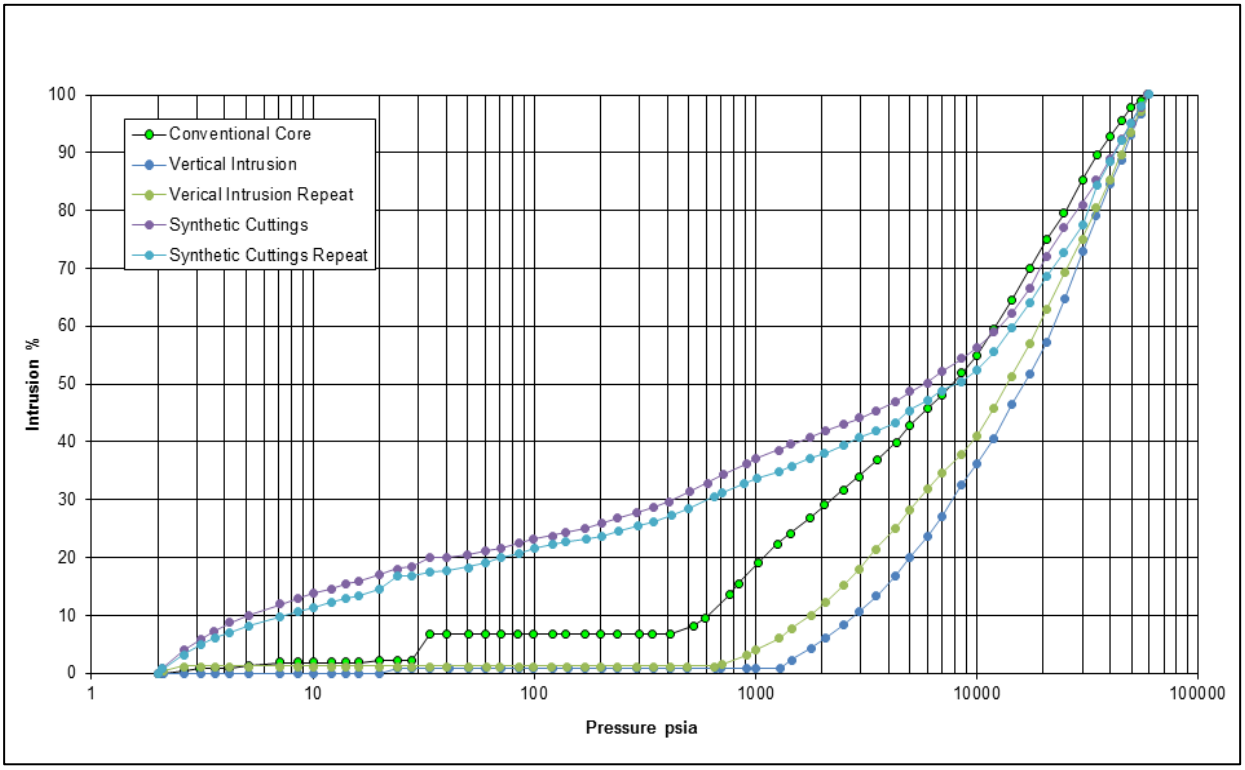

Figure C- 11: Raw MICP curves from Tenacious West-1 sample at a depth of 2846.04 m; prepared as conventional core, conventional core for vertical intrusion only, the repeated conventional core for vertical intrusion only, the synthetic cuttings and the repeated synthetic cuttings (Original analysis undertaken by Kivior, 2005).

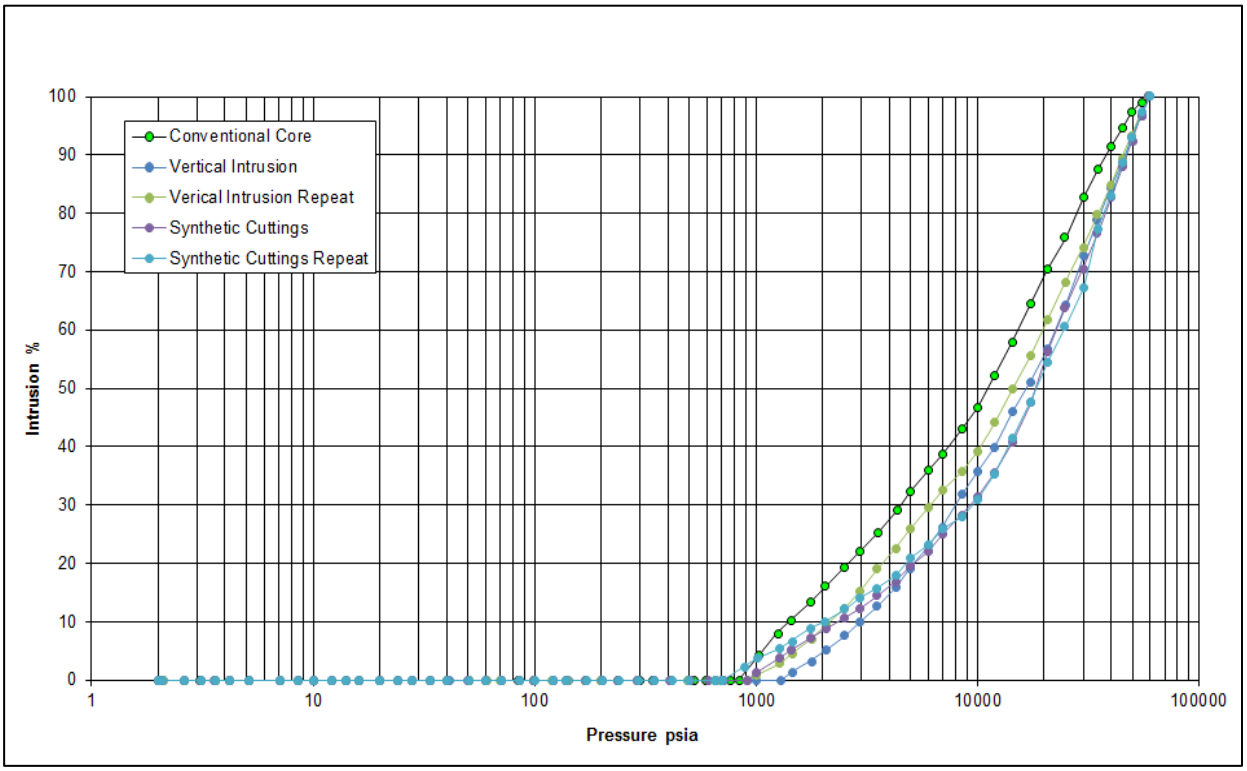

Figure C- 12: Conformance corrected MICP curves from Tenacious West-1 sample at a depth of 2846.04 m; prepared as conventional core, conventional core for vertical intrusion only, the repeated conventional core for vertical intrusion only, the synthetic cuttings and the repeated synthetic cuttings (Original analysis undertaken by Kivior, 2005).

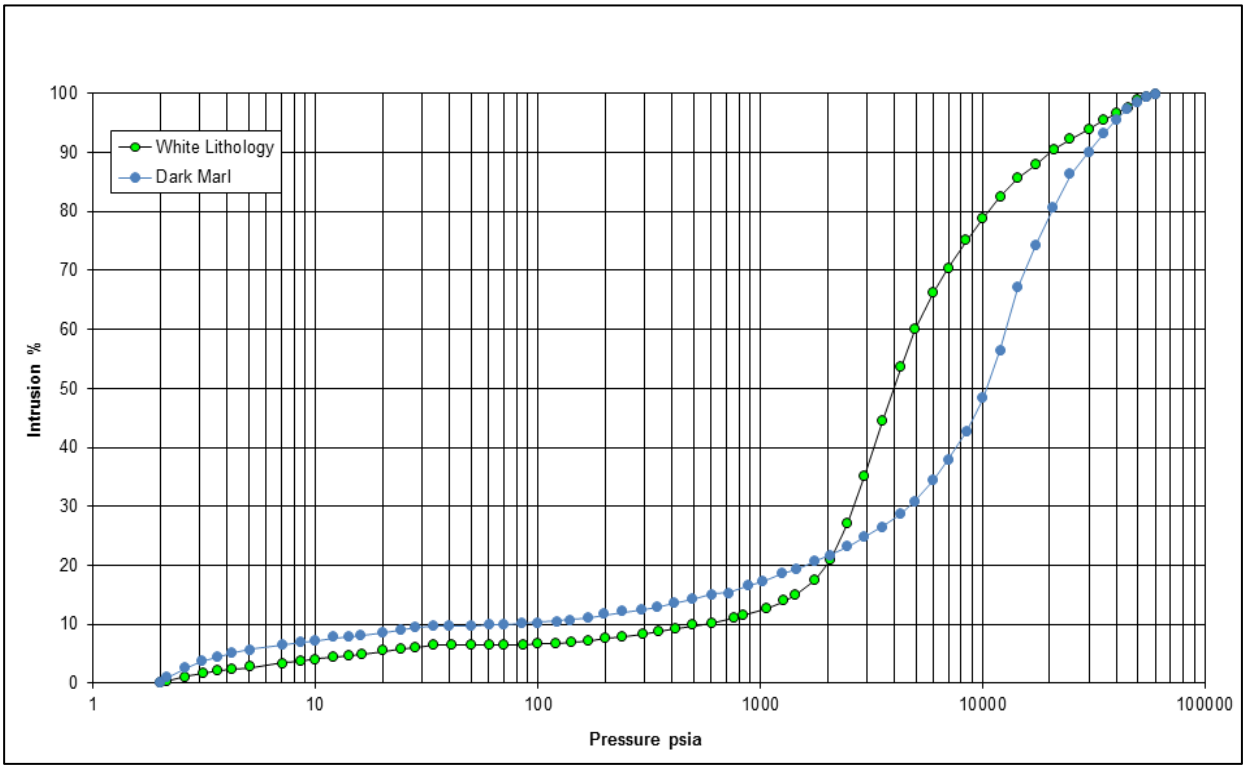

Figure C- 13: Raw MICP curves from Tenacious West-1 drill cutting sample at a depth of 2160-2165 m separated into a white lithology and a dark marl lithology.

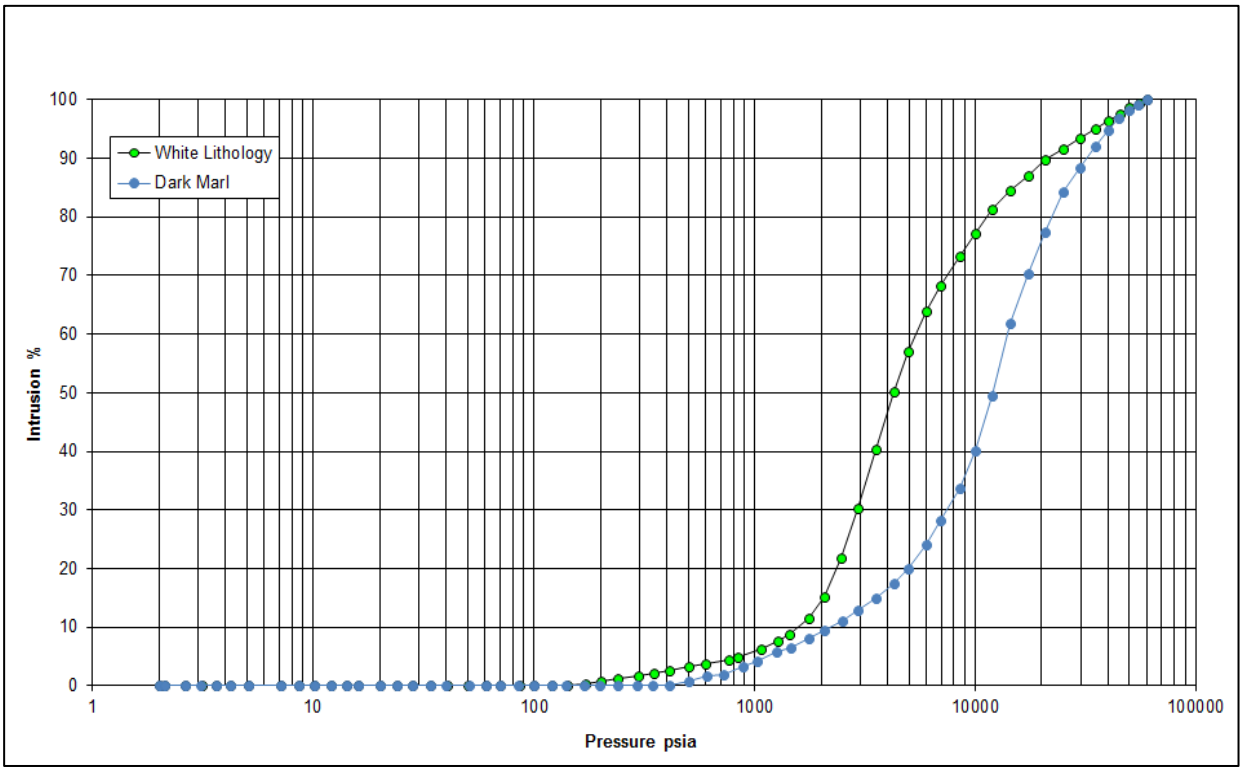

Figure C- 14: Conformance corrected MICP curves from Tenacious West-1 drill cutting sample at a depth of 2160-2165 m separated into a white lithology and a dark marl lithology.

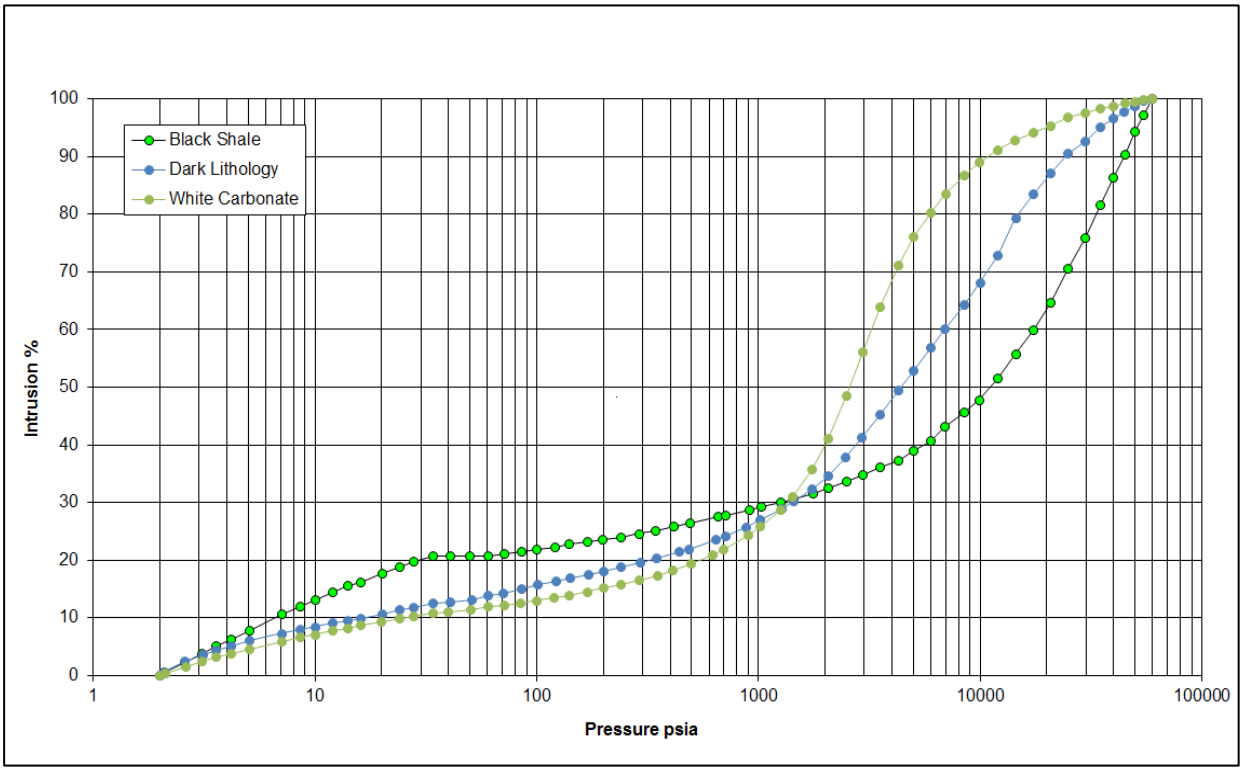

Figure C- 15: Raw MICP curves from a Tenacious West-1 drill cutting sample from a depth of 2200-2210 m separated into a black shale, a dark lithology and a white carbonate lithology.

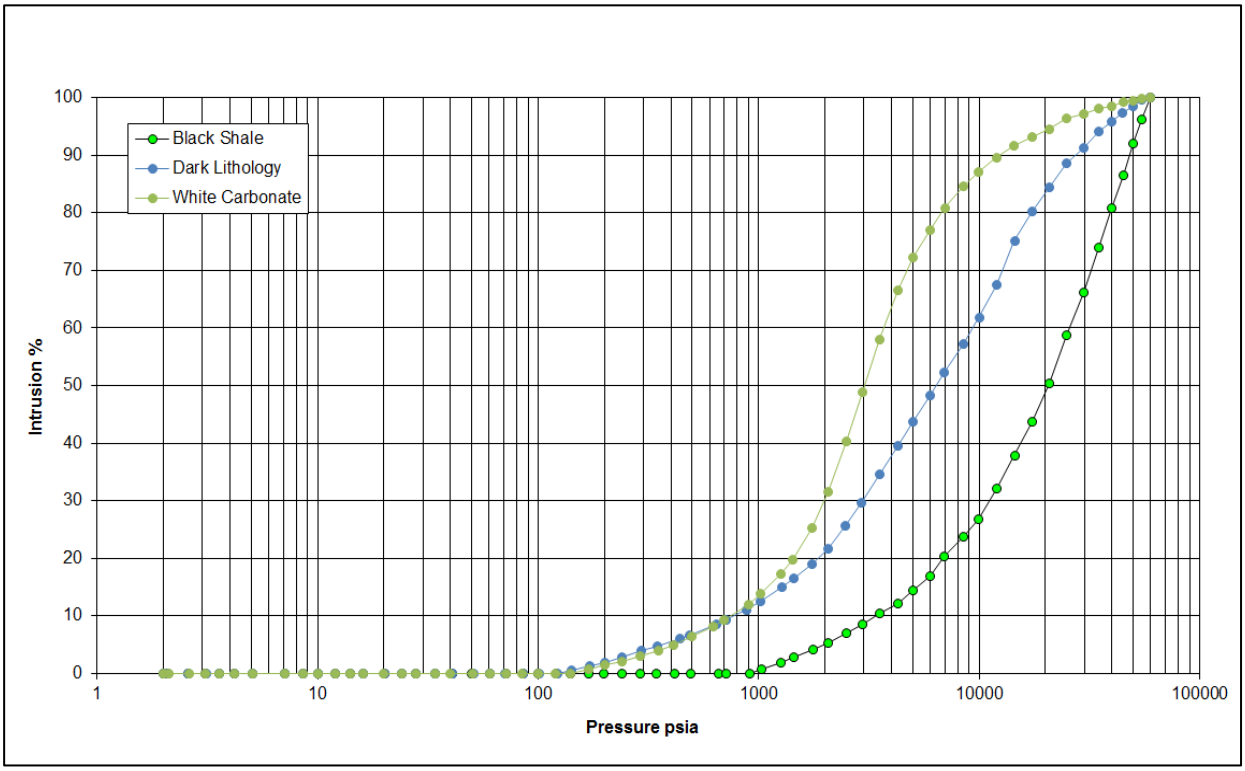

Figure C- 16: Conformance corrected MICP curves from a Tenacious West-1 drill cutting sample from a depth of 2200-2210 m separated into a black shale, a dark lithology and a white carbonate lithology.

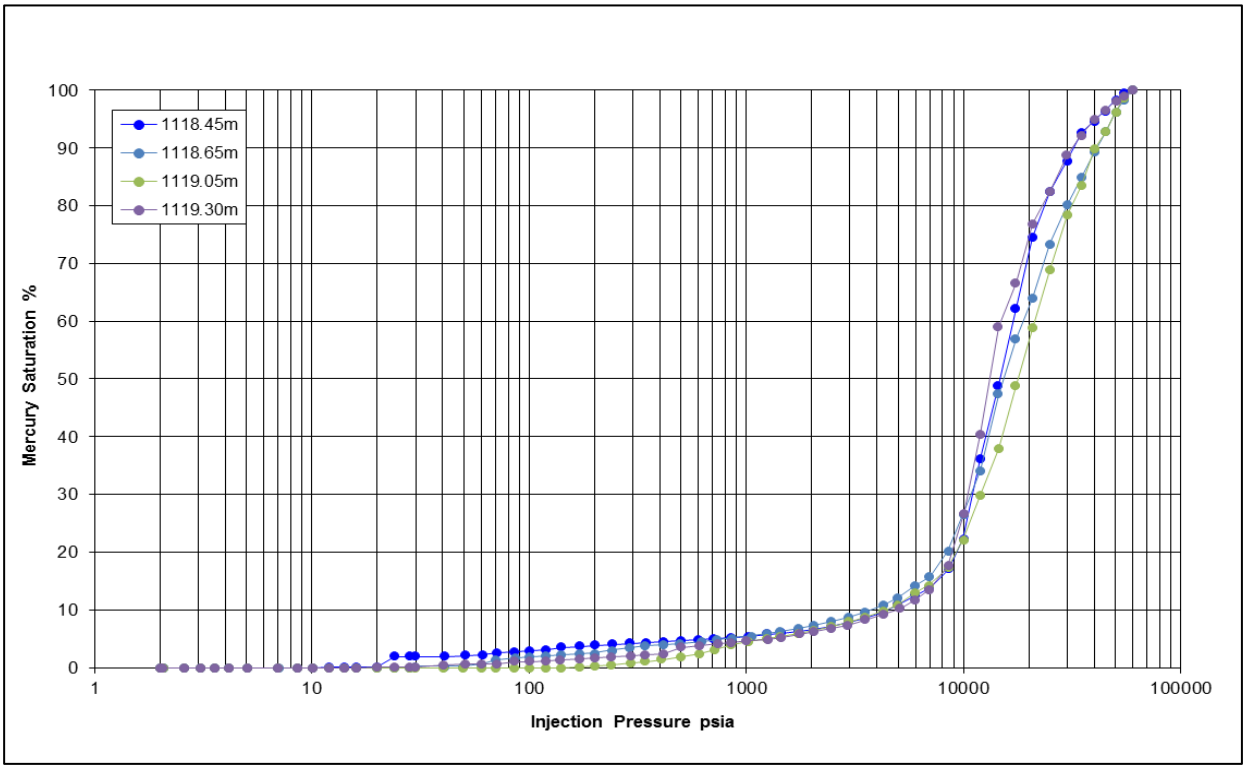

Figure C- 17: Raw MICP curves from warehoused Saracen-1 conventional core samples taken over a 1.6 m interval of conventionally cored Muderong Shale in 2013.

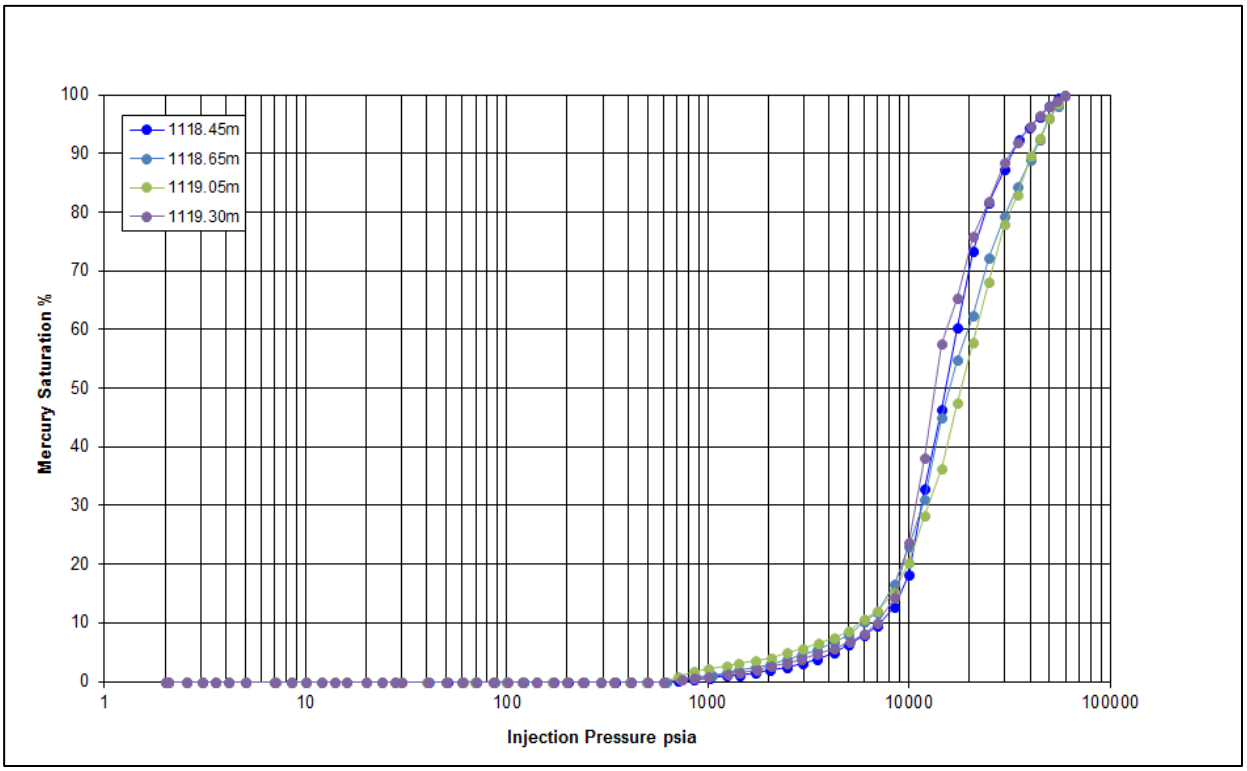

Figure C- 18: Conformance corrected MICP curves from warehoused Saracen-1 conventional core samples taken over a 1.6 m interval of conventionally cored Muderong Shale in 2013.

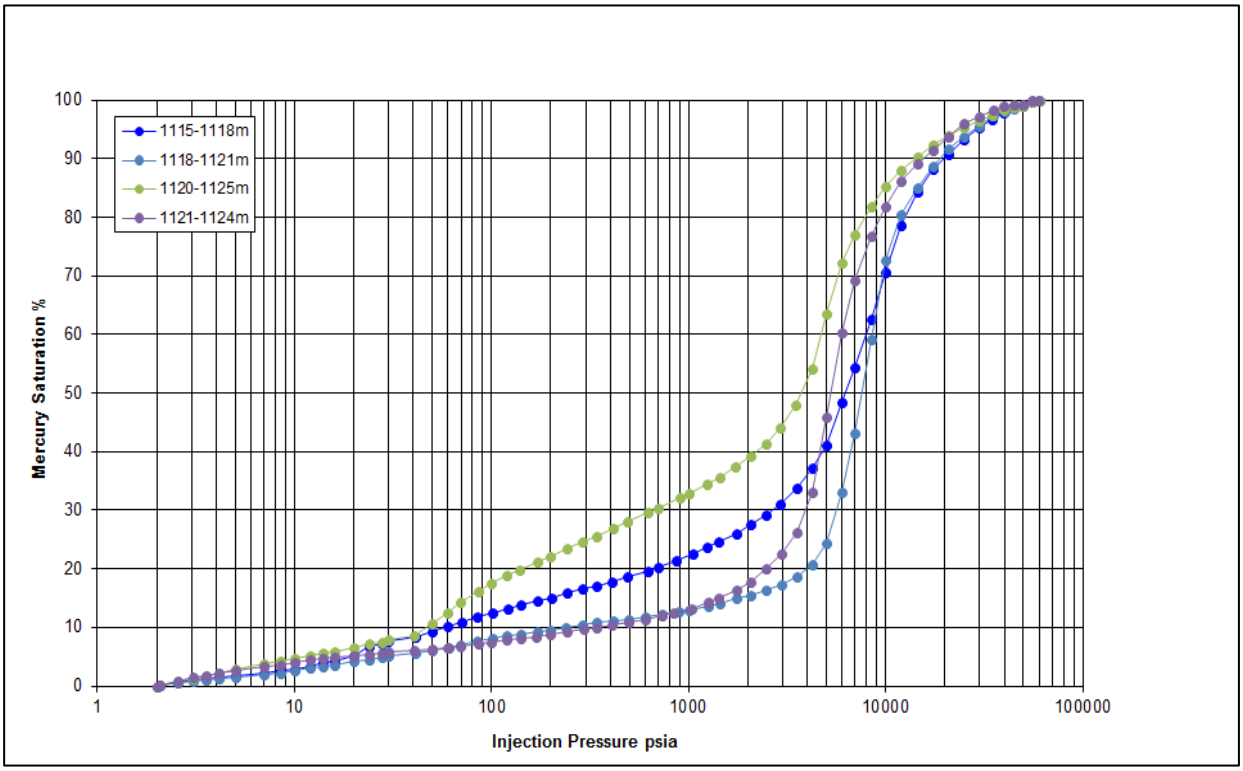

Figure C- 19: Raw MICP curves from warehoused Saracen-1 drill cutting samples taken over a 10 m interval of Muderong Shale in 2014.

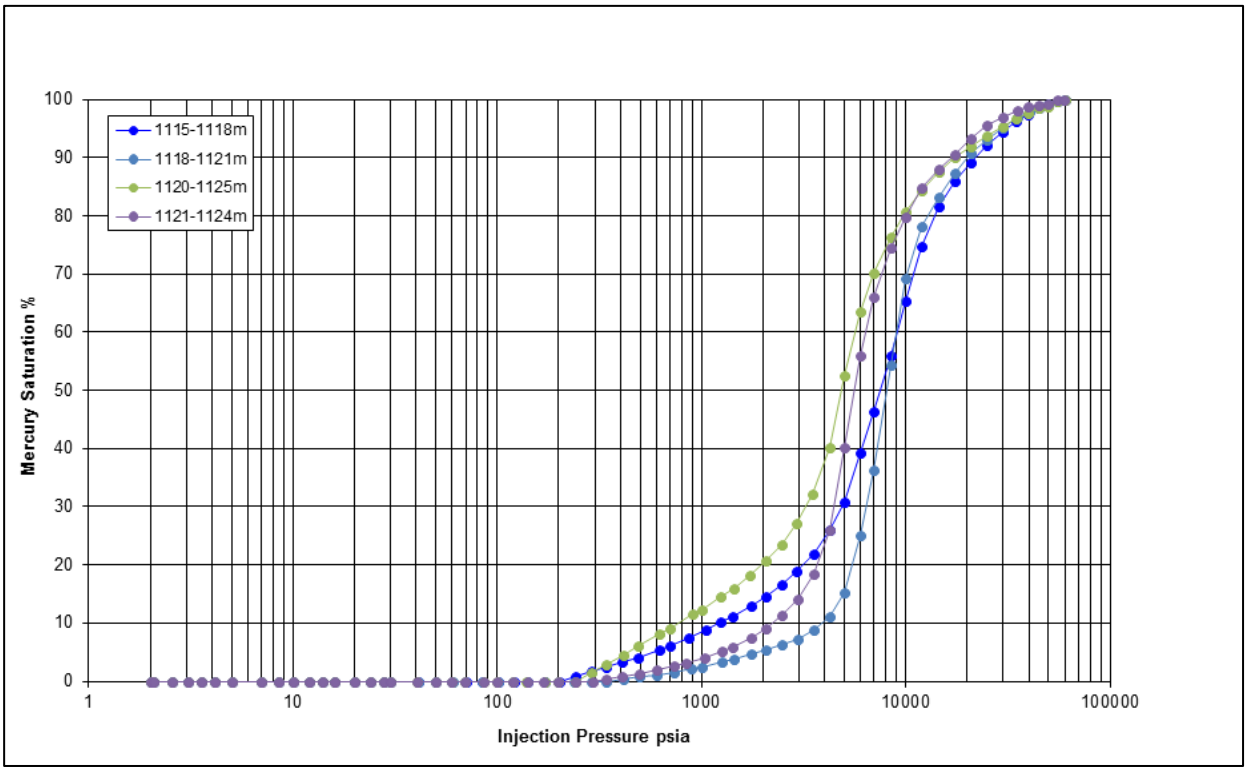

Figure C- 20: Conformance corrected MICP curves from warehoused Saracen-1 drill cutting samples taken over a 10 m interval of Muderong Shale in 2014.

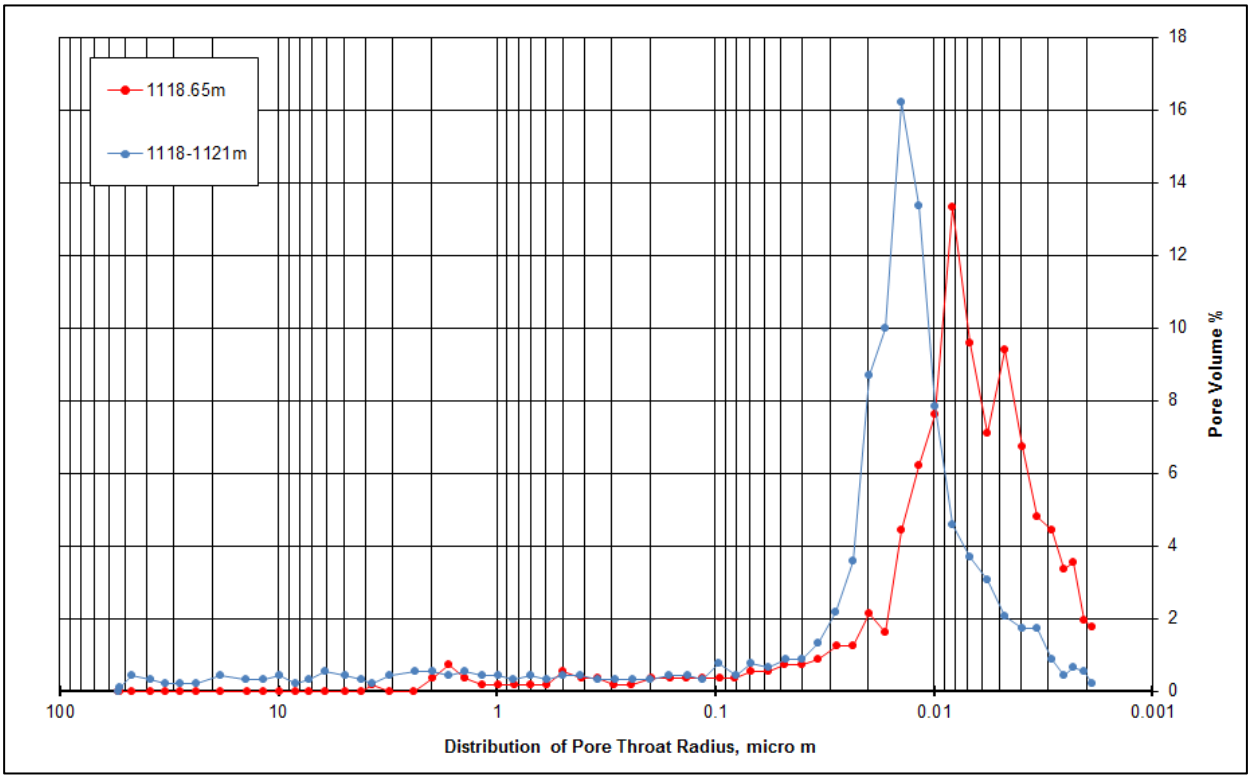

Figure C- 21: Pore throat radii distribution for conventional core sample 1118.65m and drill cutting sample 1118-1121m.

C.1 METHODOLOGY FOR THE USE OF DRILL CUTTINGS FOR MICP ANALYSIS

The use of drill cuttings need to be assessed on a case by case basis and will depend on the analyses and information required. The following guidelines are suggested for the sampling and MICP analyses of drill cuttings.

The target formation or interval should be identified with an estimated drilling depth before commencing drilling. Once the drill depth has been attained it is advisable to pump the mud column through and clear the mud and wellbore of any rock material. The mud equipment and shale shakers should be cleaned of any rock material. Recommence drilling and collect drill cutting samples of > 200 grams per metre from the interval of interest on bottoms up and place in plastic containers with sealable lids. Once the zone of interest is drilled the samples need to be laid out on a sheet of clean, absorbent paper for drying. All rock chip anomalies not representative of the sample should be removed. The remaining rock chips can then be placed in the plastic container and subsequently submerged in mineral oil. These containers can be shipped in a direct fashion to the laboratory for analysis.

On receipt of the drill cutting samples, the rock chips should be delicately held with plastic tweezers and swirled in the mineral oil to remove any loose rock debris or poorly consolidated rock material (i.e. rind of mud cake attached to the edges of the samples) and laid out on a paper towel to absorb the excess mineral oil. Obvious rock anomalies and amalgams should be removed. The rock chips should then be sorted by lithology, colour, grain size and any other distinguishing features. Four to five rock chips of medium to large size that are considered representative of the sorted groups should be selected and cleaned off the mineral oil. Proceeding the cleaning of the samples, they should be air dried at 60 ° C for 48 hours before being analysed with the mercury porosimeter.

The MICP results need to be conformance corrected as detailed in Appendix A., A.4. It is envisaged that without the washing and harsh drying of the drill cuttings the pores and pore throat networks will be less altered and provide more representative results. The threshold pressure is still likely to be an underestimate of the true threshold pressure of the formation but will provide a conservative estimate of seal capacity.

D. APPENDIX

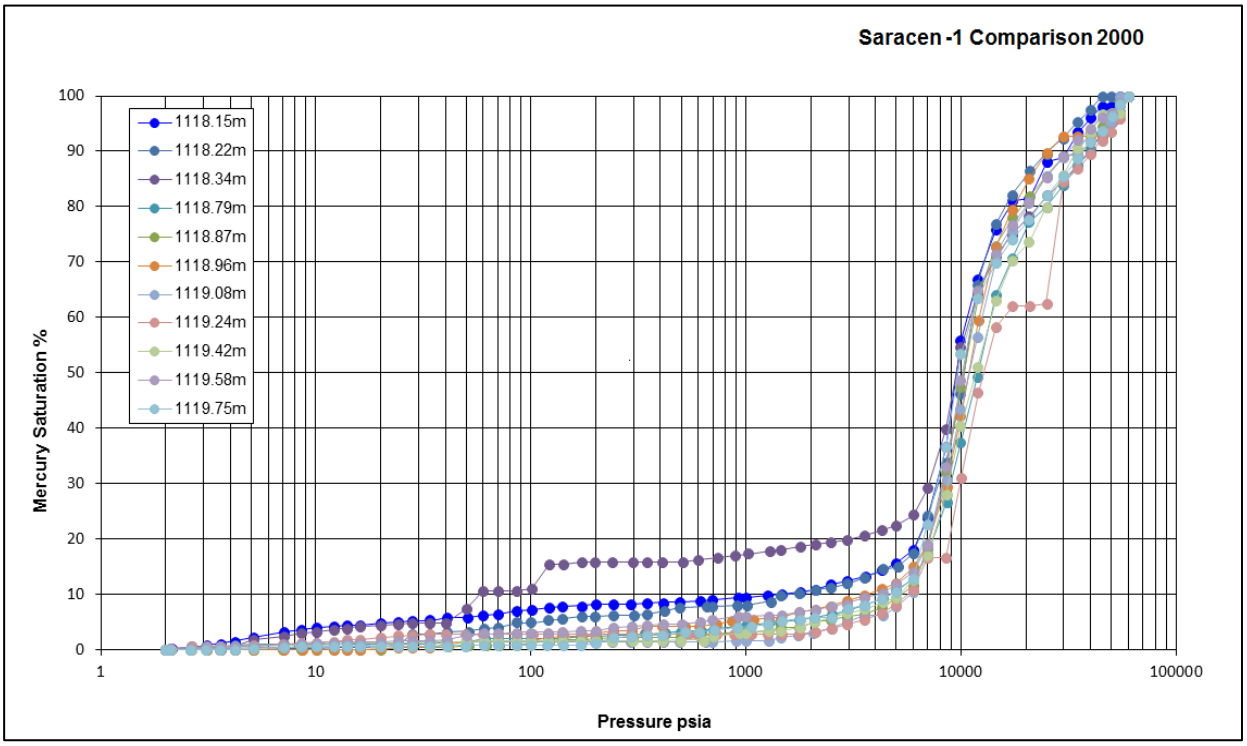

Figure D- 1: Saracen-1 fresh conventional core raw MICP curves. (Analysis conducted at the ASP on behalf of Dewhurst et al., (2002)).

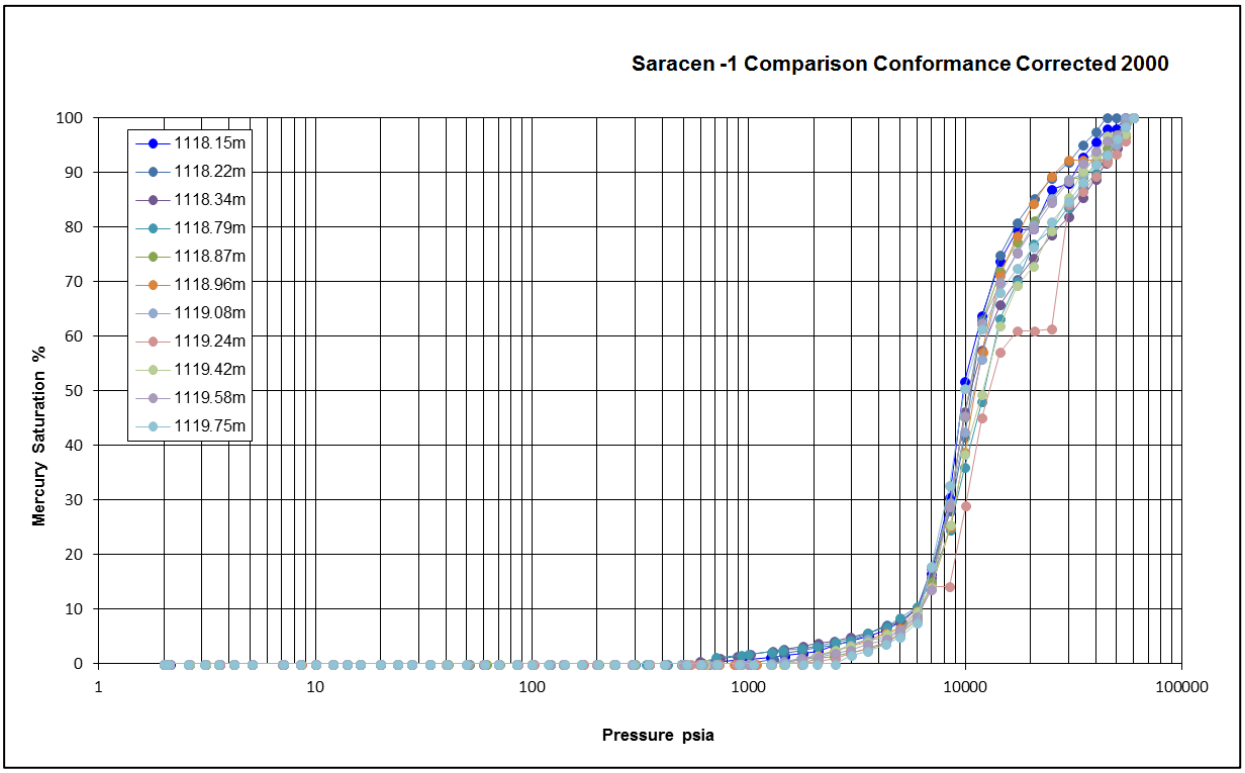

Figure D- 2: Saracen-1 fresh conventional core conformance corrected MICP curves. (Analysis conducted at the ASP on behalf of Dewhurst et al., (2002)).

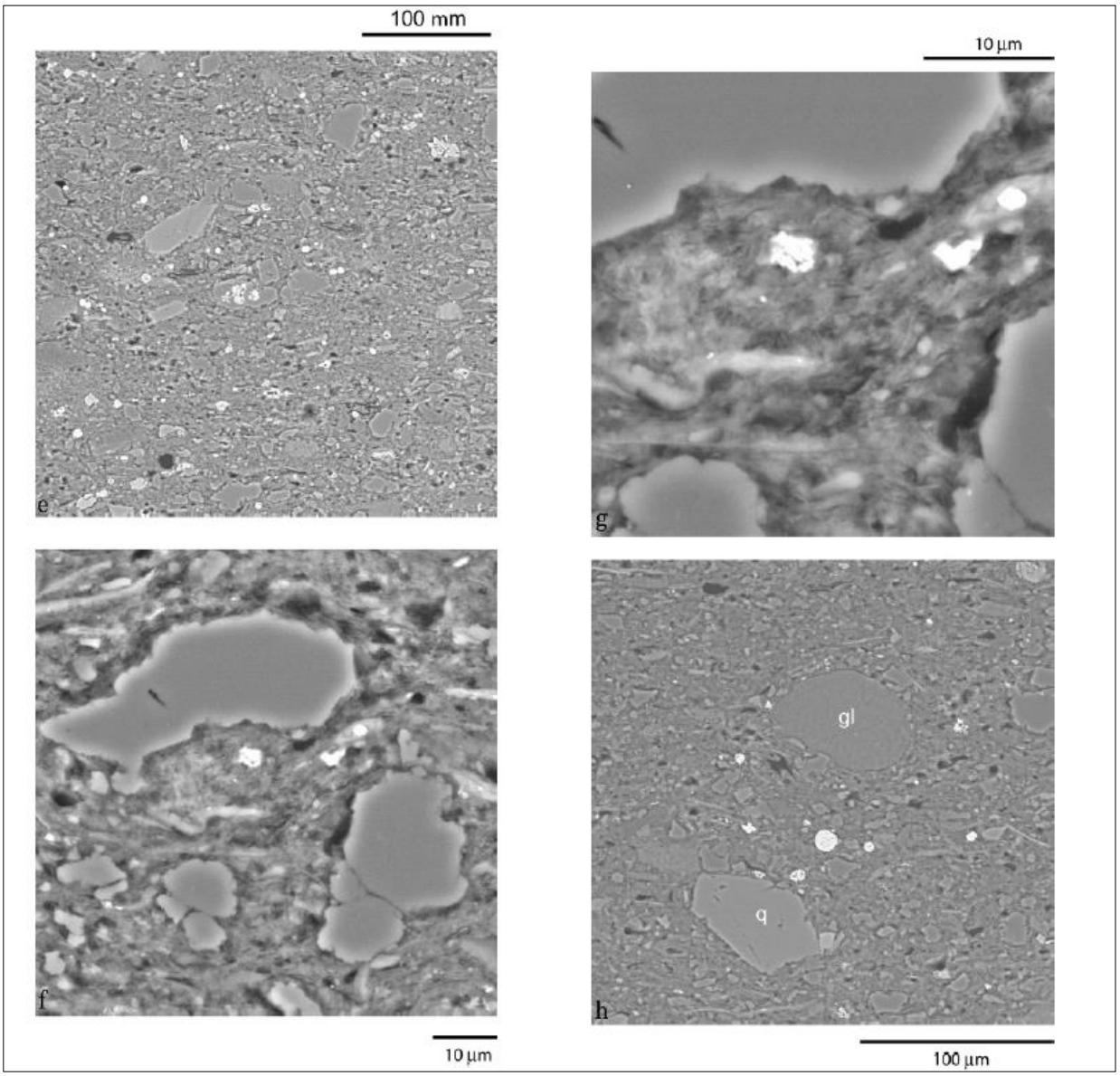

Figure D- 3: BSE images of original samples of Muderong Shale from Saracen-1. (Image is taken from Dewhurst et al., (2002)).

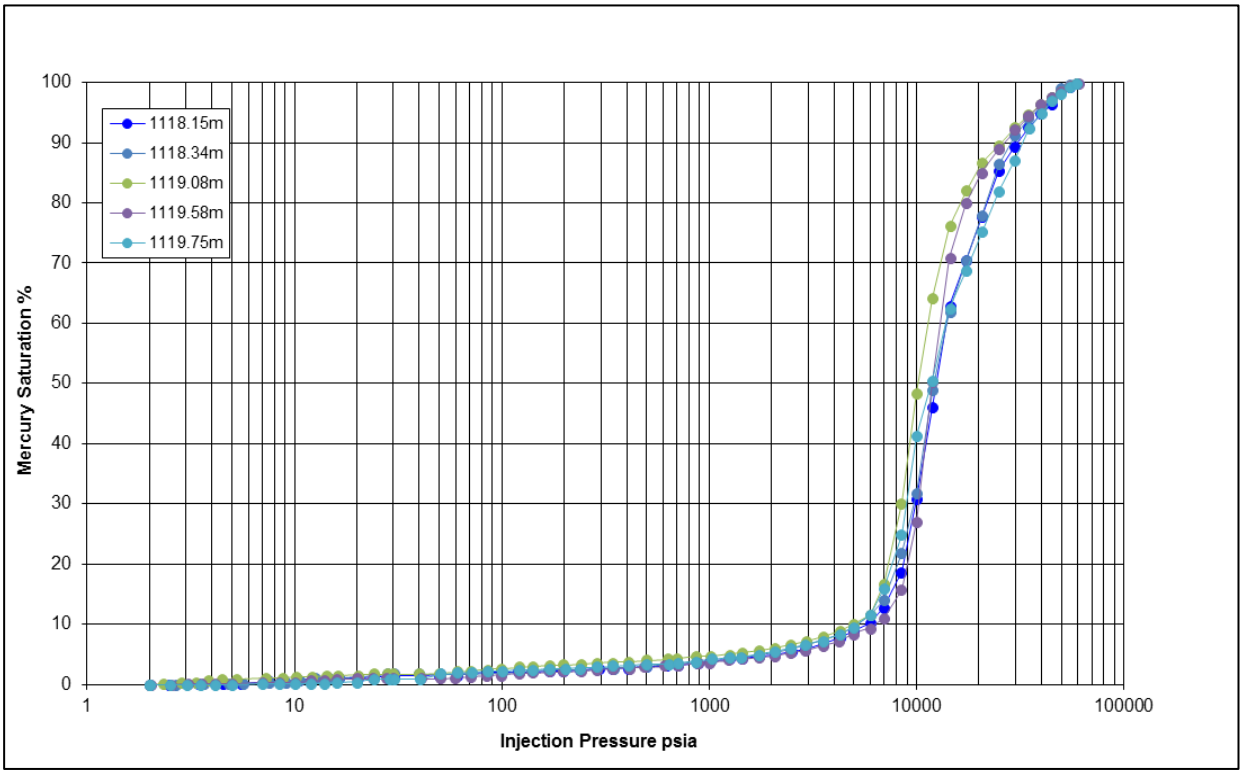

Figure D- 4: Raw MICP curves of the remaining original samples of Dewhurst et al., (2002). These samples had been stored in airtight bags since 2001 and were then analysed in 2015.

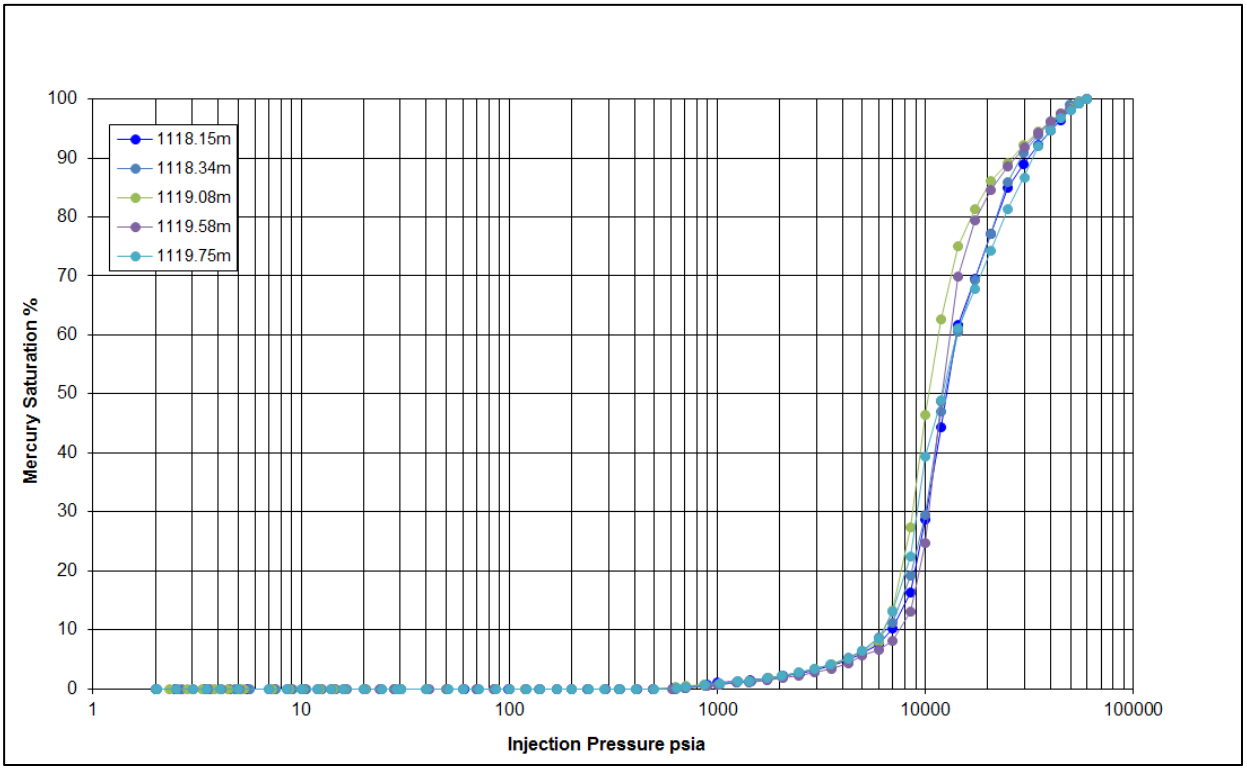

Figure D- 5: Conformance corrected MICP curves of the remaining original samples of Dewhurst et al., (2002). These samples had been stored in airtight bags since 2001 and were then analysed in 2015.

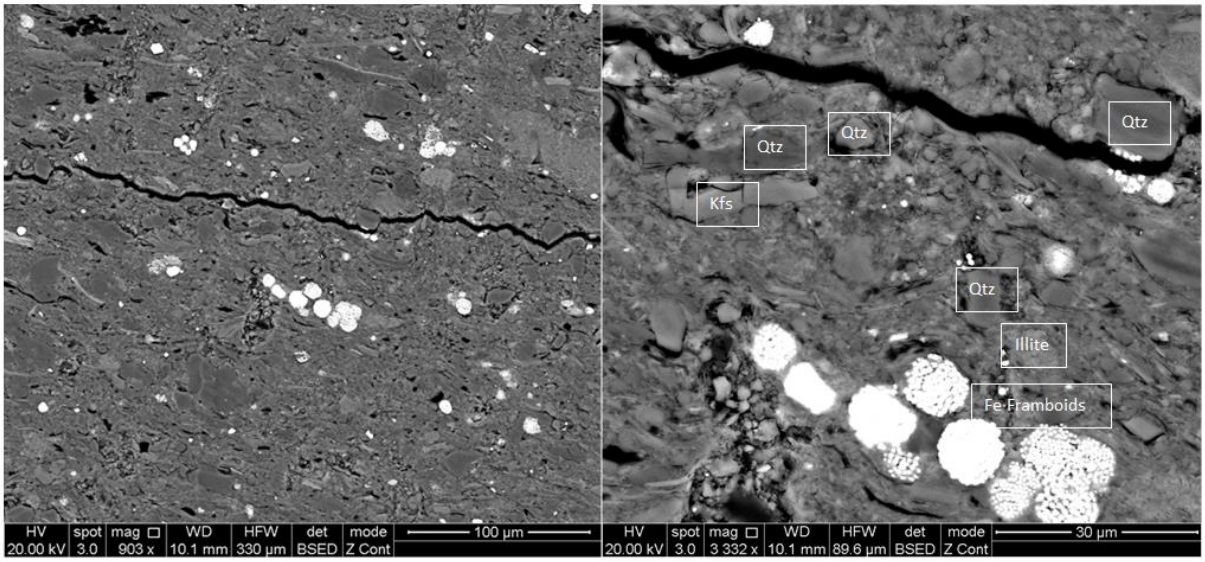

Figure D- 6: Saracen-1 BSE image of core plug 1118.15 m stored in an airtight bag. (Left hand image) The image shows a fracture through the fabric of the sample. The silty grains show a degree of orientation dotted throughout the clay matrix. (Right hand image) Saracen-1 BSE image of core plug 1118.15 m under high magnification showing pyrite framboids (Fe Framboids), illite clays (illite), potassium feldspar (Kfs) and quartz (Qtz) grains floating in a clay matrix.

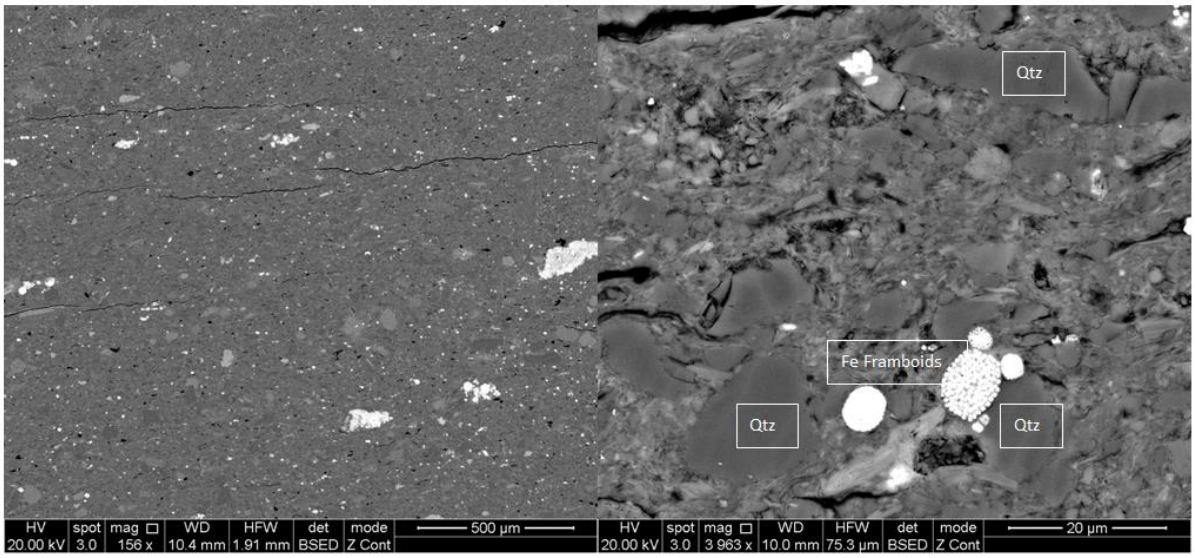

Figure D- 7: Saracen-1 BSE image of core plug 1118.34 m stored in an airtight bag. (Left hand image) The image shows a number of discontinuous parallel fractures and iron framboids dotted throughout the shale fabric. (Right hand image) Saracen-1 BSE image of core plug 1118.34 m under high magnification showing pyrite framboids (Fe Framboids) and quartz (Qtz) grains floating in a clay matrix.

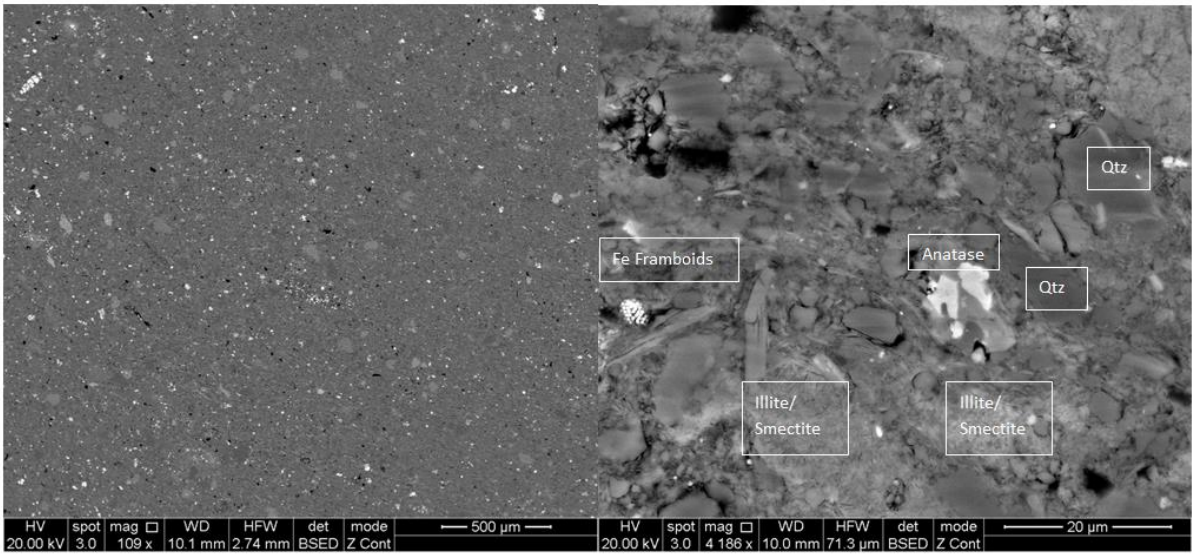

Figure D- 8: Saracen-1 BSE image of core plug 1119.08 m stored in an airtight bag. (Left hand image) The silt sized grains dotted throughout a clay matrix. (Right hand image) Saracen-1 BSE image of core plug 1119.08 m under high magnification showing pyrite framboids (Fe Framboids), illite/smectite clays, anatase and quartz (Qtz) grains floating in a clay matrix.

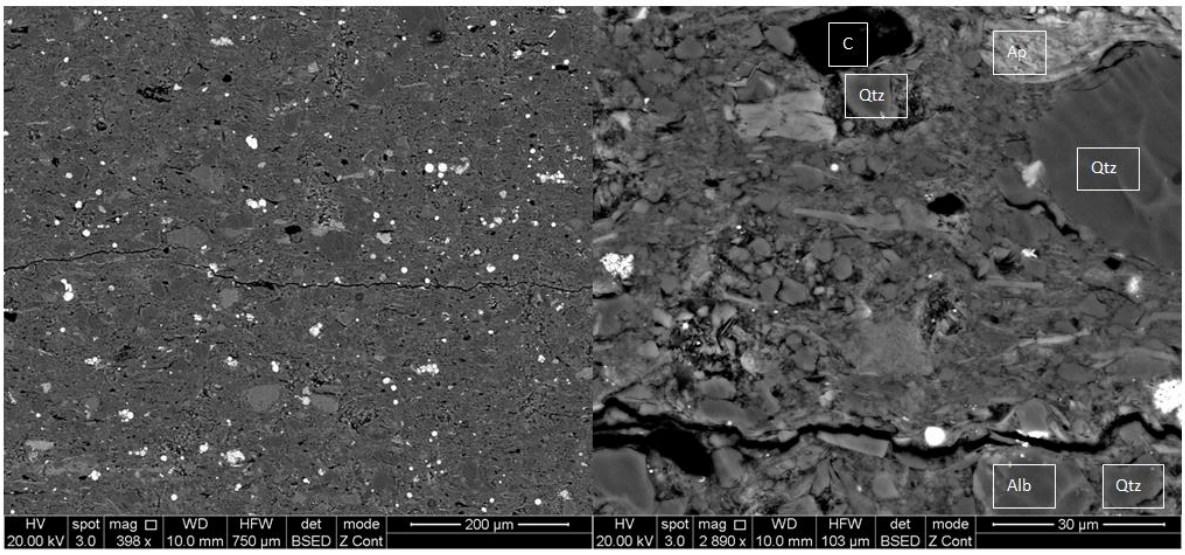

Figure D- 9: Saracen-1 BSE image of core plug 1119.75 m stored in an airtight bag. (Left hand image) The image shows a fracture traversing the sample. (Right hand image) Saracen-1 BSE image of core plug 1119.75 m under high magnification showing apatite (Ap), albite (Alb), carbon (C) and quartz (Qtz) grains interspersed throughout a clay matrix.

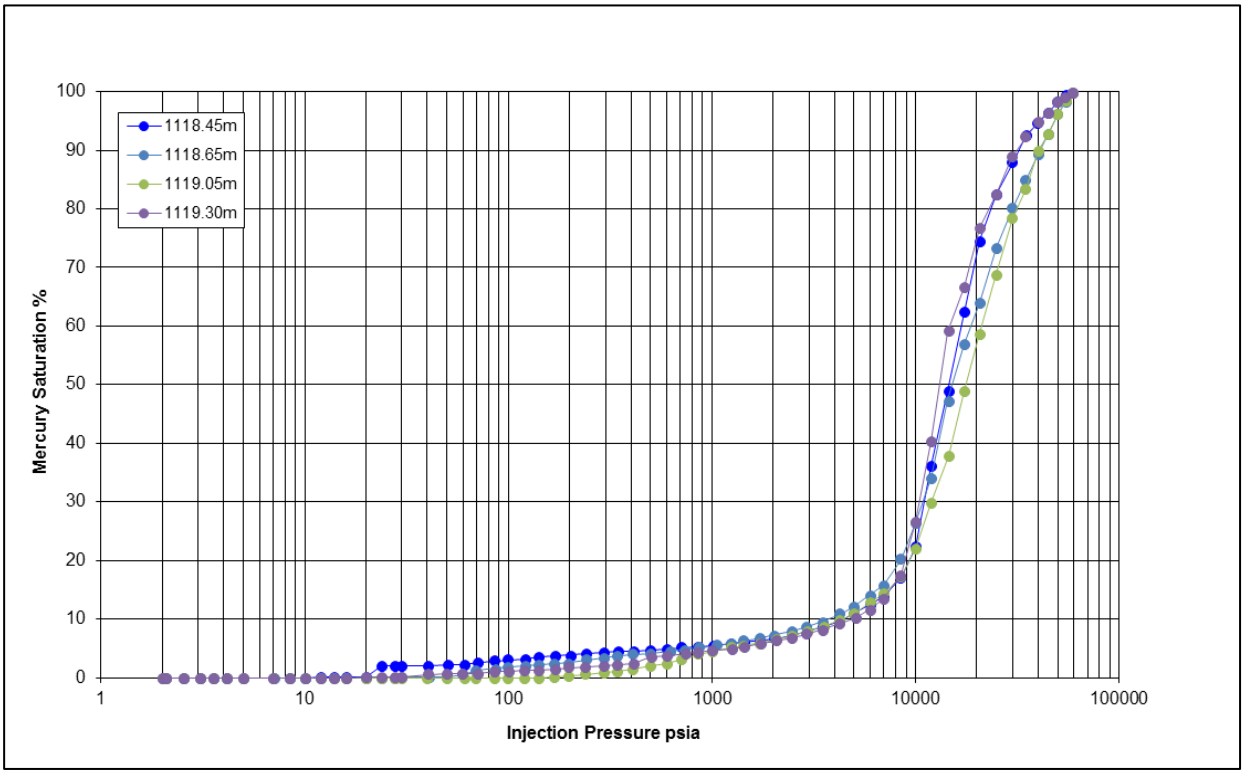

Figure D- 10: Raw MICP curves from warehoused core samples of Saracen-1 analysed in 2013

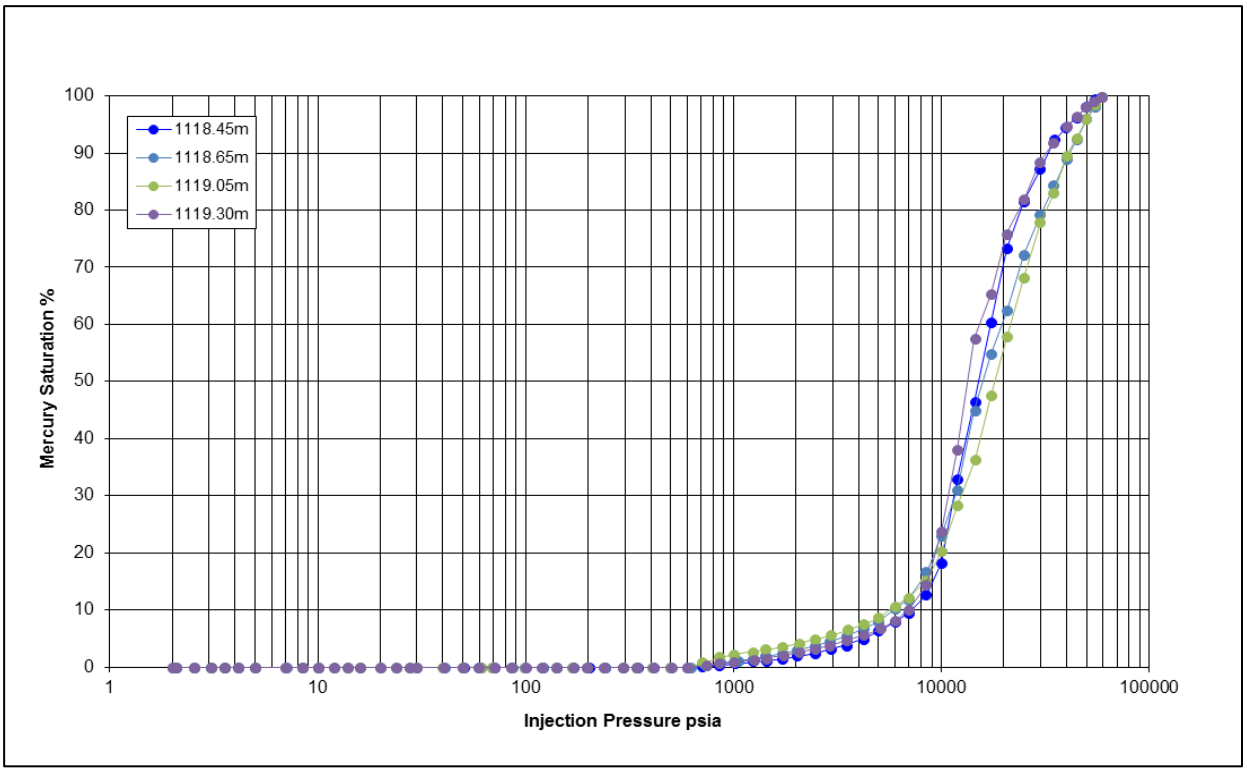

Figure D- 11: Conformance corrected MICP curves from warehoused core samples of Saracen-1 analysed in 2013

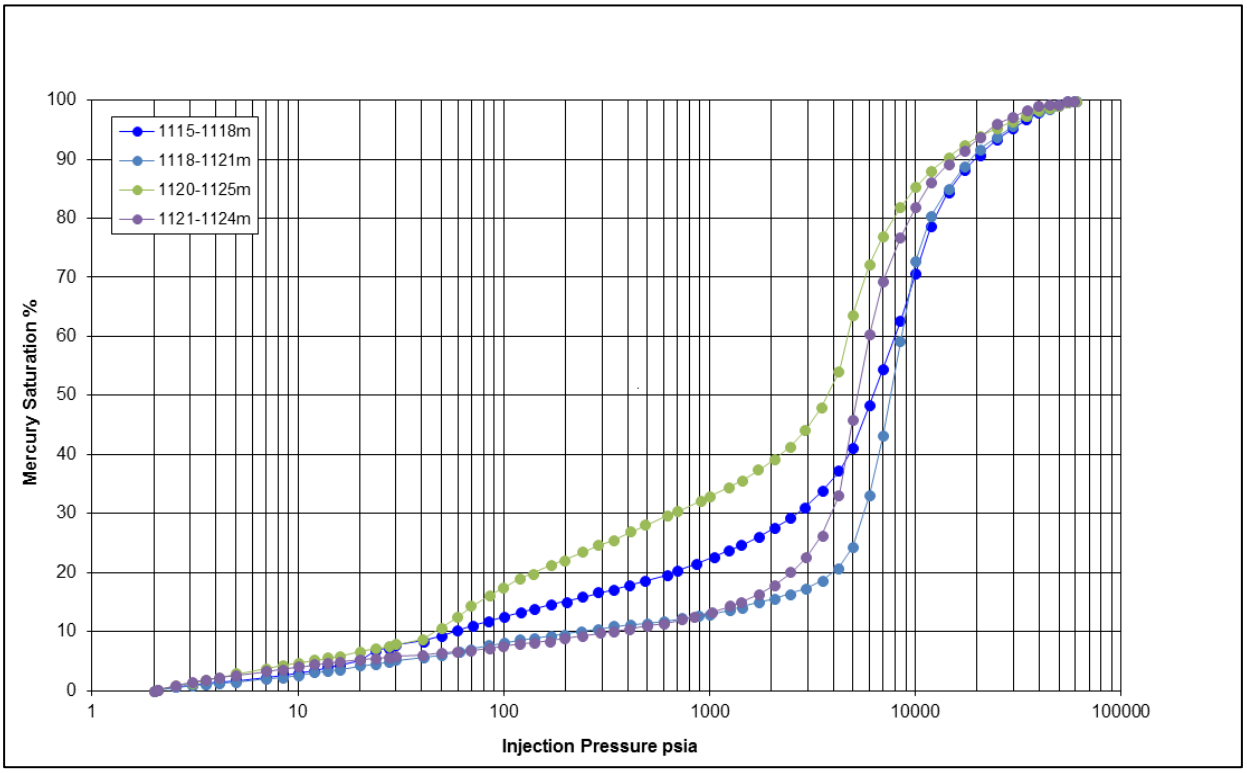

Figure D- 12: Raw MICP curves from warehoused drill cutting samples of Saracen-1 analysed in 2014.

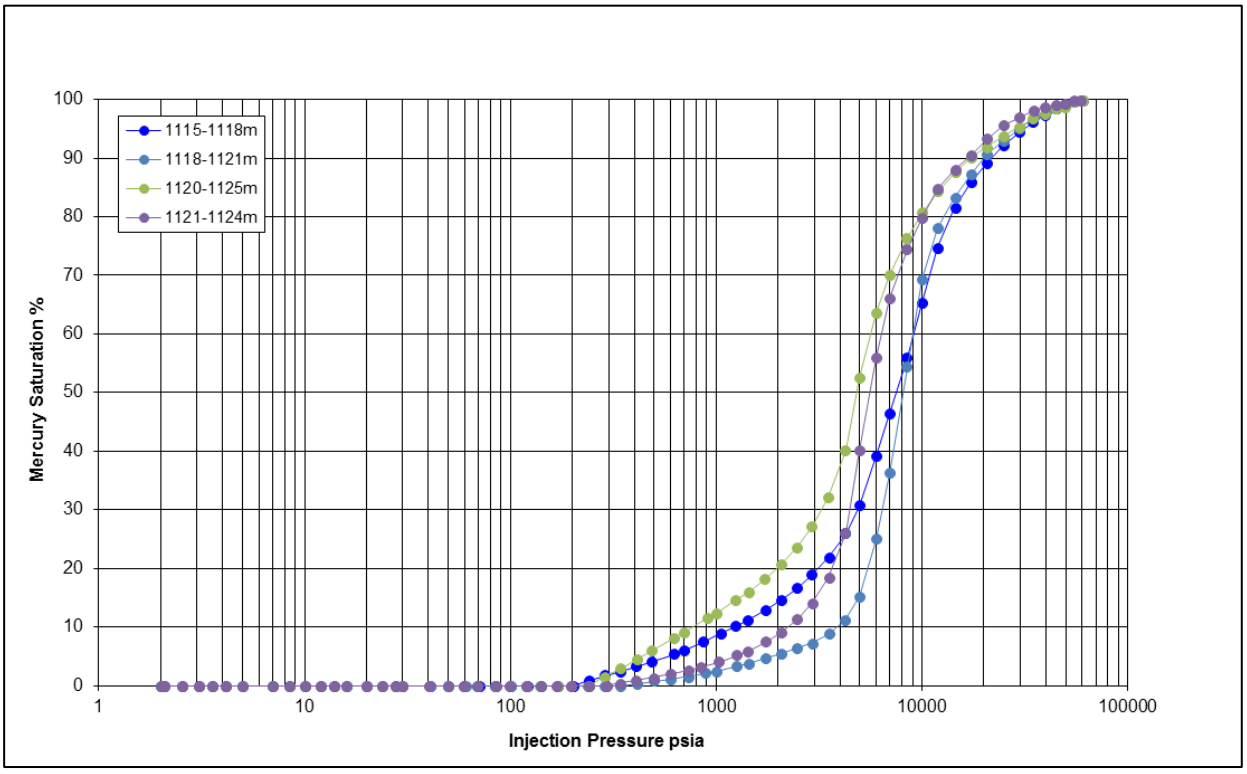

Figure D- 13: Conformance corrected MICP curves from warehoused drill cutting samples of Saracen-1 analysed in 2014.

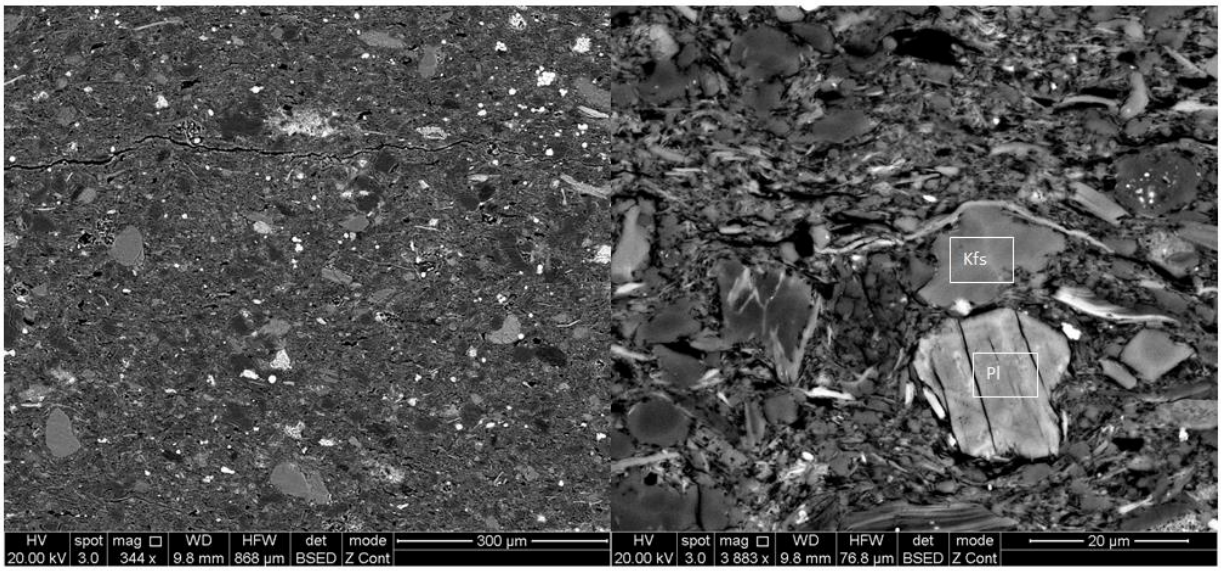

Figure D- 14: Saracen-1 BSE image of core plug 1118.45 m. (Left hand image) The image illustrates silt sized grains floating in a clay matrix. (Right hand image) Saracen-1 BSE image of core plug 1118.45 m under high magnification showing silt sized grains interspersed between clays. Potassium feldspar (Kfs) and plagioclase (Pl) grains have been identified in the clay matrix.

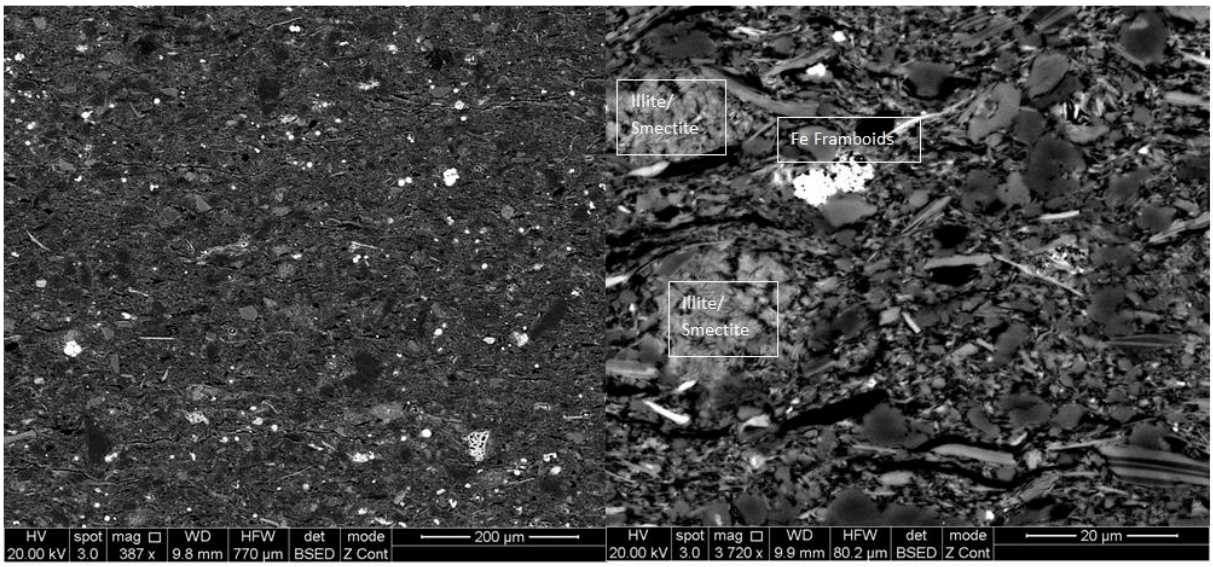

Figure D- 15: Saracen-1 BSE image of core plug 1118.65 m. (Left hand image) The image illustrates silt sized grains floating in a clay matrix. (Right hand image) Saracen-1 BSE image of core plug 1118.65 m under high magnification showing pyrite framboids (Fe Framboids) and illite/smectite clays.

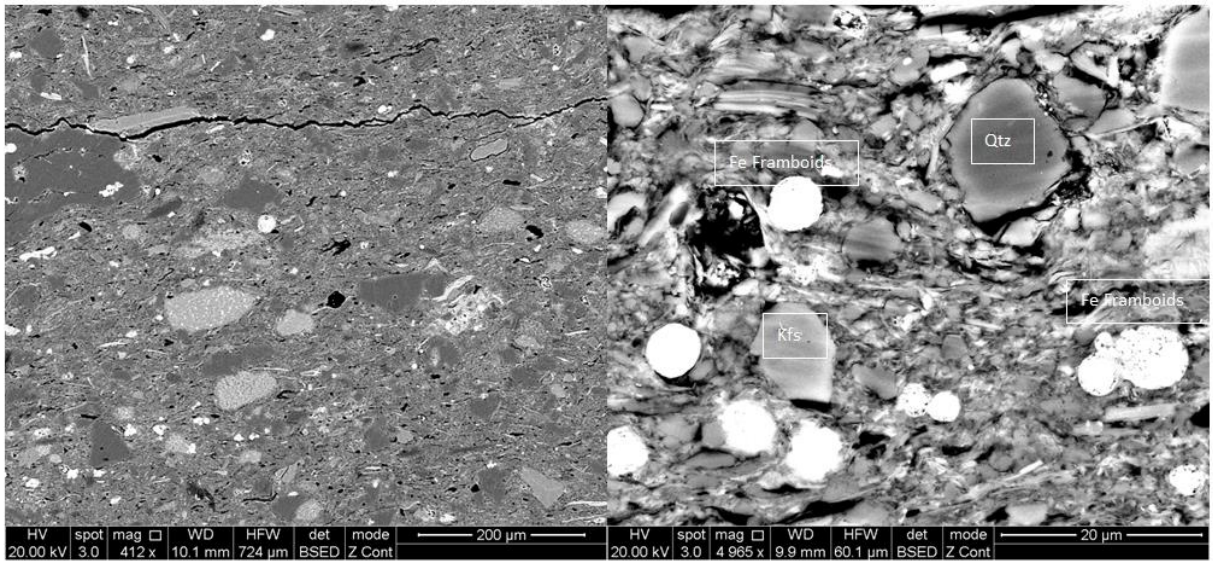

Figure D- 16: Saracen-1 BSE image of core plug 1119.05 m. (Left hand image) The image illustrates the silt sized grains floating in a clay matrix with a micro fracture traversing the image. (Right hand image) Saracen-1 BSE image of core plug 1119.05 m under high magnification showing pyrite framboids (Fe Framboids), potassium feldspar (Kfs) and quartz (Qtz) grains floating in a clay matrix.

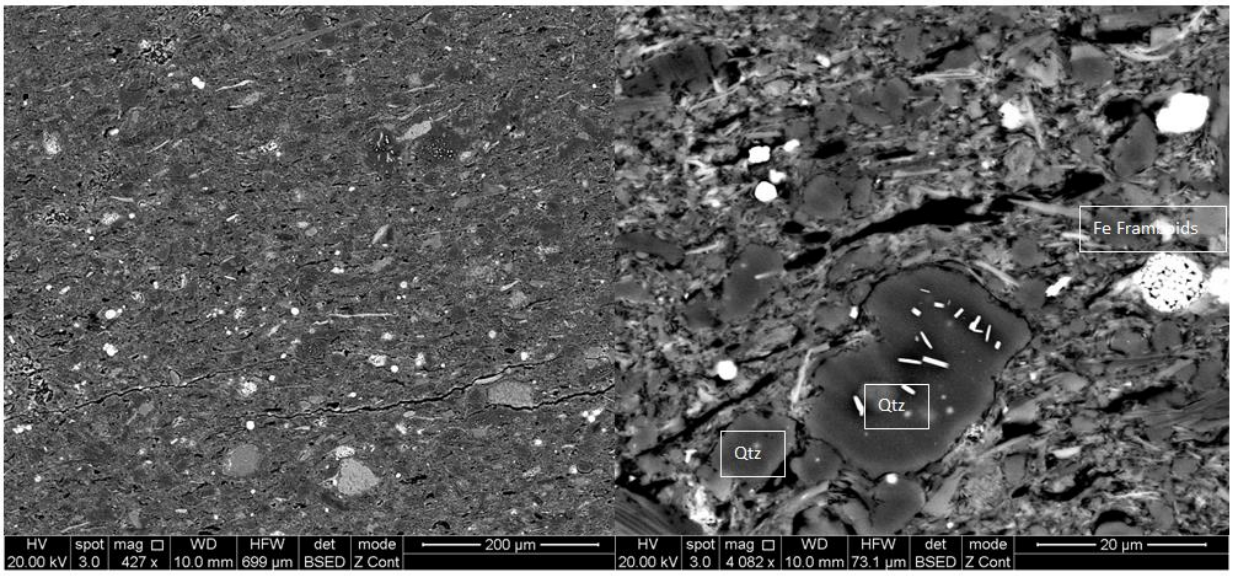

Figure D- 17: Saracen-1 BSE image of core plug 1119.30 m. (Left hand image) The image illustrates the silt sized grains floating in a clay matrix. (Right hand image) Saracen-1 BSE image of core plug 1119.30 m under high magnification showing pyrite framboids (Fe Framboids) and quartz (Qtz) grains floating in a clay matrix.

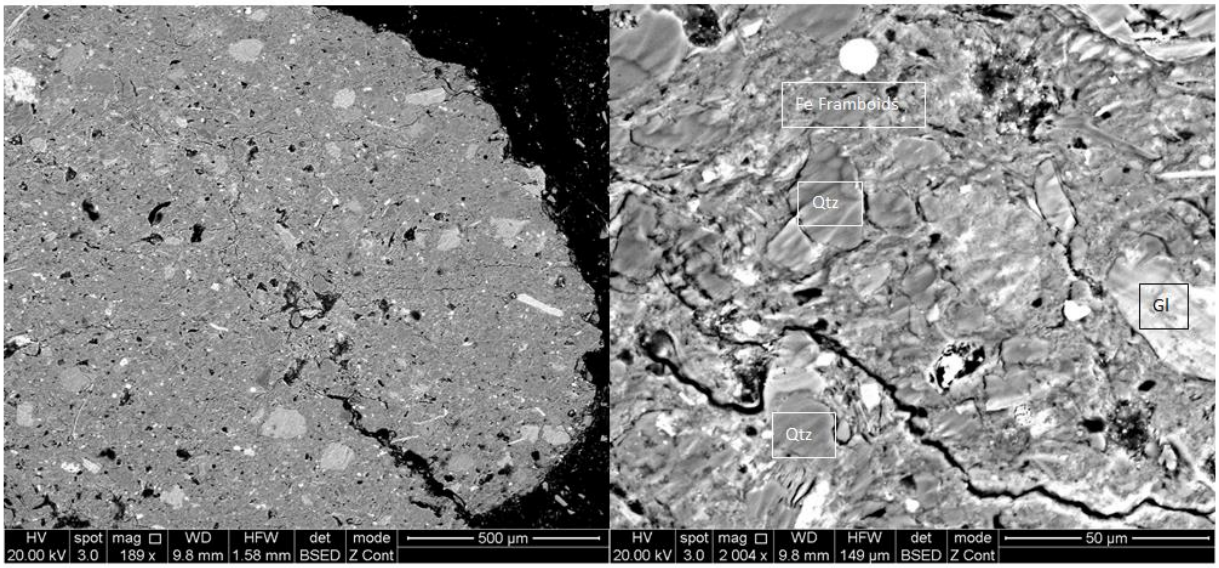

Figure D- 18: Saracen-1 BSE image of drill cutting sample 1115-1118 m. (Left hand image) Fractures linking up to one another can be observed throughout the image often connecting porosity and carbon. The silt sized grains can be seen interspersed throughout the clay matrix. (Right hand image) Saracen-1 BSE image of drill cutting sample 1115-1118 m. A fracture can be observed at the bottom of the image. Silt sized grains including quartz (Qtz), pyrite framboids (Fe Framboids) and glauconite (Gl) can be observed floating in the matrix.

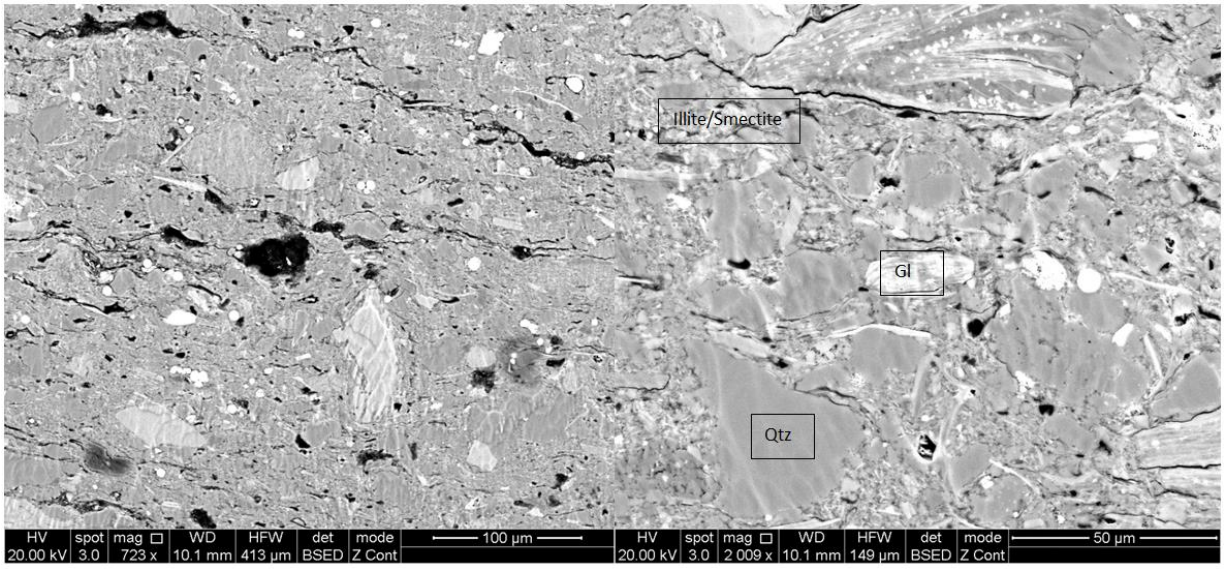

Figure D- 19: Saracen-1 BSE image of cutting sample 1118.1121 m. (Left hand image) Fractures linking up to one another can be observed throughout the image often connecting pores. The silt sized grains can be seen floating in the matrix. (Right hand image) Saracen-1 BSE image of cutting sample 1118.1121 m. A fracture can be observed at the top of the image. Silt sized grains including quartz (Qtz) and glauconite (Gl) can be observed floating in the matrix.

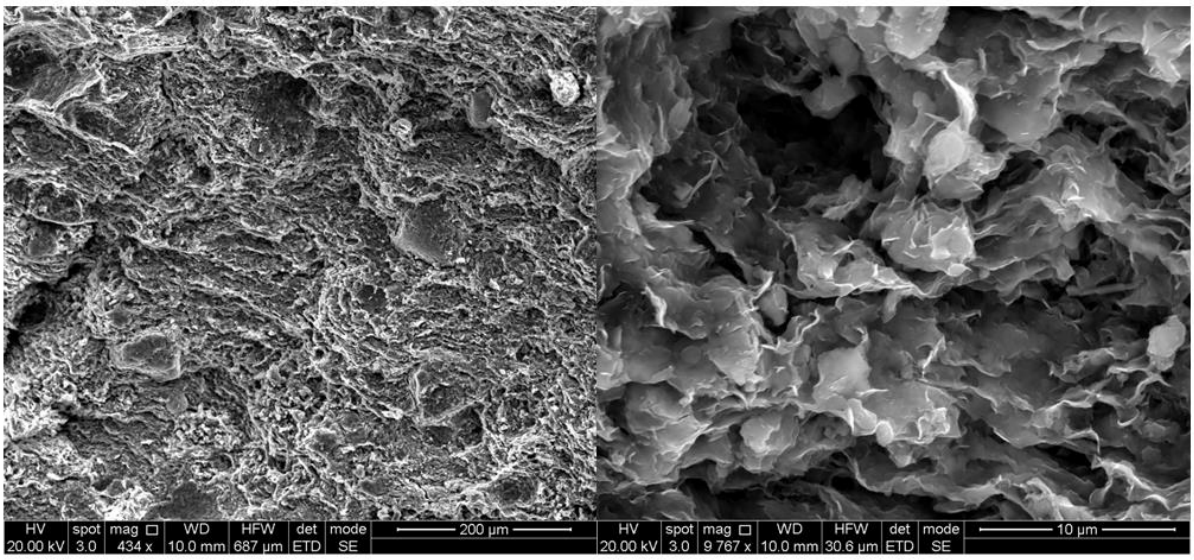

Figure D- 20: Saracen-1 SEM image of cutting sample 1120-1125 m. (Left hand image) A dominant clay matrix is observed with a micro fracture trending from the left hand side to the top of the image. (Right hand image) Saracen-1 SEM image of cutting sample 1120-1125 m. The illite smectite layered clay matrix can be observed along with a macro and micro porosity.

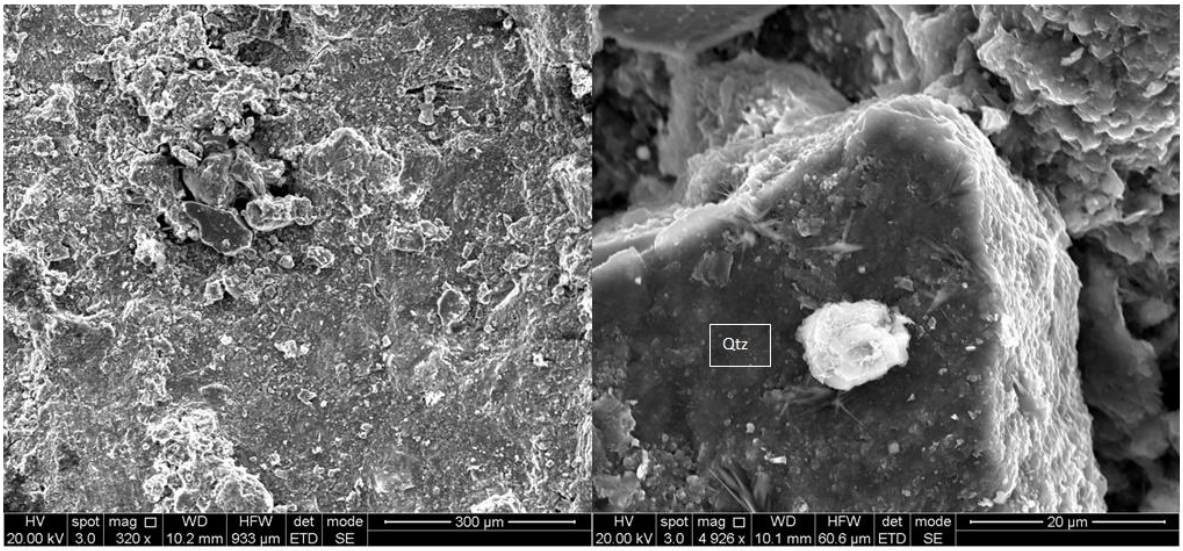

Figure D- 21: Saracen-1 SEM image of cutting sample 1121-1124 m. (Left hand image) Broken silt sized grains can be observed within the matrix. (Right hand image) Saracen-1 SEM image of cutting sample 1121-1124 m. An angular quartz grain can be observed coated with authigenic clays.

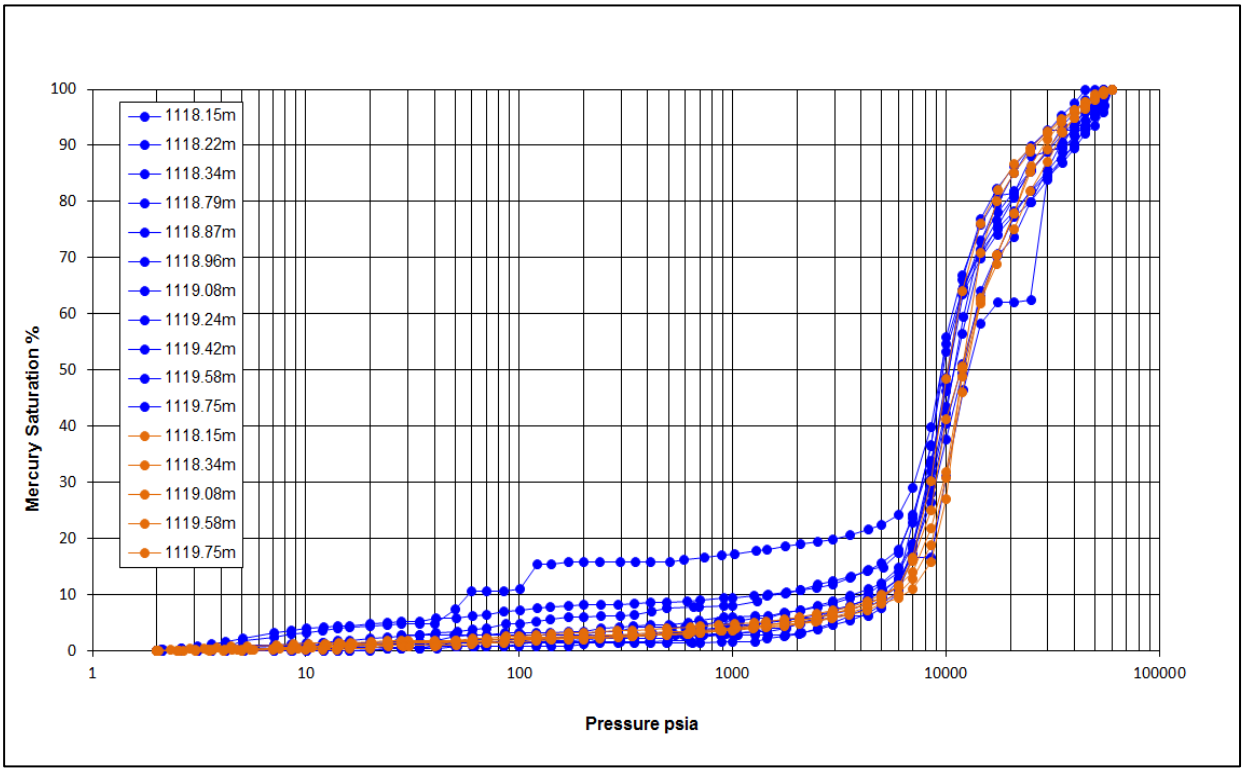

Figure D- 22:Raw MICP curves from the Muderong Shale, Saracen-1. The blue MICP curves are from the original conventional core sample analysed in 2001 by Dewhurst et al., 2002. The orange MICP curves are from the remaining conventional core samples stored in airtight bags analysed in 2015.

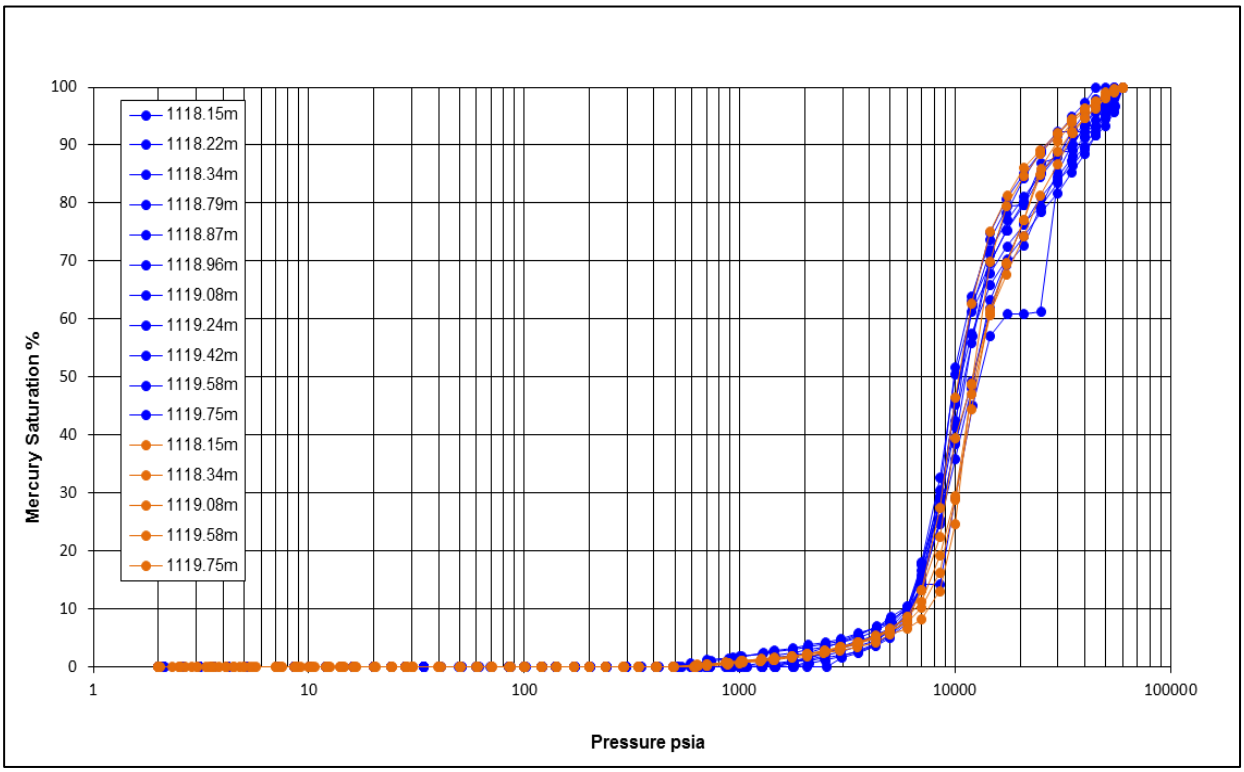

Figure D- 23: Confromance corrected MICP curves from the Muderong Shale, Saracen-1. The blue MICP curves are from the original conventional core sample analysed in 2001 by Dewhurst et al., 2002. The orange MICP curves are from the remaining 2001 conventional core samples stored in airtight bags analysed in 2015.

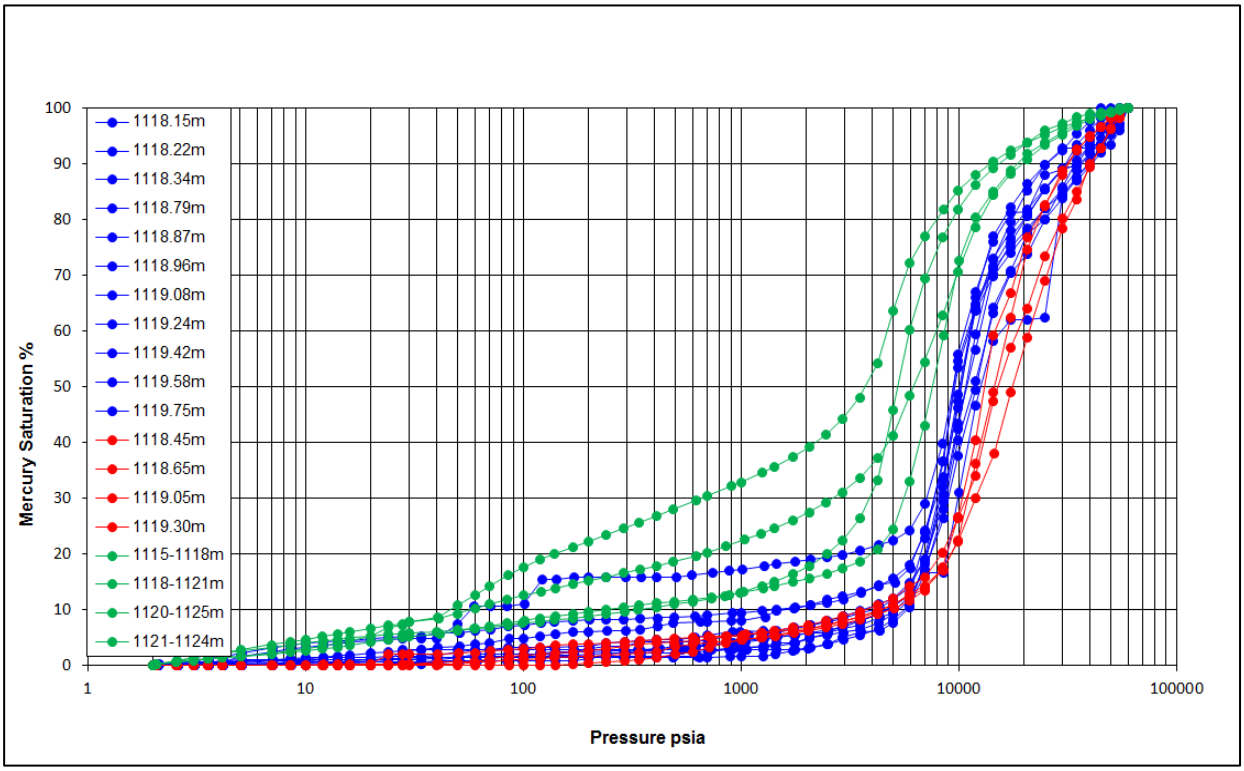

Figure D- 24: Raw MICP curves from the Muderong Shale, Saracen-1. The blue MICP curves are from the original conventional core samples analysed in 2001 by Dewhurst et al., 2002. The red MICP curves are from the warehoused conventional core samples analysed in 2013. The green MICP curves are from the warehoused drill cutting samples analysed in 2014.

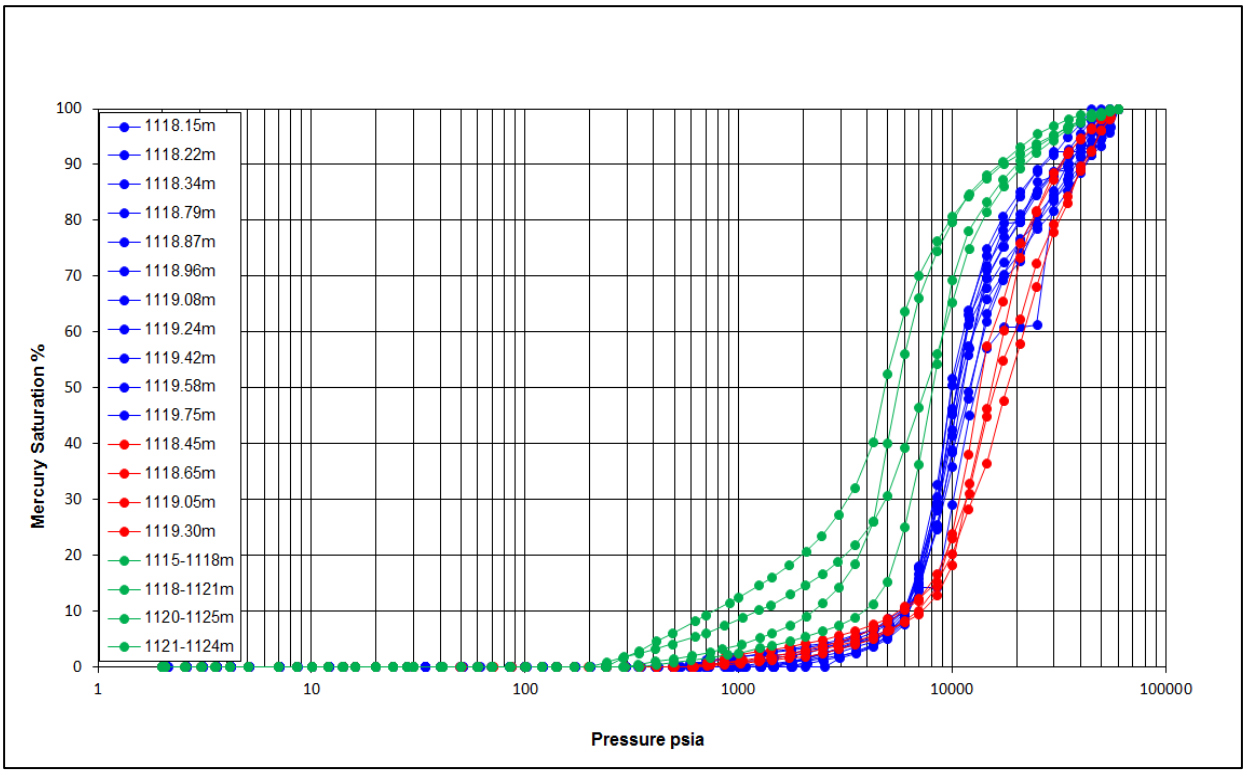

Figure D- 25: Conformance corrected MICP curves from the Muderong Shale, Saracen-1. The blue MICP curves are from the original conventional core samples analysed in 2001 by Dewhurst et al., 2002. The red MICP curves are from the warehoused conventional core samples analysed in 2013. The green MICP curves are from the warehoused drill cutting samples analysed in 2014.

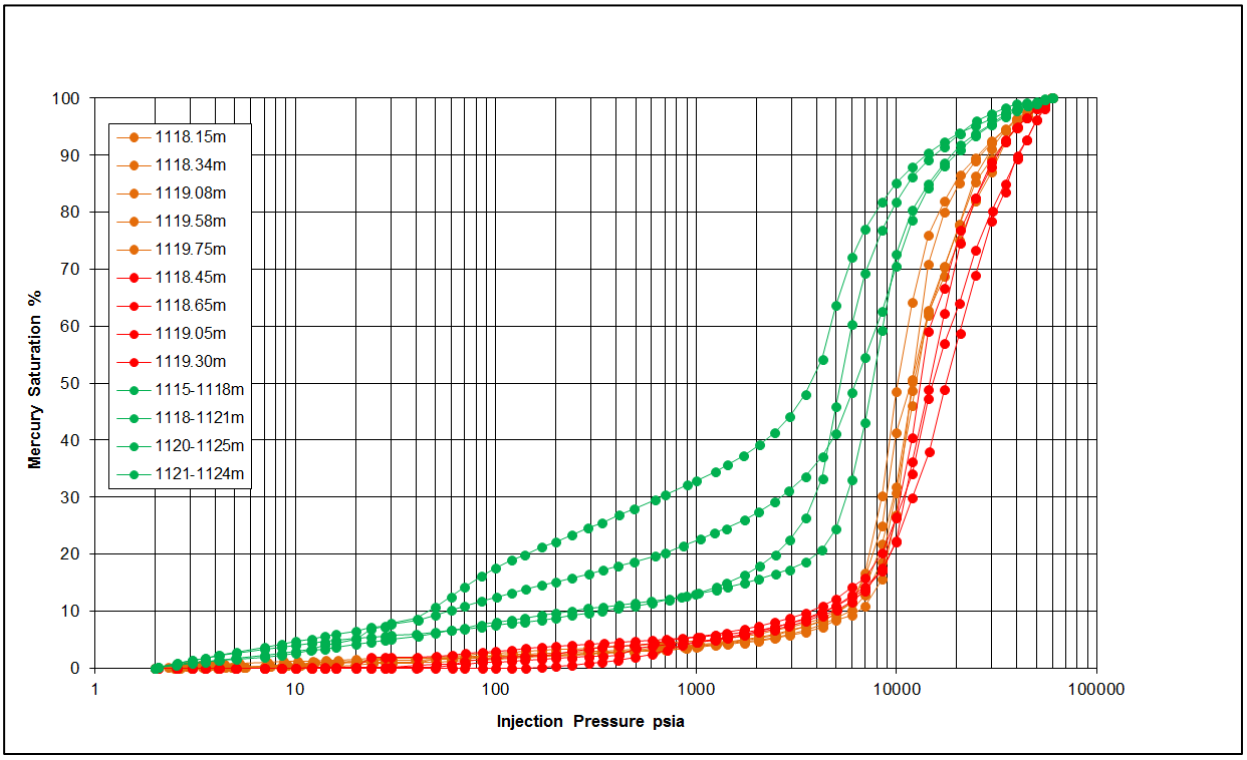

Figure D- 26: Raw MICP curves from the Muderong Shale, Saracen-1. The orange MICP curves are from the 2001 remaining conventional core samples stored in airtight bags analysed in 2015. The red MICP curves are from the warehoused conventional core samples analysed in 2013. The green MICP curves are from the warehoused drill cutting samples analysed in 2014.

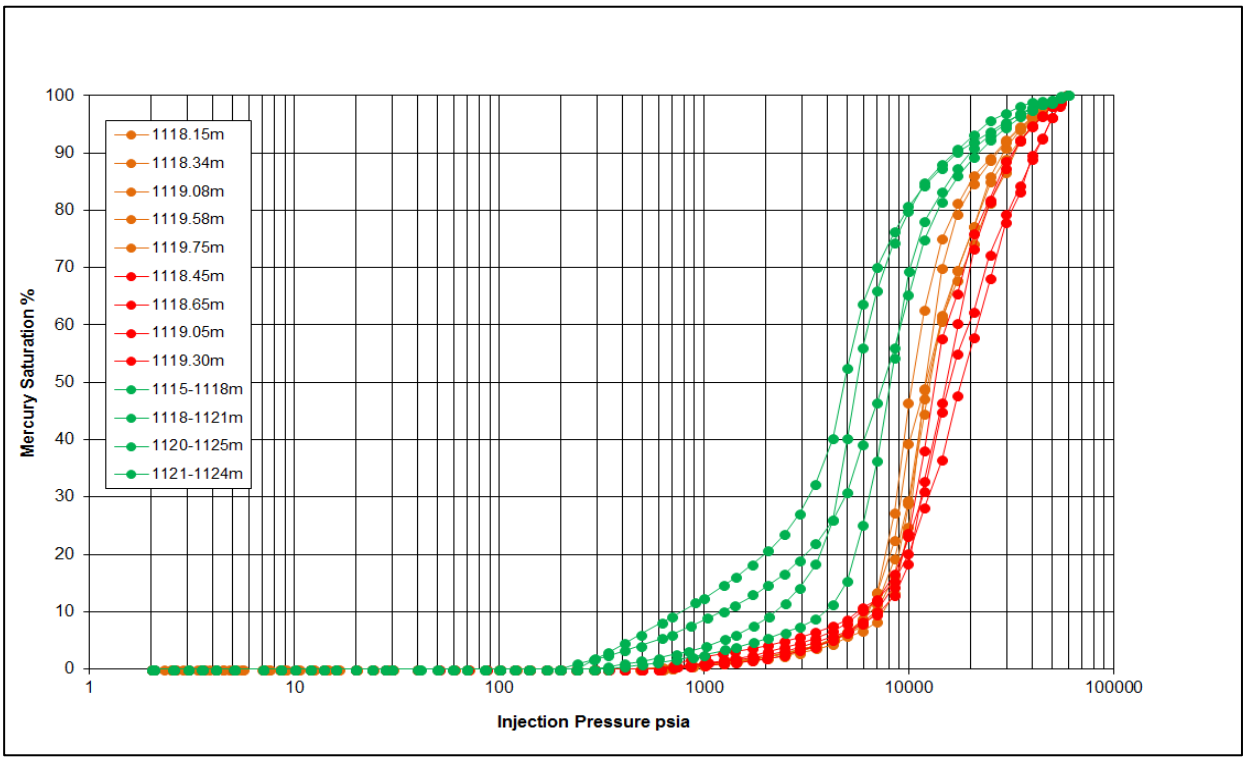

Figure D- 27: Conformance corrected MICP curves from the Muderong Shale, Saracen-1. The orange MICP curves are from the 2001 remaining conventional core samples stored in airtight bags analysed in 2015. The red MICP curves are from the warehoused conventional core samples analysed in 2013. The green MICP curves are from the warehoused drill cutting samples analysed in 2014.

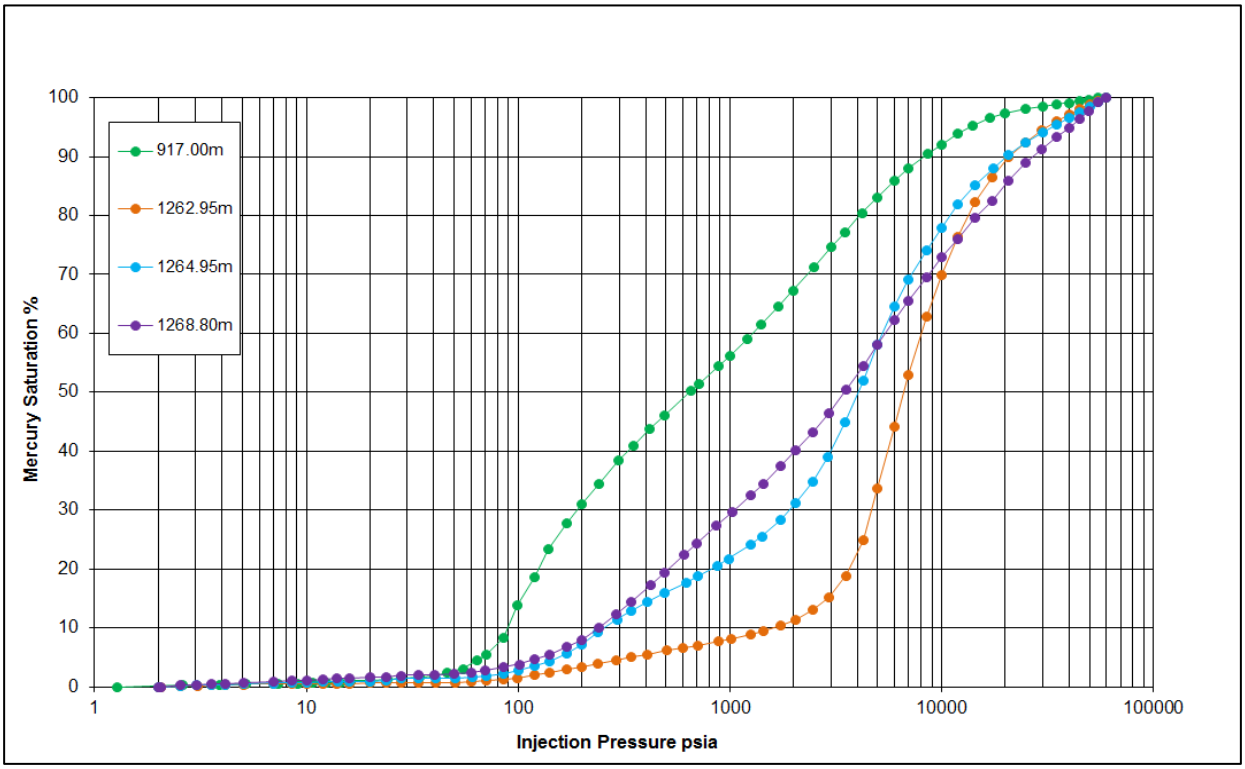

Figure D- 28: Raw MICP curves from fresh conventional core samples of the Paaratte Formation and Pember Mudstone, CRC-1. (Original analysis by Daniel, 2007)

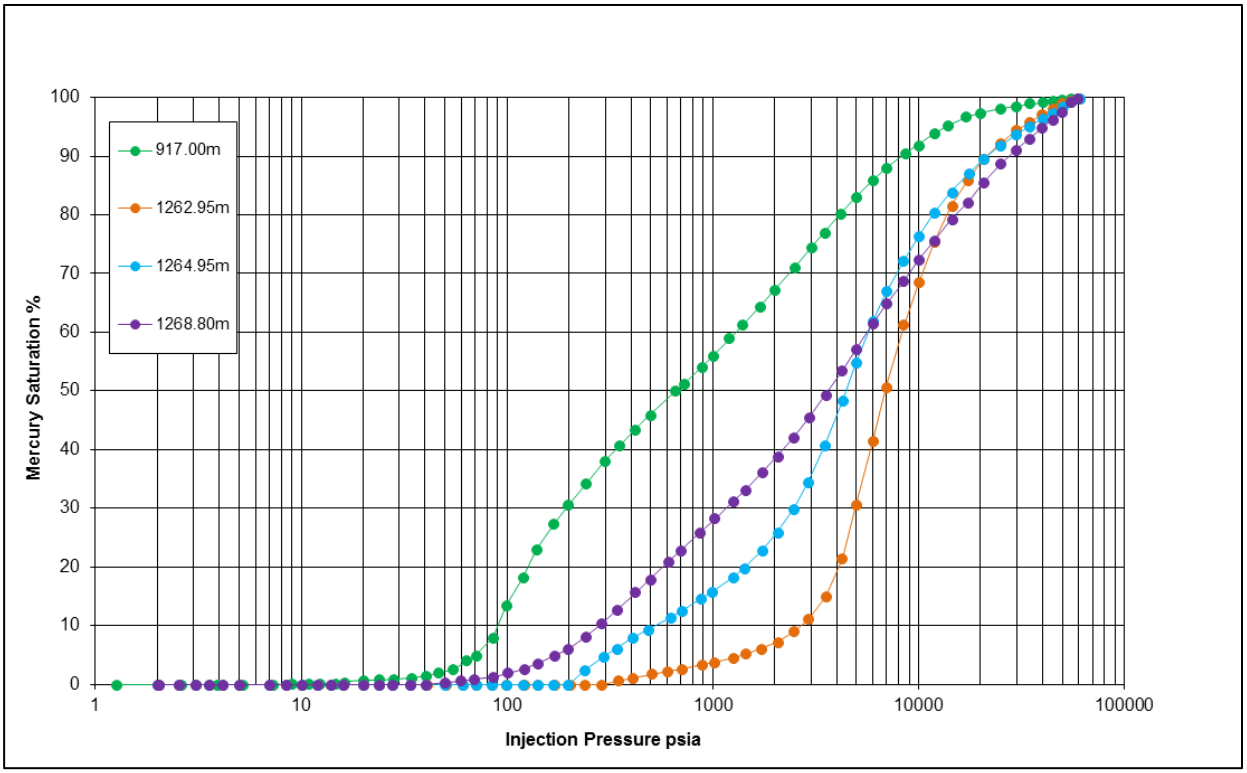

Figure D- 29: Conformance corrected MICP curves from fresh conventional core samples of the Paaratte Formation and Pember Mudstone, CRC-1. (Original analysis by Daniel, 2007)

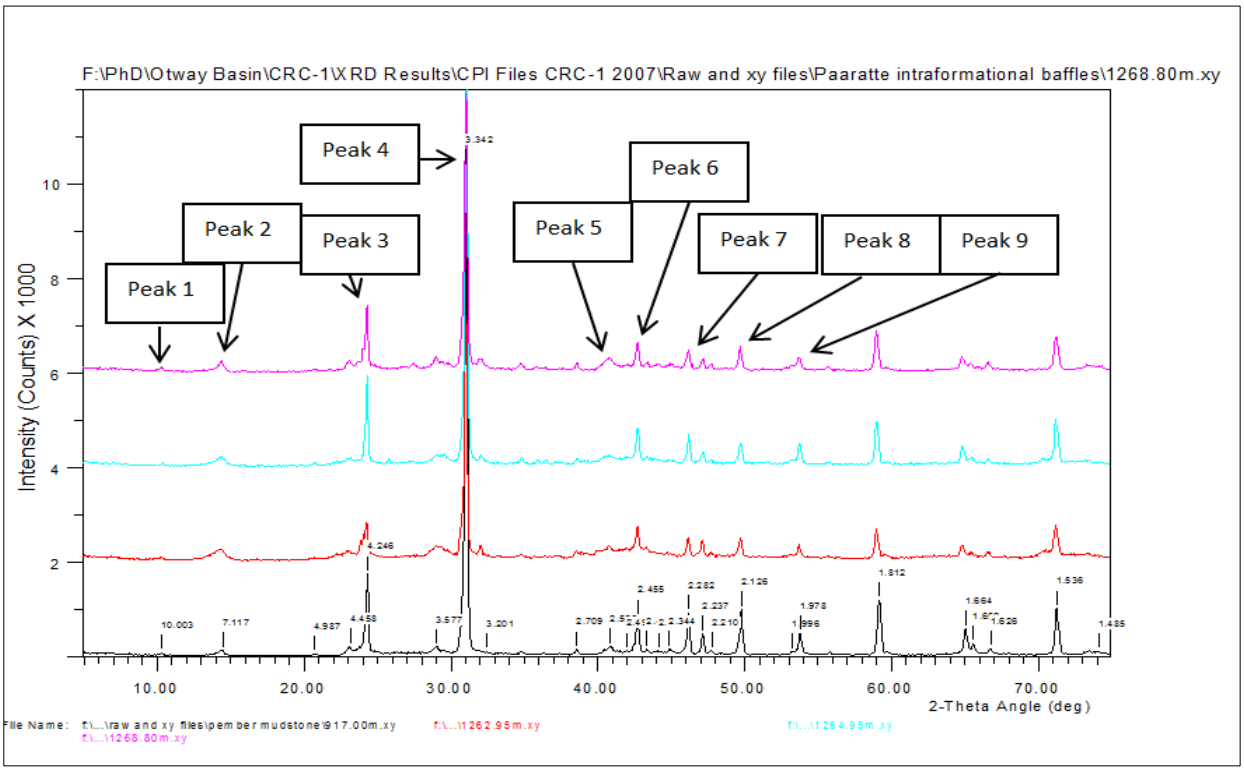

Figure D- 30: Paaratte Formation and Pember Mudstone, CRC-1 fresh conventional core sample XRD bulk diffractograms. Sample 917m (black), 1262.95m (red), 1264.95m (turquoise) and 1268.80m (pink) (Original analysis by Daniel, 2007).

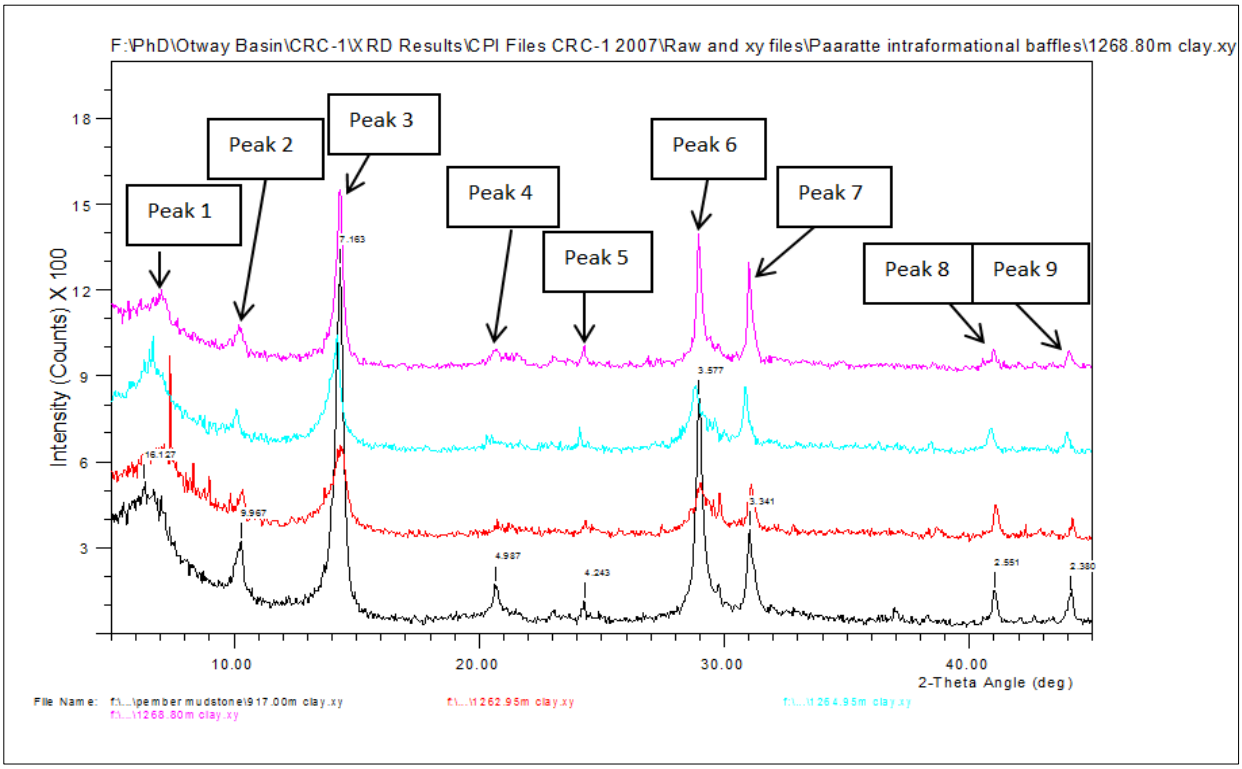

Figure D- 31: Paaratte Formation and Pember Mudstone, CRC-1 fresh conventional core sample XRD clay diffractograms. Sample 917m (black), 1262.95m (red), 1264.95m (turquoise) and 1268.80m (pink) (Original analysis by Daniel, 2007).

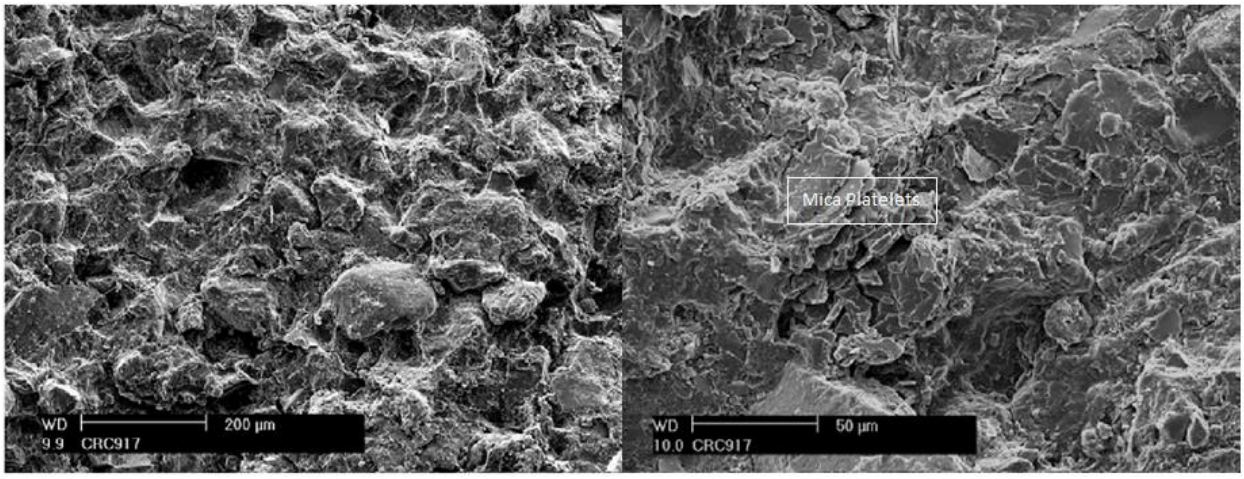

Figure D- 32: CRC-1, 2007, Images of a fresh Pember Mudstone conventional core sample 917 m. All images are perpendicular to bedding. (Left hand image) The image shows abundant clay matrix and a number of unidentified grains dotted throughout the sample. (Right hand image) CRC-1 Pember Mudstone SEM image of the conventional core sample 917 m under high magnification showing mica platelets surrounded by a clay matrix (Image and description modified from Daniel, 2007).

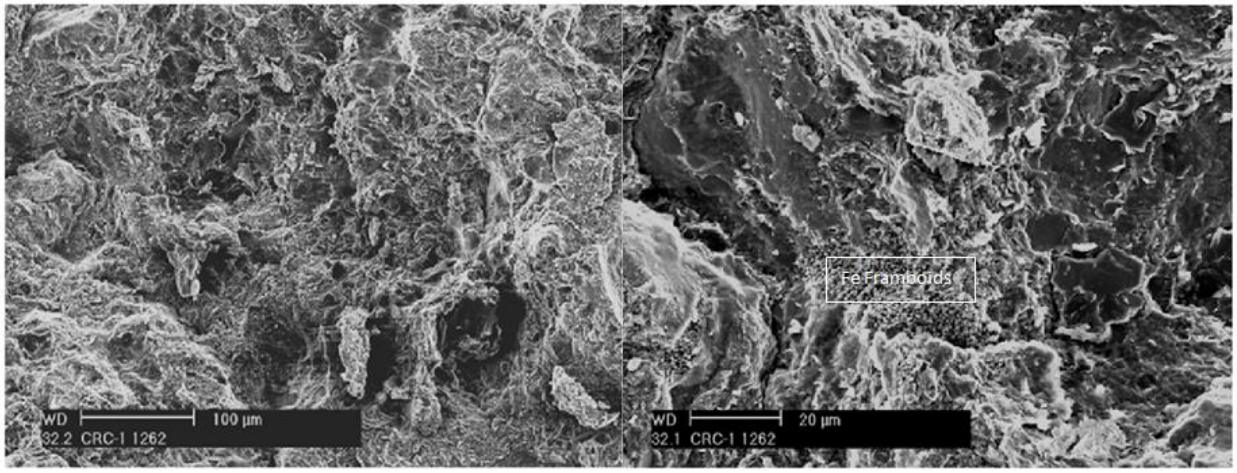

Figure D- 33: CRC-1, 2007, Images of a fresh Paaratte Formation conventional core sample 1262.95 m. All images are perpendicular to bedding. (Left Hand Image) The image shows a clay matrix, visible porosity and an angular silt sized grain. (Right Hand Image) CRC-1 Paaratte Formation SEM image of the conventional core sample 1262.95 m under high magnification showing Iron Framboids surrounded by a clay matrix. (Image and description modified from Daniel, 2007).

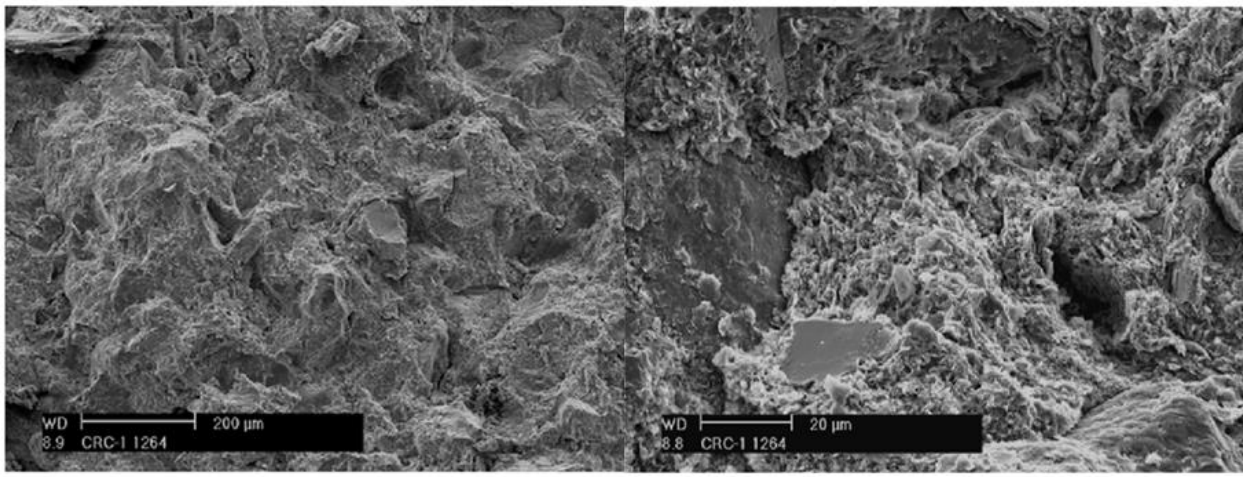

Figure D- 34: CRC-1, 2007, Images of a fresh Paaratte Formation conventional core sample 1264.95 m. All images are perpendicular to bedding. (Left Hand Image) The image shows a clay matrix, and a number of silt sized fragments. (Right Hand Image) CRC-1 Paaratte Formation SEM image of the conventional core sample 1264.95 m under high magnification showing silty fragments surrounded by clay matrix. (Image and description modified from Daniel, 2007).

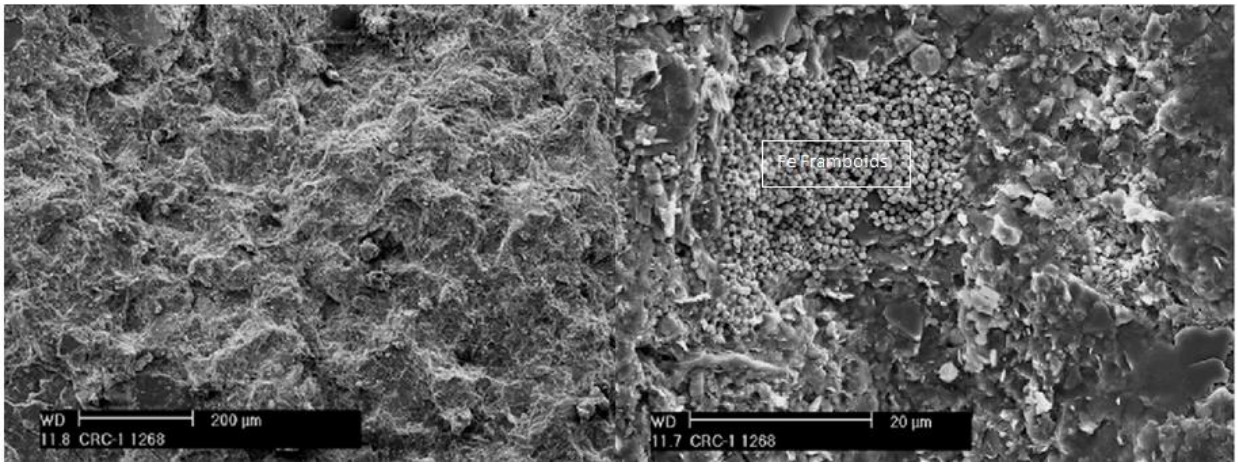

Figure D- 35: CRC-1, 2007, Images of a fresh Paaratte Formation conventional core sample 1268.90 m. All images are perpendicular to bedding. (Left Hand Image) The image shows a clay matrix with possible mica platelets. (Right Hand Image) CRC-1 Paaratte Formation SEM image of the conventional core sample 1268.80 m under high magnification showing Iron Framboids surrounded by a clay platelet matrix. (Image and description modified from Daniel, 2007).

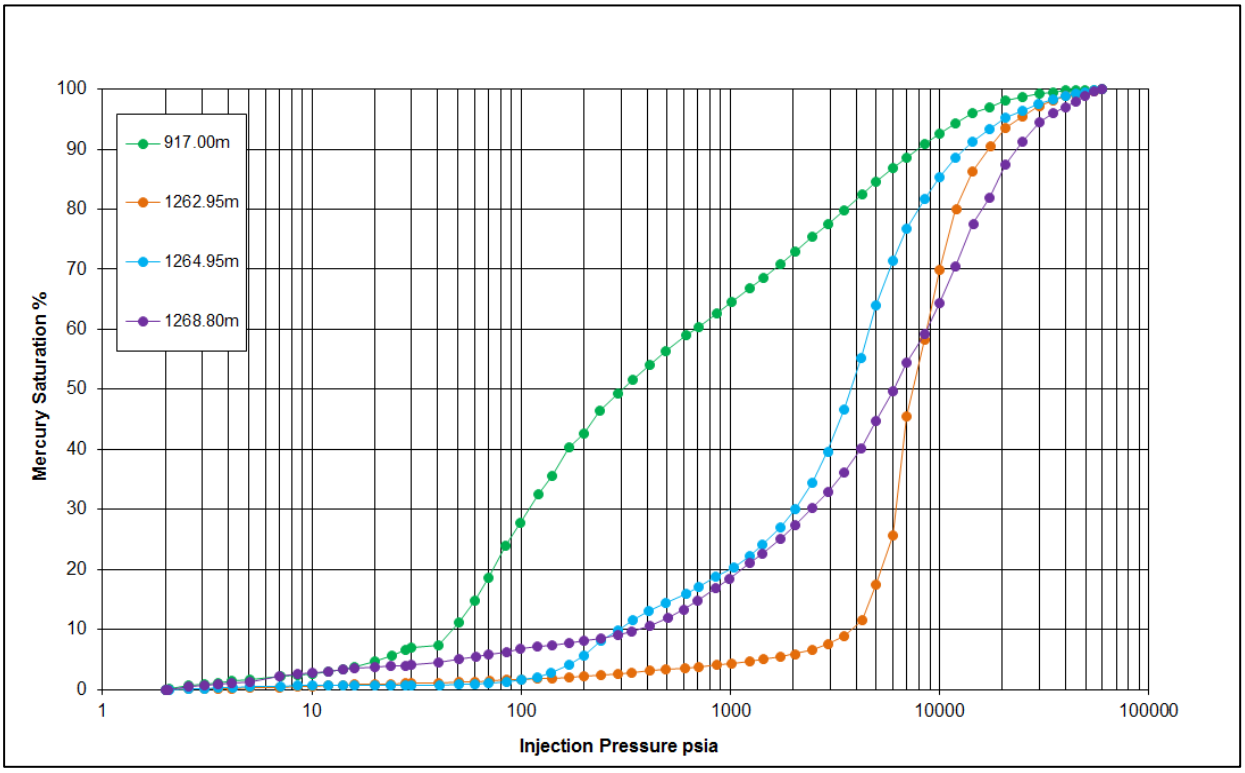

Figure D- 36: Raw MICP curves from warehoused conventional core samples of the Paaratte Formation and Pember Mudstone, CRC-1. Samples analysed in 2014.

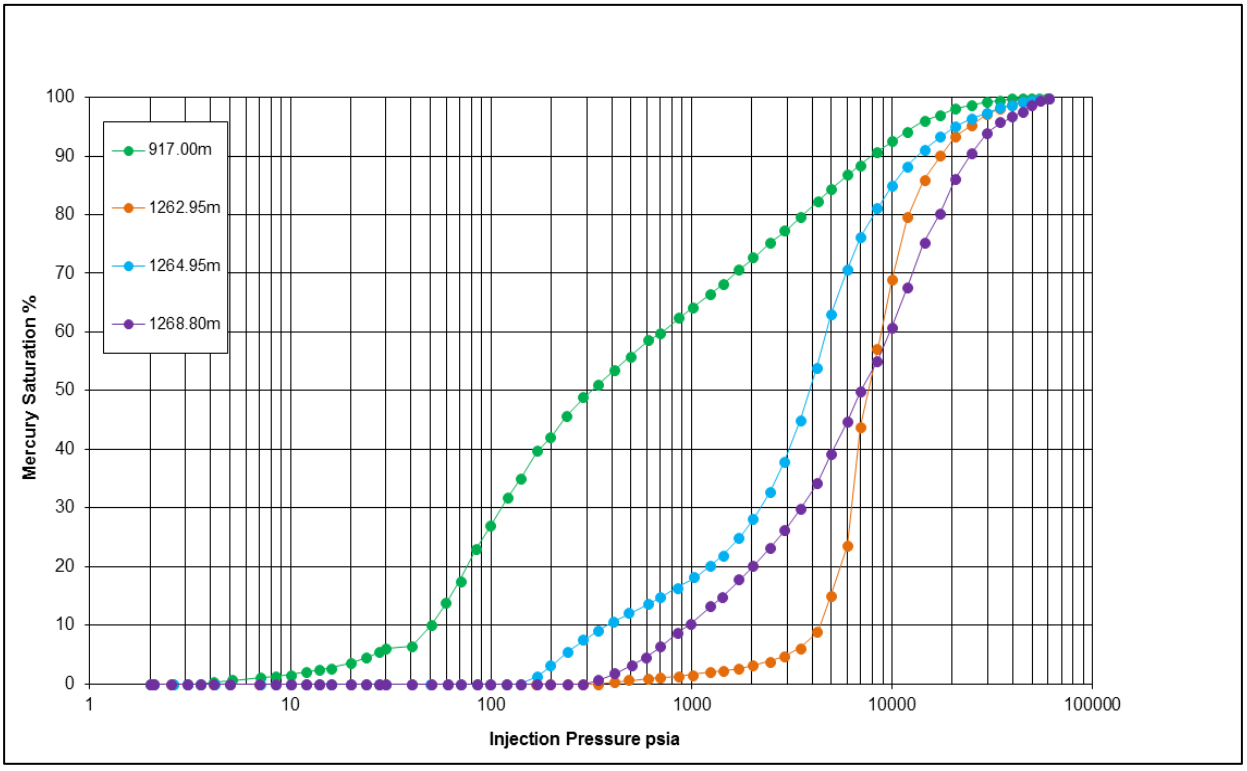

Figure D- 37: Conformance corrected MICP curves from warehoused conventional core samples of the Paaratte Formation and Pember Mudstone, CRC-1. Samples analysed in 2014.

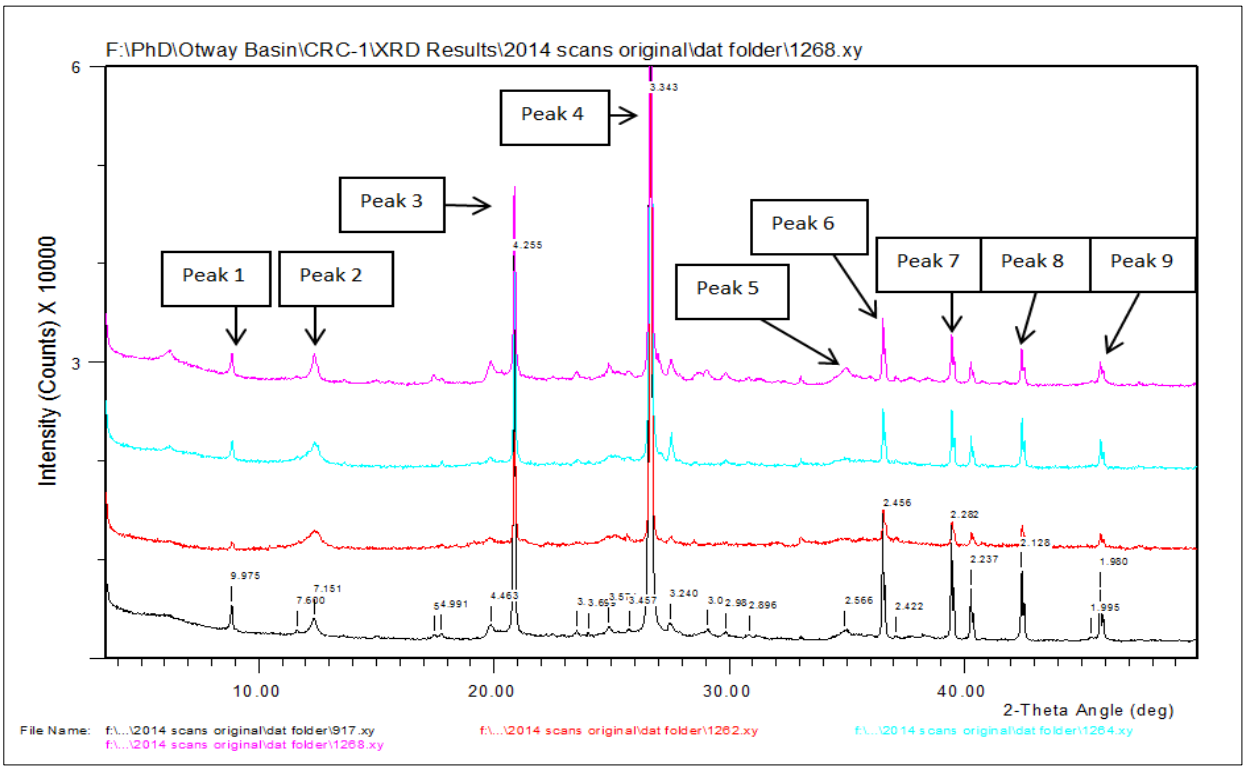

Figure D- 38: Paaratte Formation and Pember Mudstone, CRC-1 warehoused conventional core sample XRD bulk diffractograms. Sample 917m (black), 1262.95m (red), 1264.95m (turquoise) and 1268.80m (pink) (Original analysis by Daniel, 2007).Samples analysed in 2014.

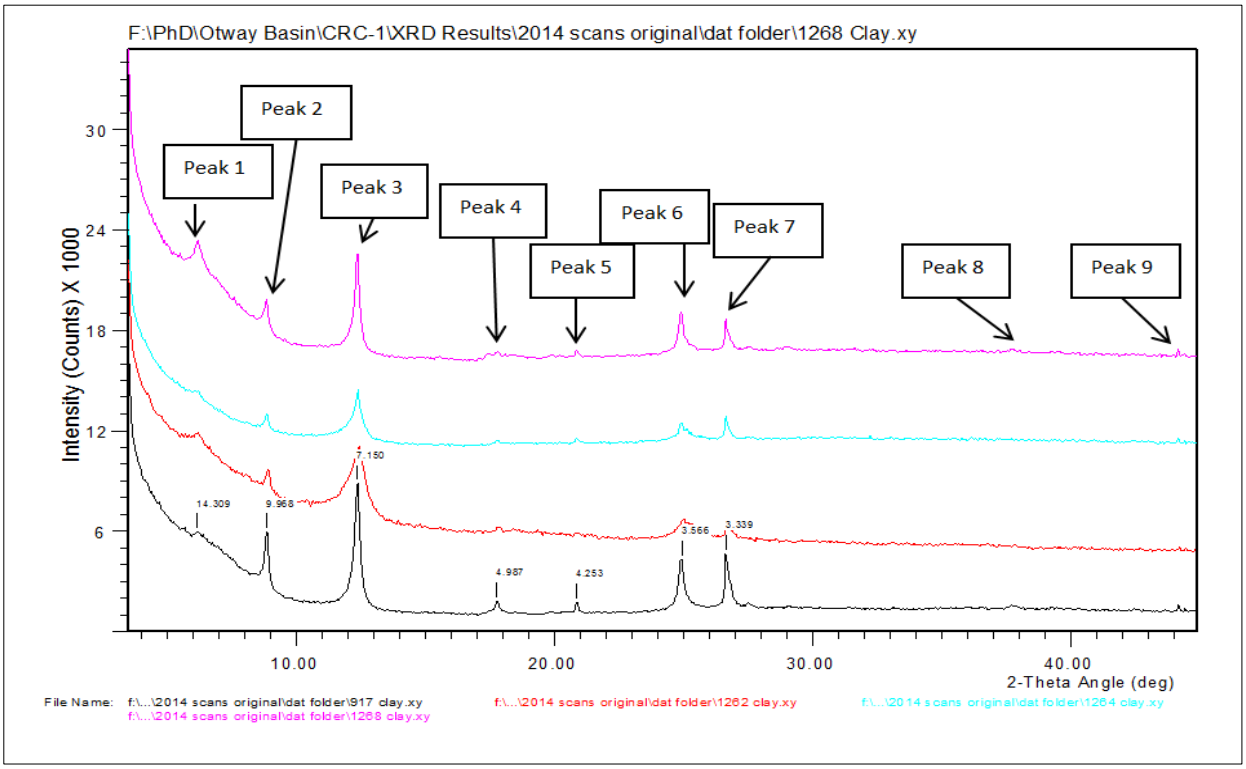

Figure D- 39: Paaratte Formation and Pember Mudstone, CRC-1 warehoused conventional core sample XRD bulk diffractograms. Sample 917m (black), 1262.95m (red), 1264.95m (turquoise) and 1268.80m (pink) (Original analysis by Daniel, 2007).Samples analysed in 2014.

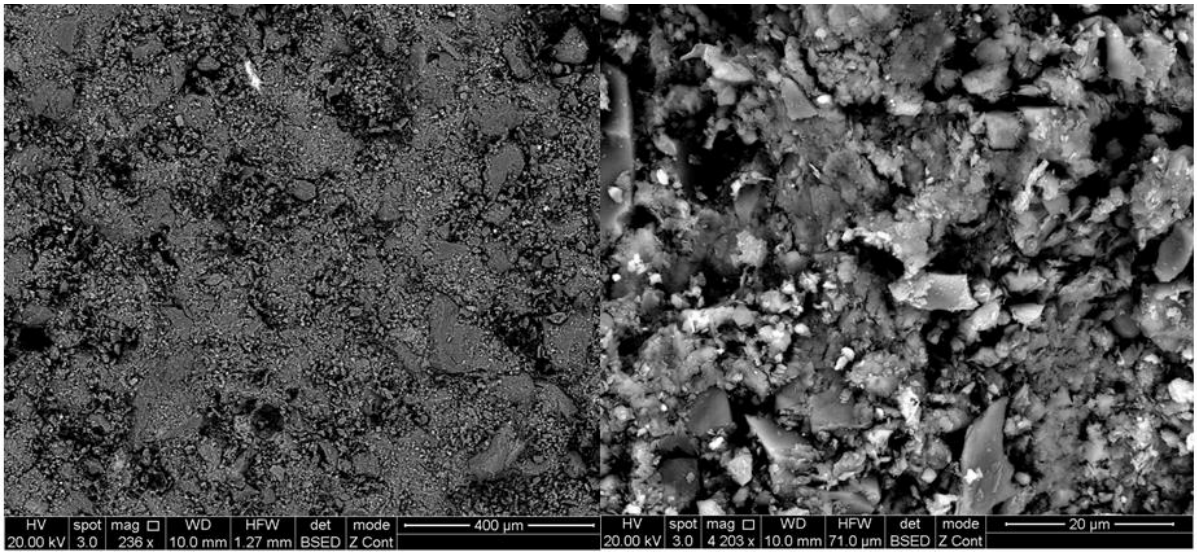

Figure D- 40: CRC-1, 2014, BSE images of warehoused Pember Mudstone conventional core sample 917 m. (Left hand image) The image shows silty grains dotted throughout a clay matrix with visible porosity. (Right hand image) CRC-1, 2014 warehoused Pember Mudstone BSE image of the conventional core sample 917 m under high magnification showing clays with interspersed angular grains. Note that the polishing of the sample was hampered by the unconsolidated nature of the sample.

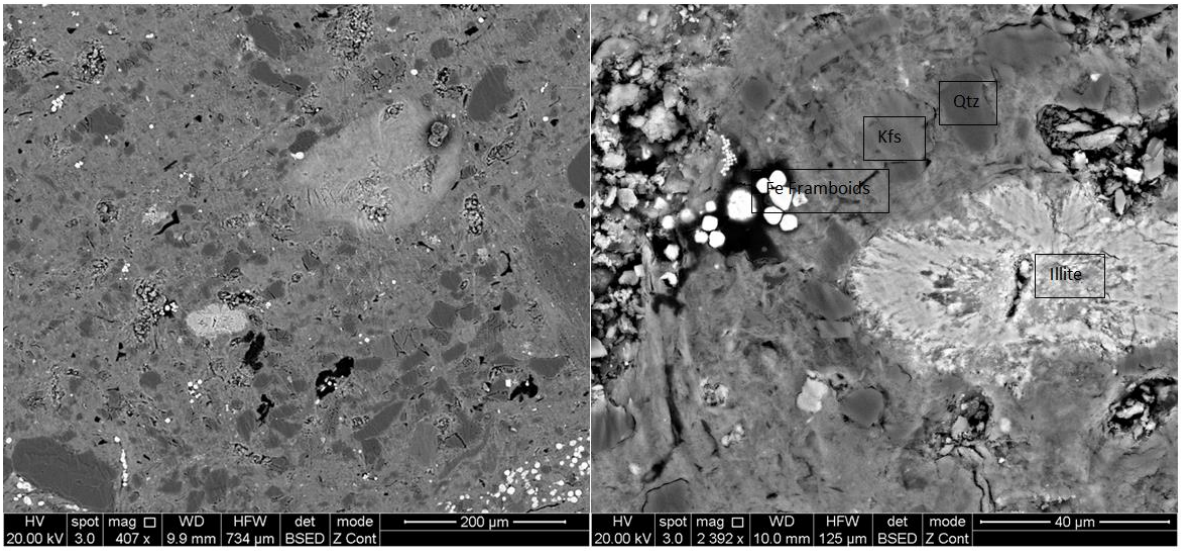

Figure D- 41: CRC-1, 2014, Images of a warehoused Paaratte Formation conventional core sample 1262.95 m. (Left hand image) The image silt sized grains, iron framboids and quartz dotted throughout the matrix. There is also porosity and organic matter visible in the sample. (Right hand image) CRC-1 Paaratte Formation BSE image of the conventional core sample 1262.95 m under high magnification showing iron framboids (Fe Framboids), porosity, illite, quartz (Qtz) and potassium feldspar (Kfs) surrounded by matrix.

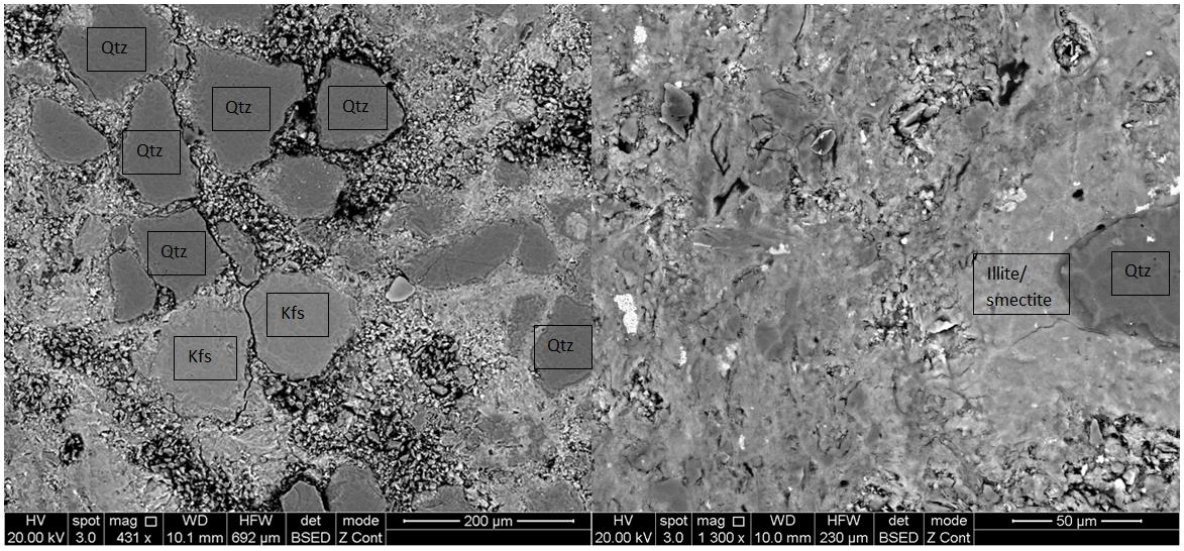

Figure D- 42: CRC-1, 2014, Images of a warehoused Paaratte Formation conventional core sample 1264.95 m. (Left hand image) The image shows quartz (Qtz) and potassium feldspar (Kfs) dotted throughout the clay matrix. There is also significant visible porosity visible. (Right hand image) CRC-1 Paaratte Formation BSE image of the conventional core sample 1264.95 m under high magnification showing a quartz grain surrounded by illite/smectite clay matrix.

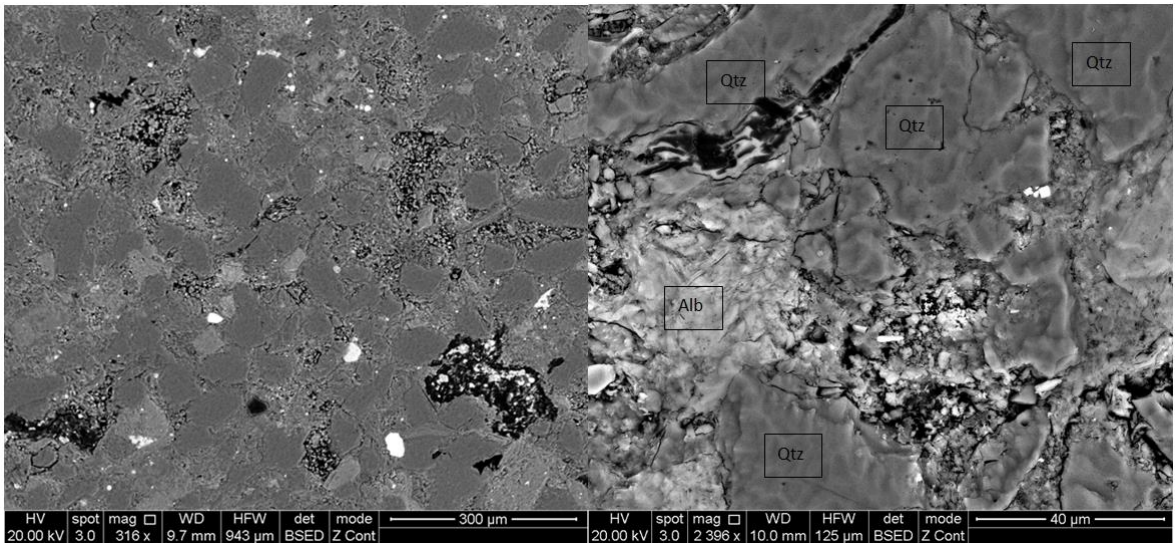

Figure D- 43: CRC-1, 2014, Images of a warehoused Paaratte Formation conventional core sample 1268.80 m. (Left hand image) The image shows dominantly quartz dotted throughout the matrix with grain to grain contact. There is also porosity and possibly organic matter visible in the sample. (Right hand image) CRC-1 Paaratte Formation BSE image of the conventional core sample 1268.80 m under high magnification showing quartz (Qtz) and albite (Alb) with visible porosity.

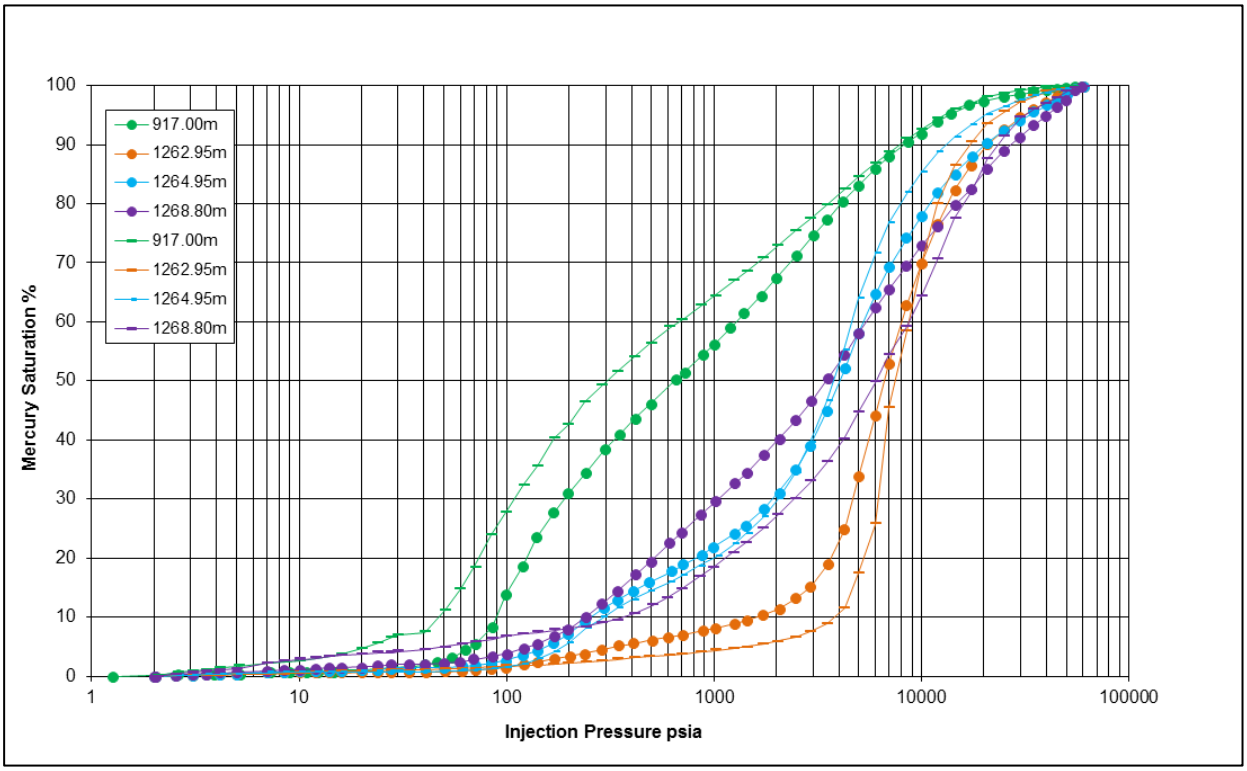

Figure D- 44: Raw MICP curves from samples of Paaratte Formation and Pember Mudstone, CRC-1. The fresh (2007) sample MICP curves are shown with dots at the pressure equilibrium points and the warehoused (2014) sample MICP curves are shown by short horizontal lines at the pressure equilibrium points.

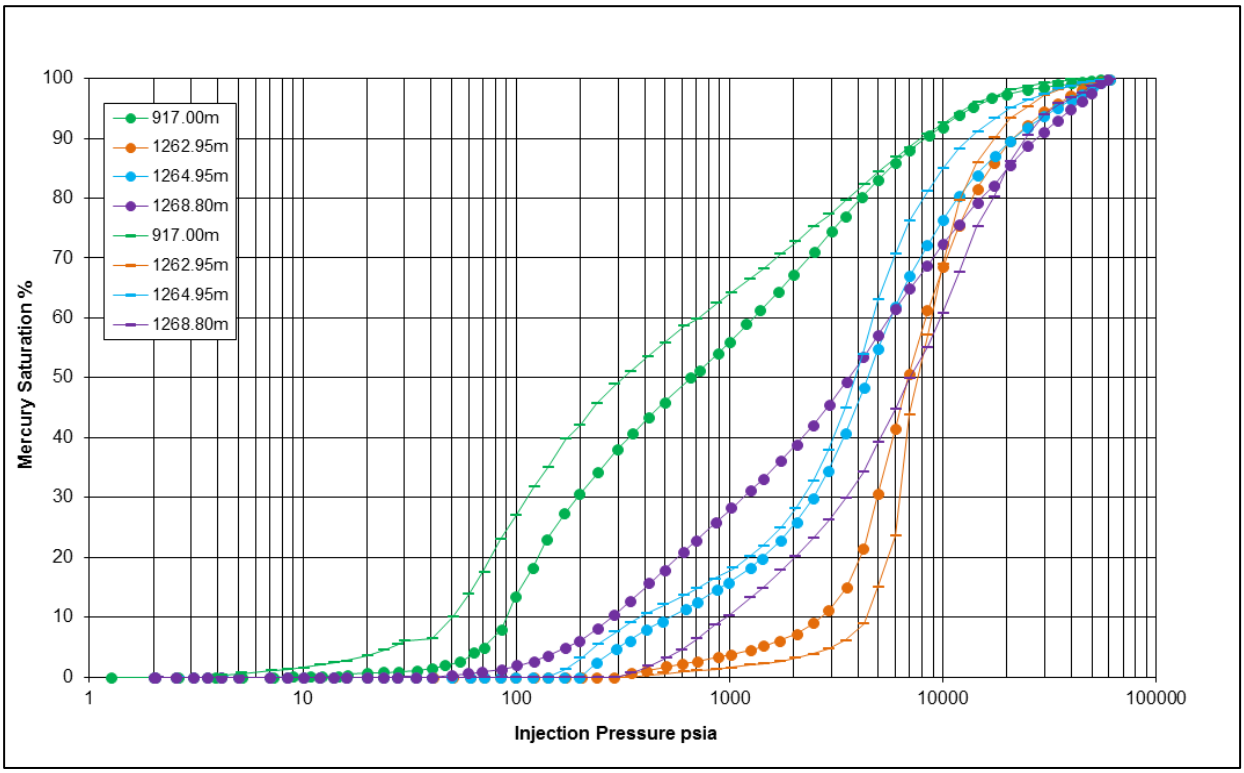

Figure D- 45: CRC-1 Conformance corrected MICP curves from samples of Paaratte Formation and Pember Mudstone, CRC-1. The fresh (2007) sample MICP curves are shown with dots at the pressure equilibrium points and the warehoused (2014) sample MICP curves are shown by short horizontal lines at the pressure equilibrium points.

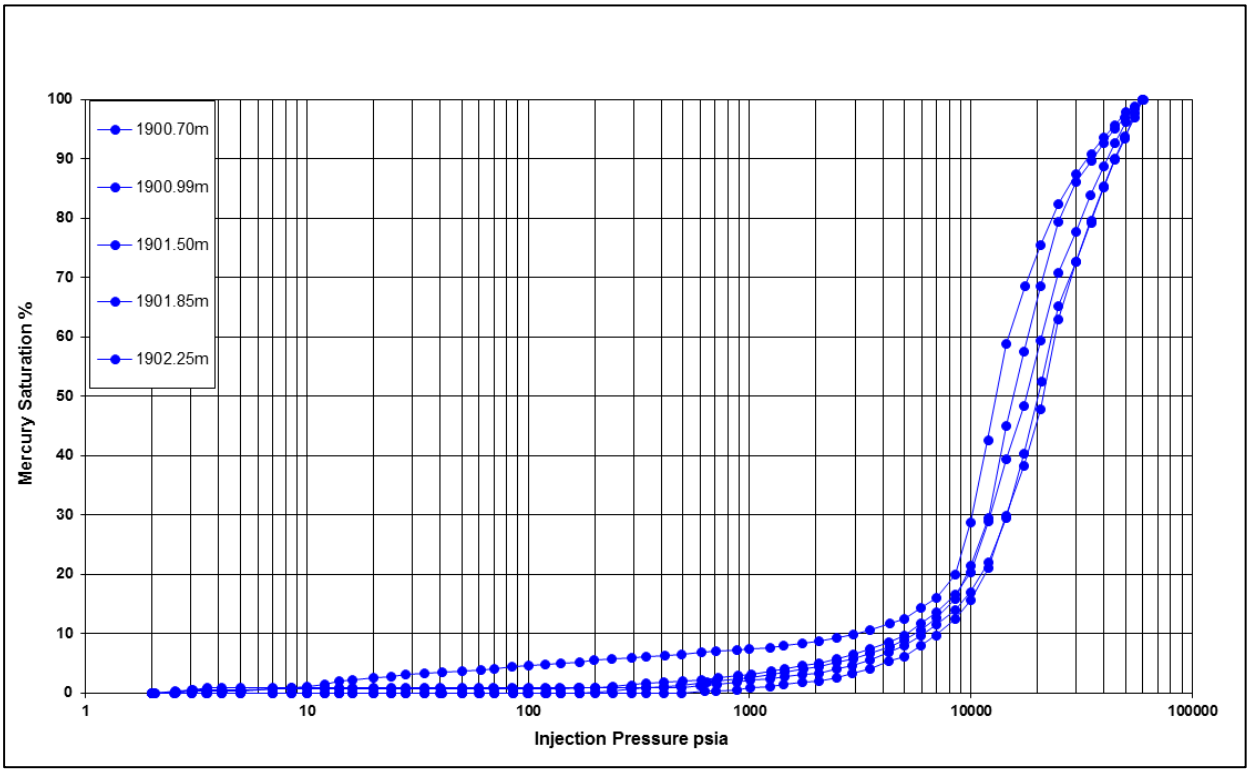

Figure D- 46: Raw MICP curves from fresh conventional core samples of the Belfast Mudstone, CRC-1. Samples analysed in 2007 (Original analysis by Daniel, 2007).

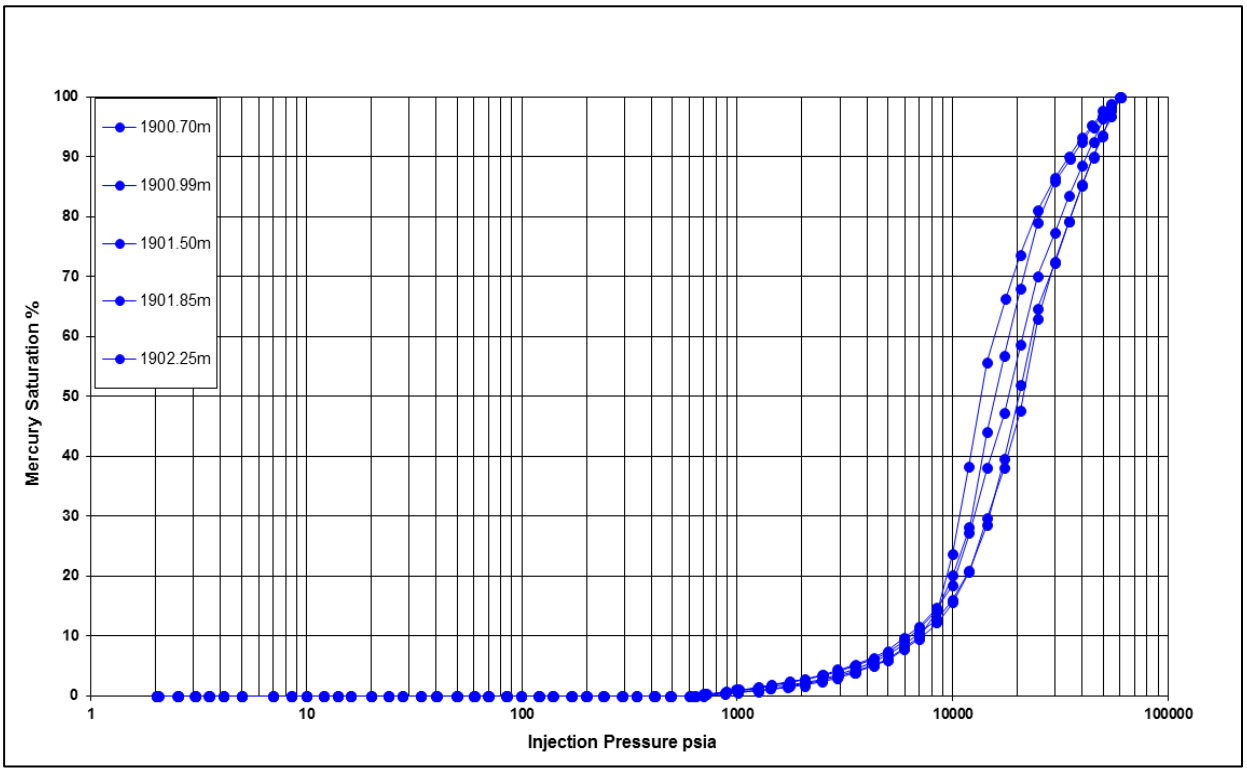

Figure D- 47: Conformance corrected MICP curves from fresh conventional core samples of the Belfast Mudstone, CRC-1. Samples analysed in 2007 (Original analysis by Daniel, 2007).

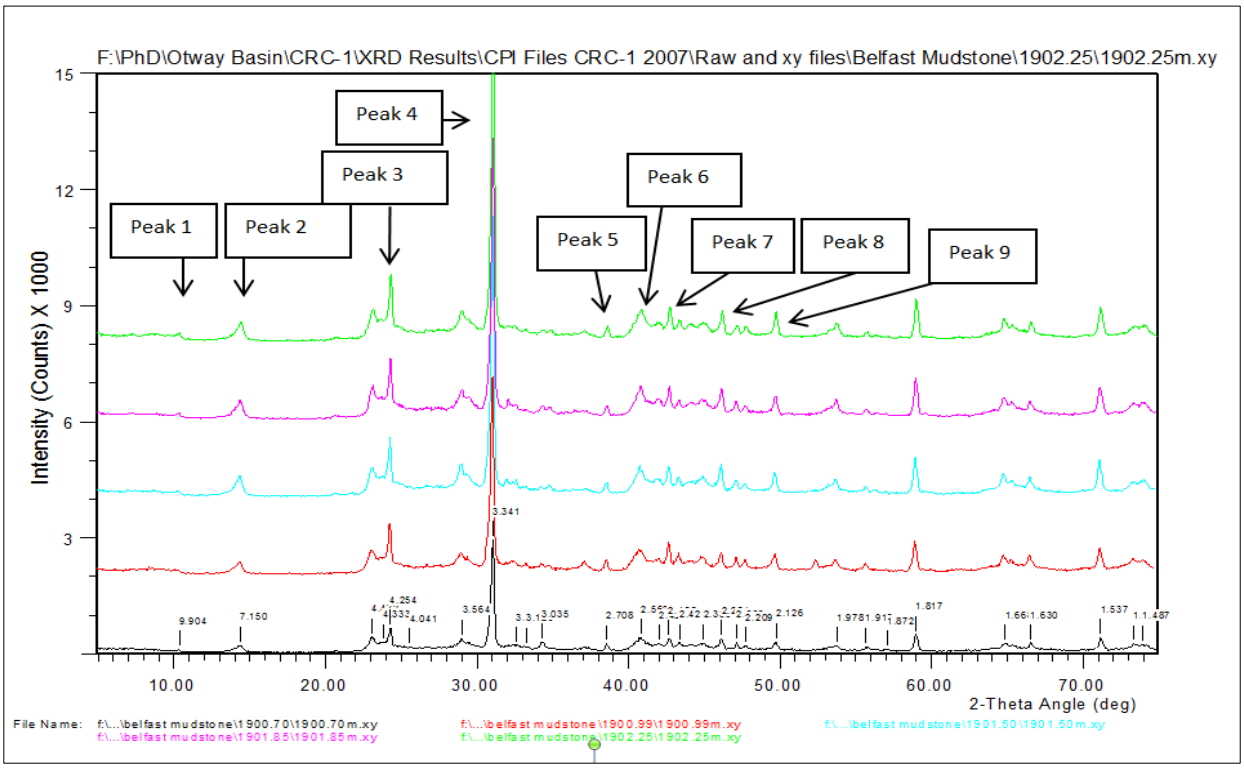

Figure D- 48: Belfast Mudstone, CRC-1 fresh (2007) conventional core sample XRD bulk diffractograms. Sample 1900.70m (black), 1900.99m (red), 1901.50m (turquoise) and 1901.85m (pink) and 1902.25m (green). (Original analysis by Daniel, 2007).

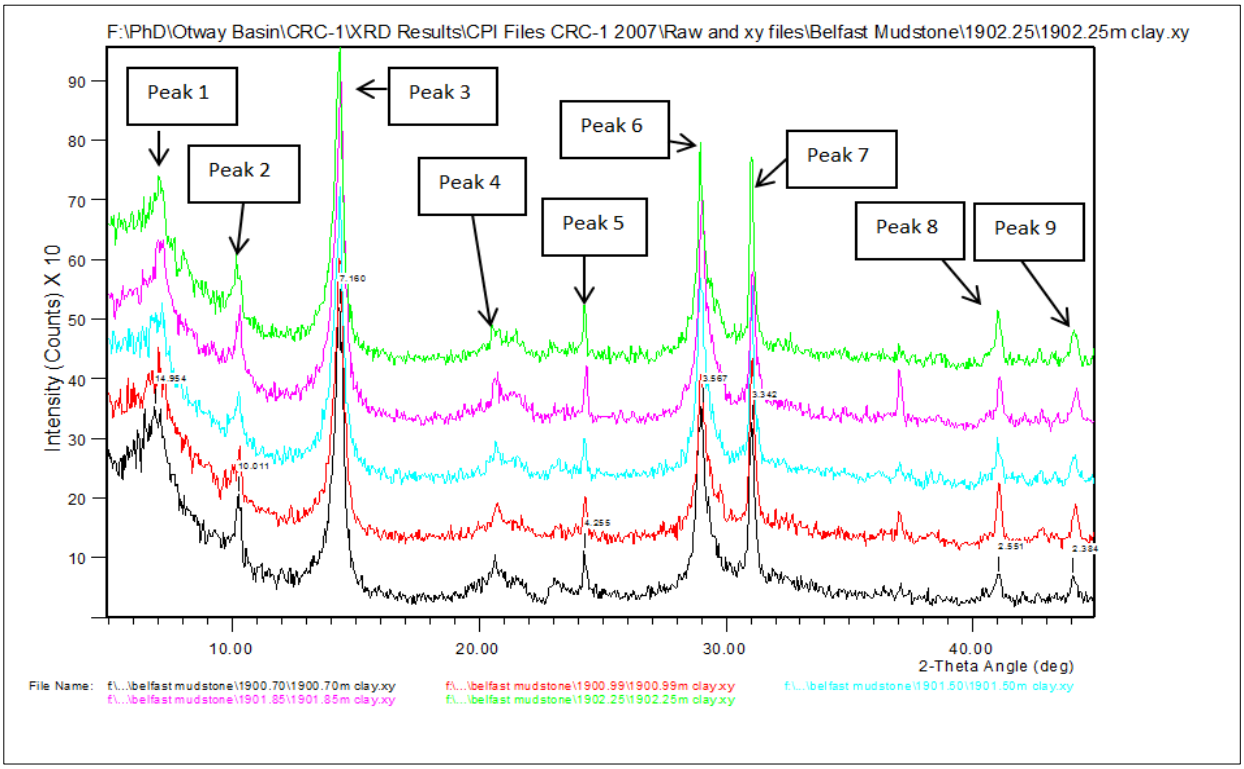

Figure D- 49: Belfast Mudstone, CRC-1 fresh (2007) conventional core sample XRD clay diffractograms Sample 1900.70m (black), 1900.99m (red), 1901.50m (turquoise) and 1901.85m (pink) and 1902.25m (green) (Original analysis by Daniel, 2007).

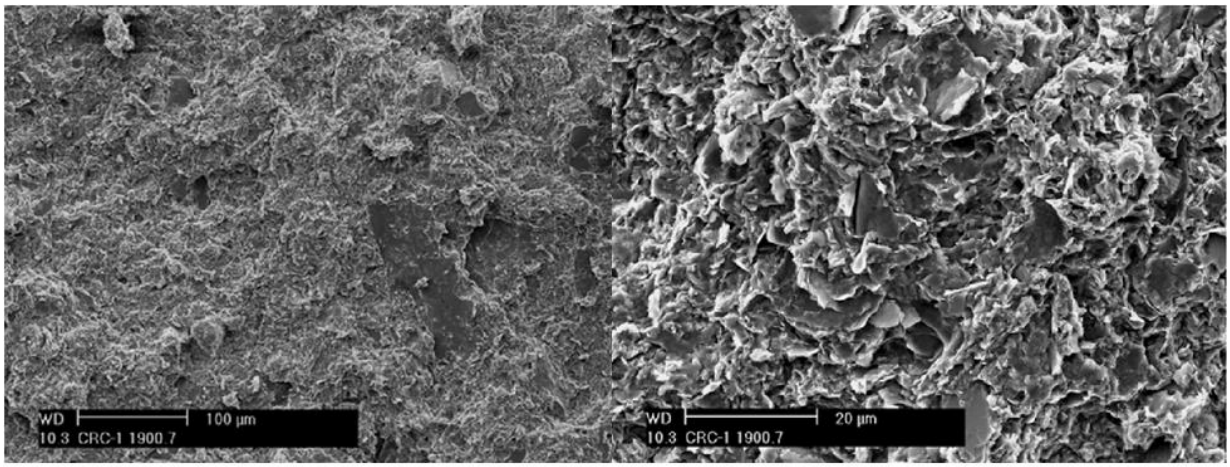

Figure D- 50: CRC-1, 2007, Images of a fresh Belfast Mudstone conventional core sample 1900.70 m. All images are perpendicular to bedding. (Left hand image) The image shows a clay matrix (Right hand image) CRC-1 Belfast Mudstone SEM image of the conventional core sample 1900.70 m under high magnification showing the clay matrix, possible mica platelets and the microporosity of the sample. (Image and description modified from Daniel, 2007).

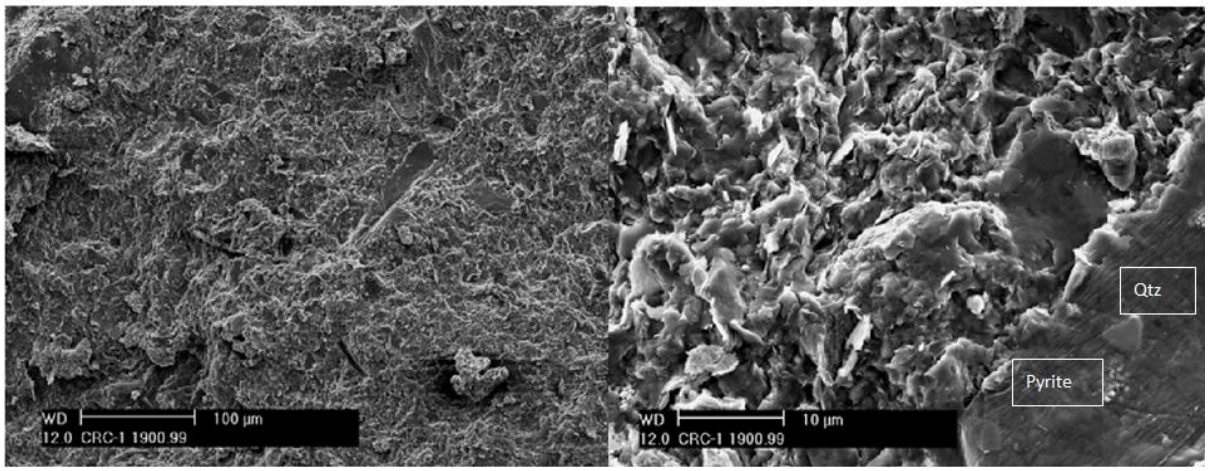

Figure D- 51: CRC-1, 2007, Images of a fresh Belfast Mudstone conventional core sample 1900.99 m. All images are perpendicular to bedding (Left hand image) The image shows a clay matrix overlaying angular grains. (Right hand image) CRC-1 Belfast Mudstone SEM image of the conventional core sample 1900.99 m under high magnification showing quartz (Qtz) and pyrite surrounded by a clay matrix. (Image and description modified from Daniel, 2007).

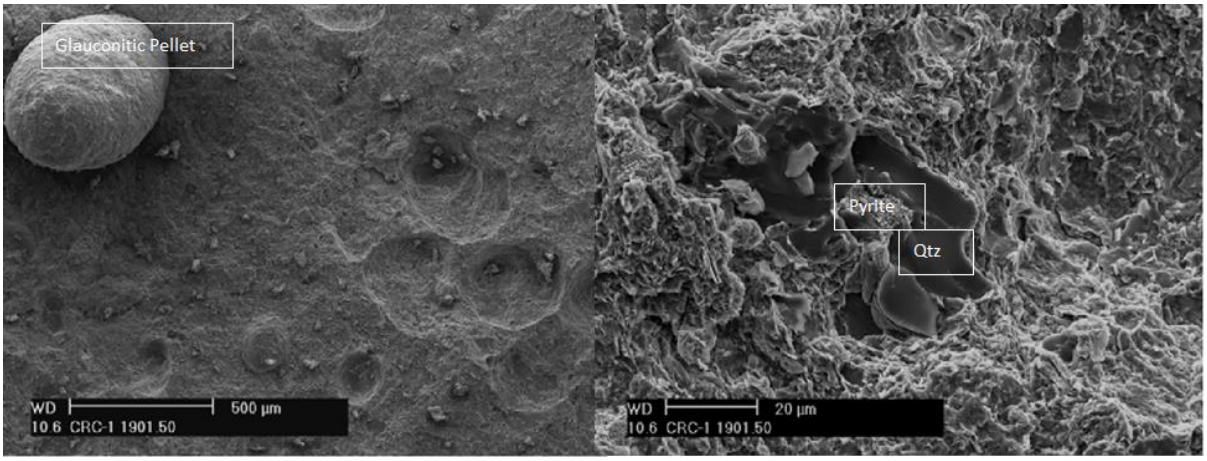

Figure D- 52: CRC-1, 2007, Images of a fresh Belfast Mudstone conventional core sample 1901.50 m. All images are perpendicular to bedding (Left Hand Image). This image shows a glauconitic pellet embedded in a clay matrix. (Right Hand Image) CRC-1 Belfast Mudstone SEM image of the conventional core sample 1901.50 m under high magnification showing quartz (Qtz) and Pyrite surrounded by a clay matrix. (Image and description modified from Daniel, 2007).

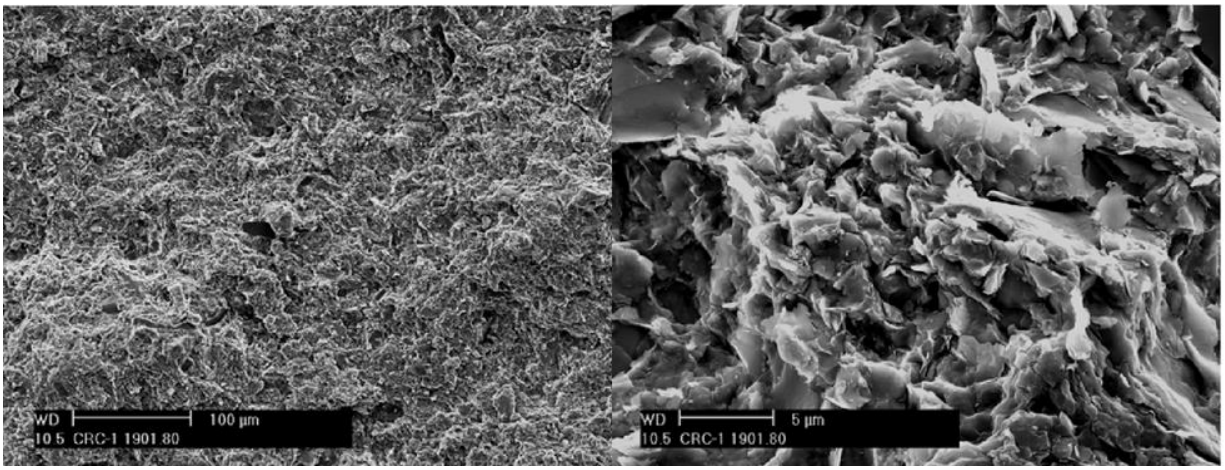

Figure D- 53: CRC-1, 2007, Images of a fresh Belfast Mudstone conventional core sample 1901.85 m. All images are perpendicular to bedding (Left hand image). This image shows microporosity within the clay matrix. (Right hand image) CRC-1 Belfast Mudstone SEM image of the conventional core sample 1901.85 m under high magnification showing the fine detail of the clay fabric identified as kaolinite/illite/smectite (Image and description modified from Daniel, 2007).

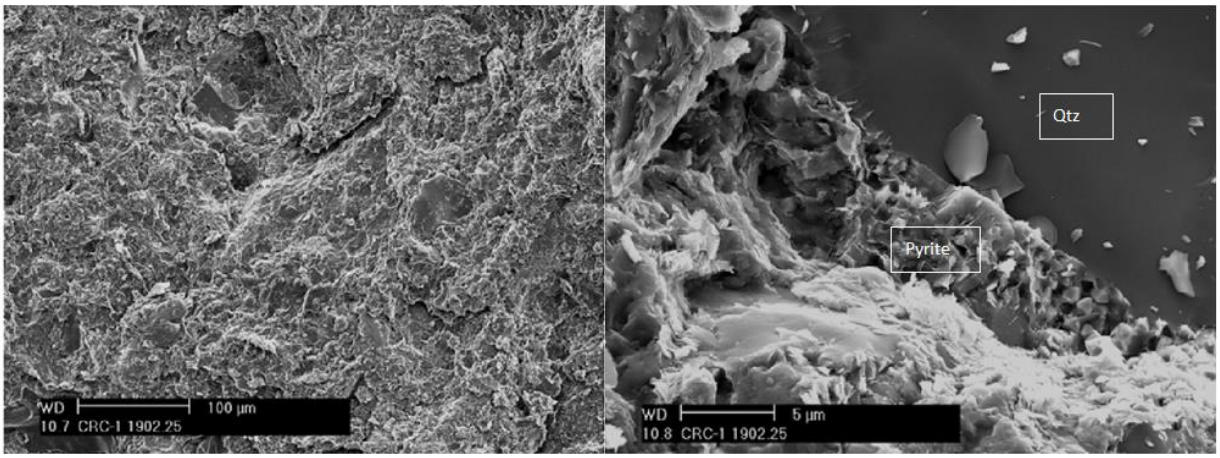

Figure D- 54: CRC-1, 2007, Images of a fresh Belfast Mudstone conventional core sample 1902.25 m. All images are perpendicular to bedding (Left hand image). This image shows the clay matrix dotted with a number of broken quartz grains dotted throughout the sample. (Right hand image) CRC-1 Belfast Mudstone SEM image of the conventional core sample 1902.25 m under high magnification showing quartz (Qtz) and pyrite. (Image and description modified from Daniel, 2007).

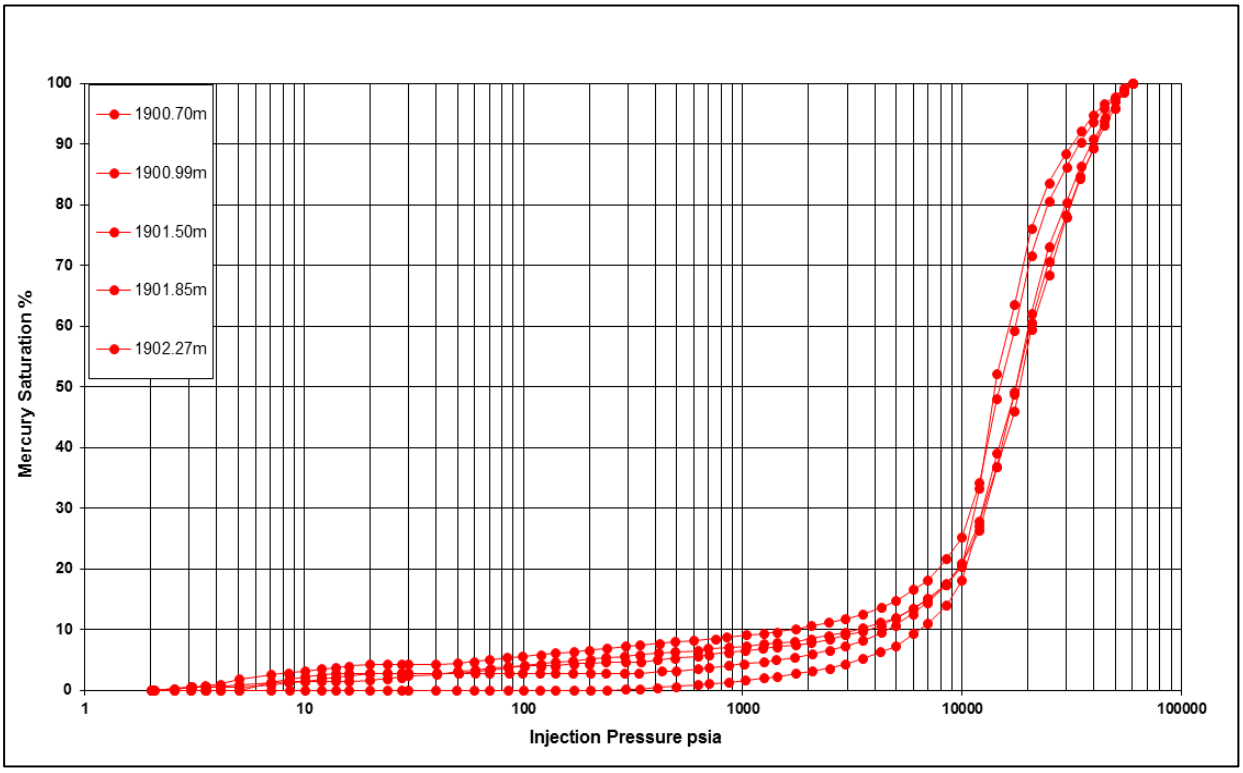

Figure D- 55: Raw MICP curves from warehoused conventional core samples of the Belfast Mudstone, CRC-1. Samples analysed in 2014.

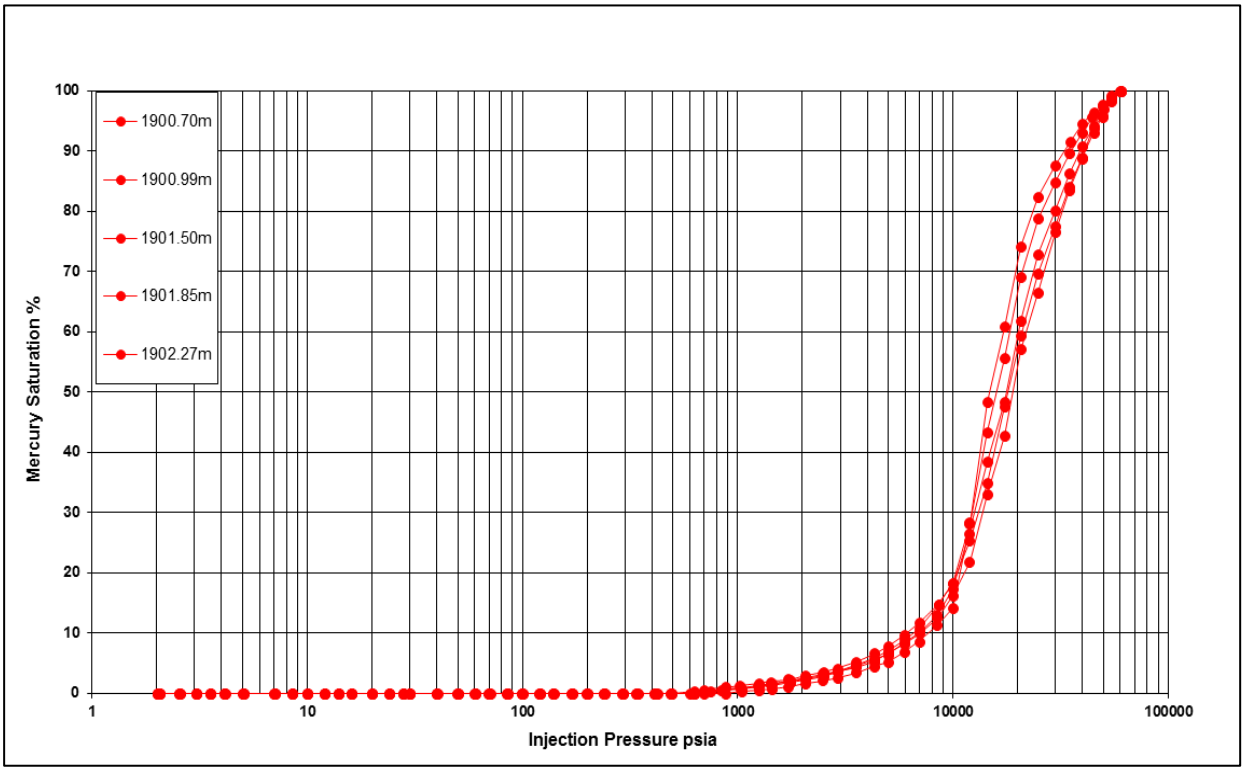

Figure D- 56: Conformance corrected MICP curves from warehoused conventional core samples of the Belfast Mudstone, CRC-1. Samples analysed in 2014.

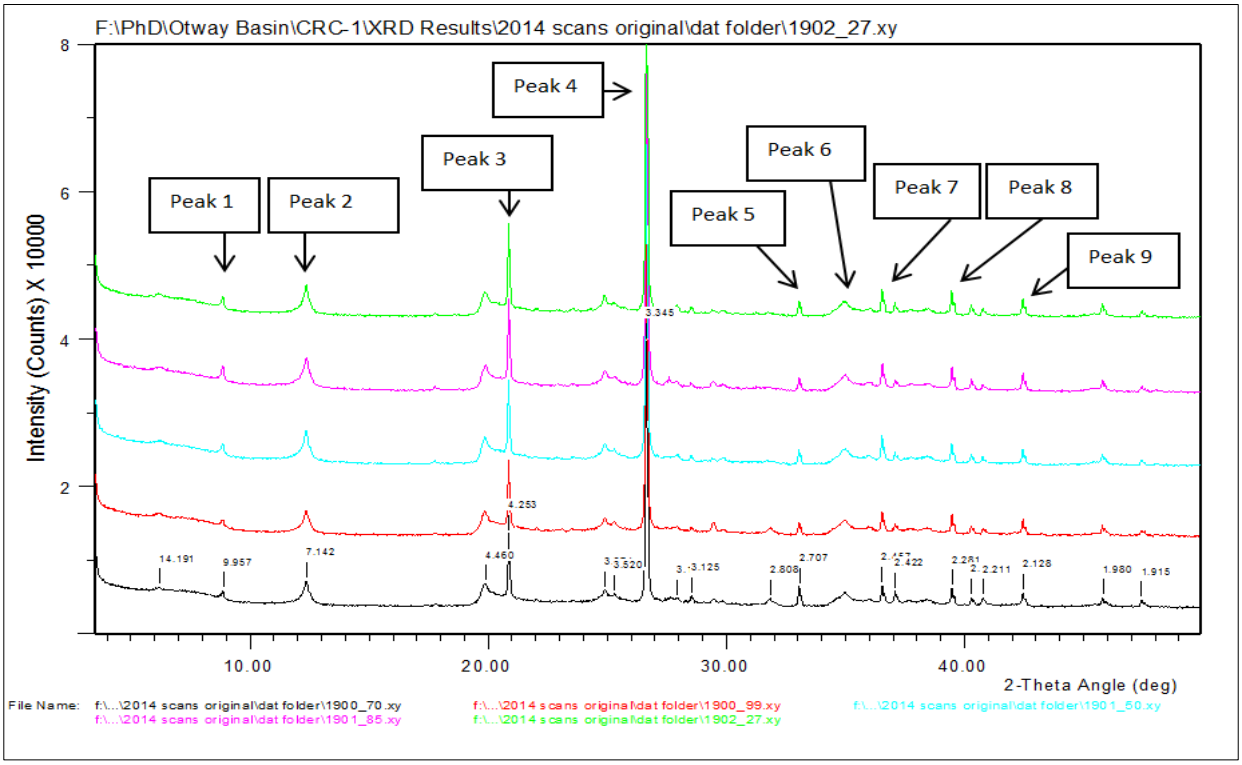

Figure D- 57: Belfast Mudstone, CRC-1 warehoused (2014) conventional core sample XRD bulk diffractograms. Sample 1900.70m (black), 1900.99m (red), 1901.50m (turquoise) and 1901.85m (pink) and 1902.25m (green). Samples analysed in 2014.

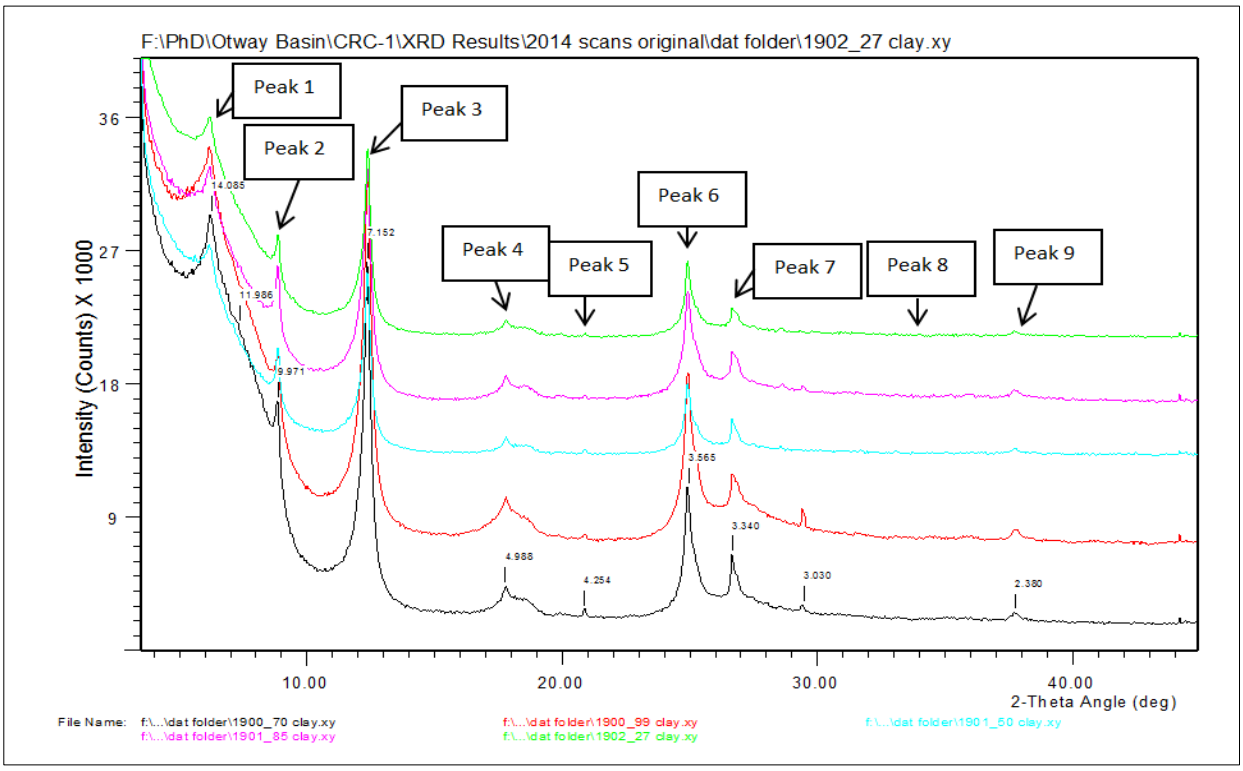

Figure D- 58: Belfast Mudstone, CRC-1 warehoused (2014) conventional core sample XRD clay diffractograms. Sample 1900.70m (black), 1900.99m (red), 1901.50m (turquoise) and 1901.85m (pink) and 1902.25m (green). Samples analysed in 2014.

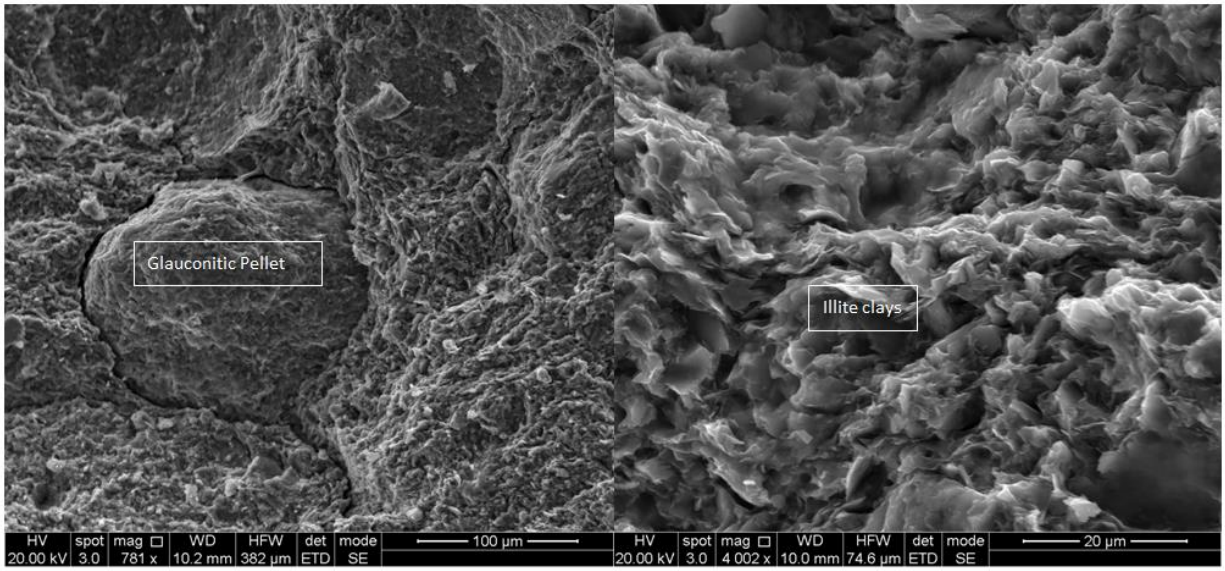

Figure D- 59: CRC-1, 2014, Images of a warehoused Belfast Mudstone conventional core sample 1900.70 m. All images are perpendicular to bedding (Left hand image). This image shows a clay matrix dotted with a number of potassium feldspar (Kfs) grains. (Right hand image) CRC-1 Belfast Mudstone BSE image of the conventional core sample 1900.70 m under high magnification showing potassium feldspar (Kfs) and iron framboids (Fe Framboids).

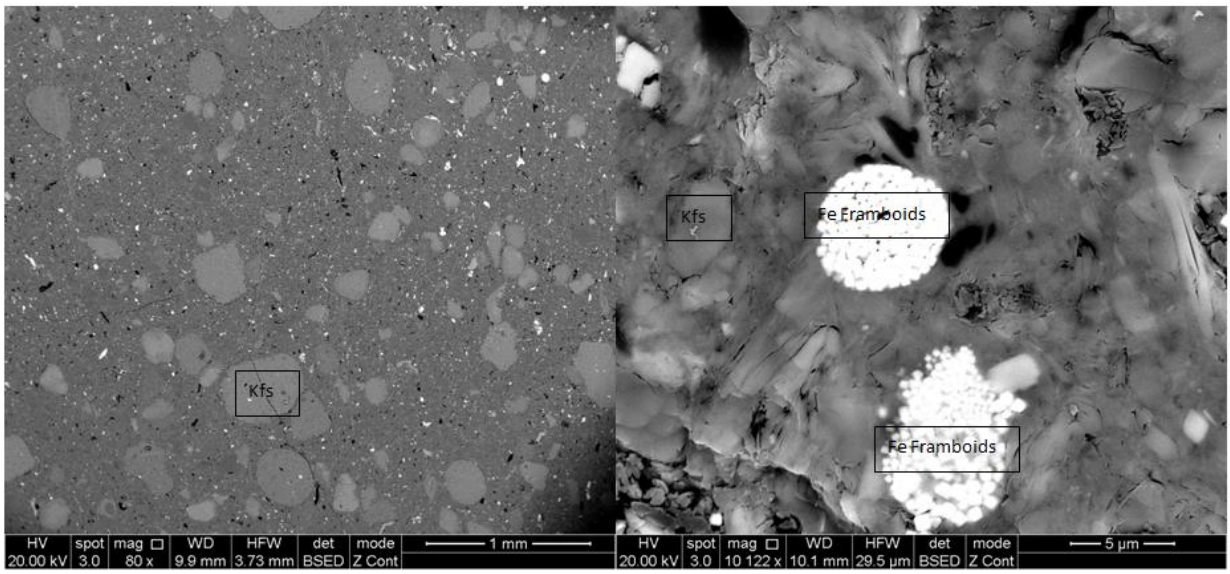

Figure D- 60: CRC-1, 2014, Images of a warehoused Belfast Mudstone conventional core sample 1900.70 m. All images are perpendicular to bedding. (Left hand image) This image shows a clay matrix dotted with a number of potassium feldspar (Kfs) grains. (Right hand image) CRC-1 Belfast Mudstone BSE image of the conventional core sample 1900.70 m under high magnification showing potassium feldspar (Kfs) and iron framboids (Fe Framboids).

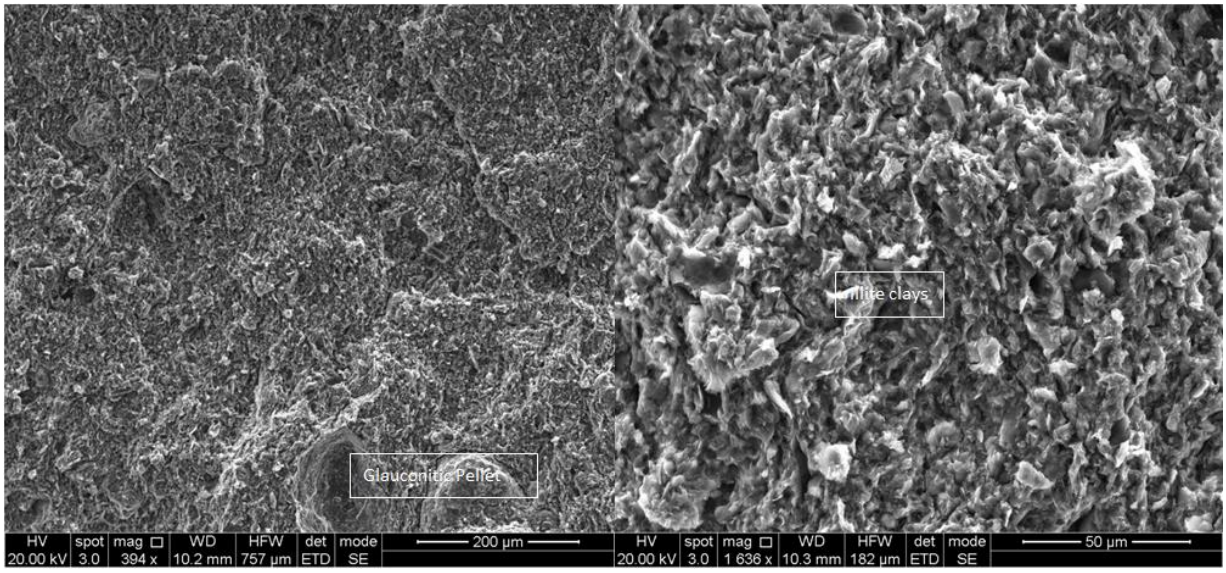

Figure D- 61: CRC-1, 2014, Images of a warehoused Belfast Mudstone conventional core sample 1900.99 m. All images are perpendicular to bedding (Left hand image). This image shows a clay matrix dotted with a number of potassium feldspar (Kfs) grains. (Right hand image) CRC-1 Belfast Mudstone BSE image of the conventional core sample 1900.99 m under high magnification showing quartz (Qtz) and iron framboids (Fe Framboids).

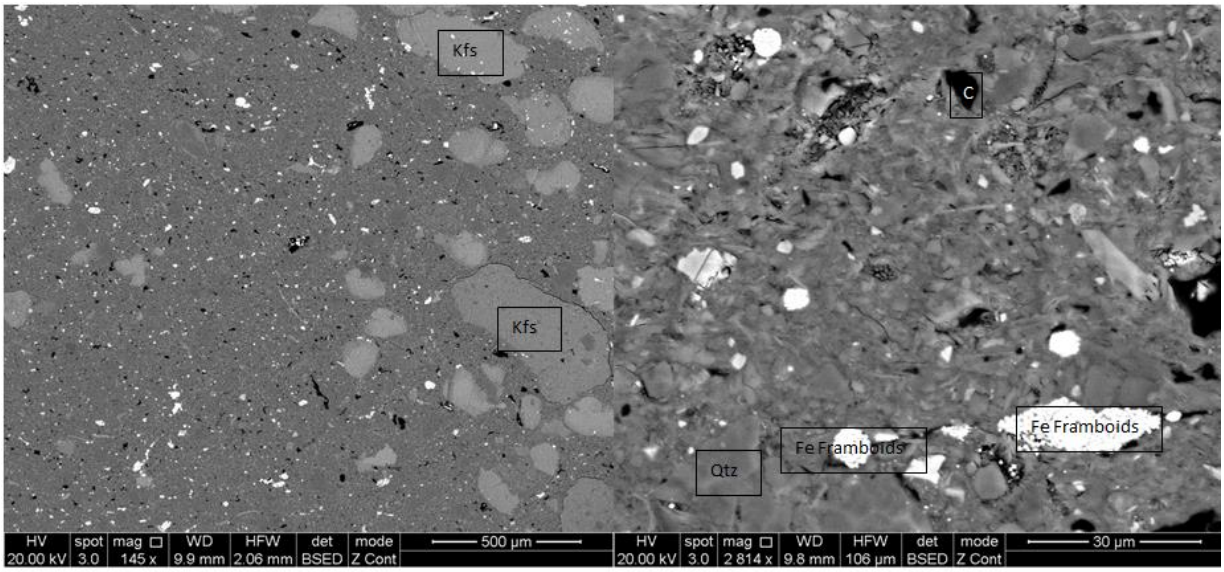

Figure D- 62: CRC-1, 2014, Images of a warehoused Belfast Mudstone conventional core sample 1900.99 m. All images are perpendicular to bedding. (Left hand image) This image shows a clay matrix dotted with a number of potassium feldspar (Kfs) grains. (Right hand image) CRC-1 Belfast Mudstone BSE image of the conventional core sample 1900.99 m under high magnification showing quartz (Qtz) and iron framboids (Fe Framboids).

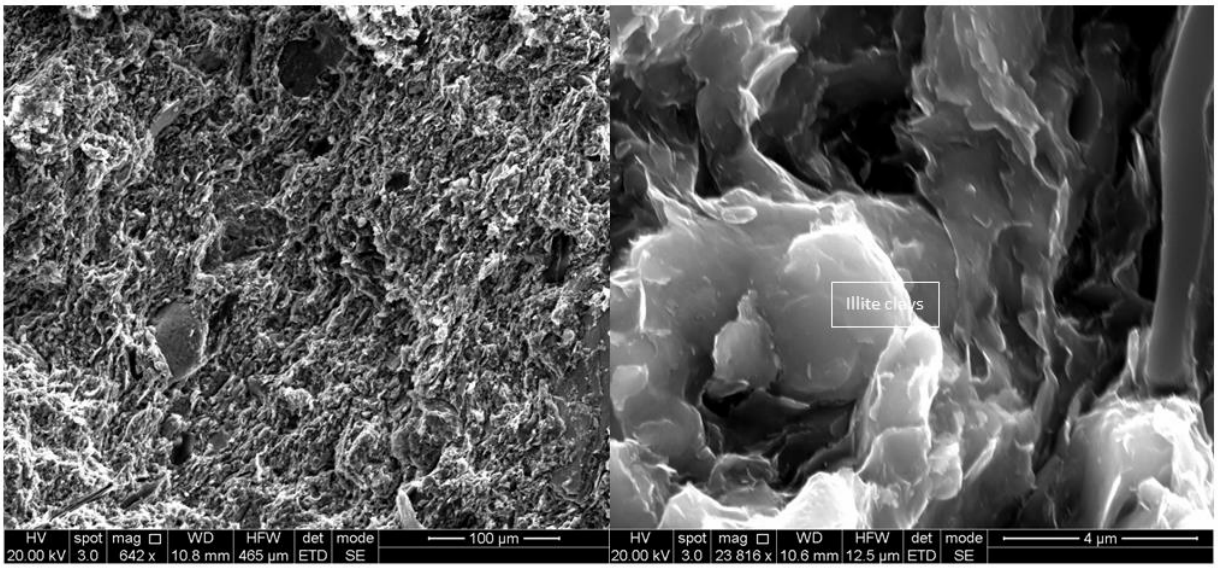

Figure D- 63: CRC-1, 2014, Images of a warehoused Belfast Mudstone conventional core sample 1901.50 m. All images are perpendicular to bedding. (Left hand image) This image shows a clay matrix dotted with potassium feldspar (Kfs) grains and carbon. (Right hand image) CRC-1 Belfast Mudstone BSE image of the conventional core sample 1901.50 m under high magnification showing quartz (Qtz), potassium feldspar (Kfs), iron framboids (Fe framboids) and rutile (TiO2).

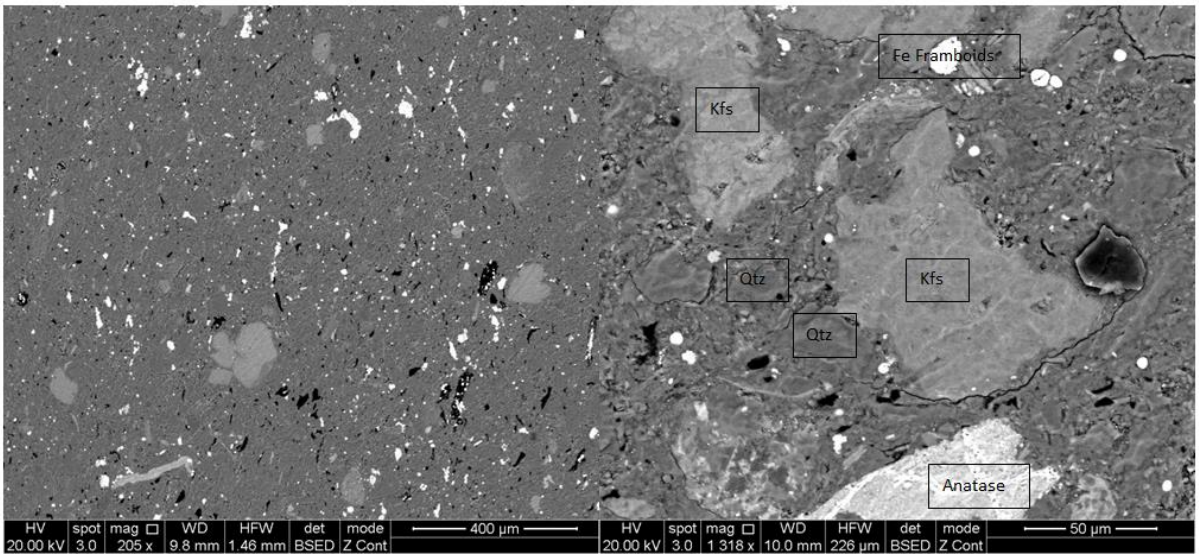

Figure D- 64: CRC-1, 2014, Images of a warehoused Belfast Mudstone conventional core sample 1901.50 m. All images are perpendicular to bedding. (Left hand image) This image shows a clay matrix dotted with potassium feldspar (Kfs) grains and carbon. (Right hand image) CRC-1 Belfast Mudstone BSE image of the conventional core sample 1901.50 m under high magnification showing quartz (Qtz), potassium feldspar (Kfs), iron framboids (Fe framboids) and anatase (TiO2).

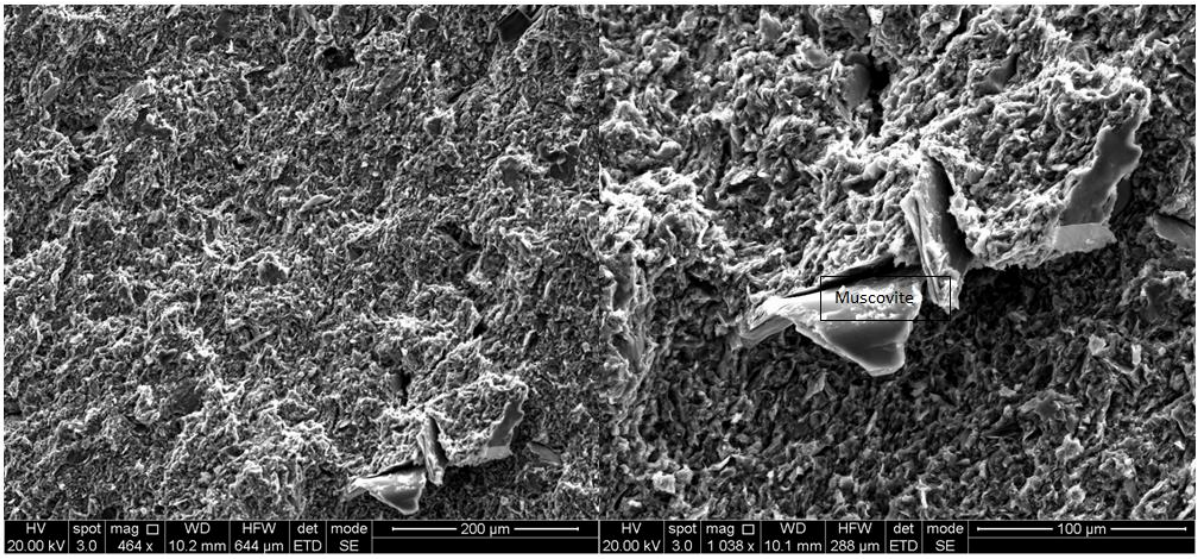

Figure D- 65: CRC-1, 2014, Images of a warehoused Belfast Mudstone conventional core sample 1901.85 m. All images are perpendicular to bedding. (Left Hand Image) This image shows the clay matrix dotted with a carbon, iron framboids, potassium feldspar and quartz. (Right Hand Image) CRC-1 Belfast Mudstone SEM image of the conventional core sample 1901.85 m under high magnification showing potassium feldspar (Kfs) and iron framboids (Fe framboids).

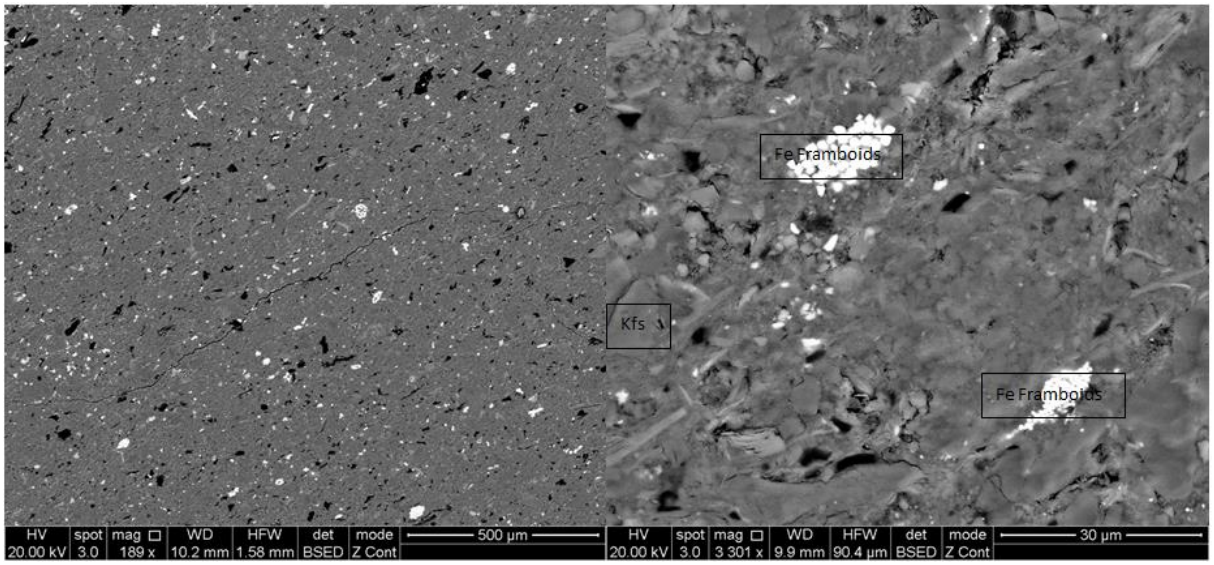

Figure D- 66: CRC-1, 2014, Images of a warehoused Belfast Mudstone conventional core sample 1901.85 m. All images are perpendicular to bedding. (Left hand image) This image shows the clay matrix dotted with a carbon, iron framboids, potassium feldspar and quartz. (Right hand image) CRC-1 Belfast Mudstone SEM image of the conventional core sample 1901.85 m under high magnification showing potassium feldspar (Kfs) and iron framboids (Fe framboids).

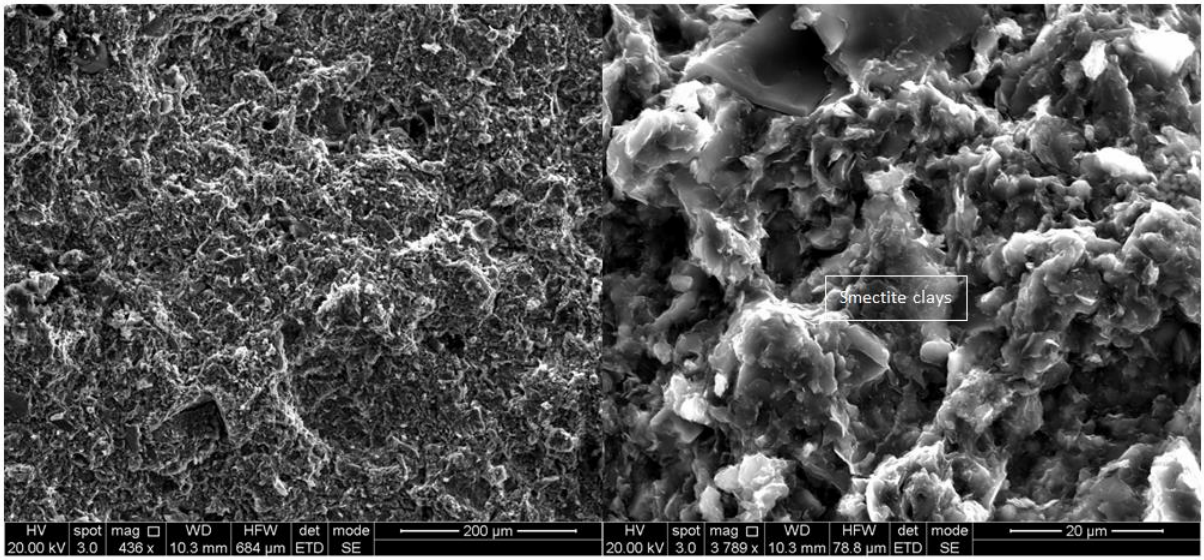

Figure D- 67: CRC-1, 2014, Images of a warehoused Belfast Mudstone conventional core sample 1902.27 m. All images are perpendicular to bedding. (Left hand image) This image shows the clay matrix dotted with a carbon and potassium feldspar. (Right hand image) CRC-1 Belfast Mudstone SEM image of the conventional core sample 1902.27 m under high magnification showing quartz (Qtz), potassium feldspar (Kfs) and iron framboids (Fe framboids).

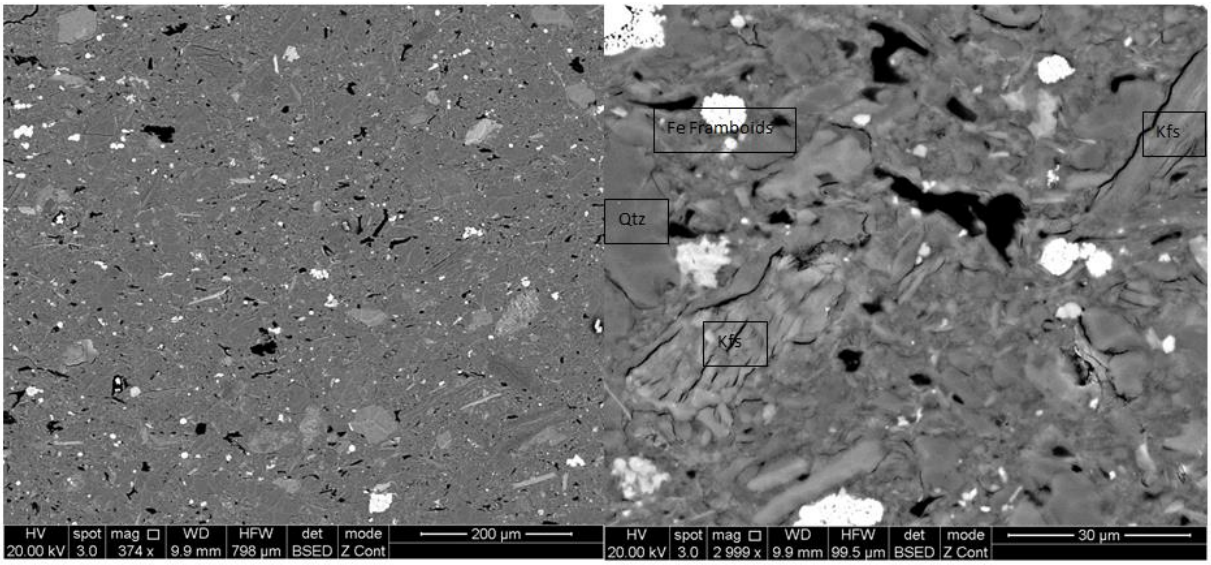

Figure D- 68: CRC-1, 2014, Images of a warehoused Belfast Mudstone conventional core sample 1902.27 m. All images are perpendicular to bedding. (Left hand image) This image shows the clay matrix dotted with a carbon and potassium feldspar. (Right hand image) CRC-1 Belfast Mudstone SEM image of the conventional core sample 1902.27 m under high magnification showing quartz (Qtz), potassium feldspar (Kfs) and iron framboids (Fe framboids).

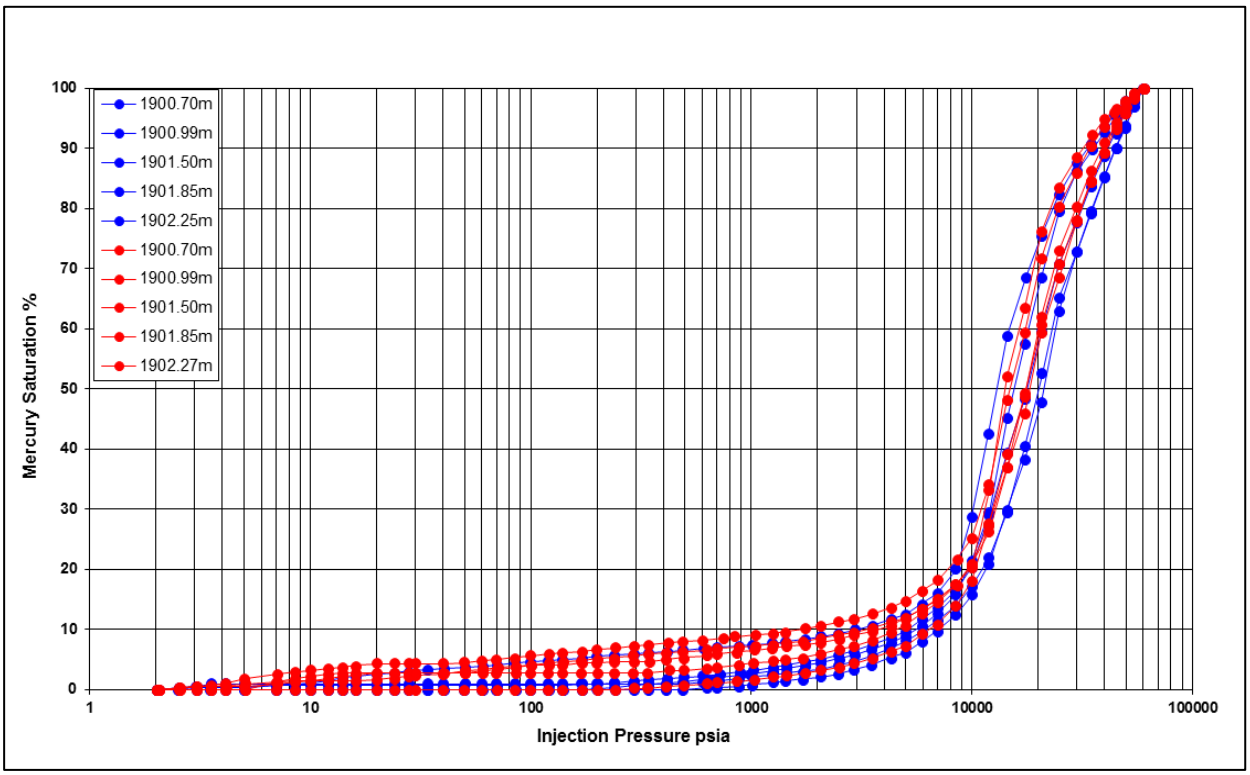

Figure D- 69: Raw MICP curves from the Belfast Mudstone, CRC-1. The blue MICP curves are from the fresh conventional core samples analysed in 2007 by Daniel, (2007). The red MICP curves are from the warehoused conventional core samples analysed in 2014.

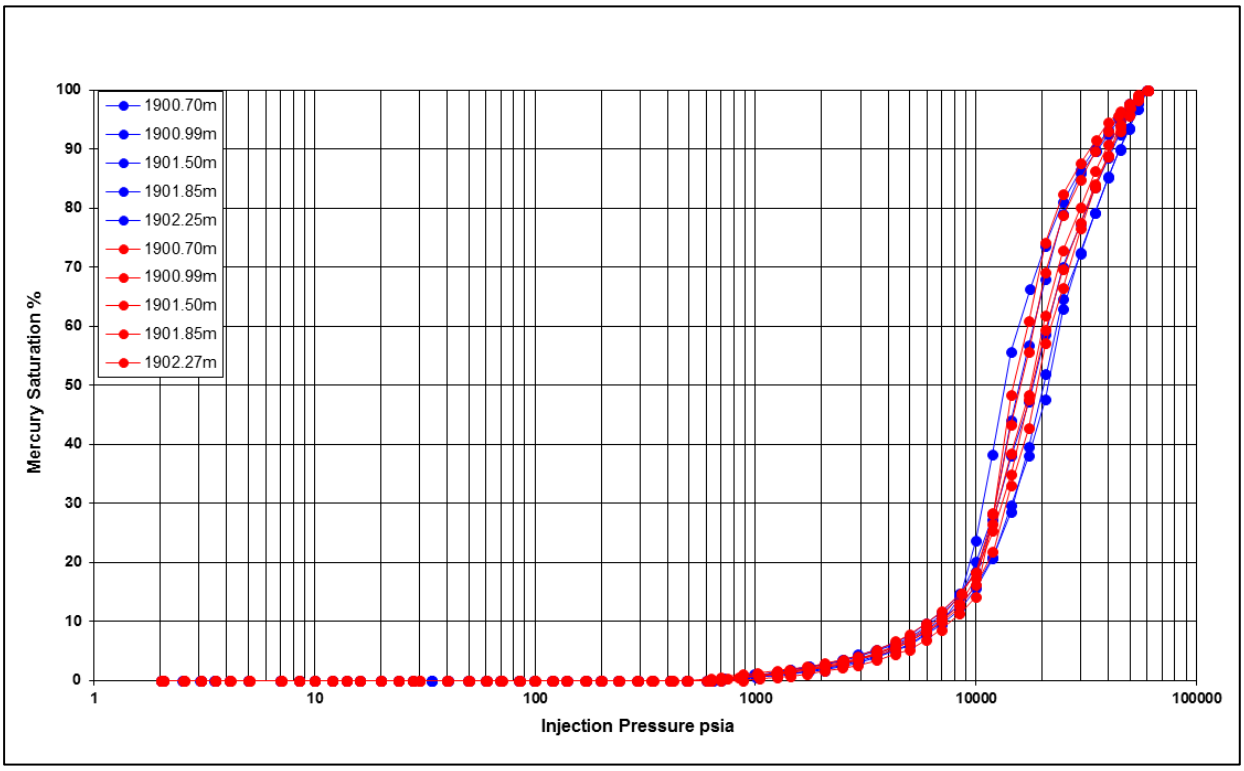

Figure D- 70: Conformance corrected MICP curves from the Belfast Mudstone, CRC-1. The blue MICP curves are from the fresh conventional core samples analysed in 2007 by Daniel, (2007). The red MICP curves are from the warehoused conventional core samples analysed in 2014

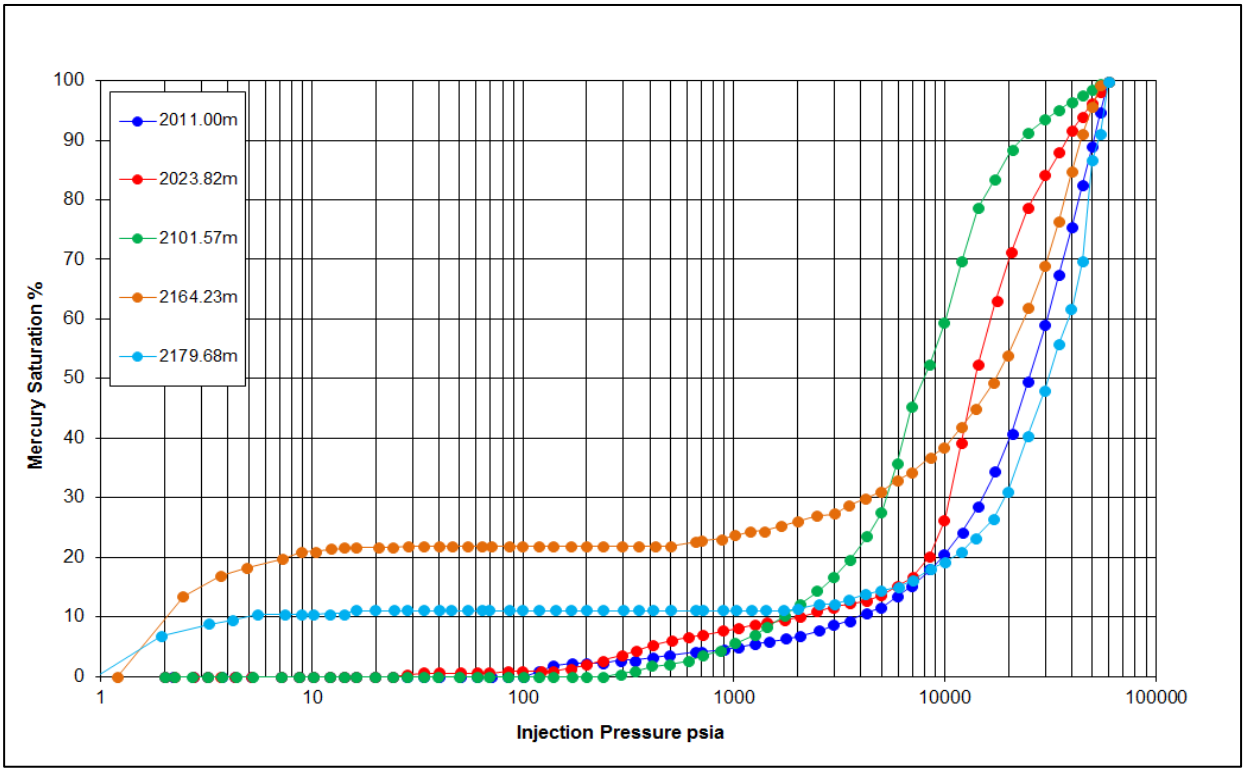

Figure D- 71: Raw MICP curves from fresh conventional core samples of the Barrow Group and Dupuy Formation, Gorgon CO2 Data Well-1 & Data Well-1ST1. Samples analysed in 2006 by Daniel and Kaldi, (2006).

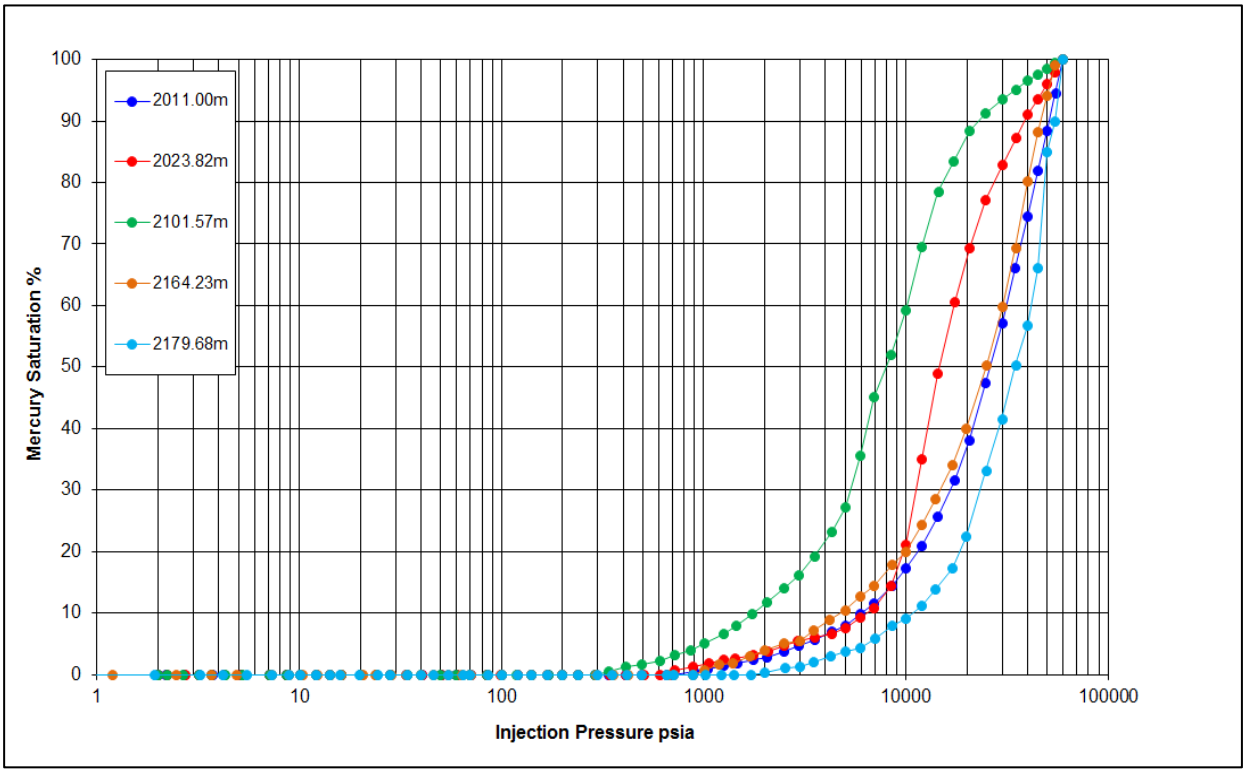

Figure D- 72: Conformance corrected MICP curves from fresh conventional core samples of the Barrow Group and Dupuy Formation, Gorgon CO2 Data Well-1 & Data Well-1ST1. Samples analysed in 2006 by Daniel and Kaldi, (2006).

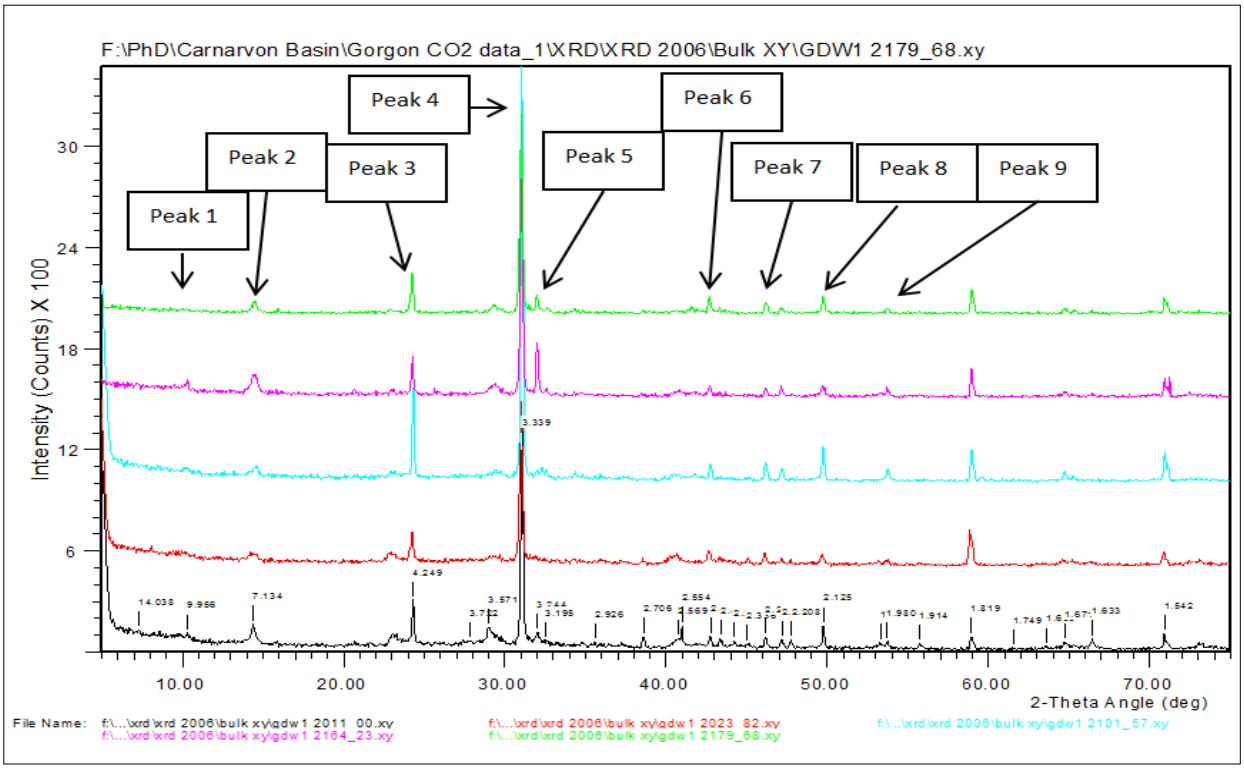

Figure D- 73: Gorgon CO2 Data Well-1 & Data Well-1ST1 fresh (2006) conventional core sample XRD bulk diffractograms. Sample 2011m (black), 2023.82m (red), 2101.57m (turquoise) and 2164.23m (pink) and 2179.68m (green) (Original analyses from Daniel and Kaldi, 2006).

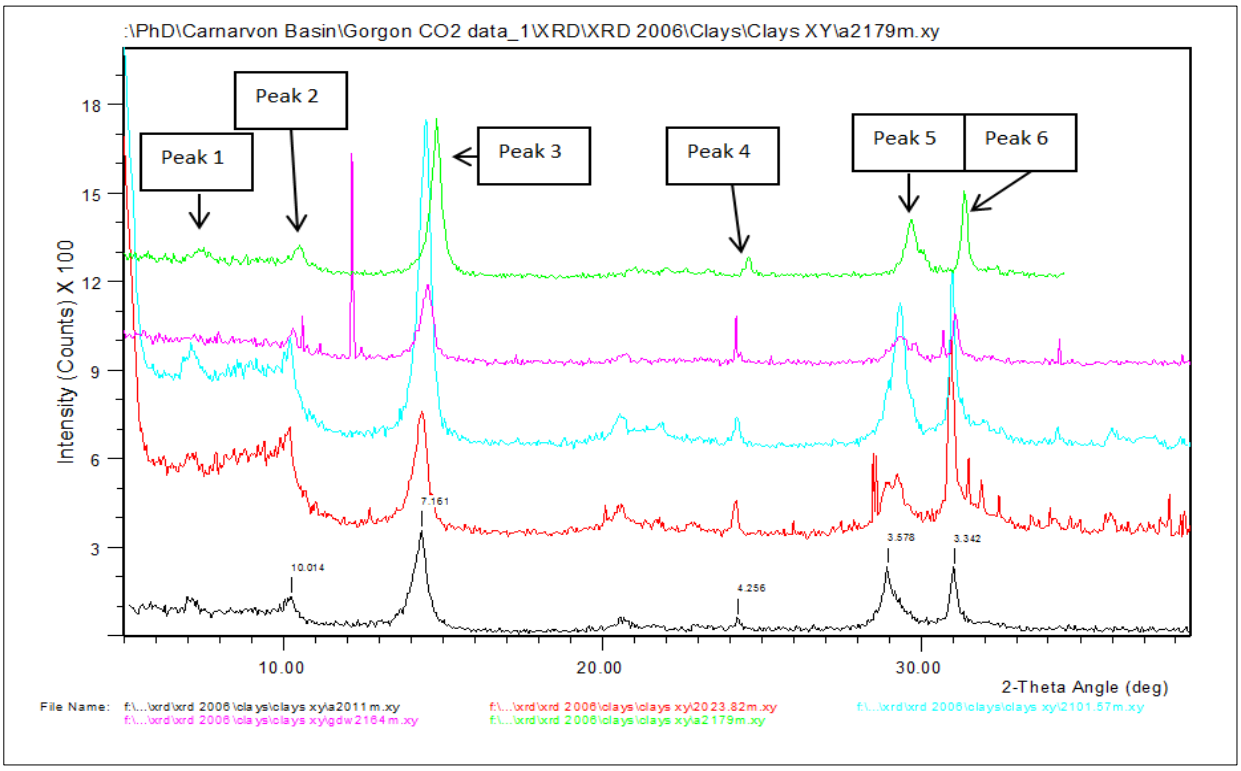

Figure D- 74: Gorgon CO2 Data Well-1 & Data Well-1ST1 fresh (2006) conventional core sample XRD clay diffractograms. Sample 2011m (black), 2023.82m (red), 2101.57m (turquoise) and 2164.23m (pink) and 2179.68m (green) (Original analyses from Daniel and Kaldi, 2006).

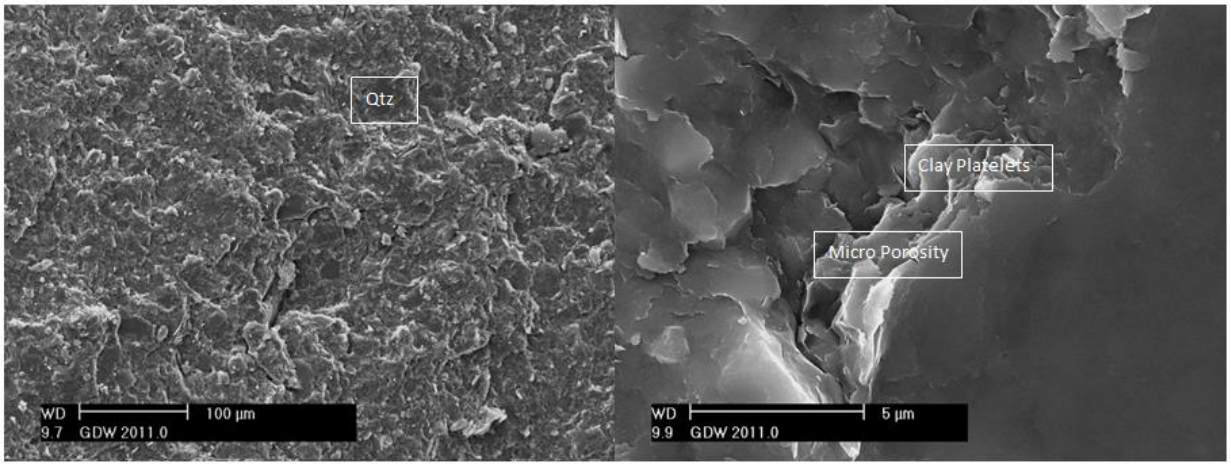

Figure D- 75: Gorgon CO2 Data-1, 2006, Images of a fresh Barrow Group conventional core sample 2011 m. All images are perpendicular to bedding. (Left hand image) This image shows the clay matrix and quartz grain. (Right hand image) Gorgon CO2 Data-1 Barrow Group SEM image of the conventional core sample 2011 m under high magnification showing clay platelets and micro porosity (Image and description modified from Daniel and Kaldi, 2006).

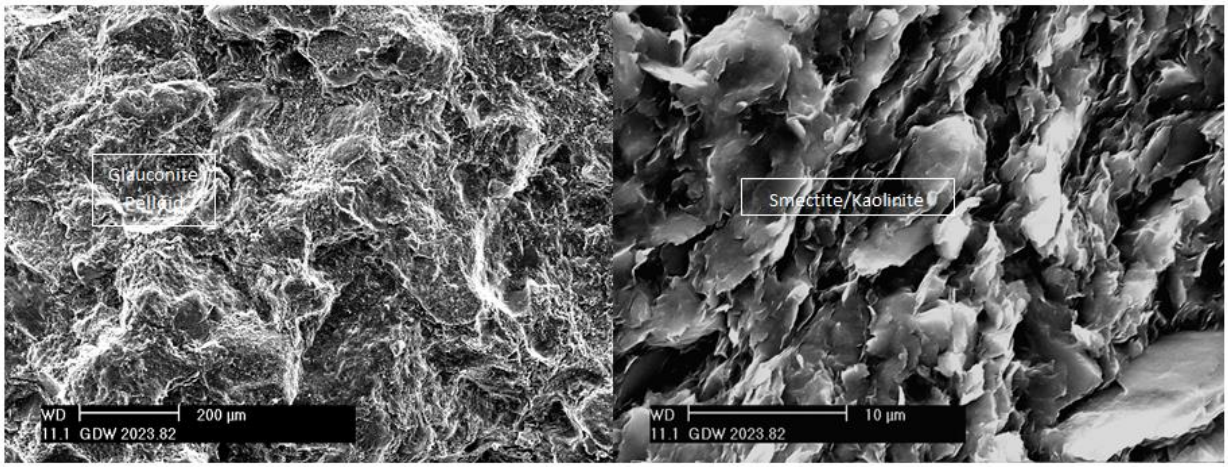

Figure D- 76: Gorgon CO2 Data-1, 2006, Images of a fresh Barrow Group conventional core sample 2023.82 m. All images are perpendicular to bedding. (Left hand image) This image shows a clay matrix and glauconite pellet. (Right hand image) Gorgon CO2 Data-1 Barrow Group SEM image of the conventional core sample 2023.82 m under high magnification showing clay smectite/kaolinite platelets and micro porosity (Image and description modified from Daniel and Kaldi, 2006).

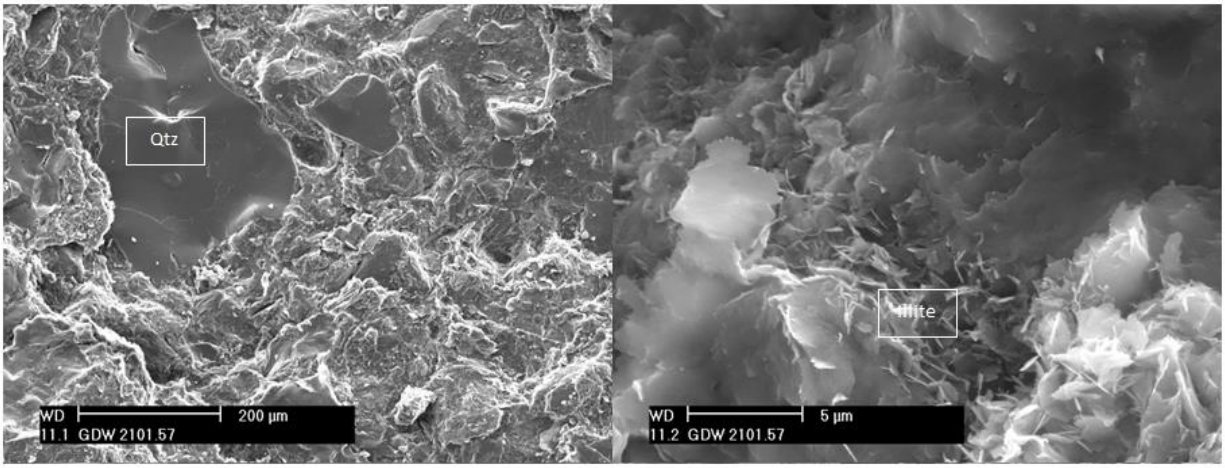

Figure D- 77: Gorgon CO2 Data-1, 2006, Images of a fresh Dupuy Formation conventional core sample 2101.57 m. All images are perpendicular to bedding (Left hand image). This image shows a quartz grain and clay matrix. (Right hand image) Gorgon CO2 Data-1 Dupuy Formation SEM image of the conventional core sample 2101.57 m under high magnification showing illite clays (Image and description modified from Daniel and Kaldi, 2006).

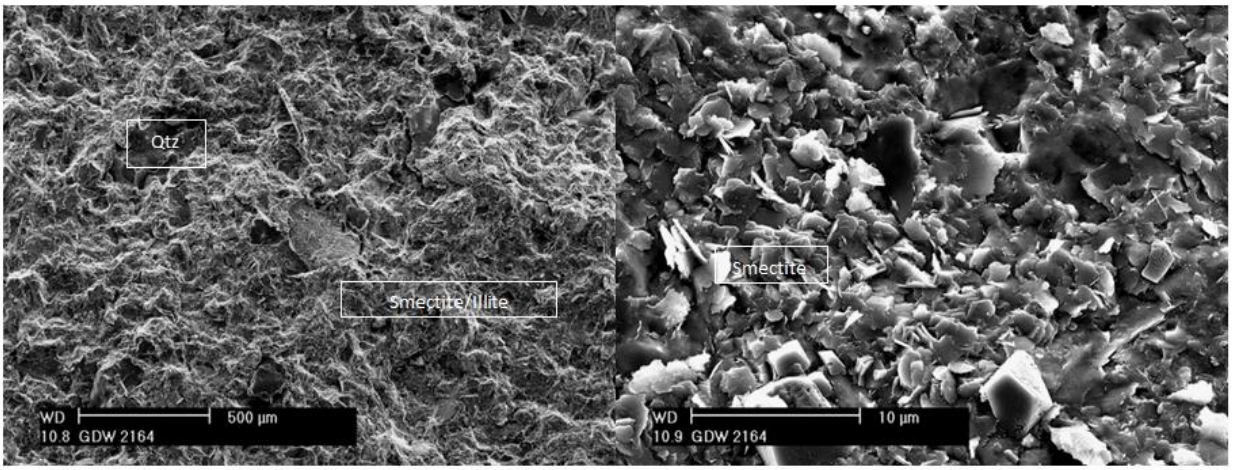

Figure D- 78: Gorgon CO2 Data-1, 2006, Images of a fresh Dupuy Formation conventional core sample 2164.23 m. All images are perpendicular to bedding. (Left hand image) This image shows a quartz grain and smectite/illite clay matrix. (Right hand image) Gorgon CO2 Data-1 Dupuy Formation SEM image of the conventional core sample 2164.23 m under high magnification showing smectite clays (Image and description modified from Daniel and Kaldi, 2006).

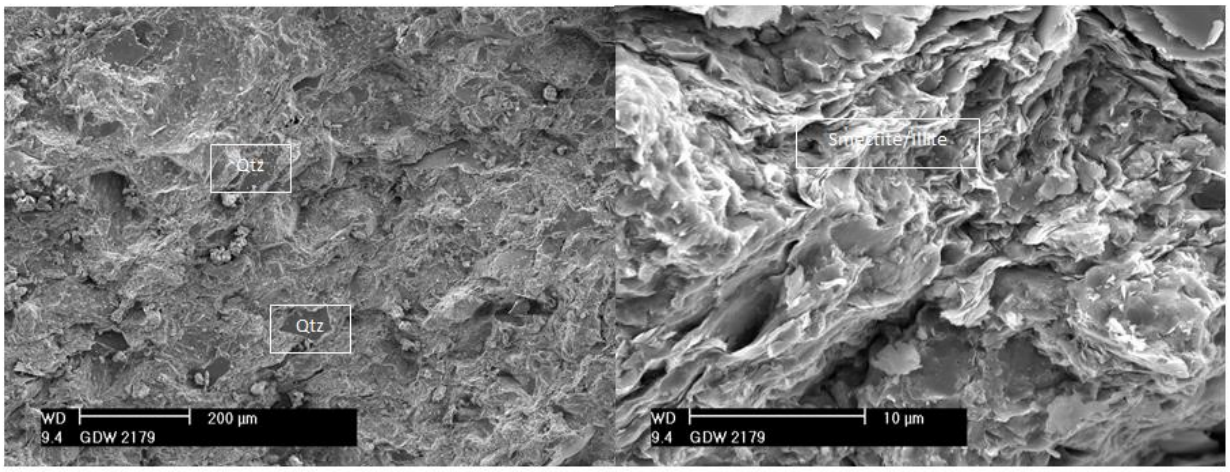

Figure D- 79: Gorgon CO2 Data-1, 2006, Images of a fresh Dupuy Formation conventional core sample 2179.68 m. All images are perpendicular to bedding. (Left hand image) This image shows quartz grains and smectite/illite clay matrix. (Right hand image) Gorgon CO2 Data-1 Dupuy Formation SEM image of the conventional core sample 2179.68 m under high magnification showing smectite/illite clays (Image and description modified from Daniel and Kaldi, 2006).

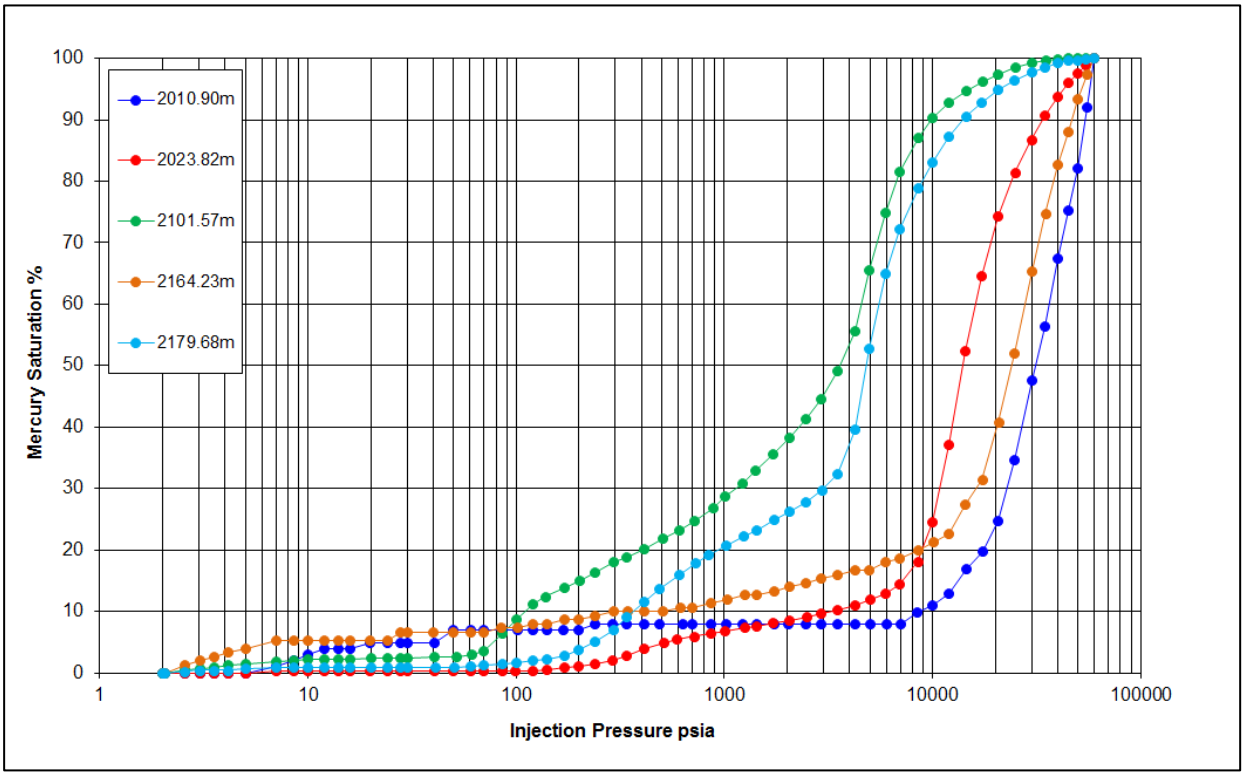

Figure D- 80: Raw MICP curves from warehoused conventional core samples of the Barrow Group and Dupuy Formation, Gorgon CO2 Data Well-1 & Data Well-1ST1. Samples analysed in 2015.

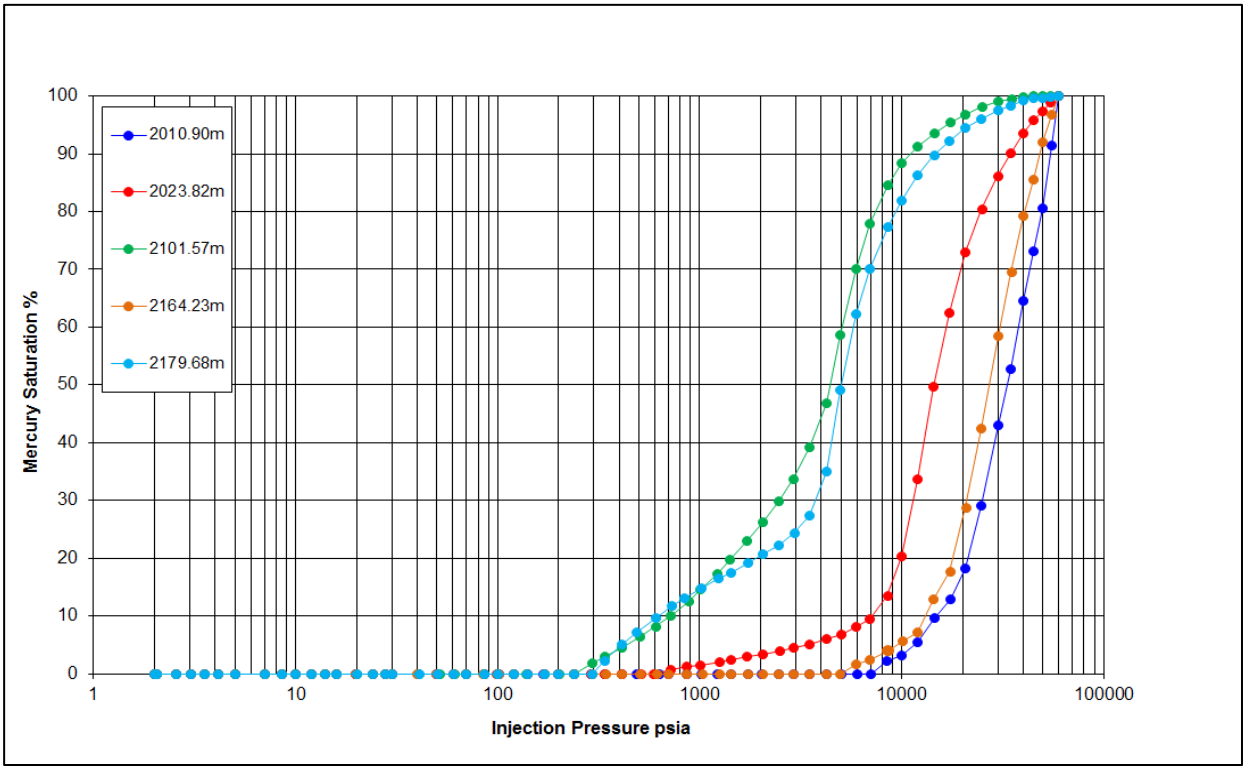

Figure D- 81: Conformance corrected MICP curves from warehoused conventional core samples of the Barrow Group and Dupuy Formation, Gorgon CO2 Data Well-1 & Data Well-1ST1. Samples analysed in 2015.

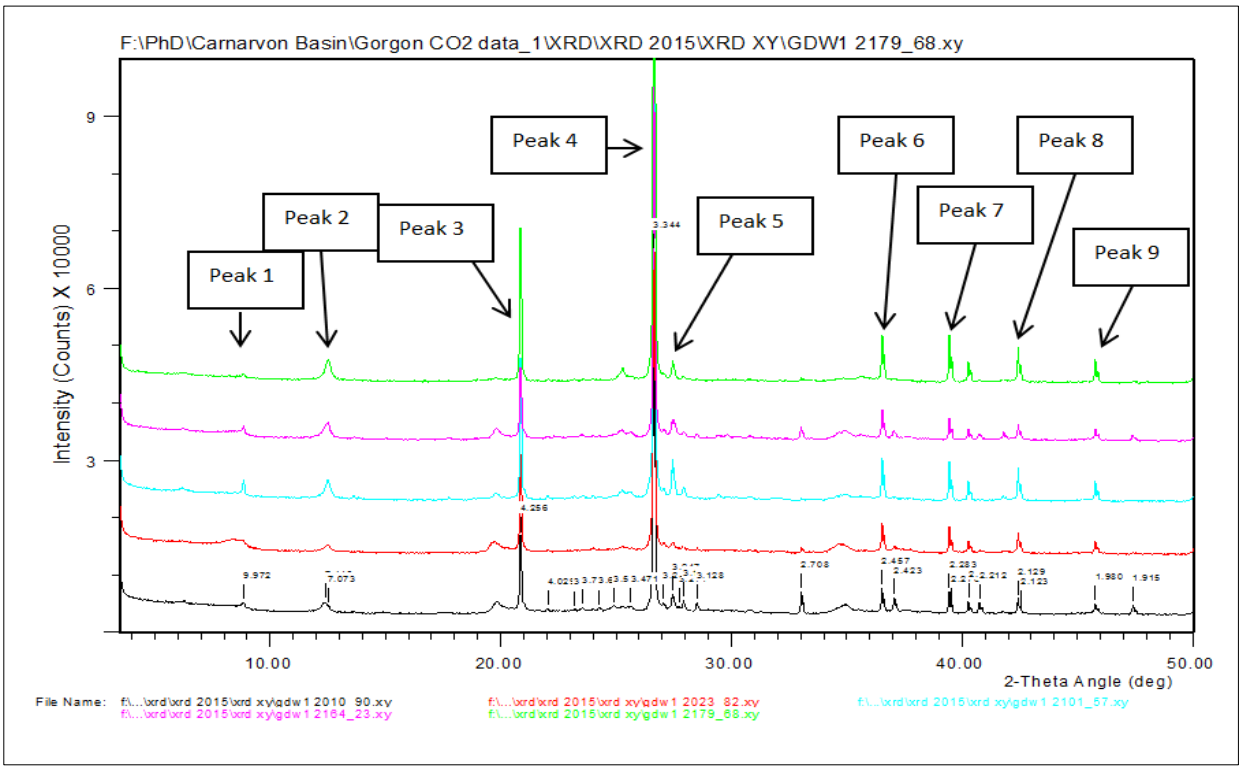

Figure D- 82: Gorgon CO2 Data Well-1 & Data Well-1ST1 warehoused (2015) conventional core sample XRD bulk diffractograms. Sample 2010.90m (black), 2023.82m (red), 2101.57m (turquoise) and 2164.23m (pink) and 2179.68m (green).

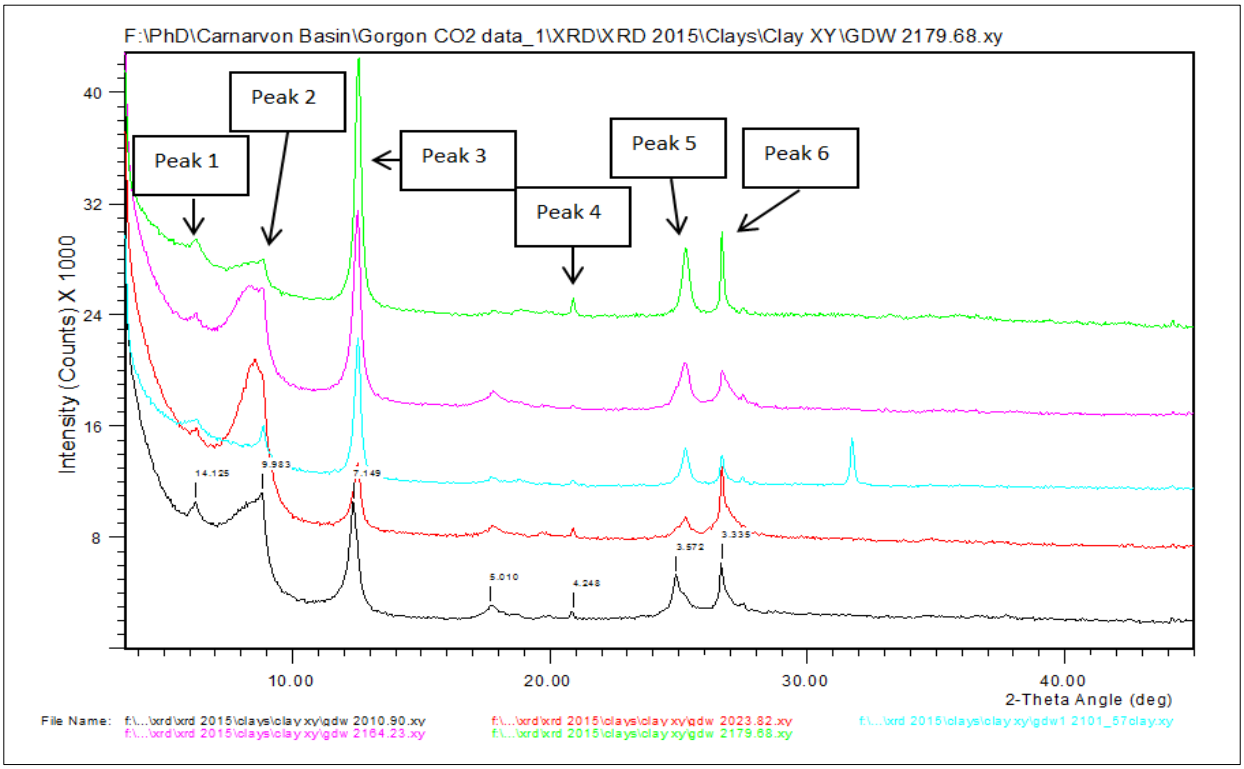

Figure D- 83: Gorgon CO2 Data Well-1 & Data Well-1ST1 warehoused (2015) conventional core sample XRD clay diffractograms. Sample 2011m (black), 2023.82m (red), 2101.57m (turquoise) and 2164.23m (pink) and 2179.68m (green).

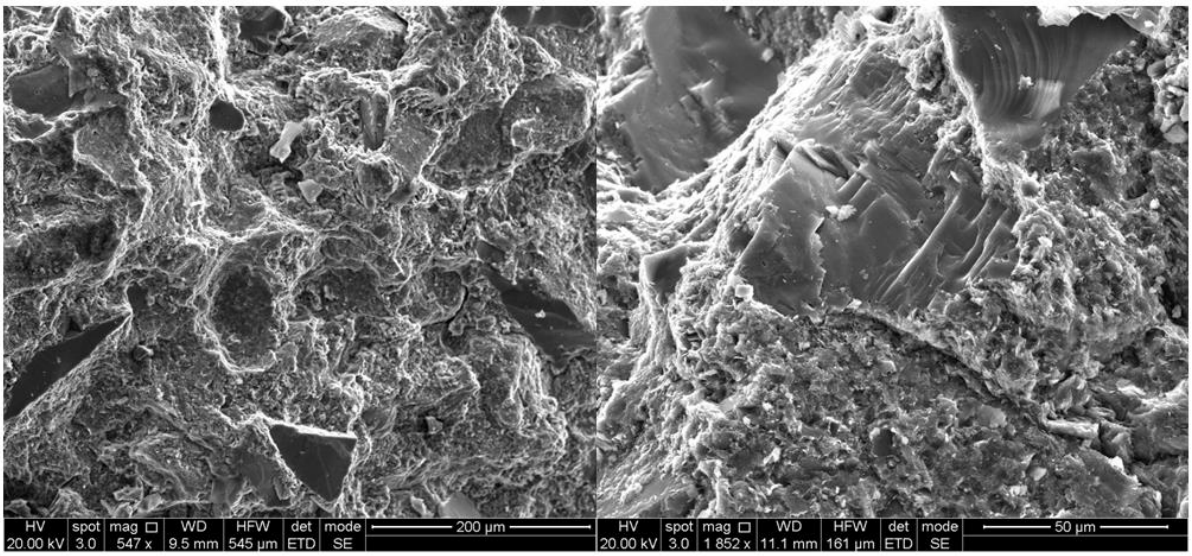

Figure D- 84: Gorgon CO2 Data-1, 2015, Images of a warehoused Barrow Group conventional core sample 2010.90 m. All images are perpendicular to bedding. (Left hand image) This image shows the clay matrix interspersed with silt sized grains and iron framboids. A number of discontinuous fractures can also be observed traversing the sample. (Right hand image) Gorgon CO2 Data-1 Barrow Group BSE image of the conventional core sample 2010.90m under high magnification the clay matrix interspersed with quartz (Qtz) grains and iron framboids (Fe Framboids). Micro porosity is visible throughout the matrix.

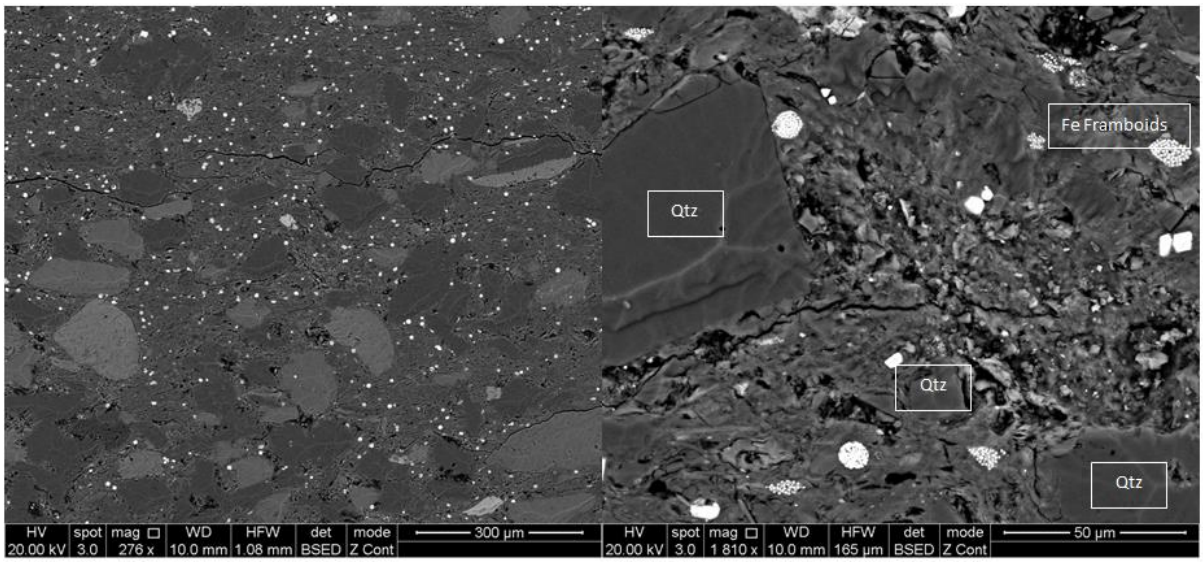

Figure D- 85: Gorgon CO2 Data-1, 2015, Images of a warehoused Barrow Group conventional core sample 2010.90m. All images are perpendicular to bedding. (Left hand image) This image shows the clay matrix interspersed with silt sized grains and iron framboids. A number of discontinuous fractures can also be observed traversing the sample. (Right hand image) Gorgon CO2 Data-1 Barrow Group BSE image of the conventional core sample 2010.90 m under high magnification the clay matrix interspersed with quartz (Qtz) grains and iron framboids (Fe Framboids). Micro porosity is visible throughout the matrix.

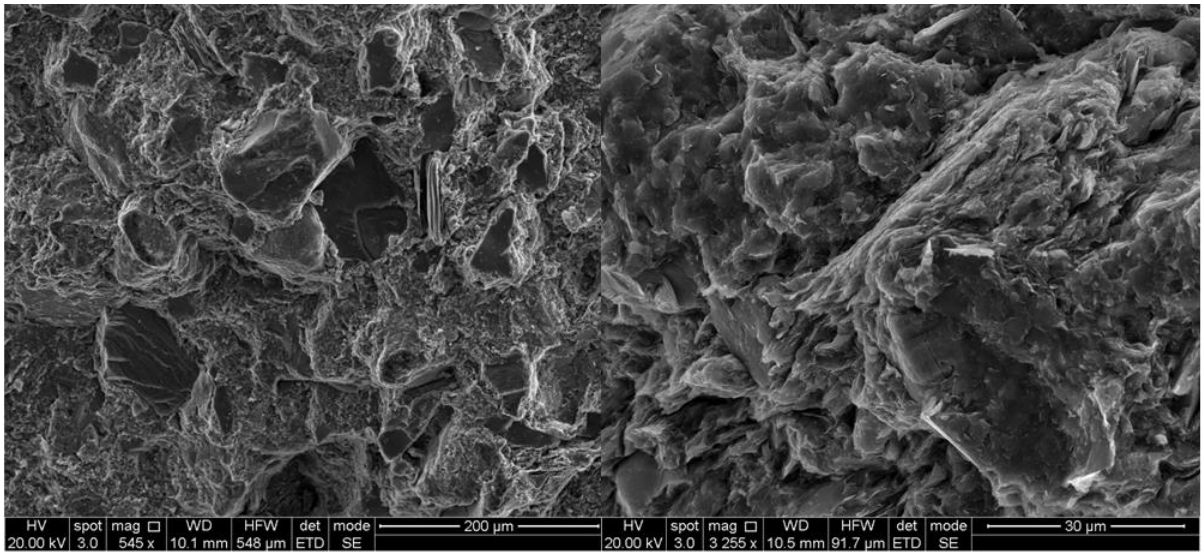

Figure D- 86: Gorgon CO2 Data-1, 2015, Images of a warehoused Barrow Group conventional core sample 2023.82m. All images are perpendicular to bedding. (Left hand image) This image tightly packed grains with authigenic iron framboids within the clay matrix. (Right hand image) Gorgon CO2 Data-1 Barrow Group BSE image of the conventional core sample 2023.82m under high magnification showing quartz (Qtz) grains and glauconite (Gl) grains dominating the sample. Clay matrix can be observed lining the grains. Authigenic iron framboids are visible within the matrix (Fe Framboids). Micro porosity is constrained to the matrix and glauconite grains.

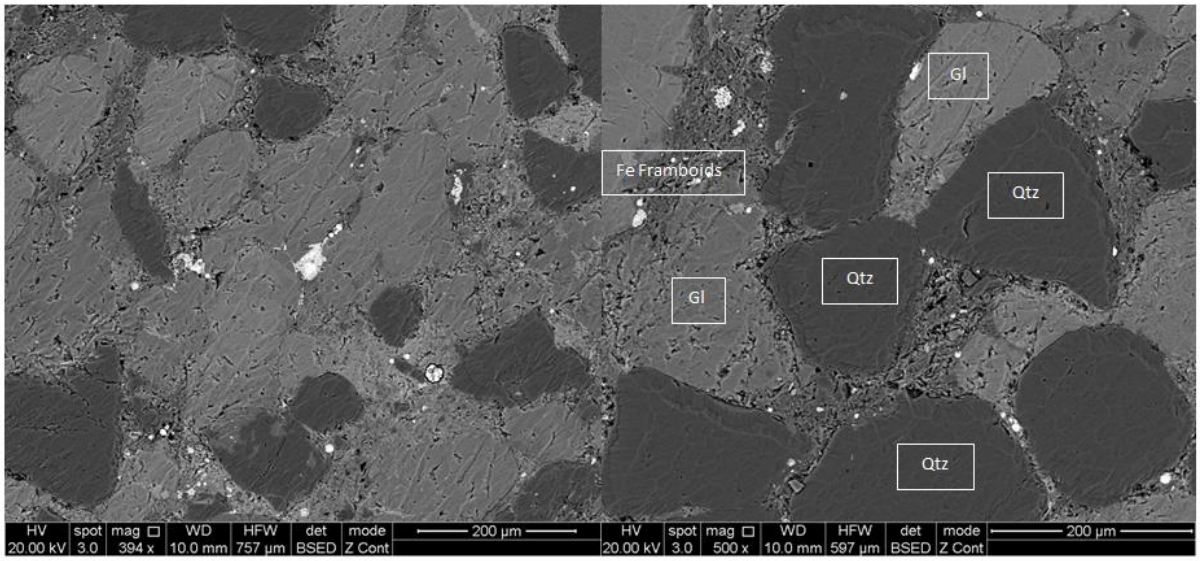

Figure D- 87: Gorgon CO2 Data-1, 2015, Images of a warehoused Barrow Group conventional core sample 2023.82 m. All images are perpendicular to bedding. (Left hand image) This image shows tightly packed grains with authigenic iron framboids within the clay matrix. (Right hand image) Gorgon CO2 Data-1 Barrow Group BSE image of the conventional core sample 2023.82 m under high magnification showing quartz (Qtz) grains and glauconite (Gl) grains dominating the sample. Clay matrix can be observed lining the grains. Authigenic iron framboids are visible within the matrix (Fe Framboids). Micro porosity is constrained to the matrix and glauconite grains.

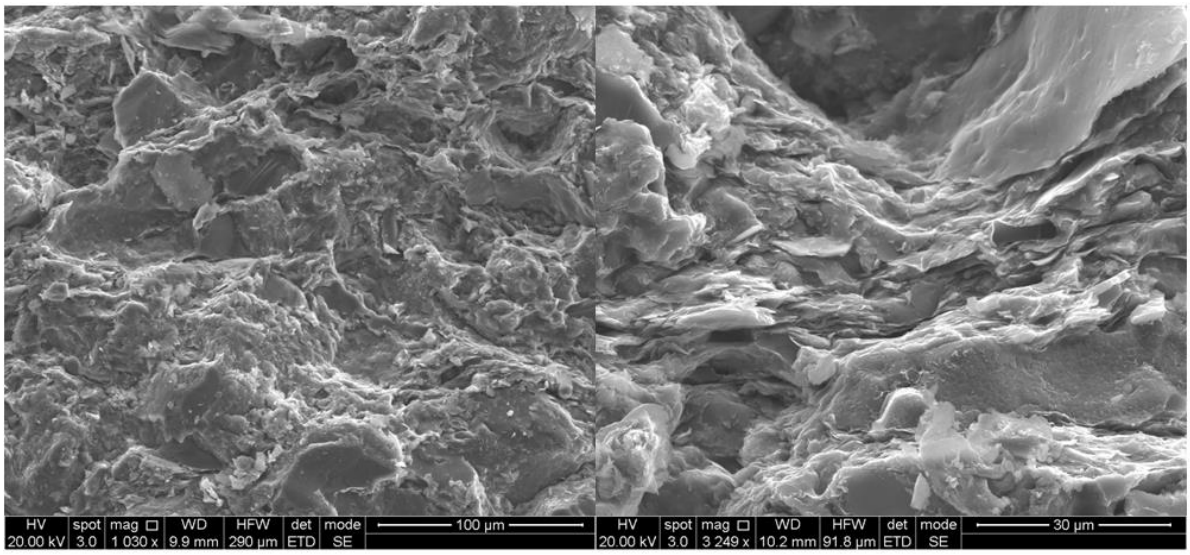

Figure D- 88: Gorgon CO2 Data-1, 2015, Images of a warehoused Dupuy Formation conventional core sample 2101.57 m. All images are perpendicular to bedding. (Left hand image) This image shows tightly packed grains with carbon/porosity dotted throughout the sample. (Right hand image) Gorgon CO2 Data-1 Barrow Group BSE image of the conventional core sample 2101.57 m under high magnification showing quartz (Qtz) grains, potassium feldspar (Kfs) and iron framboids (Fe Framboids). Micro porosity/carbon is observed throughout the sample.

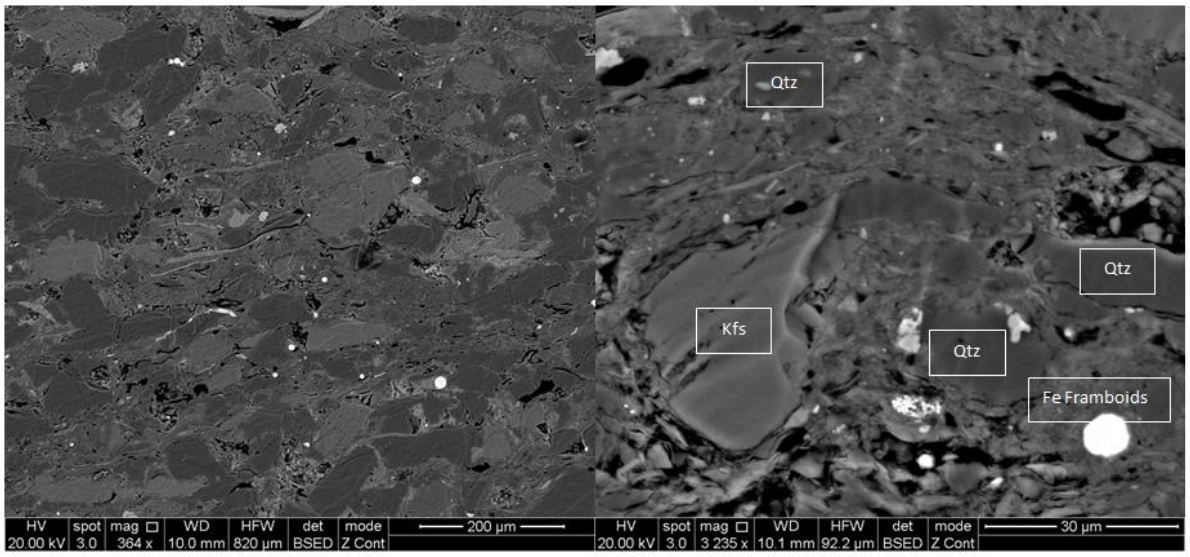

Figure D- 89: Gorgon CO2 Data-1, 2015, Images of a warehoused Dupuy Formation conventional core sample 2101.57 m. All images are perpendicular to bedding. (Left hand image) This image shows tightly packed grains with carbon/porosity dotted throughout the sample. (Right hand image) Gorgon CO2 Data-1 Barrow Group BSE image of the conventional core sample 2101.57 m under high magnification showing quartz (Qtz) grains, potassium feldspar (Kfs) and iron framboids (Fe Framboids). Micro porosity/carbon is observed throughout the sample.

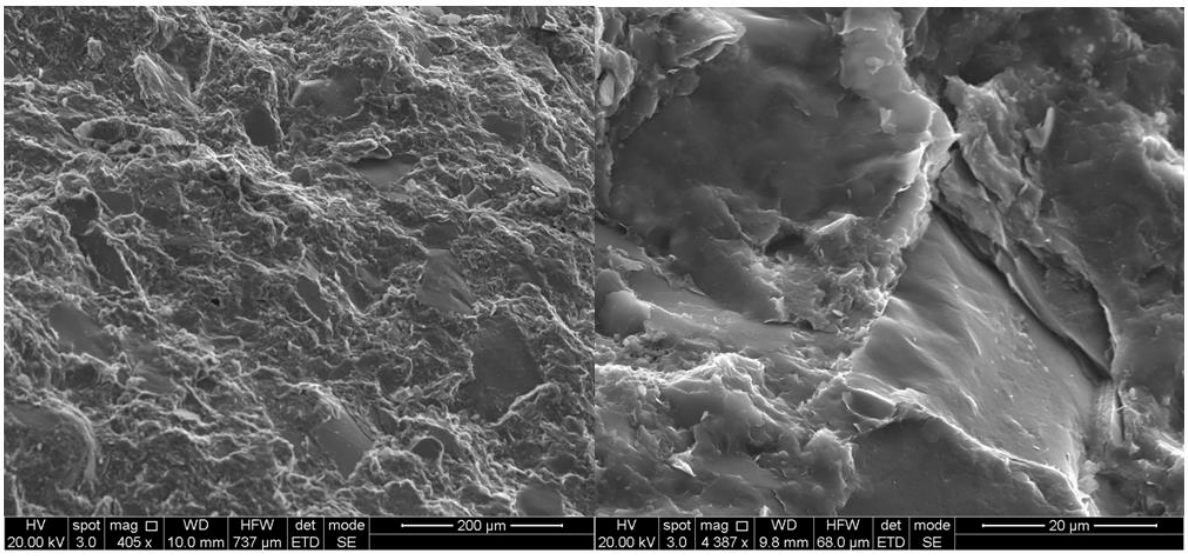

Figure D- 90: Gorgon CO2 Data-1, 2015, Images of a warehoused Dupuy Formation conventional core sample 2164.23 m. All images are perpendicular to bedding. (Left hand image) This image shows significant porosity surrounding some of the quartz grains. (Right hand image) Gorgon CO2 Data-1 Barrow Group BSE image of the conventional core sample 2164.23 m under high magnification showing quartz (Qtz) grains and iron framboids (Fe Framboids). Micro porosity/carbon is observed throughout the sample next to quartz grains and within the matrix.

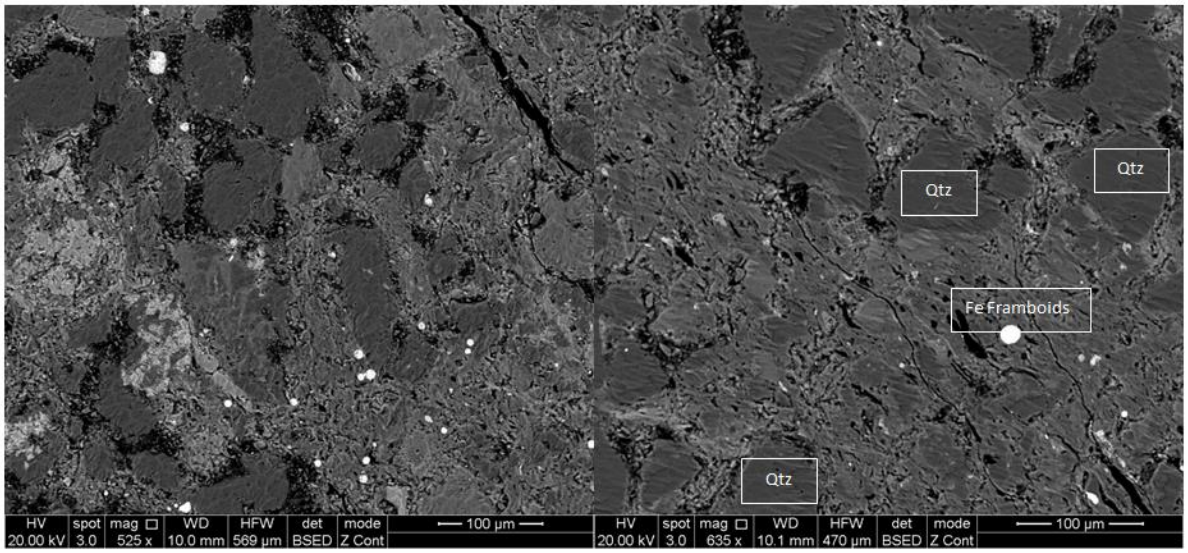

Figure D- 91: Gorgon CO2 Data-1, 2015, Images of a warehoused Dupuy Formation conventional core sample 2164.23 m. All images are perpendicular to bedding. (Left hand image) This image shows significant porosity surrounding some of the quartz grains. (Right hand image) Gorgon CO2 Data-1 Barrow Group BSE image of the conventional core sample 2164.23 m under high magnification showing quartz (Qtz) grains and iron framboids (Fe Framboids). Micro porosity/carbon is observed throughout the sample next to quartz grains and within the matrix.

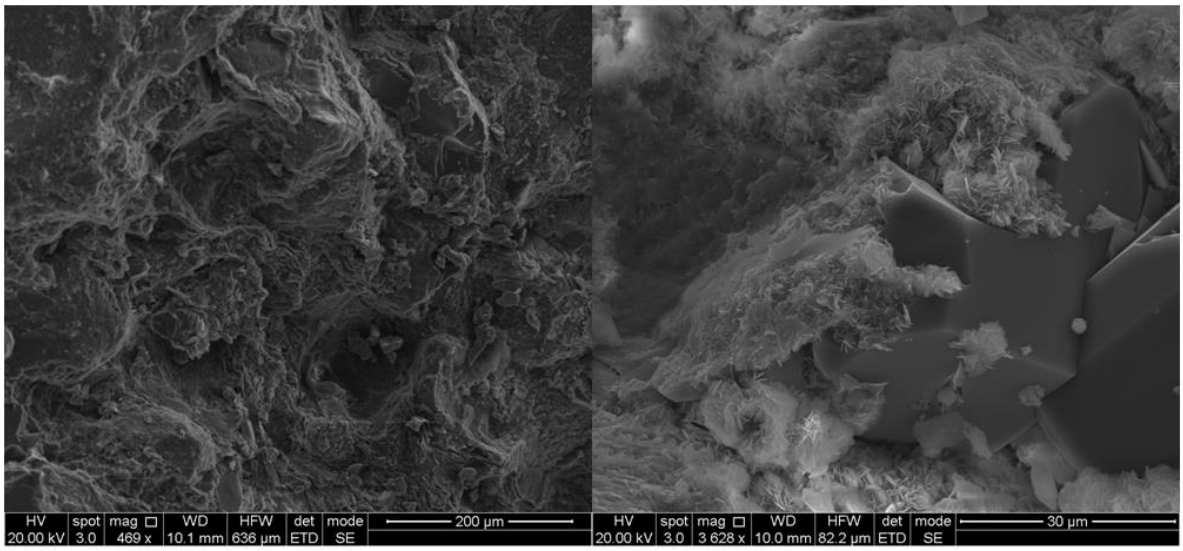

Figure D- 92: Gorgon CO2 Data-1, 2015, Images of a warehoused Dupuy Formation conventional core sample 2179.68 m. All images are perpendicular to bedding. (Left hand image) This image shows quartz grains surrounded by matrix. Dissolution of the matrix resulting in significant porosity surrounding some of the quartz grains can be observed. (Right hand image) Gorgon CO2 Data-1 Barrow Group BSE image of the conventional core sample 2179.68 m under high magnification showing quartz (Qtz) grains, matrix and porosity.

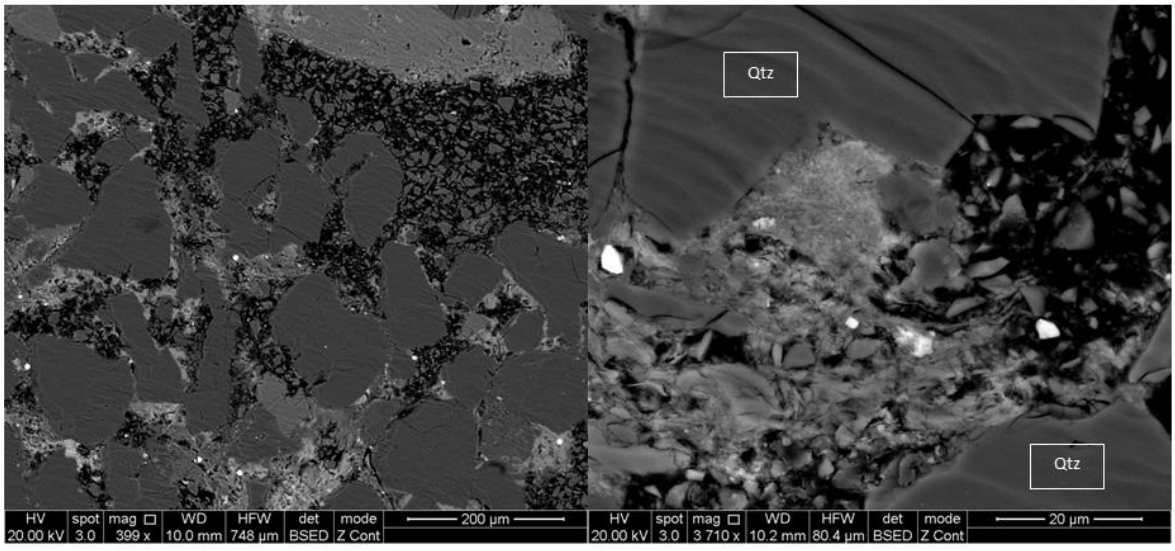

Figure D- 93: Gorgon CO2 Data-1, 2015, Images of a warehoused Dupuy Formation conventional core sample 2179.68 m. All images are perpendicular to bedding. (Left hand image) This image shows quartz grains surrounded by matrix. Dissolution of the matrix resulting in significant porosity surrounding some of the quartz grains can be observed. (Right hand image) Gorgon CO2 Data-1 Barrow Group BSE image of the conventional core sample 2179.68 m under high magnification showing quartz (Qtz) grains, matrix and porosity.

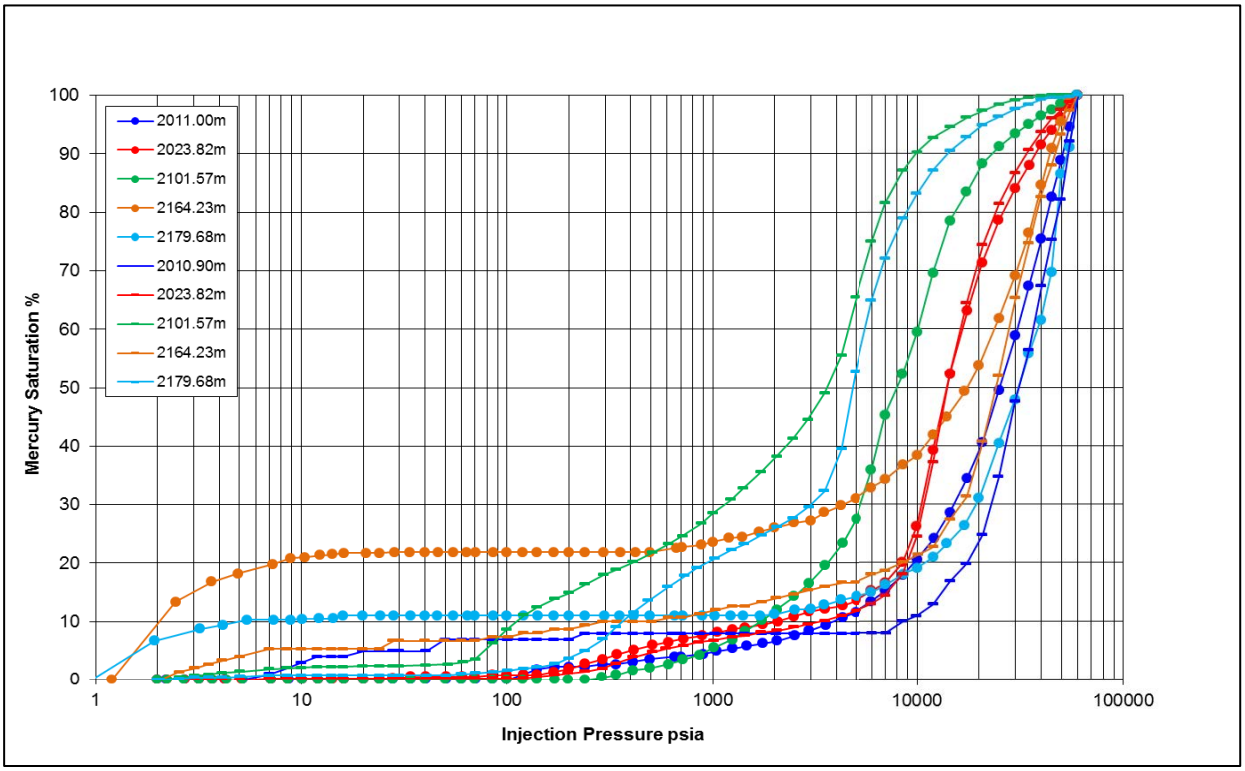

Figure D- 94: Raw MICP curves from samples of Barrow Group and Dupuy Formation, Gorgon CO2 Data Well-1 & Data Well-. The fresh (2006) sample MICP curves are shown with dots at the pressure equilibrium points (Daniel and Kaldi, 2006) and the warehoused (2015) sample MICP curves are shown by short horizontal lines at the pressure equilibrium points

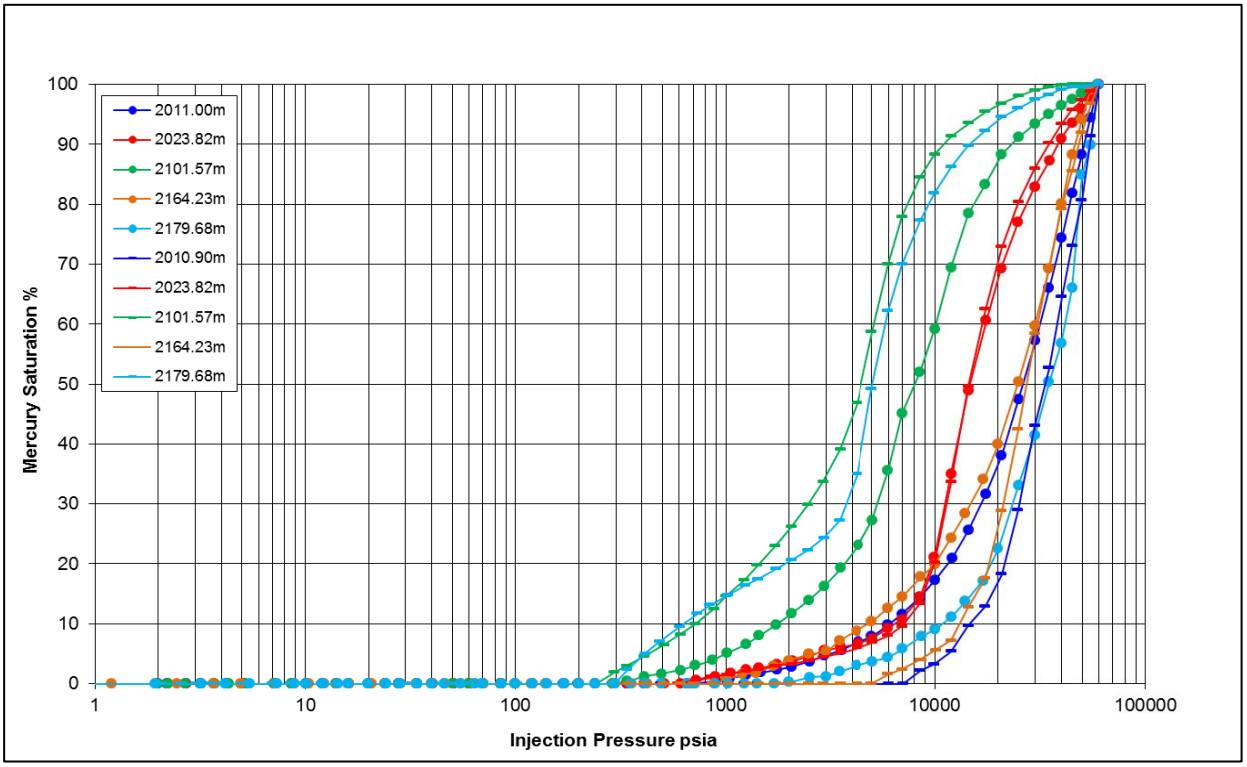

Figure D- 95: Conformance corrected MICP curves from samples of Barrow Group and Dupuy Formation, Gorgon CO2 Data Well-1 & Data Well-. The fresh (2006) sample MICP curves are shown with dots at the pressure equilibrium points (Daniel and Kaldi, 2006) and the warehoused (2015) sample MICP curves are shown by short horizontal lines at the pressure equilibrium points

E. APPENDIX

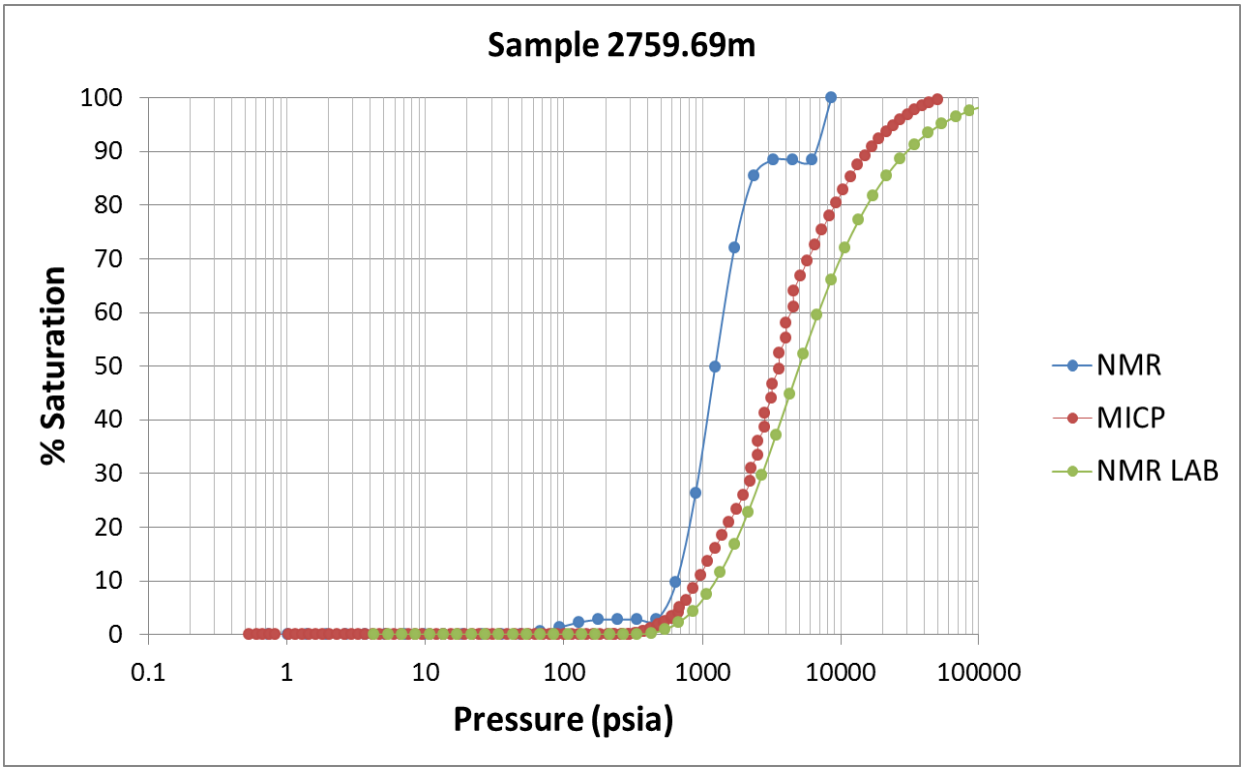

Figure E- 1: Tindilpie-11 MICP curve from the core sample (MICP) at 2759.69 m. Also shown is the laboratory synthetic NMR (NMR LAB) and well synthetic NMR (NMR) over the same depth interval.

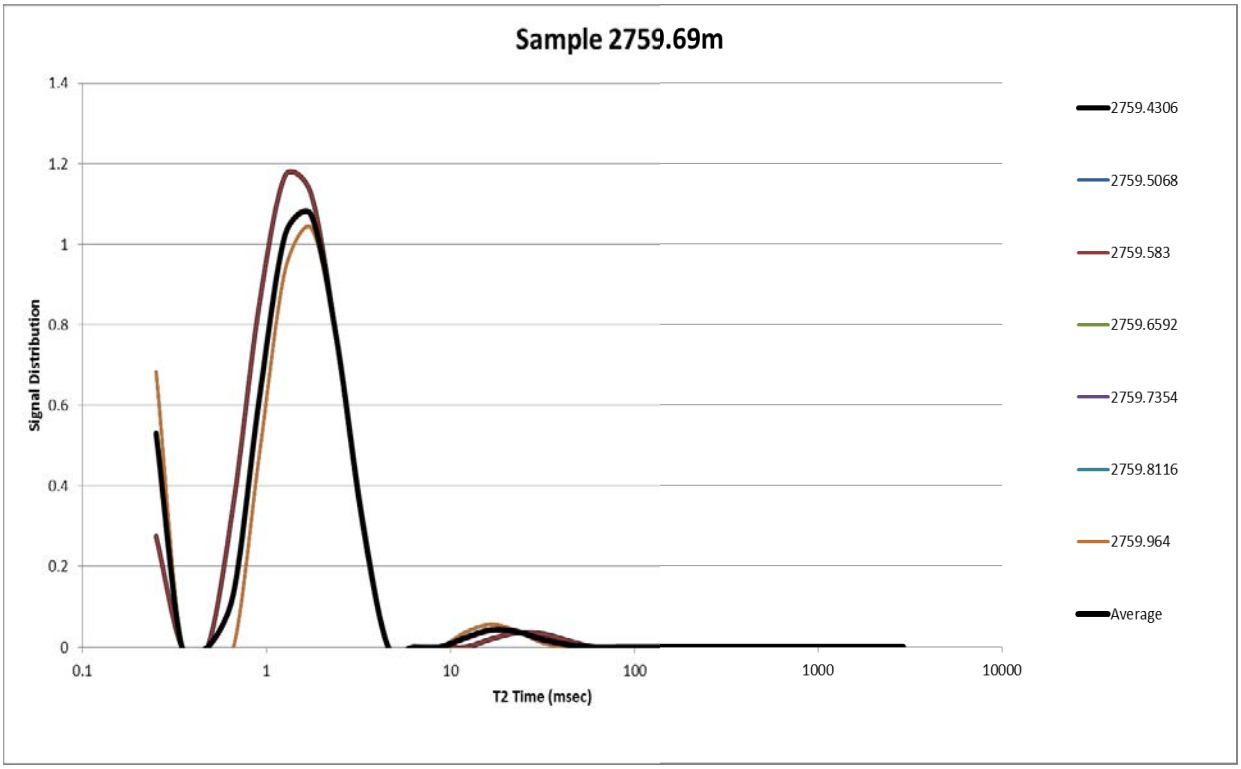

Figure E- 2: Tindilpie -11 NMR T_2 distributions over the 1.6 m interval used to produce the well synthetic MICP curve at 2759.69 m depth.

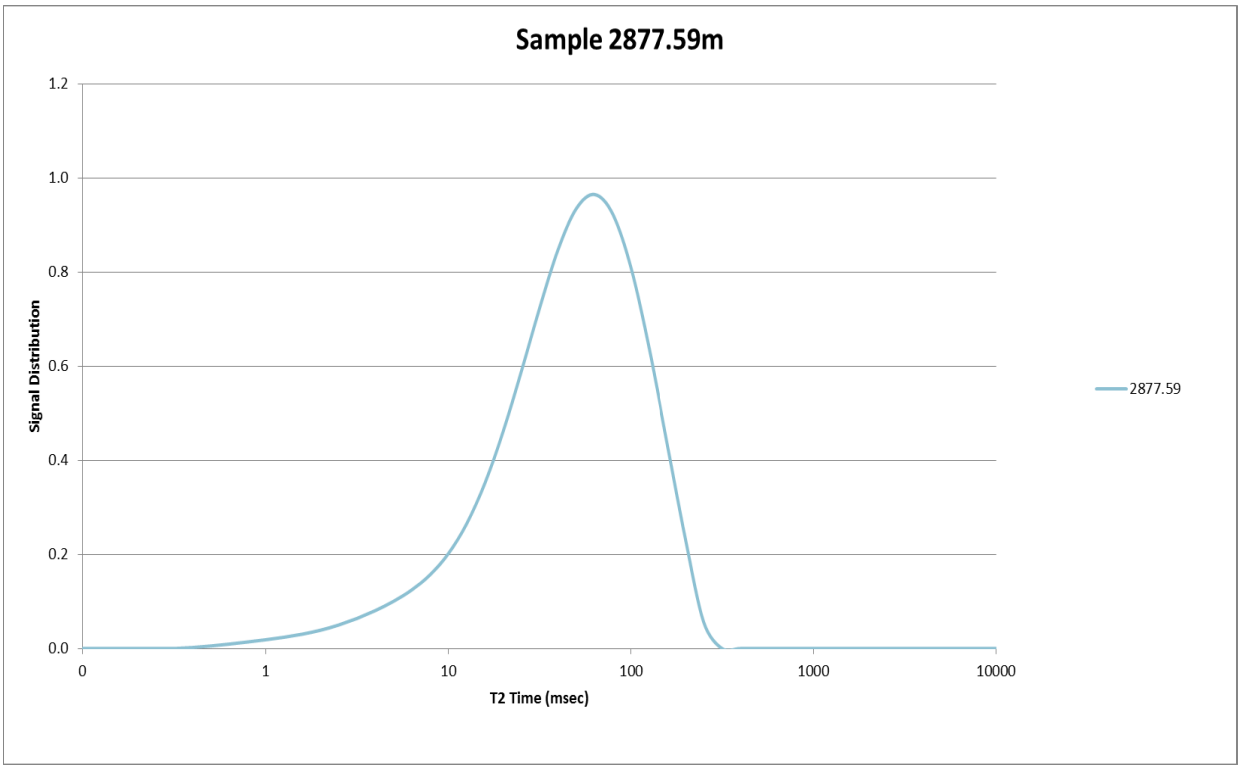

Figure E- 3: Tindilpie-11 NMR T_2 distribution from the laboratory sample at 2759.69 m used to produce the laboratory synthetic MICP curve.

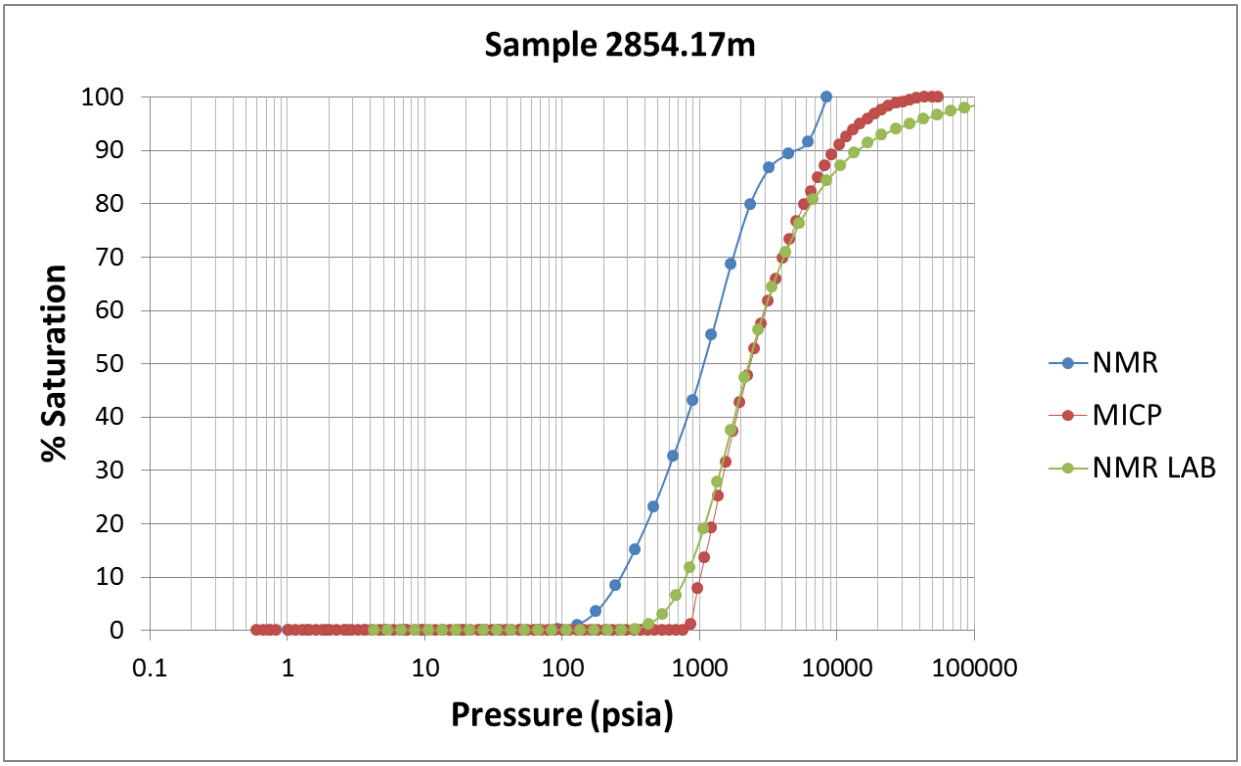

Figure E- 4: Tindilpie-11 MICP curve from the core sample (MICP) at 2854.17 m. Also shown is the laboratory synthetic NMR (NMR LAB) and well synthetic NMR (NMR) over the same depth interval.

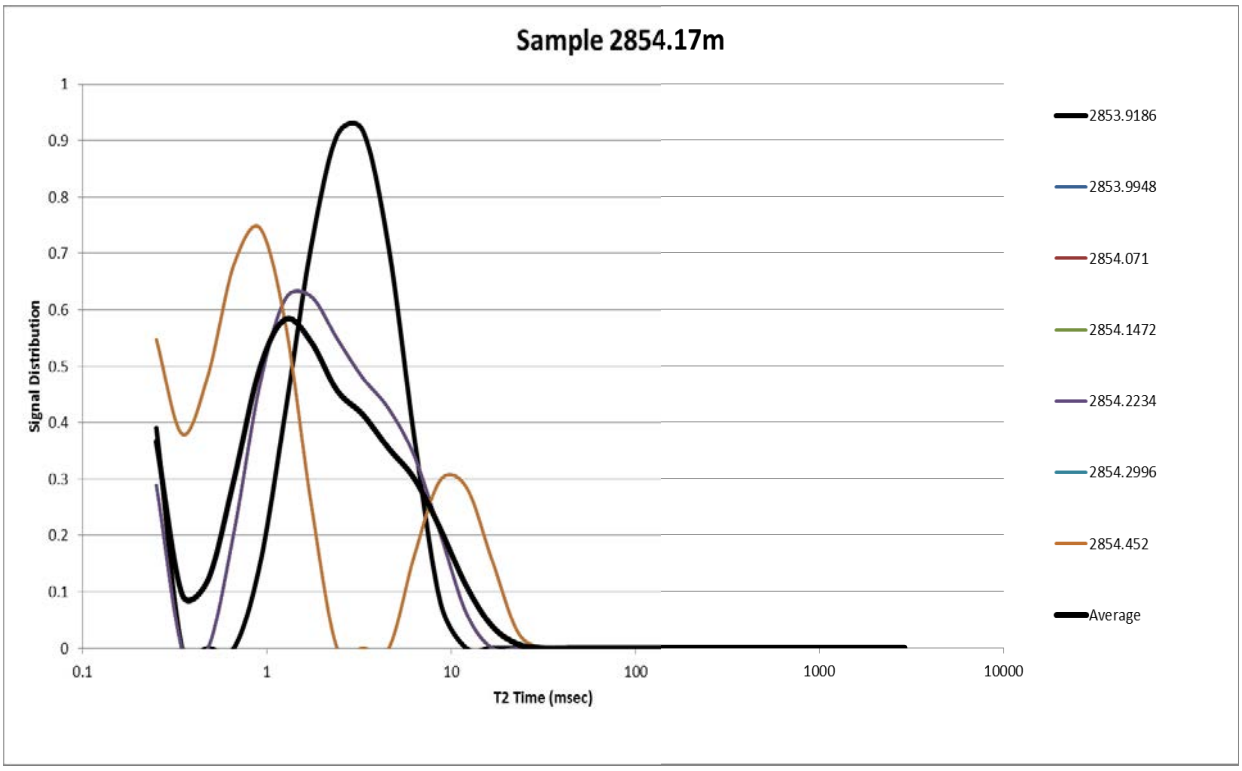

Figure E- 5: Tindilpie -11 NMR T_2 distributions over the 1.6 m interval used to produce the well synthetic MICP curve at 2854.17 m depth.

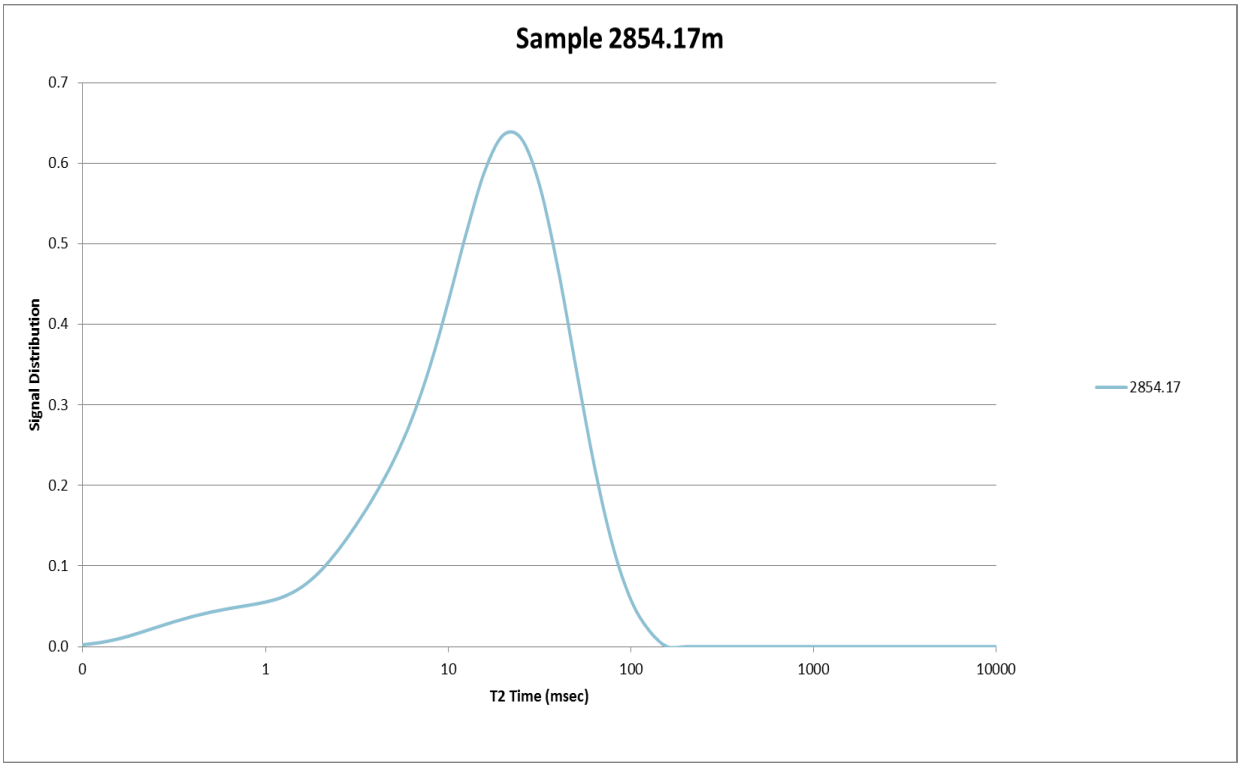

Figure E- 6: Tindilpie-11 NMR T_2 distribution from the laboratory sample at 2854.17 m used to produce the laboratory synthetic MICP curve.

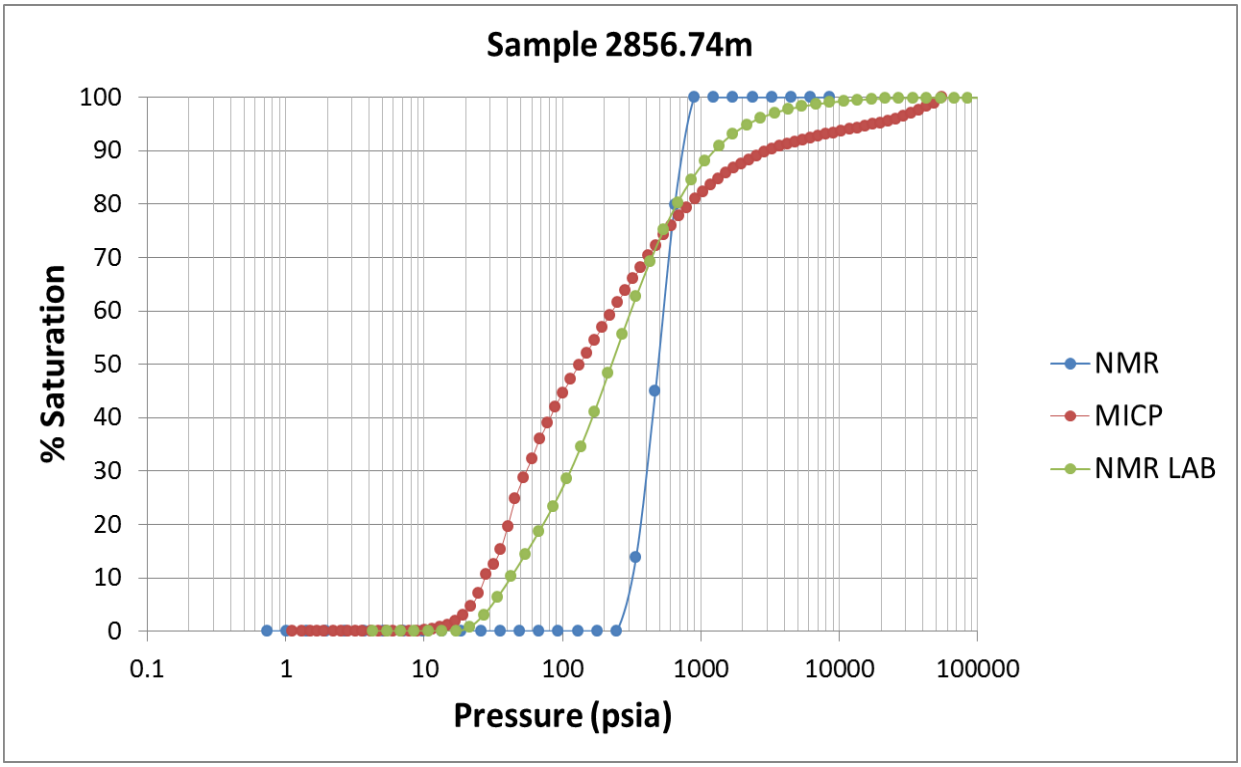

Figure E- 7: Tindilpie-11 MICP curve from the core sample (MICP) at 2856.74 m. Also shown is the laboratory synthetic NMR (NMR LAB) and well synthetic NMR (NMR) over the same depth interval.

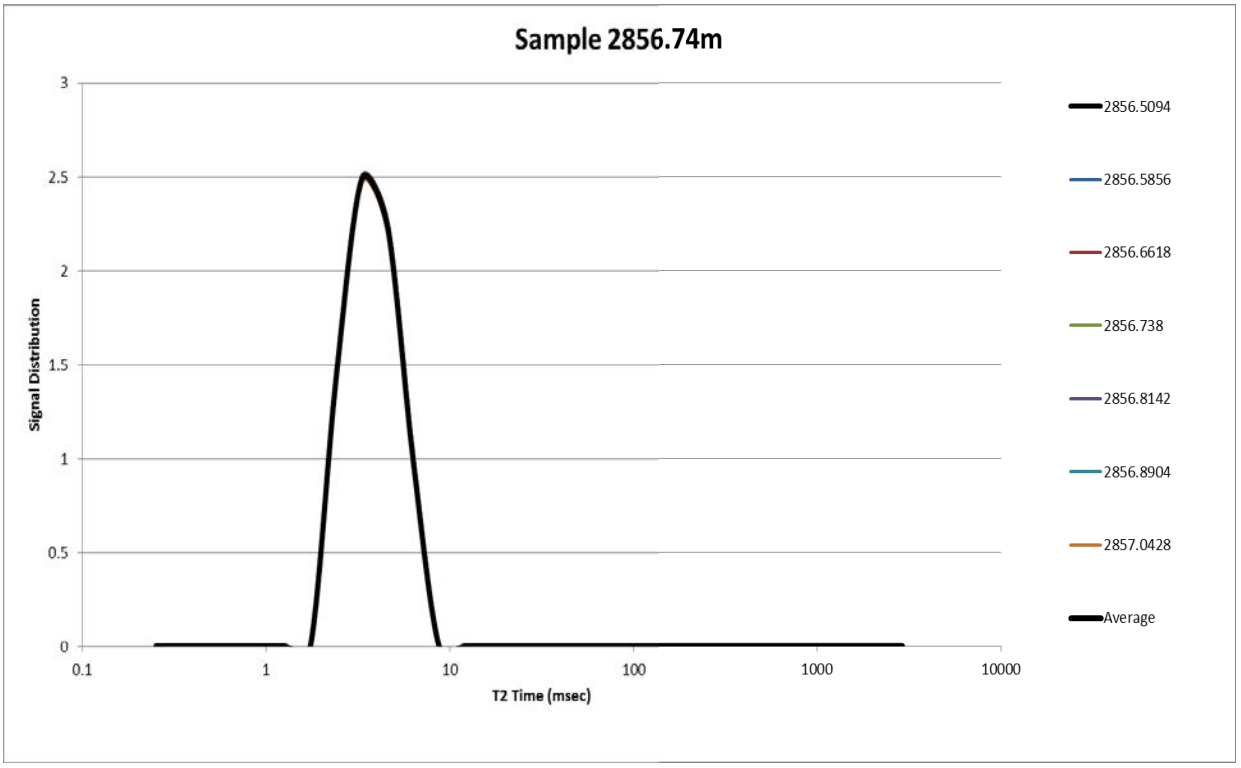

Figure E- 8: Tindilpie -11 NMR T_2 distributions over the 1.6 m interval used to produce the well synthetic MICP curve at 2856.7 4m depth.

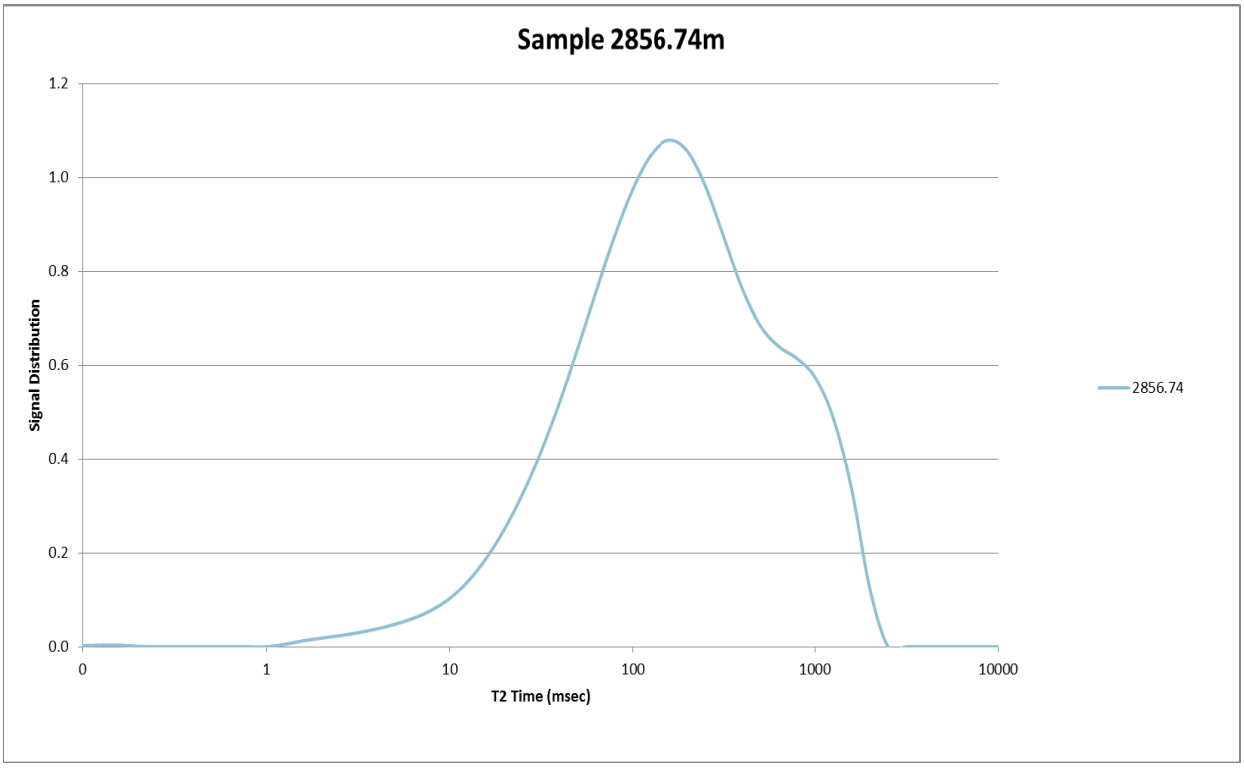

Figure E- 9: Tindilpie-11 NMR T_2 distribution from the laboratory sample at 2856.74 m used to produce the laboratory synthetic MICP curve.

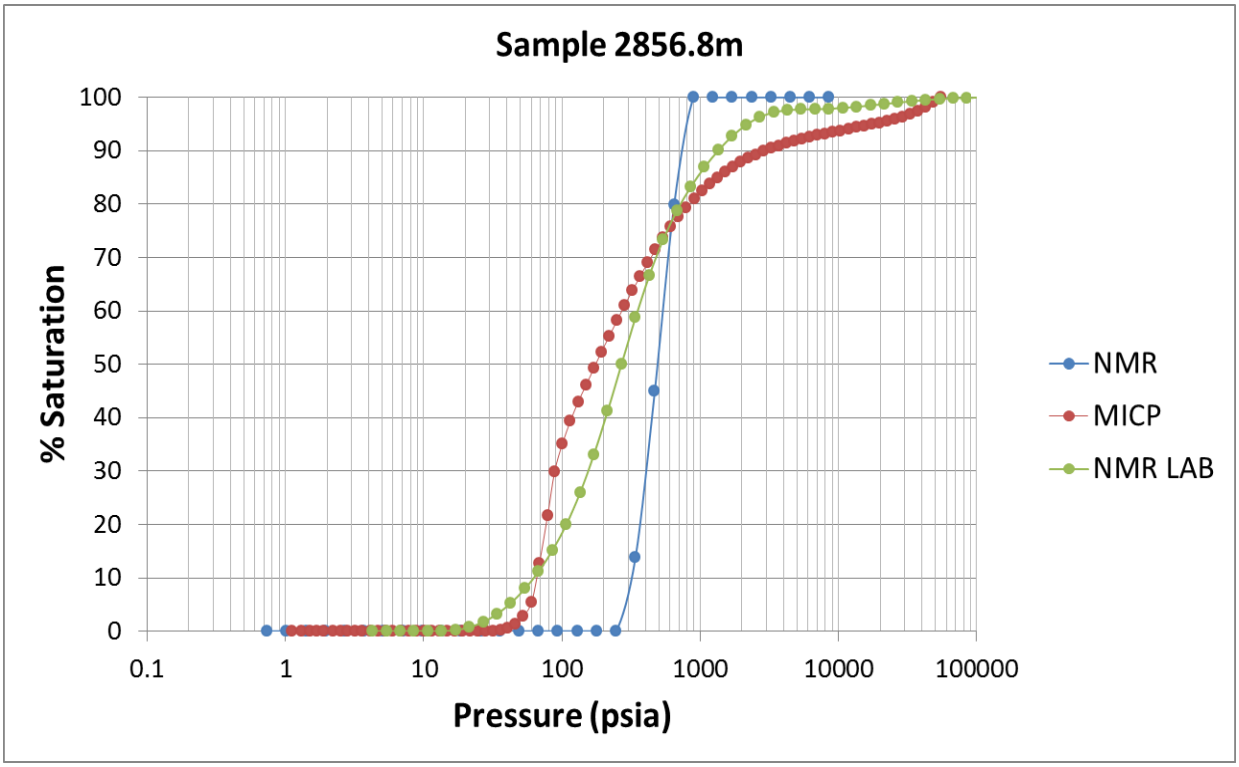

Figure E- 10: Tindilpie-11 MICP curve from the core sample (MICP) at 2856.8 m. Also shown is the laboratory synthetic NMR (NMR LAB) and well synthetic NMR (NMR) over the same depth interval.

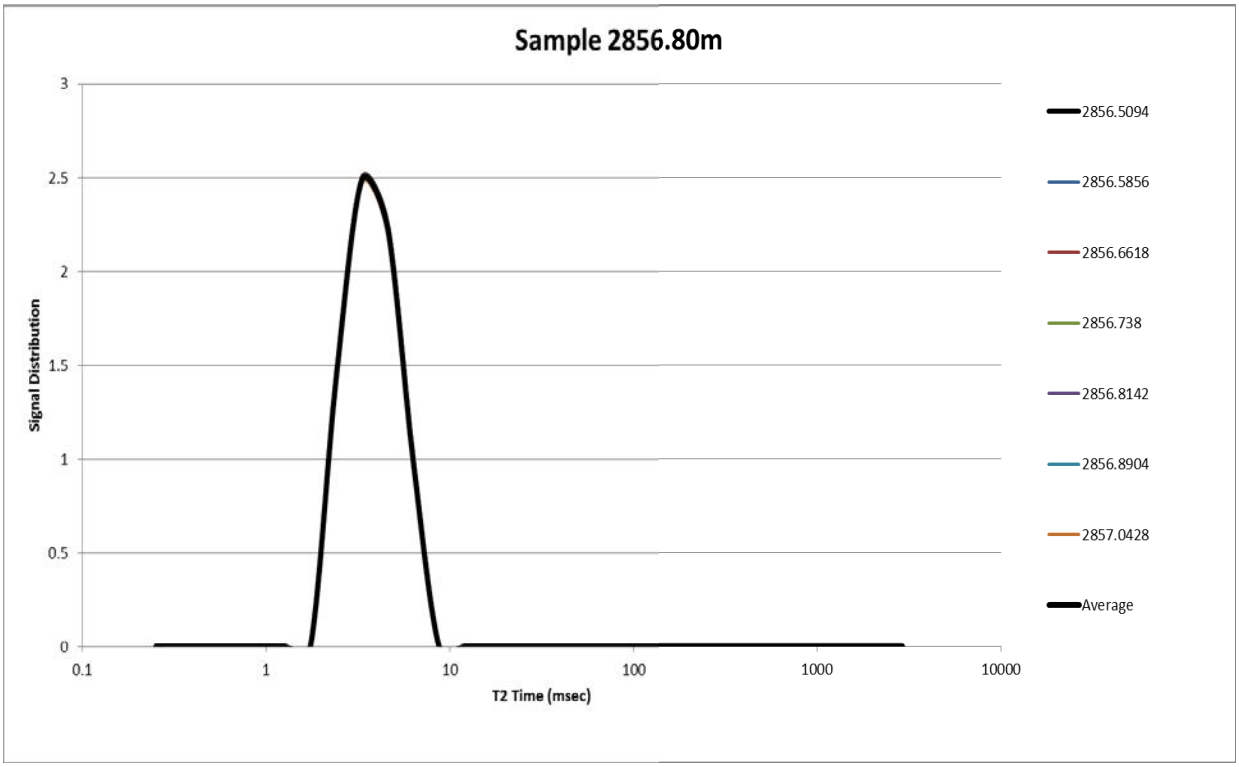

Figure E- 11: Tindilpie -11 NMR T_2 distributions over the 1.6 m interval used to produce the well synthetic MICP curve at 2856.8 m depth.

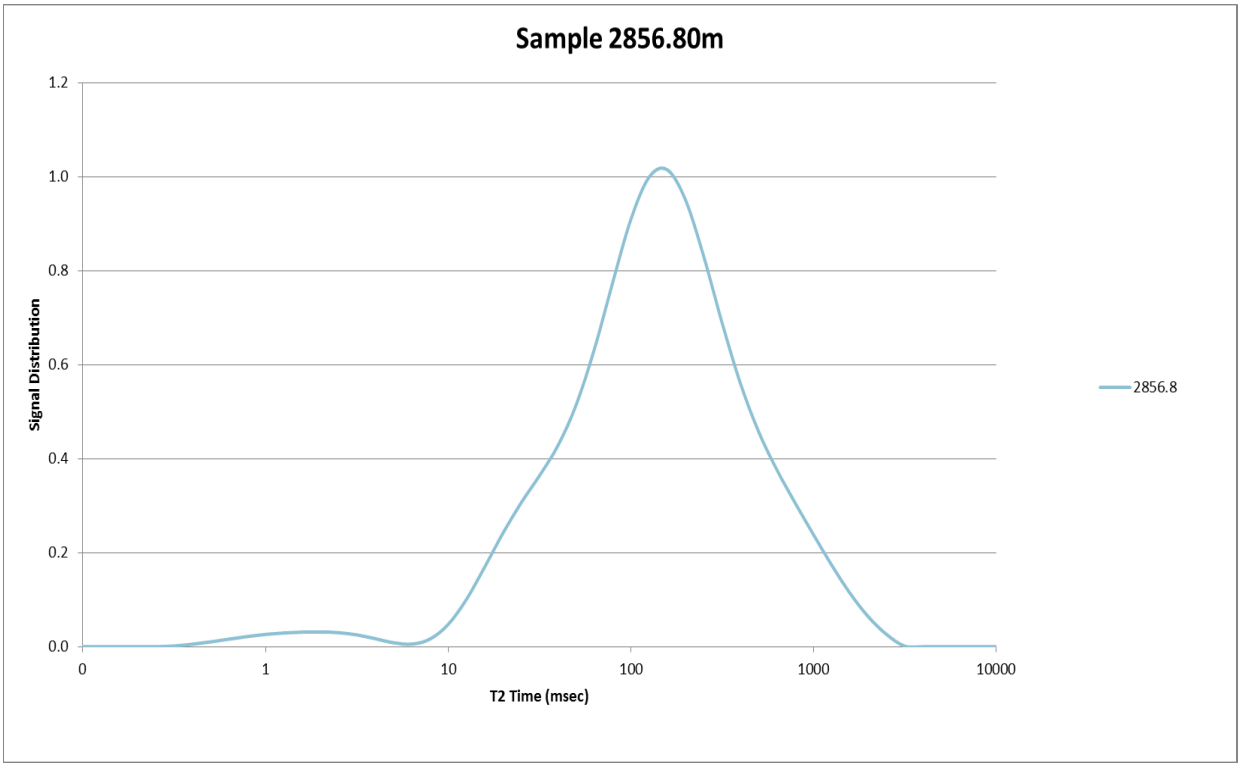

Figure E- 12: Tindilpie-11 NMR T_2 distribution from the laboratory sample at 2856.8 m used to produce the laboratory synthetic MICP curve.

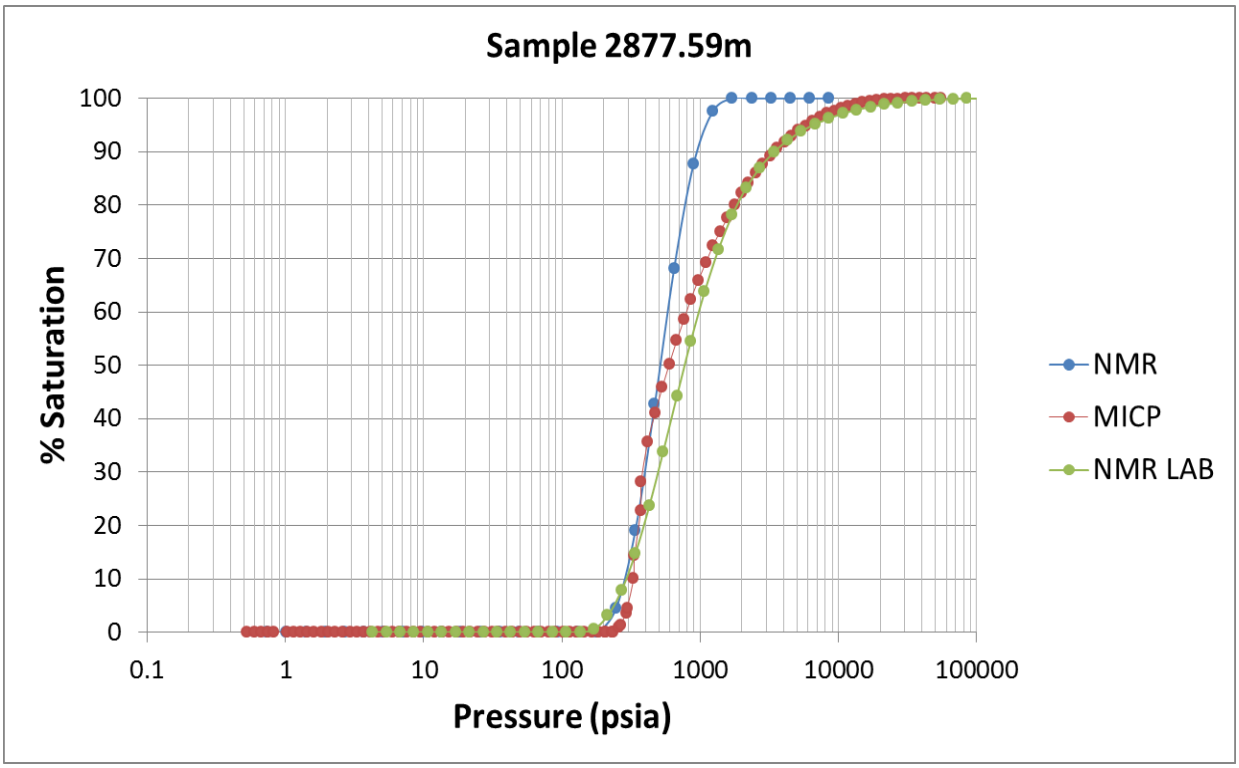

Figure E- 13: Tindilpie-11 MICP curve from the core sample (MICP) at 2877.59 m. Also shown is the laboratory synthetic NMR (NMR LAB) and well synthetic NMR (NMR) over the same depth interval.

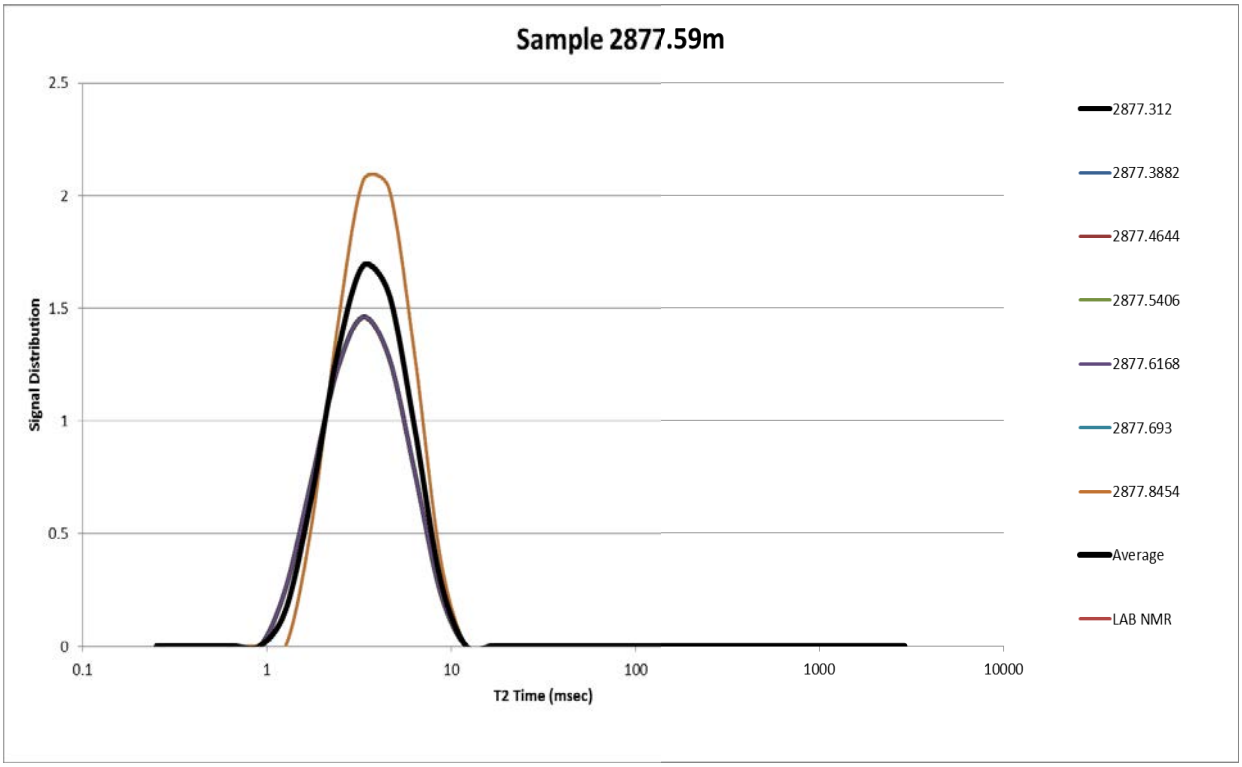

Figure E- 14: Tindilpie -11 NMR T_2 distributions over the 1.6m interval used to produce the well synthetic MICP curve at 2877.59 m depth

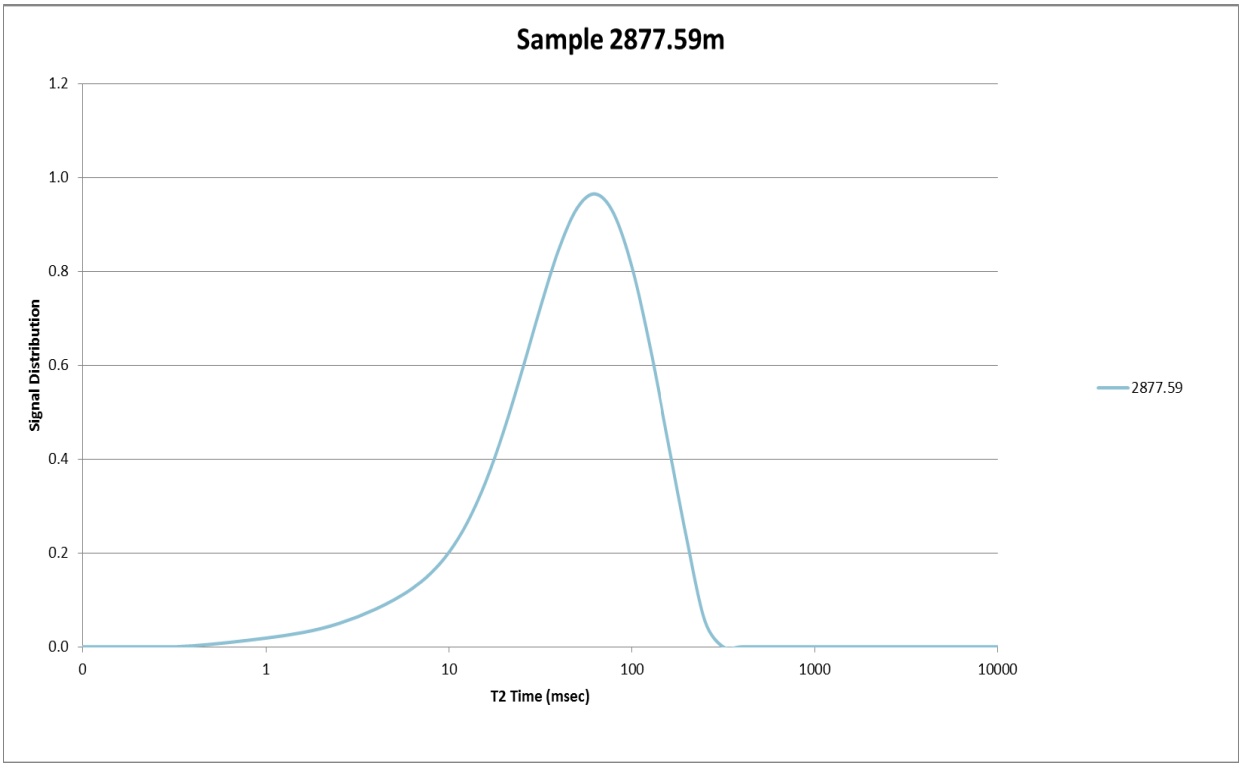

Figure E- 15: Tindilpie-11 NMR T_2 distribution from the laboratory sample at 2877.59 m used to produce the laboratory synthetic MICP curve.

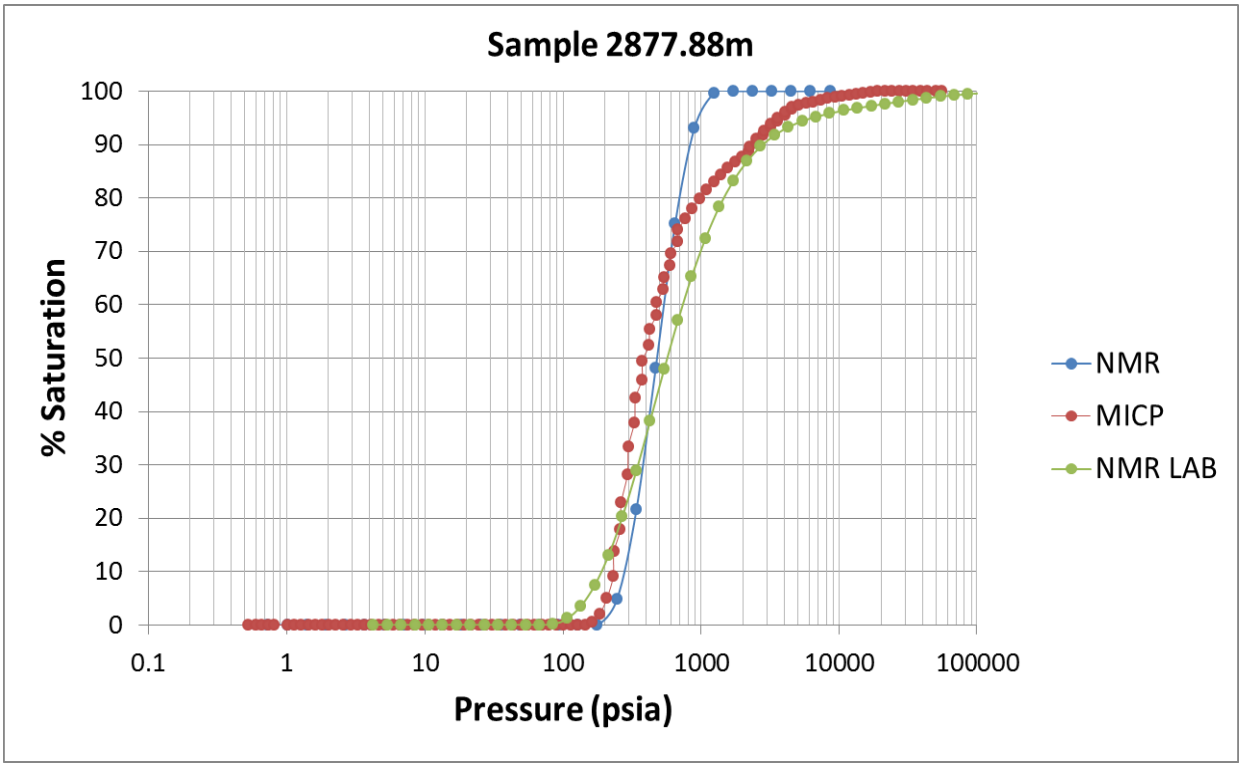

Figure E- 16: Tindilpie-11 MICP curve from the core sample (MICP) at 2877.88 m. Also shown is the laboratory synthetic NMR (NMR LAB) and well synthetic NMR (NMR) over the same depth interval.

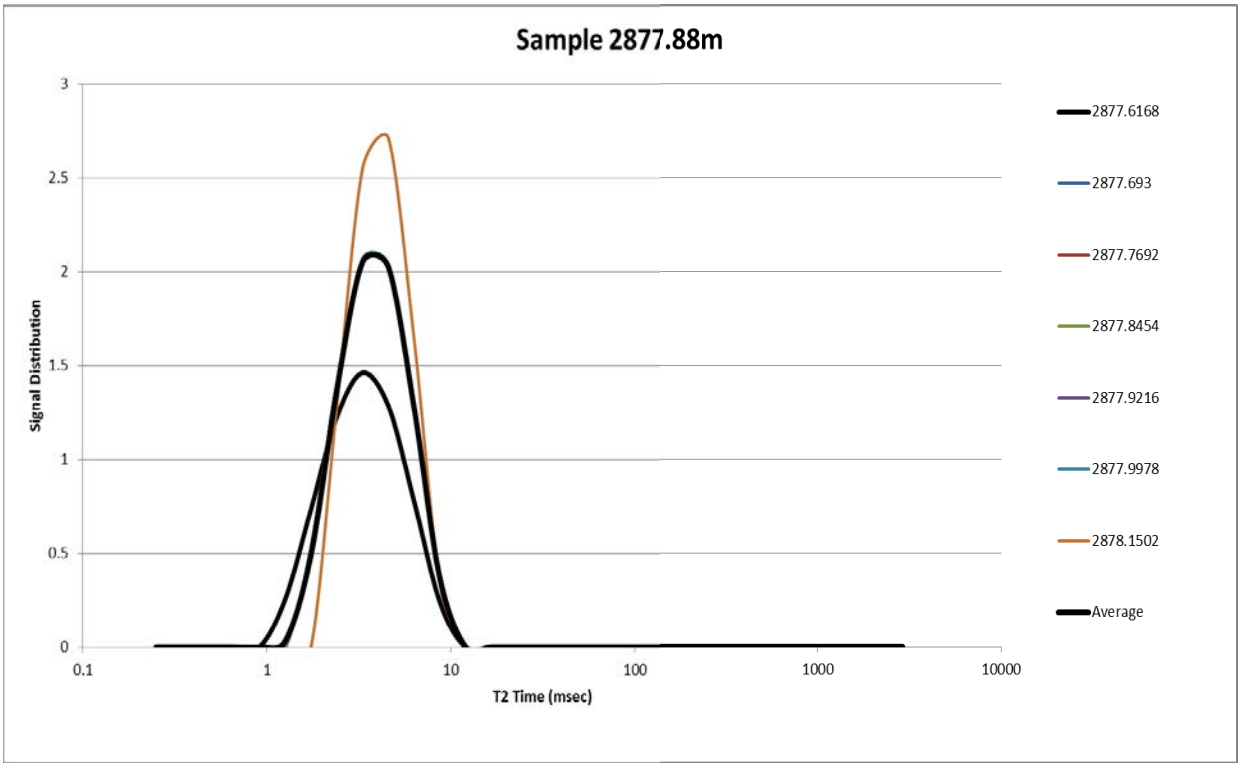

Figure E- 17: Tindilpie -11 NMR T_2 distributions over the 1.6 m interval used to produce the well synthetic MICP curve at 2877.88 m depth.

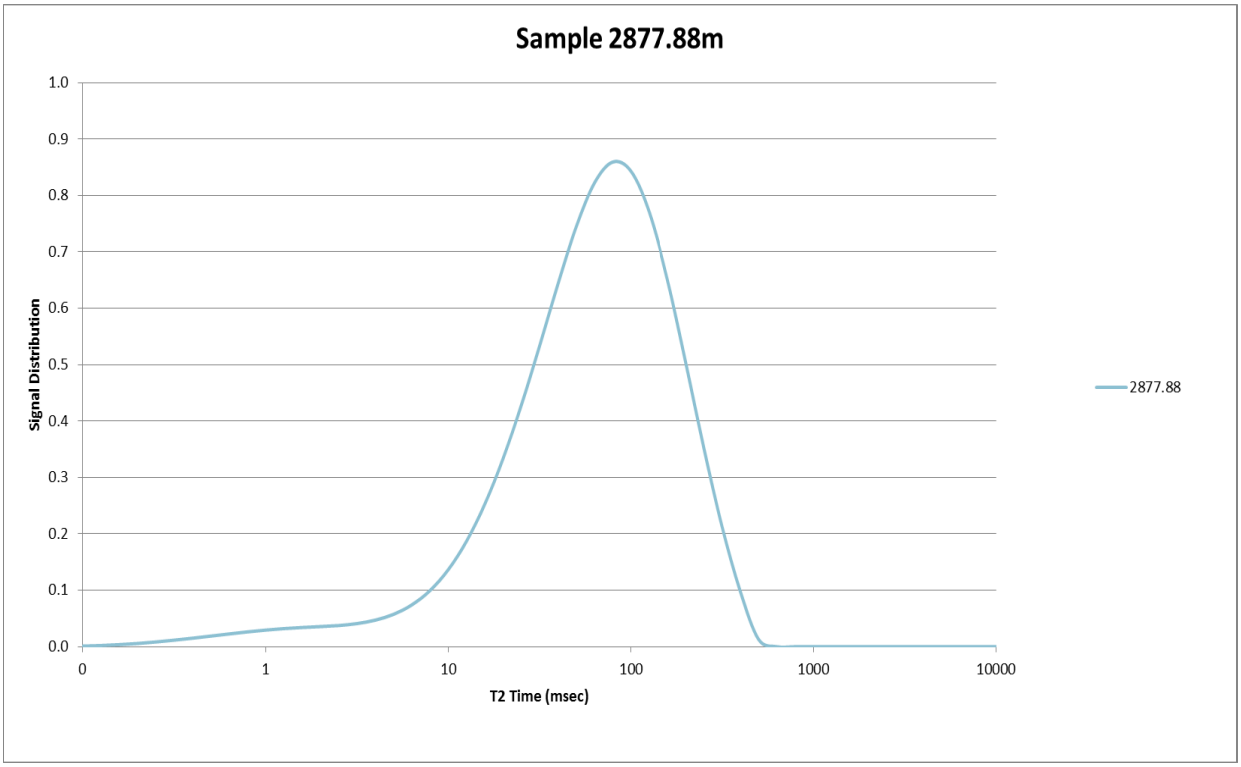

Figure E- 18: Tindilpie-11 NMR T_2 distribution from the laboratory sample at 2877.88 m used to produce the laboratory synthetic MICP curve.

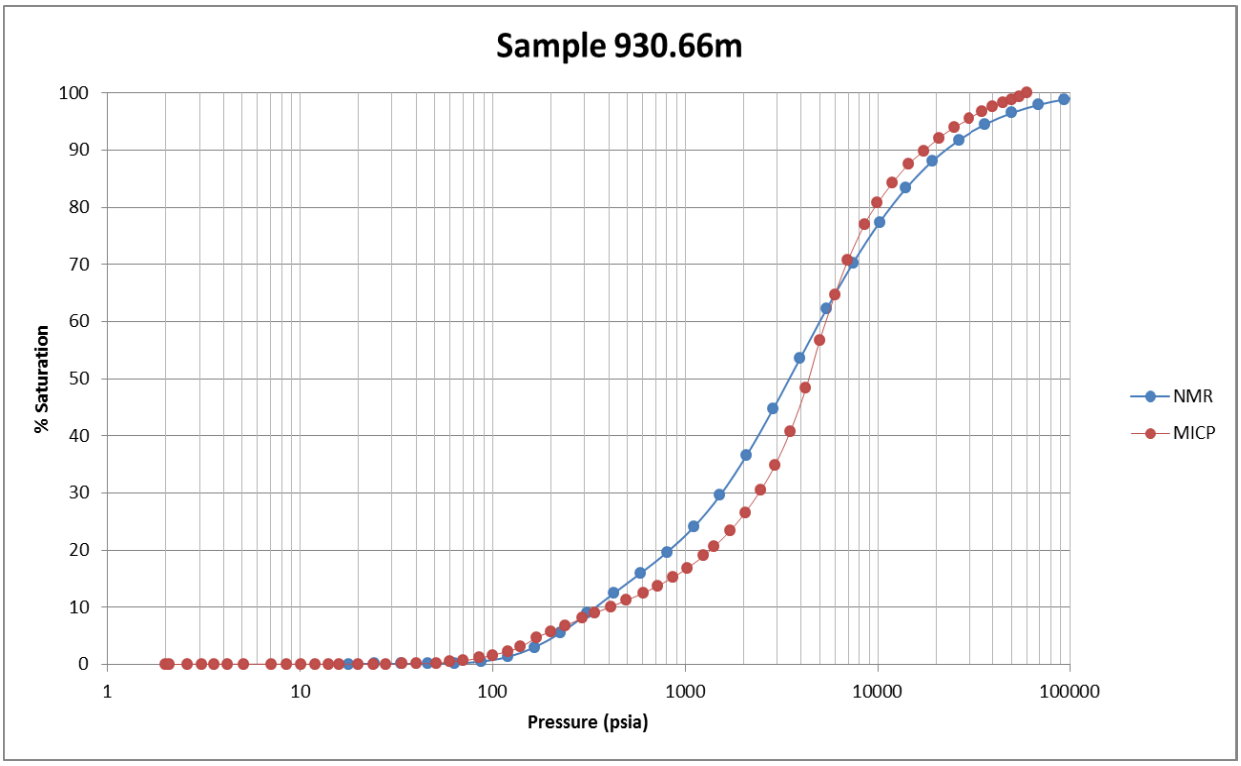

Figure E- 19: CRC-2 MICP curve from the core sample (MICP) at 930.66 m. Also shown is the well synthetic NMR (NMR) over the same depth interval.

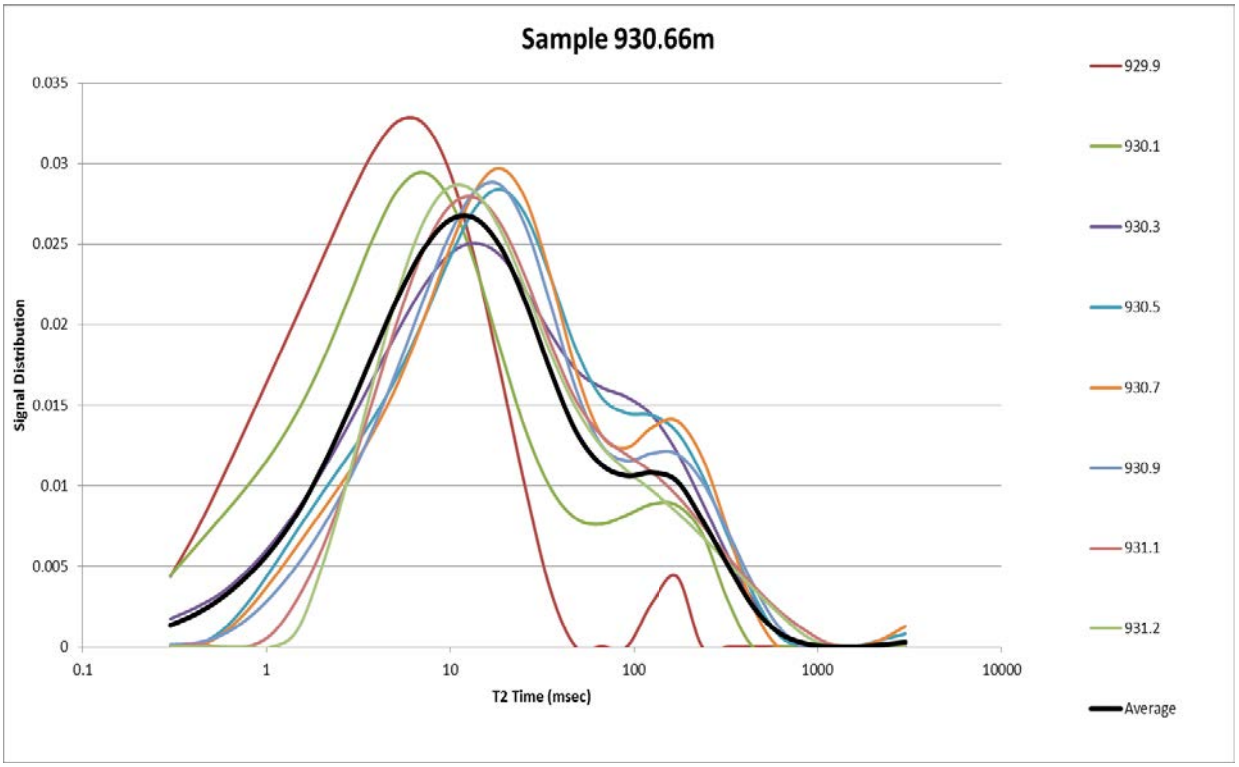

Figure E- 20: CRC-2 NMR T_2 distributions over the 1.6 m interval used to produce the well synthetic MICP curve at 930.66 m depth

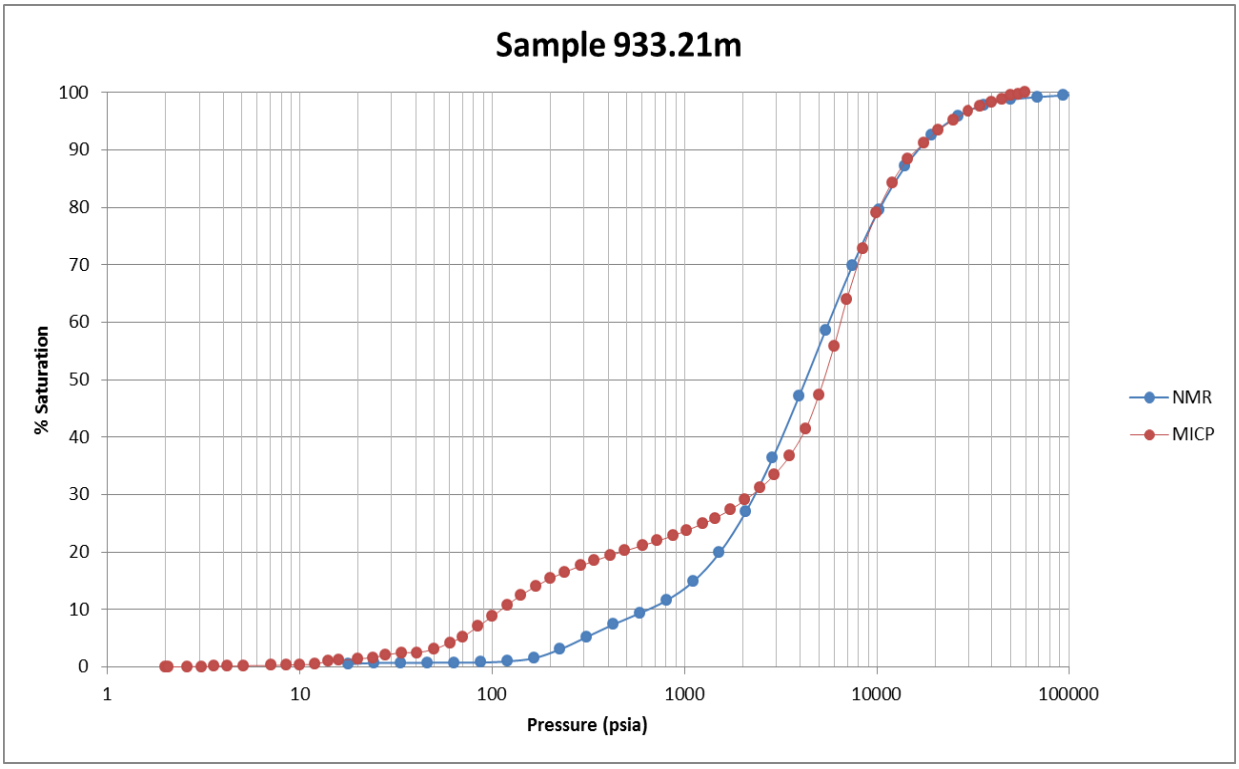

Figure E- 21: CRC-2 MICP curve from the core sample (MICP) at 933.21 m. Also shown is the well synthetic NMR (NMR) over the same depth interval.

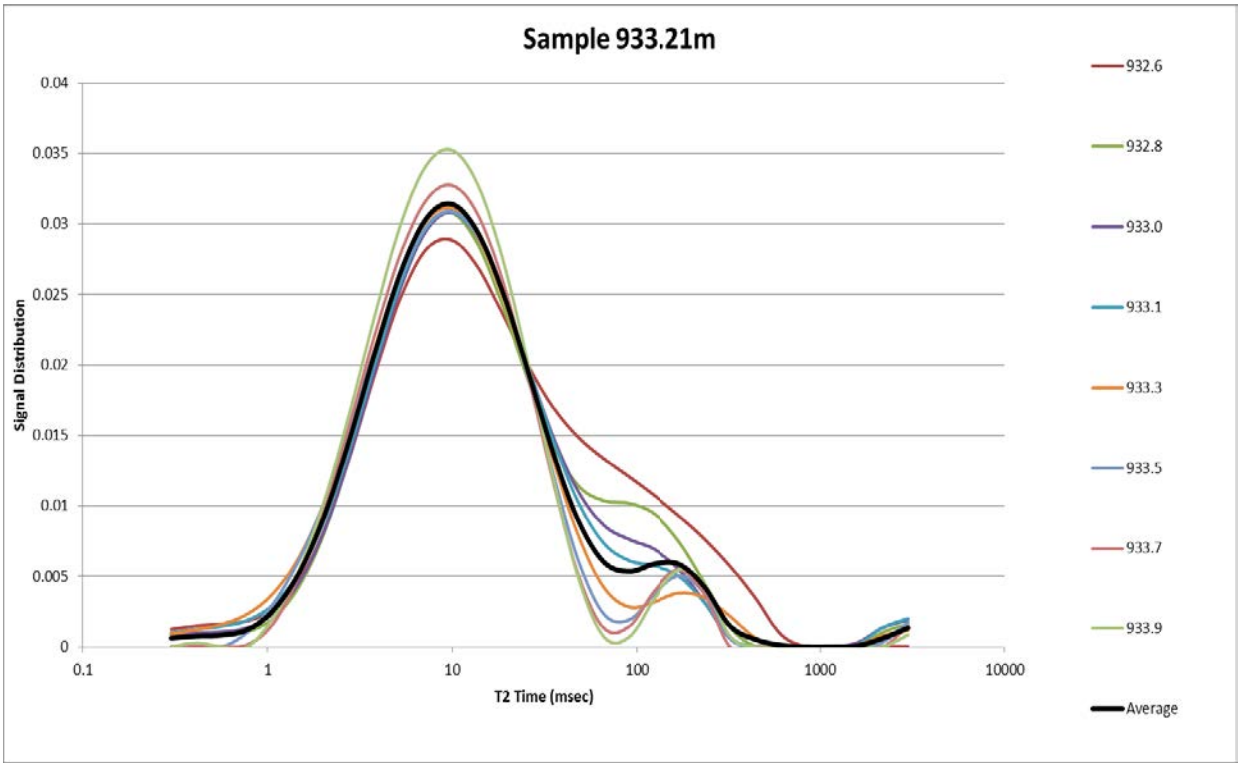

Figure E- 22: CRC-2 NMR T_2 distributions over the 1.6 m interval used to produce the well synthetic MICP curve at 933.21 m depth.

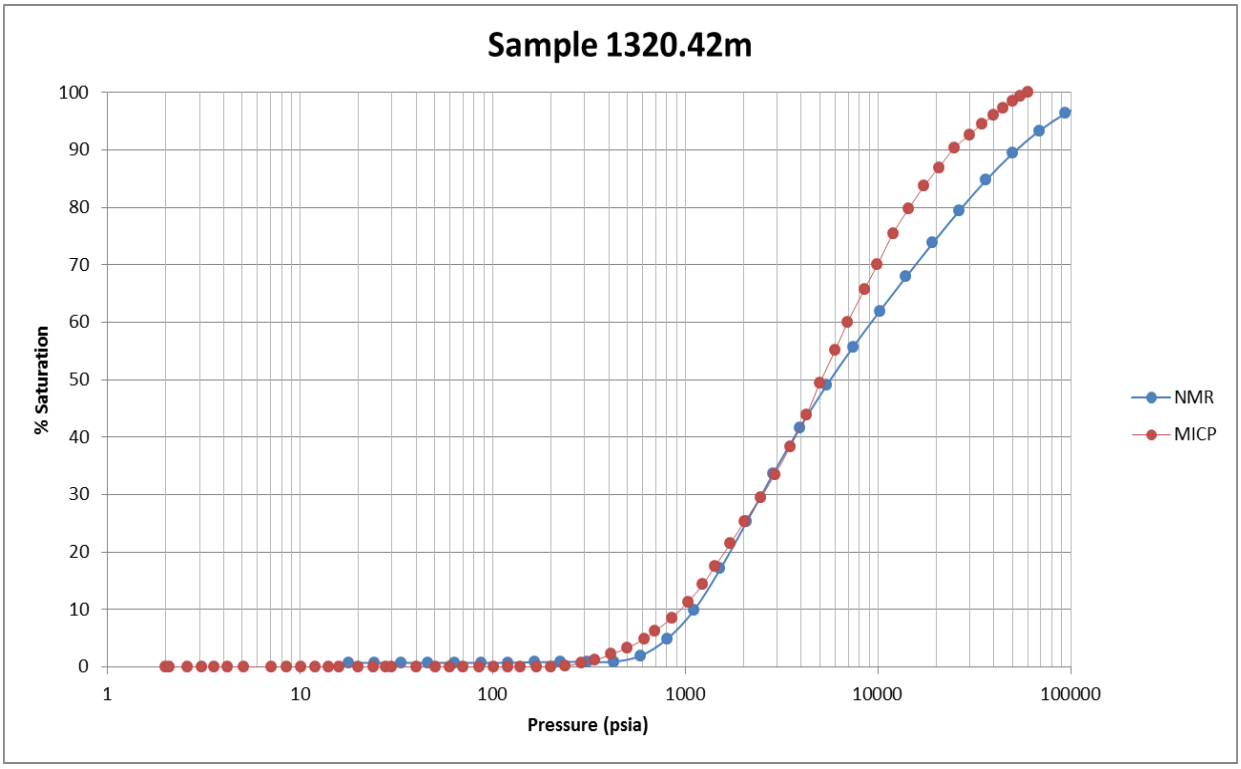

Figure E- 23: CRC-2 MICP curve from the core sample (MICP) at 1320.42 m. Also shown is the well synthetic NMR (NMR) over the same depth interval.

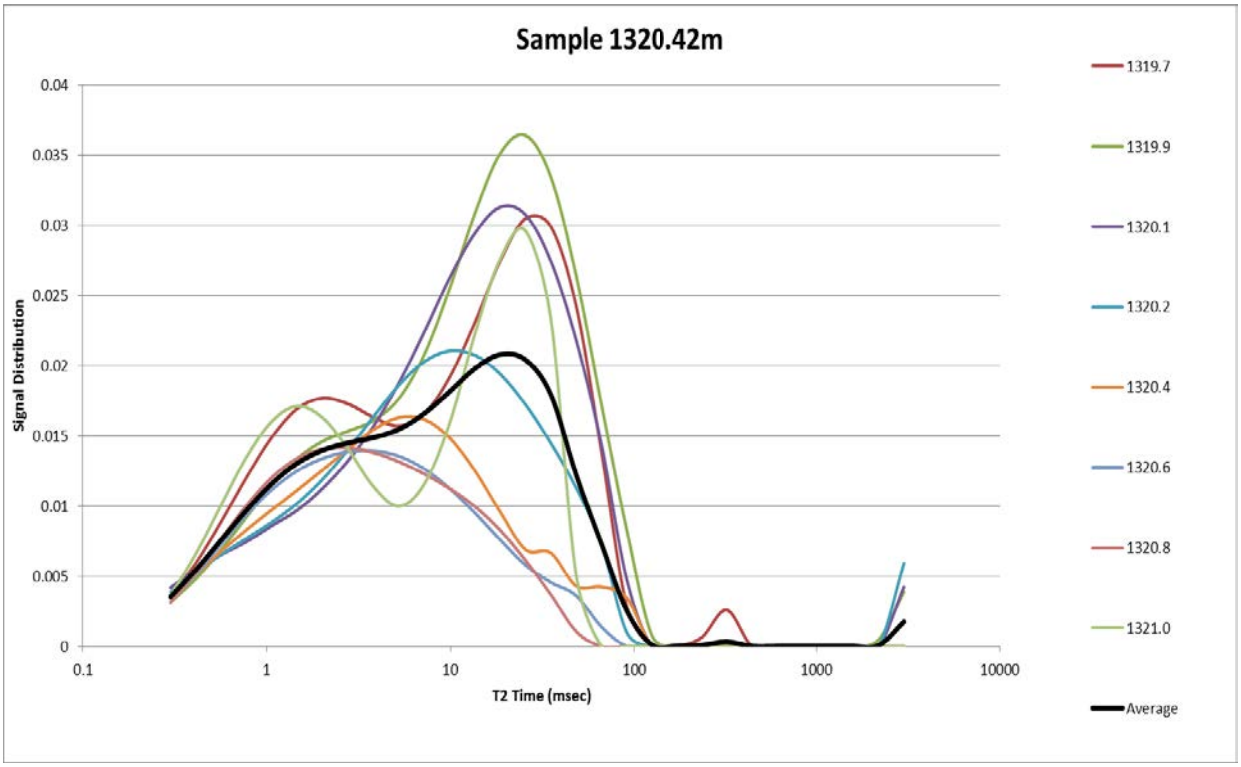

Figure E- 24: CRC-2 NMR T_2 distributions over the 1.6m interval used to produce the well synthetic MICP curve at 1320.42m depth.

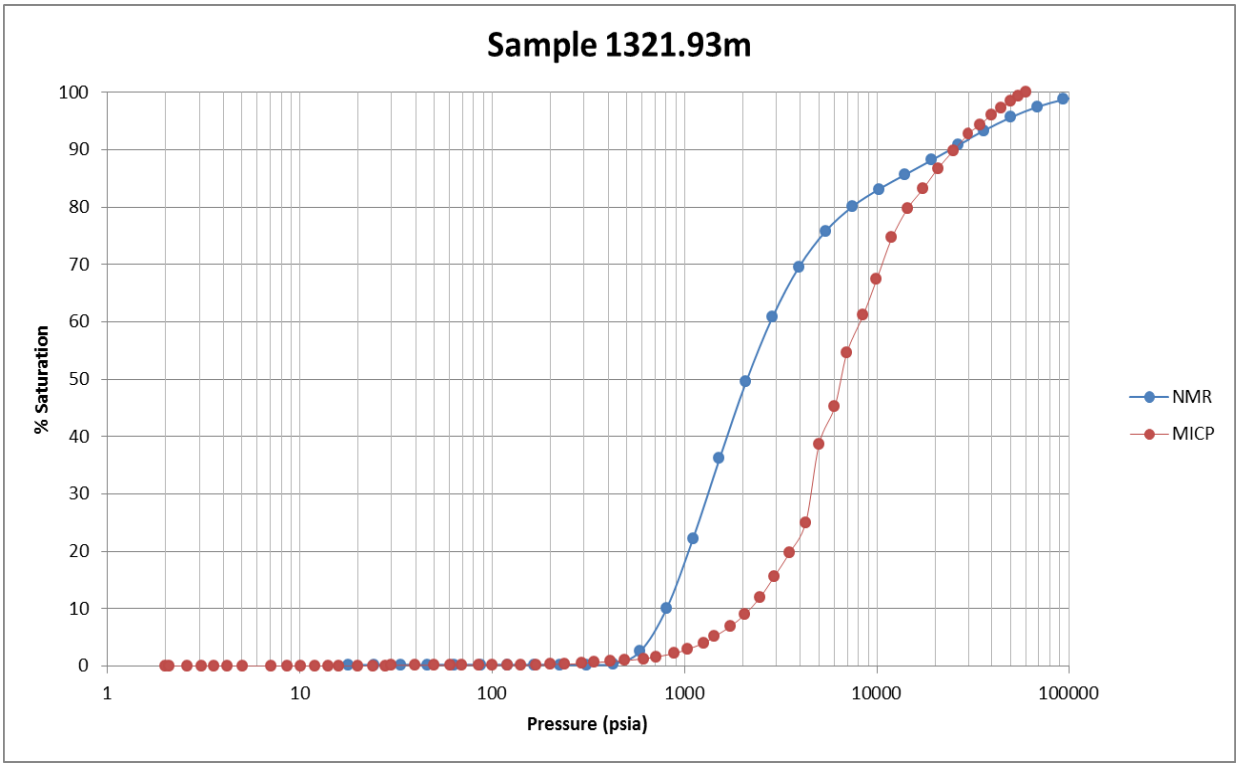

Figure E- 25: CRC-2 MICP curve from the core sample (MICP) at 1321.93m. Also shown is the well synthetic NMR (NMR) over the same depth interval.

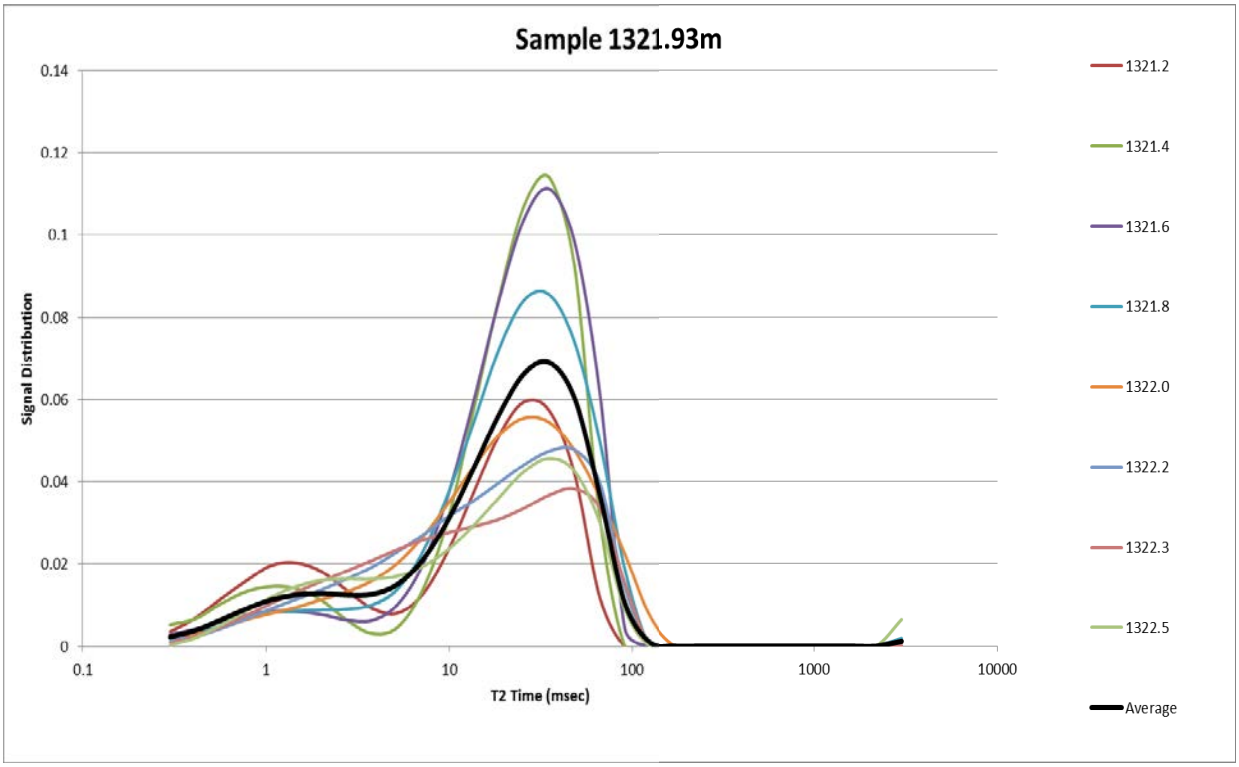

Figure E- 26: CRC-2 NMR T_2 distributions over the 1.6 m interval used to produce the well synthetic MICP curve at 1321.93 m depth.

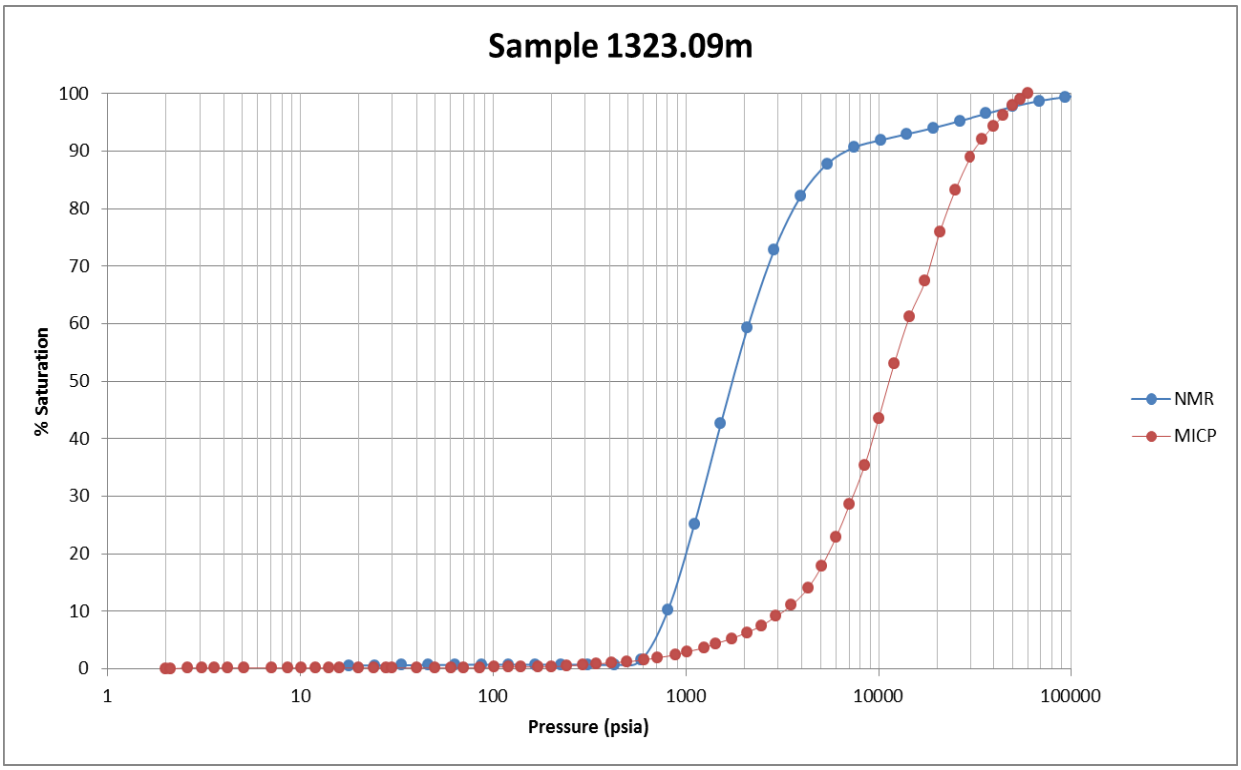

Figure E- 27: CRC-2 MICP curve from the core sample (MICP) at 1323.09 m. Also shown is the well synthetic NMR (NMR) over the same depth interval.

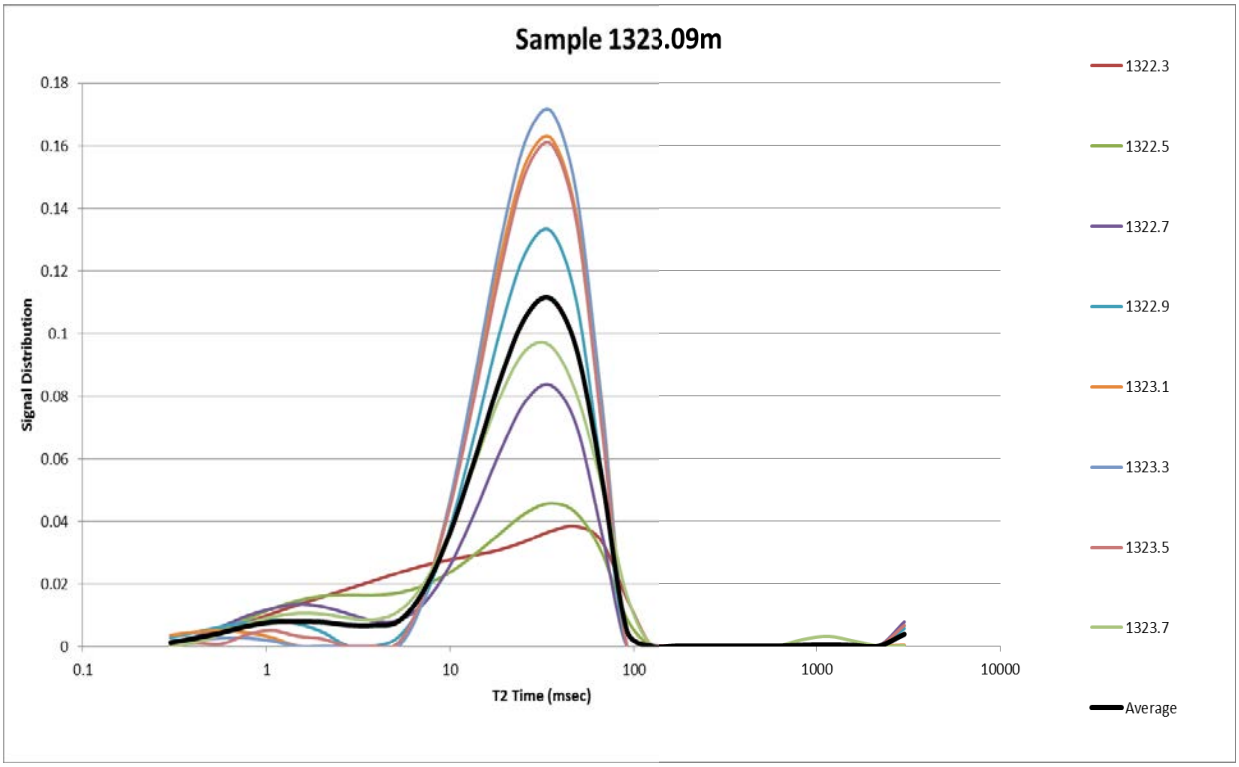

Figure E- 28: CRC-2 NMR T_2 distributions over the 1.6 m interval used to produce the well synthetic MICP curve at 1323.09 m depth.

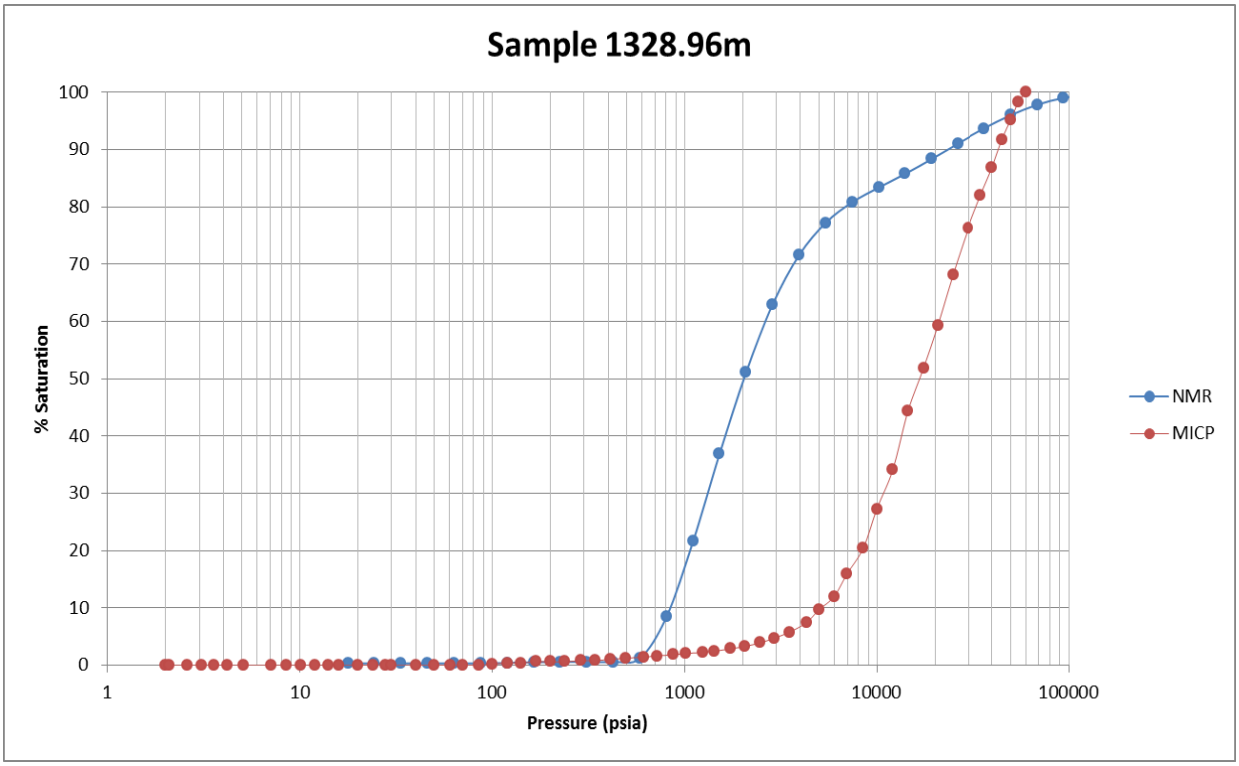

Figure E- 29: CRC-2 MICP curve from the core sample (MICP) at 1328.96 m. Also shown is the well synthetic NMR (NMR) over the same depth interval.

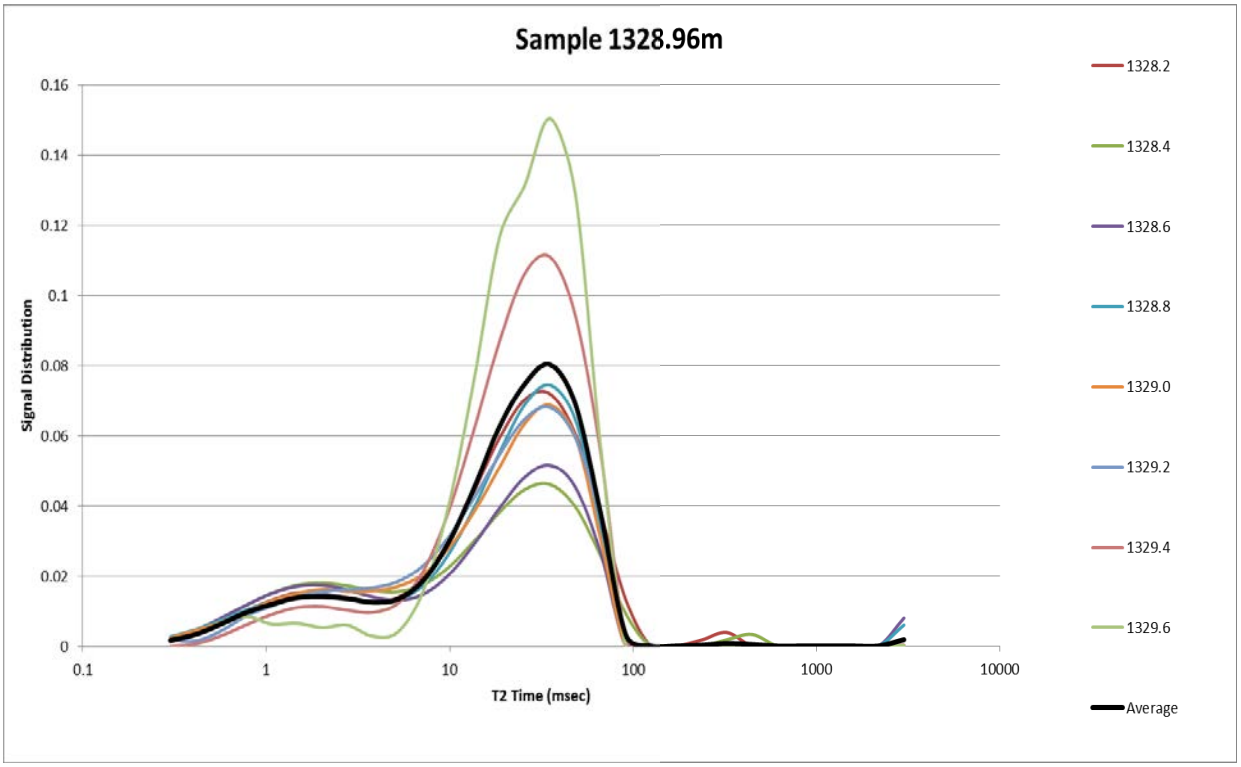

Figure E- 30: CRC-2 NMR T_2 distributions over the 1.6 m interval used to produce the well synthetic MICP curve at 1328.96 m depth.

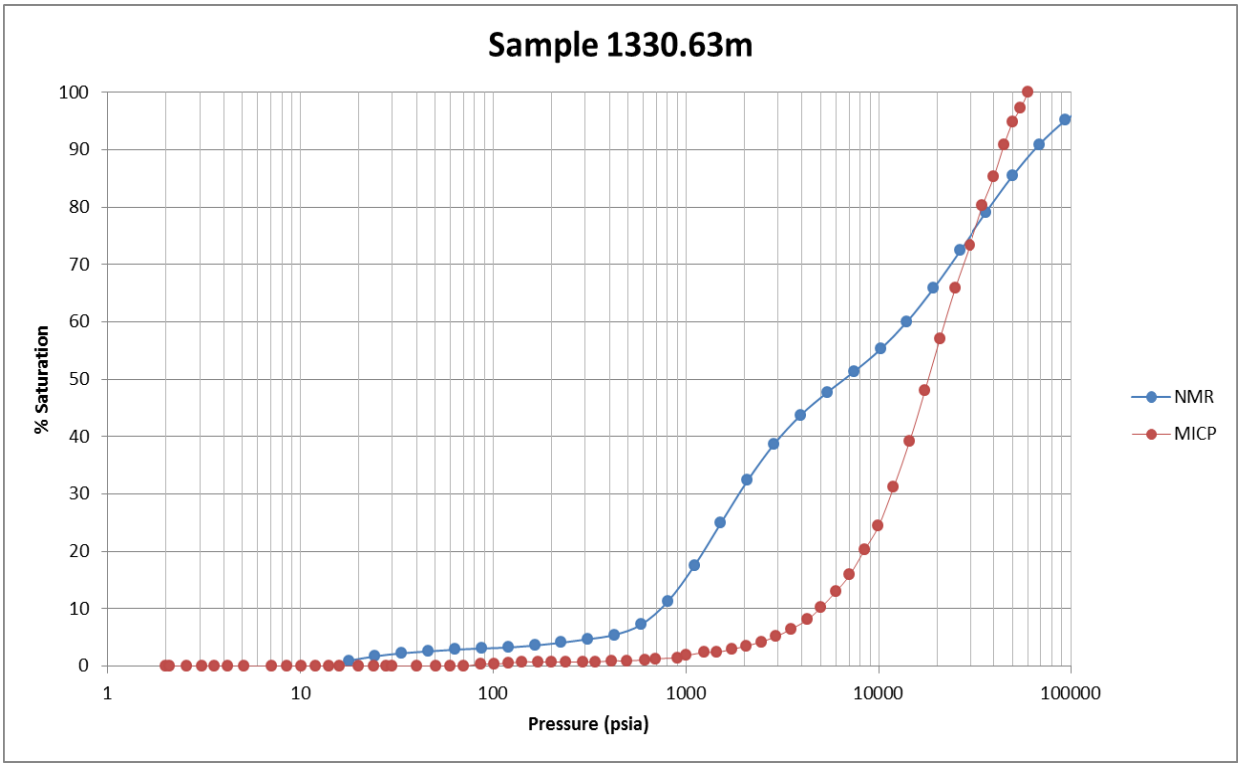

Figure E- 31: CRC-2 MICP curve from the core sample (MICP) at 1330.63 m. Also shown is the well synthetic NMR (NMR) over the same depth interval.

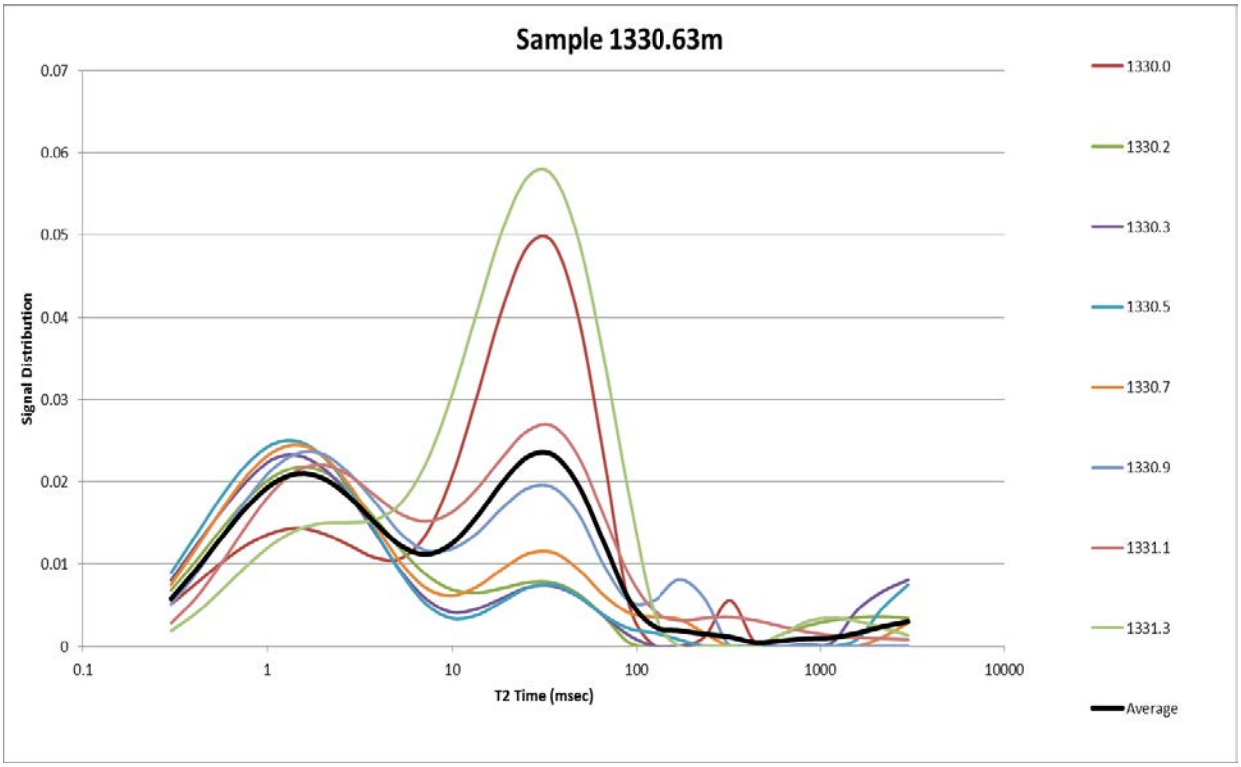

Figure E- 32: CRC-2 NMR T_2 distributions over the 1.6 m interval used to produce the well synthetic MICP curve at 1330.63 m depth.

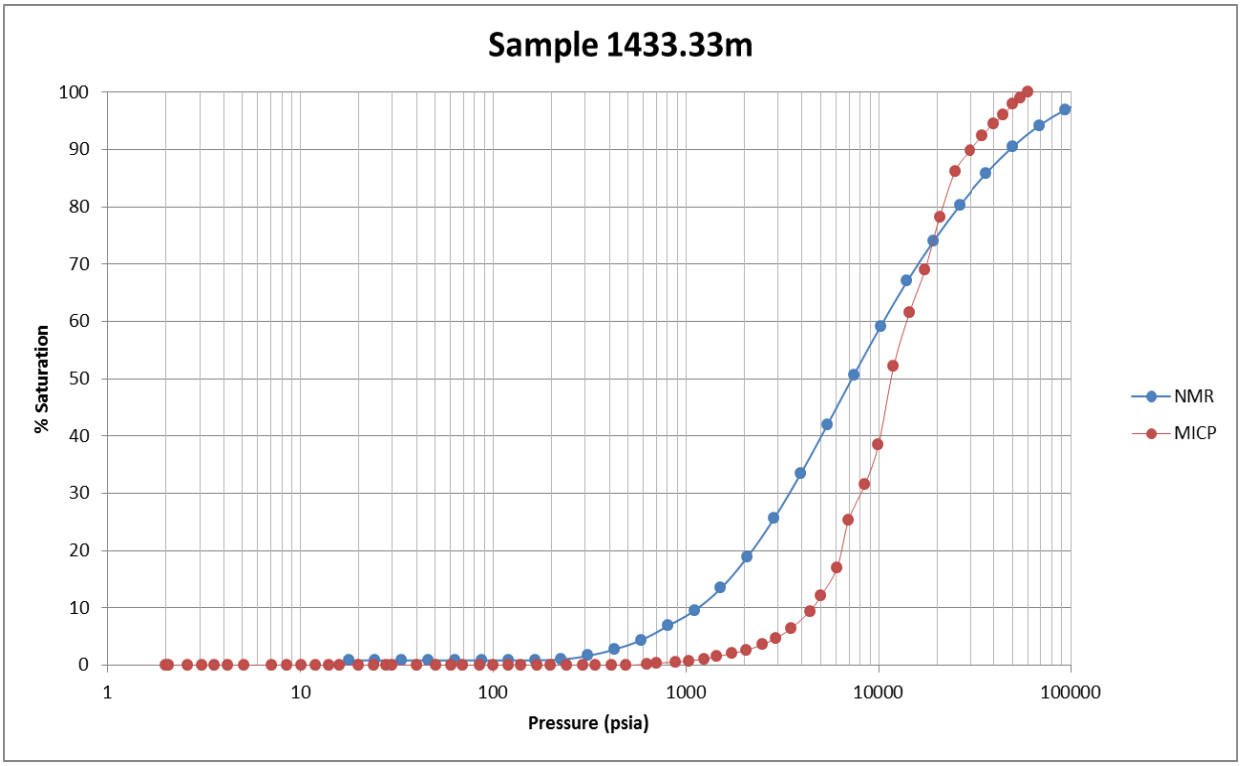

Figure E- 33: CRC-2 MICP curve from the core sample (MICP) at 1433.33 m. Also shown is the well synthetic NMR (NMR) over the same depth interval.

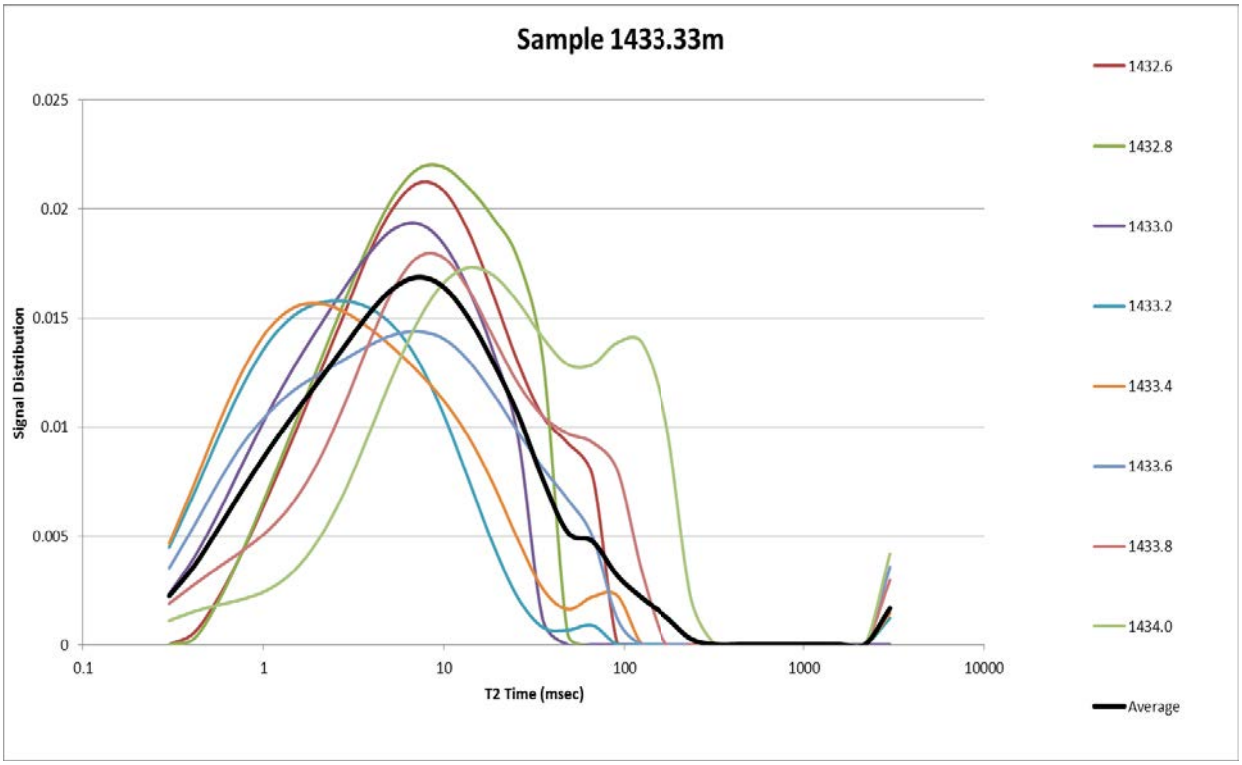

Figure E- 34: CRC-2 NMR T_2 distributions over the 1.6 m interval used to produce the well synthetic MICP curve at 1433.33 m depth.

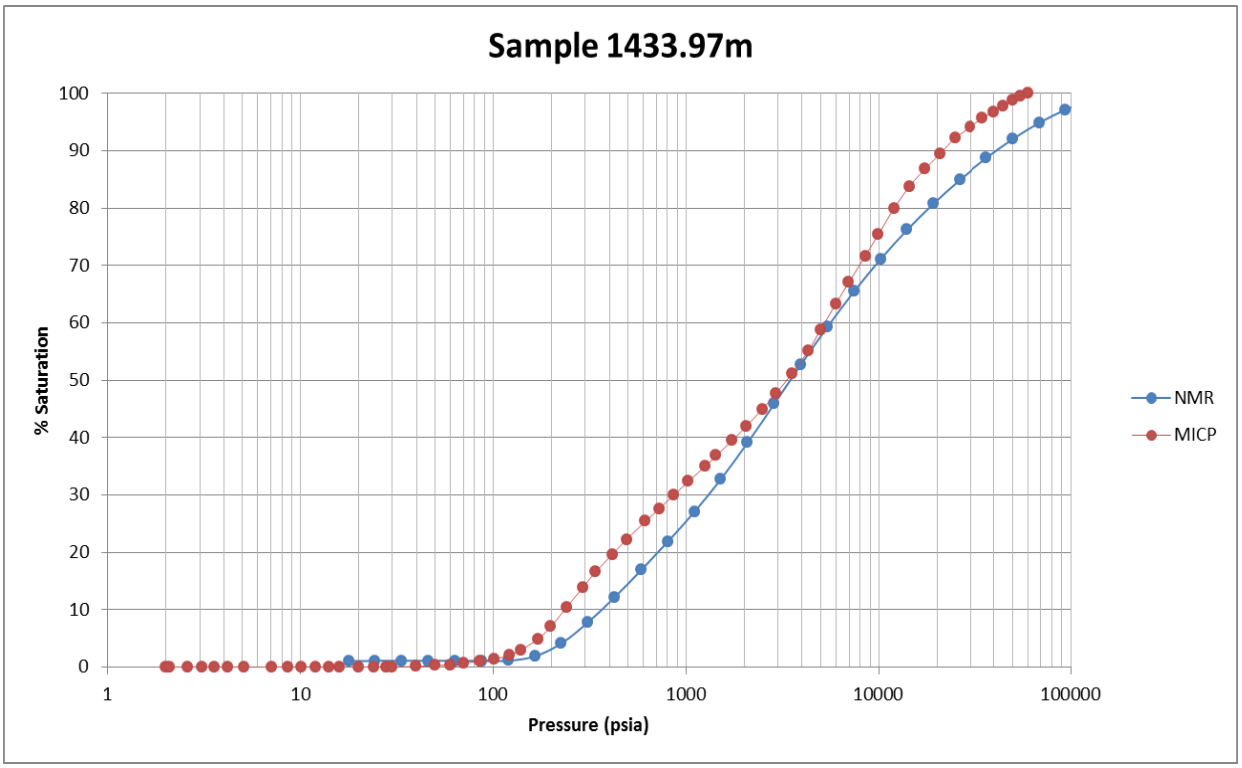

Figure E- 35: CRC-2 MICP curve from the core sample (MICP) at 1433.97 m. Also shown is the well synthetic NMR (NMR) over the same depth interval.

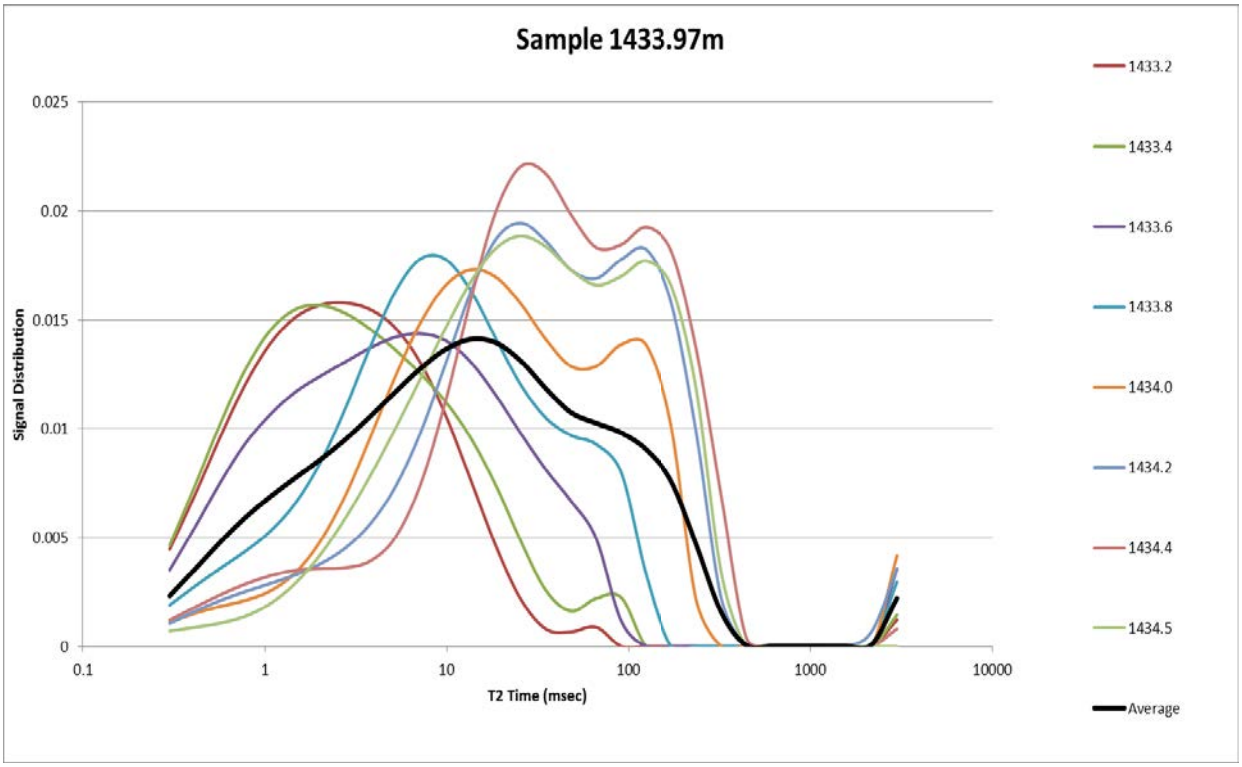

Figure E- 36: CRC-2 NMR T_2 distributions over the 1.6 m interval used to produce the well synthetic MICP curve at 1433.97 m depth.

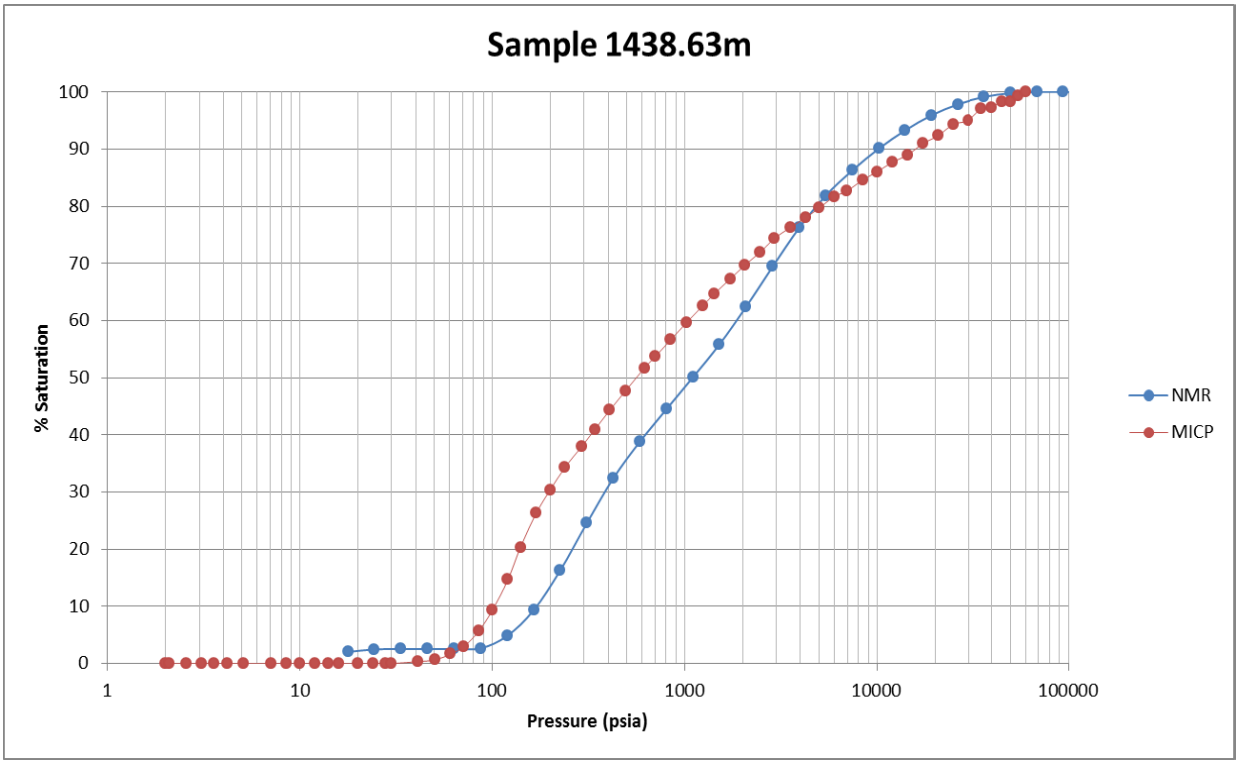

Figure E- 37: CRC-2 MICP curve from the core sample (MICP) at 1438.63 m. Also shown is the well synthetic NMR (NMR) over the same depth interval.

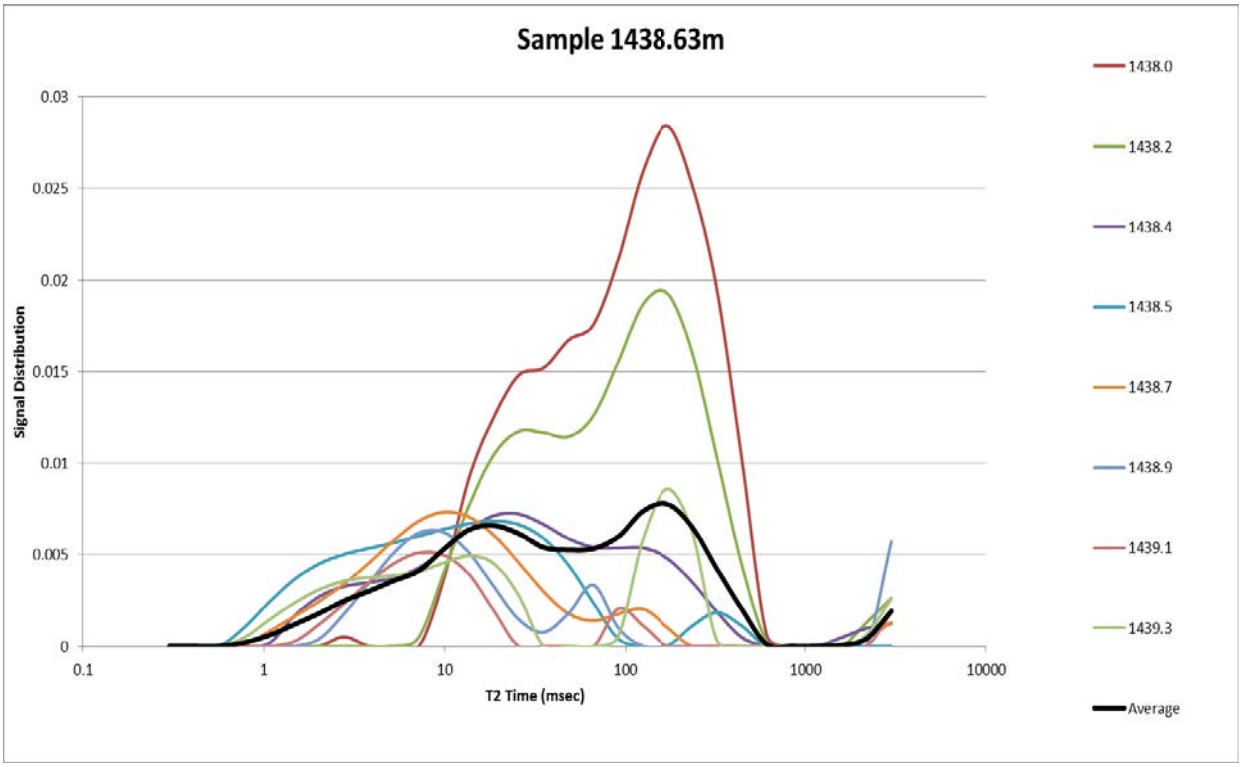

Figure E- 38: CRC-2 NMR T_2 distributions over the 1.6 m interval used to produce the well synthetic MICP curve at 1438.63m depth.

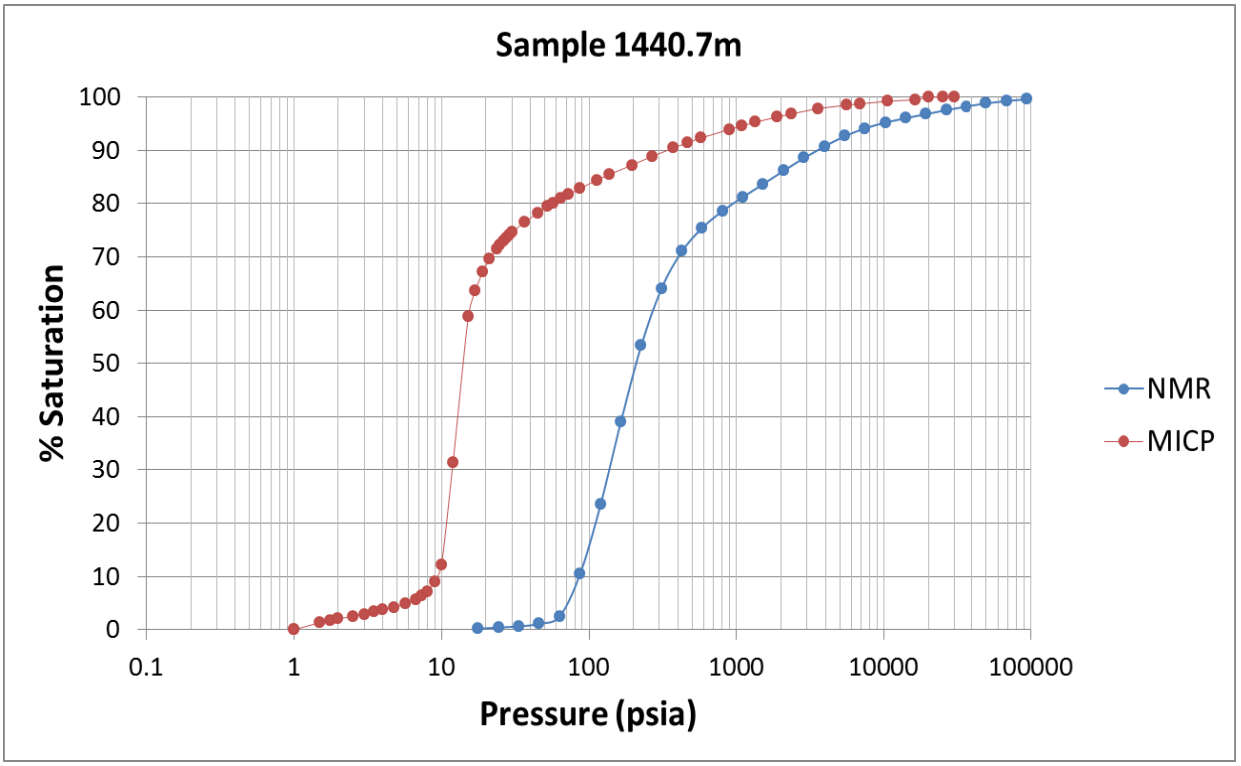

Figure E- 39: CRC-2 MICP curve from the core sample (MICP) at 1440.7 m. Also shown is the well synthetic NMR (NMR) over the same depth interval.

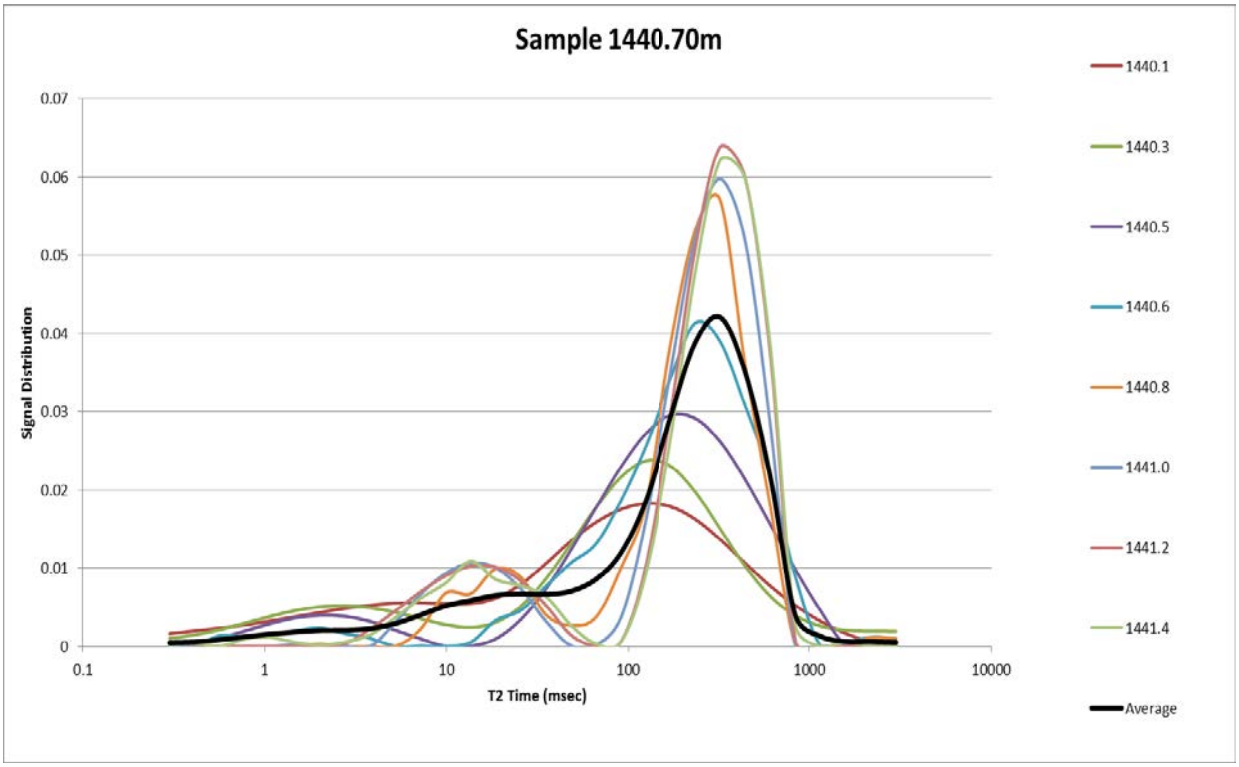

Figure E- 40: CRC-2 NMR T_2 distributions over the 1.6 m interval used to produce the well synthetic MICP curve at 1440.7 m depth.

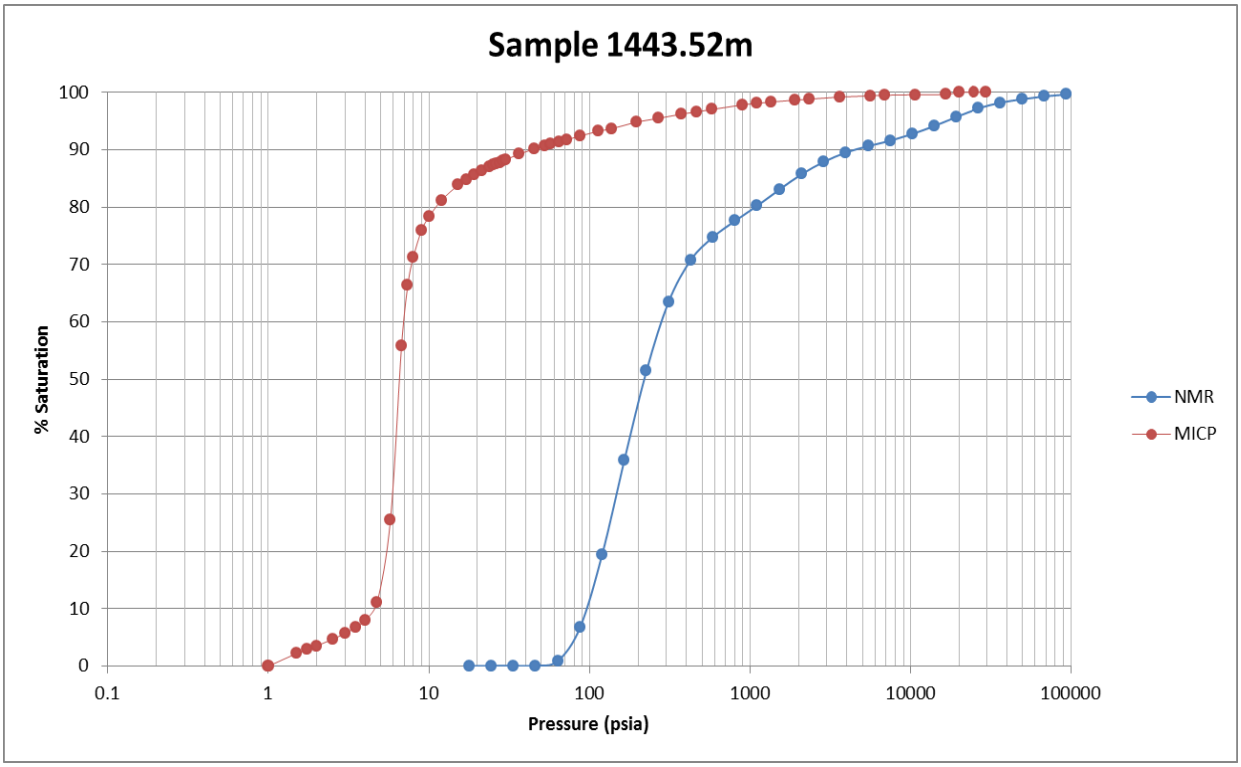

Figure E- 41: CRC-2 MICP curve from the core sample (MICP) at 1443.52 m. Also shown is the well synthetic NMR (NMR) over the same depth interval.

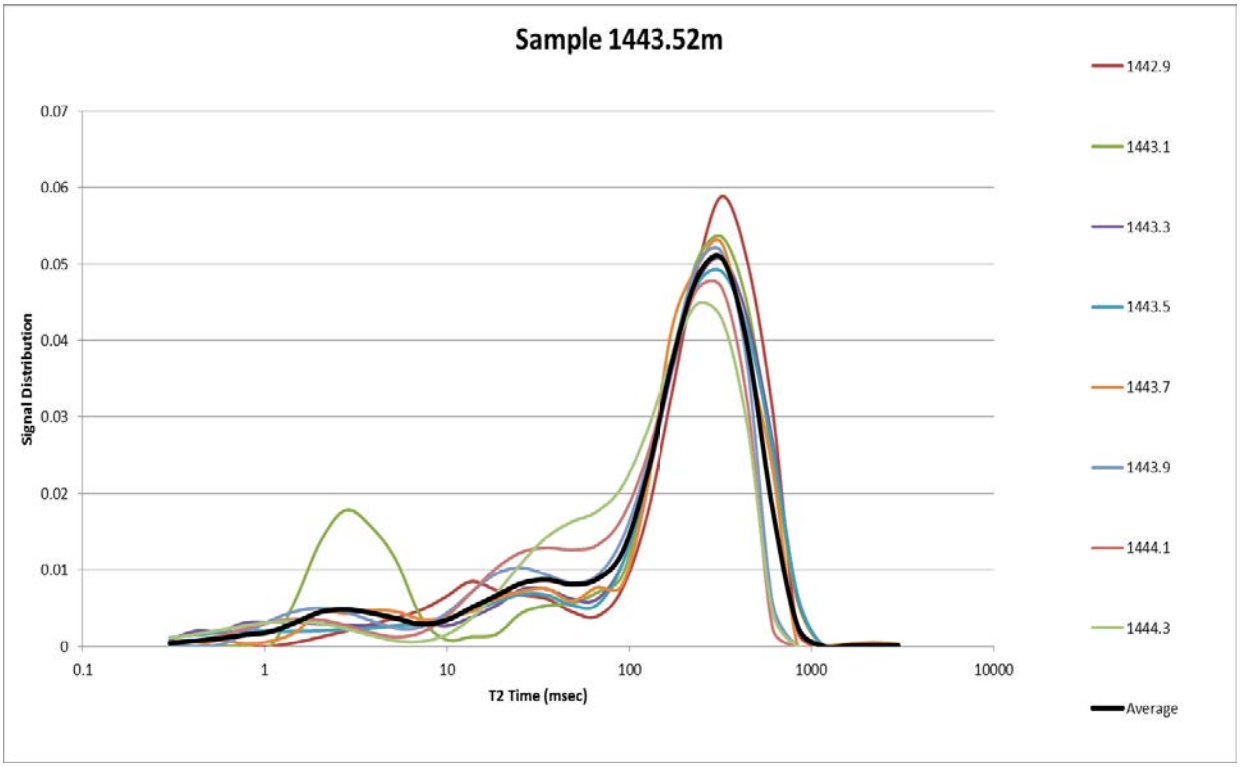

Figure E- 42: CRC-2 NMR T_2 distributions over the 1.6 m interval used to produce the well synthetic MICP curve at 1443.52 m depth.

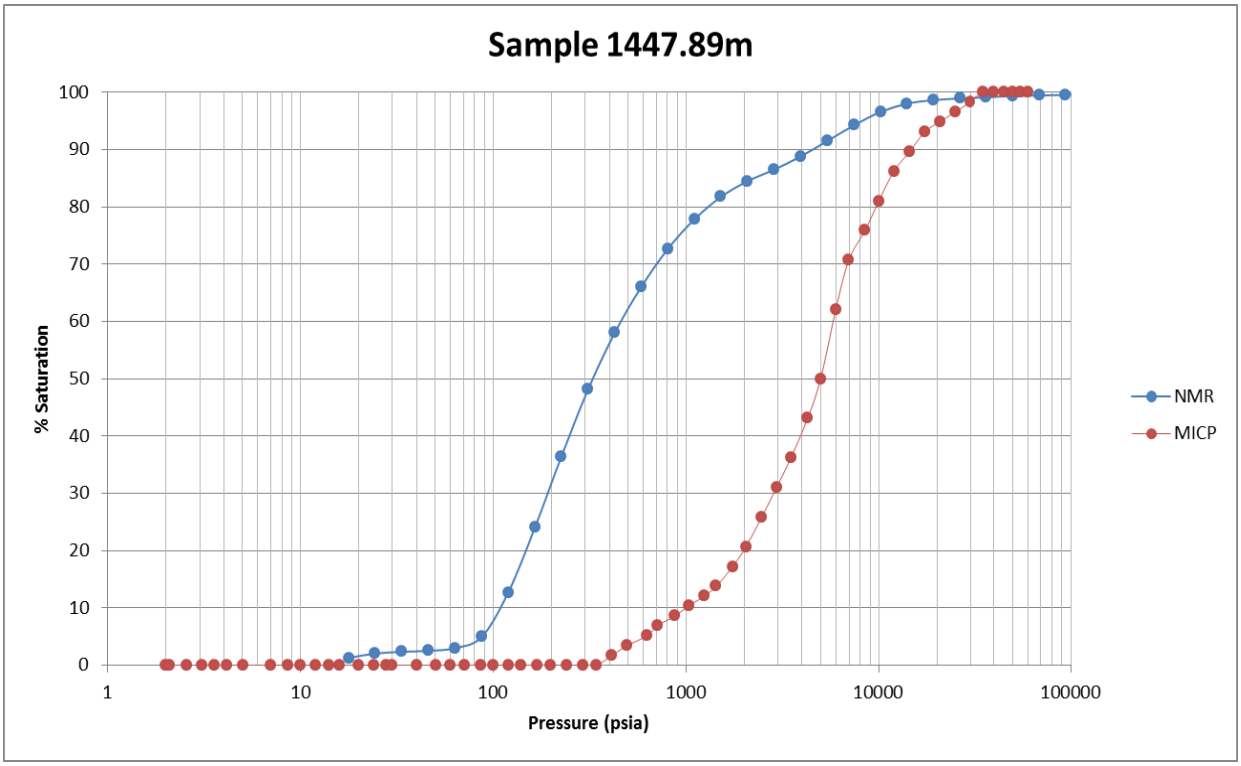

Figure E- 43: CRC-2 MICP curve from the core sample (MICP) at 1447.89 m. Also shown is the well synthetic NMR (NMR) over the same depth interval.

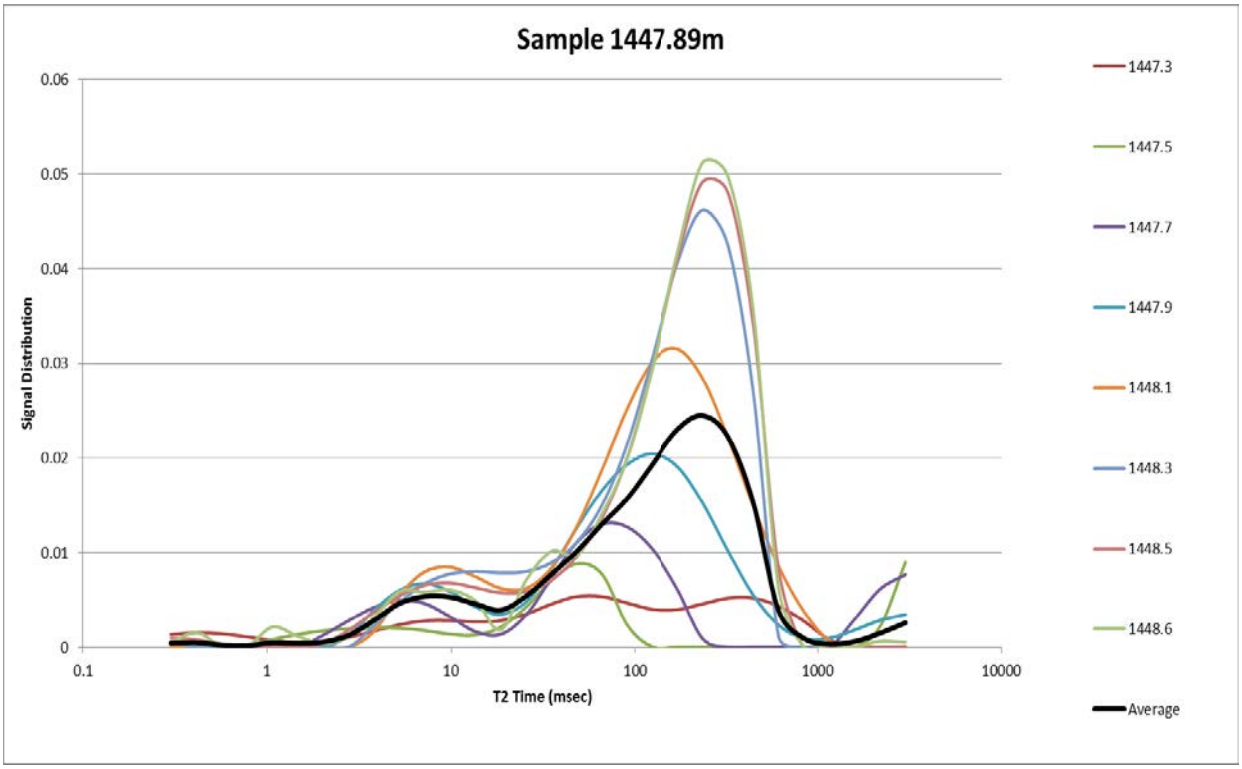

Figure E- 44: CRC-2 NMR T_2 distributions over the 1.6 m interval used to produce the well synthetic MICP curve at 1447.89 m depth.

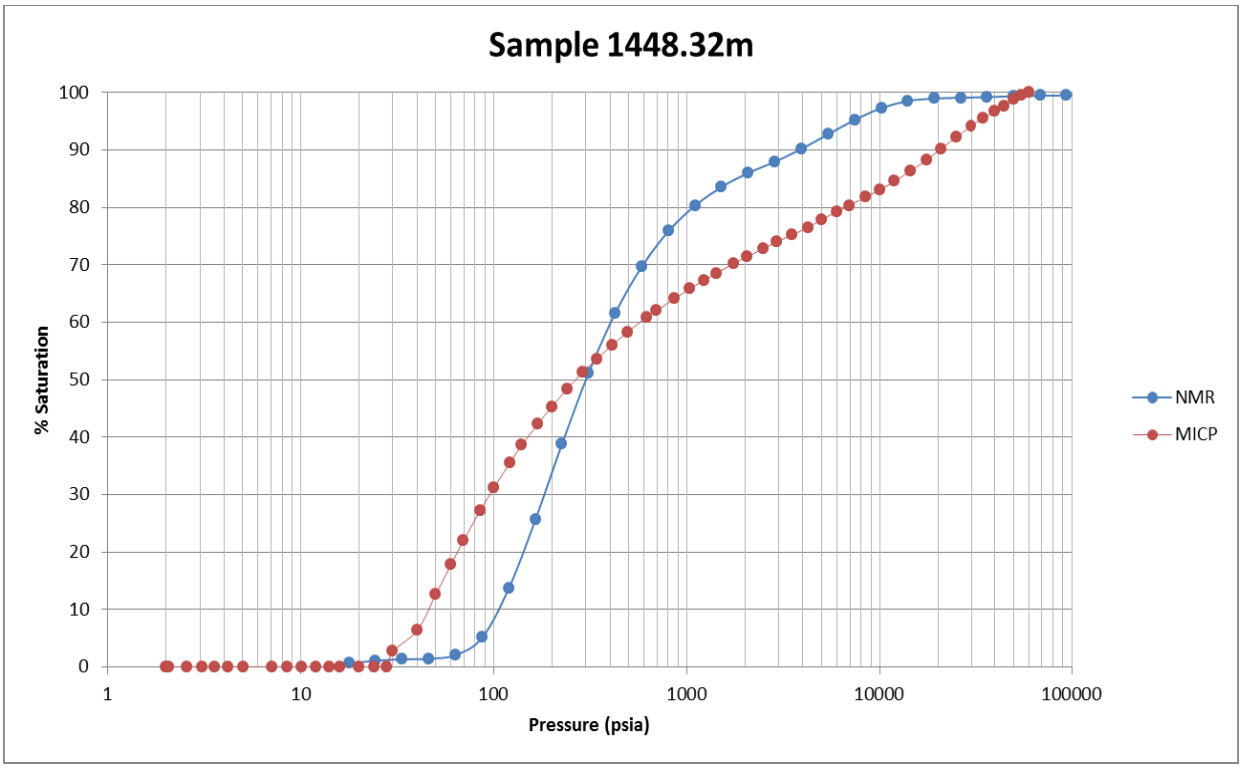

Figure E- 45: CRC-2 MICP curve from the core sample (MICP) at 1448.32 m. Also shown is the well synthetic NMR (NMR) over the same depth interval.

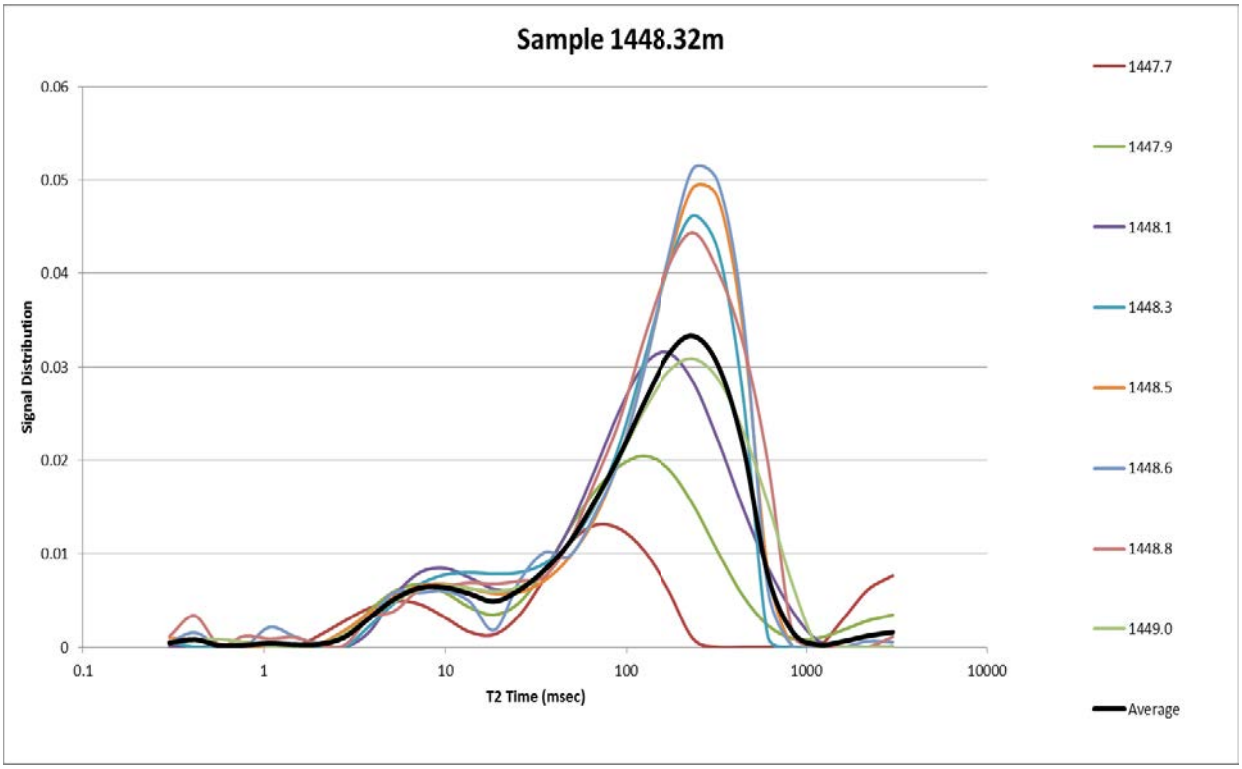

Figure E- 46: CRC-2 NMR T_2 distributions over the 1.6 m interval used to produce the well synthetic MICP curve at 1448.32 m depth.

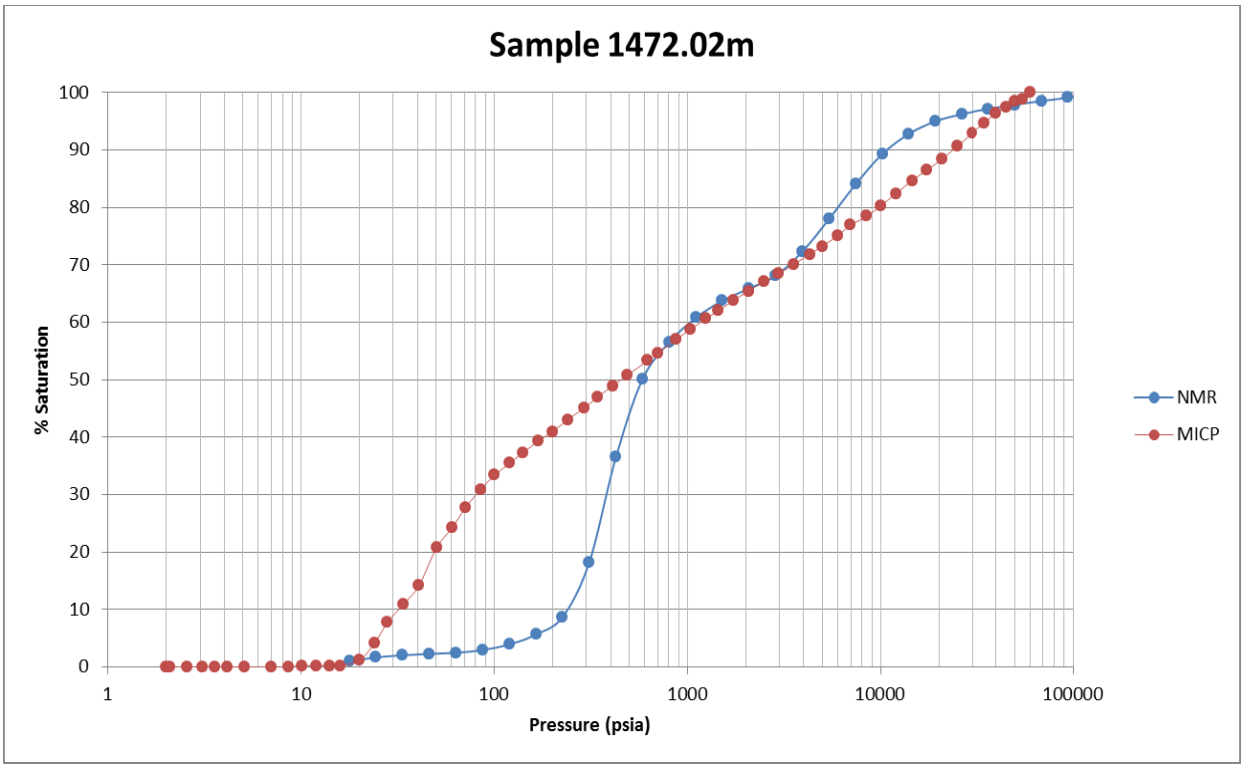

Figure E- 47: CRC-2 MICP curve from the core sample (MICP) at 1472.02 m. Also shown is the well synthetic NMR (NMR) over the same depth interval.

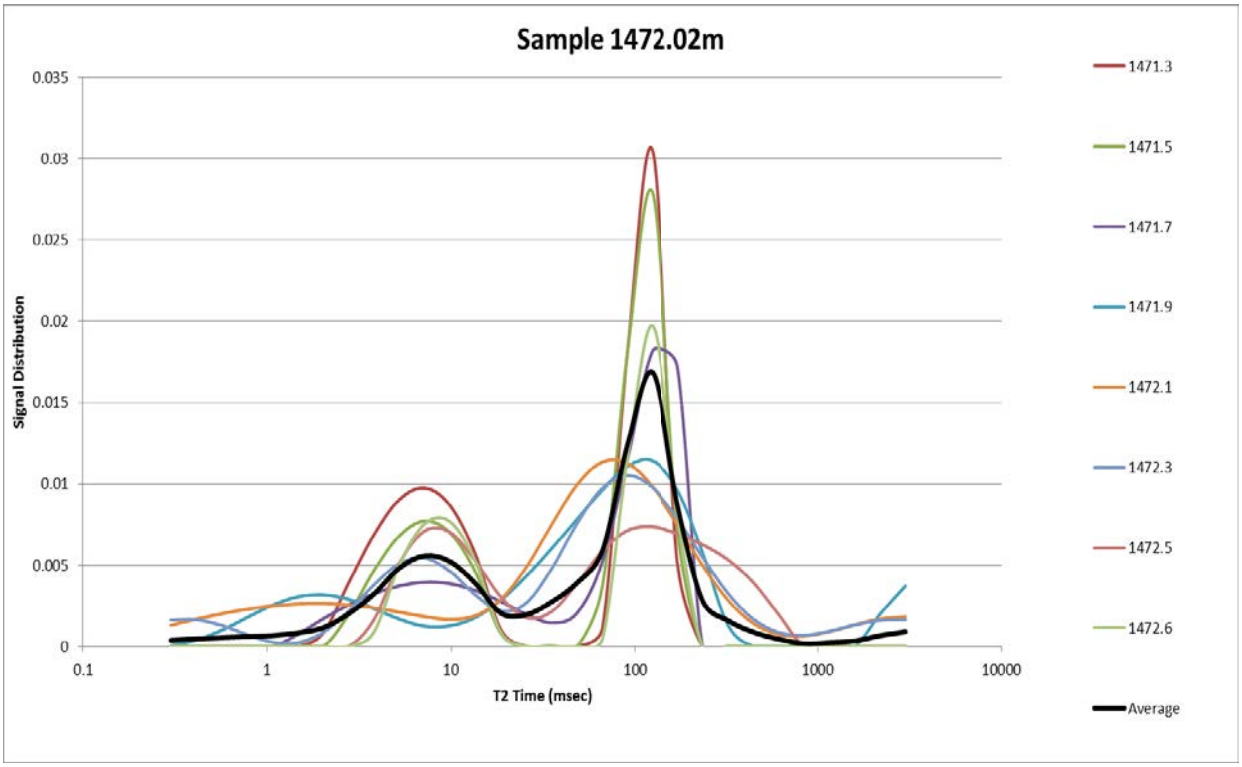

Figure E- 48: CRC-2 NMR T_2 distributions over the 1.6 m interval used to produce the well synthetic MICP curve at 1472.02 m depth.

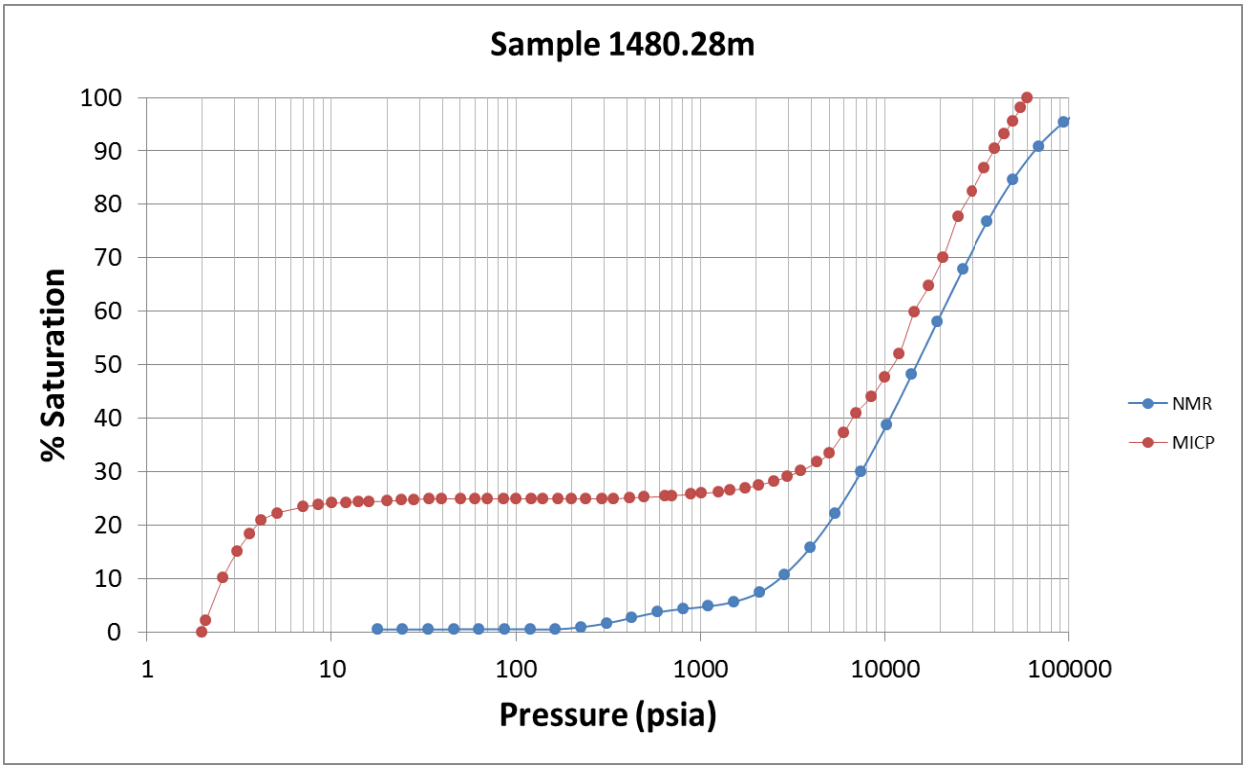

Figure E- 49: CRC-2 MICP curve from the core sample (MICP) at 1480.28 m. Also shown is the well synthetic NMR (NMR) over the same depth interval.

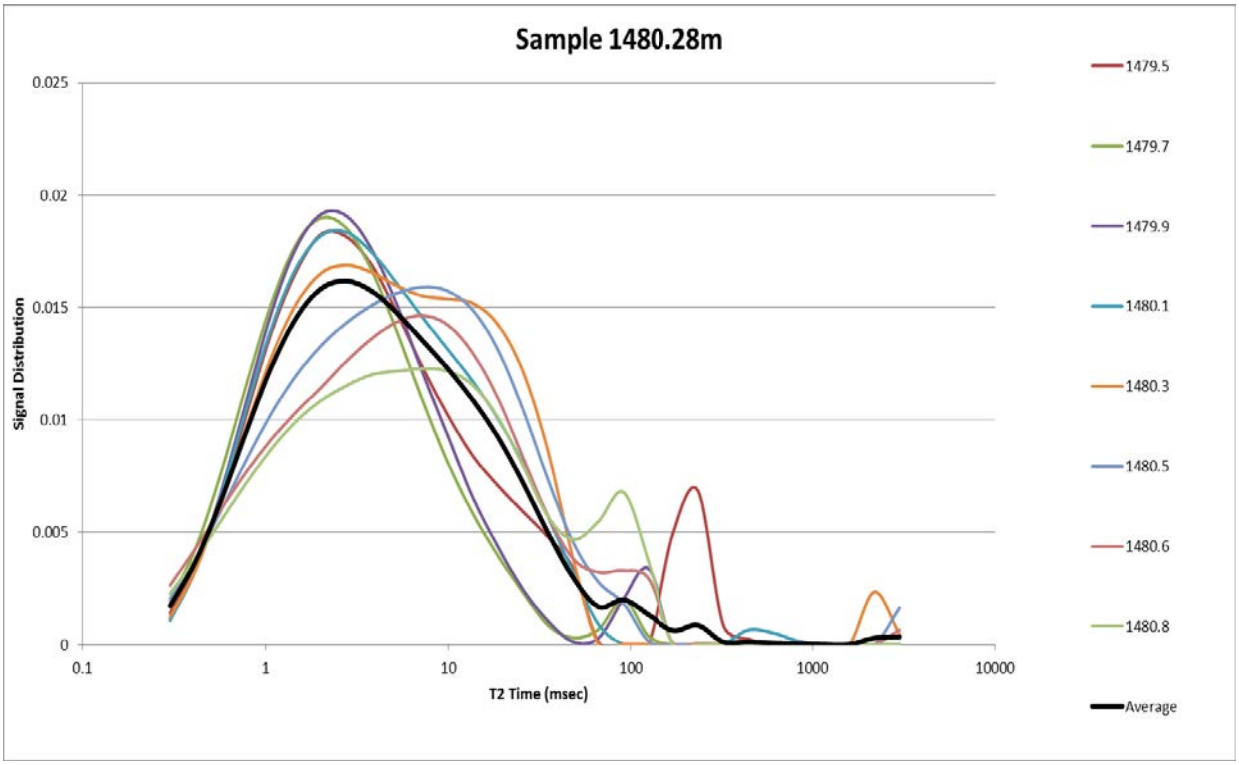

Figure E- 50: CRC-2 NMR T_2 distributions over the 1.6 m interval used to produce the well synthetic MICP curve at 1480.28 m depth.

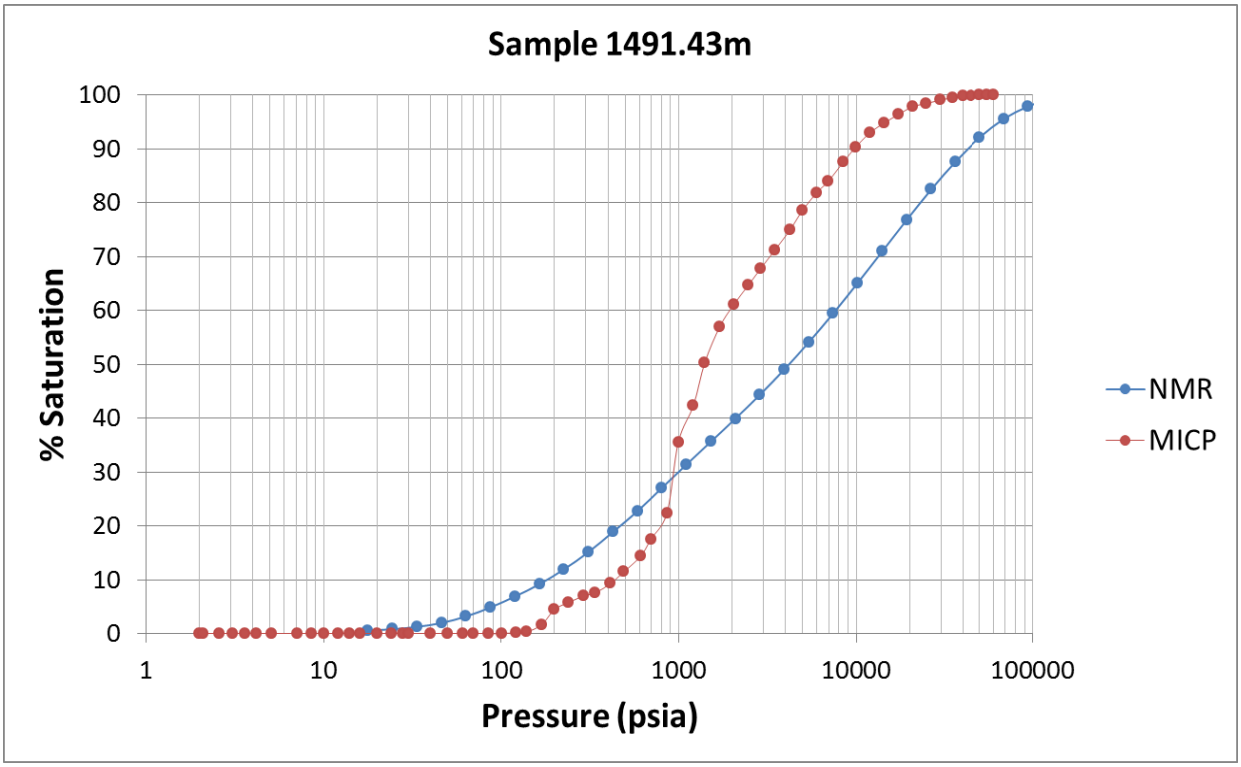

Figure E- 51: CRC-2 MICP curve from the core sample (MICP) at 1491.43 m. Also shown is the well synthetic NMR (NMR) over the same depth interval.

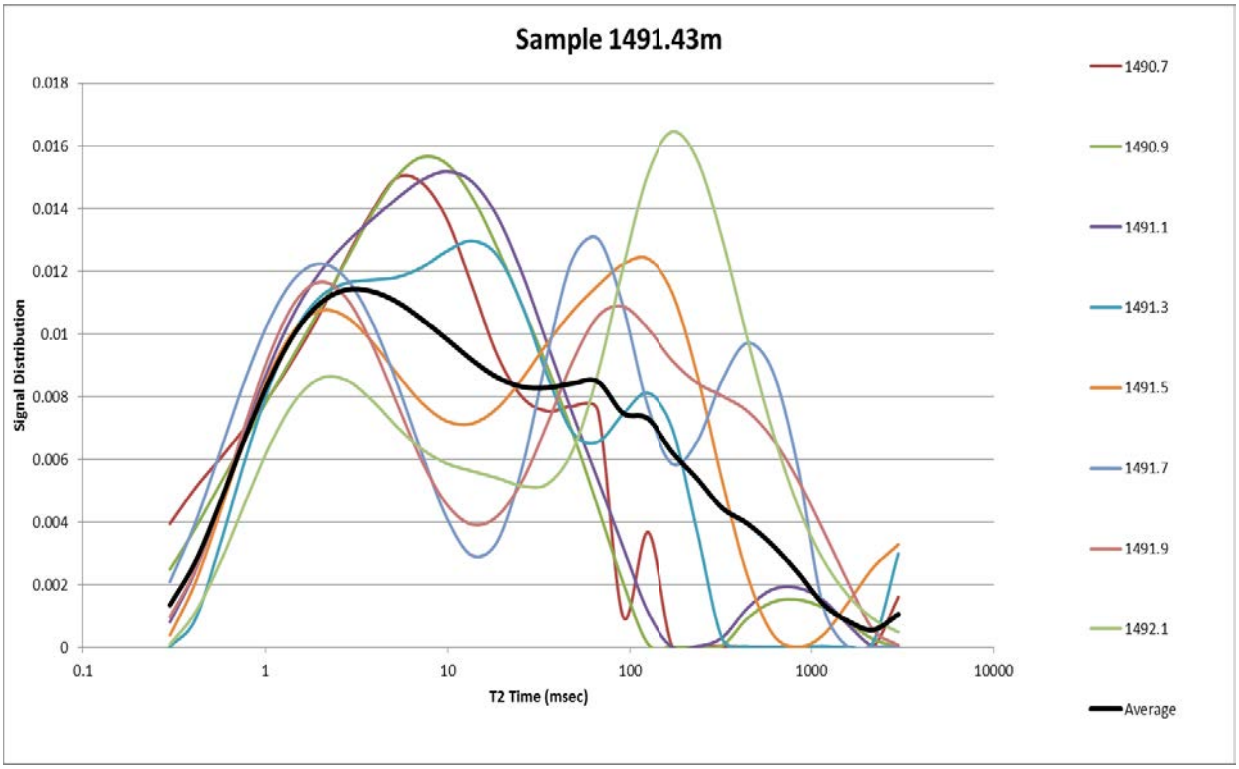

Figure E- 52: CRC-2 NMR T_2 distributions over the 1.6 m interval used to produce the well synthetic MICP curve at 1491.43 m depth.

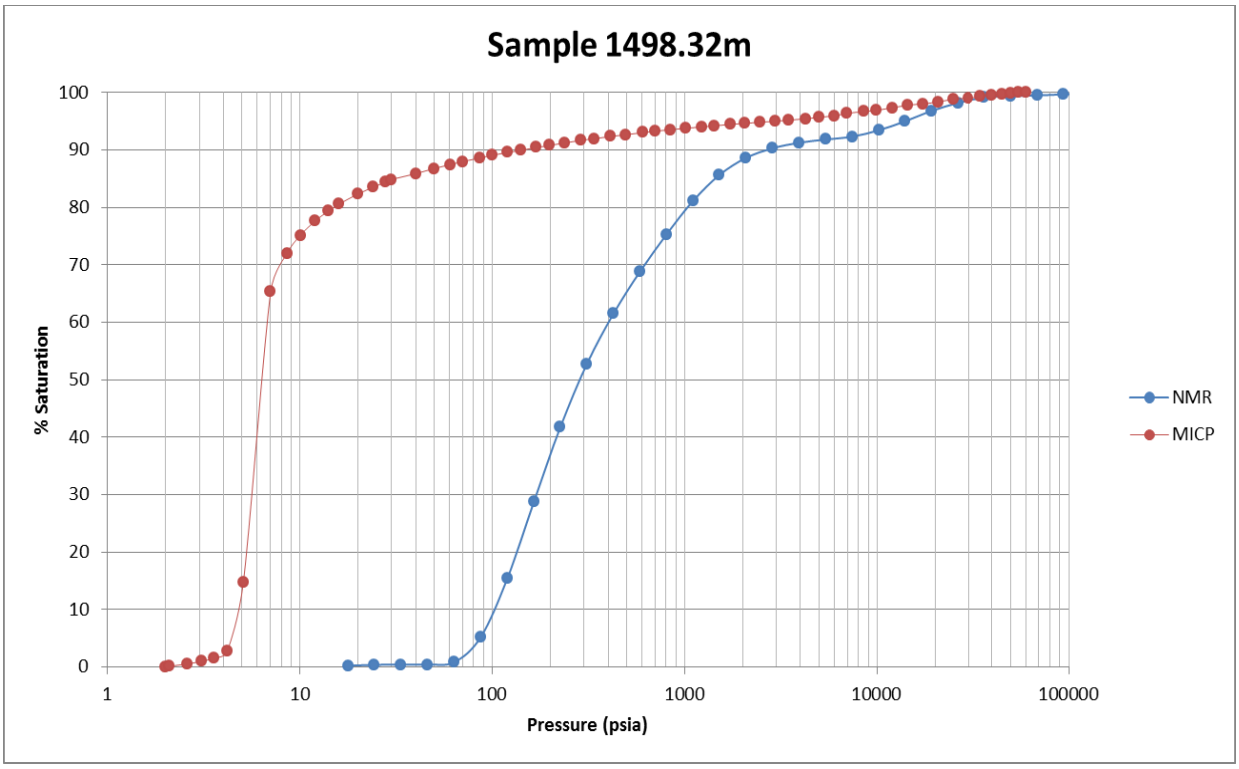

Figure E- 53: CRC-2 MICP curve from the core sample (MICP) at 1498.32 m. Also shown is the well synthetic NMR (NMR) over the same depth interval.

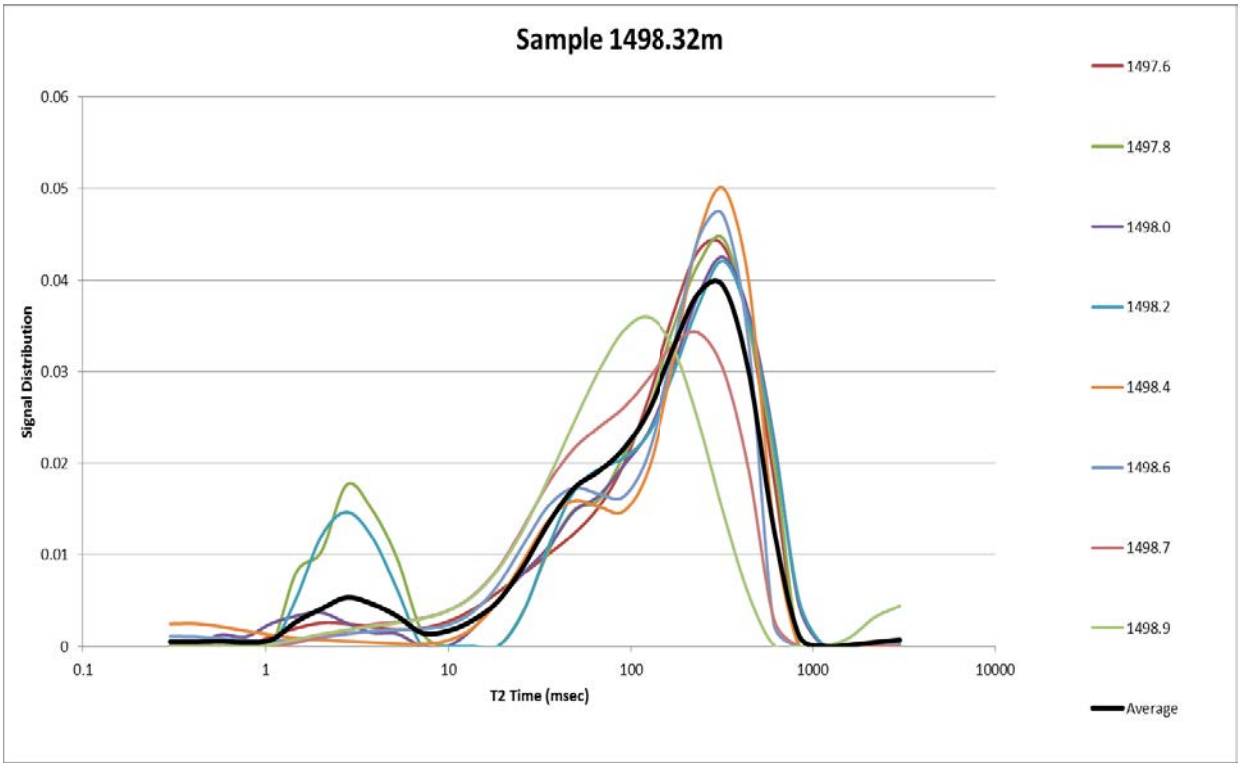

Figure E- 54: CRC-2 NMR T_2 distributions over the 1.6 m interval used to produce the well synthetic MICP curve at 1498.32 m depth.

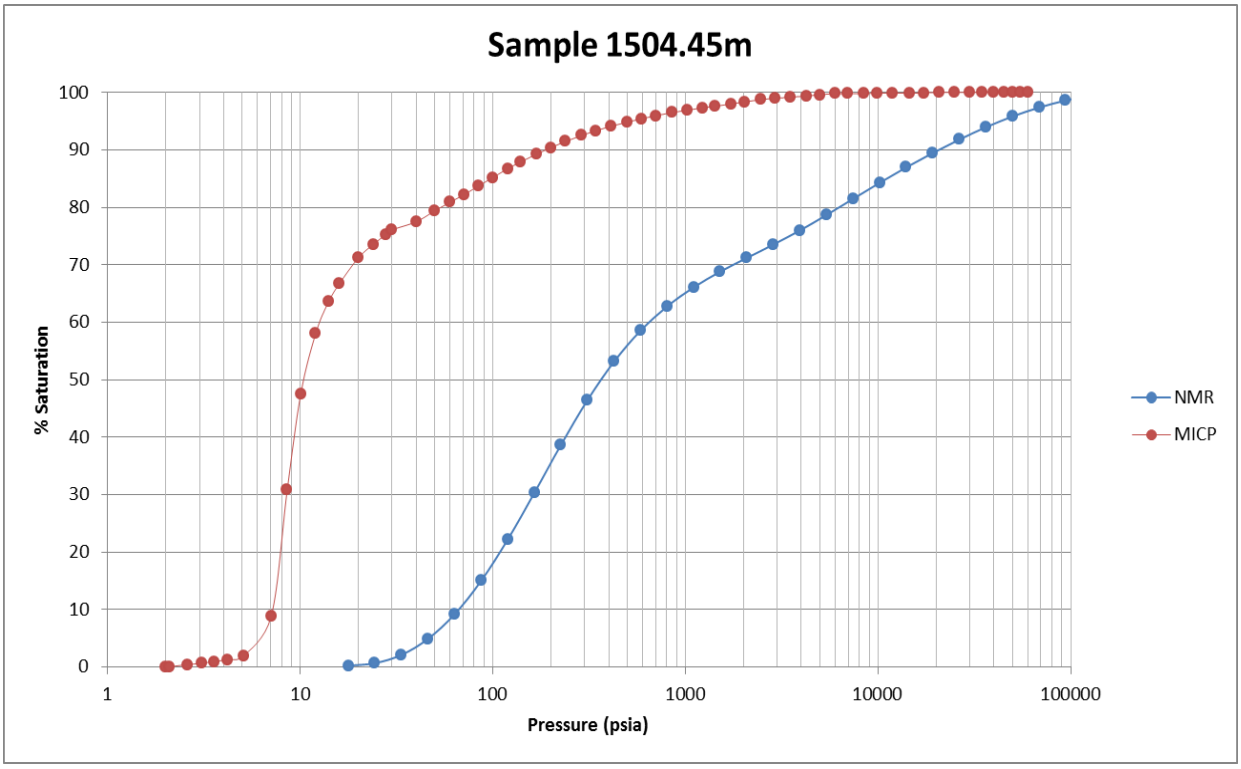

Figure E- 55: CRC-2 MICP curve from the core sample (MICP) at 1504.45 m. Also shown is the well synthetic NMR (NMR) over the same depth interval.

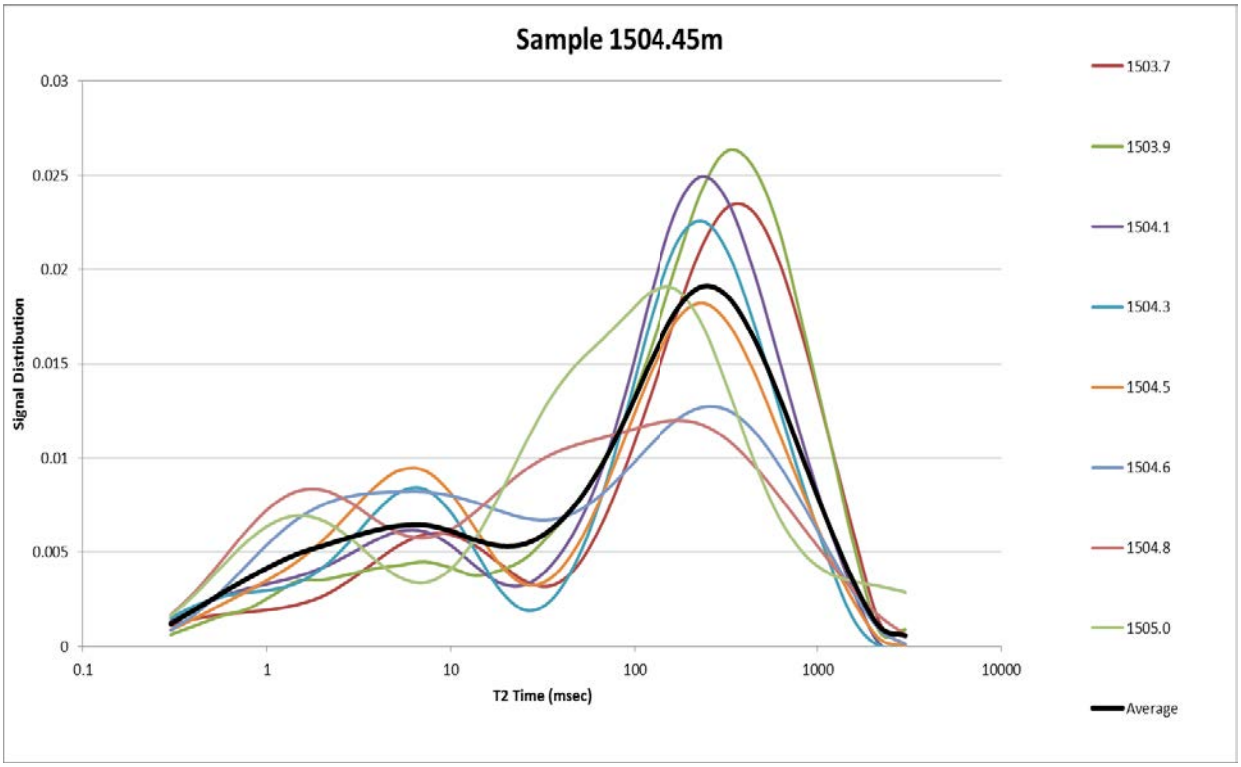

Figure E- 56: CRC-2 NMR T_2 distributions over the 1.6 m interval used to produce the well synthetic MICP curve at 1504.45 m depth.

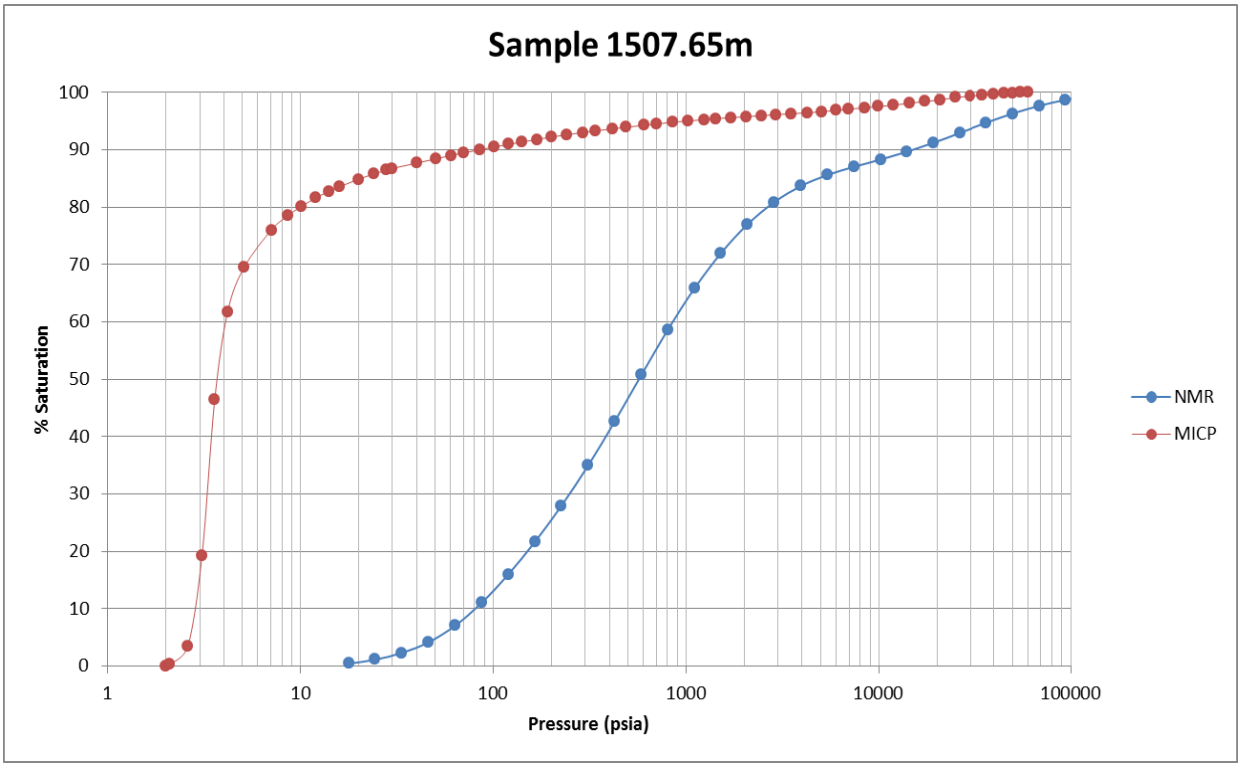

Figure E- 57: CRC-2 MICP curve from the core sample (MICP) at 1507.65 m. Also shown is the well synthetic NMR (NMR) over the same depth interval.

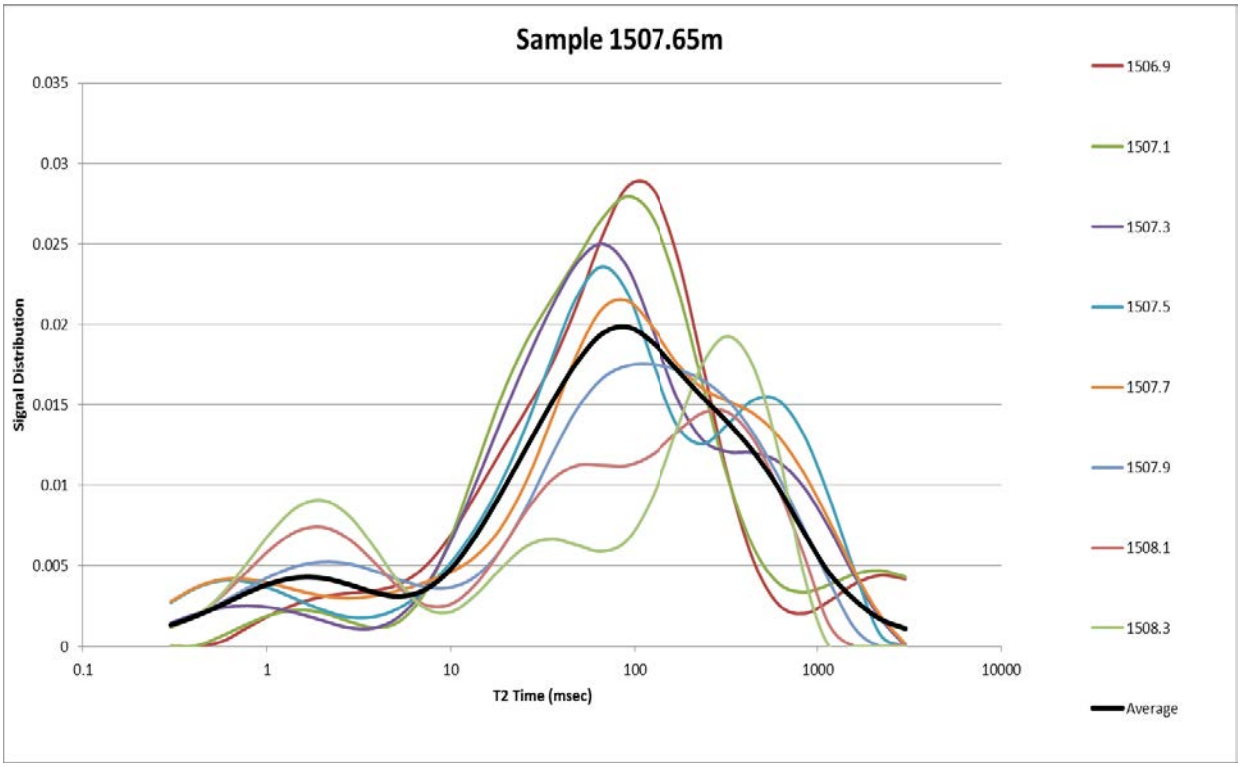

Figure E- 58: CRC-2 NMR T_2 distributions over the 1.6 m interval used to produce the well synthetic MICP curve at 1507.65 m depth.

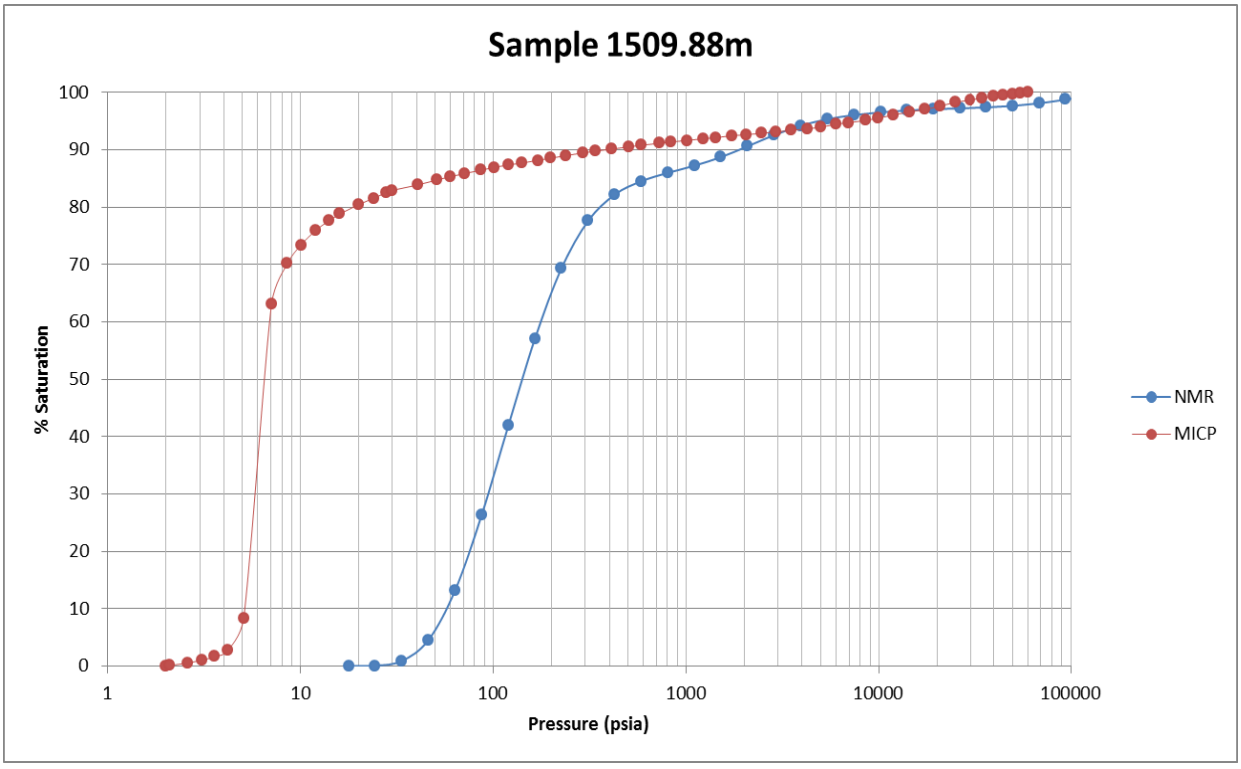

Figure E- 59: CRC-2 MICP curve from the core sample (MICP) at 1509.88 m. Also shown is the well synthetic NMR (NMR) over the same depth interval.

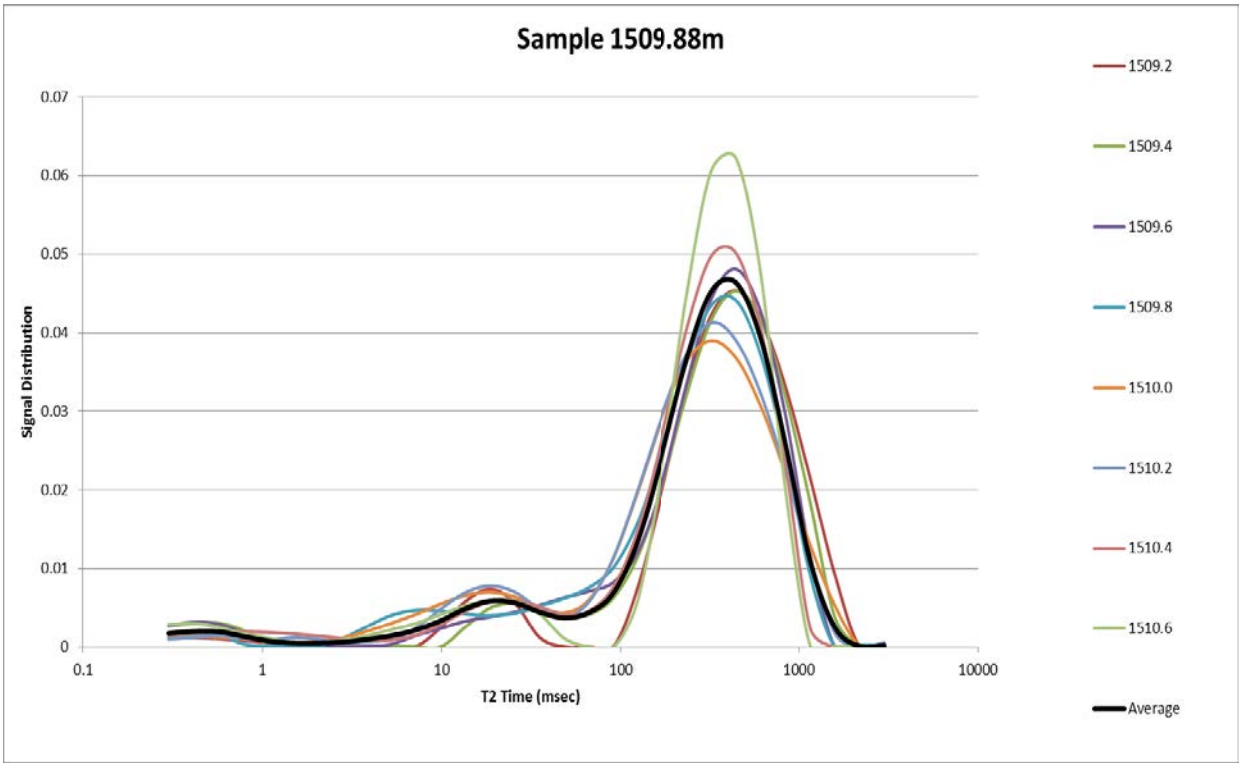

Figure E- 60: CRC-2 NMR T_2 distributions over the 1.6 m interval used to produce the well synthetic MICP curve at 1509.88 m depth.

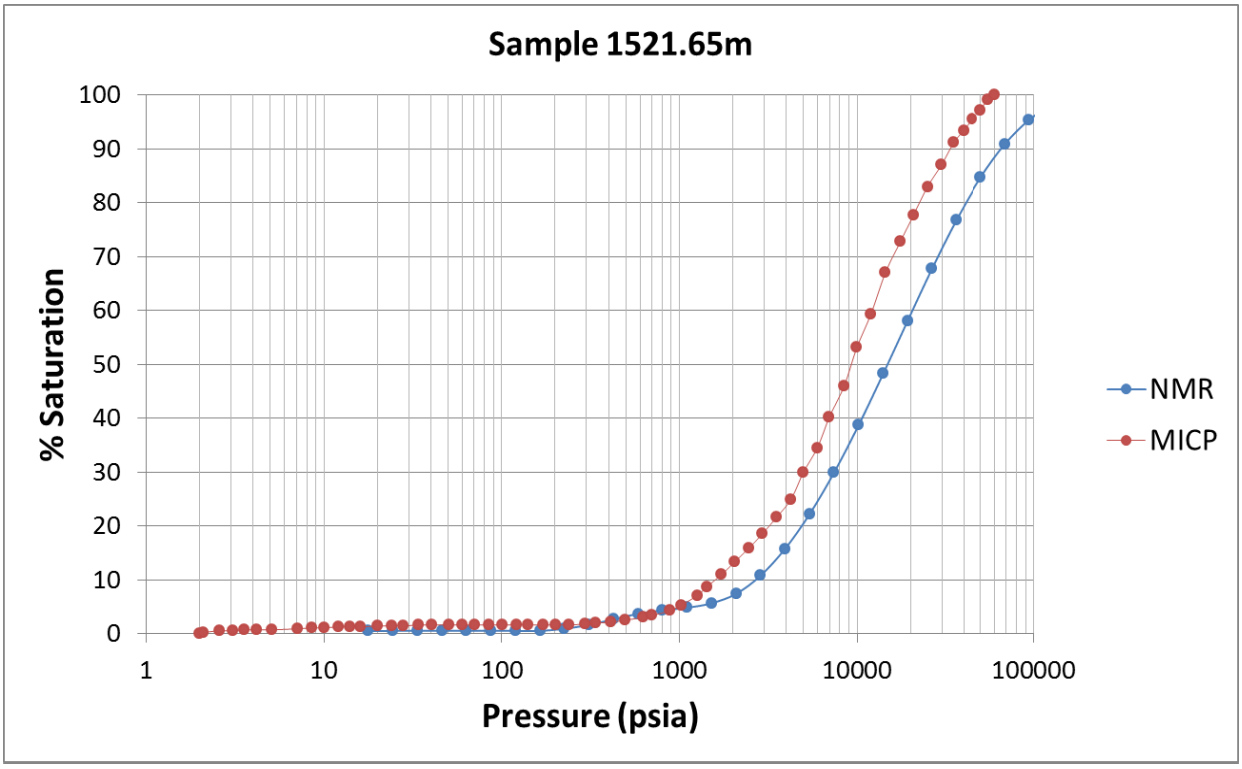

Figure E- 61: CRC-2 MICP curve from the core sample (MICP) at 1521.65 m. Also shown is the well synthetic NMR (NMR) over the same depth interval.

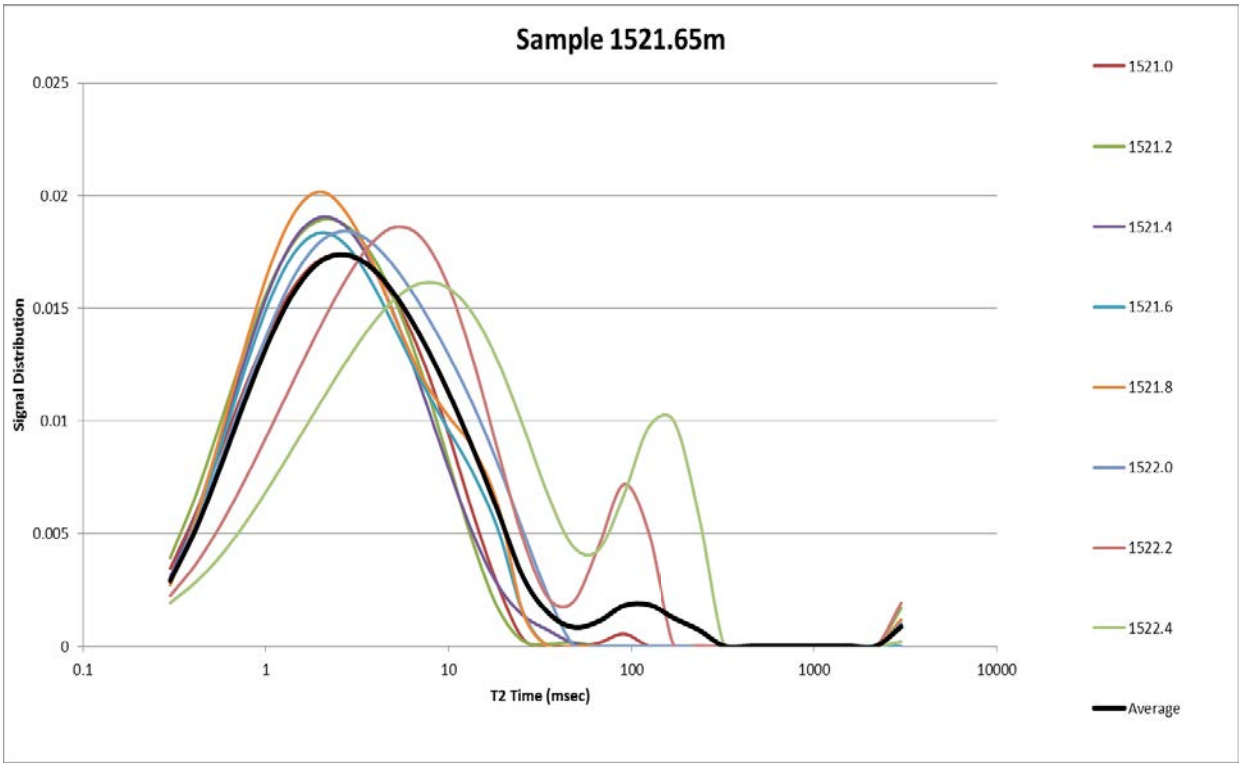

Figure E- 62: CRC-2 NMR T_2 distributions over the 1.6 m interval used to produce the well synthetic MICP curve at 1521.65 m depth.

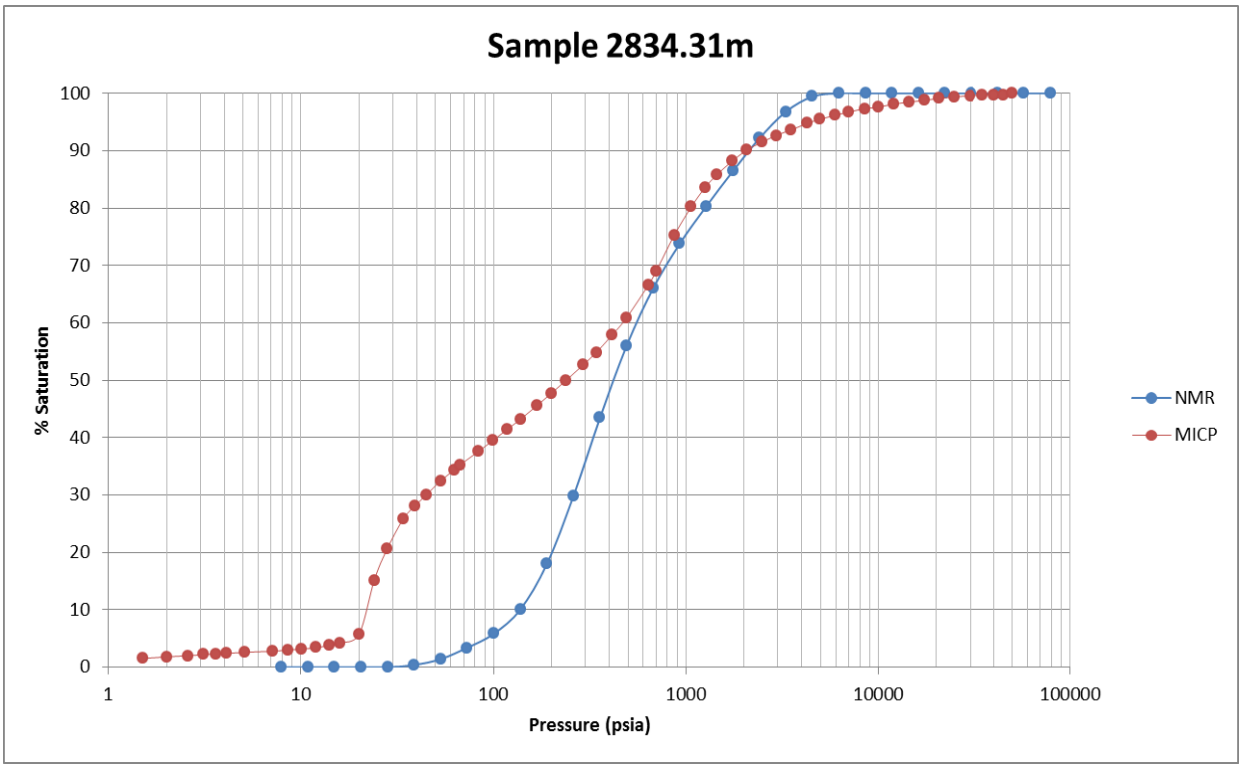

Figure E- 63: Redman-1 MICP curve from the core sample (MICP) at 2834.31 m. Also shown is the well synthetic NMR (NMR) over the same depth interval.

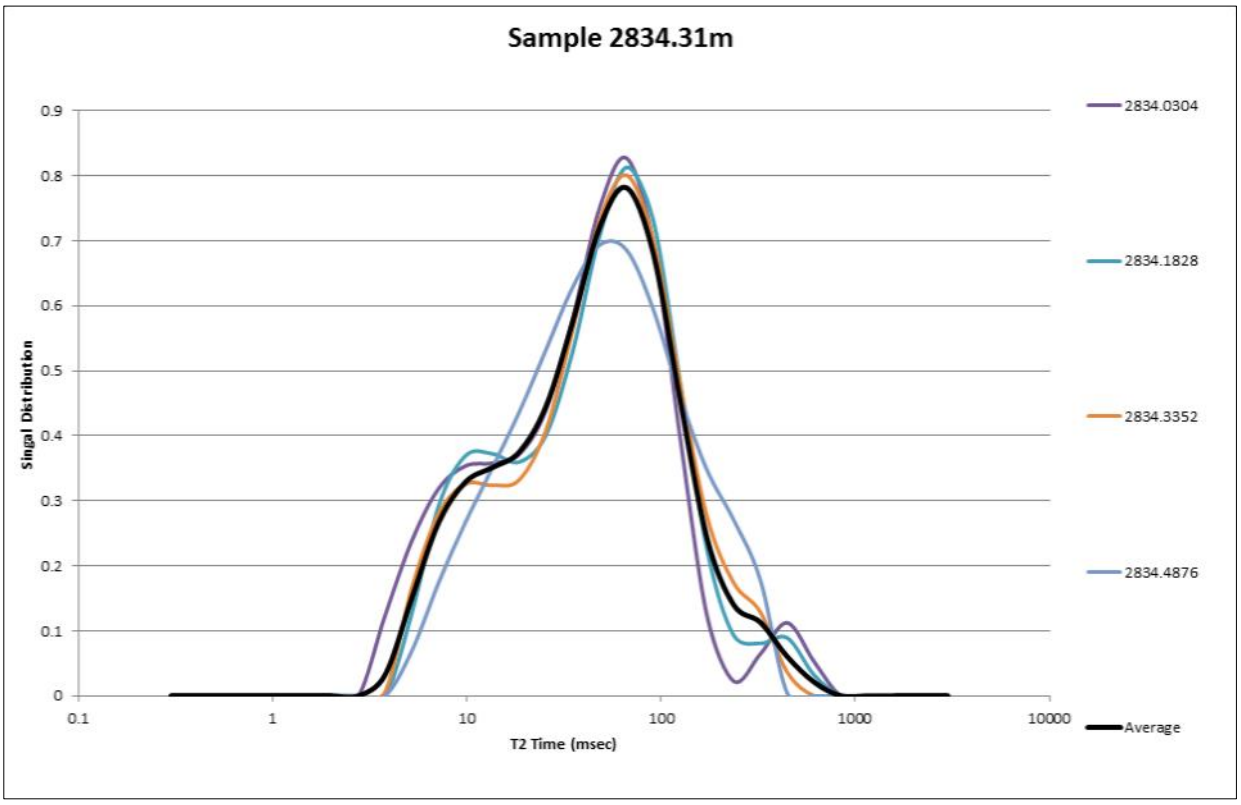

Figure E- 64: Redman-1 NMR T_2 distributions over the 80 cm interval used to produce the well synthetic MICP curve at 2834.31 m depth.

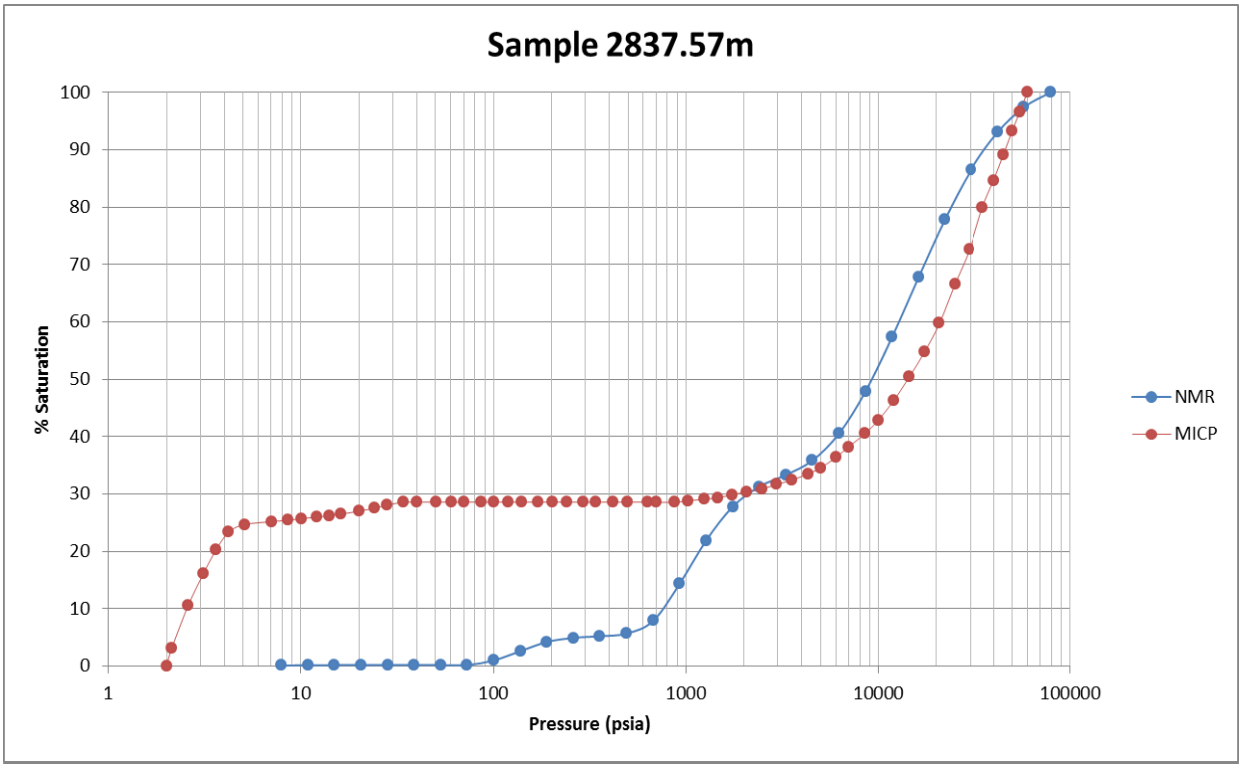

Figure E- 65: Redman-1 MICP curve from the core sample (MICP) at 2837.57 m. Also shown is the well synthetic NMR (NMR) over the same depth interval.

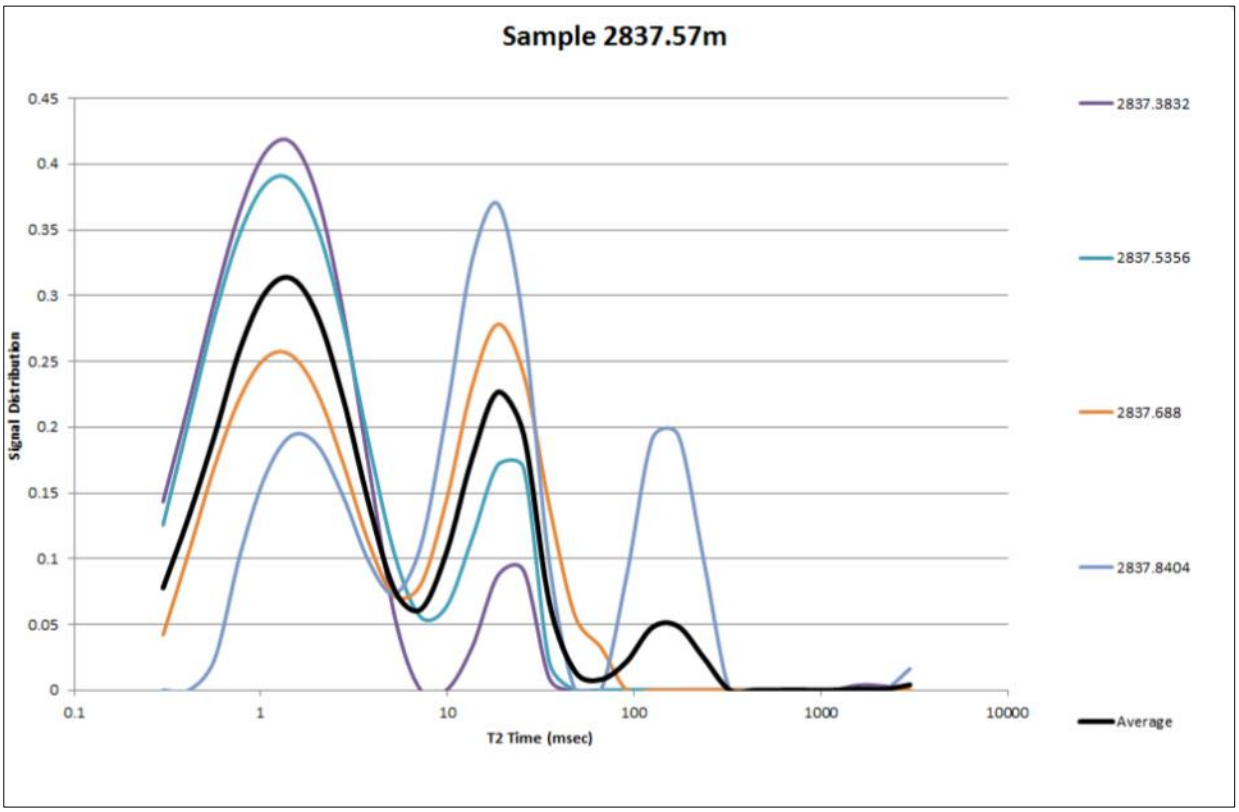

Figure E- 66: Redman-1 NMR T_2 distributions over the 80 cm interval used to produce the well synthetic MICP curve at 2837.57 m depth.

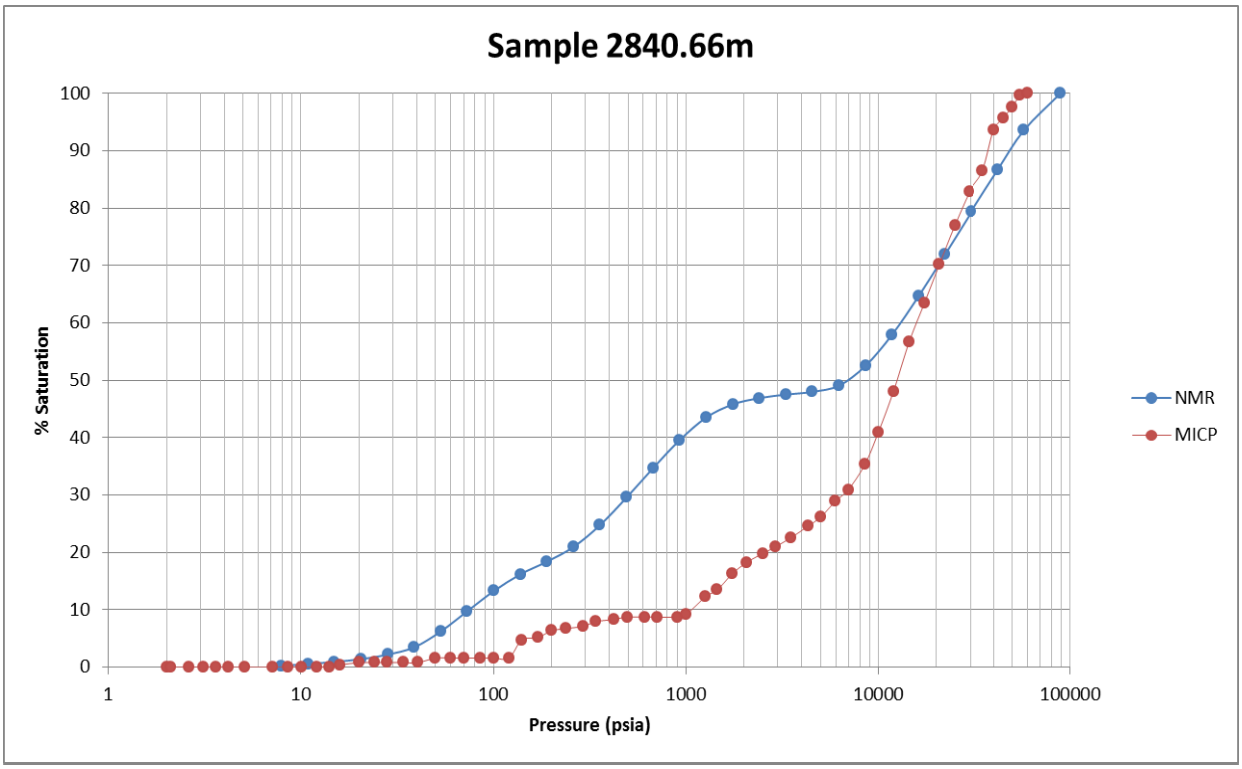

Figure E- 67: Redman-1 MICP curve from the core sample (MICP) at 2840.66 m. Also shown is the well synthetic NMR (NMR) over the same depth interval.

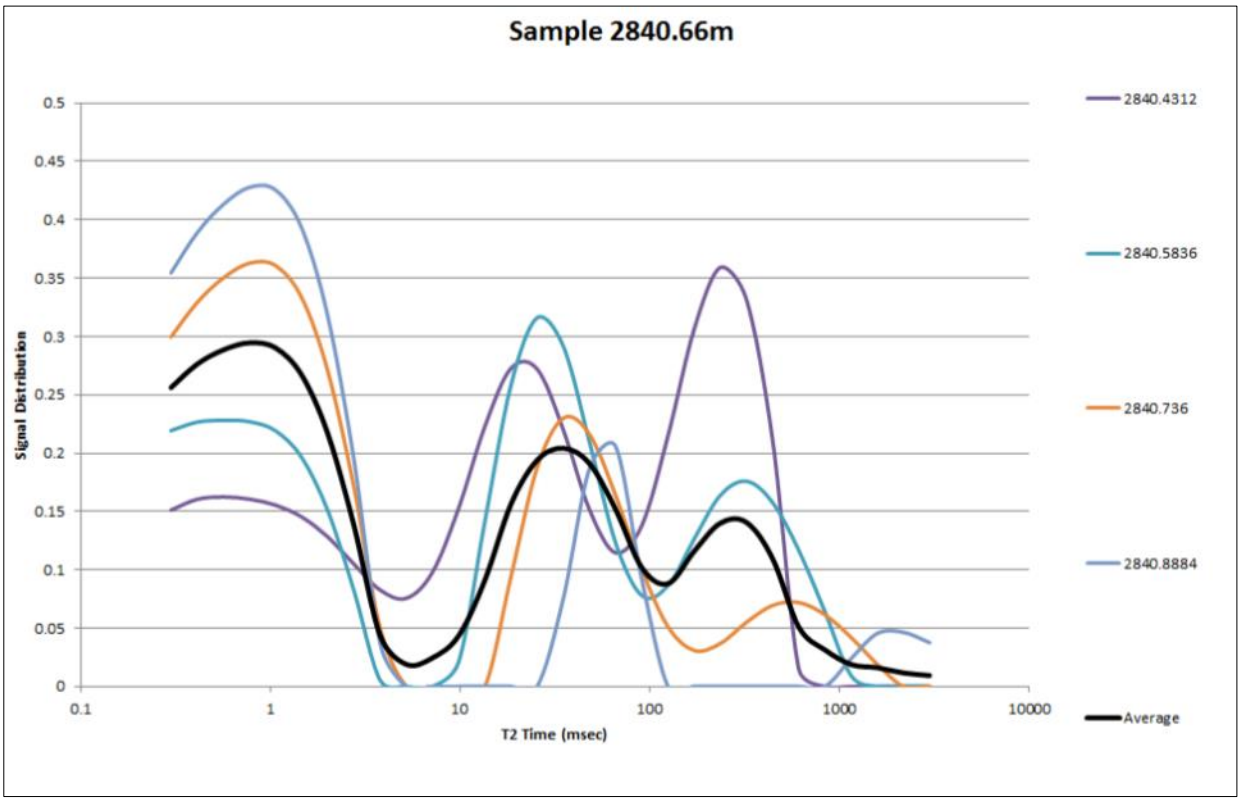

Figure E- 68: Redman-1 NMR T_2 distributions over the 80 cm interval used to produce the well synthetic MICP curve at 2840.66 m depth.

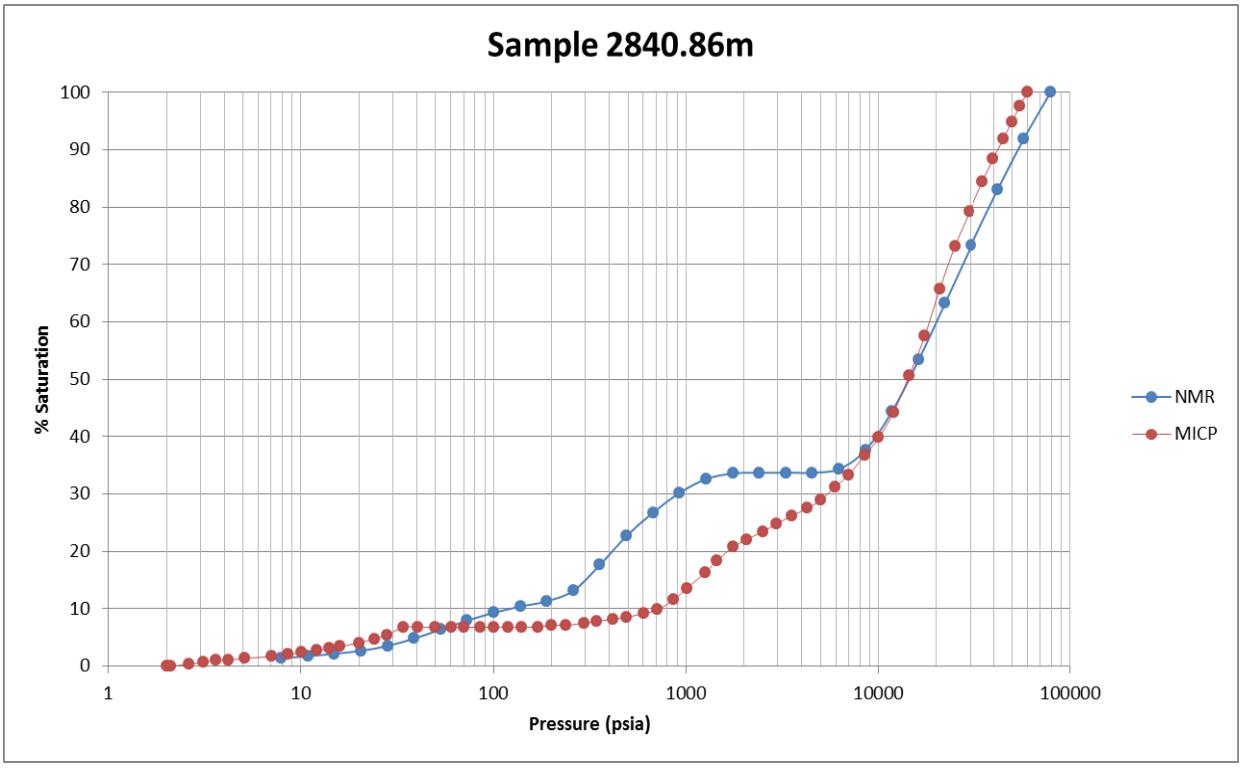

Figure E- 69: Redman-1 MICP curve from the core sample (MICP) at 2840.86 m. Also shown is the well synthetic NMR (NMR) over the same depth interval.

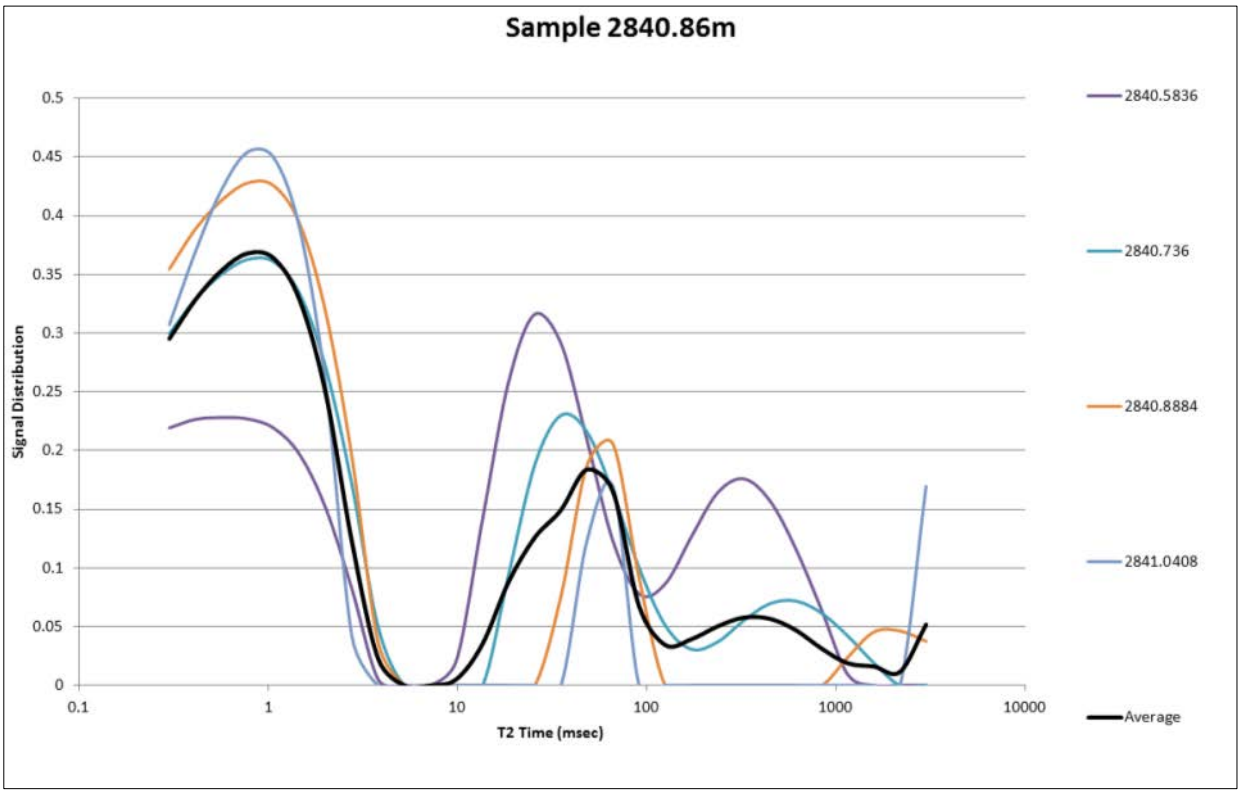

Figure E- 70: Redman-1 NMR T_2 distributions over the 80 cm interval used to produce the well synthetic MICP curve at 2840.86 m depth.

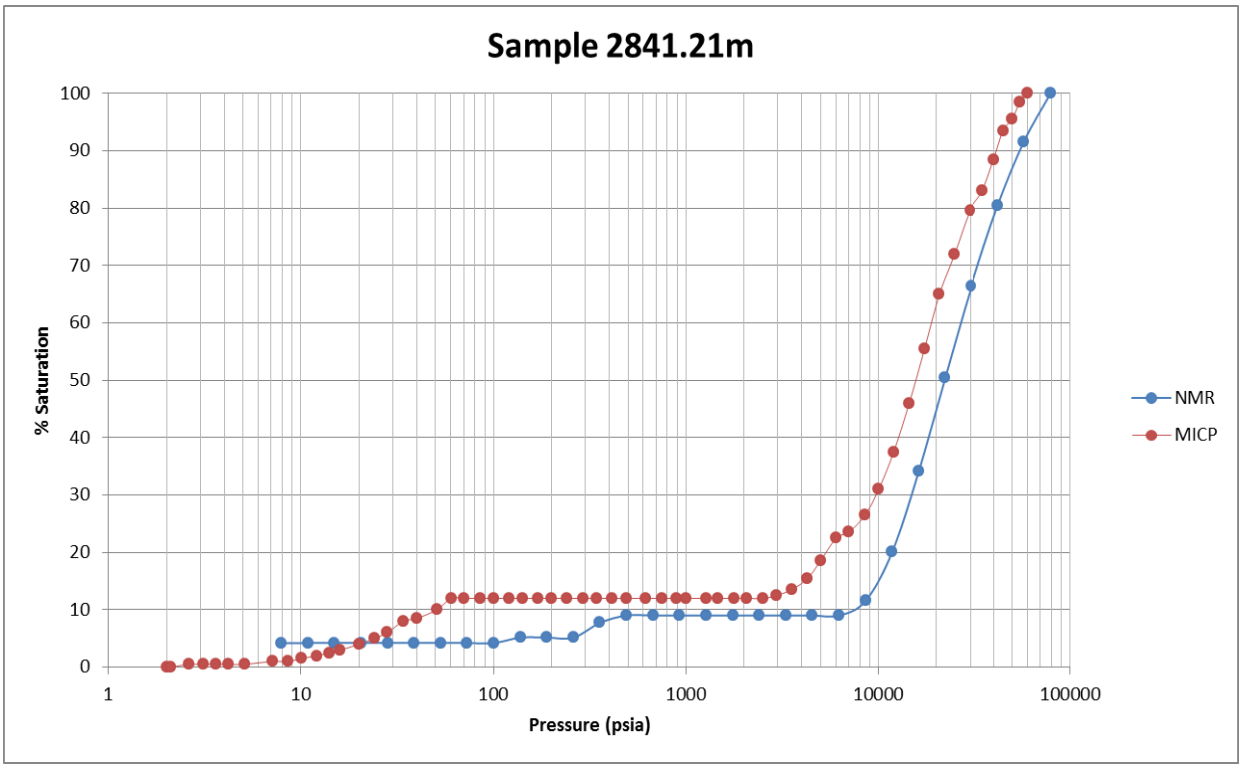

Figure E- 71: Redman-1 MICP curve from the core sample (MICP) at 2841.21 m. Also shown is the well synthetic NMR (NMR) over the same depth interval.

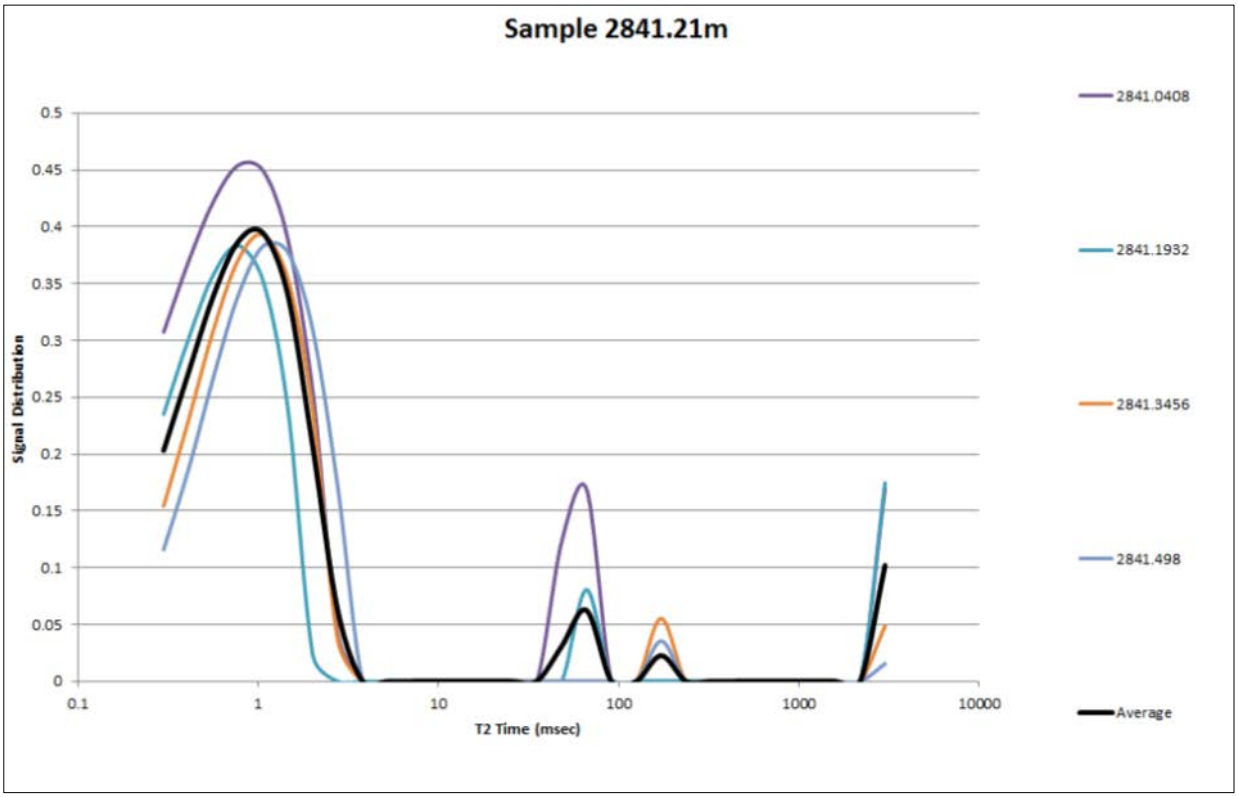

Figure E- 72: Redman-1 NMR T_2 distributions over the 80 cm interval used to produce the well synthetic MICP curve at 2841.21 m depth.

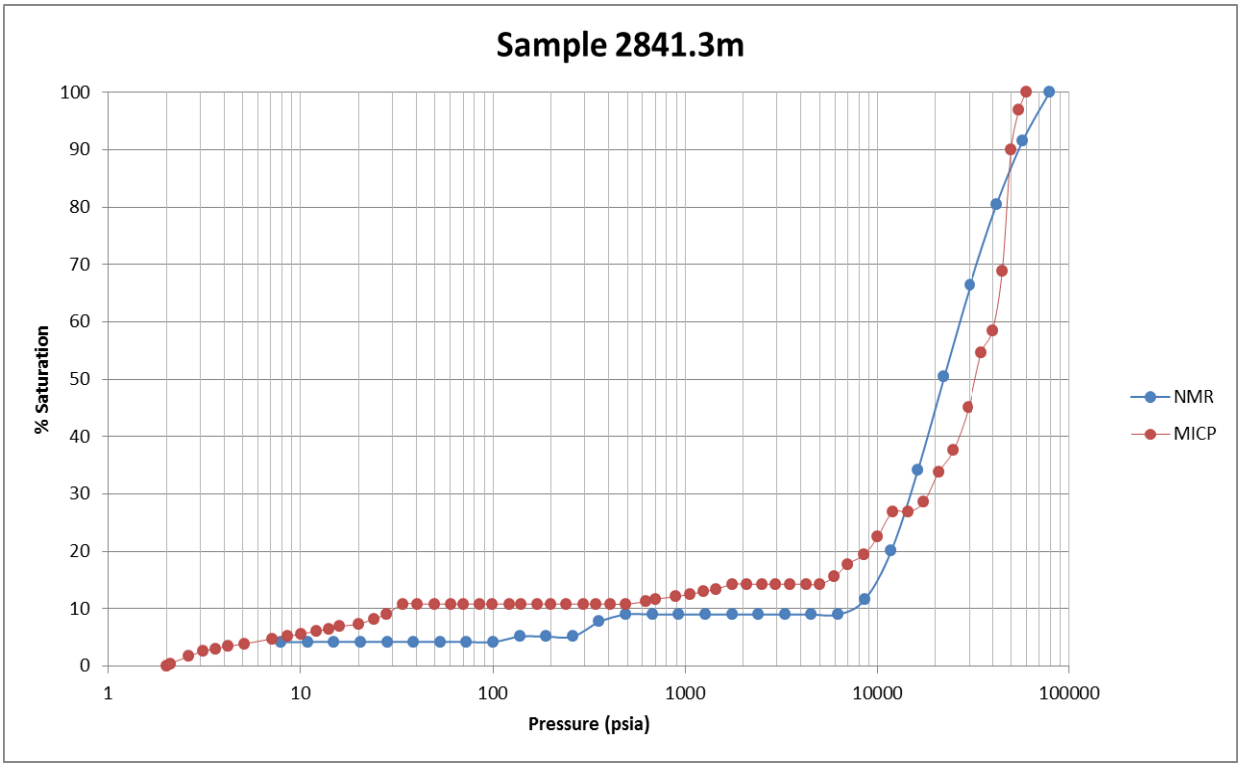

Figure E- 73: Redman-1 MICP curve from the core sample (MICP) at 2841.3 m. Also shown is the well synthetic NMR (NMR) over the same depth interval.

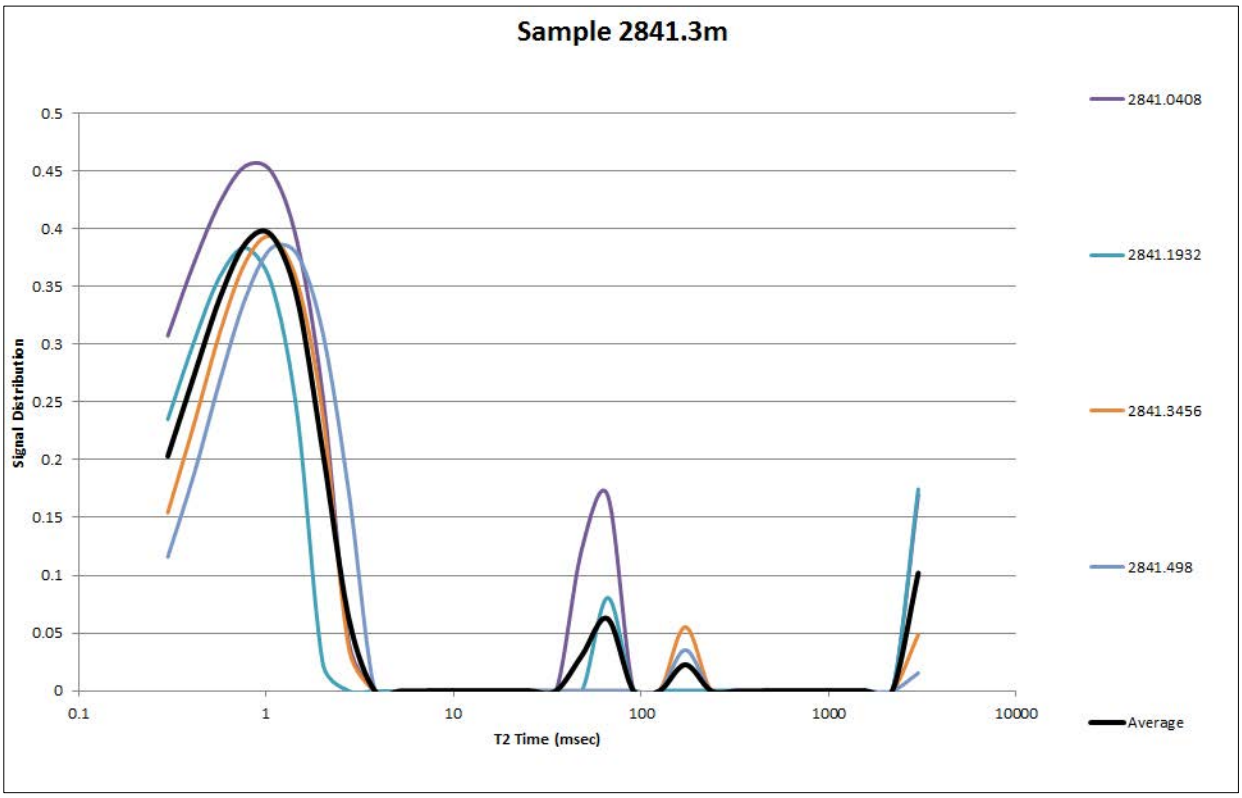

Figure E- 74: Redman-1 NMR T_2 distributions over the 80 cm interval used to produce the well synthetic MICP curve at 2841.3 m depth.

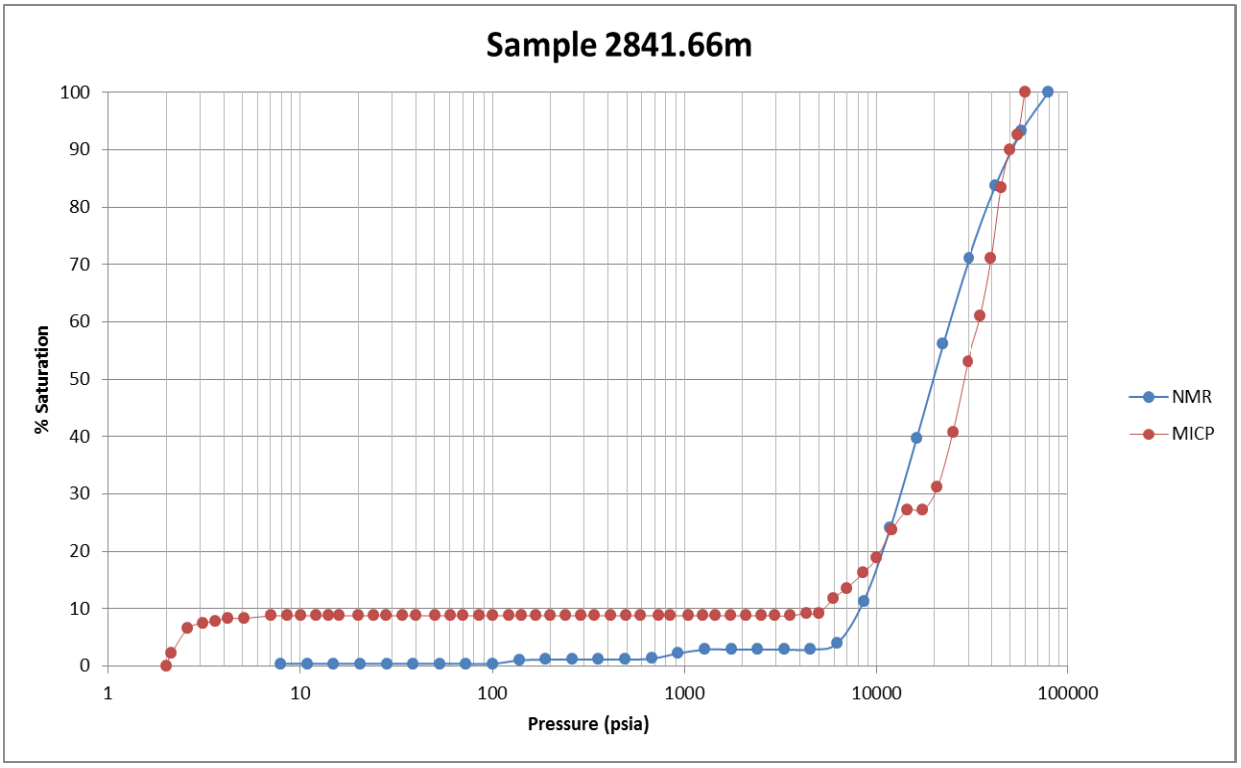

Figure E- 75: Redman-1 MICP curve from the core sample (MICP) at 2841.66 m. Also shown is the well synthetic NMR (NMR) over the same depth interval.

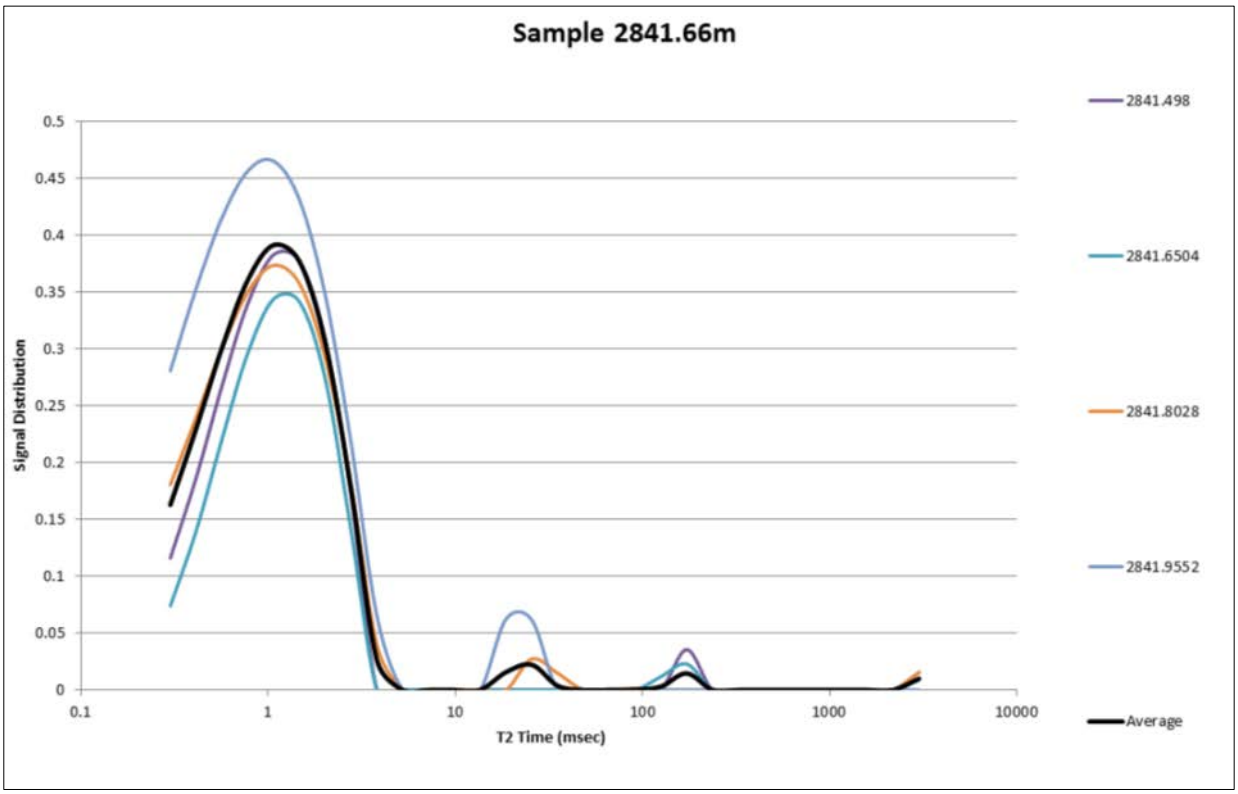

Figure E- 76: Redman-1 NMR T_2 distributions over the 80 cm interval used to produce the well synthetic MICP curve at 2841.66 m depth.

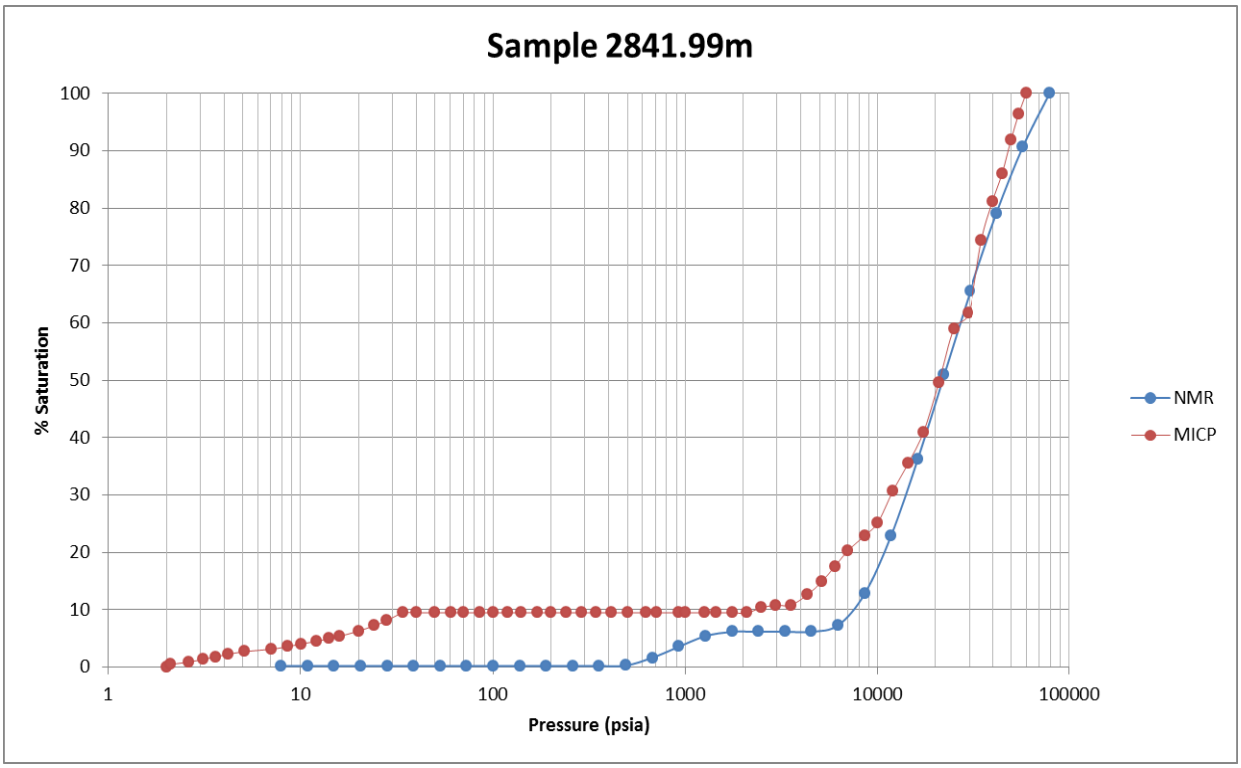

Figure E- 77: Redman-1 MICP curve from the core sample (MICP) at 2841.99 m. Also shown is the well synthetic NMR (NMR) over the same depth interval.

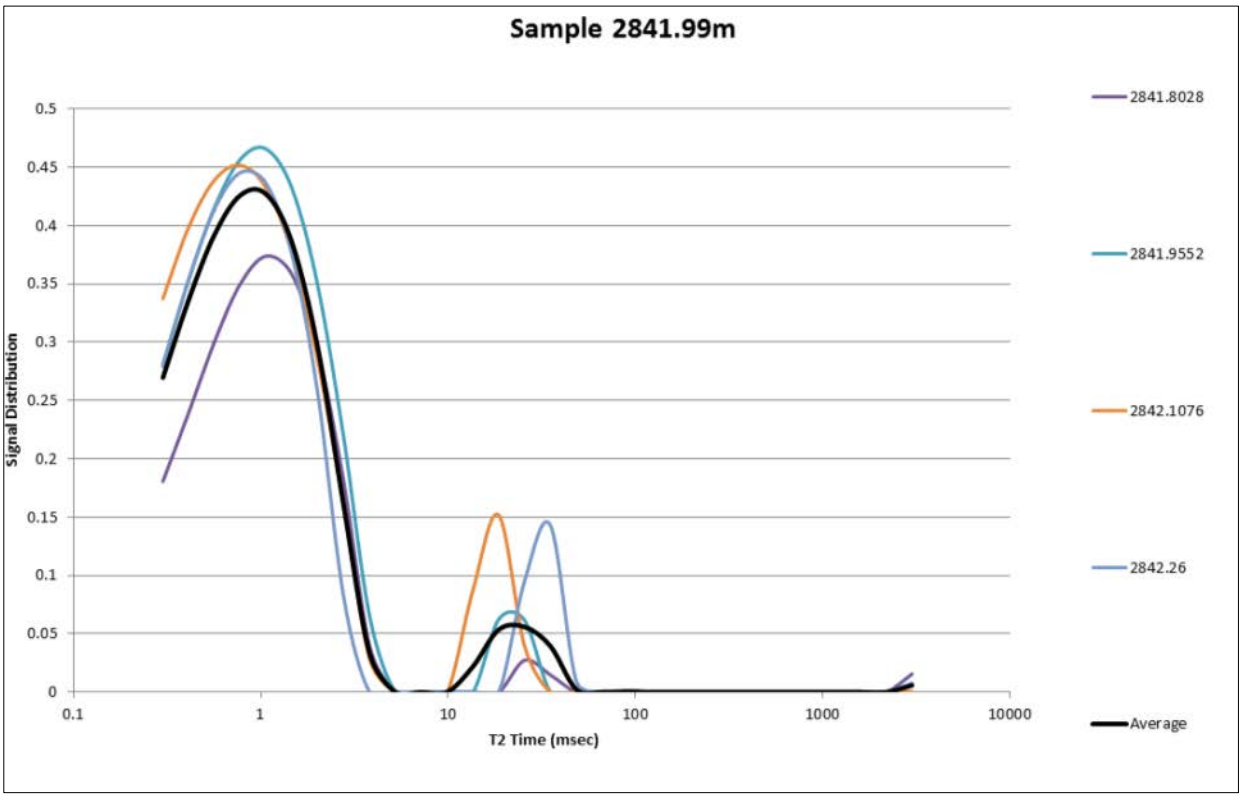

Figure E- 78: Redman-1 NMR T_2 distributions over the 80 cm interval used to produce the well synthetic MICP curve at 2841.99 m depth.

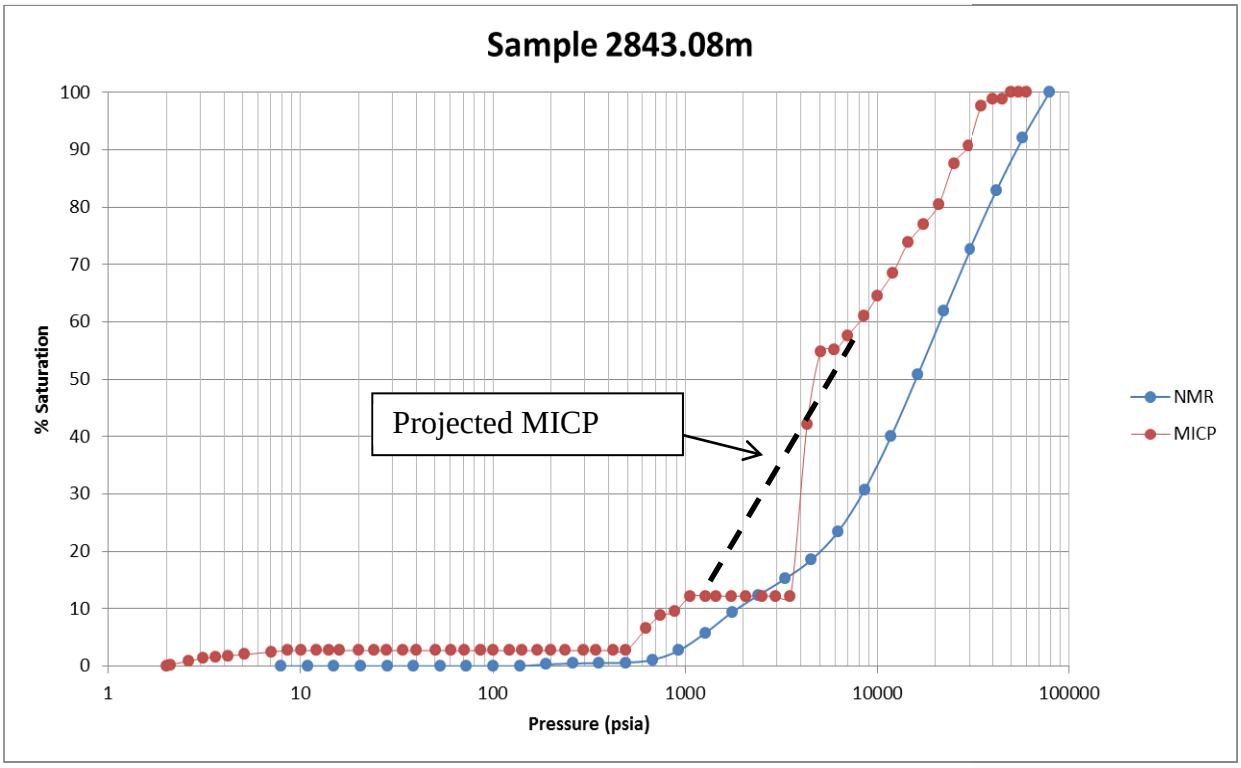

Figure E- 79: Redman-1 MICP curve from the core sample (MICP) at 2841.99 m. Also shown is the well synthetic NMR (NMR) over the same depth interval.

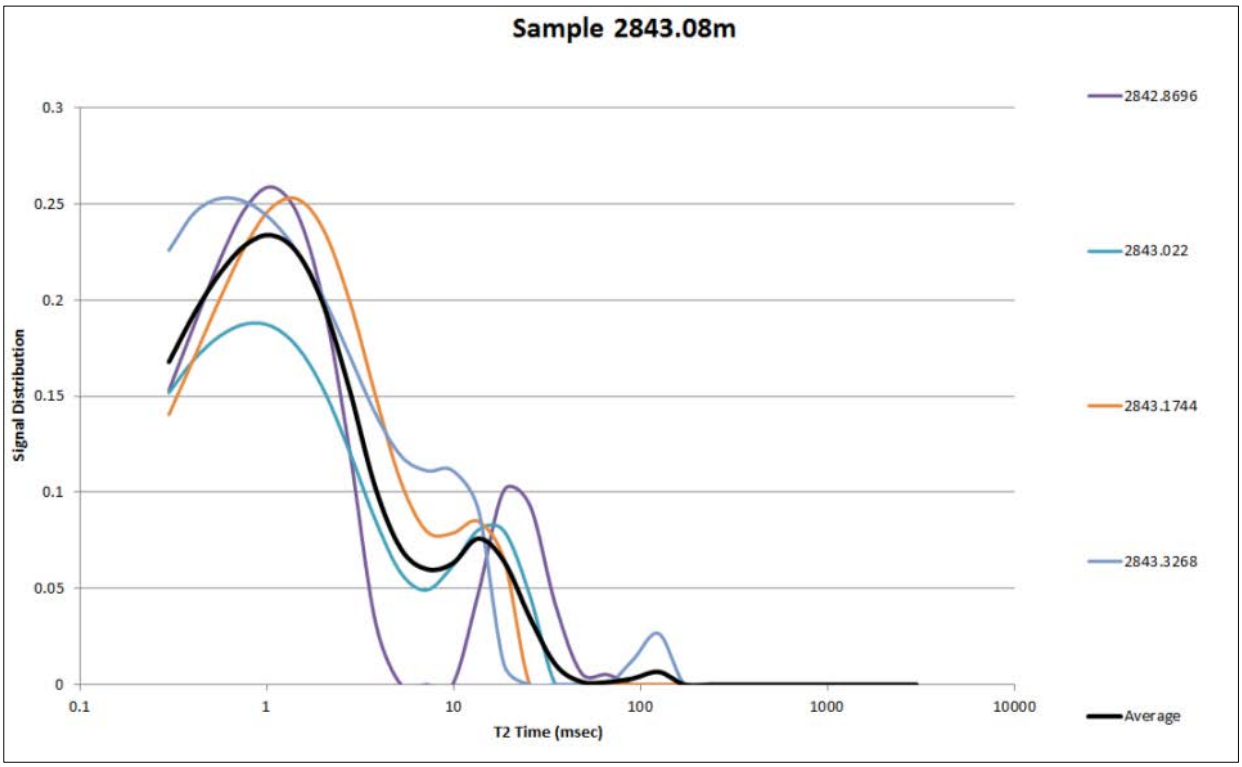

Figure E- 80: Redman-1 NMR T_2 distributions over the 80 cm interval used to produce the well synthetic MICP curve at 2843.08 m depth.

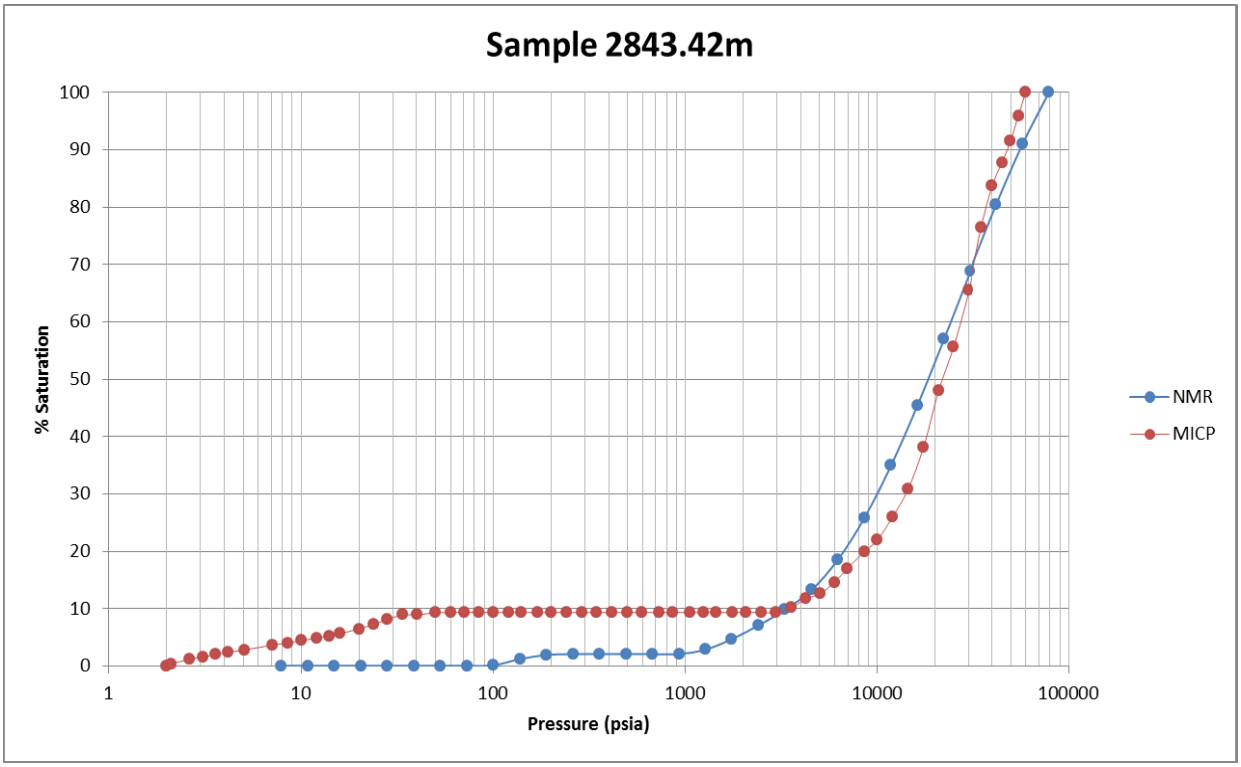

Figure E- 81: Redman-1 MICP curve from the core sample (MICP) at 2843.42 m. Also shown is the well synthetic NMR (NMR) over the same depth interval.

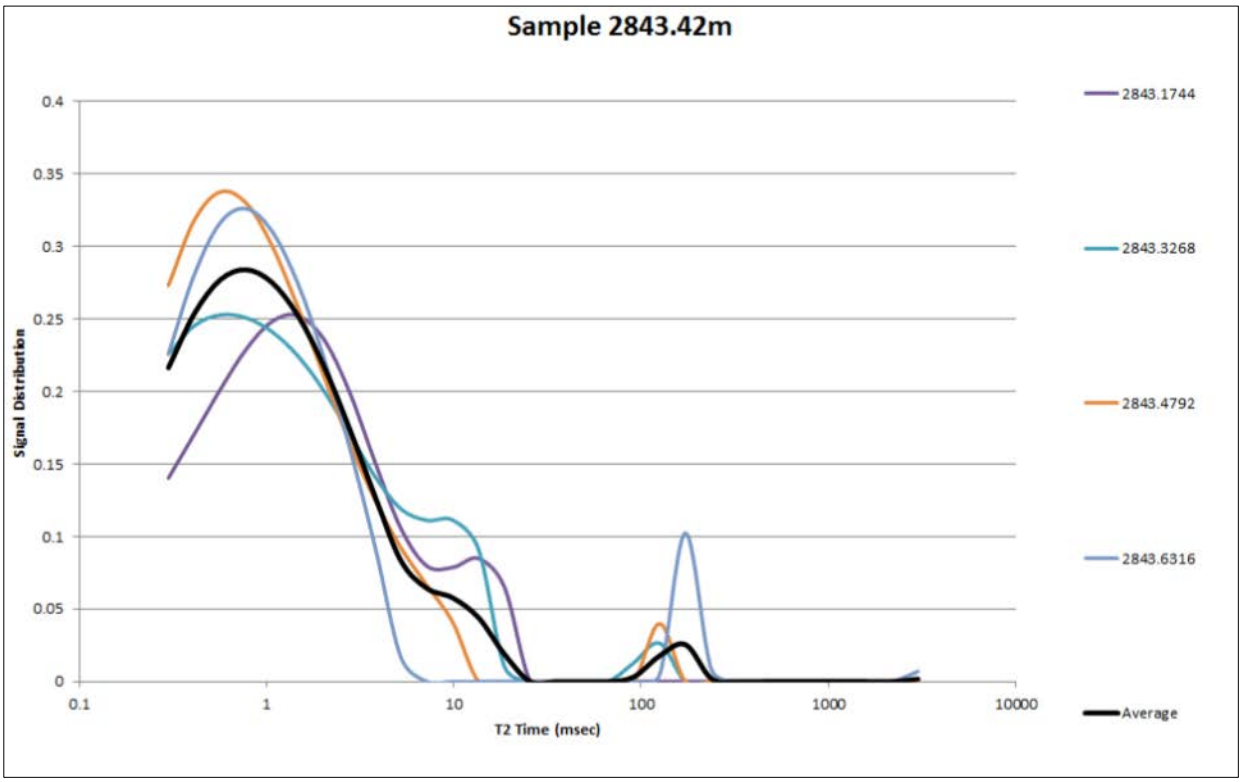

Figure E- 82: Redman-1 NMR T_2 distributions over the 80 cm interval used to produce the well synthetic MICP curve at 2843.42 m depth.

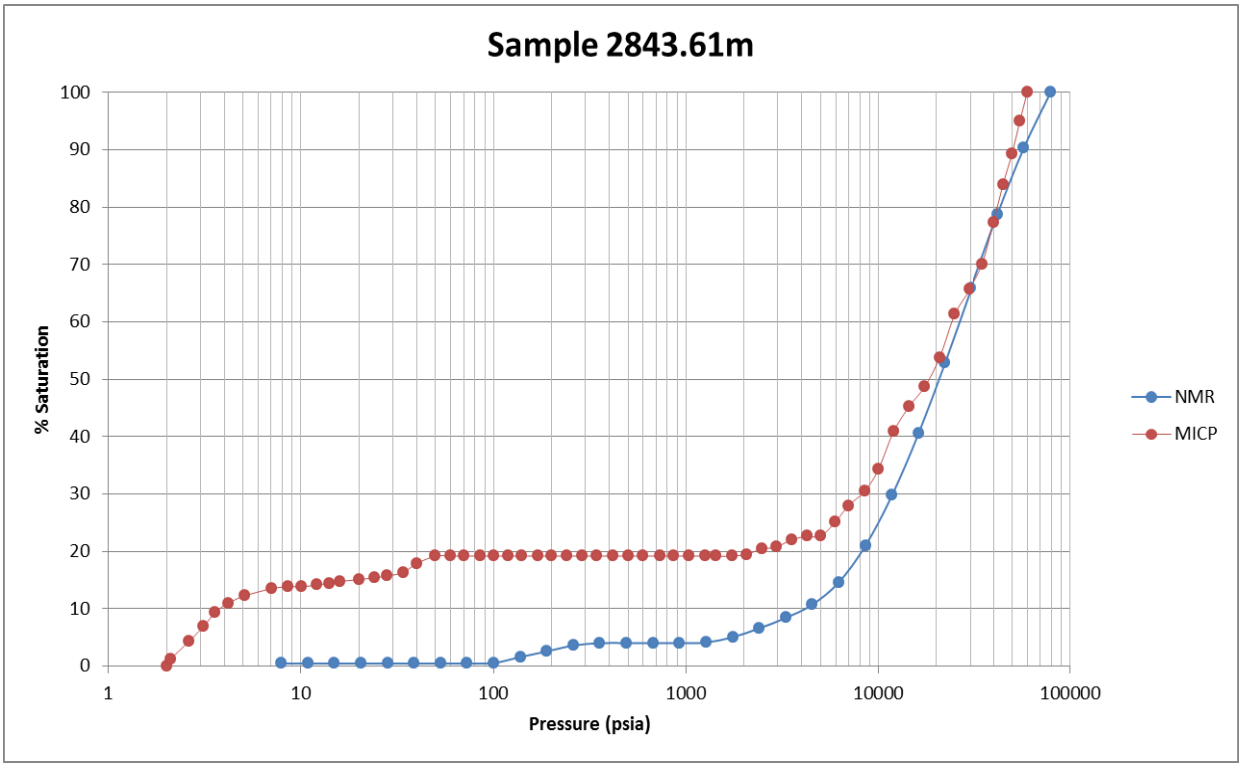

Figure E- 83: Redman-1 MICP curve from the core sample (MICP) at 2843.61 m. Also shown is the well synthetic NMR (NMR) over the same depth interval.

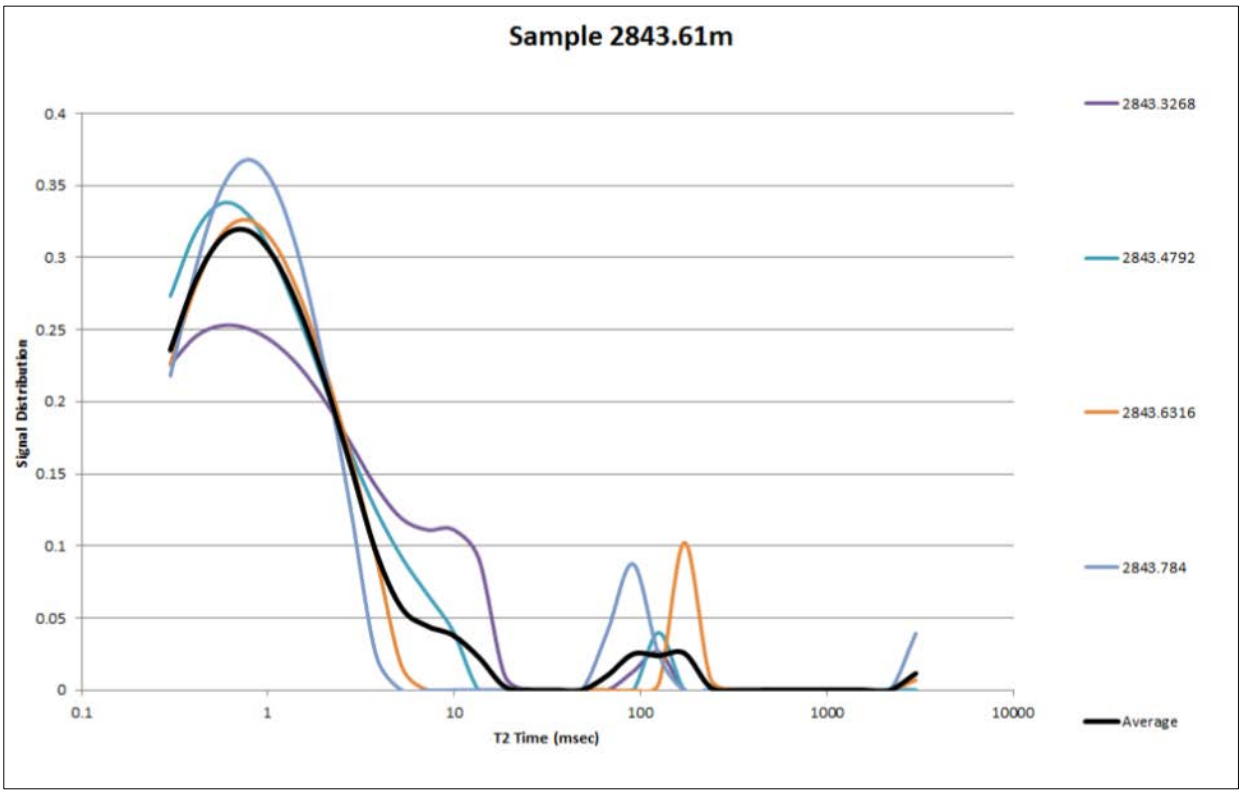

Figure E- 84: Redman-1 NMR T_2 distributions over the 80 cm interval used to produce the well synthetic MICP curve at 2843.61 m depth.

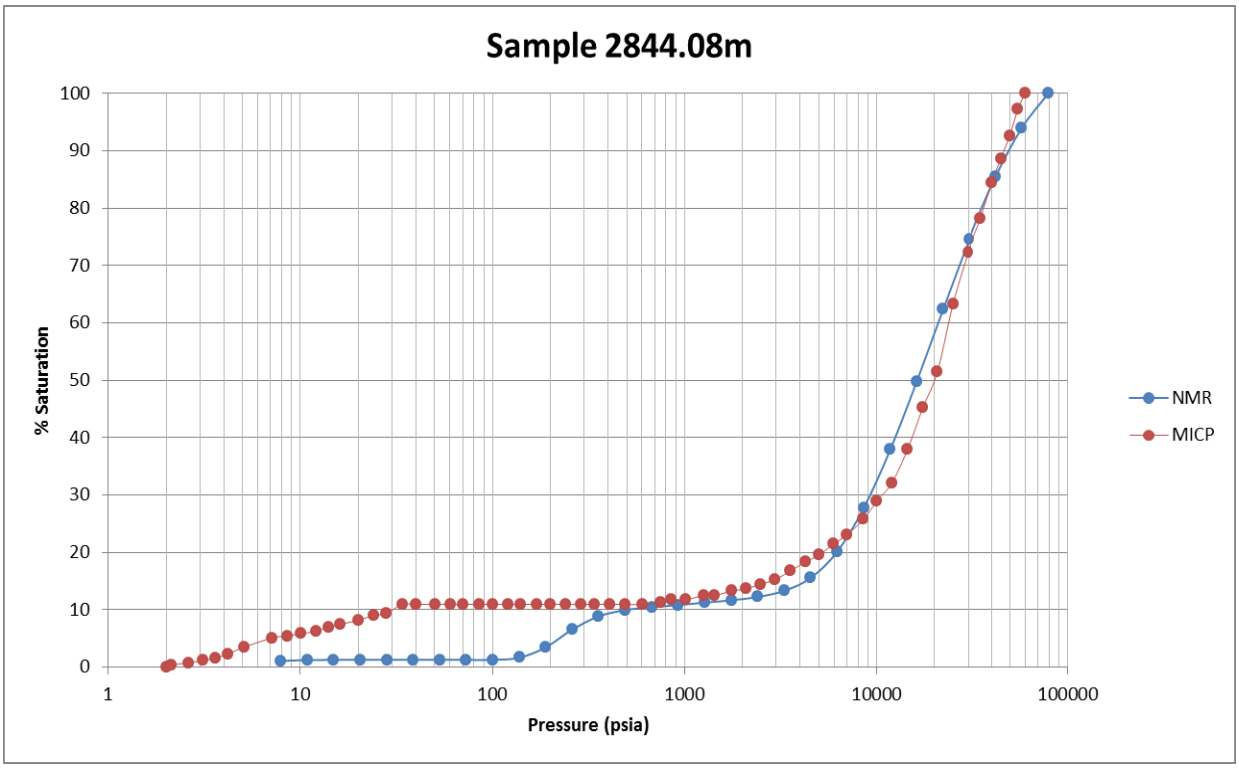

Figure E- 85: Redman-1 MICP curve from the core sample (MICP) at 2844.08 m. Also shown is the well synthetic NMR (NMR) over the same depth interval.

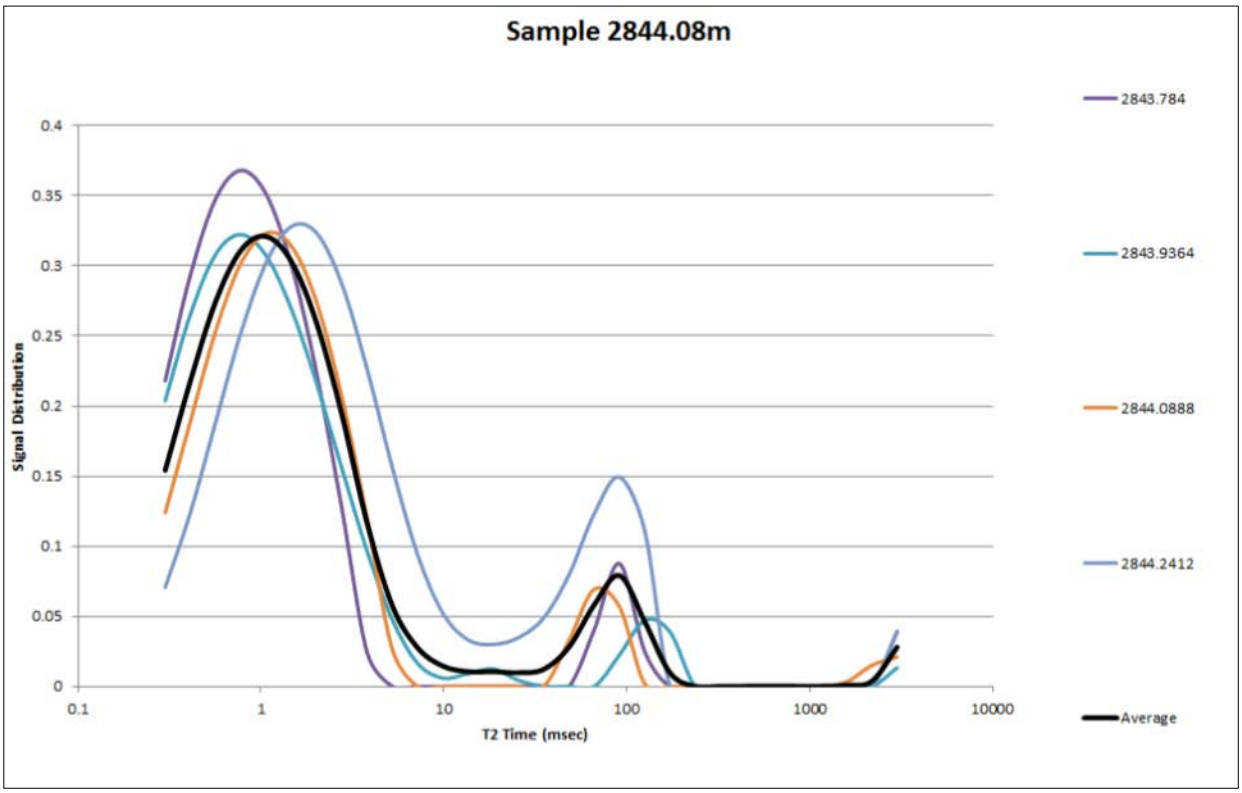

Figure E- 86: Redman-1 NMR T_2 distributions over the 80 cm interval used to produce the well synthetic MICP curve at 2844.08 m depth.

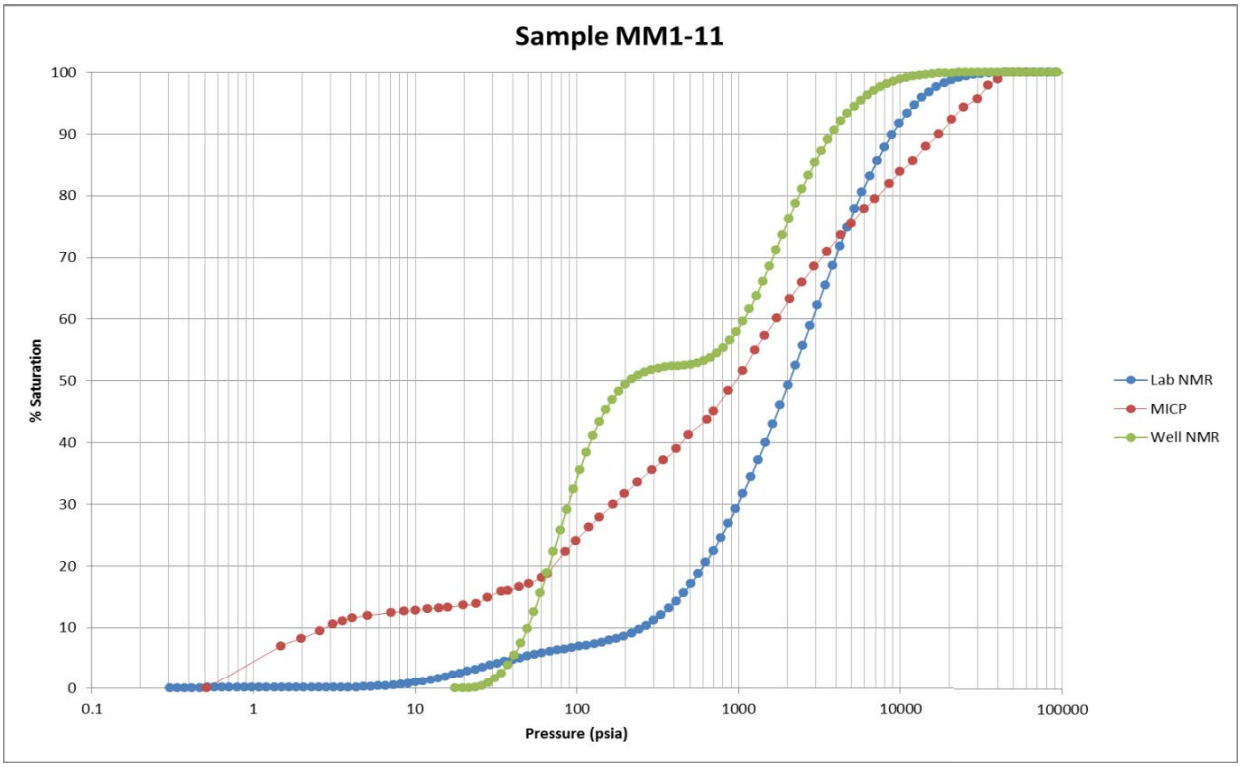

Figure E- 87: Mena Murtee-1 MICP curve from the core sample (MICP) at 1604.965 m. Also shown is the laboratory synthetic NMR (NMR LAB) and well synthetic NMR (NMR) over the same depth interval.

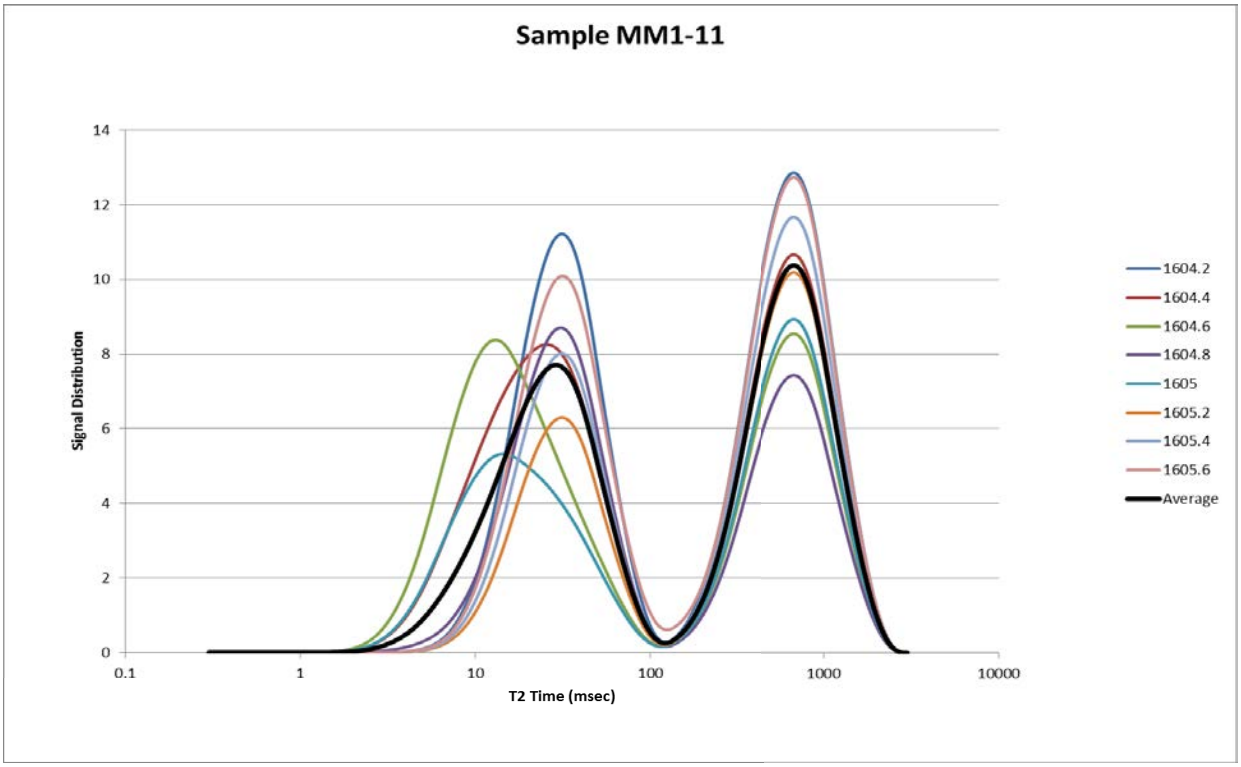

Figure E- 88: Mena Murtee-1 NMR T_2 distributions over the 1.6 m interval used to produce the well synthetic MICP curve at 1604.965 m depth.

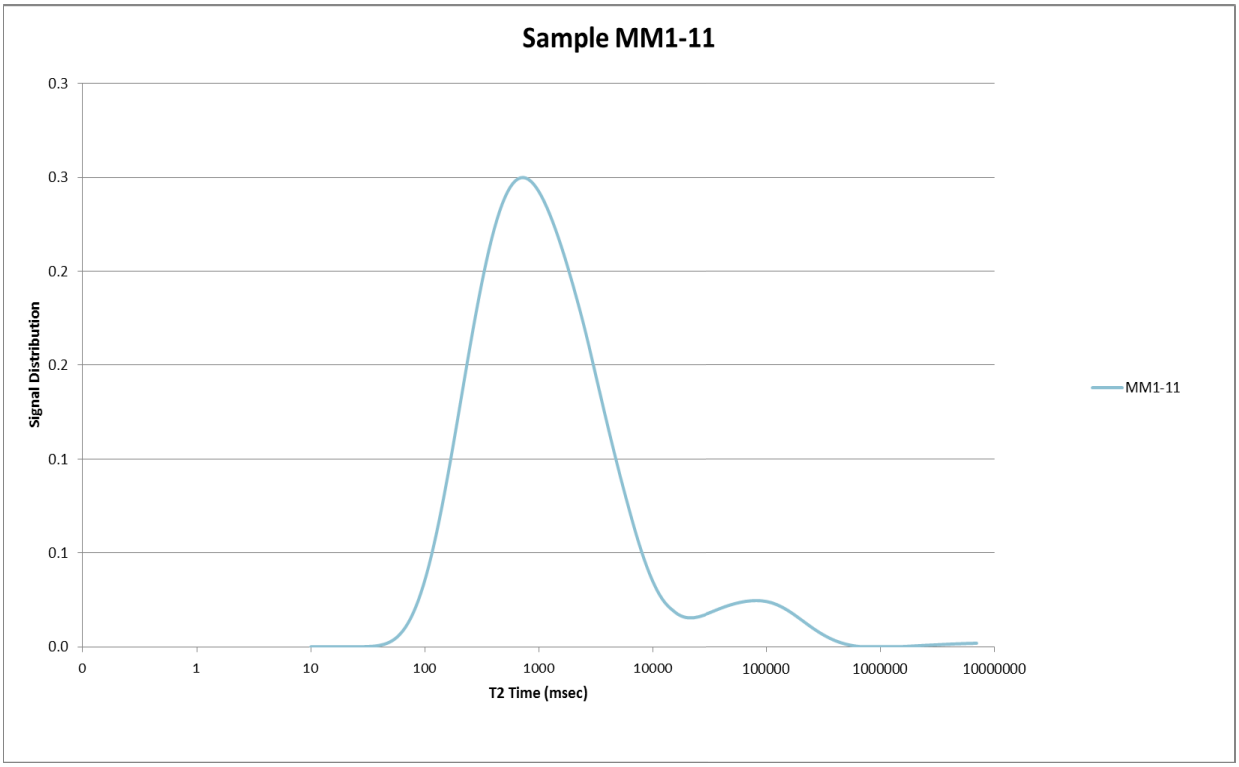

Figure E- 89: Mena Murtee-1 NMR T_2 distribution from the laboratory sample at 1604.965 m used to produce the laboratory synthetic MICP curve.

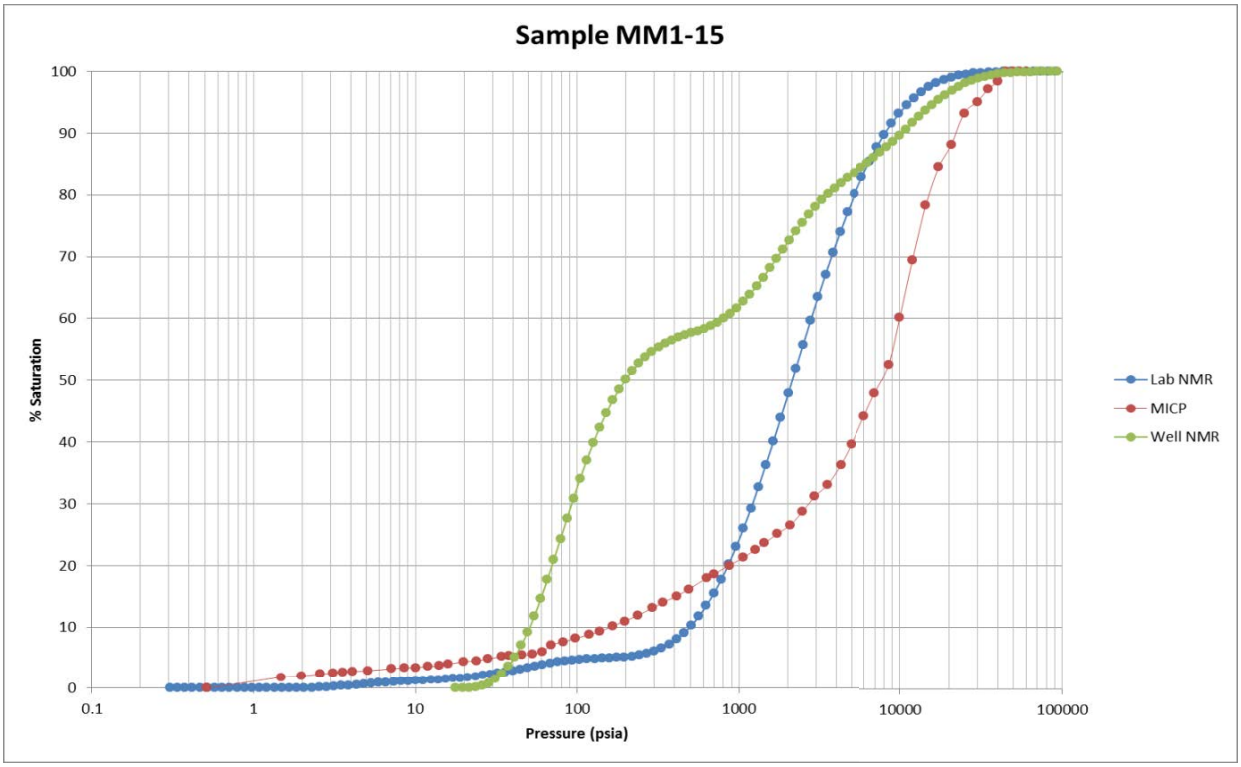

Figure E- 90: Mena Murtee-1 MICP curve from the core sample (MICP) at 1606.91 m. Also shown is the laboratory synthetic NMR (NMR LAB) and well synthetic NMR (NMR) over the same depth interval.

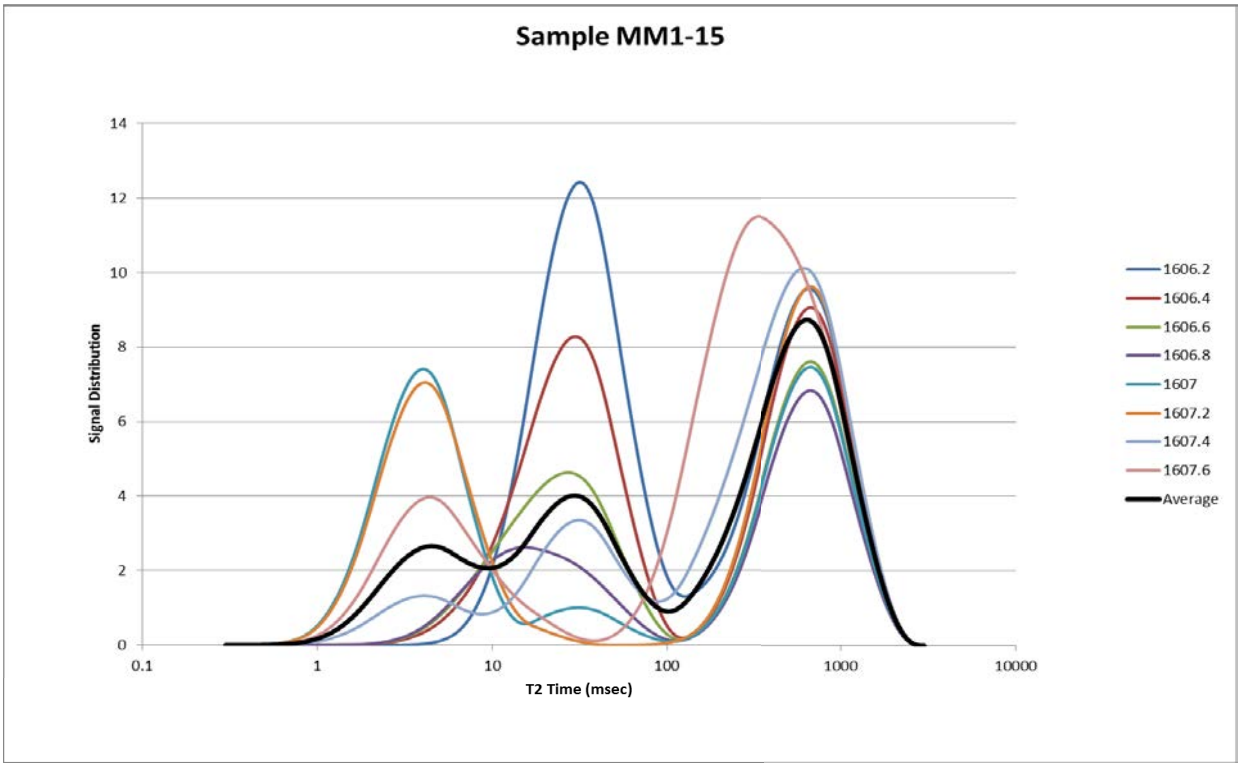

Figure E- 91: Mena Murtee-1 NMR T_2 distributions over the 1.6 m interval used to produce the well synthetic MICP curve at 1606.91 m depth.

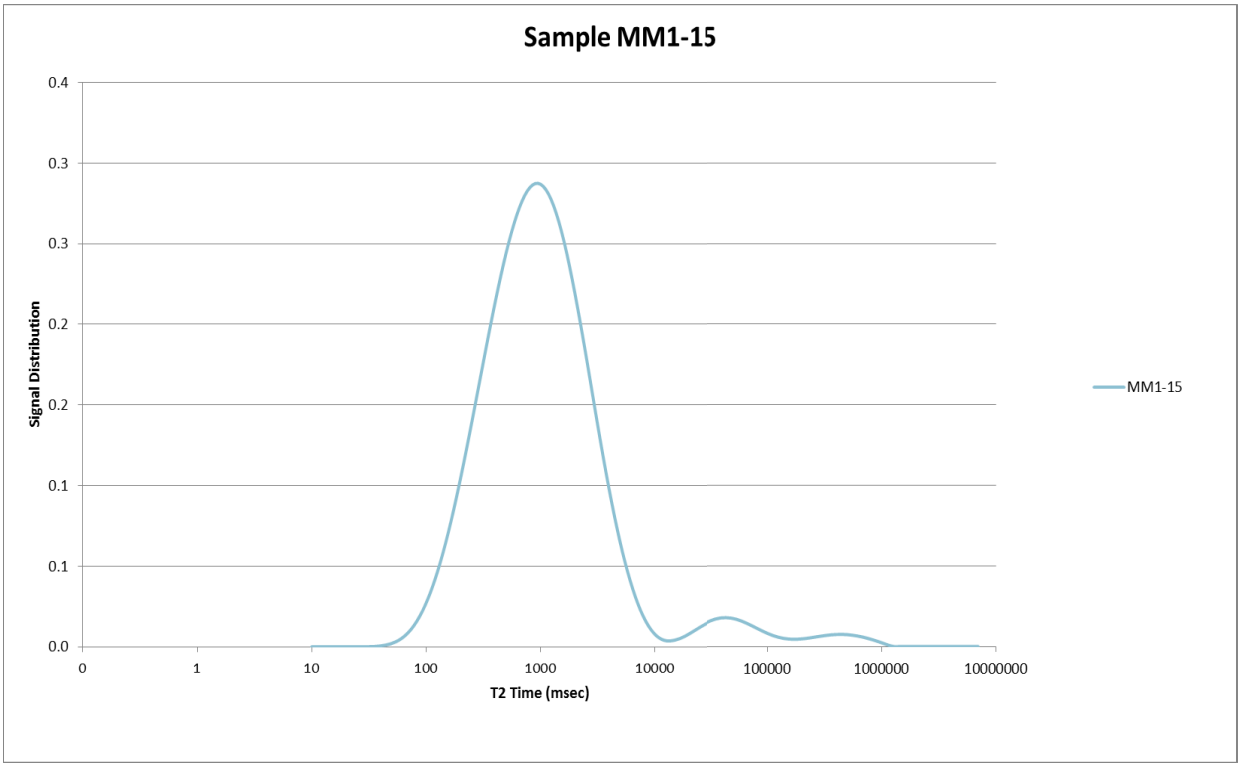

Figure E- 92: Mena Murtee-1 NMR T_2 distribution from the laboratory sample at 1606.91 m used to produce the laboratory synthetic MICP curve.

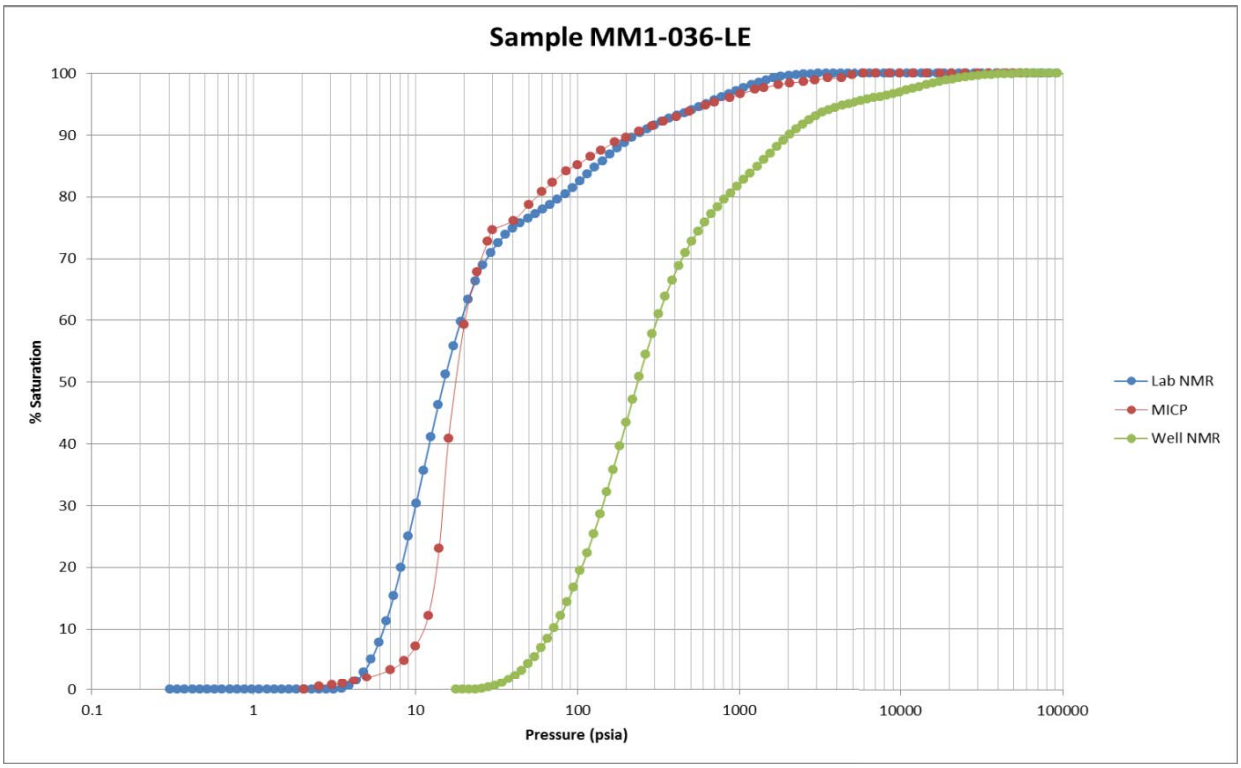

Figure E- 93: Mena Murtee-1 MICP curve from the core sample (MICP) at 1629.05 m. Also shown is the laboratory synthetic NMR (NMR LAB) and well synthetic NMR (NMR) over the same depth interval.

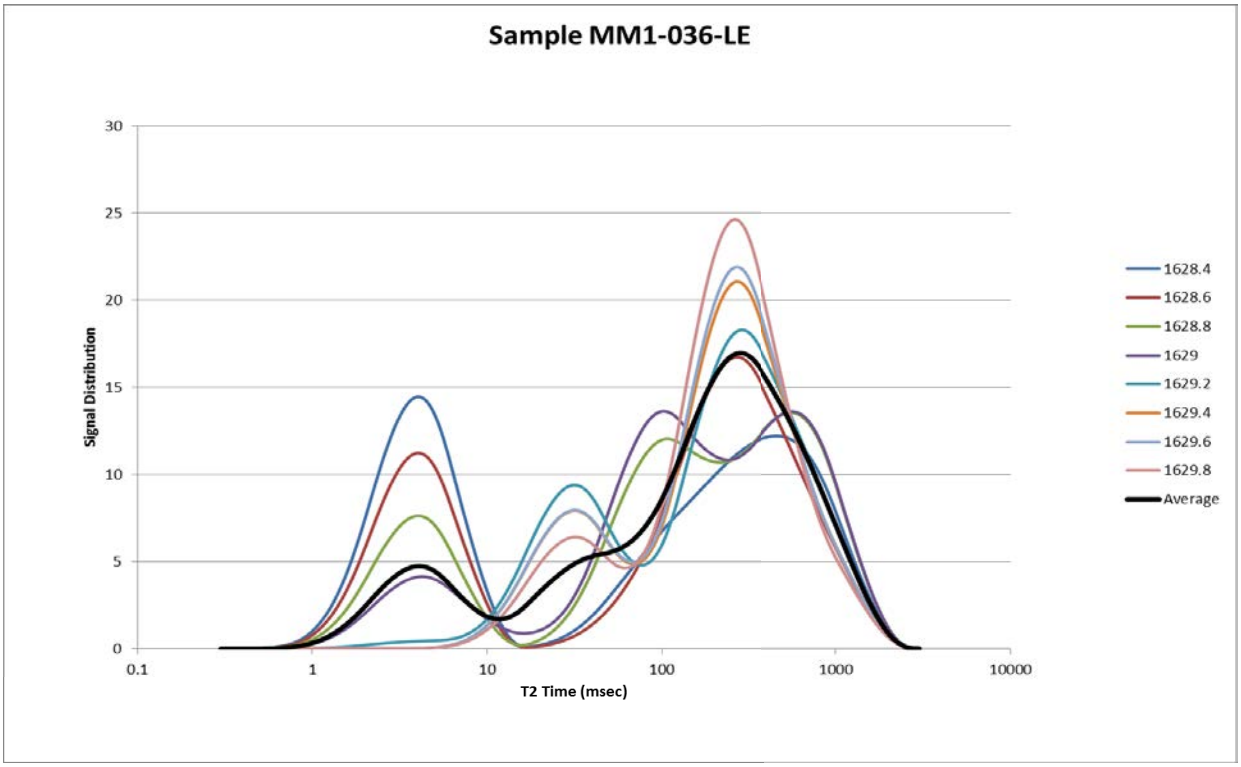

Figure E- 94: Mena Murtee-1 NMR T_2 distributions over the 1.6 m interval used to produce the well synthetic MICP curve at 1629.05 m depth.

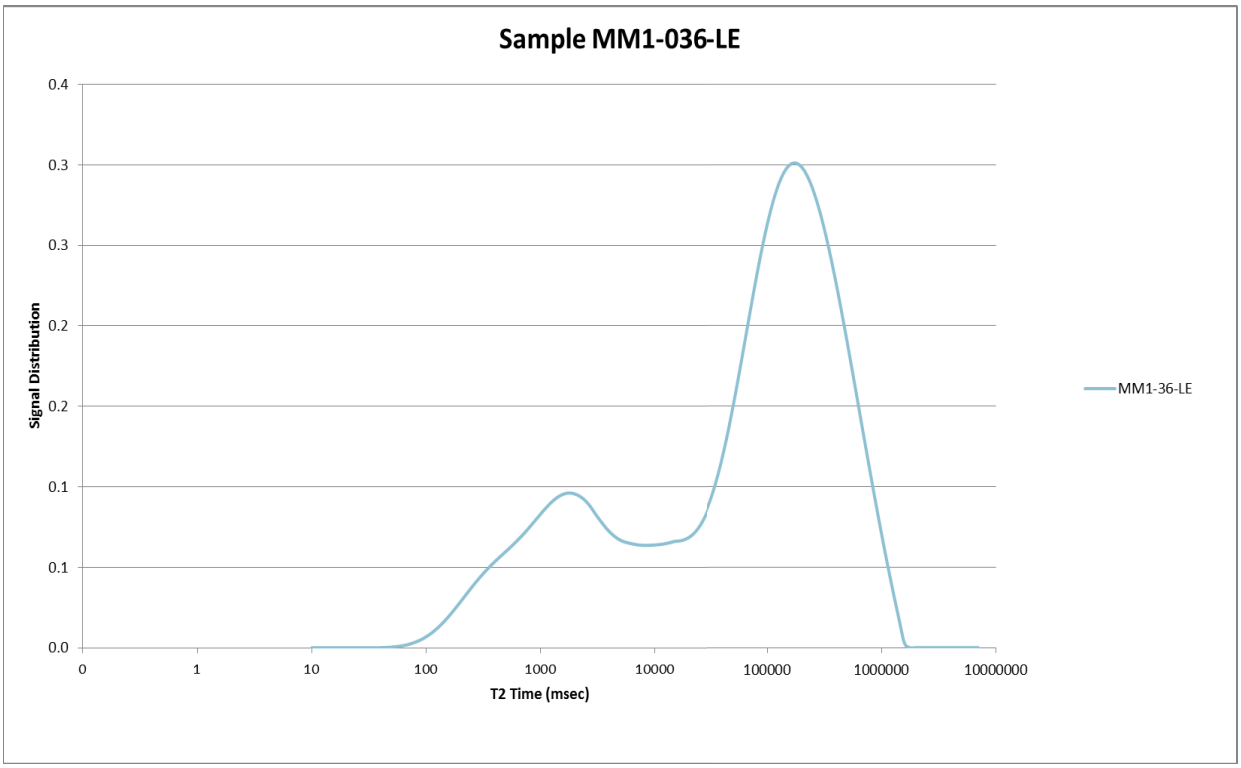

Figure E- 95: Mena Murtee-1 NMR T_2 distribution from the laboratory sample at 1629.05 m used to produce the laboratory synthetic MICP curve.

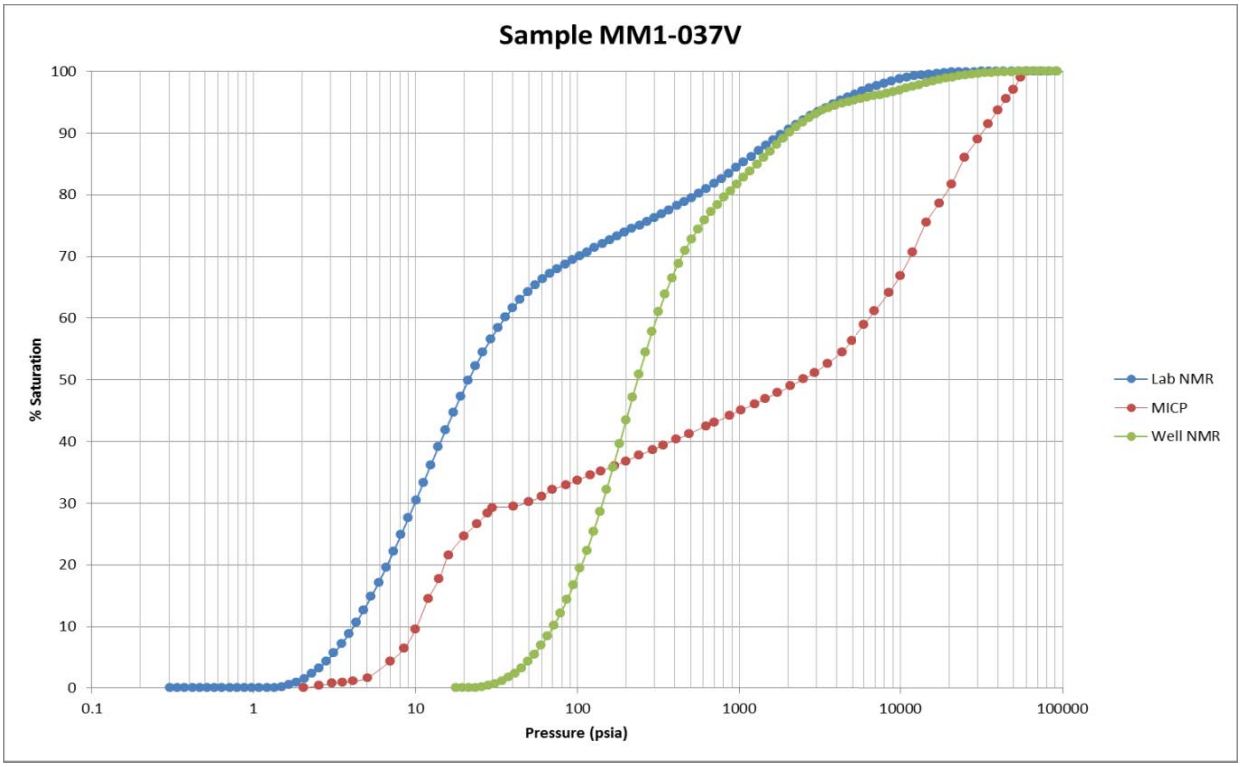

Figure E- 96: Mena Murtee-1 MICP curve from the core sample (MICP) at 1629.98 m. Also shown is the laboratory synthetic NMR (NMR LAB) and well synthetic NMR (NMR) over the same depth interval.

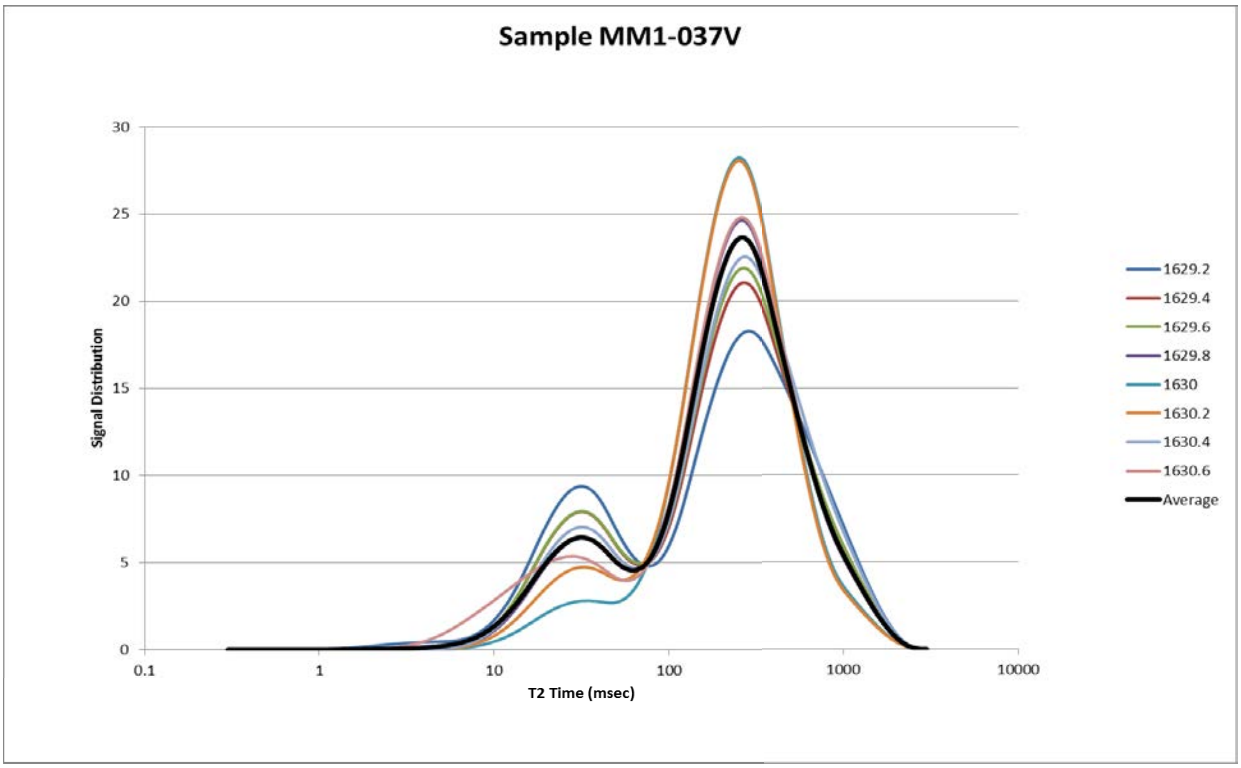

Figure E- 97: Mena Murtee-1 NMR T_2 distributions over the 1.6 m interval used to produce the well synthetic MICP curve at 1629.98 m depth.

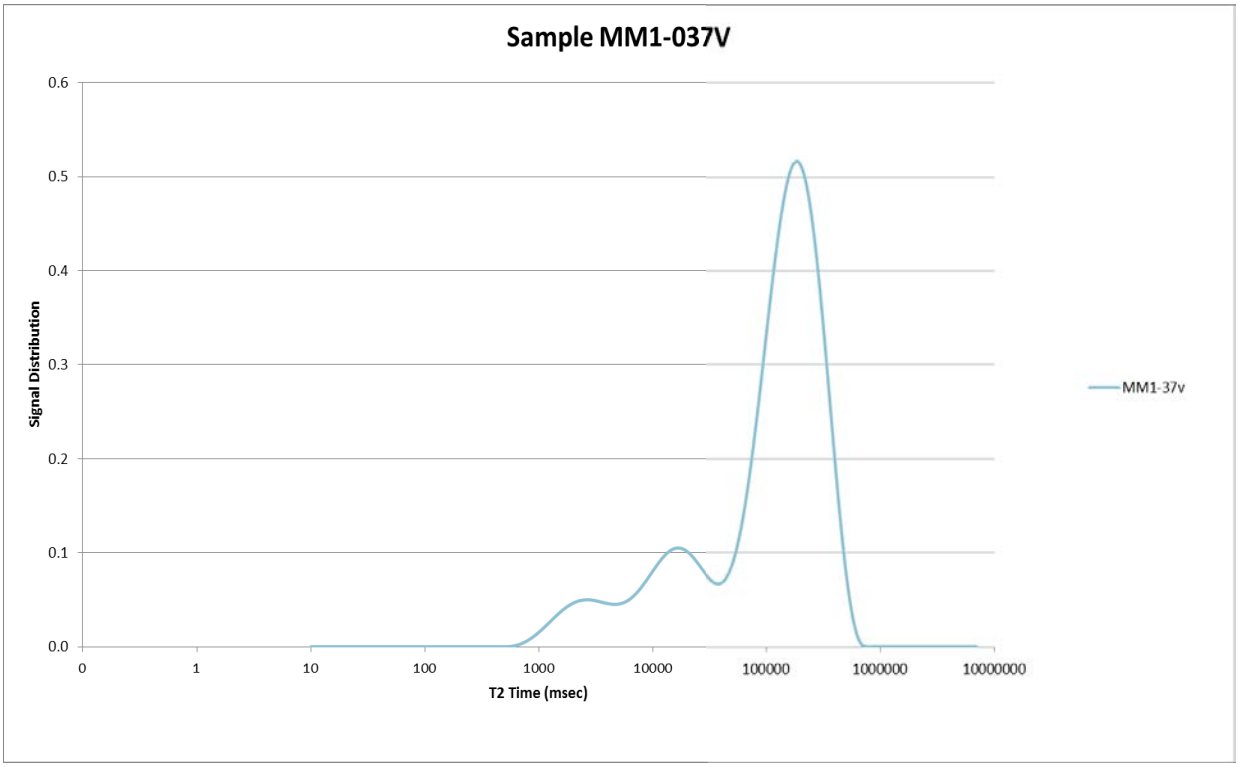

Figure E- 98: Mena Murtee-1 NMR T_2 distribution from the laboratory sample at 1629.05 m used to produce the laboratory synthetic MICP curve.

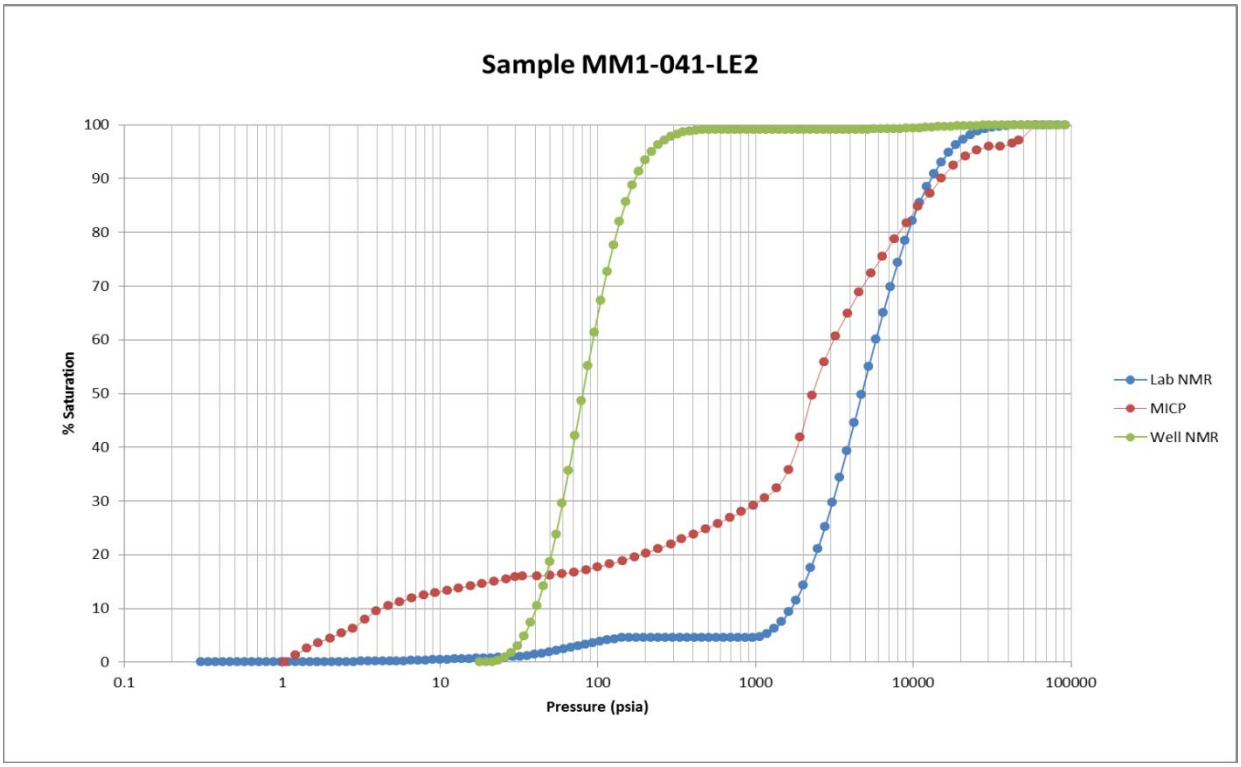

Figure E- 99: Mena Murtee-1 MICP curve from the core sample (MICP) at 1859.75 m. Also shown is the laboratory synthetic at 1859.025 m NMR (NMR LAB) and well synthetic NMR (NMR) over the 1859.75 m depth interval.

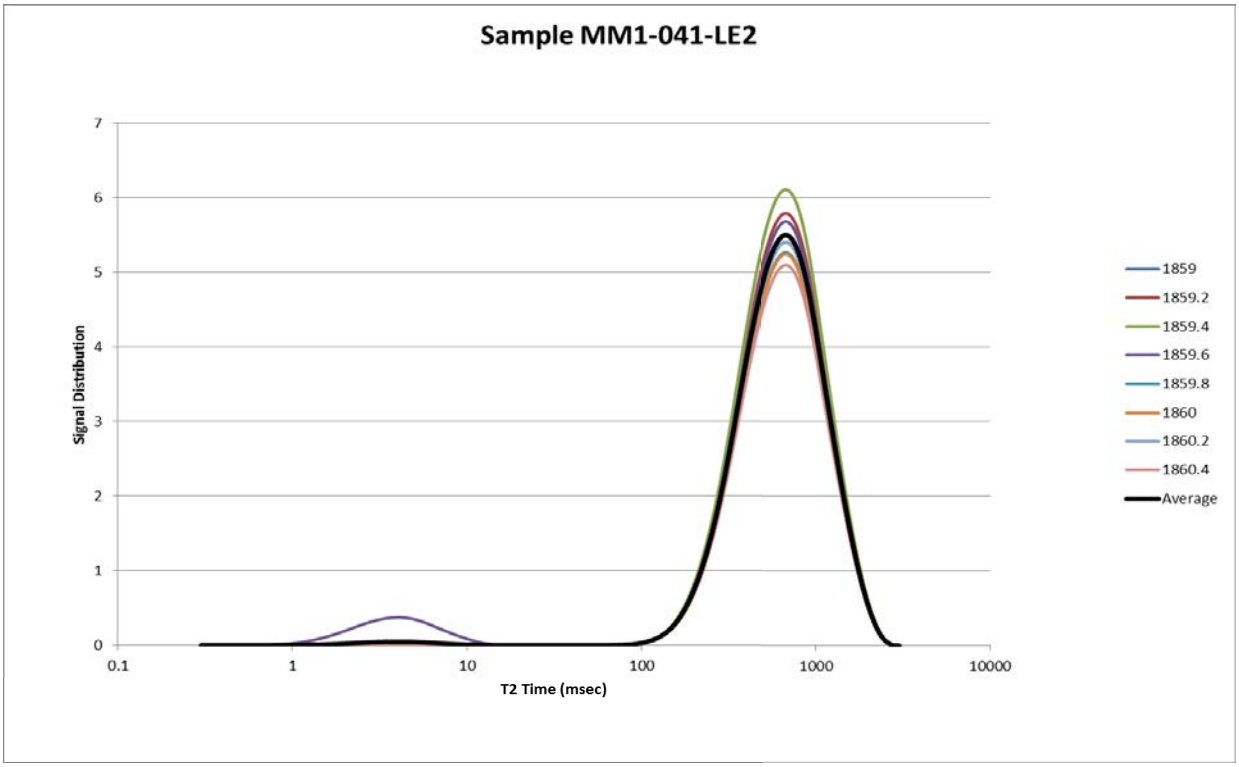

Figure E- 100: Mena Murtee-1 NMR T_2 distributions over the 1.6 m interval used to produce the well synthetic MICP curve at 1859.75 m depth.

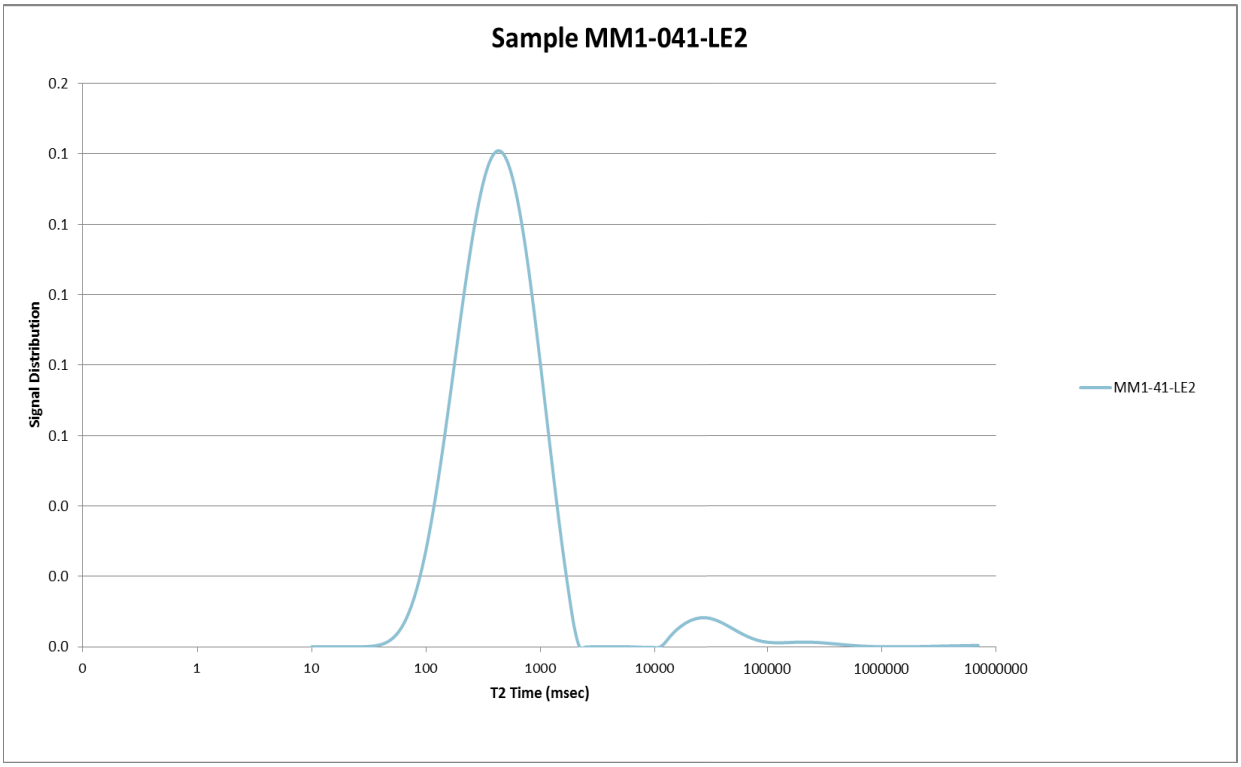

Figure E- 101: Mena Murtee-1 NMR T_2 distribution from the laboratory sample at 1859.025 m used to produce the laboratory synthetic MICP curve.

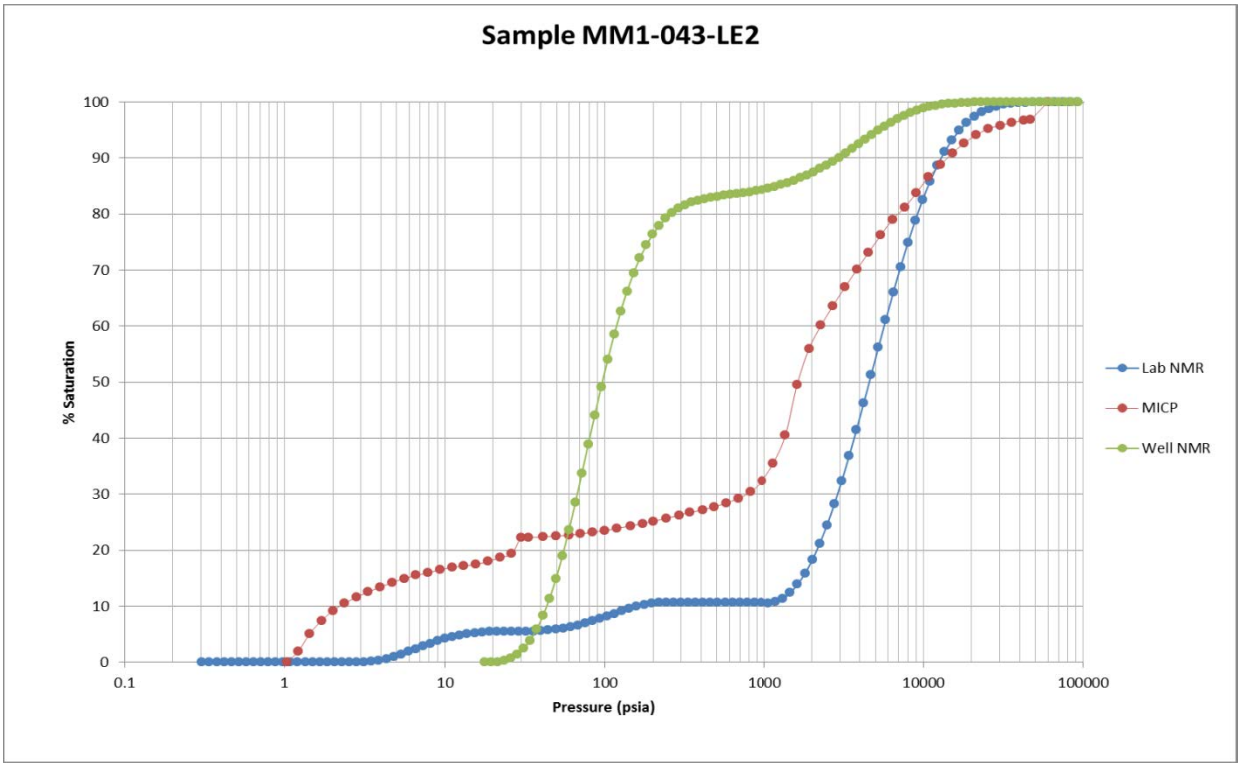

Figure E- 102: Mena Murtee-1 MICP curve from the core sample (MICP) at 1865.06 m. Also shown is the laboratory synthetic at 1866.035 m NMR (NMR LAB) and well synthetic NMR (NMR) over the 1865.06 m depth interval.

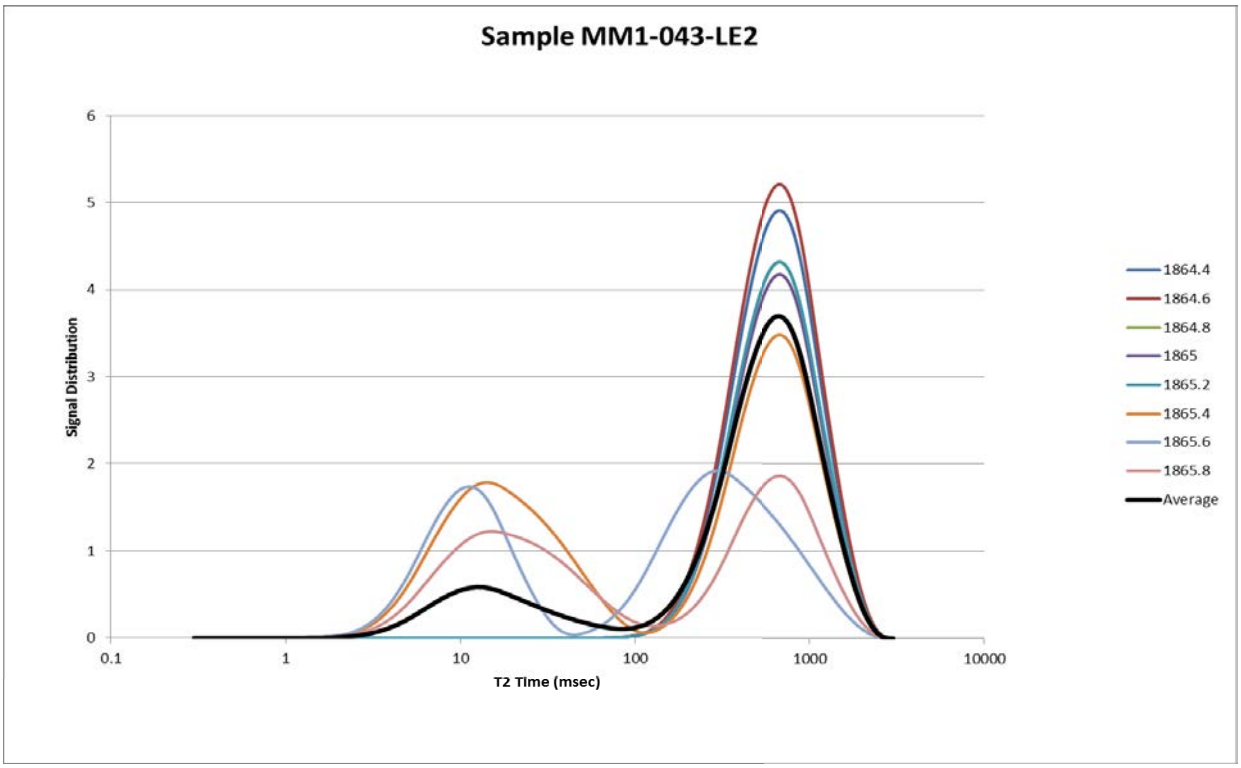

Figure E- 103: Mena Murtee-1 NMR T_2 distributions over the 1.6 m interval used to produce the well synthetic MICP curve at 1865.06 m depth.

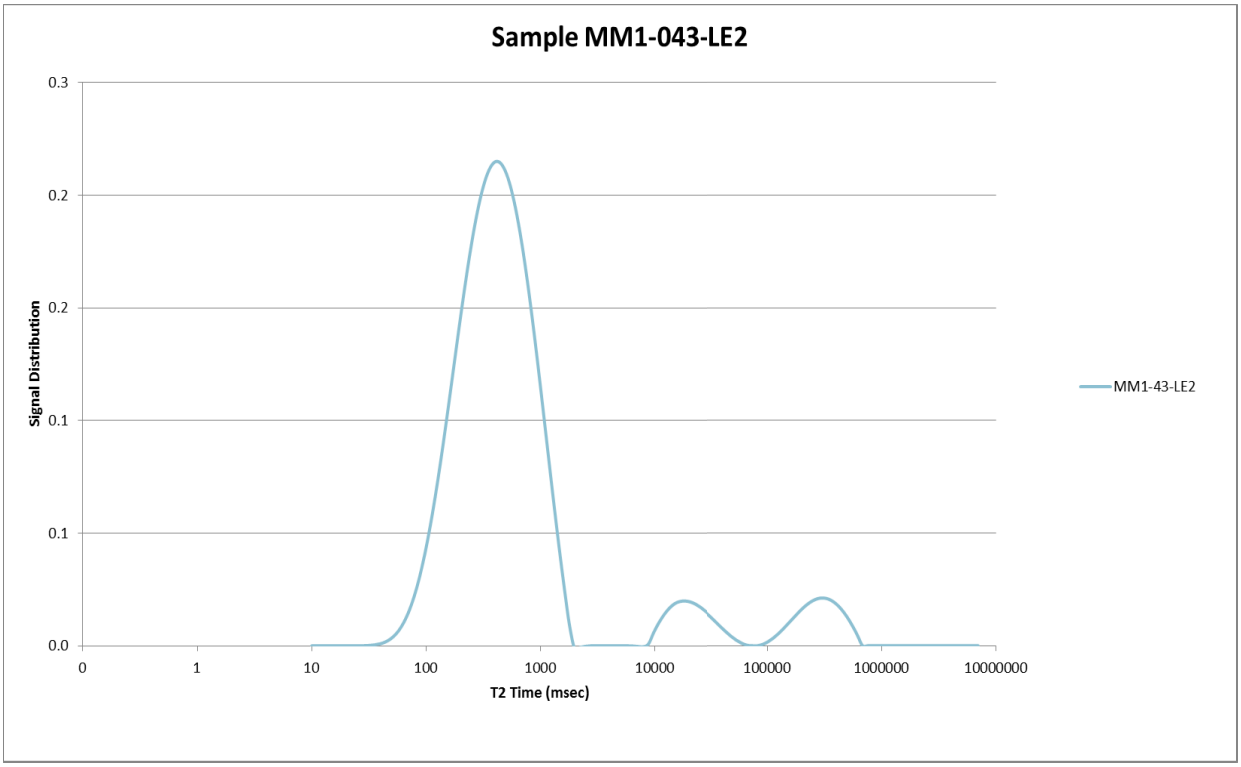

Figure E- 104: T_2 Distributions for the laboratory measurement at 1866.035 m. Mena Murtee-1 NMR T_2 distribution from the laboratory sample at 1865.06 m used to produce the laboratory synthetic MICP curve.

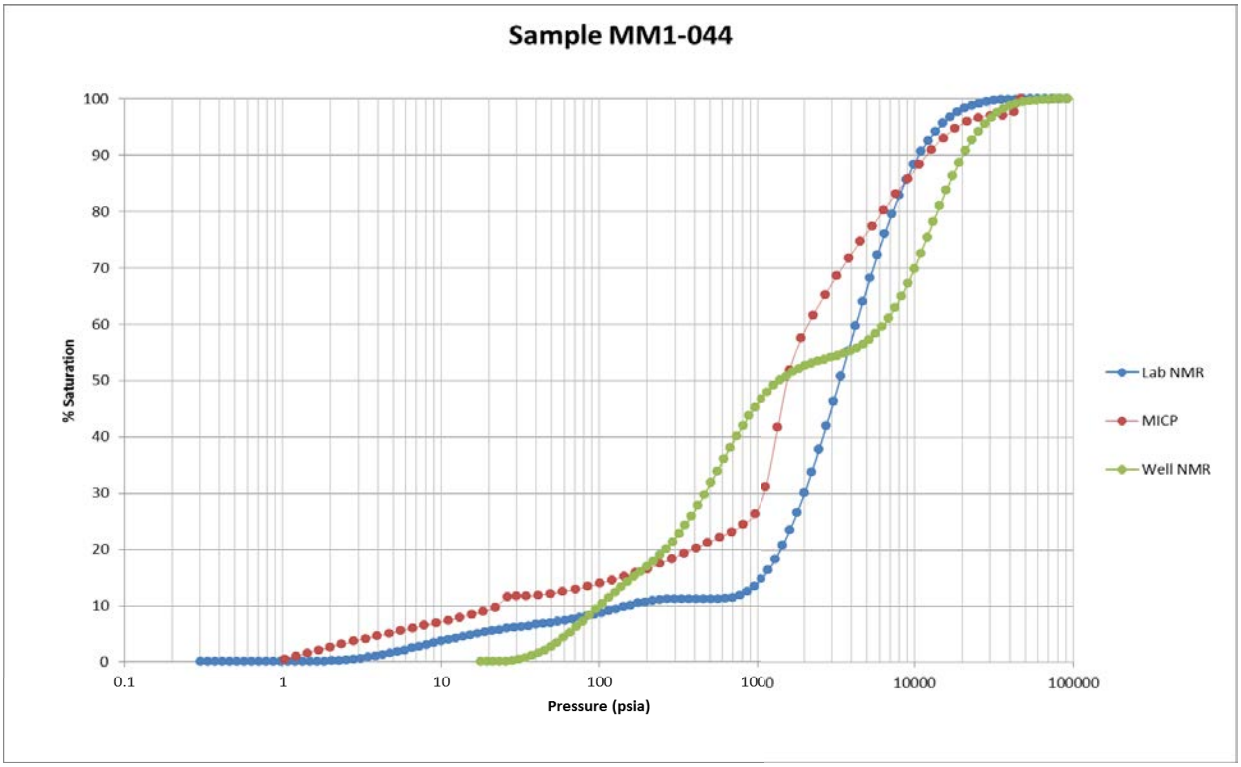

Figure E- 105: Mena Murtee-1 MICP curve from the core sample (MICP) at 1872.32 m. Also shown is the laboratory synthetic at 1873.03 m NMR (NMR LAB) and well synthetic NMR (NMR) over the 1872.32 m depth interval.

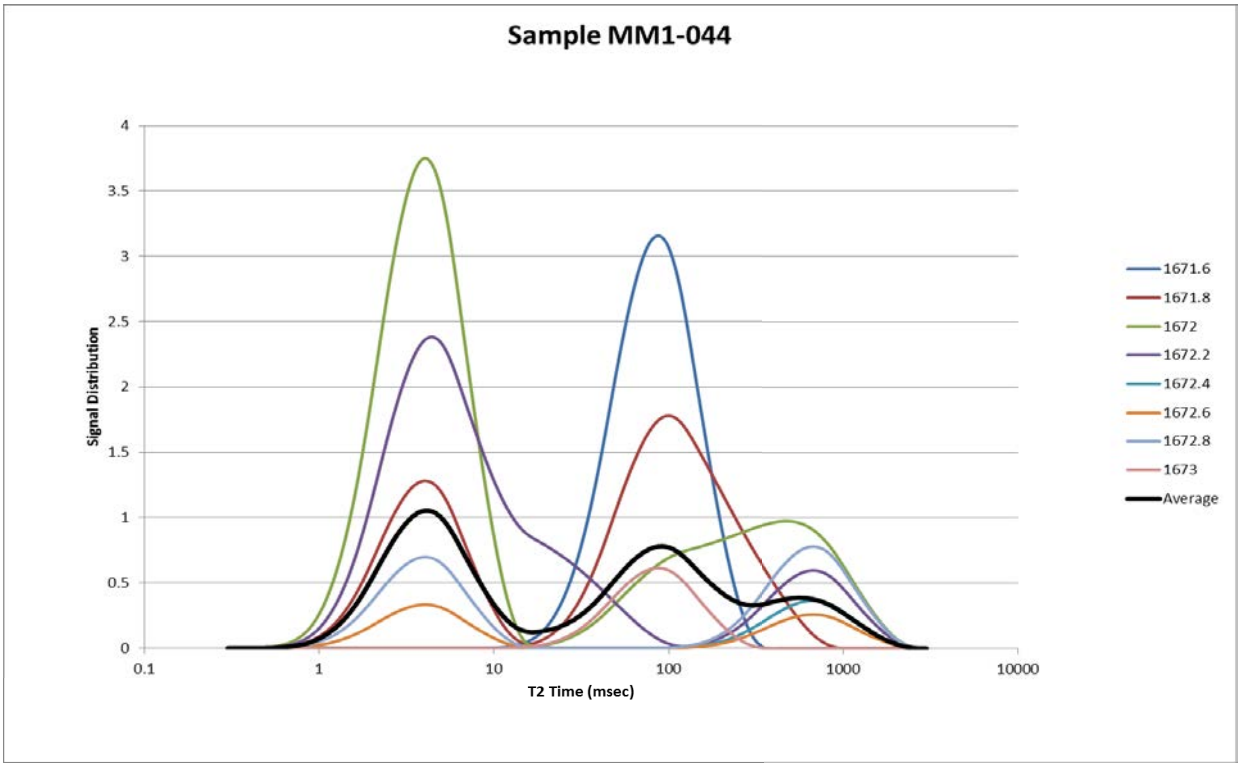

Figure E- 106: Mena Murtee-1 NMR T_2 distributions over the 1.6 m interval used to produce the well synthetic MICP curve at 1872.32 m depth.

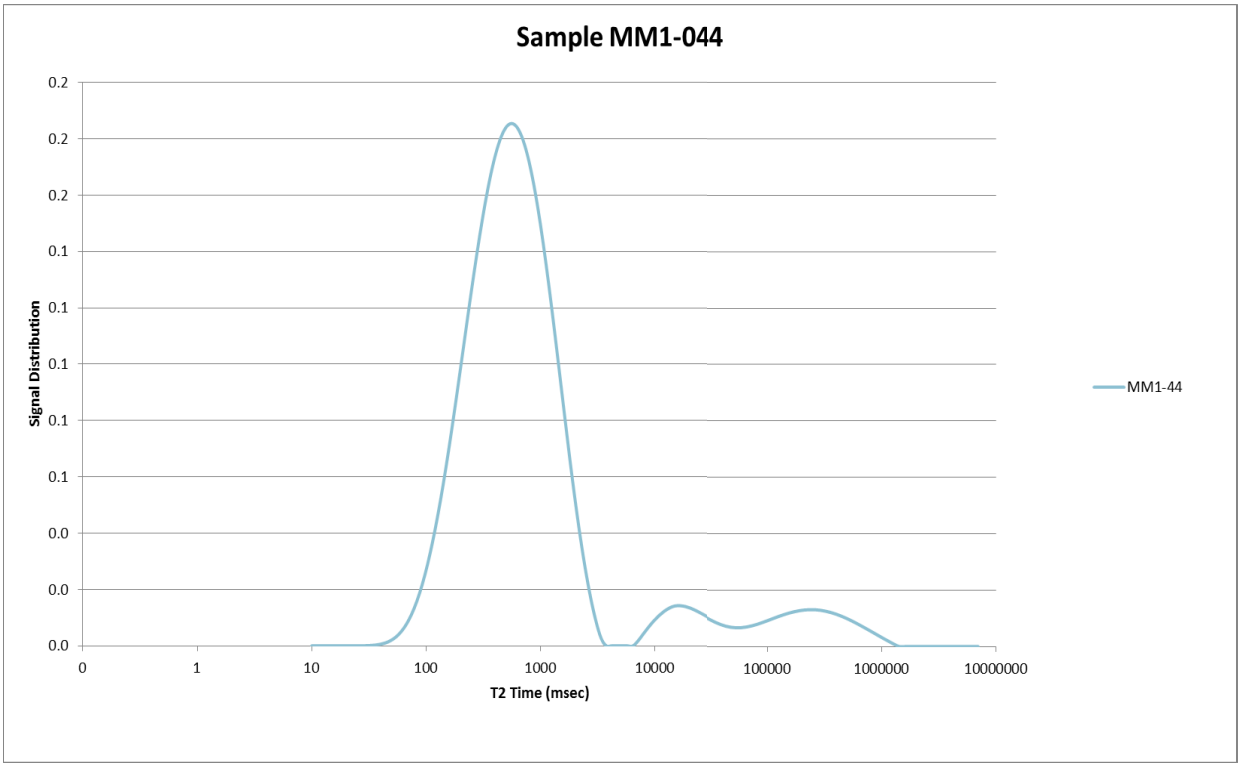

Figure E- 107: Mena Murtee-1 NMR T_2 distribution from the laboratory sample at 1873.03 m used to produce the laboratory synthetic MICP curve.

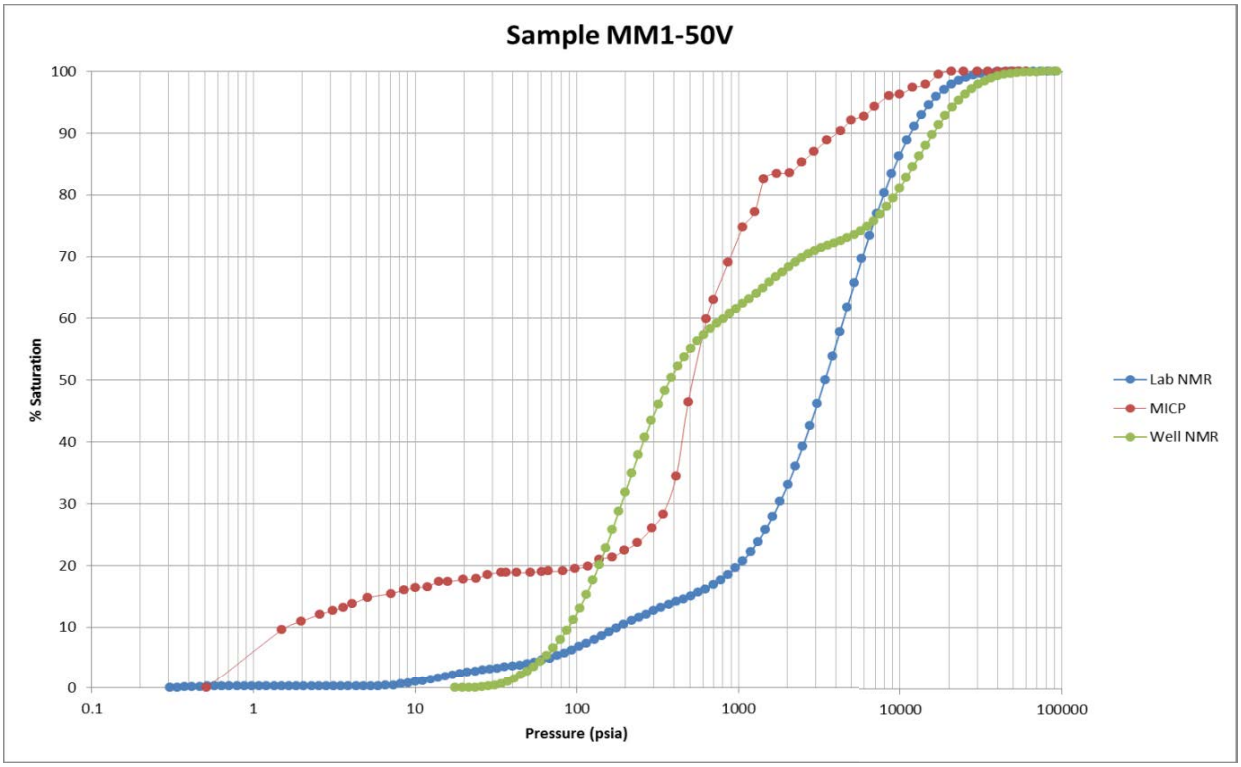

Figure E- 108: Mena Murtee-1 MICP curve from the core sample (MICP) at 2035.39 m. Also shown is the laboratory synthetic NMR (NMR LAB) and well synthetic NMR (NMR) over the same depth interval.

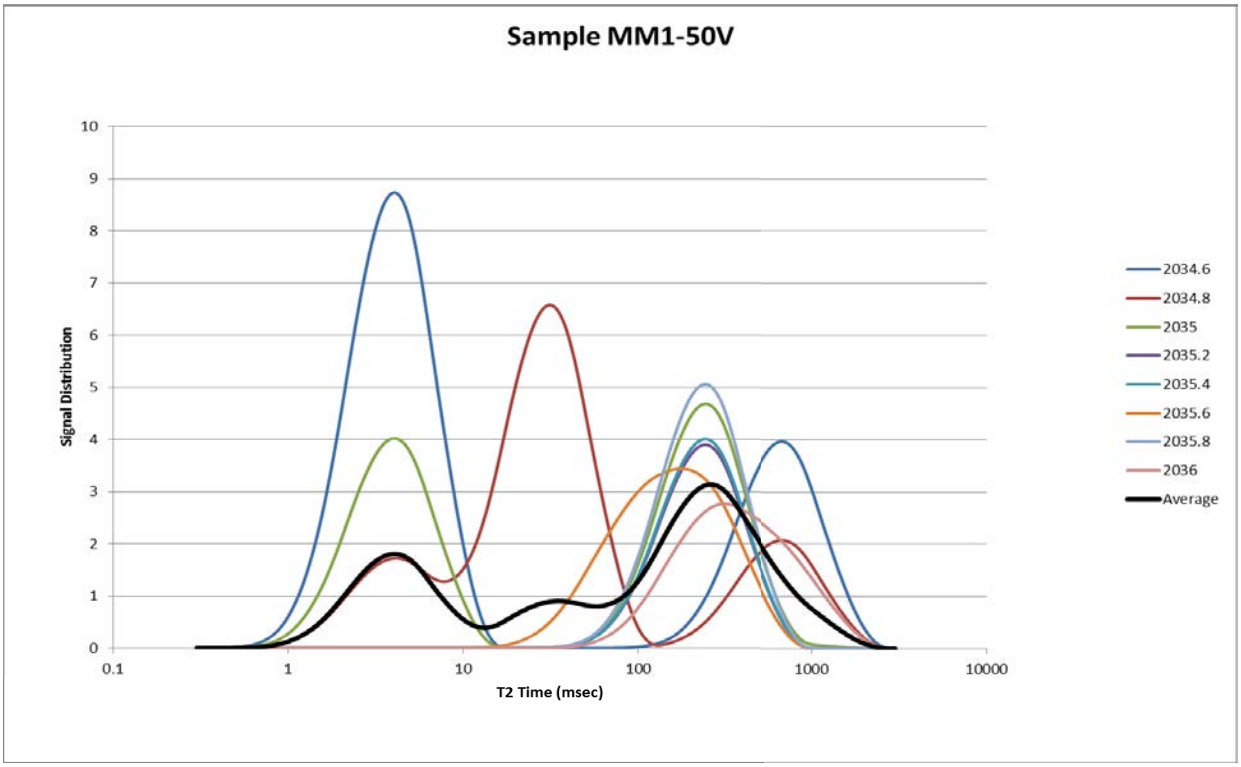

Figure E- 109: Mena Murtee-1 NMR T_2 distributions over the 1.6 m interval used to produce the well synthetic MICP curve at 2035.39 m depth.

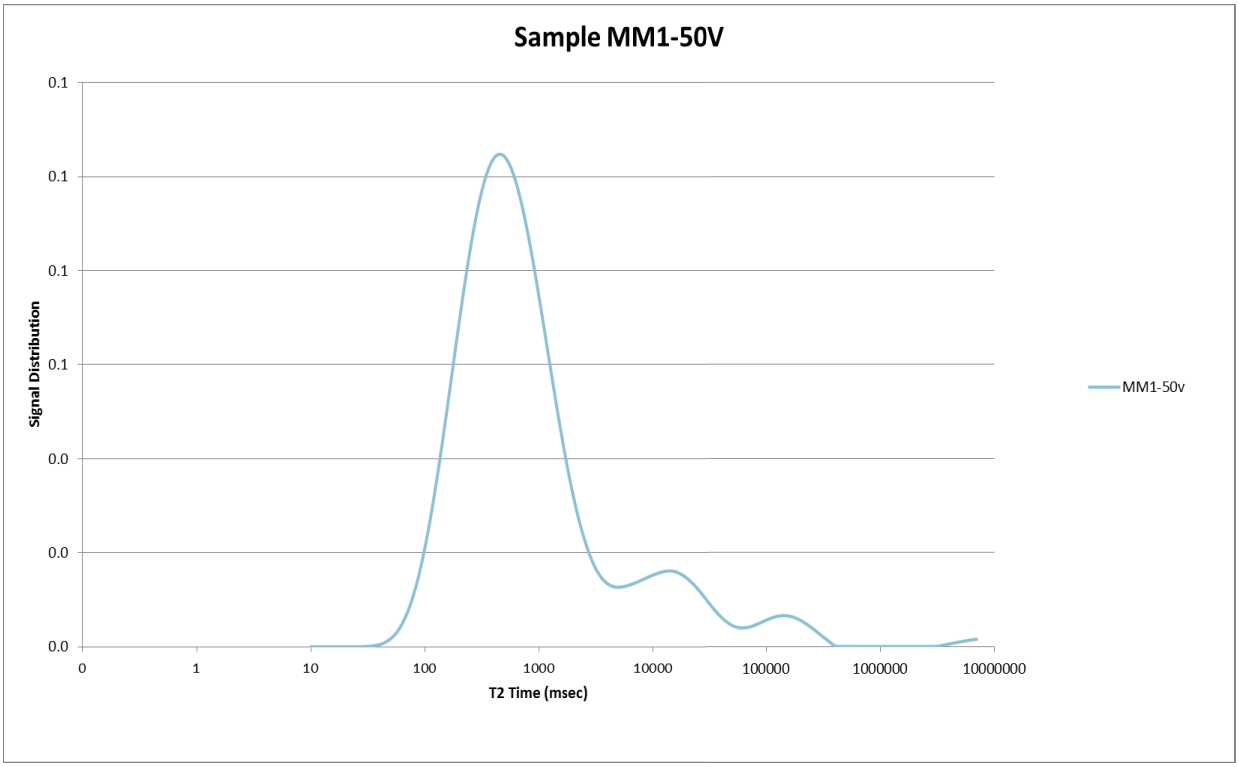

Figure E- 110: Mena Murtee-1 NMR T_2 distribution from the laboratory sample at 2035.39 m used to produce the laboratory synthetic MICP curve.

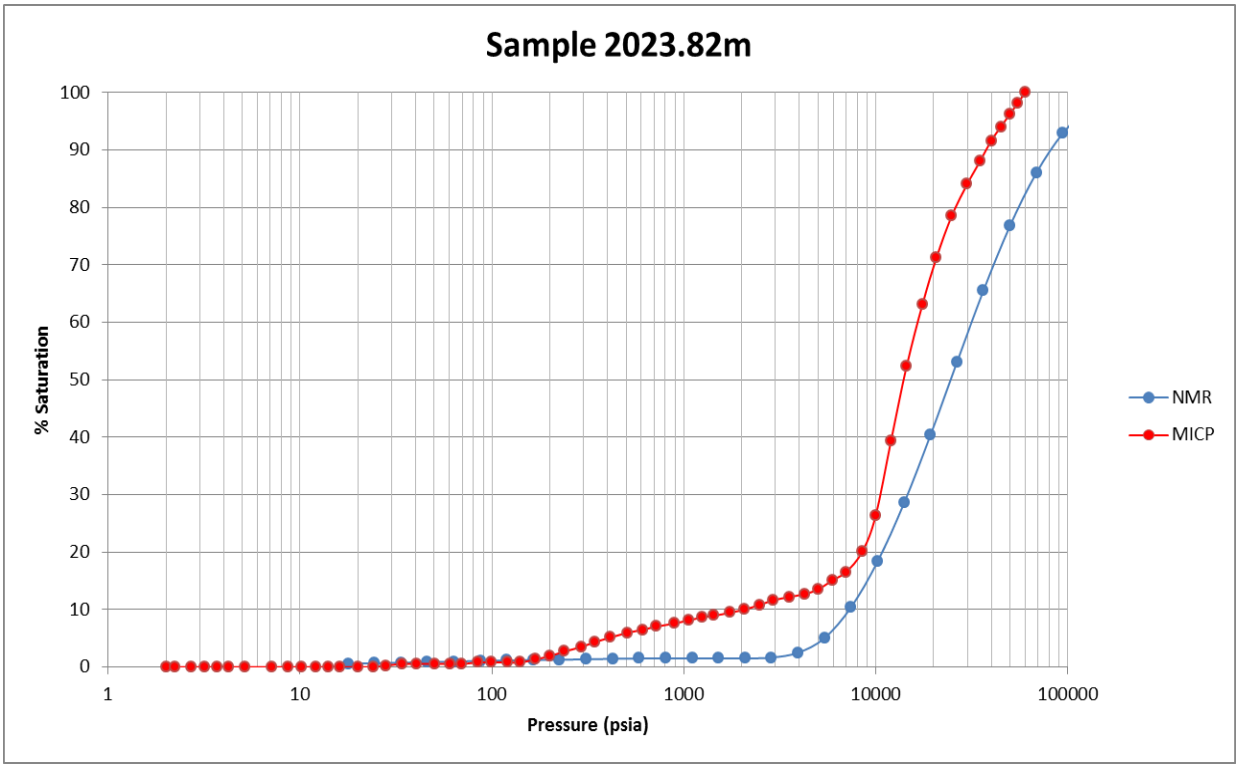

Figure E- 111: Gorgon CO2 Data Well-1& Data Well-1ST1 MICP curve from the core sample (MICP) at 2023.82 m. Also shown is the well synthetic NMR (NMR) over the same depth interval.

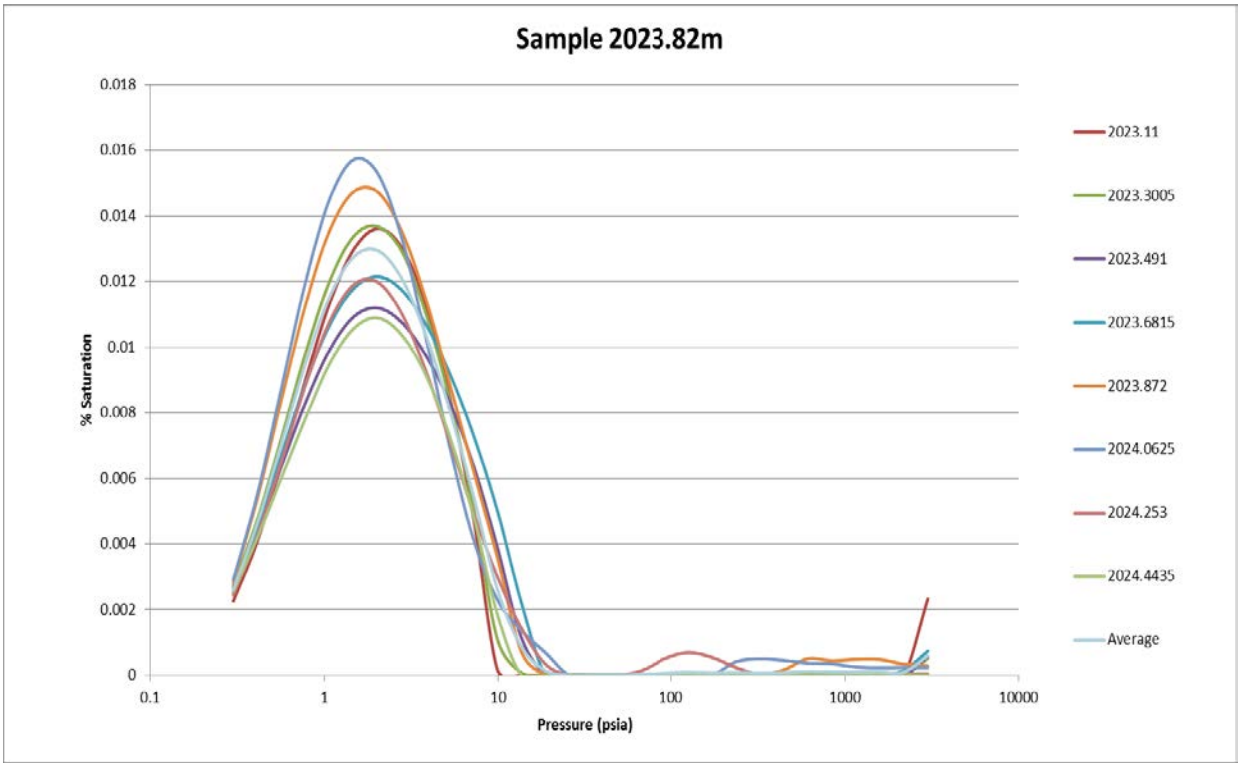

Figure E- 112: Gorgon CO2 Data Well-1& Data Well-1ST1 NMR T_2 distributions over the 1.6 m interval used to produce the well synthetic MICP curve at 2023.82 m depth.

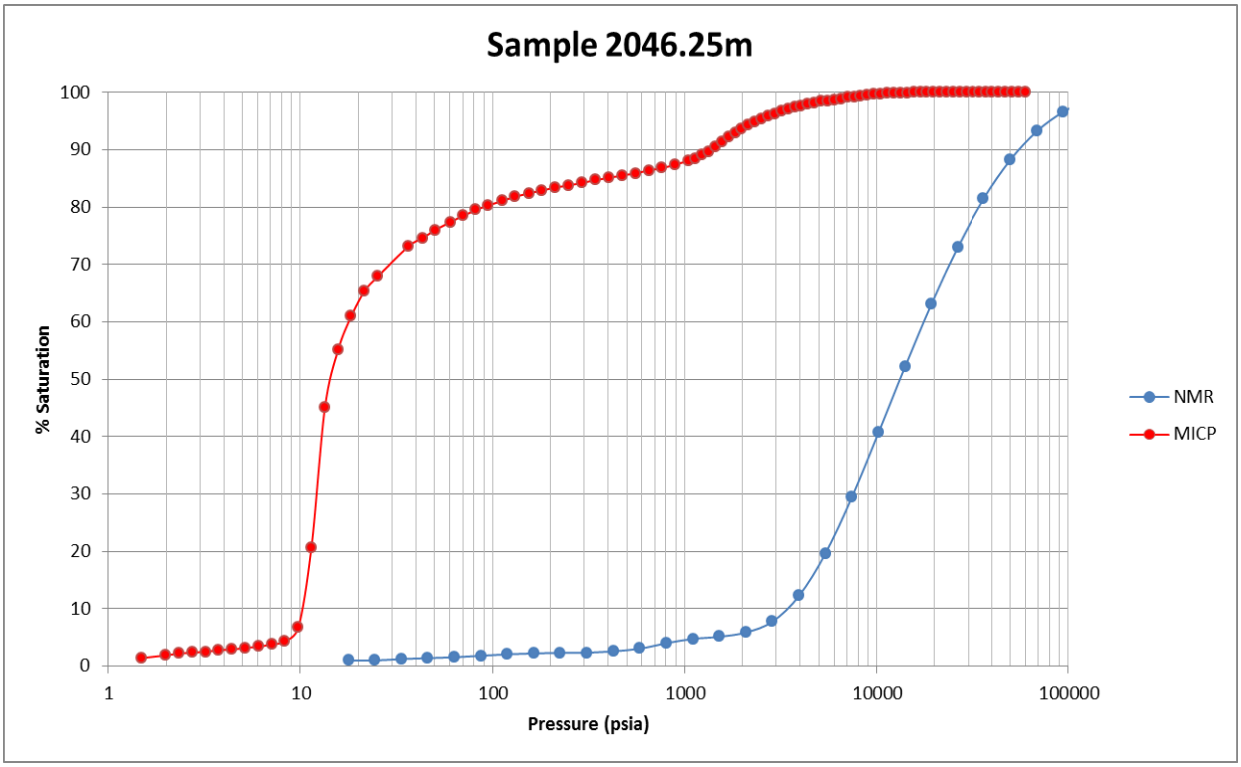

Figure E- 113: Gorgon CO2 Data Well-1& Data Well-1ST1 MICP curve from the core sample (MICP) at 2046.25 m. Also shown is the well synthetic NMR (NMR) over the same depth interval.

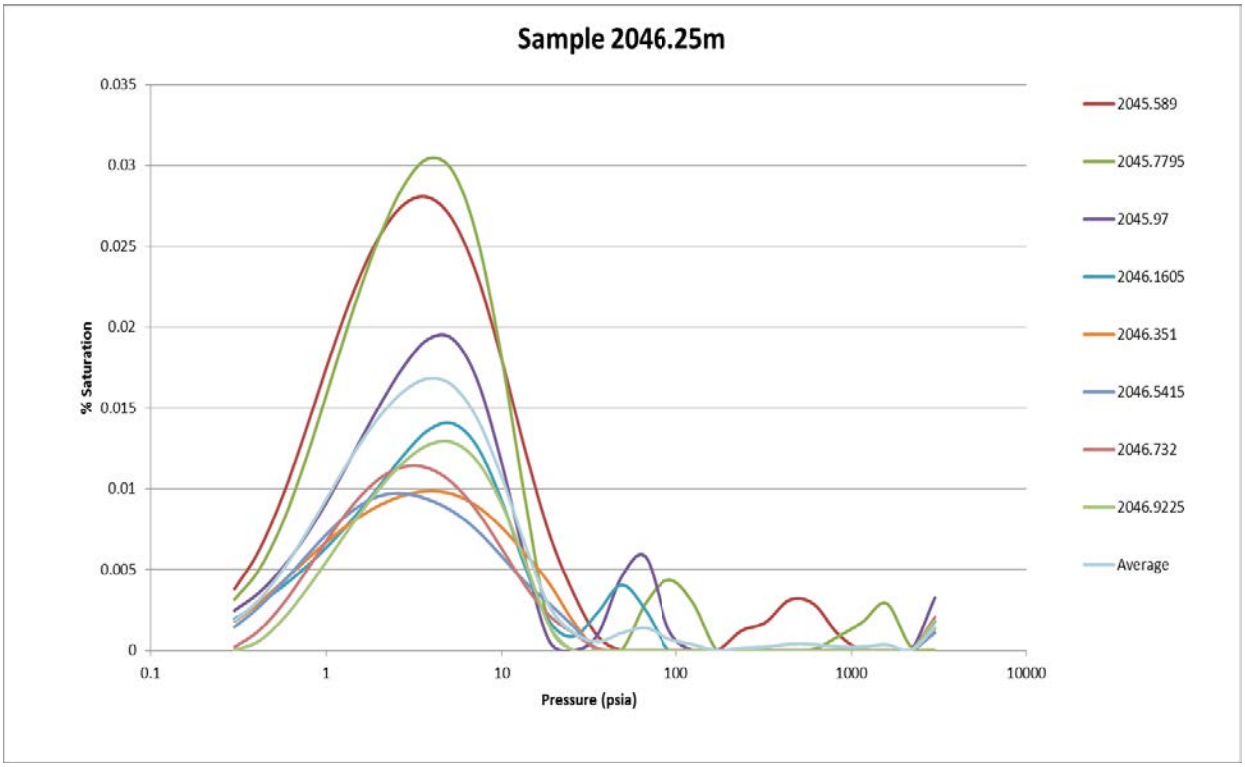

Figure E- 114: Gorgon CO2 Data Well-1& Data Well-1ST1 NMR T_2 distributions over the 1.6 m interval used to produce the well synthetic MICP curve at 2046.25 m depth.

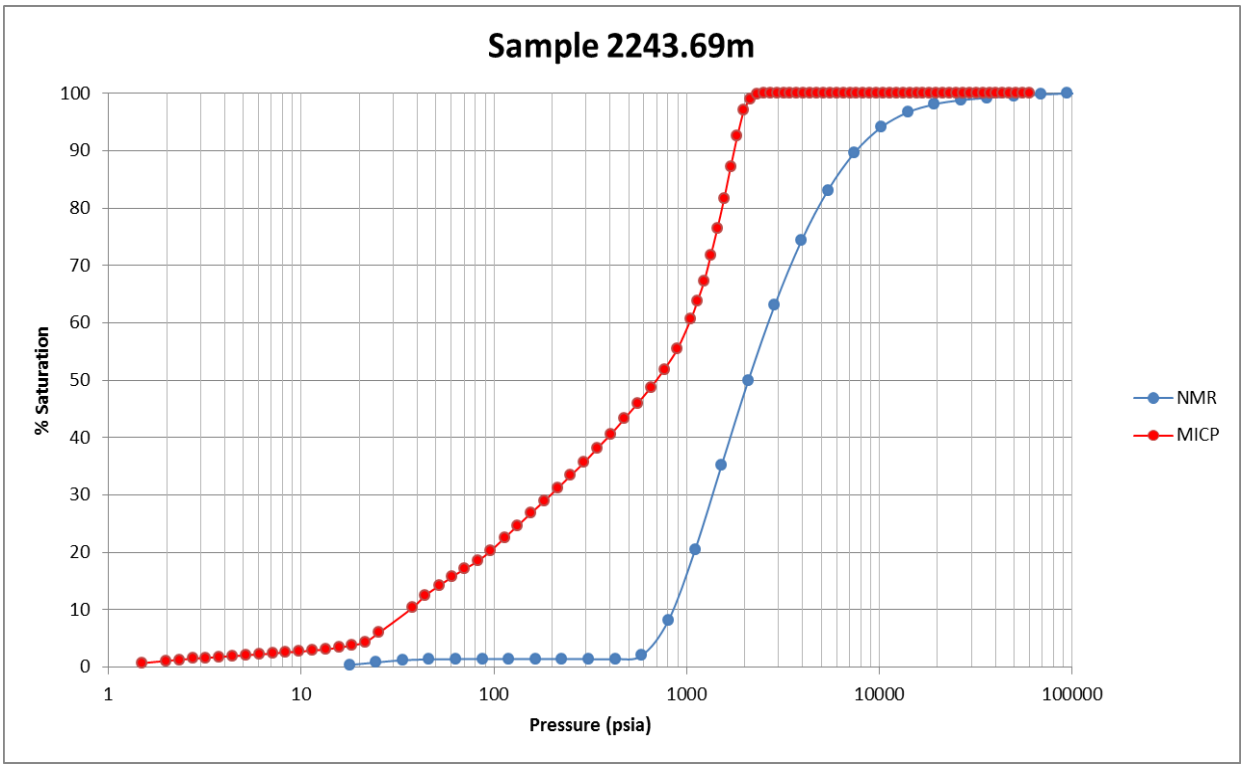

Figure E- 115: Gorgon CO2 Data Well-1& Data Well-1ST1 MICP curve from the core sample (MICP) at 2243.69 m. Also shown is the well synthetic NMR (NMR) over the same depth interval.

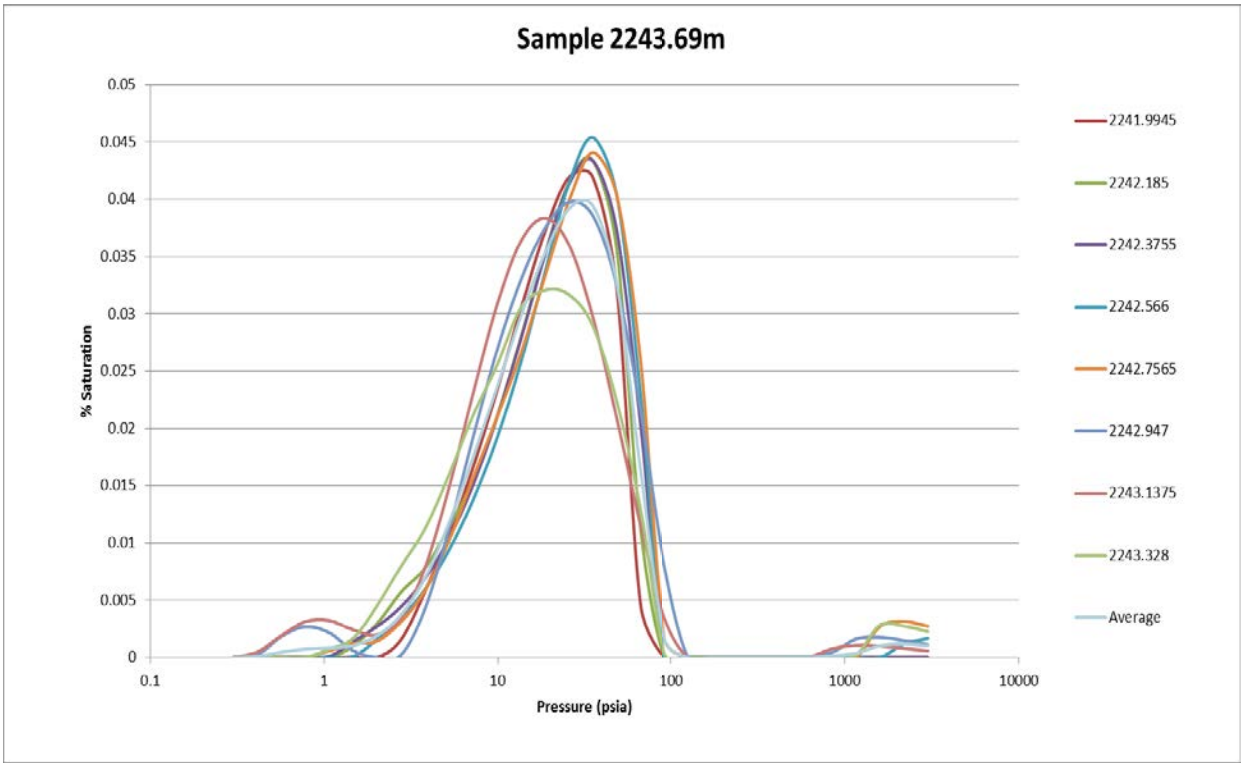

Figure E- 116: Gorgon CO2 Data Well-1& Data Well-1ST1 NMR T_2 distributions over the 1.6 m interval used to produce the well synthetic MICP curve at 2243.69 m depth.

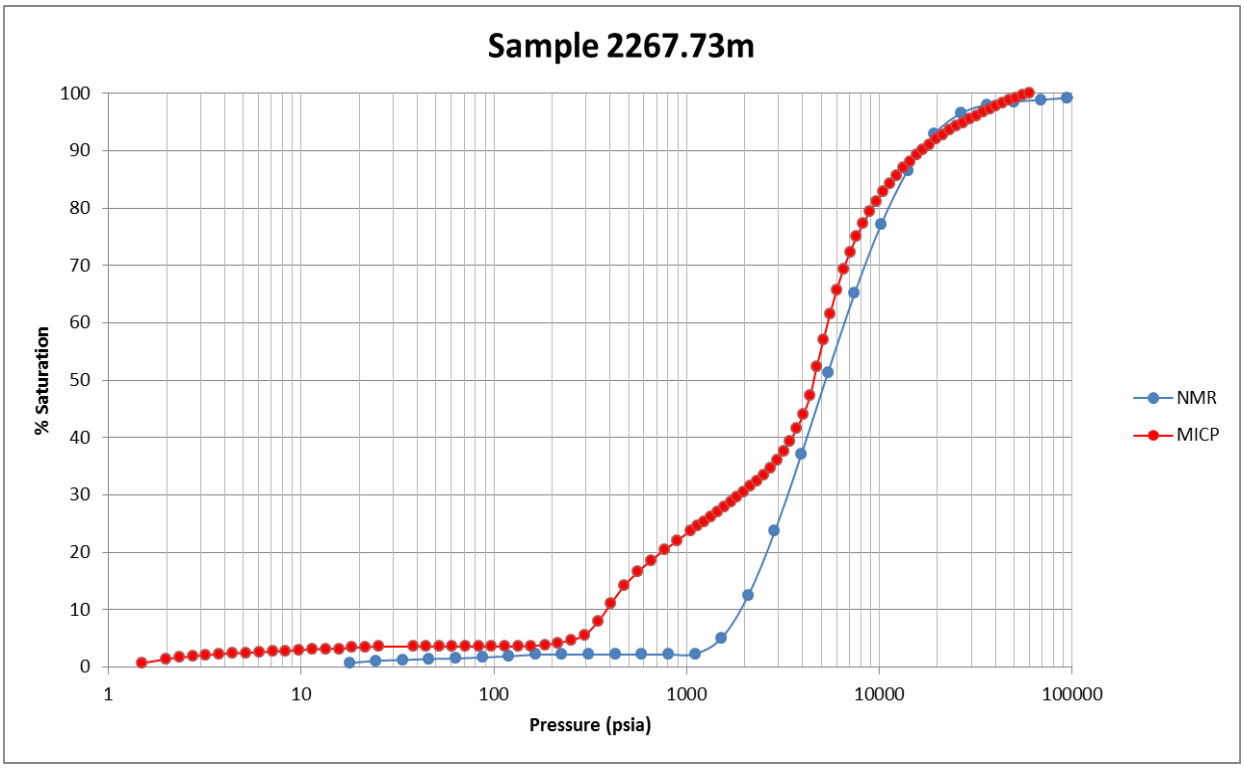

Figure E- 117: Gorgon CO2 Data Well-1& Data Well-1ST1 MICP curve from the core sample (MICP) at 2267.73 m. Also shown is the well synthetic NMR (NMR) over the same depth interval.

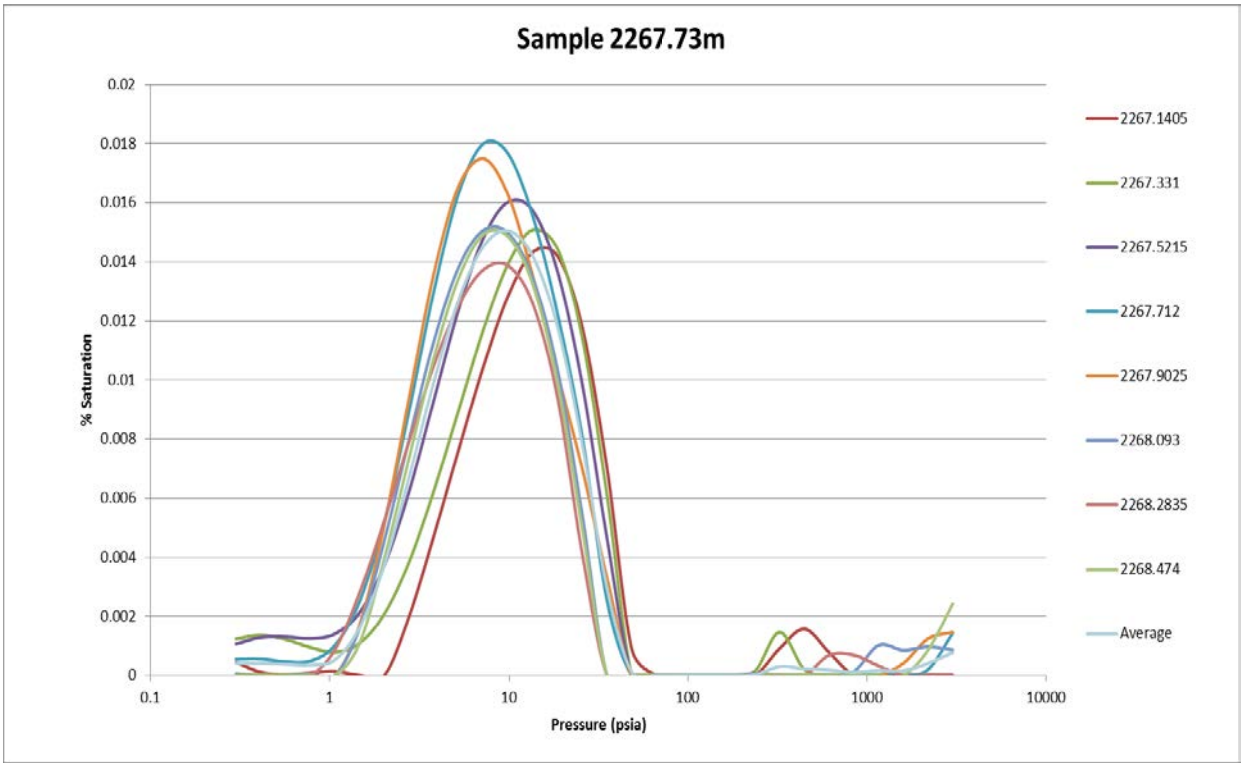

Figure E- 118: Gorgon CO2 Data Well-1& Data Well-1ST1 NMR T_2 distributions over the 1.6 m interval used to produce the well synthetic MICP curve at 2267.73 m depth.

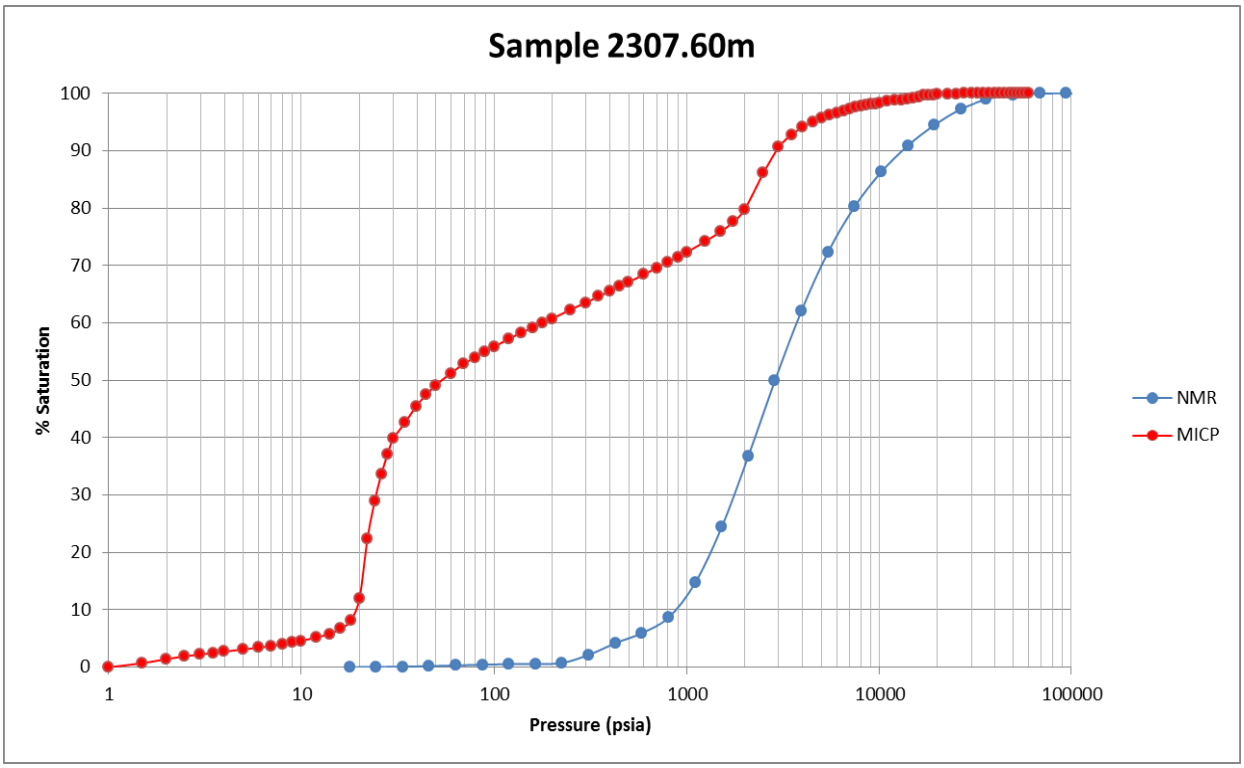

Figure E- 119: Gorgon CO2 Data Well-1& Data Well-1ST1 MICP curve from the core sample (MICP) at 2307.60 m. Also shown is the well synthetic NMR (NMR) over the same depth interval.

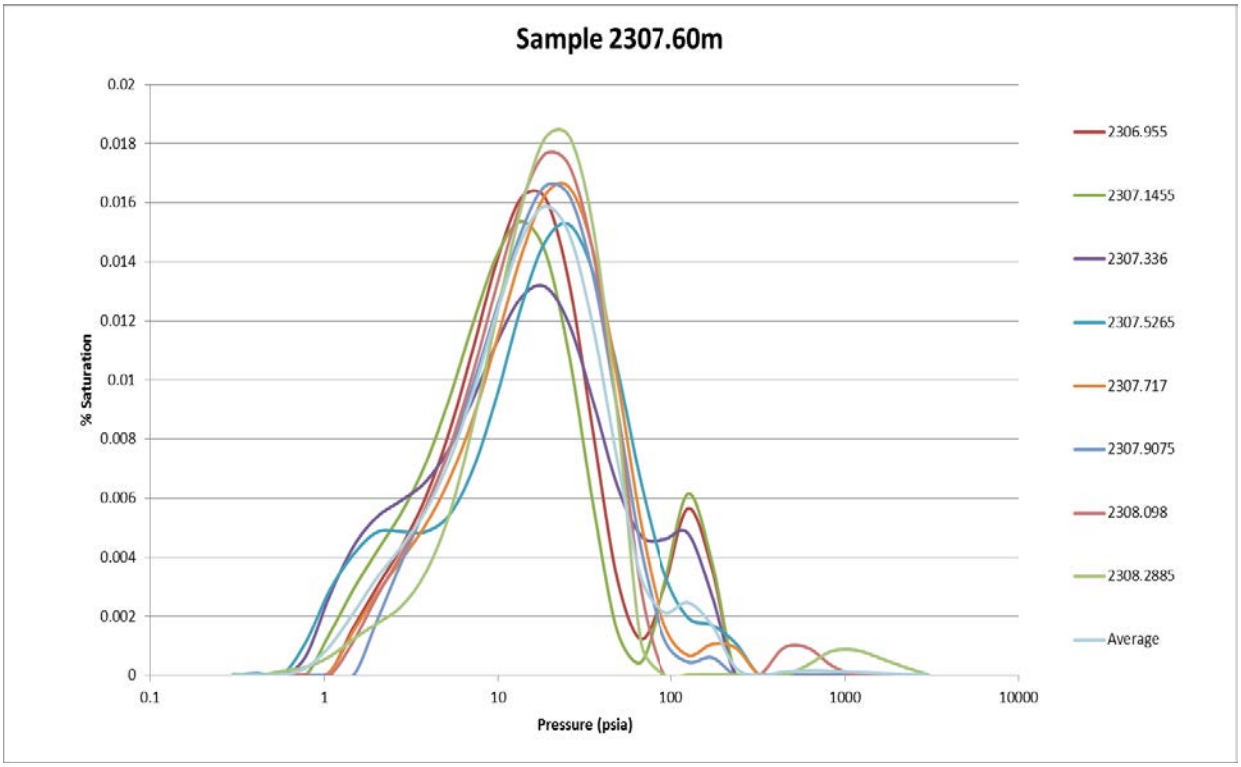

Figure E- 120: Gorgon CO2 Data Well-1& Data Well-1ST1 NMR T_2 distributions over the 1.6 m interval used to produce the well synthetic MICP curve at 2307.60 m depth.

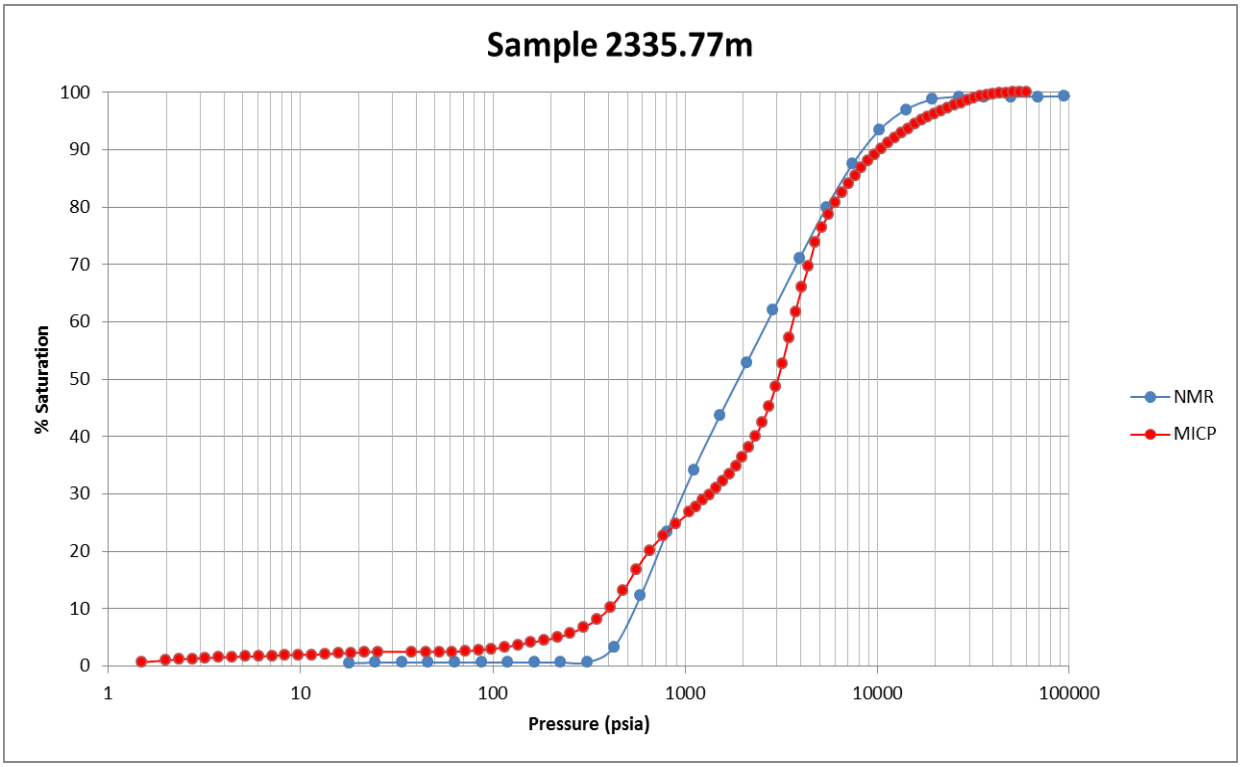

Figure E- 121: Gorgon CO2 Data Well-1& Data Well-1ST1 MICP curve from the core sample (MICP) at 2335.77 m. Also shown is the well synthetic NMR (NMR) over the same depth interval.

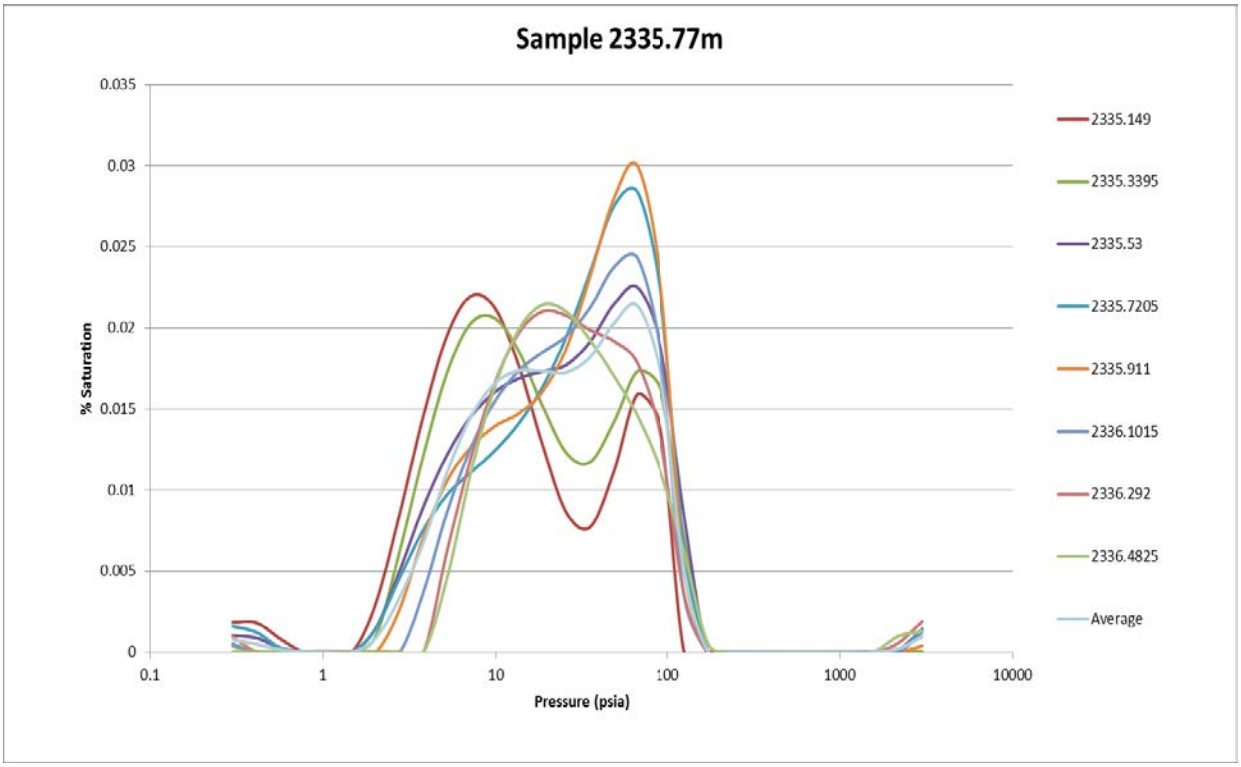

Figure E- 122: Gorgon CO2 Data Well-1& Data Well-1ST1 NMR T_2 distributions over the 1.6 m interval used to produce the well synthetic MICP curve at 2335.77 m depth.

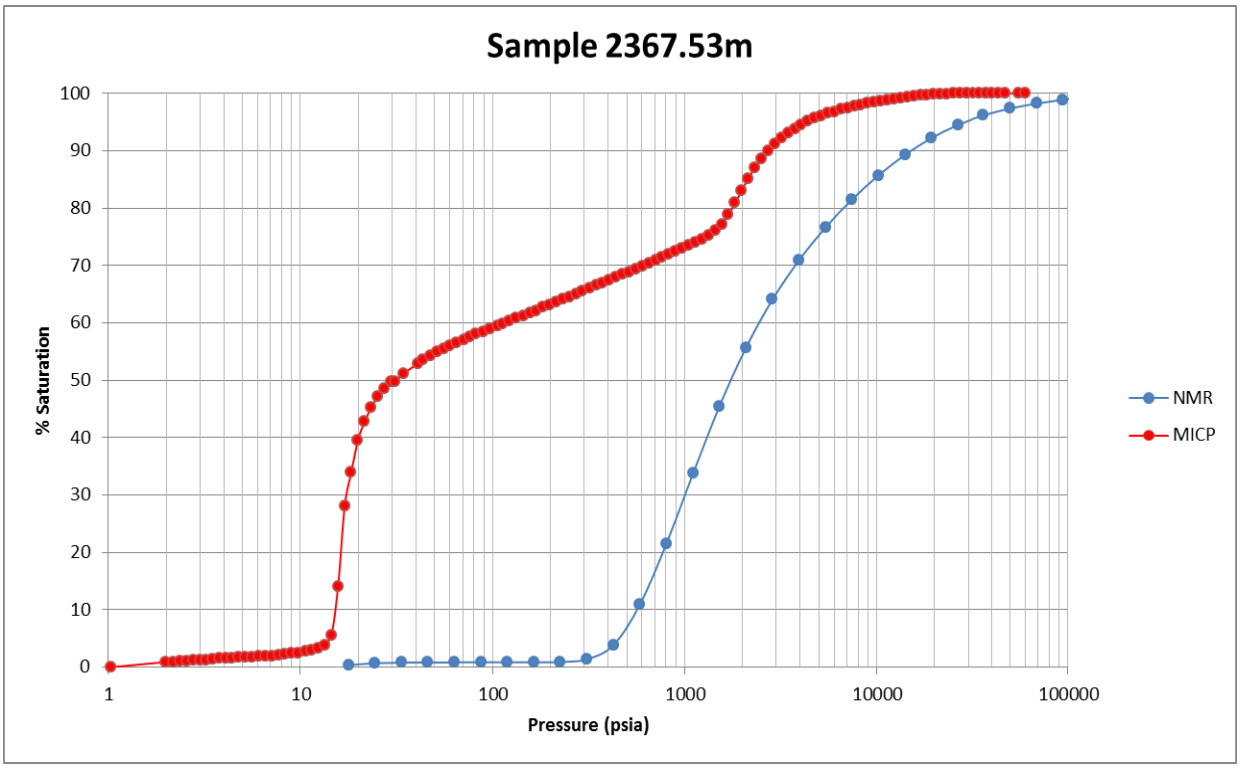

Figure E- 123: Gorgon CO2 Data Well-1& Data Well-1ST1 MICP curve from the core sample (MICP) at 2367.53 m. Also shown is the well synthetic NMR (NMR) over the same depth interval.

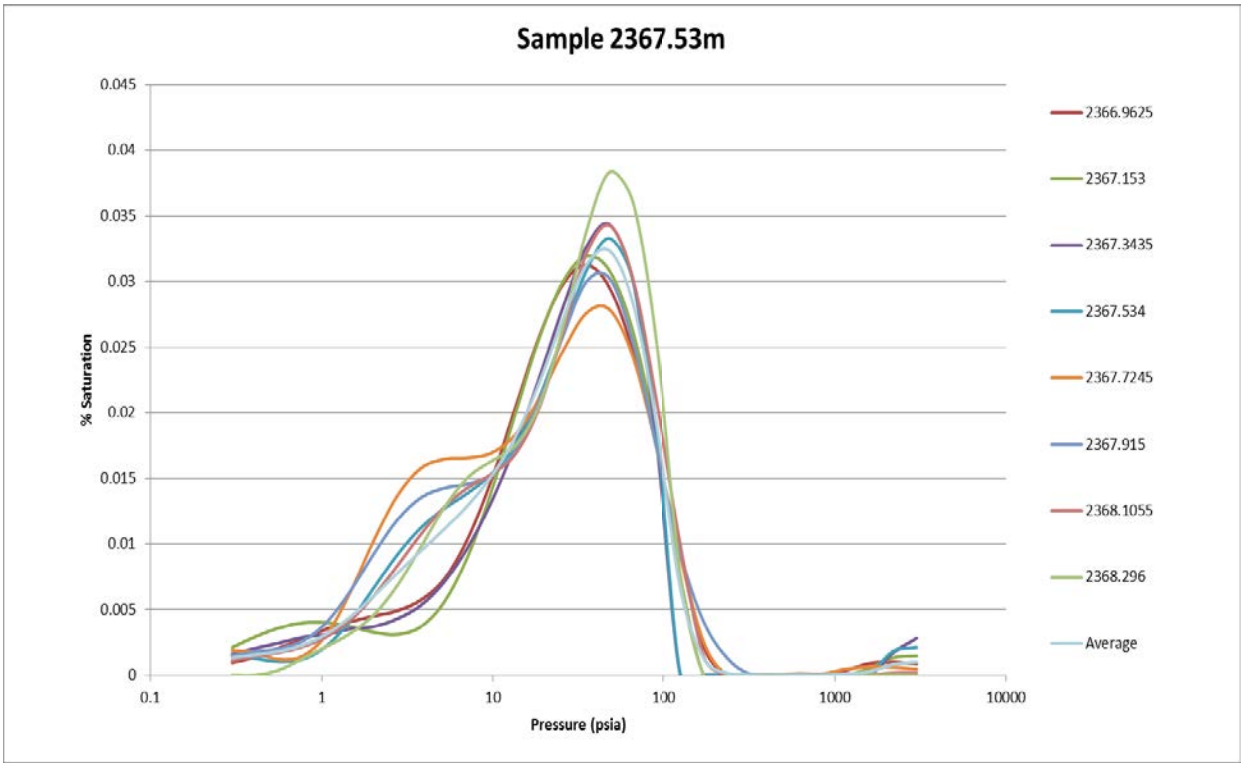

Figure E- 124: Gorgon CO2 Data Well-1& Data Well-1ST1 NMR T_2 distributions over the 1.6 m interval used to produce the well synthetic MICP curve at 2367.53 m depth.

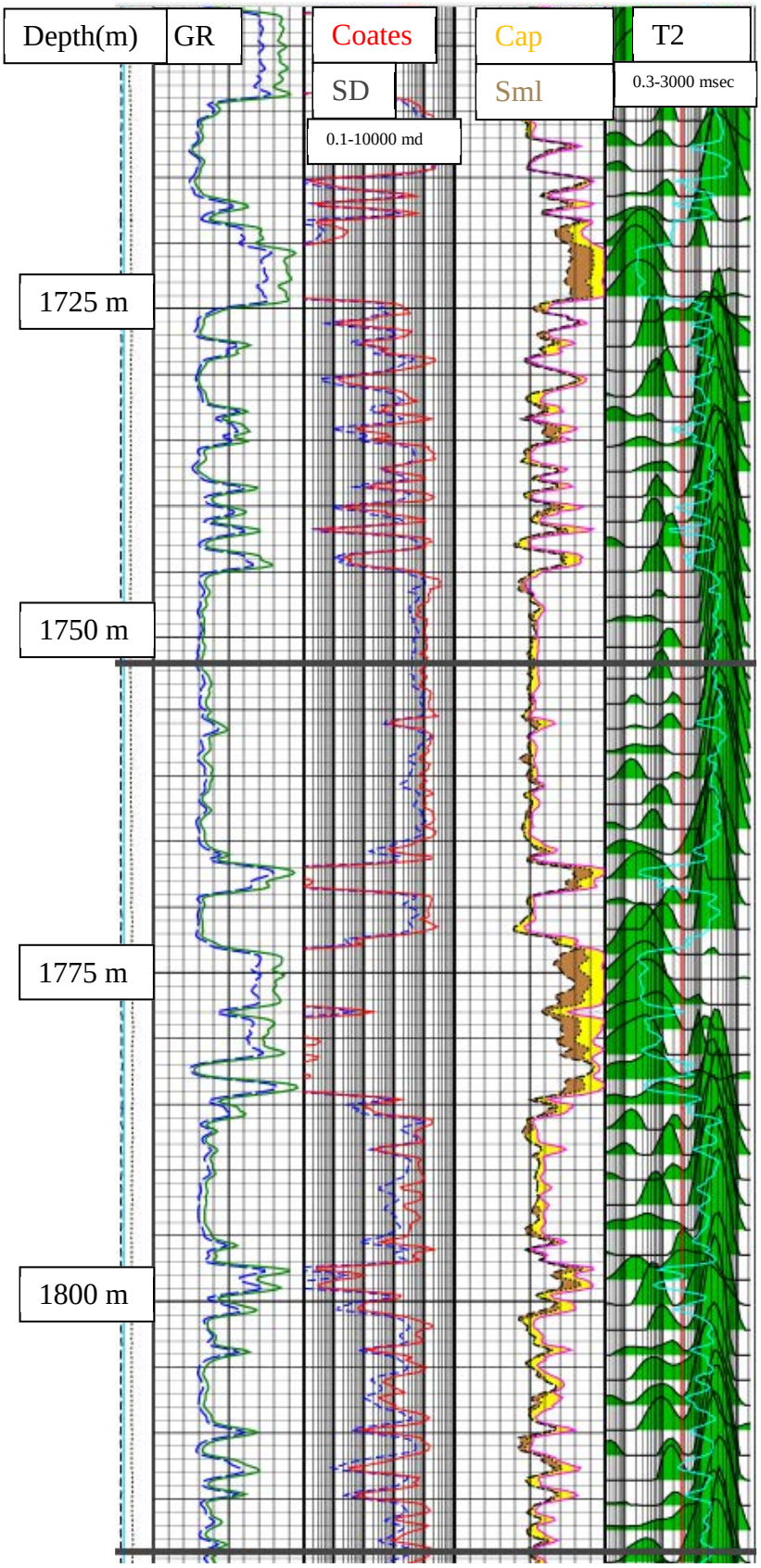

Figure E- 125: Gorgon CO2 Data Well-1& Data Well-1ST1 CMR (NMR) log between 1700m-1825 m depth. The composite log shows gamma (GR), Timur Coates (Coates) Schlumberger Doll Research (SDR) permeability, capillary bound (Cap Bnd) and small pore (Sml Pore) porosity and the T_2 distribution (T_2 Dist) (Image modified from WCR, Ellis, 2009).

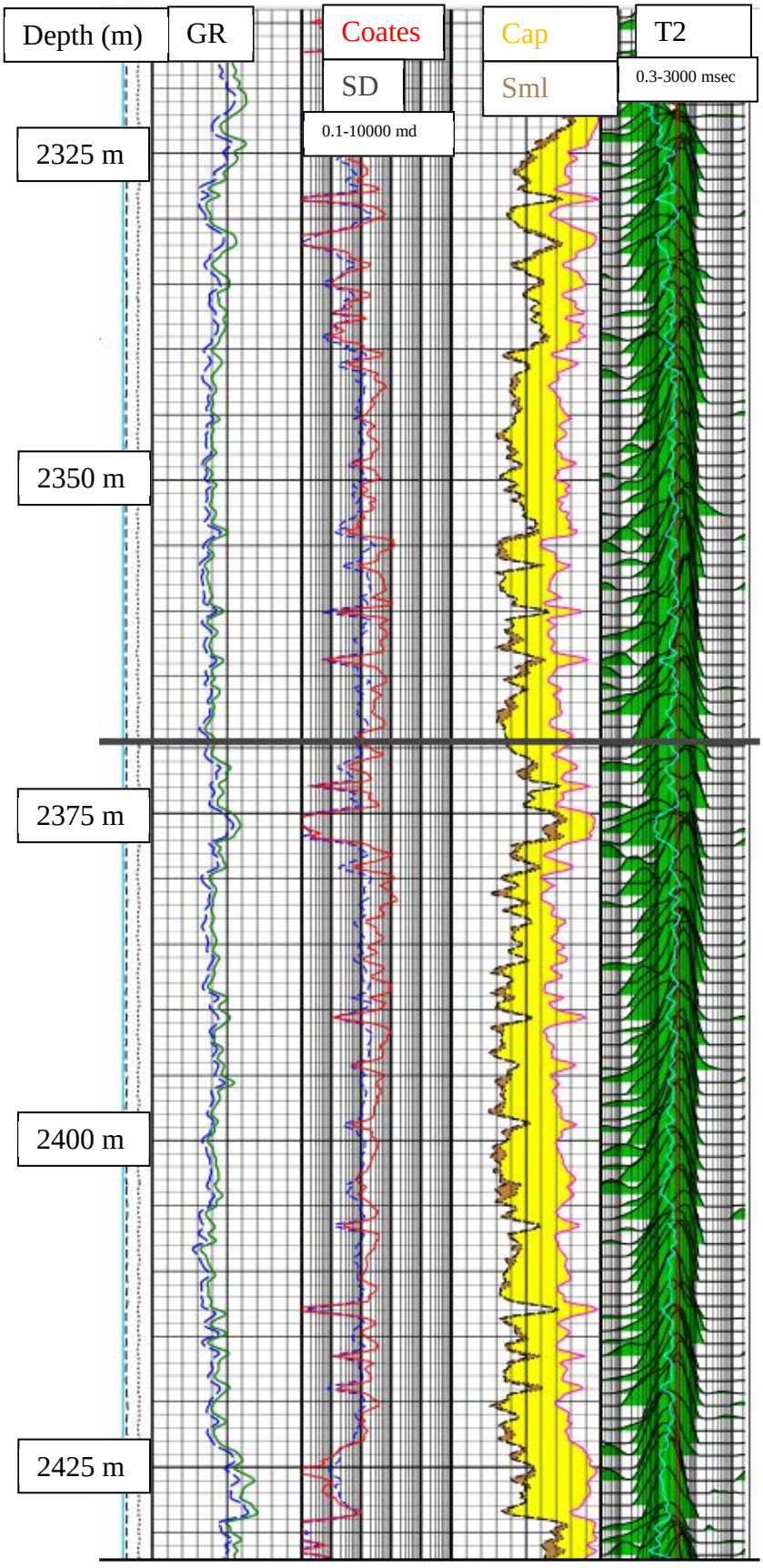

Figure E- 126: Gorgon CO2 Data Well-1& Data Well-1ST1 CMR (NMR) log between 2300m-2450 m depth. The composite log shows gamma (GR), Timur Coates (Coates) Schlumberger Doll Research (SDR) permeability, capillary bound (Cap Bnd) and small pore (Sml Pore) porosity and the T_2 distribution (T_2 Dist) (Image modified from WCR, Ellis, 2009).

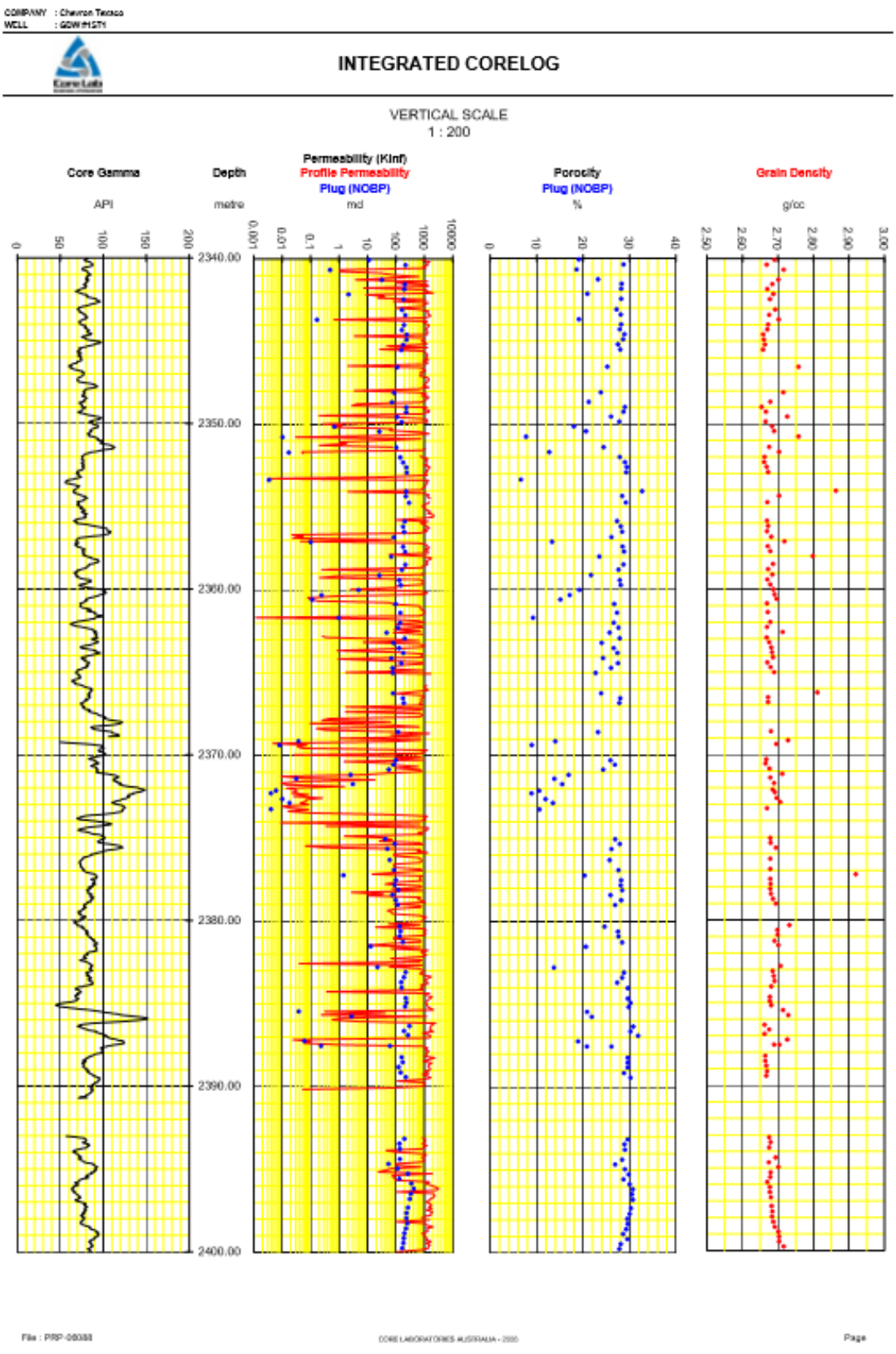

Figure E- 127: Gorgon CO2 Data Well-1& Data Well-1ST1 conventional core log between 2340 m -2400 m depth. The composite log shows gamma, permeability, porosity and grain density (Image from WCR, Ellis, 2009).

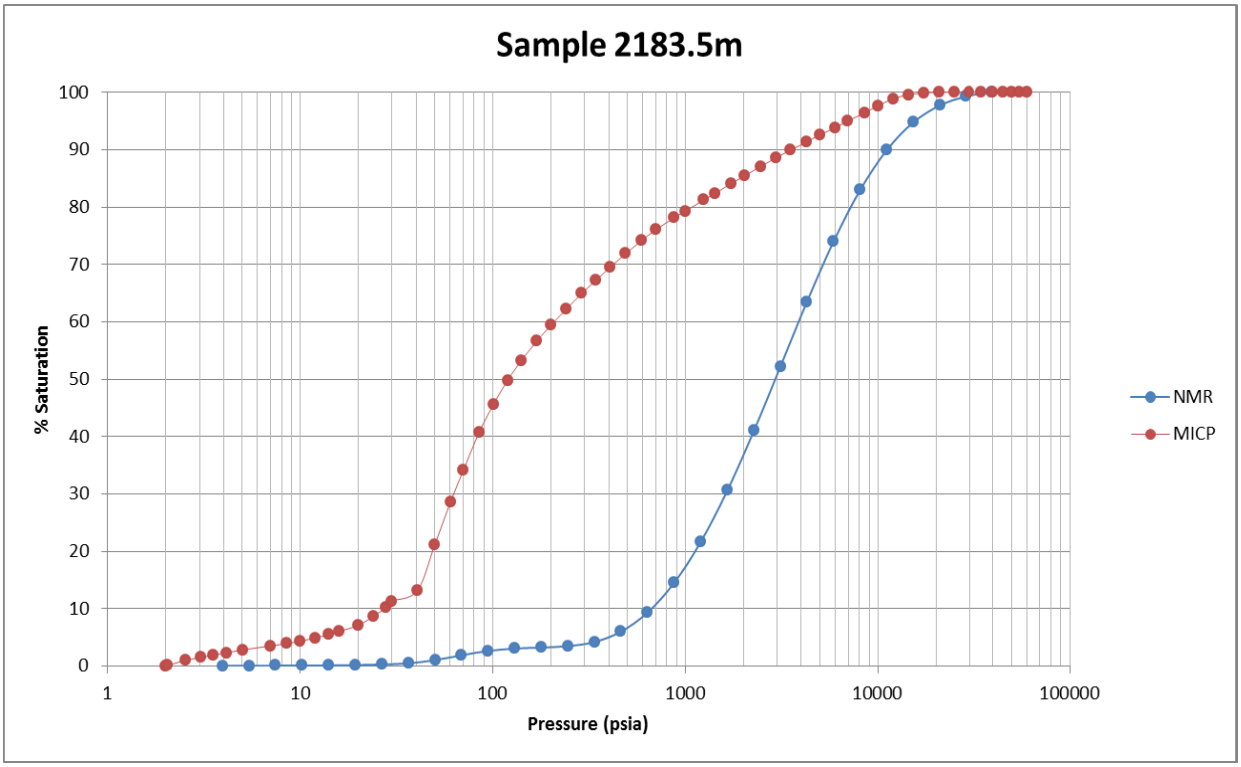

Figure E- 128: Thebe-2 MICP curve from the core sample (MICP) at 2183.5 m. Also shown is the well synthetic NMR (NMR) over the same depth interval.

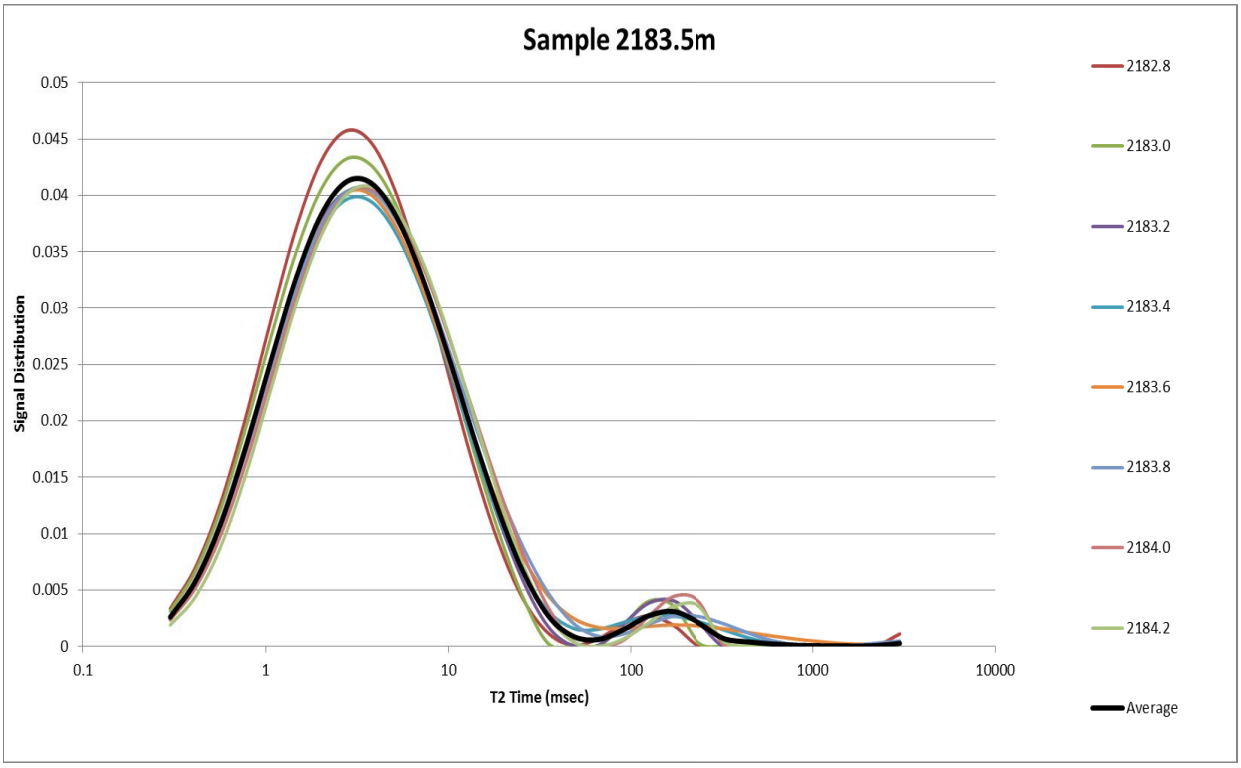

Figure E- 129: Thebe-2 NMR T_2 distributions over the 1.6 m interval used to produce the well synthetic MICP curve at 2183.5 m depth.

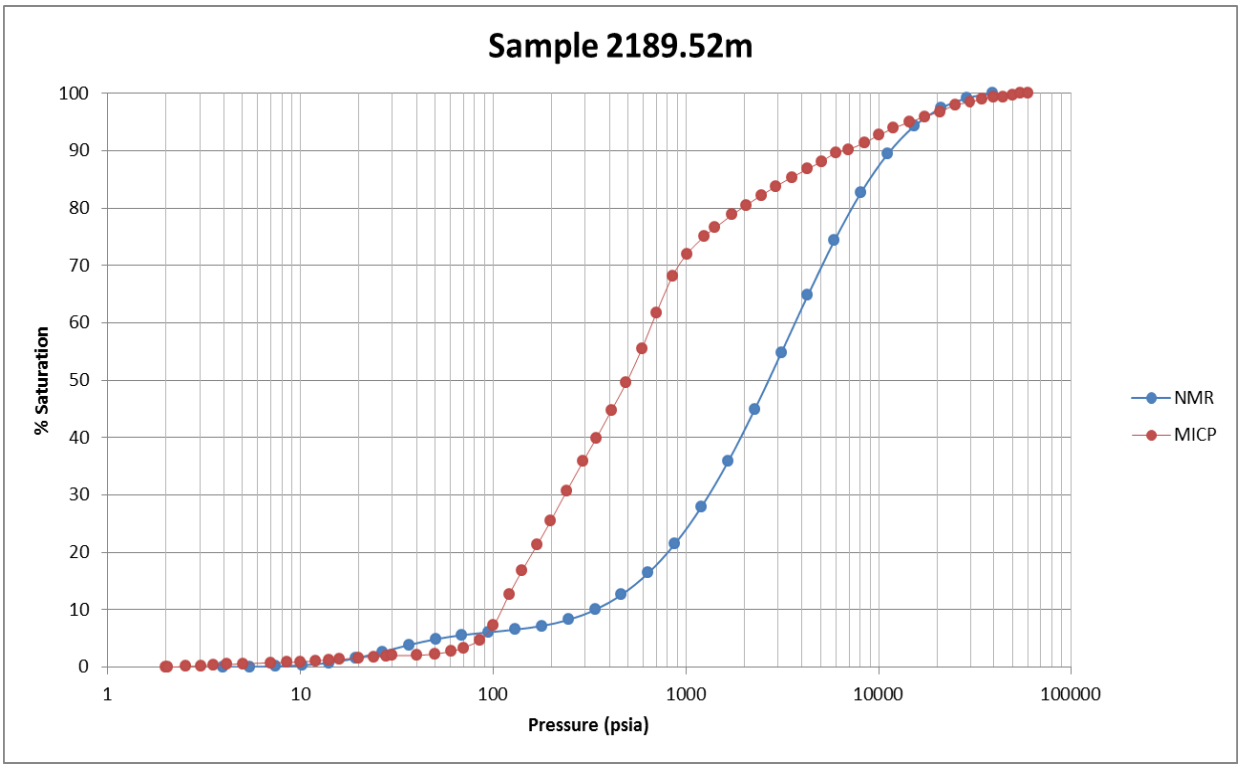

Figure E- 130: Thebe-2 MICP curve from the core sample (MICP) at 2189.52 m. Also shown is the well synthetic NMR (NMR) over the same depth interval.

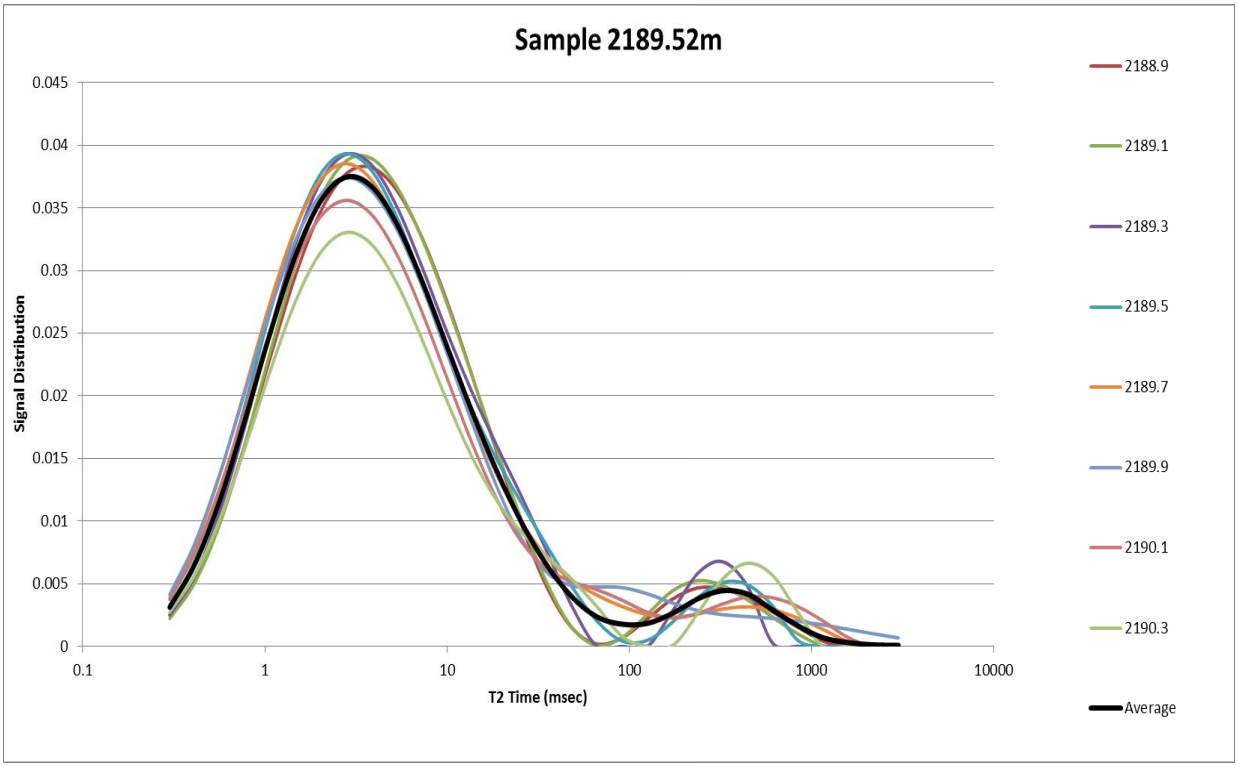

Figure E- 131: Thebe-2 NMR T_2 distributions over the 1.6 m interval used to produce the well synthetic MICP curve at 2189.52 m depth.

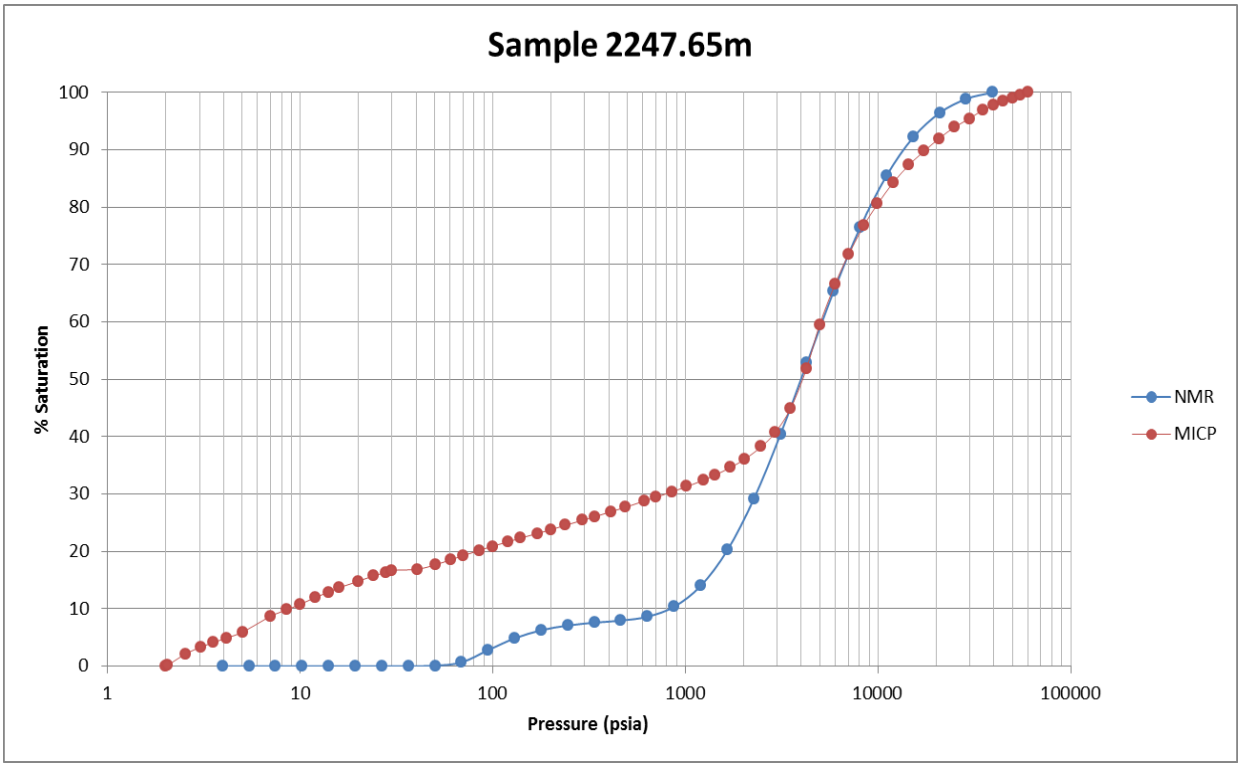

Figure E- 132: Thebe-2 MICP curve from the core sample (MICP) at 2247.65 m. Also shown is the well synthetic NMR (NMR) over the same depth interval.

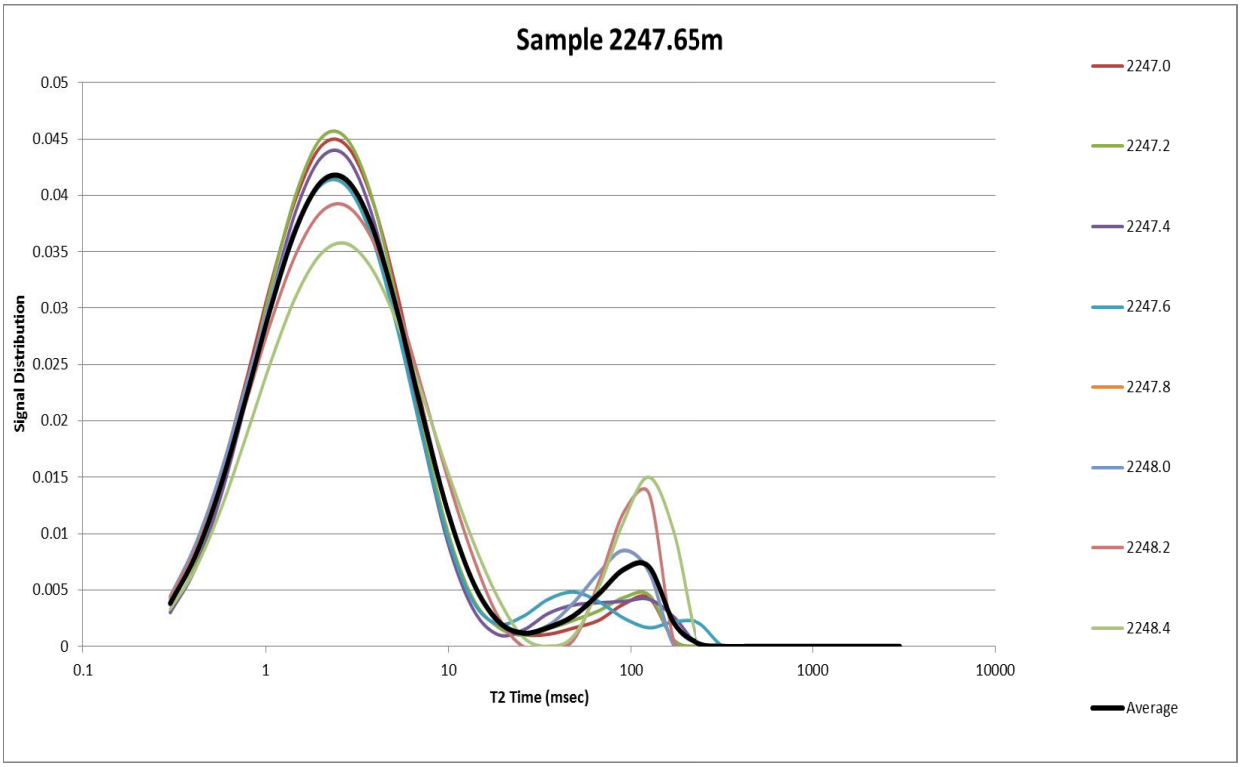

Figure E- 133: Thebe-2 NMR T_2 distributions over the 1.6 m interval used to produce the well synthetic MICP curve at 2247.65 m depth.

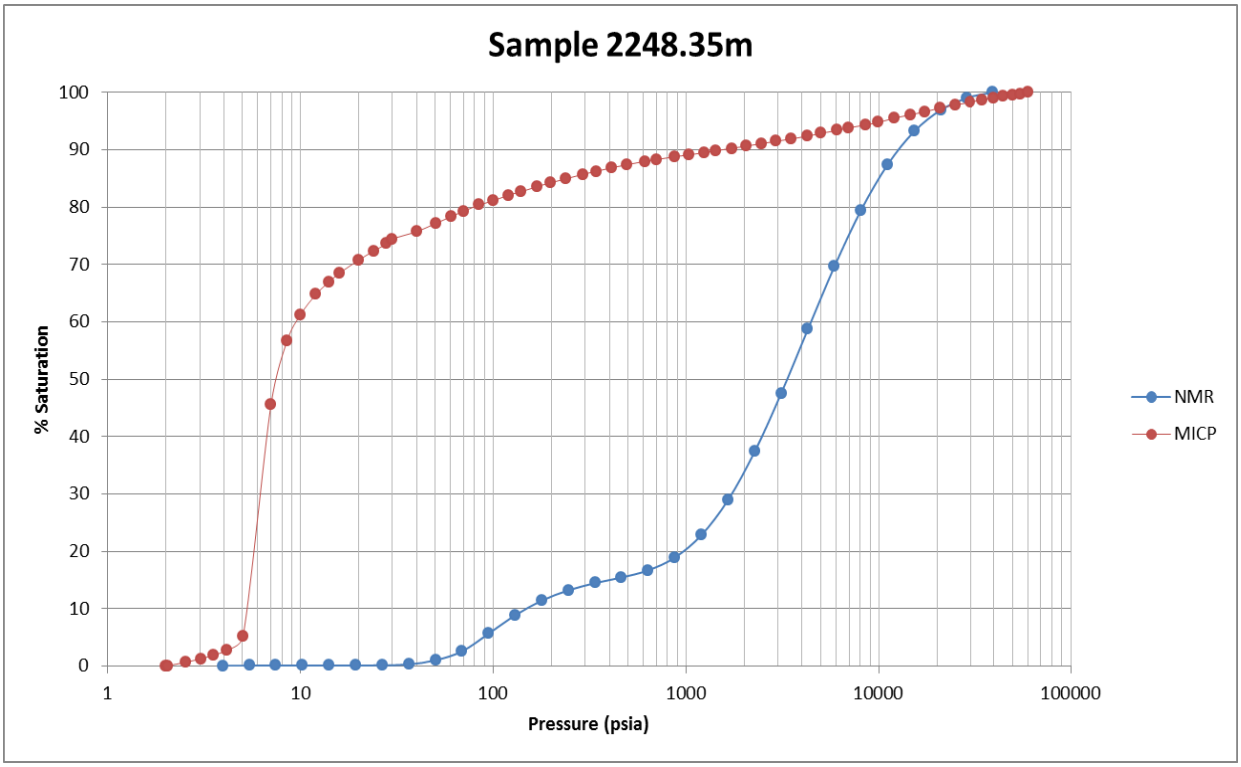

Figure E- 134: Thebe-2 MICP curve from the core sample (MICP) at 2248.35 m. Also shown is the well synthetic NMR (NMR) over the same depth interval.

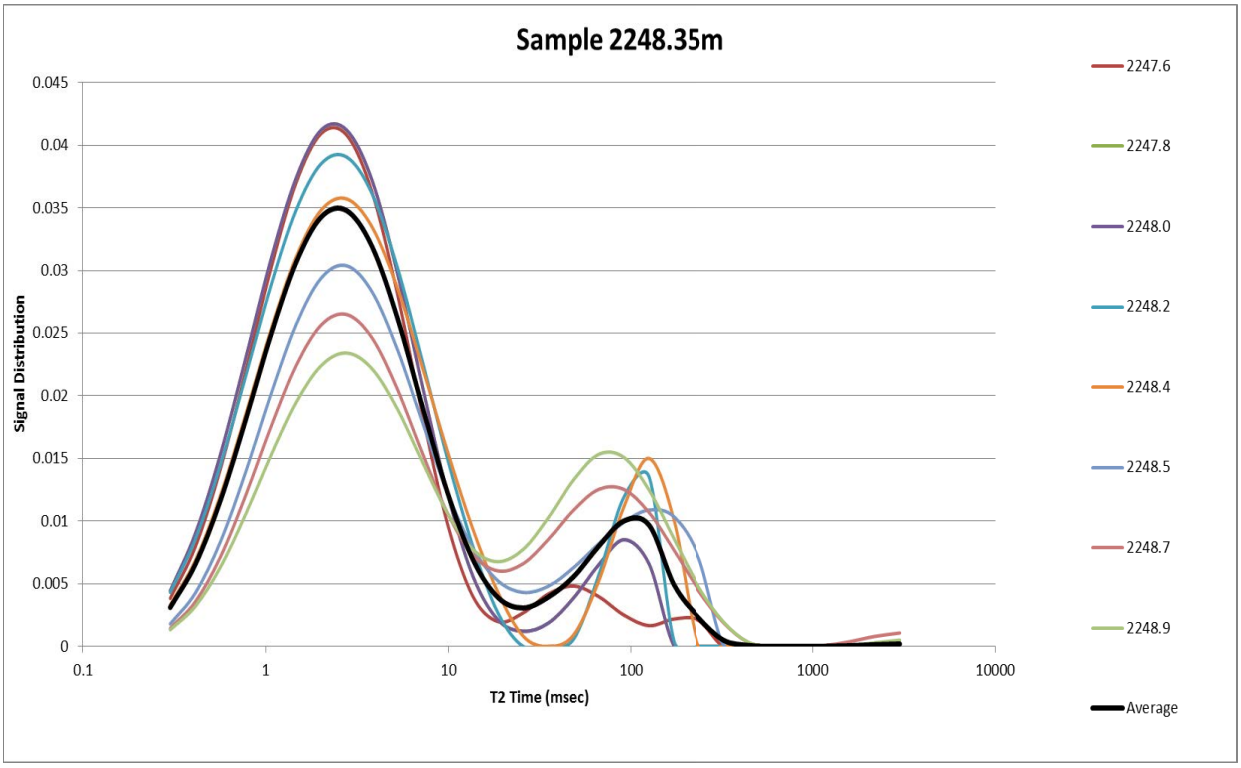

Figure E- 135: Thebe-2 NMR T_2 distributions over the 1.6 m interval used to produce the well synthetic MICP curve at 2248.35 m depth.

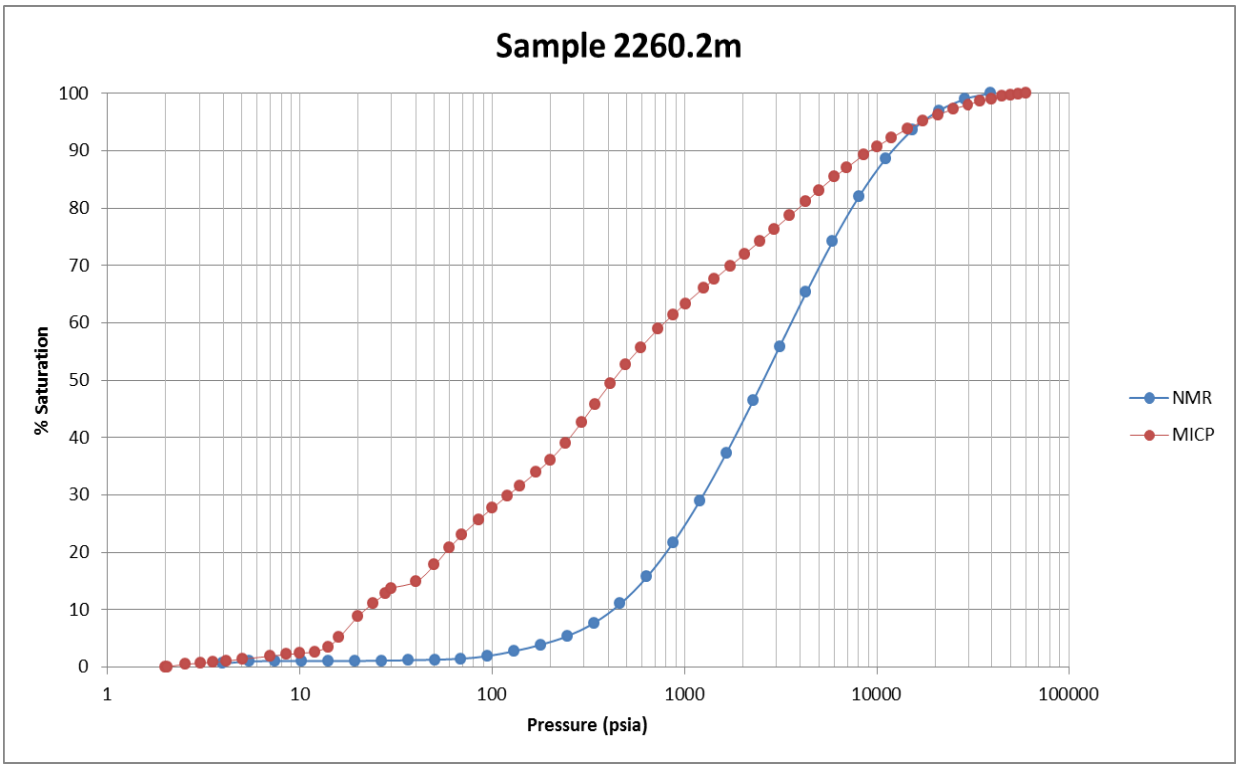

Figure E- 136: Thebe-2 MICP curve from the core sample (MICP) at 2260.2 m. Also shown is the well synthetic NMR (NMR) over the same depth interval.

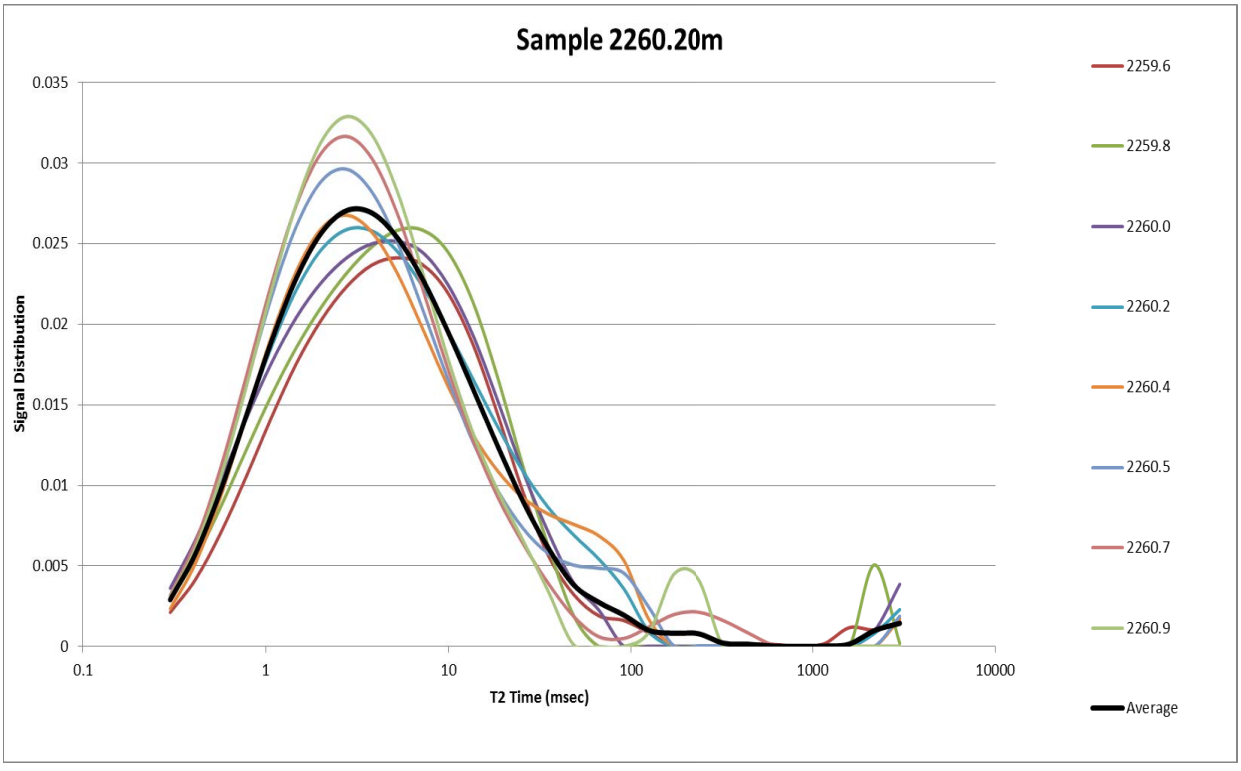

Figure E- 137: Thebe-2 NMR T_2 distributions over the 1.6 m interval used to produce the well synthetic MICP curve at 2260.2 m depth.

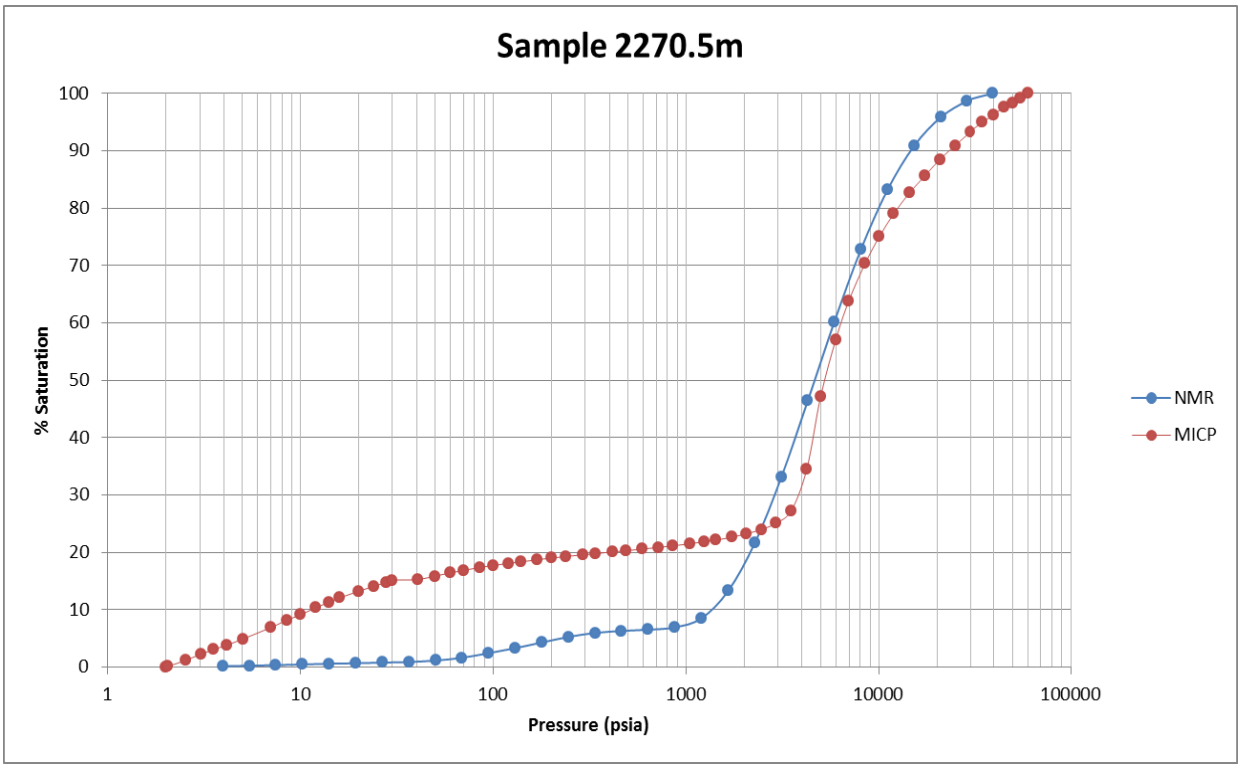

Figure E- 138: Thebe-2 MICP curve from the core sample (MICP) at 2270.5 m. Also shown is the well synthetic NMR (NMR) over the same depth interval.

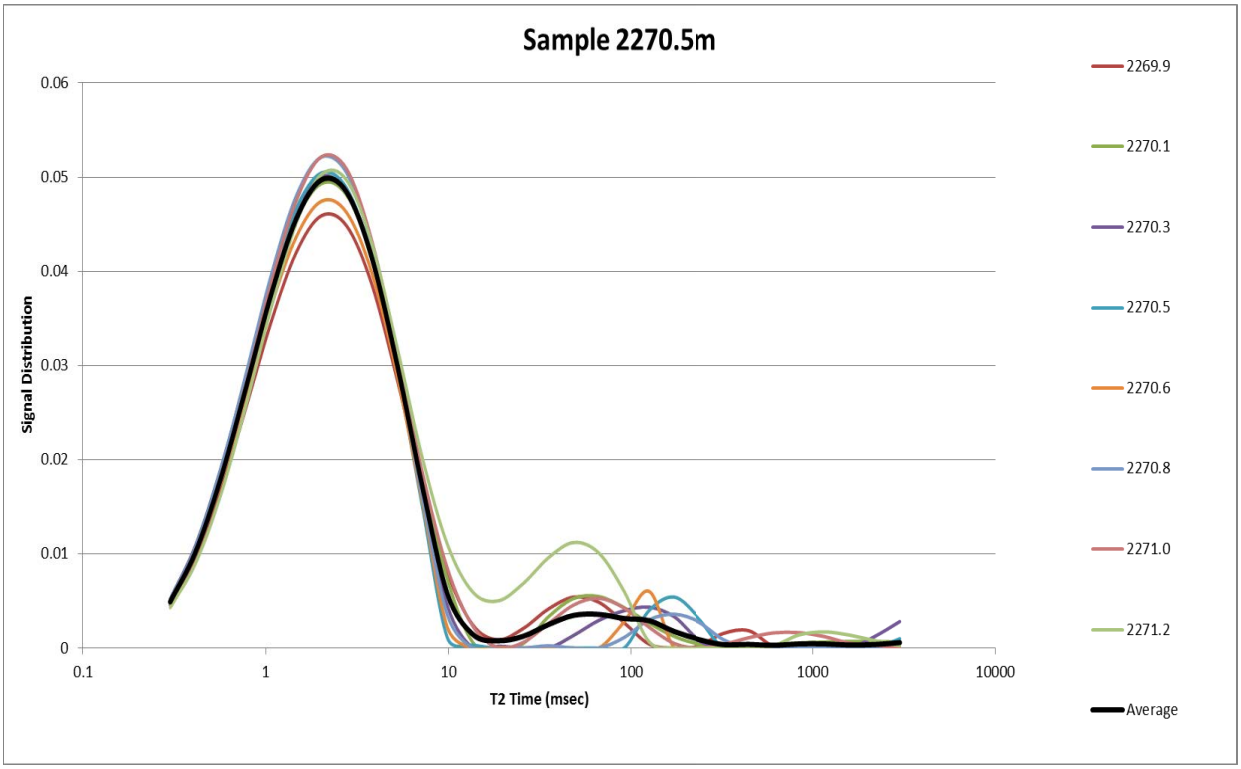

Figure E- 139: Thebe-2 NMR T_2 distributions over the 1.6 m interval used to produce the well synthetic MICP curve at 2270.5 m depth.

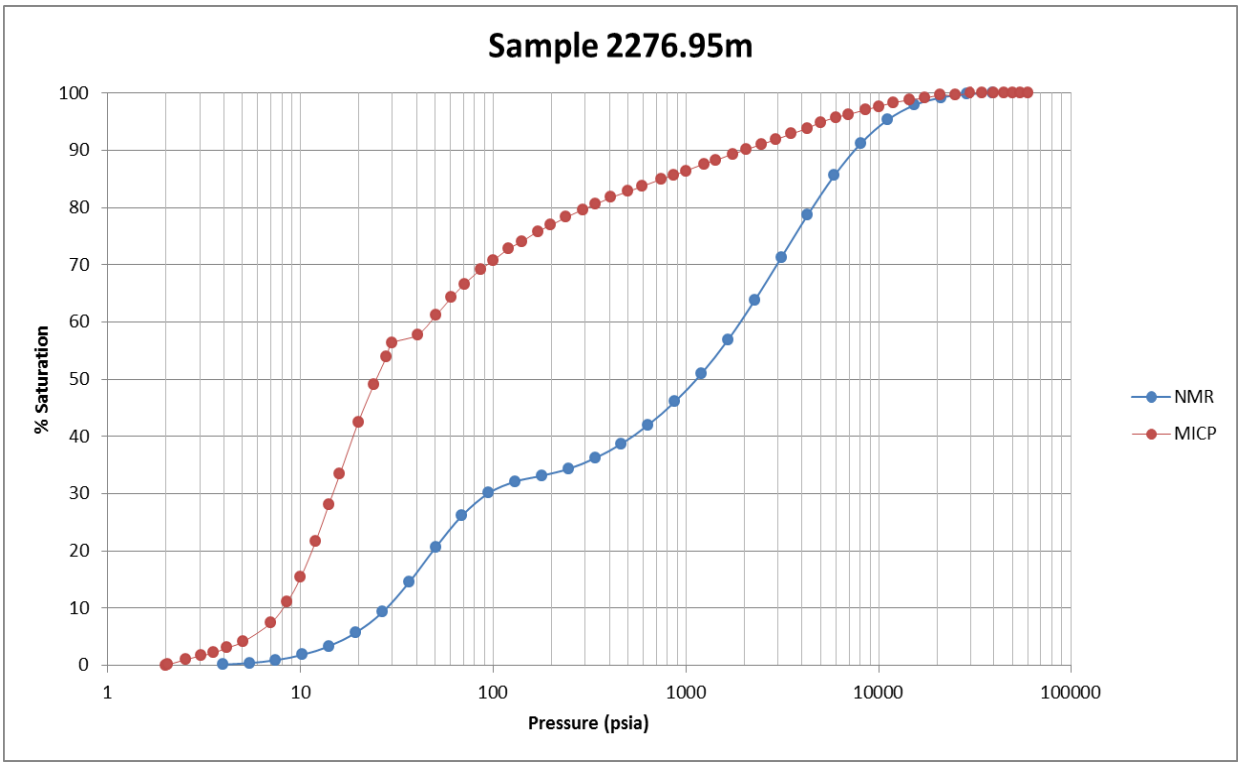

Figure E- 140: Thebe-2 MICP curve from the core sample (MICP) at 2276.95 m. Also shown is the well synthetic NMR (NMR) over the same depth interval.

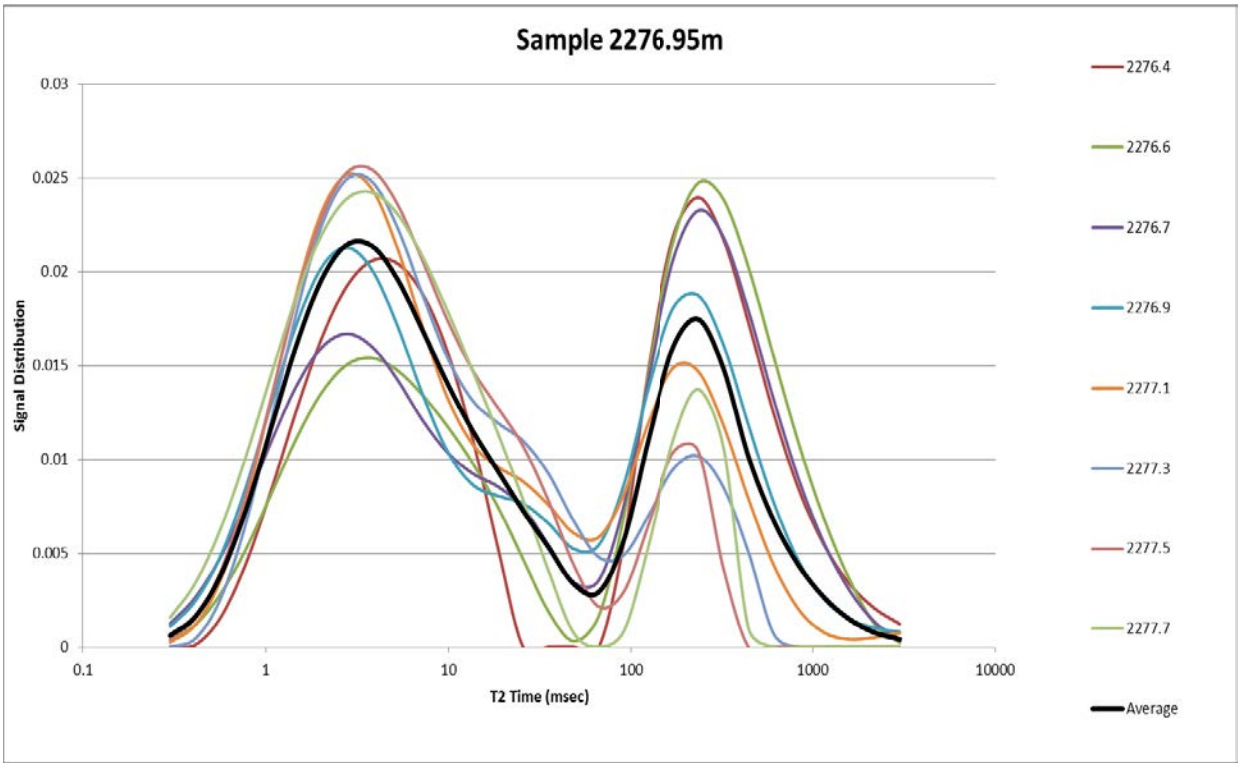

Figure E- 141: Thebe-2 NMR T_2 distributions over the 1.6 m interval used to produce the well synthetic MICP curve at 2276.95 m depth.

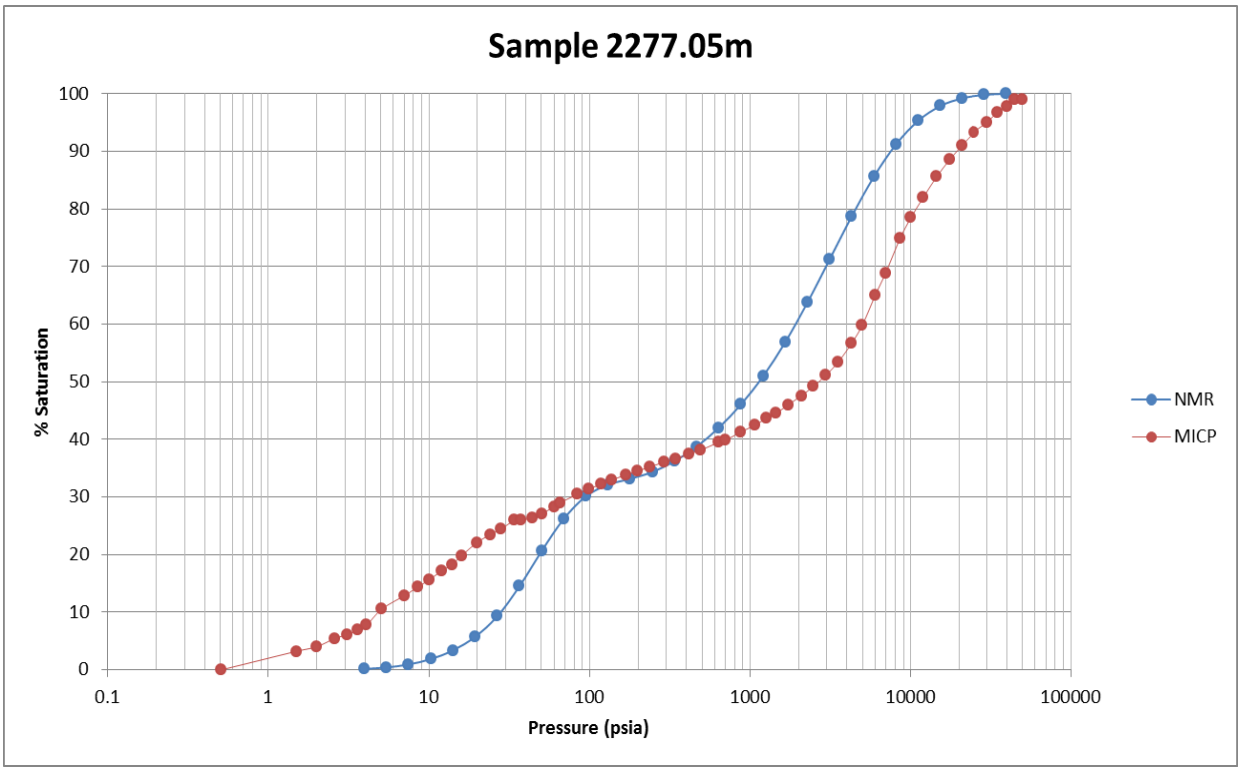

Figure E- 142: Thebe-2 MICP curve from the core sample (MICP) at 2277.05 m. Also shown is the well synthetic NMR (NMR) over the same depth interval.

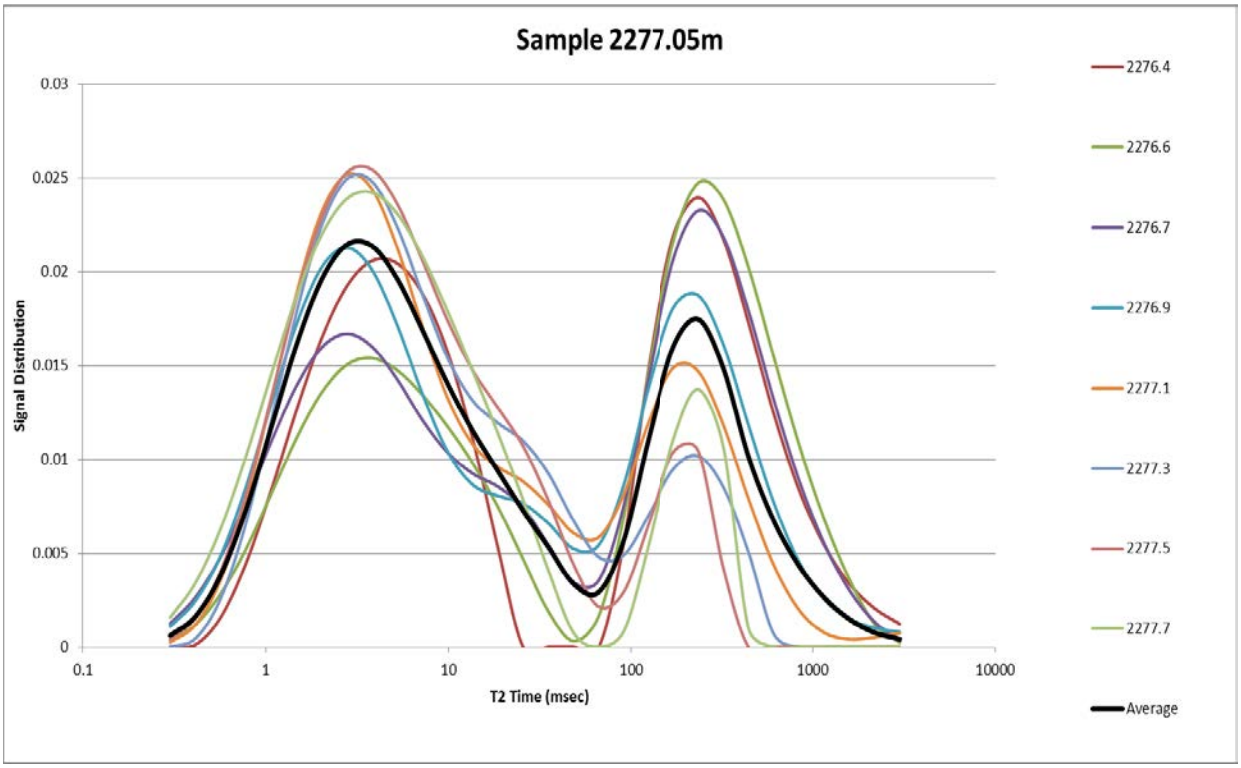

Figure E- 143: Thebe-2 NMR T_2 distributions over the 1.6 m interval used to produce the well synthetic MICP curve at 2277.05 m depth.

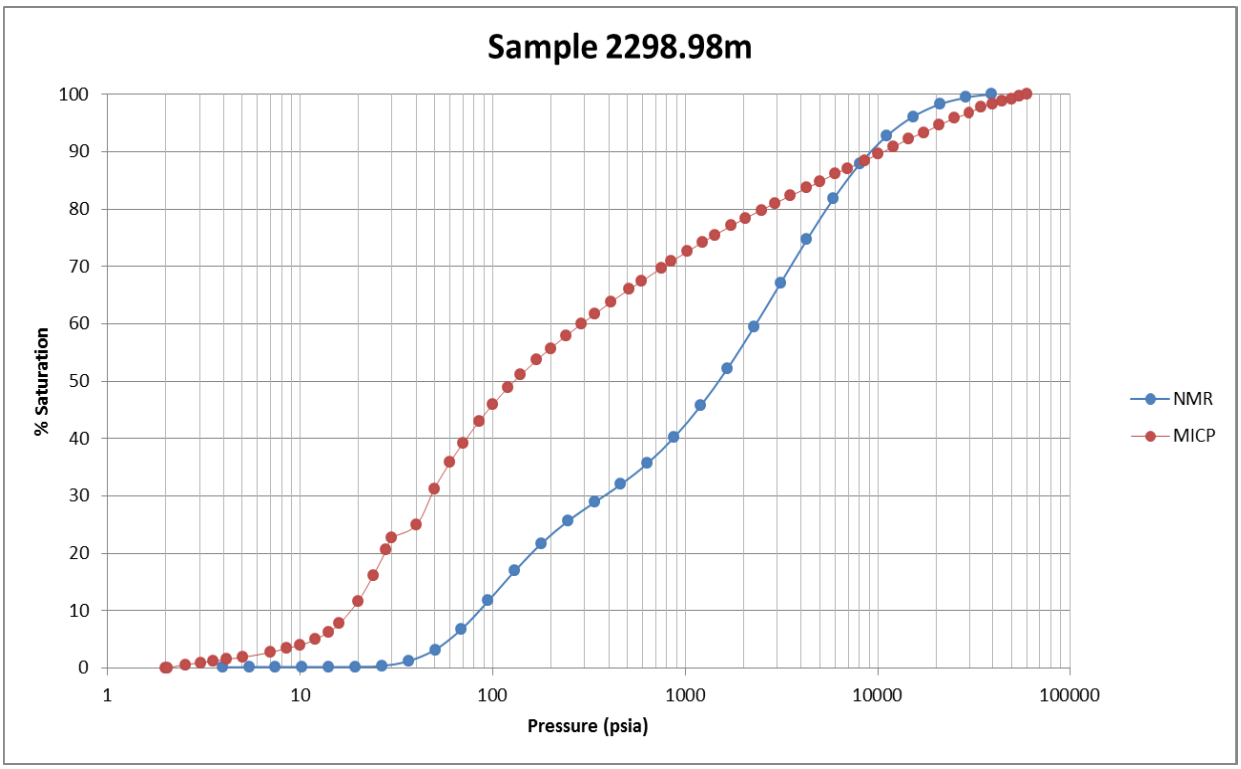

Figure E- 144: Thebe-2 MICP curve from the core sample (MICP) at 2298.28 m. Also shown is the well synthetic NMR (NMR) over the same depth interval.

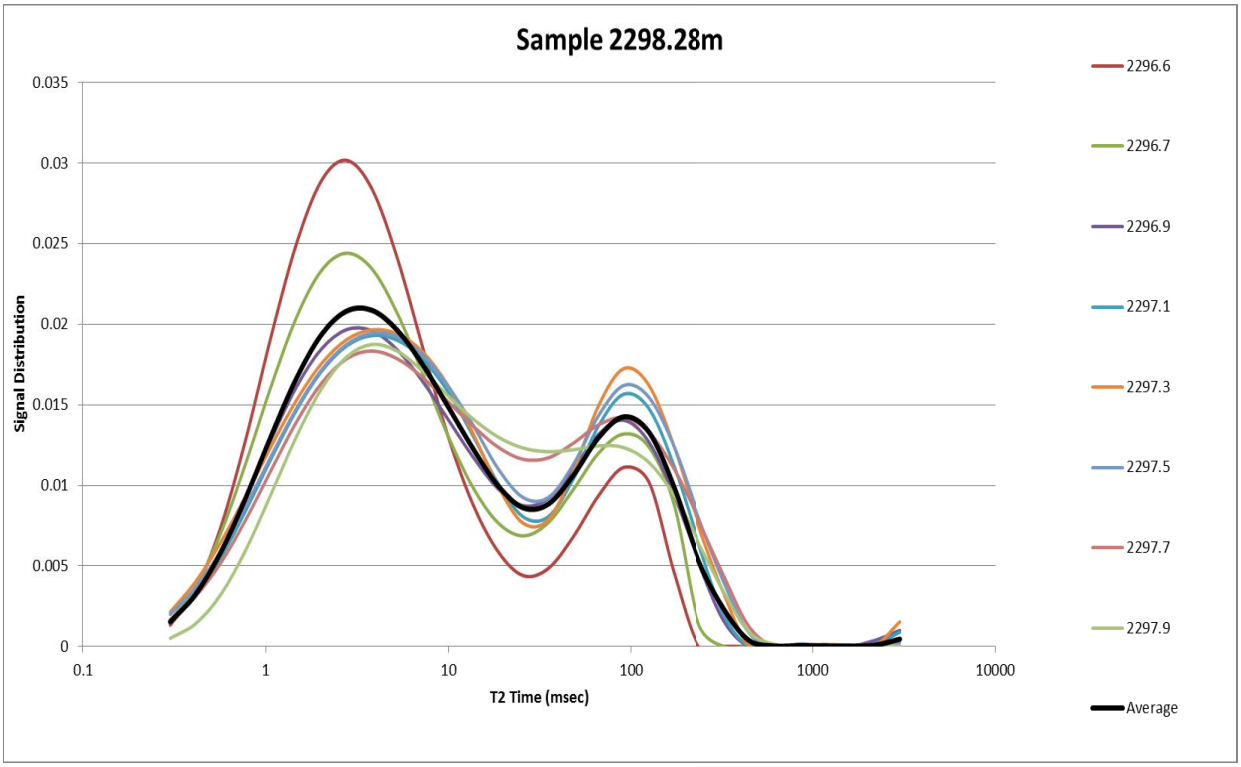

Figure E- 145: Thebe-2 NMR T_2 distributions over the 1.6 m interval used to produce the well synthetic MICP curve at 2298.28 m depth.

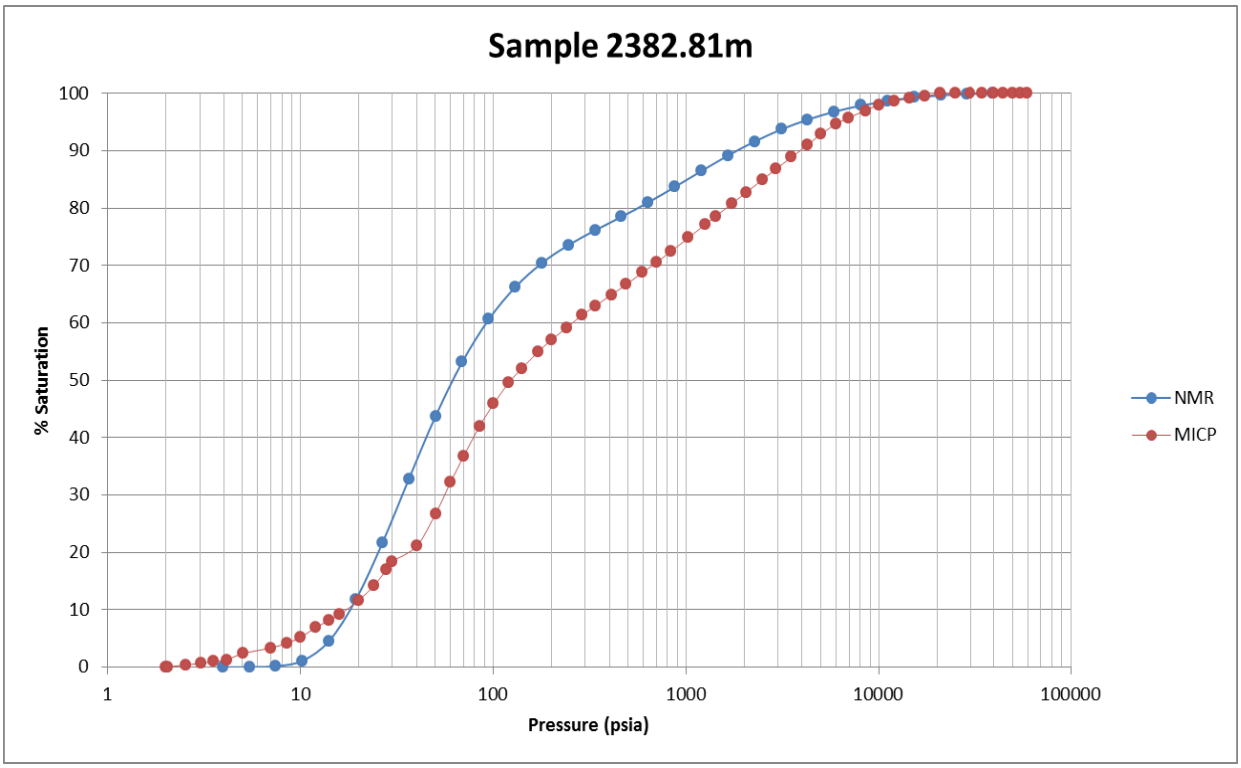

Figure E- 146: Thebe-2 MICP curve from the core sample (MICP) at 2382.81 m. Also shown is the well synthetic NMR (NMR) over the same depth interval.

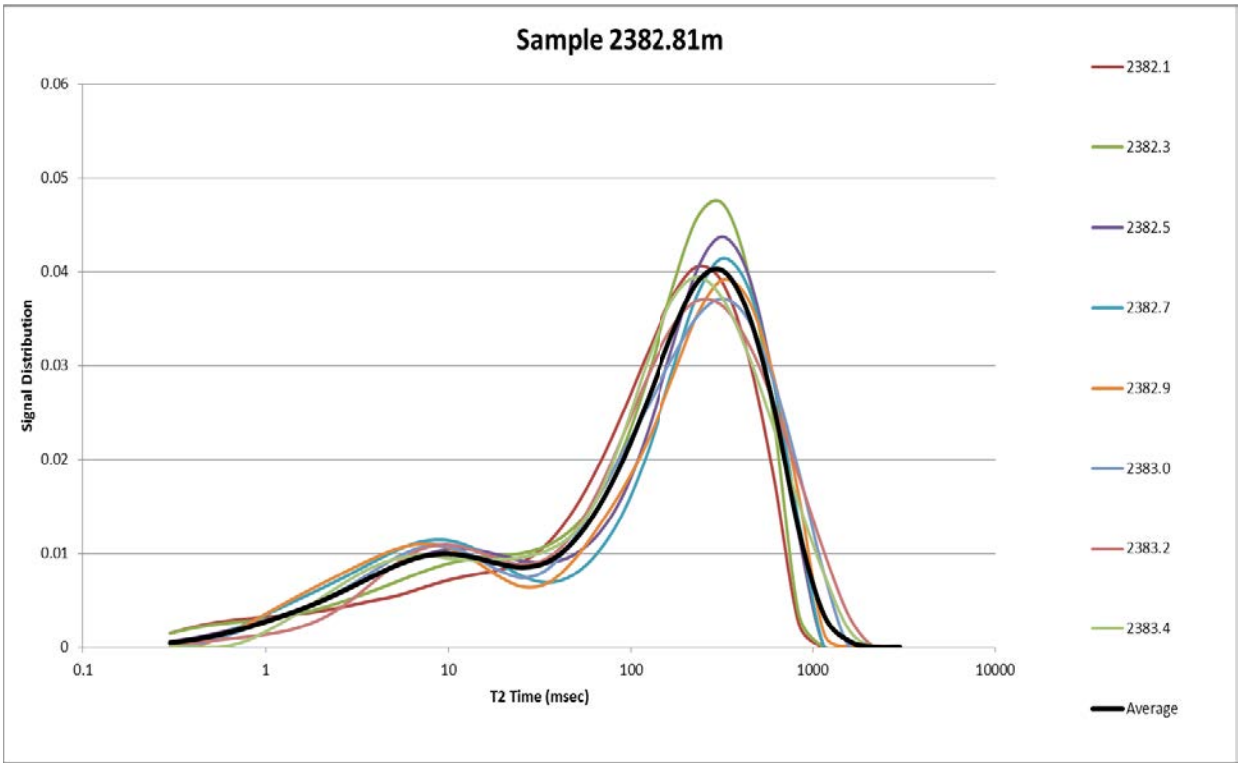

Figure E- 147: Thebe-2 NMR T_2 distributions over the 1.6 m interval used to produce the well synthetic MICP curve at 2382.81 m depth.

E.1 METHODOLOGY TO USE NMR SYNTHETIC MICP CURVES TO DETERMINE SEAL CAPACITY

The key learnings from Chapter 7 are:

- The laboratory based NMR tool is the most accurate device available to date and tool developers should strive to incorporate its components into the down-hole NMR logging tools.
- The Schlumberger CMR well log and possibly the Baker Hughes MREX well log have had some success in this study.
- The wellbore NMR log needs to be checked for accuracy – e.g. Gorgon CO2 Data Well-1.
- An accurate depth for samples is vital.
- The formation of interest needs to be identified and a rock sampling program needs to be devised for each formation in which synthetic MICP curves are produced. Each formation should have rock samples for calibration.
- Existing basin knowledge should be utilised to pick the most homogeneous interval for sampling for MICP analysis and calibration of synthetic MICP curves – the more rock samples taken and analysed with MICP the better the accuracy of the pore body to pore throat correction and thus the more accurate the synthetic MICP curves.
- The most accurate sample use to calibrate the synthetic MICP curves is conventional core with an accurate depth conversion, but it is the most expensive sample to obtain.
- Sidewall core (SWC) may provide numerous advantages (No depth correction required, relatively cheap and can sample numerous intervals) –The well logs and drill cuttings can be used to identify the most homogenous zones for sampling. SWC‘s can be taken in close proximity to one another (over the 1.6m interval used to generate the synthetic), averaged, and used to calibrate the synthetic MICP curve. Numerous intervals can be sampled relatively cheaply and without depth correction.
- The relationship between the pore throat and pore body differs between fine grained and coarse grained lithologies. Thus a correction factor needs to be selected for the formation of interest (seal, reservoir or baffle) but caution needs to be exercised when using the same correction factor for different lithologies.
- Different lithologies have different efficacies in relaxing hydrogen protons and thus no single correction factor suits all lithologies.

- Hydrocarbon or fluids with different hydrogen indices in the wellbore or used in the drilling fluids will affect the NMR measurements and derived synthetic MICP curves.
- In addition, there is a compromise between the signal to noise ratio and the scale of measurement. Thus if the signal to noise ratio is improved by averaging adjacent samples, then the scale on which the measurement is taken is increased.

The target reservoir and seal couplet for the storage and retention of CO_2 need to be identified before drilling commences. The thickness of the sealing formation will ultimately determine the rock sampling regime. Ideally, a minimum of 6 samples should be taken; 2 times 3 samples within 1.6 m that has been identified as fairly homogeneous. Correct sample depth is vital for the calibration of the synthetic MICP curves.

The MICP analysis of the three samples over the 1.6 m interval will provide an indication of the homogeneity of the sampling. Ideally, the three samples will have similar MICP curves and can be used to determine the pore body to pore throat calibration of the synthetic MICP curves by adding a multiplier to the predicted pressure and aligning the MICP curve. If the MICP analyses of the three samples show significant variation from one another then the three samples can be averaged and use to correct the synthetic MICP curve. This is less optimal and if the second group of three samples is more uniform then the correction factor established for these samples should be used.

The technique then needs to be checked to make sure that it is working correctly. The synthetic MICP curves should show a similar shape to the MICP curves from the rock samples. The synthetic MICP curves should be located in the same position as the conventional core MICP curves on the graph. Further, the pore body to pore throat correction should adequately correct for both sample intervals of the one formation. If the produced synthetic MICP curves do not meet each of these guidelines, then the technique should be abandoned. If the technique appears to be working adequately then all derived synthetic MICP curves should be accurate for that formation and less accurate with distance from the rock sample depth used to calibrate pore body to pore throats. The results from this study would suggest that the synthetic threshold pressures calculated from the maximum point of inflection method will be on average conservative in comparison to that interpreted from conventional core.

E.2 METHODOLOGY TO USE NMR SYNTHETIC MICP CURVES TO DETERMINE PERFORATION ZONES OF HYDROCARBON RESERVOIRS

The synthetic MICP curves can be used to determine perforation zones for hydrocarbon production.

The added difficulty of applying this technique to hydrocarbon reservoirs is threefold. Firstly, the NMR measurement is designed to measure hydrogen proton relaxation due to the contact with the pore surface. In water wet hydrocarbon reservoirs the hydrocarbon is immiscible with the water, therefore between the rock and the hydrocarbon is a film of water separating the two components. Thus the hydrocarbon in the pore is not in contact with the surface of the rock and is not relaxed by the pore surface. The relaxation method that dominates is bulk relaxation and not surface relaxation. Thus the NMR measurement of hydrocarbon reservoirs may be an incorrect estimate of pore body size as a result of the T_2 distribution shifting to longer relaxation times. However, depending on the hydrogen index of the fluid (Table E- 1) approximately 1 for oil and < 0.5 for Methane (USA Society of Petroleum Engineers, 2007) the T_2 distribution could indicate a lower porosity if the tool is calibrated to water. Additionally, the hydrogen in gas requires longer polarization times and thus in the normal logging environment will lead to an underestimate of porosity and shorter relaxation times than is the reality (Freedman et al., 1998).

Table E- 1: Hydrocarbon content of some common earth elements (USA Society of Petroleum Engineers, 2007).

TABLE 3D.4—HYDROGEN CONTENT OF SOME COMMON EARTH ELEMENTS		
Material	Hydrogen Density ($atm/cm^3 \times 10^{23}$)	Hydrogen Index
Water (60°F, 14.7 psi)	0.669	1.000
Water (200°F, 2,000 psi)	0.667	1.000
Brine (200 kppm NaCl)	0.614	0.920
Methane (60°F, 14.7 psi)	0.001	0.002
Methane (200°F, 2,000 psi)	0.329	0.490
n-octane (60°F, 14.7 psi)	0.667	1.000
n-octane (200°F, 2,000 psi)	0.639	0.960
Gypsum	0.325	0.490
Anthracite	0.268	0.400
Kaolinite	0.250	0.370
Chlorite	0.213	0.320
Illite	0.059	0.090

There are two proposed methodologies for determining capillary pressure curves over hydrocarbon reservoirs. The first methodology involves using the well log in its current form and using the hydrocarbon filled reservoirs and any rock samples and their MICP analysis taken from within these formations to calibrate the log over these intervals and selecting desirable intervals to perforate for the production of hydrocarbon. The second methodology as described by Freedman et al., (1998) and Freedman (1997) involves using the density log to correct the NMR log. This is referred to as the Density Magnetic Resonance (DMR) method and is detailed in both of the previous references. This methodology uses the density log to correct the NMR log over gas filled reservoirs.

The first methodology is designed to be applicable to a heterogeneous hydrocarbon reservoir containing gas and oil. The first task is to assess and constrain the hydrocarbon reservoir vertical limits/extent. This will require the identification of the caprock and thus the top of the hydrocarbon column to be determined, the gas oil contact if applicable and the oil water contact or bottom of the reservoir. The methodology will work on the assumption that the column height will be 100 percent hydrocarbon saturated.

The suggested tools to delineate the hydrocarbon reservoir limits/extent include:

- The density and neutron well log plotted together and identify the crossover and subsequently interpreting the gas column.
- The resistivity well log (high resistivity most in sandstone lithologies often corresponds to oil/gas).
- Any hydrocarbon shows on the core; sidewall core, conventional core or cuttings
- Spikes in the well pressure above the hydrostatic pressure

Once the hydrocarbon reservoir limits have been defined any rock samples from within that zone that can be accurately assigned a depth need to be identified. Rotary side wall core and conventional core will be adequate providing that the sample remains intact and that an accurate depth can be assigned to the sample. Drill cuttings are unlikely to be sufficient as an accurate depth cannot be assigned to the sample. However, drill cuttings may suffice where the interval is relatively homogeneous. Ideally, more than 2 samples of both reservoir rock and sealing rock from within both the gas and oil reservoir limits need to be analysed with MICP. These samples will need to be cleaned of their hydrocarbon before being analysed with MICP.

The MICP analysis will provide the calibration of the synthetic MICP curves for both the gas and oil reservoir. The calibrated synthetic MICP curves will only be accurate over oil and gas hydrocarbon reservoirs respectively – If there are hydrocarbon reservoirs elsewhere in the stratigraphy, then the appropriate gas or oil calibration should be adequate although ideally another sample should be taken and analysed with MICP. Note one calibration should be fine for oil and one for gas over the entire well, but as a precaution, it is suggested that another sample is analysed.

The MICP results should be plotted against the generated NMR synthetic MICP curves and the one calibration factor for that type of hydrocarbon should be applied. There should be a close relationship between the curves although as noted in the introduction there may be additional differences due to the different lithologies and pore body to pore throat ratio variations. If a relationship is successfully established then calibrated NMR synthetic MICP curves can be generated over the entire hydrocarbon column. A capillary pressure cut off can then be applied and the zones from which hydrocarbon can be produced on a commercial scale can then be identified and perforated. If this technique is successful, it will allow the identification of zones that should be preferentially perforated in heterogeneous conventional reservoirs that may have otherwise been missed.

The second methodology requires the NMR log to be corrected using the density log as detailed by Freedman et al., (1998) and Freedman (1997). Once this correction has been applied to the NMR log the generated synthetic MICP curves can be used in much the same way as the NMR log where no hydrocarbon was encountered i.e. gas reservoirs, brine-filled reservoir and seals can have synthetic MICP curves produced over the formations without the concern of gas affecting the results. As mentioned in the above methodology the closer the synthetic MICP curves are to the core samples used to calibrate the results the more confidence in the synthetic MICP curve.

To determine the perforation zones, it is suggested that the resistivity log in conjunction with the density neutron log be utilised to identify all hydrocarbon filled reservoirs penetrated by the well. Once the hydrocarbon filled reservoirs have been identified a synthetic MICP curve can be produced every 1.6 m over the hydrocarbon column. The synthetic MICP curves can be used to pick zones of low threshold pressure that are likely to readily produce hydrocarbons.